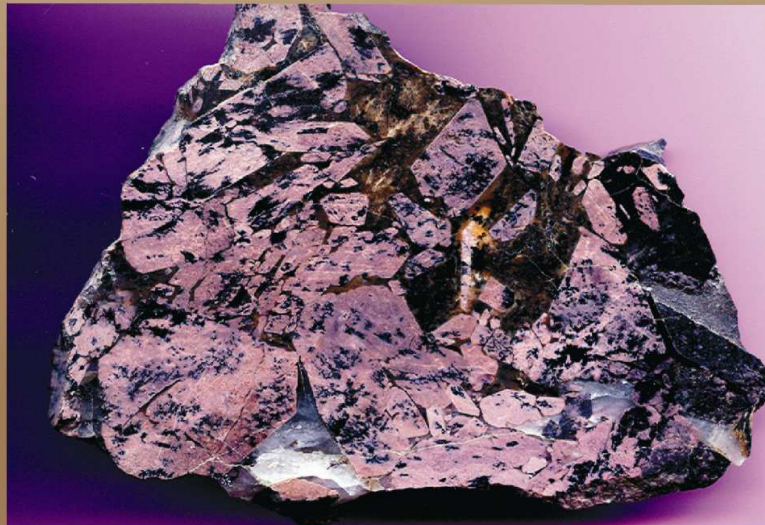




DEEP SEATED MAGMATISM, Its sources and plumes

Глубинный магматизм, его источники и плюмы



**IRKUTSK
2011**

**Russian Academy of Sciences
Vinogradov Institute of Geochemistry
Siberian Branch
Russian Foundation of Basic Research**



Deep-seated magmatism, its sources and plumes

(Глубинный магматизм, его источники и плюмы)

PROCEEDING
of XI International Workshop
«Deep-seated magmatism, its
sources and plumes »

Edited by Dr. N.V. Vladykin

IRKUTSK

2011

UDK 552.33+ 552.33

Deep-seated magmatism, its sources and plumes

Proceedings of the XI International Conference. Publishing House of the Institute of Geography SB RAS, 2011, 244 p., ISBN 978-5-94797-154-5. Vol.3

The annual publication of the materials of the 11th International seminar is dedicated to the memory of outstanding petrologist and geochemist, prominent specialist in rare-metal magmatism of the Central Asia academician of RAS Vjacheslav Ivanovich Kovalenko.

New data on the composition of the alkaline complexes of the South Goby and detailed geochemical data on the comendite complex of Khan-Bogdo are given in the book. By composition of melt inclusions the compositions of magmas from diverse geodynamic settings were calculated, silicate-carbonate immiscibility in alkaline lavas of Vulture volcano (Italy) was found. Geochemical features of the North Fenoscandian volcanism is discussed. New data on the age of Guli intrusion in North Priabarje and Vishnevogorskij complex of the Urals are reported. The interesting data on PT-conditions of mantle in Colorado and behavior of chlorine in kimberlites of the pipe Udachnaja in Yakutia are discussed.

The book is of great importance for petrologists, geochemists, and specialists studying deep alkaline and kimberlite magmatism, students and teaching staff of Universities.

*Published following the decision of the Scientific Council
of Vinogradov Institute of Geochemistry SB RAS*

Editor: Prof. N.V. Vladykin

Reviewers: Prof. V.S. Antipin

Original-model: M.D.Sedunova

Institute of Geography SB RAS
664033, Irkutsk, Ulanbatorskaja str. 1

Published in Glazkovskaya printing House

Irkutsk, Gogol str., 53.

Order № 2256. Edition 100 copies.

ISBN 978-5-94797-154-5

© Institute of Geochemistry SB RAS, 2011

© Irkutsk Geography SB RAS, 2011

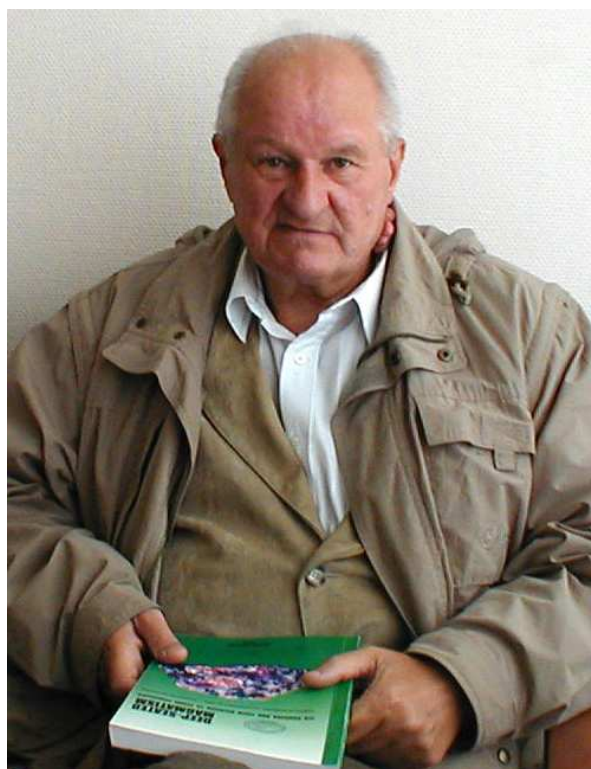
On the cover there is the photo of new mineral – kovalenkoite

(Ca, Ba, Sr), Nb₂ [SiO₄] · O₄ 5H₂O

CONTENTS

Foreword	4
1. Kovalenko V.I., Kozlovsky A.M., Yarmolyuk V.V. Comendite-Bearing Subduction-Related Volcanic Associations in the Khan-Bogd Area, Southern Mongolia: Geochemical Data.	5
2. Ryabchikov I.D. Redox potential of diamond formation in the Earth's lower mantle.	39
3. Vladykin N.V. Petrology and composition of rare-metal alkaline complexes of the South Gobi, Mongolia.	46
4. Kogarko L.N., Zartman R.E. A Pb isotope investigation of the Guli massif, Maymecha-Kotuy alkaline-ultramafic complex, Siberian flood basalt province, Polar Siberia.	76
5. Arzamastsev A.A., Petrovsky M.N. Paleozoic Alkaline Volcanism of the Northeastern Fennoscandia: Geochemical Features and Petrologic Consequences.	96
6. Anfilogov V.N., Khachai. Yu.V. A Possible Scenario of Material Differentiation at the Initial Stage of the Earth's Formation.	126
7. Kamenetsky V.S., Maas R., Kamenetsky M.B., Paton C., Phillips D., Golovin A.V. Chlorine from the mantle: magmatic halides in the Udachnaya-East kimberlite, Siberia.	132
8. Solovova I.P., Girnis A.V., Kogarko L.N., Kononkova N.N. Compositions of magmas and carbonate-silicate liquid immiscibility in the Vulture alkaline igneous complex, Italy.	150
9. Naumov V.B., Kovalenko V.I., Dorofeeva V.A., Girnis A.V., Yarmolyuk V.V. Average Compositions of Igneous Melts from Main Geodynamic Settings According to the Investigation of Melt Inclusions in Minerals and Quenched Glasses of Rocks.	171
10. Nedosekova I.L., Belousova E.A., Sharygin V.V. Sources for the Il'menoVishnevogorsky Alkaline Complex: Evidence from Lu–Hf Isotopic Data for Zircons.	205
11. Ashchepkov I.V., Downes H., Vladykin N.V., Mitchell R., Nigmatulina E., Palessky S.V. Reconstruction of mantle sequences beneath the Wyoming craton using xenocrysts from Sloan and Kelsey Lake - 1 kimberlite pipes, northern Colorado.	213
12. Krasnova N., Petrov T., Korolev N. The RHA coding of mineral compositions of alkaline rocks exemplified by the nepheline syenite family.	234

FOREWORD



The annual publication of the materials of the 11th International seminar is dedicated to the memory of outstanding petrologist and geochemist, prominent specialist in rare-metal magmatism of the Central Asia academician of RAS Vjacheslav Ivanovich Kovalenko. From 1960 to 1977 his scientific activity was related to the Institute of Geochemistry SB RAS Irkutsk. The objects of his study were alkaline and granite complexes of Tuva and Sajany, and from 1967 – those of Mongolia. Together with the collaborators of the laboratory guided by him they found the South-goby belt of the alkaline rocks with the deposit of Zr,Nb,TR in Khan-Bogdo massif, the South-goby carbonatite province with the rare earth' and apatite deposit, the Lulingol massif of pseudoleucite syenite with rare earth carbonatite deposit. For the first time he subdivided five geochemical types of granites and based the magmatic origin of the alkaline-granite and Li-F type of rare metal granites, found ongonites – volcanic analogues of Li-F granites. From 1977 to 2010 V.I. Kovalenko worked at the IGEM RAS Moscow. Last years he dealt with the problems of global magmatism of the Central Asia and deep-seated geodynamics.

New data on the composition of the alkaline complexes of the South Goby and detailed geochemical data on the comendite complex of Khan-Bogdo are given in the book. By composition of melt inclusions the compositions of magmas from diverse geodynamic settings were calculated, silicate-carbonate immiscibility in alkaline lavas of Vulture volcano (Italy) was found. Geochemical features of the North Fenoscandian volcanism is discussed. New data on the age of Guli intrusion in North Prianabarje and Vishnevogorskij complex of the Urals are reported. The interesting data on PT-conditions of mantle in Colorado and behavior of chlorine in kimberlites of the pipe Udachnaja in Yakutia are discussed.

The book might present interest to specialists involved in petrological and geochemical investigations as well as those studying deep alkaline and kimberlite magmatism.

Chairman of Organizing Committee,
Chief Editor

Dr. N.V. Vladykin

COMENDITE-BEARING SUBDUCTION-RELATED VOLCANIC ASSOCIATIONS IN THE KHAN-BOGD AREA, SOUTHERN MONGOLIA: GEOCHEMICAL DATA

V. I. Kovalenko, A. M. Kozlovsky, and V. V. Yarmolyuk

Institute of the Geology of Ore Deposits, Petrography, Mineralogy, and Geochemistry (IGEM), Russian Academy of Sciences, Staromonetnyi per. 35, Moscow, 109017 Russia e-mail:

ABSTRACT

The vertical section of volcanic rocks in the Khan-Bogd Late Paleozoic depression, southern Mongolia, in the belt of southern Mongolian Hercynides contains comendites. The basement of the depression is made up of Devonian ophiolites (older than 362 Ma) overlain by volcanic associations of an active continental margin (ACM) (dated at 330 Ma) and a bimodal association (dated at approximately 290 Ma), which is subdivided into a lower unit (BLU), dacites of the intermediate layer (IL), and a bimodal association of the upper unit (BUU). The volcanic associations of the Devonian and ACM are calc-alkaline and poor in TiO₂. The BLU rocks have higher alkalinity and TiO₂ concentrations and show a transition from the tholeiitic to calc-alkaline series in the 4-Deep-seated magmatism, its sources and plumes and course of differentiation with the origin of comendites and trachyrhyolites, including those with adakite characteristics. The IL dacites are analogues of calc-alkaline magmas of the ACM type. The BUU volcanic association is composed of tholeiite basalts with moderate Ti concentrations (of the MORB type), comendites, and trachyrhyolites, with a compositional gap at rocks of intermediate composition. The variations in the canonical ratios of incompatible trace elements and petrochemical parameters of the Khan-Bogd volcanic rocks show that their parental magmas were derived mostly from a source of basalts of the arc type (IAB) with the addition of variable proportions of a source of the MORB type. The greatest role of the latter is identified in the magmas of the bimodal association. BLU and BUU are separated by IL, a fact testifying that the bimodal volcanism occurred simultaneously with normal dacite continental-marginal volcanism. Although the geodynamic environments in which volcanic rocks were formed somewhat varied during the development of the Khan-Bogd depression, a subduction environment remained predominant, and the volcanic rocks were derived from an IAB-type source. The subduction volcanic associations produced thereby are differentiated and vary in composition from basites to dacite and rhyolite, which could be formed at the assimilation of continental crustal material

(CC). Conceivably, the bimodal volcanic association was generated when the subduction zone was approached by a

mid-oceanic ridge, whose material could be added in appreciable amounts to the subduction sources. The volcanic evolution of the Khan-Bogd depression shows an evolution of geodynamic environments and the composition of the volcanic rocks generally resembling those in the western margin of North America in the Cenozoic. The acid BLU and BUU rocks were most probably generated by different mechanisms. The BLU comendites and trachyrhyolites were likely formed by the crystallization differentiation of an arc basite magma of elevated alkalinity. The acid BUU rocks resulted from the anatexis of basites of this association, particularly spilitized ones (as well as any other basites) and the subsequent crystallization differentiation of the anatexic magmas.

INTRODUCTION

The Khan-Bogd alkali-granite massif in southern Mongolia has a unique size and mineralogy. Its southern and northern outer-contact zones contain volcanic associations with typical comendites and their plutonic analogues (alkali granites). Geological, geochronologic, and some geochemical data on the territory were published in our earlier papers (Durante et al., 1976; Kovalenko et al., 2006, 1973; Vladykin et al., 1981; Yarmolyuk and Kovalenko, 1991; *Types...*, 2006). The multielement rare-metal mineralization discovered at the massif (Kovalenko et al., 1971; Kovalenko, 1977; Vladykin et al., 1981) and the general geochemical specifics of the magmatic rocks make this massif notably different from rare-metal alkali granitoids derived from mantle–plume sources (Kovalenko et al., 2007). The specifics characterize the alkali granitoids of the Khan-Bogd Massif and the bimodal association in surrounding structures rather as a bimodal association but not as a plume association, which is more typical of such rocks. We are aware only of two published descriptions of such rare associations of alkali agpaite rocks: one in Mayor Island in the vicinity of the New Zealand island arc (Ewart et al., 1968; Houghton et al., 1992; Liu et al., 2006; Dundar and Kyle, 1992) and the other in the Mexican Volcanic Belt (Nelson et al., 1990). In light of these data, it seemed to be important to examine the vertical section of volcanic rocks in the area of the Khan-Bogd alkali granite massif to elucidate the reasons for the origin of the acid agpaite rocks. This paper is focused on the solution of this problem. The geological setting of the magmatic rocks and the southern Mongolian Hercynides (which host the massif) as a whole were discussed in much detail in our earlier publications [16.30]

GEOLOGY AND PETROCHEMISTRY OF THE AREA OF THE KHAN-BOGD ALKALI-GRANITE MASSIF

The study area known for the Khan-Bogd massif of alkali granitoids, one of the world's largest massifs of the type (>1500 km²) (Fig. 1), is located in the southern Gobi desert, Mongolia (Kovalenko et al., 2006, 2007). The massif was formed in a Late Paleozoic (Hercynian) active continental margin of the Siberian paleocontinent (Yarmolyuk et al., 1983, 2008; Yarmolyuk and Kovalenko, 1991). Our studies were centered on the Devonian arc rock associations, Carboniferous units of predominantly andesite lavas (of varies alkalinity), which are grouped into a differentiated complex of a continental-marginal magmatic belt (ACM), and rocks that we previously classed with a bimodal basalt–comendite–alkali granite association (this association was supposedly formed in the Late Carboniferous or at the Carboniferous–Permian boundary).

The aforementioned Middle and Late Paleozoic sedimentary–volcanic sequences surrounding the Khan-Bogd Massif in the south, east, and north and exposed in the outer-contact zones of the massif and its more distant peripheral part (Fig. 1) compose the Late Paleozoic Khan-Bogd depression (Durantebet et al., 1976; Yarmolyuk et al., 1983; Kovalenko et al., 2006; Khashgerel et al., 2006; our unpublished data).

The oldest (pre-Carboniferous) rocks of the area (in the basement of the Khan-Bogd depression) are greenstone siliceous and terrigenous–volcanic sequences 1500 m thick,

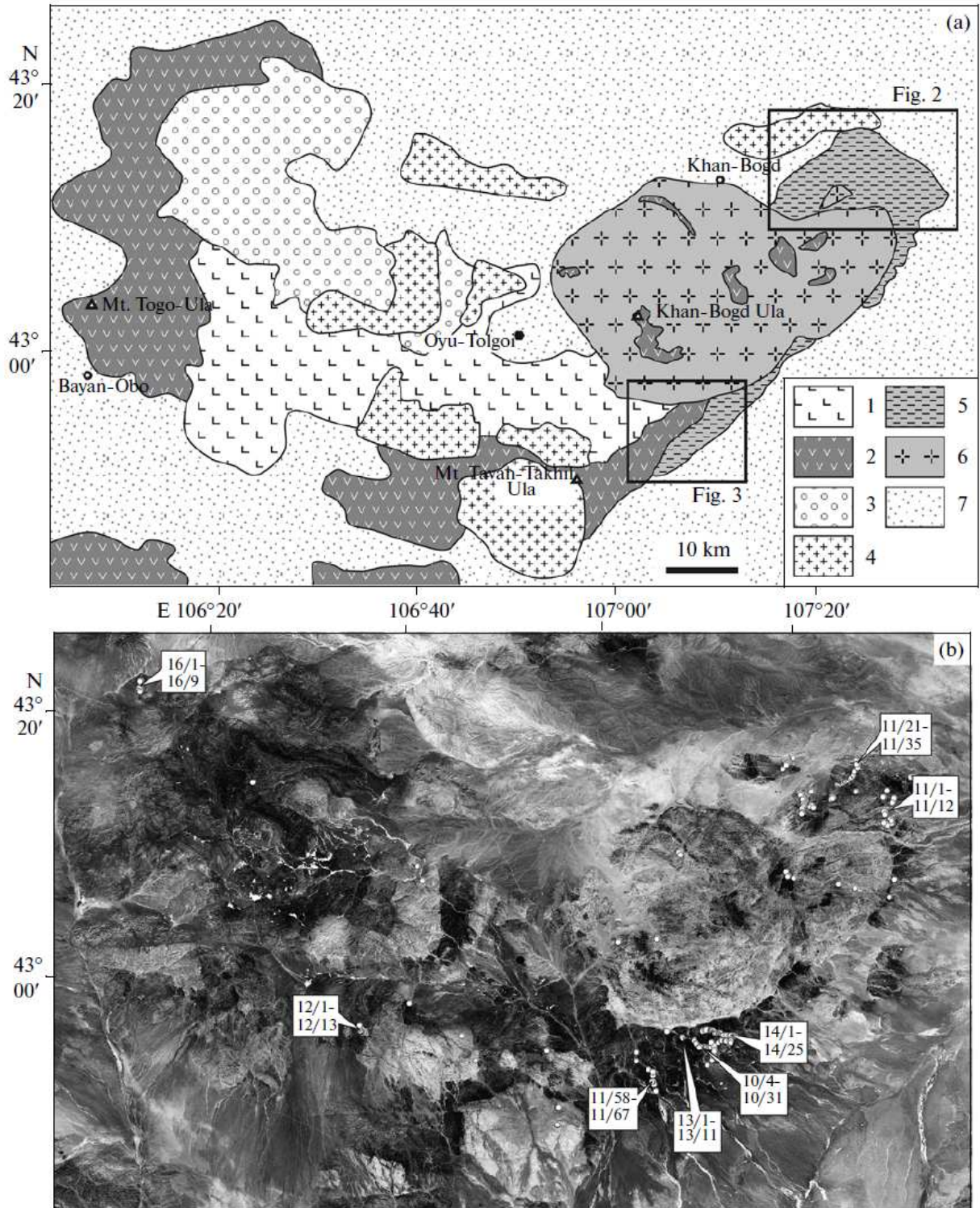


Fig. 1. (a) Schematic geological map and (b) Landsat-7 image of structures surrounding the Khan-Bogd alkali-granite massif. (1) Devonian arc volcanic rocks; (2) Carboniferous volcanic complexes of an active continental margin; (3) Carboniferous terrigenous rocks; (4) Paleozoic granitoids of normal alkalinity; (5) Permian rocks of a bimodal volcanic association; (6) Permian alkali granitoids; (7) loose Middle Mesozoic-Cenozoic deposits. Fig. 1b shows sampling sites and their numbers at reference sections of the volcanic sequence.

which are exposed along the southwestern boundary of the Khan-Bogd Massif (exposures in the area of Gashun-Sukhoi-Khuduk well and in the area of the Oyu-Tolgoi Cu-Au porphyry deposit). The lower unit of the complex of the depression basement consists (Durante et al., 1976) of basic volcanics, which are transformed into greenstones and intruded by numerous bodies of hornblende gabbro, and siliceous and clayey–siliceous shales and jaspers. The upper unit of this complex is made up of siliceous–clay shales, polymictic sandstones, and conglomerates. The age of this complex was determined in (Durante et al., 1976) as pre-Carboniferous (supposedly Ordovician), and this complex was ascribed to Hercynian ophiolites (eugeosyncline rocks, according to Durante et al., 1976) based on its formation composition. The age of the basement of the Khan-Bogd depression was later specified in the course of exploration of the Oyu-Tolgoi Cu–Au porphyry deposit west of the southwestern margin of the massif (Fig. 1). Similar to the southwestern outer-contact zone of the massif, the younger magmatic rocks in this area are the aforementioned arc associations of the folded basement dated at 362 Ma (Khashgerel et al., 2006). As elsewhere in the southern Mongolian Hercynides, these rocks are Devonian. Most of our samples of volcanic rocks from the Devonian basement of the Khan-Bogd depression are andesite with rare beds of basalt and rhyolite, which were sampled southwest of the Oyu-Tolgoi deposit (Fig. 1; table, samples 12/1–12/13) and in the westernmost part of the volcanic sequence adjacent to the Khan-Bogd Massif (Fig. 1; table, samples 13/1–13/3 and 13/8).

The Late Paleozoic stratified sequences of the Khan-Bogd depression itself are thought to be ACM sequences of Carboniferous and Permian age (348–290

Ma; ovalenko et al., 2006; Khashgerel et al., 2006) surrounding the massif and filling sags in its roof, which unconformably overlay rocks of the ophiolite complex in the basement of the depression.

The oldest Late Paleozoic sequence of the depression is the sedimentary succession consisting of sandstone, siltstone, and conglomerate with Tournaisian–Visean faunal fossils and the Carboniferous tuff–sedimentary succession with Middle Carboniferous floral fossils. The overlying units are dominated by volcanic rocks, which are grouped into an andesite (differentiated) and bimodal (basalt–andesite–trachyrhyolite–comendite) associations (Yarmolyuk, 1983)

The *andesite (differentiated) association* is further subdivided into a lower sedimentary–volcanic (500–600 m thick) and upper (up to 2500 m thick) units. The stratigraphic section of the sedimentary–volcanic unit begins with a series of brown andesite lava flows, which give way upsection to conglomerates with pebbles of andesite porphyries and, more rarely, granites and granodiorites and, farther upward, to cyclically alternating tuff-sandstones, tuff-siltstones, and tuffites with floral remnants of the Middle–Late Carboniferous (Durante et al., 1976). The upper part of the vertical section contains subordinate volumes of andesite flows.

The lava pile is made up mostly of andesite, basaltic andesite, dacite, and rhyolite flows (Fig. 2, table). The geology of the sequence was described in detail

Component	13/3	13/8	16/3	16/5	10/1	10/2	13/5	13/7	10/4	10/5
	Dev	Dev	ACM	ACM	ACM	ACM	ACM	ACM	BLU	BLU
SiO ₂	55.61	56.85	47.62	53.54	57.29	61.83	66.81	71.92	51.80	57.59
TiO ₂	1.08	0.99	0.56	0.95	0.97	0.78	0.75	0.25	1.69	1.21
Al ₂ O ₃	18.47	16.66	23.58	17.52	17.11	16.53	15.45	14.47	17.50	16.95
FeO	7.79	6.84	6.62	8.57	6.79	4.99	3.95	1.76	8.55	6.35
MnO	0.14	0.10	0.10	0.16	0.14	0.11	0.08	0.04	0.10	0.12
MgO	3.17	4.34	4.24	4.72	2.94	1.95	1.10	0.29	3.36	2.61
CaO	7.08	6.46	13.41	9.57	6.17	4.10	2.80	0.73	7.53	5.95
Na ₂ O	3.02	3.51	2.20	2.87	3.72	4.08	3.97	5.06	4.28	3.35
K ₂ O	0.81	2.47	0.25	0.39	2.55	3.31	2.29	4.15	2.14	2.87
P ₂ O ₅	0.33	0.30	0.11	0.20	0.27	0.22	0.20	0.05	0.84	0.44
L.O.I.	1.60	0.65	0.72	0.56	1.34	1.50	1.89	1.00	1.13	1.74
Total	99.09	99.16	99.40	99.06	99.28	99.39	99.29	99.73	98.90	99.18
Be	2.11	1.48	0.303	0.639	1.31	1.79	1.75	3.01	1.70	1.53
Sc	15.2	5.65	0.376	23.5	14.2	13.9	4.10	0.938	14.0	11.9
V	183	163	167	244	165	98.6	91.8	17.9	210	143
Co	25.8	22.9	22.1	25.3	15.5	11.5	7.31	29.1	22.6	13.8
Ga	21.6	17.8	15.2	17.6	15.1	18.2	15.8	15.7	17.4	15.7
Rb	21.1	61.4	2.36	6.13	35.7	74.6	56.7	93.4	20.1	34.1
Sr	615	550	634	462	448	506	599	511	1021	962
Y	19.7	16.6	7.56	19.4	16.5	21.8	34.6	20.0	16.2	16.1
Zr	200	172	23.3	64.8	86.1	200	212	467	94.1	108
Nb	9.96	7.92	0.629	1.70	5.68	10.0	8.71	11.9	8.94	7.08
Cs	1.33	2.09	0.180	0.482	0.523	0.727	1.62	2.41	0.434	0.407
Ba	335	567	130	236	459	742	810	678	582	740
La	22.1	19.5	5.71	5.07	13.4	21.9	45.4	35.2	22.9	18.1
Ce	48.7	42.9	12.4	13.0	29.6	50.3	52.1	65.9	52.4	40.2
Pr	6.08	5.27	1.65	2.01	3.67	5.80	9.31	8.12	6.73	5.22
Nd	24.7	21.9	7.48	10.2	15.6	24.6	37.2	29.2	27.5	20.7
Sm	5.23	4.64	1.69	2.88	3.50	4.71	6.94	5.35	5.51	4.22
Eu	1.49	1.41	0.651	0.936	0.991	1.34	1.26	0.837	1.54	1.24
Gd	4.59	4.05	1.64	3.32	3.24	4.47	6.37	4.16	4.27	3.57
Tb	0.693	0.602	0.256	0.566	0.533	0.686	0.923	0.623	0.617	0.576
Dy	3.93	3.41	1.58	3.75	2.87	3.80	5.41	3.83	3.13	2.80
Ho	0.768	0.693	0.328	0.791	0.595	0.856	1.17	0.777	0.626	0.607
Er	2.13	1.90	0.891	2.28	1.58	2.29	3.26	2.25	1.52	1.54
Tm	0.318	0.280	0.131	0.340	0.260	0.337	0.474	0.369	0.193	0.255
Yb	1.90	1.70	0.787	2.200	1.64	2.11	2.87	2.43	1.34	1.53
Lu	0.277	0.248	0.119	0.350	0.235	0.340	0.433	0.379	0.206	0.233
Hf	5.16	4.45	0.715	1.90	3.17	4.33	5.51	11.1	3.12	3.63
Ta	0.584	0.472	0.020	0.020	0.361	0.715	0.606	0.900	0.409	0.444
Pb	6.82	6.12	2.30	2.34	8.13	9.22	4.92	7.69	7.04	8.05
Th	6.32	5.25	0.659	0.180	2.86	6.33	7.85	9.27	1.82	3.35
U	1.95	1.58	0.214	0.183	1.08	1.81	2.61	2.48	0.558	1.14

Table. (Contd.)

Component	10/6	14/1	14/5	14/8	10/14	14/11	10/15a	10/15b	10/17	10/19
	BLU	BLU	BLU	BLU	BLU	BLU	IL	IL	BUU	BUU
SiO ₂	53.64	50.36	52.87	58.74	69.37	68.61	63.40	61.56	48.53	51.13
TiO ₂	1.49	1.62	1.54	1.50	0.59	0.57	0.56	0.62	1.37	1.26
Al ₂ O ₃	17.01	17.14	17.27	16.98	16.25	16.16	16.25	16.89	16.58	16.45
FeO	8.34	8.73	7.72	6.11	1.97	1.57	4.54	5.14	8.51	8.14
MnO	0.12	0.13	0.14	0.09	0.02	0.02	0.06	0.06	0.15	0.13
MgO	2.48	4.83	3.78	1.33	0.06	0.22	1.86	1.71	2.93	2.72
CaO	6.08	7.92	6.67	2.71	0.32	0.33	4.51	4.39	10.29	9.66
Na ₂ O	3.71	3.98	3.81	4.74	7.31	5.51	3.60	4.17	3.01	2.96
K ₂ O	3.49	2.02	2.70	4.59	2.89	5.69	2.48	2.17	0.78	0.54
P ₂ O ₅	1.11	0.64	0.74	0.53	0.08	0.09	0.17	0.24	0.39	0.41
L.O.I.	1.57	1.49	1.67	1.71	0.78	0.92	2.05	2.43	6.59	5.73
Total	99.03	98.86	98.90	99.02	99.64	99.68	99.46	99.38	99.14	99.12
Be	1.99	1.54	2.28	3.35	1.65	2.41	1.34	1.38	1.01	1.06
Sc	9.81	7.46	4.38	0.396	4.83	0.556	6.15	6.72	17.0	14.1
V	128	229	186	91.3	25.9	25.9	105	112	162	151
Co	13.2	26.9	24.8	6.49	0.434	0.484	12.5	13.5	25.7	19.7
Ga	14.8	18.5	19.4	20.7	15.1	19.9	16.6	17.9	13.9	13.4
Rb	51.4	26.0	33.8	93.0	35.7	81.3	56.3	46.9	6.12	1.57
Sr	896	1330	1269	951	56.5	67.5	519	665	448	501
Y	19.6	19.2	19.7	29.6	27.9	31.0	10.4	16.8	20.1	19.2
Zr	111	156	218	358	223	360	133	130	75.7	86.5
Nb	9.21	8.64	12.2	19.1	15.7	17.5	4.54	5.32	4.24	5.49
Cs	0.847	0.537	0.487	1.37	0.376	0.885	0.502	0.564	0.060	0.119
Ba	791	679	1026	1223	748	1275	836	1097	215	320
La	24.2	27.3	30.6	41.8	32.3	43.6	14.7	20.8	11.3	14.8
Ce	55.7	62.6	69.7	94.4	71.3	97.8	31.3	38.8	26.4	33.4
Pr	7.02	8.12	8.83	12.0	9.11	11.9	3.60	4.87	3.58	4.27
Nd	29.5	34.2	35.7	47.6	35.5	45.9	14.5	19.4	16.1	18.3
Sm	5.60	6.815	6.73	9.09	6.83	8.39	2.99	3.88	3.95	4.11
Eu	1.66	2.09	2.05	2.38	1.67	2.10	0.703	0.906	1.14	1.15
Gd	4.75	5.39	5.31	7.13	5.66	6.68	2.53	3.21	3.97	3.82
Tb	0.704	0.752	0.749	1.054	0.904	1.00	0.369	0.473	0.674	0.666
Dy	3.71	4.06	4.05	6.04	4.90	6.04	2.08	2.88	3.39	3.62
Ho	0.725	0.801	0.801	1.22	1.08	1.24	0.417	0.583	0.775	0.716
Er	1.94	2.17	2.17	3.42	2.90	3.50	1.16	1.63	2.05	1.95
Tm	0.307	0.311	0.322	0.537	0.436	0.548	0.187	0.246	0.305	0.323
Yb	1.91	1.87	1.86	3.32	2.74	3.43	1.08	1.57	2.08	1.96
Lu	0.254	0.268	0.281	0.496	0.443	0.513	0.158	0.246	0.276	0.292
Hf	3.74	3.79	4.91	8.93	6.54	8.57	3.41	3.22	2.76	3.29
Ta	0.479	0.394	0.591	1.07	0.890	1.03	0.280	0.321	0.235	0.285
Pb	8.31	4.50	4.85	8.94	12.868	5.08	6.77	5.63	3.61	5.73
Th	2.16	2.25	2.84	5.94	3.88	5.66	4.19	4.76	0.589	1.12
U	0.762	0.728	1.00	2.41	0.843	1.24	1.39	1.65	0.265	0.457

Table. (Contd.)

Component	14/14	14/18	14/19	14/21	14/20	10/21	10/27	10/28	10/29	14/24	14/13	14/26	14/29
	BUU	SB	SB	SB									
SiO ₂	49.65	48.29	50.76	48.60	70.94	68.50	71.08	67.87	68.25	75.29	66.51	67.34	71.06
TiO ₂	1.46	1.50	1.28	1.52	0.55	0.56	0.30	0.46	0.48	0.23	0.50	0.50	0.27
Al ₂ O ₃	16.29	16.65	16.44	15.95	12.29	11.74	14.00	14.43	14.49	11.76	14.35	15.33	14.38
FeO	8.11	8.90	8.35	9.85	5.56	5.97	2.50	4.09	4.09	3.05	3.77	3.60	2.12
MnO	0.17	0.15	0.22	0.14	0.14	0.14	0.08	0.13	0.23	0.04	0.08	0.13	0.05
MgO	3.67	3.20	2.61	1.93	0.27	0.41	0.21	0.13	0.14	0.16	0.91	0.27	0.27
CaO	9.54	10.39	9.86	10.58	0.30	1.27	0.38	0.37	0.39	0.30	2.24	0.95	0.72
Na ₂ O	2.84	3.07	3.33	3.17	3.00	1.81	3.93	4.16	4.24	3.44	5.05	4.66	4.11
K ₂ O	0.82	0.56	1.32	1.23	4.61	7.00	5.79	6.61	6.24	4.79	3.20	4.78	5.46
P ₂ O ₅	0.51	0.40	0.42	0.48	0.05	0.05	0.05	0.07	0.08	0.03	0.11	0.11	0.05
L.O.I.	6.12	5.87	4.35	5.39	1.77	1.90	1.35	1.28	0.89	0.58	2.79	1.69	1.22
Total	99.18	98.99	98.94	98.83	99.48	99.35	99.67	99.59	99.50	99.68	99.51	99.37	99.71
Be	1.47	1.38	1.60	1.52	2.58	2.49	3.43	2.96	3.77	3.62	3.17	4.40	4.60
Sc	11.1	18.5	15.8	19.4	0.747	6.12	3.70	17.0	16.2	0.726	0.659	0.904	0.227
V	184	194	182	210	2.779	0.511	2.98	12.0	4.24	19.2	6.16	5.84	11.6
Co	26.4	31.1	28.2	30.7	0.137	0.602	1.11	0.755	0.384	1.42	1.56	1.23	1.20
Ga	17.7	17.5	18.8	18.4	26.0	21.3	17.1	19.5	19.0	23.7	21.5	22.9	19.0
Rb	5.20	4.91	14.8	12.0	68.5	126	104	106	102	140	69.5	107	115
Sr	726	545	580	533	75.5	34.2	43.3	19.4	26.8	32.6	245	104	51.5
Y	26.3	24.0	24.2	27.3	62.4	54.0	27.4	38.5	38.0	72.8	56.2	60.4	56.1
Zr	194	168	181	192	657	290	191	225	203	647	570	559	426
Nb	8.22	7.06	7.43	7.70	17.9	15.4	17.9	16.2	15.2	19.5	16.8	17.7	16.6
Cs	0.460	0.190	0.205	0.747	0.957	0.897	2.61	3.81	5.65	2.33	1.10	1.63	1.08
Ba	356	277	566	486	84.8	108	387	25.8	40.9	110	900	1014	455
La	20.8	17.5	20.5	21.3	38.5	34.2	23.7	23.8	20.0	53.8	41.1	43.3	43.6
Ce	48.1	40.2	46.4	48.6	101	84.1	54.8	51.1	44.9	122.391	96.0	99.2	99.6
Pr	6.37	5.34	5.88	6.41	12.7	10.8	7.12	7.65	6.53	15.1	12.2	12.7	12.4
Nd	27.5	23.2	25.4	28.3	54.1	45.1	28.8	33.3	27.3	60.8	49.7	51.7	48.3
Sm	6.22	5.41	5.62	6.31	12.7	10.1	5.78	7.55	6.41	13.2	10.9	11.3	10.3
Eu	1.86	1.67	1.48	1.75	1.52	1.09	0.600	0.470	0.406	0.320	2.32	2.59	1.13
Gd	5.86	5.38	5.30	6.04	12.3	9.45	5.11	6.65	6.24	12.3	9.97	10.5	9.53
Tb	0.901	0.819	0.825	0.937	2.12	1.722	0.942	1.16	1.20	2.12	1.67	1.77	1.61
Dy	5.24	4.93	4.81	5.37	13.1	9.96	5.52	7.05	6.56	13.5	10.6	11.4	10.6
Ho	1.07	1.02	0.976	1.13	2.68	2.24	1.23	1.58	1.53	2.89	2.27	2.43	2.25
Er	3.06	2.80	2.74	3.08	7.40	6.24	3.50	4.57	4.20	8.26	6.80	7.13	6.72
Tm	0.453	0.420	0.419	0.463	1.17	0.992	0.602	0.713	0.698	1.30	1.09	1.13	1.09
Yb	2.69	2.51	2.52	2.83	7.48	6.31	4.39	4.71	4.40	8.00	6.96	7.30	7.20
Lu	0.417	0.391	0.384	0.444	1.19	0.898	0.602	0.678	0.659	1.22	1.08	1.14	1.10
Hf	4.48	3.98	4.19	4.52	15.5	11.5	9.36	8.41	7.78	15.9	13.8	14.1	12.2
Ta	0.382	0.341	0.320	0.323	1.11	0.952	1.10	0.876	0.841	1.42	1.06	1.14	1.21
Pb	4.04	4.14	3.64	6.15	9.81	13.7	10.5	6.81	7.95	10.7	4.97	9.75	5.39
Th	1.47	0.896	1.34	1.04	6.66	4.72	4.94	3.29	3.15	12.6	8.09	8.28	10.1
U	0.574	0.435	0.595	0.498	2.22	0.955	1.22	0.837	0.755	2.80	3.25	3.17	3.88

Note: Volcanic associations: Dev—Devonian island_arc association, ACM—in (Kovalenko et al., 2006). The volcanic units were formed in subaerial environments in the northern part of the depression and mostly in aqueous environments in the southern part. The stratigraphic section is crowned by a unit of brown normal and welded dacite–trachydacite tuffs. This systematic alternation of basic, intermediate, and acid rocks is fairly typical of Carboniferous volcanic

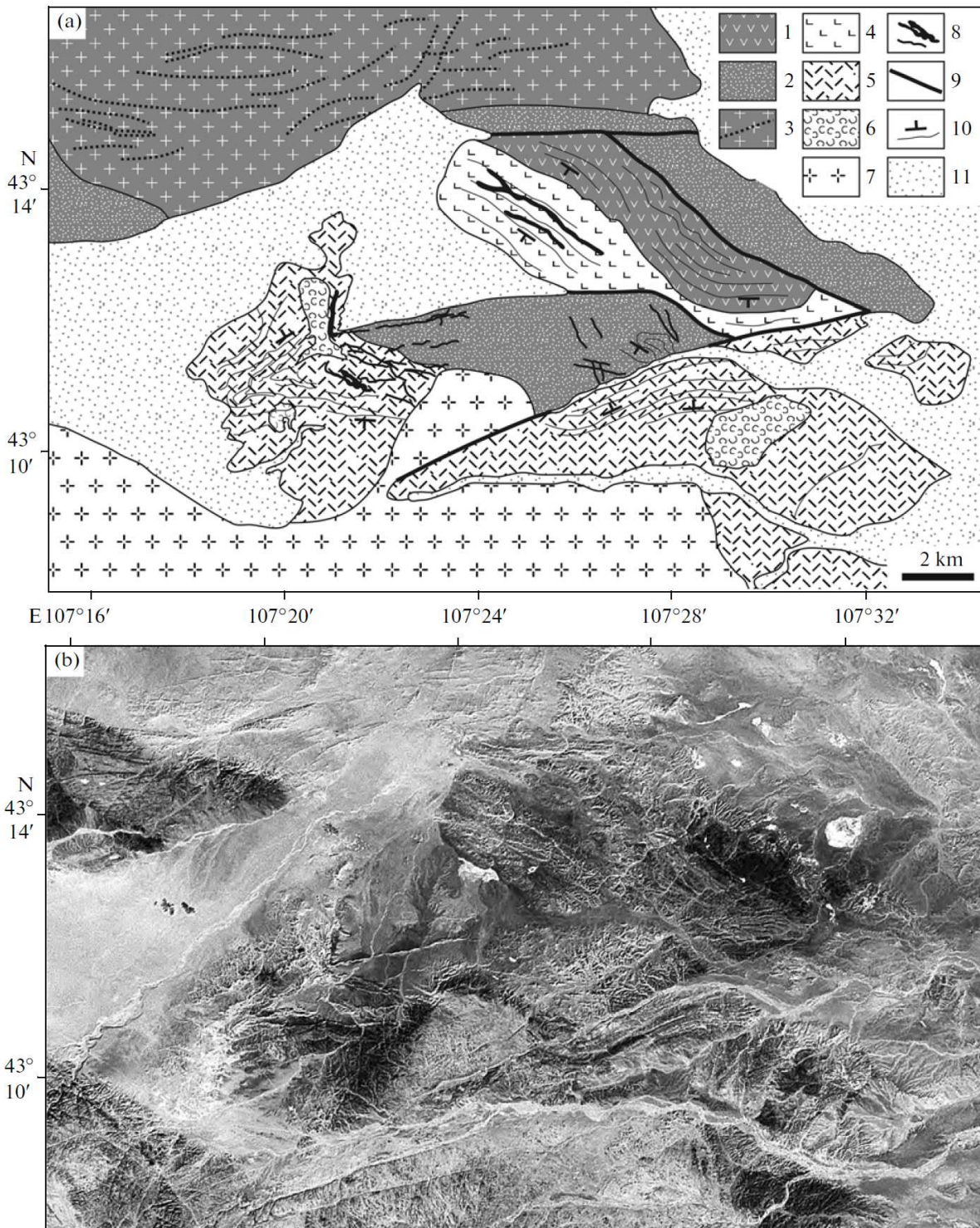


Fig. 2. (a) Schematic geological map and (b) Landsat-7 image of the northeastern volcanic field in the surroundings of the Khan-Bogd alkali-granitoid massif. (1□3) Rocks of the continental-margin evolutionary stage (ACM): (1) volcanic rocks, (2) terrigenous rocks; (3) granitoids of normal alkalinity and their dikes; (4-6) volcanic rocks of the bimodal association: (4) basaltoids, (5) trachytes, trachydacites, trachyrhyolites, comendites, and pantellerites; (6) extrusions of alkali salic rocks; (7) alkali granites; (8) dikes of rocks of the bimodal association; (9) faults; (10) boundaries of volcanic flows and their dips; (11) loose Middle Mesozoic-Cenozoic deposits.

sequences in southern Mongolia, and this led us to recognize these rock associations as a differentiated volcanic complex (Yarmolyuk and Kovalenko, 1991).

The U–Pb zircon age of dacites from roof sags in the alkali granites is 330 Ma and is in good agreement with the age of the floral imprints (Durante et al., 1976; Yarmolyuk, 1983). It should also be mentioned that arc magmatic rocks (ophiolites in the depression basement, which are referred to as the Devonian association below) and ACM complexes not only have similar ages but are also close in composition, including geochemical and isotopic characteristics, and hence, they can be collectively considered to be a group of volcanic rocks related to subduction-zone magmatism (subduction associations).

The *bimodal volcanic association* comprises alternating units of various composition: basaltic and acid lavas, on the one hand, and tuffs, ignimbrites, and lavas and subvolcanic bodies of comendite and trachyrhyolite composition, on the other. The rocks of the bimodal complex were traced along the northeastern (northern field) and southern (southern field) boundaries of the Khan-Bogd Massif and overly the ACM units.

The northeastern field (Fig. 2) is extensively broken into blocks at gentle dip angles of the volcanic units and the rolling topography of the territory. Because of this, rocks of the complex are exposed in this field as relatively thin fragments of usually homogeneous composition. The area hosts red granitoids and syenites in contact with the terrigenous complex, which are classed with arc rocks produced before the development of the ACM. The terrigenous complex is exposed as fault-bounded blocks among the comendites of the bimodal unit. The volcanic comendites and their extrusions overly the terrigenous unit. The differentiated basalt–andesite–dacite ACM complex and the overlying basalts of the bimodal association occur in a block that is in fault contact with the terrigenous complex. The northern field of the bimodal association includes widespread subvolcanic rocks in the form of dikes and tabular bodies of alkali granite porphyries, comendites, trachyrhyolites and more rare basalts. In the field, they cut through practically the whole subvolcanic complex, except only the upper series of acid lavas, ignimbrites, and welded tuffs, and belong to two differently oriented and spatially separated systems. Near the fault, these are almost exclusively steeply dipping bodies of east–northeastern strike, which occur on the continuations of major faults and accompanying dikes, which were traced throughout the whole alkali-granite massif. Away from the massif, dikes of porphyritic alkali granites are predominant and occur as a crescent-shaped (ring) array of bodies that dip at angles of approximately 45° to the west and southwest, i.e., toward the alkali granite massif. The density of dike bodies in the system is very high: dikes 5–9 m

thick are spaced approximately 50 m apart (across the strike of the dike array) in the southern part of the system, and the number of dikes increases northward.

The most complete stratigraphic section of the ACM and bimodal association occurs in the volcanic field in the southern outer-contact zone of the KhanBogd Massif (Fig. 3), in which these rocks were thoroughly sampled (sometimes practically at each distinct unit) at a number of localities (Fig. 3a). Figure 3b presents a generalized vertical section. The rocks of the bimodal complex subconformably overlay the ACM volcanic sequence and are separated from the latter by a sandstone and gritstone unit of broadly varying thickness. This is, in turn, overlain by the following succession of more or less compositionally homogeneous volcanic units, which were subdivided into a BLU (bimodal lower unit; numeral in parentheses show the thicknesses in m): (1) basaltic andesite (400), (2) trachydacite and comendite tuff and ignimbrite (200), (3) olivine basalt (350), (4) comendite and trachyrhyolite (100), and (5) dacite (100); and BUU (bimodal upper unit): (1) olivine basalt (400), and (2) trachyrhyolite, comendite, and corresponding welded tuff and ignimbrite (>800). The dacite layer in the top of the BLU is referred to as the intermediate layer (IL). The total thickness of section is more than 2000 m. The volcanic pile includes tabular bodies of usually hydrothermally altered trachyrhyolites and alkali granites. In the southern part of the volcanic field, rock of the bimodal association are cut across by a body of complicated morphology consisting of trachy- rhyolites and rachyrhyodacites.

The southeastern and eastern boundaries of the Khan-Bogd Massif are marked by a narrow stripe of exposures of rocks of the bimodal complex. This is an extension of the northern and southern fields as a continuous stripe of exposures (Fig. 1), which testifies that both volcanic areas belong to a single larger volcanic field. The original area of the latter was likely no smaller than 1800–2000 km².

Figures 4 and 5 illustrate the petrochemistry of all of the rocks described above.

The (Na₂O + K₂O)–SiO₂ diagram (Fig. 4) shows that the Devonian volcanics are basalts, andesites, dacites, trachydacites, and more rare rhyolites. They are mostly rocks of normal alkalinity or, occasionally subalkaline (trachydacites). This is a typical differentiated low-Ti (<1.5 wt % TiO₂) volcanic association of the calc–alkaline series with a characteristic increase in the SiO₂ concentration and a decrease in the contents of total Fe and TiO₂ (Fig. 5) at an increase in the Fe# of the rocks.

The volcanic rocks in the lower part of the KhanBogd depression, which were classed with the ACM association, are only insignificantly different petrochemically from the Devonian rocks (Figs. 4, 5). This is a continuous series, from basalt to rhyolite, of a lowTi (<1.5 wt % TiO₂) volcanic association of normal alkalinity or that transitional to the subalkaline series (Fig. 4), which belongs to the calc–alkaline series (the increase in the SiO₂ concentration is associated with a decrease in the concentrations of total Fe and TiO₂ at increasing Fe# of the rocks;

Fig. 5). The TiO_2 concentration in the ACM rocks passes through a maximum due to magma saturation with Ti and the further crystallization of Ti-concentrating minerals, a process to which the origin of acid magmas is commonly thought to be related [20]

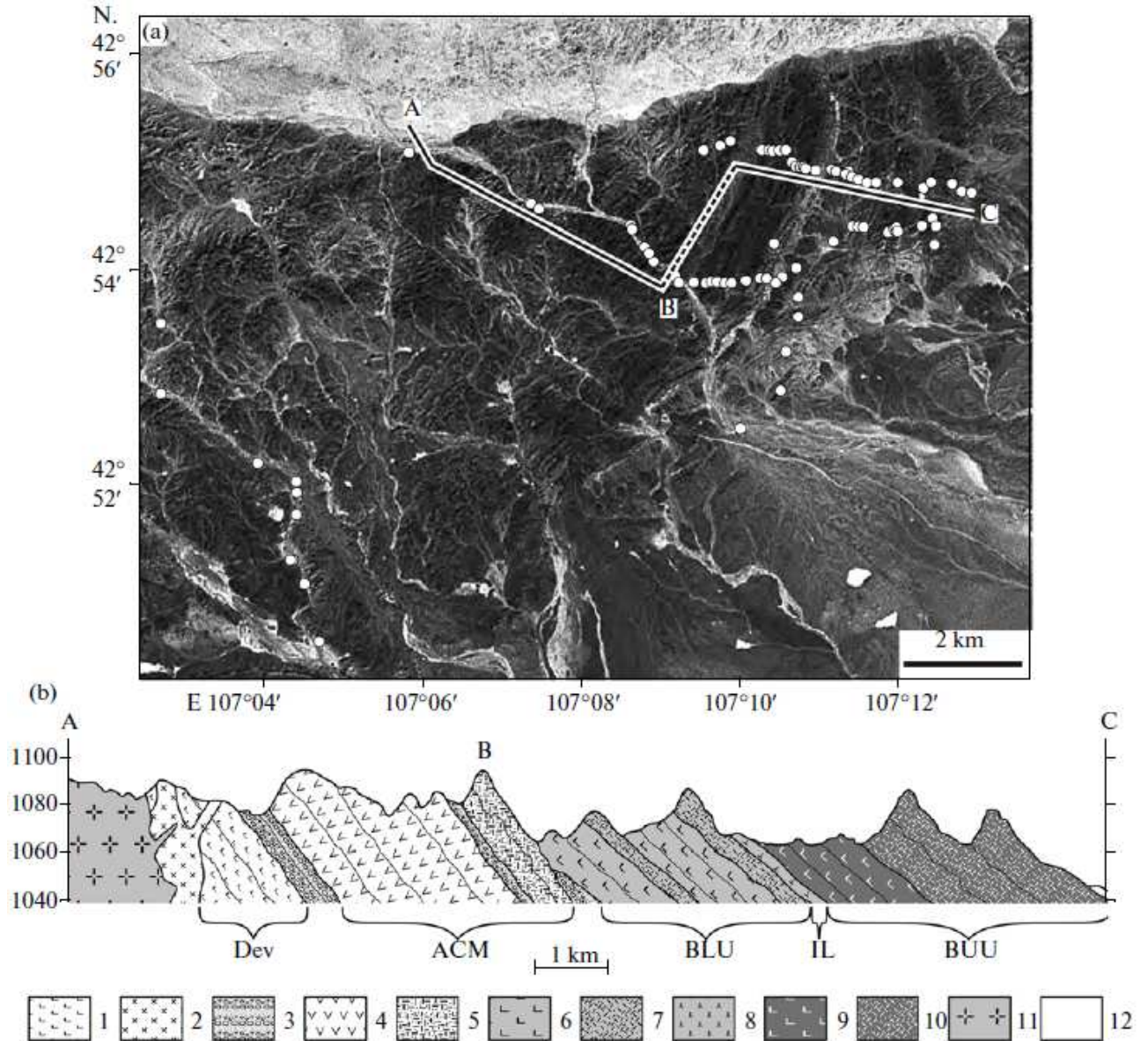


Fig. 3. (a) Landsat-7 image and (b) geological section of the southern volcanic field in the surroundings of the Khan-Bogd alkali-granitoid massif. (1) Devonian basaltoids of the island-arc type (Dev); (2) monzonite-granodiorite intrusion of supposedly Devonian age; (3) conglomerates and sandstones between volcanic units; (4, 5) continental-marginal volcanic rocks (ACM): (4) basaltoids and andesites, (5) dacite ignimbrites; (6, 7) volcanic rocks of the lower units of the bimodal association (BLU): (6) basaltoids, (7) alkali salic rocks; (8) dacites of the intermediate layer (IL); (9, 10) volcanic rocks of the upper units of the bimodal association (BUU): (9) basaltoids, (10) alkali salic rocks; (11) alkali granites; (10) loose Middle Mesozoic-Cenozoic deposits. The satellite image shows the section line and sampling sites.

According to the stratigraphic section described above and to the petrochemistry of volcanic rocks in the bimodal association, it is subdivided into a lower (BLU) and upper (BUU) units, with an intermediate dacite layer (IL) in

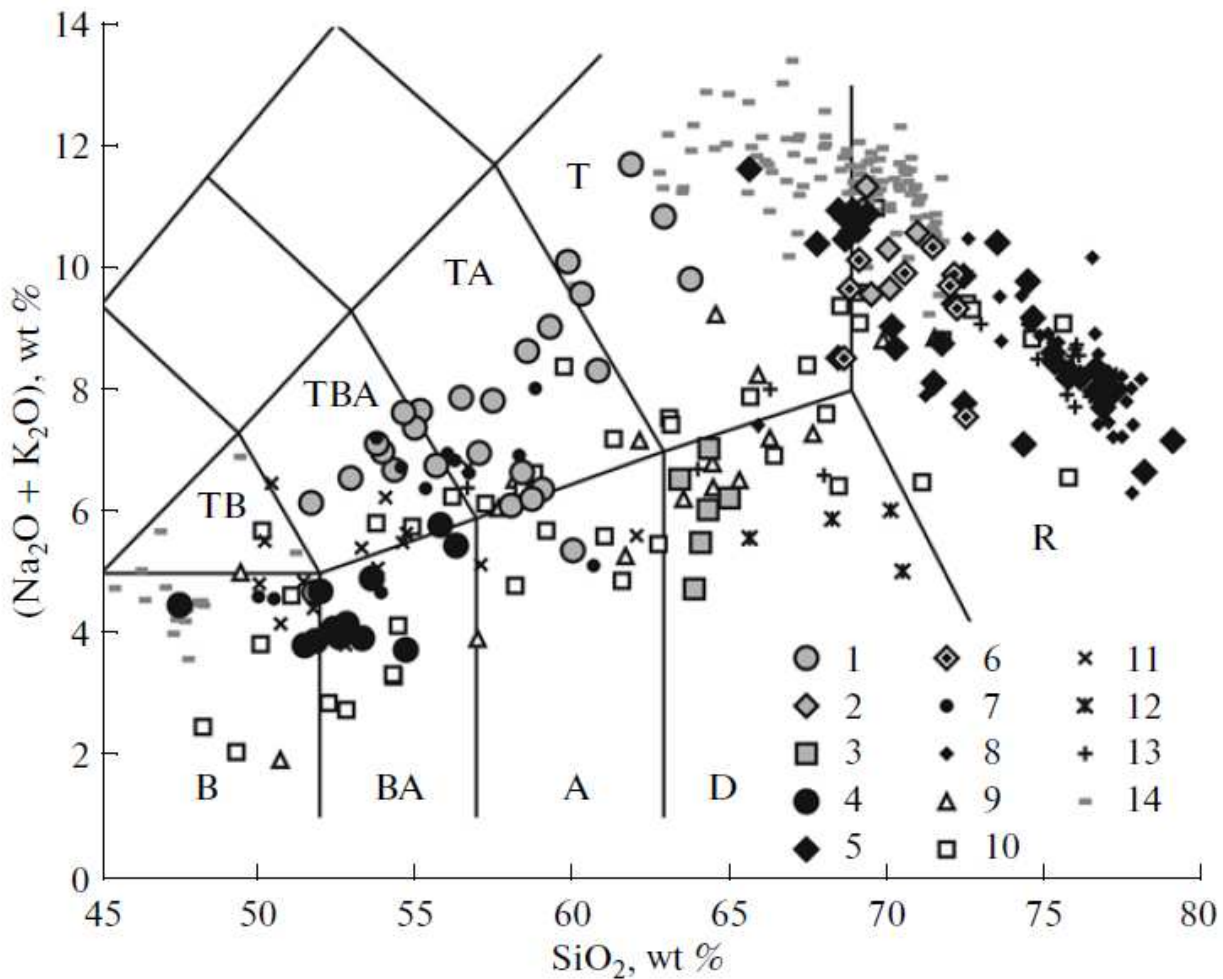


Fig. 4. $(\text{Na}_2\text{O} + \text{K}_2\text{O})$ vs. SiO_2 classification diagram for Paleozoic rocks of the Khan-Bogd area. (1, 2) Volcanic rocks of the lower unit of the bimodal association (BLU): (1) basaltoids-trachytes, (2) alkali salic rocks; (3) dacites of the intermediate layer (IL); (4, 5) volcanic rocks of the upper unit of the bimodal association (BUU): (4) basaltoids, (5) alkali salic rocks; (6) acid subvolcanic rocks; (7, 8) undifferentiated rocks of the northeastern field: (7) basaltoids, (8) alkali salic rocks; (9) volcanic rocks of the Devonian arc association; (10) continental-marginal volcanic rocks; (11, 12) ophiolites of the southern Mongolian belt of Hercynides: (11) volcanic rocks, (12) sedimentary rocks; (13) various granitoids of normal alkalinity in the Khan-Bogd area; (14) volcanic rocks of Pantelleria Island. Fields in the classification diagram: B—basalts, BA—basaltic andesites, A—andesites, D—dacites, TB—trachybasalts, TBA—trachybasaltic andesites, TA—trachyandesites, T—trachytes and trachydacites; R—rhyolites.

between, which is principally different from these units (Fig. 3b). The BLU (trachybasaltic andesite, trachyandesite, trachydacite and comendite tuffs and ignimbrites, lava comendite, and trachyrhyolite; Fig. 3b) is dominated by subalkaline rocks (Fig. 4) with a narrow composition gap between 65 and 70 wt %

SiO₂. The petrochemical parameters of the BLU are intermediate between those of the calc-alkaline and tholeiite series (Fig. 5): more basic rocks are characterized by

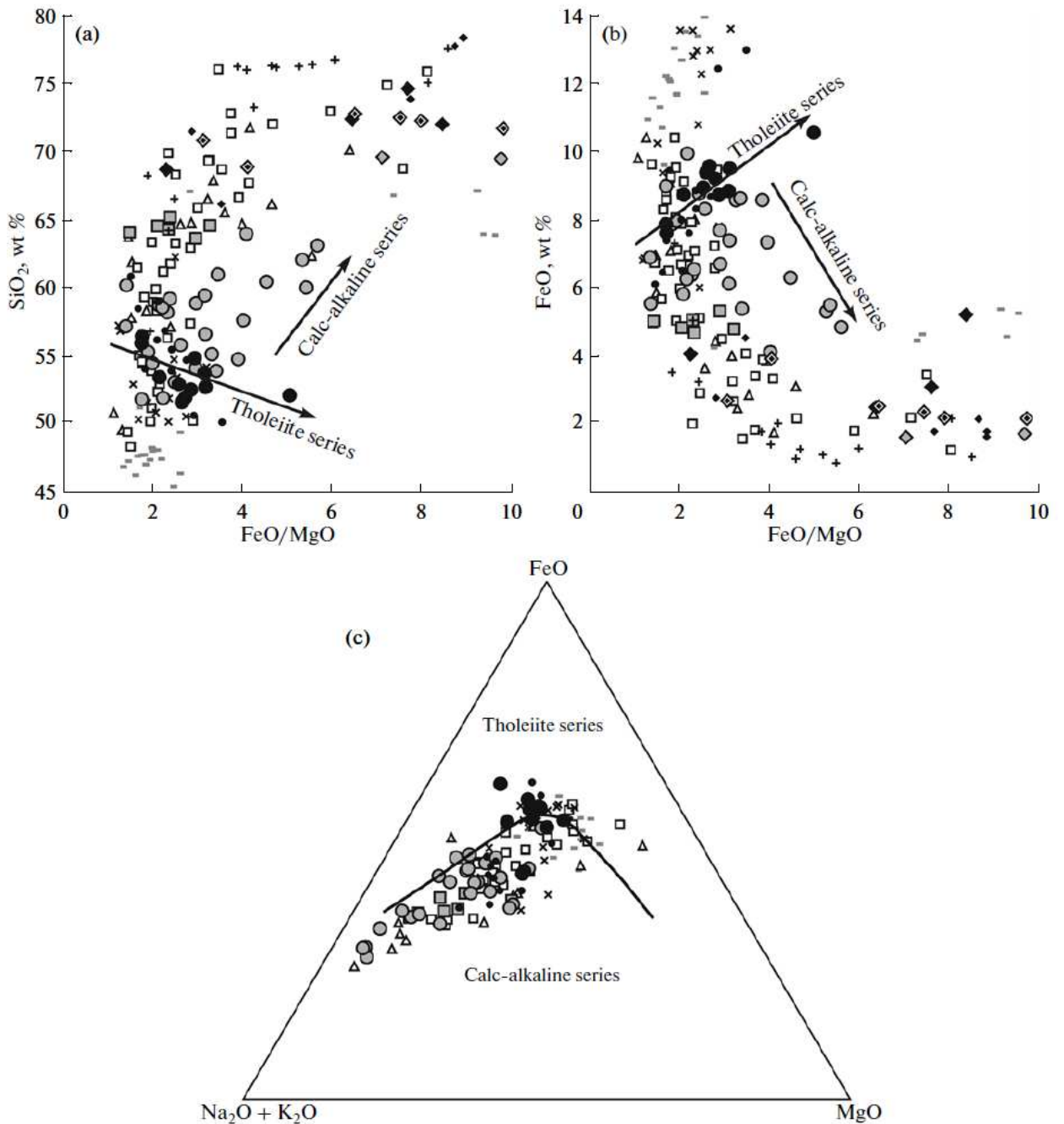


Fig. 5. Diagrams illustrating variations in the concentrations of elements in the calc-alkaline and tholeiite series of volcanic rocks in the Khan-Bogd depression. See Fig. 4 for symbol explanations. Arrows indicate characteristic compositional trends of the basic-intermediate rocks of the tholeiite and calc-alkaline series.

a trend with a decrease in the SiO₂ concentration at an increase in the content of total Fe and the Fe# of the rocks, whereas more acid rocks show opposite trends: the more basic volcanics are closer to the tholeiite series and the more acid rocks

displaying features transitional to the calc-alkaline series. The basite BLU compositions are the richest in TiO_2 among all of the compositions discussed herein and belong to moderate-Ti varieties whose TiO_2 concentrations are higher than those not only in average arc basalts but also in basalts from mid-oceanic ridges (MORB).

It is pertinent to mention the compositional specifics of the comendites and trachyrhyolites that directly pertain not only to BLU but also to BUU (see below). The comendites and trachyrhyolites are often indistinguishable. The rocks consist of phenocrysts of perthitic alkali feldspar and quartz in a vitreous or devitrified quartz-alkali feldspar groundmass but are noted for the presence of alkali amphiboles and aegirine in the groundmass of the comendites and the absence of these minerals from the trachyrhyolites, which contain small grains of oxidized magnetite. Accordingly, the comendites more often have an agpaite coefficient greater than one, and the trachyrhyolites have this coefficient smaller than one. The transition from the comendites to trachyrhyolites is often obviously related to secondary alterations of the former because of the instability of alkali amphiboles and pyroxenes and their replacement by Fe oxides at the removal of Na_2O and K_2O . This transition is associated with the reddening of the rocks. As a result, the altered comendites look closely similar to normal ACM rhyolites (which are, however, devoid of plagioclase). In view of this, we differentiated between the comendites and trachyrhyolites of the bimodal association and ACM rhyolites using the concentrations of Nb, an element little mobile during secondary alterations, whose concentrations in agpaite comendites and trachyrhyolites are much higher than in any ACM and arc rhyolites. Figure 6 shows the correlations of the SiO_2 concentrations of the rocks and their agpaite coefficients with the Nb concentrations for rocks of all of the associations in question. All comendite and trachyrhyolite compositions have higher Nb concentrations. At 70 wt % SiO_2 , the boundary Nb concentration between acid ACM rocks and comendites, on the one hand, and trachyrhyolites, on the other, is drawn at approximately 13 ppm.

The boundary layer between the upper and lower units of the bimodal volcanic association is a dacite layer about 100 m thick, which is traced for a long distance along the strike of the sequence (Fig. 3). The chemical composition of this volcanic layer has no analogues among any other rocks of the bimodal association. Its composition could be considered intermediate between those of basanites and acid rocks of the upper unit of the bimodal association (Fig. 4), but Fig. 5 shows that all petrochemical and geochemical parameters of the dacite of the intermediate layer are principally different from those of any rocks of the upper unit (see below), and hence, these rocks should rather be classed with the Devonian calc-alkaline volcanic association and ACM than with the bimodal association.

The BUU conformably overlying IL can be, strictly speaking, considered bimodal because it contains practically only basalts and basaltic andesites, on the one hand, and comendites and trachyrhyolites, on the other. The compositional gap in the SiO_2 concentration corresponds to the range of 57–65 wt %. In contrast to

the association of BLU, which is dominated by subalkaline volcanics, the basites of BUU have normal alkalinity and are close to the Devonian and ACM basites (Fig. 4). However, the silica concentrations in the BUU basites rather decreases with increasing Fe#, and the total Fe concentration increases, which allowed us to class these rocks with the tholeiite petrochemical series. The TiO₂ concentrations of the rocks are at the level in MORB.

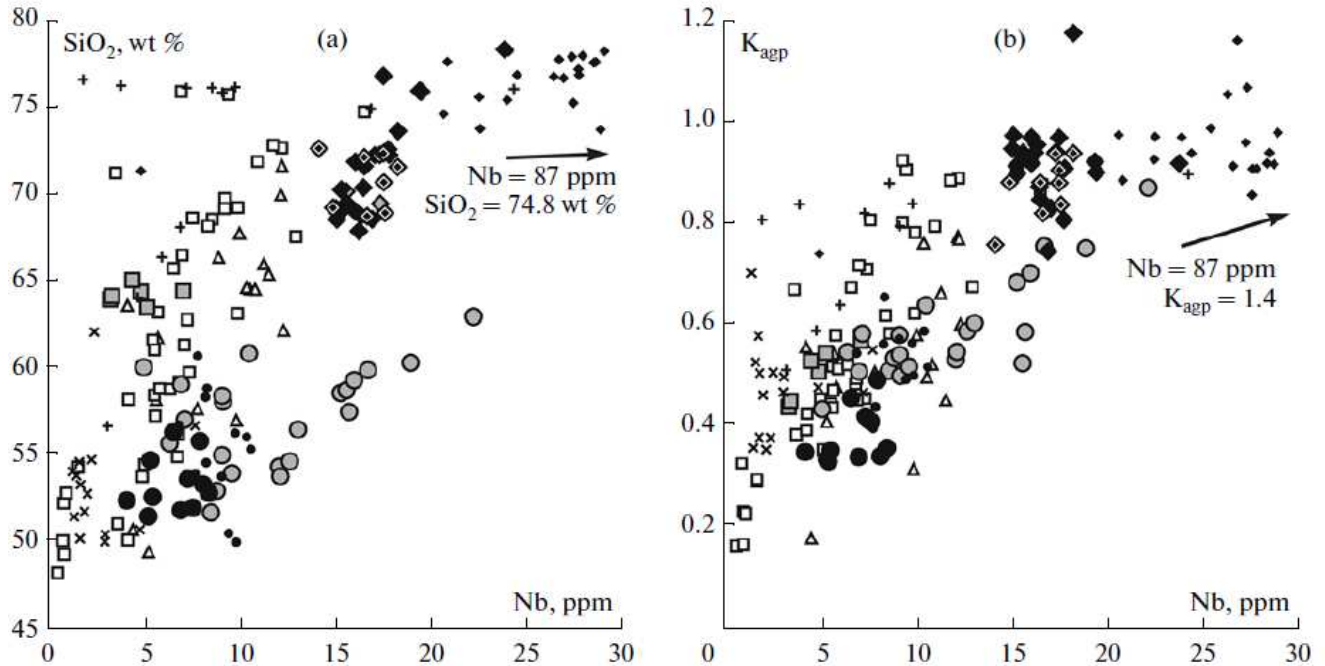


Fig. 6. Variations in the SiO₂ concentration and agpaite coefficient K_{agp} as a function of Nb concentration in volcanic rocks of the Khan-Bogd territory. See Fig. 4 for symbol explanations.

Figure 7 shows the compositions of the rocks in the compositional fields of adakites and normal arc volcanics according to (Martin, 1999). The overwhelming majority of the compositions of rocks of the Devonian series, ACM, and bimodal association plot within the field of normal arc volcanic rocks. The exception is the least differentiated compositions of the volcanic rocks of ACM, BLU, and IL dacites, which fall into either the intermediate field between adakites and normal arc volcanics or the field of adakites. The compositions of BLU rocks that partly correspond to adakites define a negative correlation line $\text{Sr}/\text{Y} = 1571\text{Y}^{-1.2339}$, $R^2 = 0.5822$ in Fig. 7b, and the analogous line for the Devonian associations is $\text{Sr}/\text{Y} = -1.8415\text{Y} + 73.023$, $R^2 = 0.6326$.

The ACM and Devonian volcanic associations are typical island-arc calc-alkaline, low-Ti rock associations. The transition from the Devonian to ACM associations is not accompanied by any appreciable compositional changes. Starting with BLU, the conditions under which the magmas were derived changed: the first indications of bimodality became discernible, the alkalinity and TiO₂

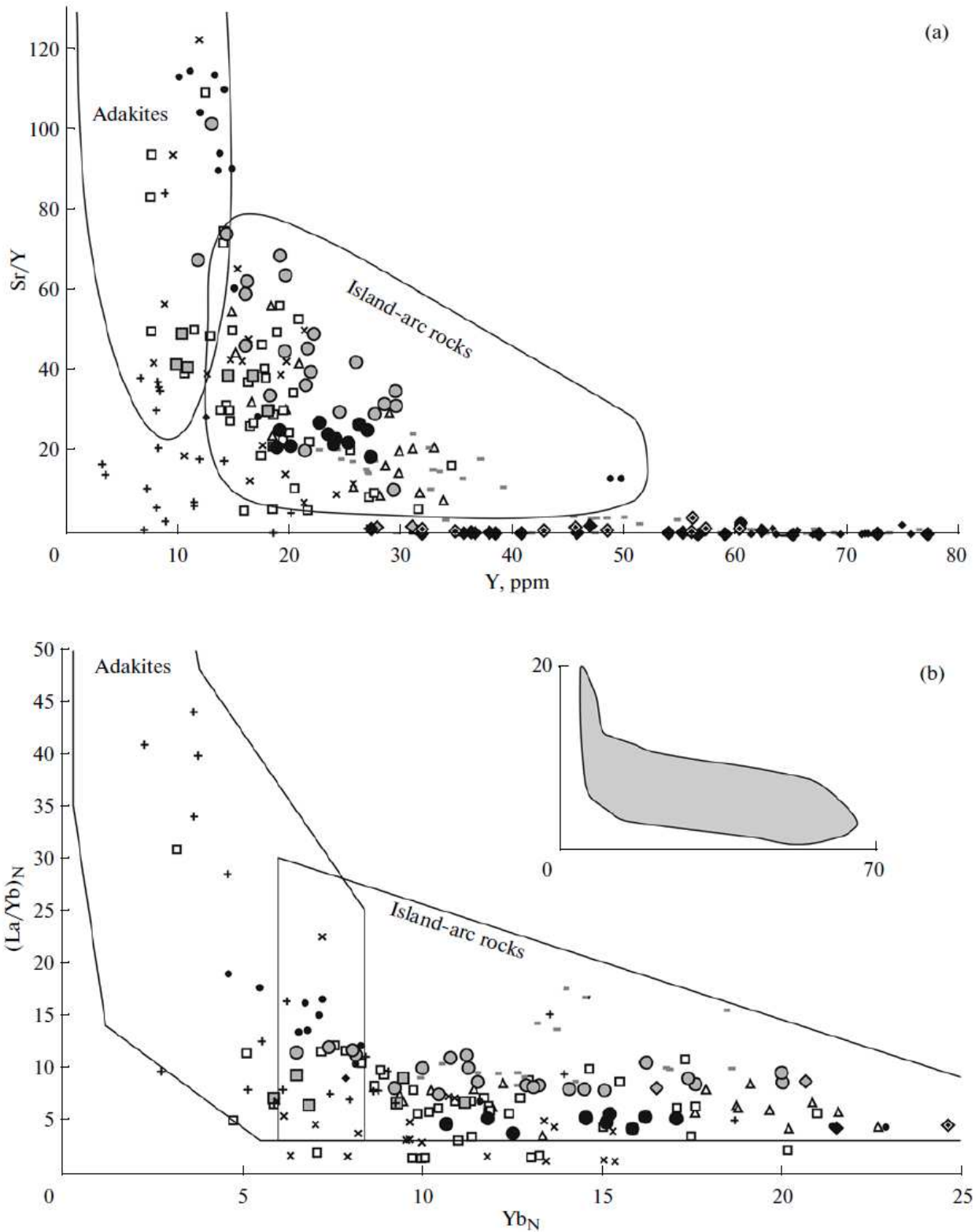


Fig. 7. Position of the composition of volcanic rocks from the Khan_Bogd area relative to compositional fields of adakites and normal arc rocks (Martin, 1999). See Fig. 4 for symbol explanations. The gray field in the inset shows the overall compositional field of volcanic rocks of the Khan-Bogd bimodal association.

concentrations of the magmas increased, their differentiation was associated with the transition from the tholeiite to calc-alkaline series with the origin of comendites and trachyrhyolites. The analogues of calc-alkaline magmas of the ACM type reappeared in the form of IL dacites. The least evolved basite varieties of this part of the bimodal association and the boundary dacites are close to adakites. BLU characterizes the origin of tholeiite basalts with moderate TiO₂ concentrations (of the MORB type), comendites, and trachyrhyolites, with a compositional gap between them. This can be seen in the generalized vertical section.

DISTRIBUTION OF TRACE ELEMENTS VOLCANIC ROCKS

Geochemical Methods Used to Identify the Magma Sources and Estimate the Differentiation and Mixing of the Magmas

Our approaches to estimating the sources of magmatic rocks were described in (Kovalenko et al., 2007) with reference to rare-metal granitoids and their parental rocks. The sources of any magmatic rocks are inferred from the proportions of the concentrations of incompatible elements with close values of bulk crystal-magma distribution coefficients. Such ratios are referred to as canonical (Workman and Hart, 2005). Equations for the dependence of trace-element ratios in magmas and their sources on the various degrees of incompatibility, degree of melting of the source or magma differentiation were presented in our earlier publication (Kovalenko et al., 2007). The trace elements selected for this purpose are characterized by enrichment in a magma of any composition in the course of its differentiation (Fig. 8), and these pairs of trace elements are Nb-U, Nb-Zr, La-Yb, Th-Ta, Ce-Pb, and Nb-La. Ratios of the concentrations of these elements can be applied to estimate the sources of various mantle magmas. It is also important that these trace-element pairs have different values in the model sources (mantle sources: depleted mantle, whose derivatives are MORB and within-plate oceanic basalts OIB; arc basites IAB, continental crust CC, etc.) with which rocks are conventionally compared. In addition to these global sources, certain magmas can be derived with the participation of local sources (such as ophiolites, sediments, and others). It is pertinent to mention that our experience in the geochemical study of various magmatic rocks indicates that the involvement of any pure sources alone in the generation of natural magmas is rare, and accordingly, magma evolution trajectories commonly intersect lines of equal values of canonical ratios (Fig. 8), which testifies that the magmas were generated with the participation not only of crystallization differentiation (or fractional melting) but also of the mixing of magmas or their sources.

The behavior of pairs of incompatible trace elements during the differentiation or anatexis of magmas derived from different sources is portrayed as straight lines passing through the source compositions in diagrams of the

logarithms of concentrations of elements that enrich residual magmas in the course of their differentiation.

Canonical Ratios of Incompatible Elements in Volcanic Rocks of the Khan-Bogd Depression

In addition to the compositions of the rocks, Fig. 8 also shows lines of equal ratios of concentrations of incompatible elements and data on volcanic rocks from Pantelleria Island (model OIB source). As can be seen in this figure, the evolutionary compositional trajectories of various associations deviate from equal concentration lines of the elements and become subparallel (for the La/Yb and Zr/Nb ratios) or intersecting at acute angles (for Nb/U and Ce/Pb). In all of the diagrams (Fig. 8), acid rocks of the bimodal association define a curve, which is approximated for the Nb/U ratio by the equation $Nb = 14.453e^{0.1167U}$, $R^2 = 0.6501$.

Figure 8 also shows that all individual canonical ratios of the great majority of our rock compositions are close to those in the model arc source with variable amounts of the MORB source, enriched sources (OIB or CC), and with the contribution of crystallization differentiation, which characterizes the enrichment of elements.

Below we discuss these conclusions in more detail in Fig. 9. For this purpose we selected combinations of canonical ratios that highlight relations between the volcanic associations discussed herein and model sources: mantle (N-MORB, E-MORB, OIB), crustal (CC), and mixed (IAB). Crustal sources can also include ophiolites in the southern Mongolian Hercynides, which characterize the oceanic-crustal compositions of the Late Paleozoic Paleotethys (Yarmolyuk et al., 2008).

The Th/Ta–Nb/U diagram (Fig. 9a) definitely shows that most compositions of the volcanic associations comply with near-hyperbolic dependences and plot within the field bounded by near-hyperbolic curves approximated by the equations $Th/Ta = 80.288(Nb/U)^{-1.3299}$, $R^2 = 0.7848$ for ophiolite compositions and $Th/Ta = 43.456(Nb/U)^{-0.6899}$, $R^2 = 0.4835$ for the compositions of granitoids from the southern Mongolia Hercynides. The line for ophiolite compositions is close to the compositions of basite rocks from almost all of the volcanic associations: Devonian (except for two samples of composition close to granitoids), ACM (except the compositions of volcanic rocks sampled in the western part of the Khan-Bogd depression: samples 16/3–16.9; table), and some BLU compositions. The compositions plotting away from this line correspond to most samples from BLU, comendites, and trachyrhyolites. Judging from Fig. 8, the line approximating the compositions of ophiolites and most other rocks considered herein was defined by various processes that contributed to the origin of the rocks. At constant values of the canonical ratios during magma differentiation, it should have correlated to the mixing line of two groups of magma sources: an island-arc source of the IAB type and a mantle source (of either the MORB or the OIB type). The La/Yb–Nb/U

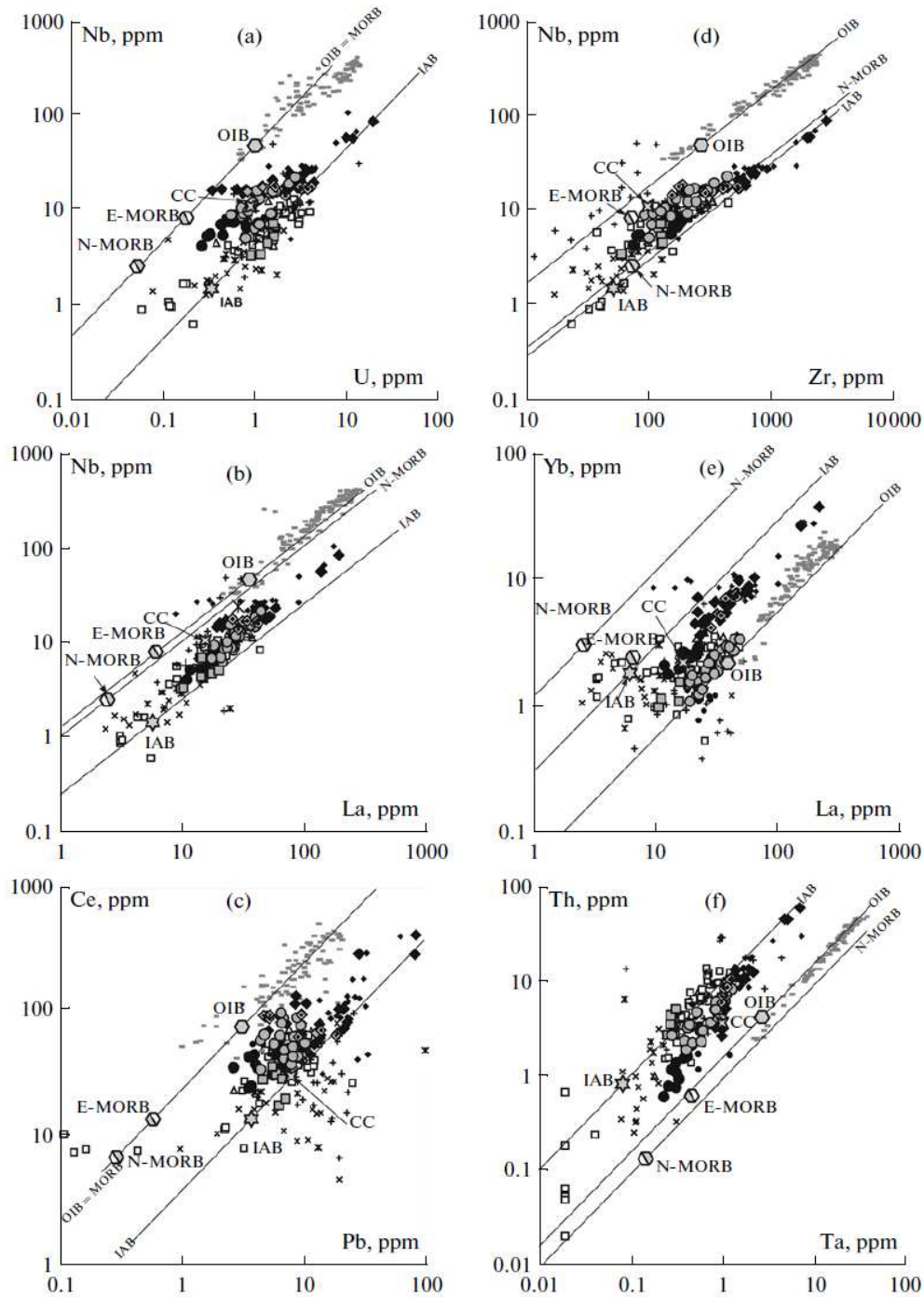


Fig. 8. Variations in the concentrations of incompatible trace elements in volcanic rocks of the Khan-Bogd area. The diagram shows model compositions of mid-oceanic ridge basalts (N-MORB are normal MORB, E-MORB are enriched MORB), oceanic-island basalts (OIB), island-arc basalts (IAB), and the continental crust (CC) as the possible sources of the rocks. Lines in the diagrams correspond to equal ratios of certain sources.

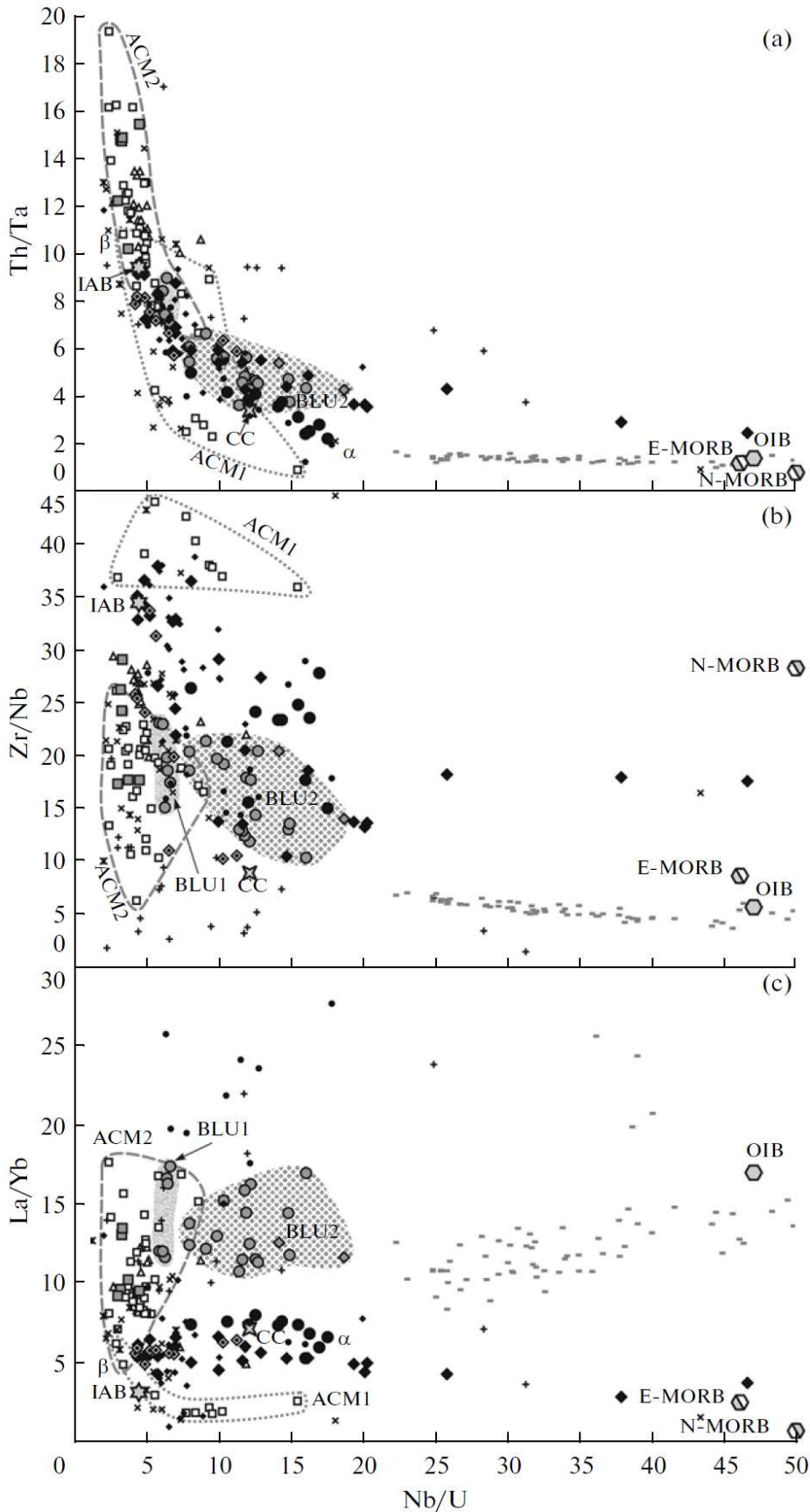


Fig. 9. Variations in (a) the Th/Ta, (b) Zr/Nb, and (c) La/Yb ratios versus the Nb/U ratio in volcanic rocks of the Khan-Bogd area. See Fig. 4 for symbol explanations and Fig. 8 for model sources.

diagram (Fig. 9c) makes it possible to distinguish between the sources because the OIB- and MORB-type sources notable differ in the La/Yb ratio. Figure 9c shows that one of the end members of the mantle sources for the magmas of the volcanic associations was a source of the MORB type, but not that of the OIB type. Figure 9a demonstrates that the other source end member of these magmas was a subduction-related source of the IAB type. The Zr/Nb–Nb/U diagram in Fig. 9b confirms this conclusion and shows that the mantle endmember source of the Devonian, ACM, and BLU volcanic association was a mixture of the depleted (of the N-MORB type) and enriched (E-MORB type) mantle material of mid-oceanic ridges. The same tendencies, but with the obvious involvement of CC, are discernible in the compositions of comendites, trachyrhyolites, and BLU (Fig. 9a).

The analysis of the distribution of the compositions of volcanic rocks in each of the associations in such diagrams provides insight into important specifics of magma differentiation and the origin of volcanism in the Khan-Bogd area.

First, many rock compositions in Fig. 9a (the Devonian association, some ACM compositions, and IL dacites) plot near the region of high Th/Ta ratios (>9 , with the model value of the IAB source being close to 9) at the practical constancy of the Nb/U ratio of 3–6. This implies either a regionally higher Th/Ta ratio in the magma source than in the model source or an increase in this ratio during magma differentiation.

The effect of magma differentiation on the Th/Ta ratio can be tested using such indicators of magma differentiation as Nb or SiO₂ concentrations (Figs. 10, 11). Figures 10a and 11a show that volcanic rocks of the Devonian association, IL dacites, and some ACM rocks have Th/Ta ratios higher than the global model value of the IAB source, and this ratio increases with increasing Nb and SiO₂ concentrations in the rocks, i.e., with increasing degree of magma differentiation (or a decrease in the degree of source melting). Inasmuch the SiO₂ concentration in these associations increases at Th/Ta ratios higher than this is permitted by the average CC composition, it is more realistic to explain this effect by the differentiation of the magmas of the Devonian and ACM associations but not by CC assimilation. This is corroborated by the high SiO₂ concentration in the acid volcanic and plutonic rocks with high Th/Ta ratios. Note that the compositional fields of BLU and BUU in Figs. 10a and 11a continue one another with increasing Th/Ta ratio and concentrations of Nb and SiO₂, although this could result not only from magma differentiation but also from the mixing of such sources as MORB, IAB, and CC.

Second, it is pertinent to consider more closely the behavior of the Nb/U ratio during magma differentiation (Figs. 10b, 11b). The Nb/U ratio in most of the rocks varies within ranges corresponding to a suprasubduction IAB source and is plotted as a nearly horizontal evolutionary trajectory at Nb concentrations up to 37 ppm (at a practically unvarying Nb/U ratio of 3–6), as is typical of crystallization differentiation. This conclusion is consistent with correlations between the Nb/U

ratio and silicity of the rocks ($\text{Nb/U} = 46418(\text{SiO}_2)^{-2.2182}$, $R^2 = 0.4438$; Fig. 11b) and between the Nb/U and Eu/Eu* ratios ($\text{Nb/U} = 5.281 \text{ Eu/Eu}^* + 0.3119$, when an increase in the Nb concentration is directly correlated with an increase in the silicity and a decrease in the Eu/Eu* ratio from 1.2 to 0.7 (Fig. 12b). This type of differentiation with an increase in the SiO₂ concentration and with the fractionation of feldspars is typical of classic calc-alkaline magmatic associations. Hence, this provides us with an argument in support of the hypothesis that the rocks with high Th/Ta ratios resulted from magma differentiation. The least differentiated compositions of the Devonian and ACM rocks deviate toward mantle sources, namely, toward MORB (see above; samples with Nb/U > 10). According to their indicators of the degree of differentiation and canonical ratios, the ACM volcanic rocks are subdivided into (i) ACM1 basites (<55 wt % SiO₂) with very low Nb concentrations (no higher than 2 ppm), low Nb/U ratios (<18), high Zr/Nb (>35), and low La/Yb (<7), low Ce/Pb (<6), and low Nb/La (<0.5); this group also includes volcanic rocks exposed northeast of the Khan-Bogd granite massif (samples 16/3–16/9, table); and (ii) ACM2 volcanics of variable composition (50–65 wt % SiO₂), low and moderate Nb concentrations (>2 ppm), low Zr/Nb (<30), variable La/Yb (4–18), Ce/Pb (1.5 to almost 10), and high Th/Ta (7–19). The first group of basites has all of the above parameters closest to the subduction source of the IAB type, with an admixture of a source of the MORB type (according to Nb/U ~ 16, Ce/Pb ~ 19, and Th/Ta ~ 1). This group differs from the second one in showing a greater spread of the canonical ratios. The other group is close to the ACM rock group with the most compact range of the Nb/U ratio (3–6).

It is now pertinent to turn to the characterization of the bimodal association. The Nb/U ratio and Nb concentrations are not principally different in the BLU and BUU compositions (Fig. 10b), but significant differences are discernible between the bimodal association and the aforementioned compositions of the Devonian and ACM rocks. A small number of samples from the BLU association falls into the field of the Devonian association and ACM2 (association BLU1), with Nb/U = 5–7 and the lowest Nb concentration (approximately 5 ppm). The rest of the complexes (i.e., most of them, which are referred to as association BLU2) plot along lines α and β and most likely was produced by a combination of the differentiation of magma of composition α and mixing of component α with Nb/U \geq 18 (5 ppm Nb) and component β with Nb/U ~ 5 (20 ppm Nb). The differentiation trends of the Devonian, ACM, IL, and BLU1 merge with the line of differentiation and mixing for BLU2 at point β . Component β is a typical subduction source of the IAB type as the main magma source for all of the described volcanic associations. Component α is a mixture of IAB and MORB sources (Fig. 9). Given that the least differentiated magmas of the lower unit of the bimodal association contain practically no compositions intermediate between α and β , it is likely that component α is a mixture of sources but not magmas, and this component

obviously contains a certain fraction of the MORB source. This source is

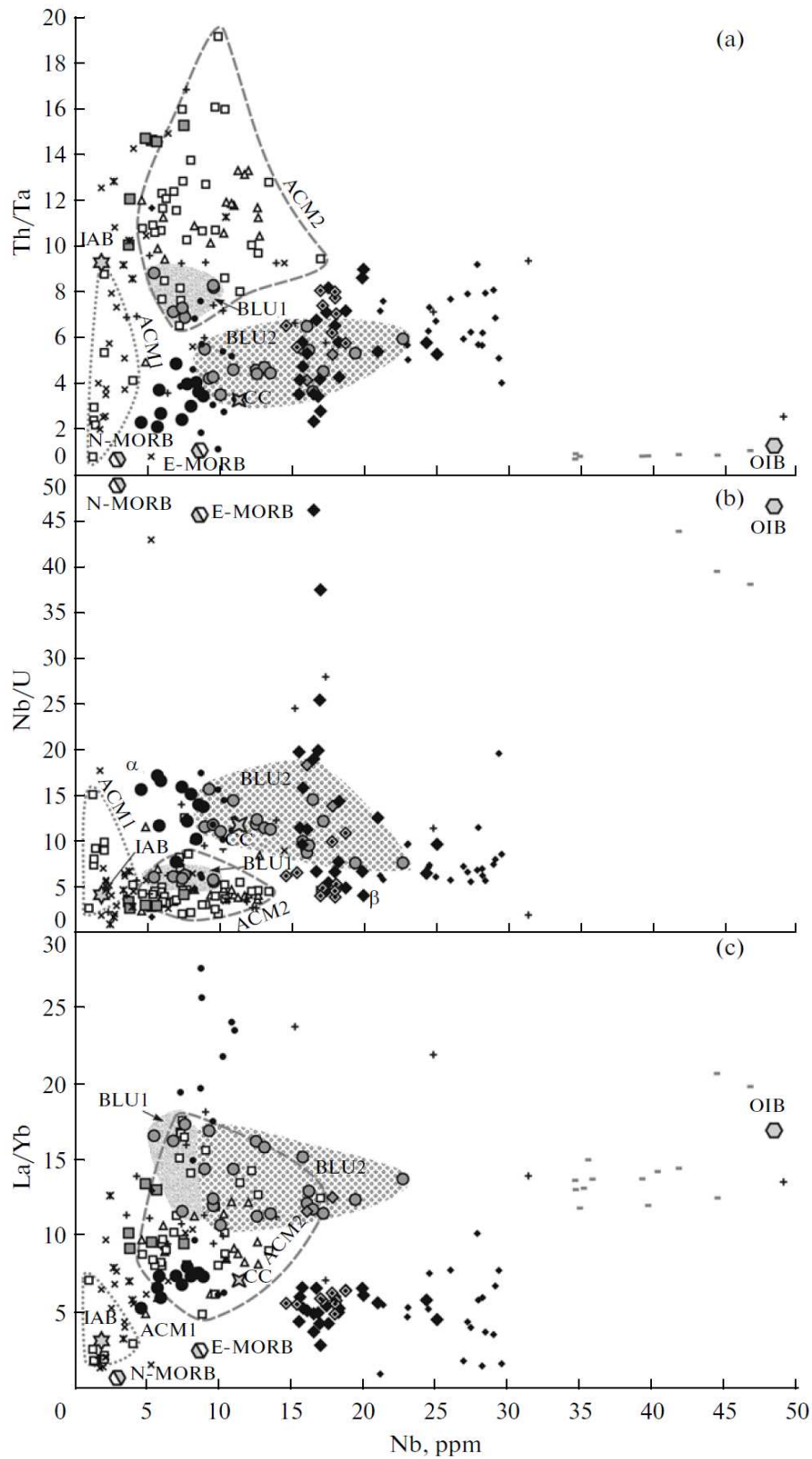


Fig. 10. Variations in (a) the Th/Ta, (b) Nb/U, and (c) La/Yb ratios versus Nb concentration in volcanic rocks of the Khan-Bogd area.

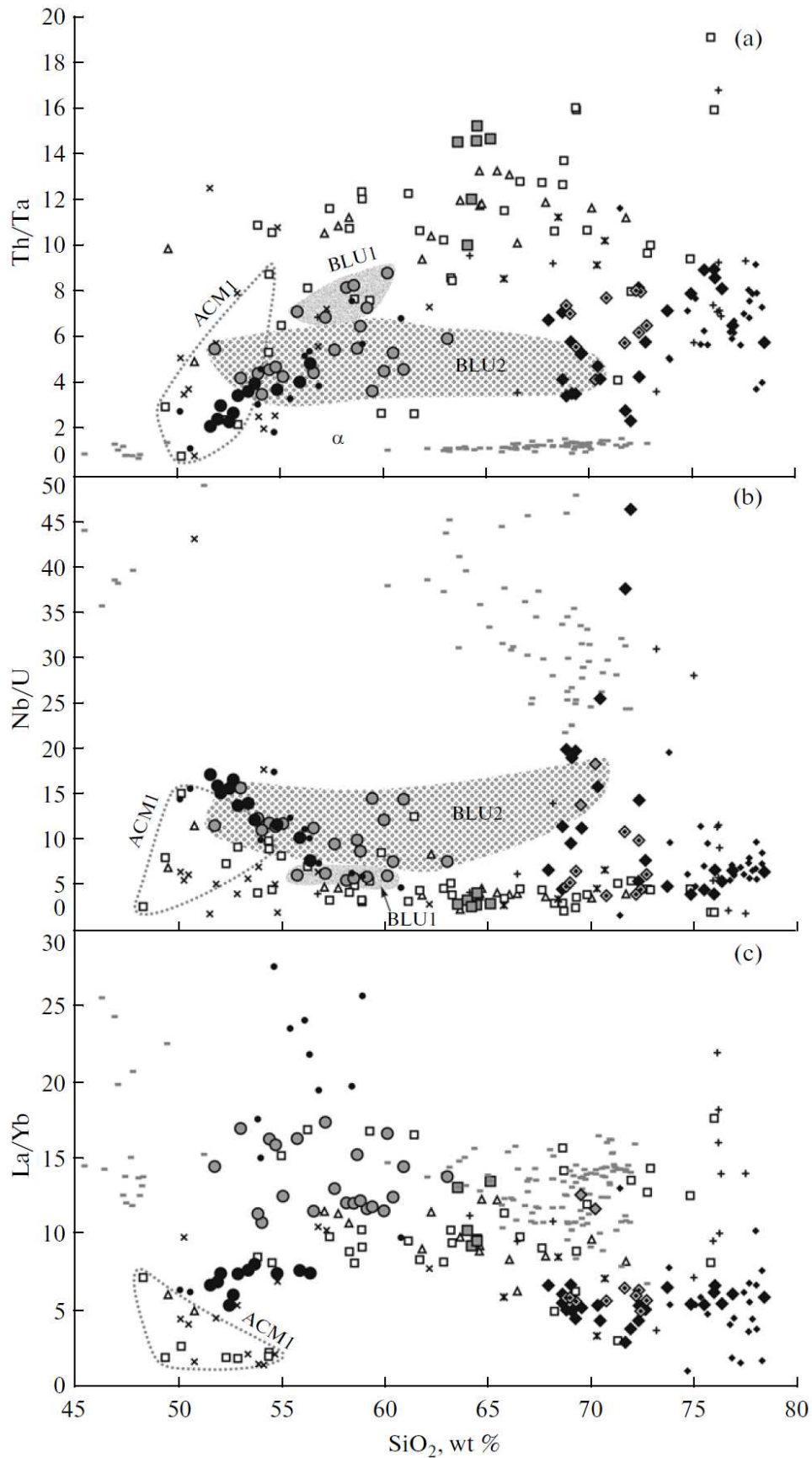


Fig. 11. Variations in (a) the Th/Ta, (b) Nb/U, and (c) La/Yb ratios versus SiO₂ concentration in volcanic rocks of the Khan-Bogd area.

discernible even in the ophiolites of the Hercynides and ACM1 volcanics. Most compositions of BLU2 volcanics are richer in Nb than BUU volcanics, which can be explained by either the involvement of a source of the OIB type or the assimilation of BLU2 magmas with an average CC composition (Fig. 9a). The BLU and BUU compositions enrich in SiO₂ with increasing degree of differentiation (Fig. 13), which can be explained by either magma differentiation or the assimilation of the upper crust (and sediments of ophiolites and granitoids) by the magmas.

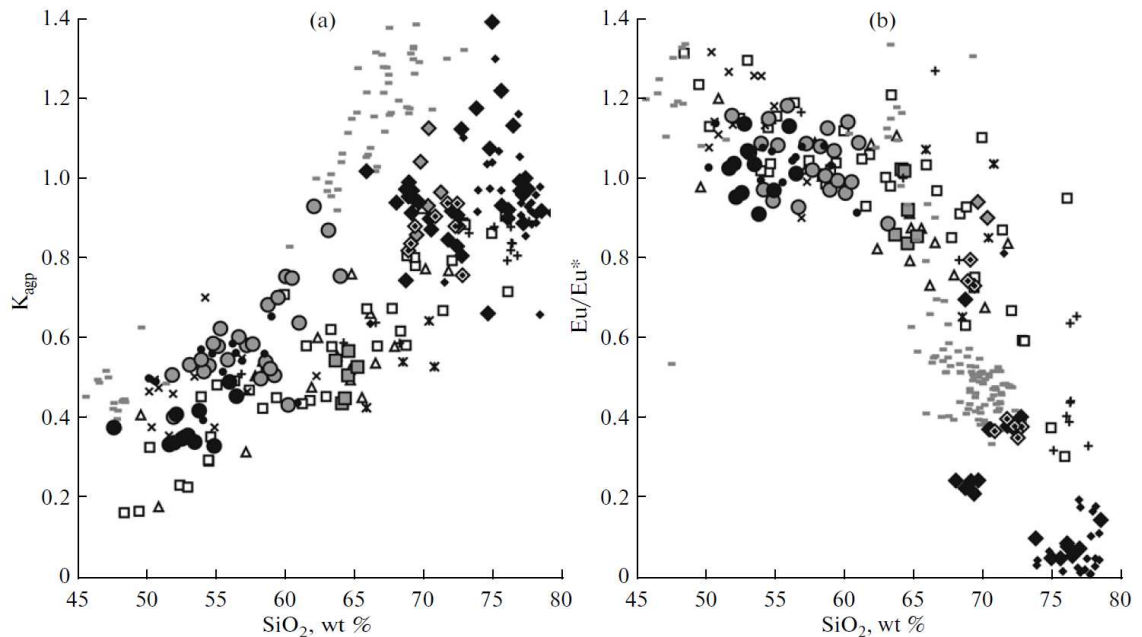


Fig. 12. Variations in (a) the apgaitic coefficient and (b) Eu minimum versus SiO₂ concentration in volcanic rocks of the Khan-Bogd area. See Fig. 4 for symbol explanations.

IL dacites of the bimodal association are obviously related to a source of the IAB type (Fig. 10b), although it is uncertain whether an increase in their SiO₂ contents resulted from the differentiation of the Devonian or ACM magmas (the Nb concentrations are too low for this) or from the assimilation of the rocks or magmas from the same IAB source by the aforementioned basite magmas. It is most probable that the IL dacites were generated by the differentiation of the Nb-poorest magmas of the ACM1 type.

Figure 13 shows an obvious direct correlation between the Nb and Si concentrations in all of the volcanic associations. This figure also implies that (1) the sources of the SiO₂-poorest basite magmas of all associations vary from IAB through N-MORB to EMORB [with the Nb concentration increasing in the succession ACM1–IAB; ACM2 and Devonian–IAB (or N-MORB) + E-MORB; BUU, BLU1—same but with enrichment in E-MORB; BLU2—E-MORB] at unchanging silicity, which testifies that the magma compositions were affected by

their sources but not magma derivatives; and (2) the reason for the direct correlation between the Nb and SiO₂ concentrations in the BLU2 association can be either magma differentiation or upper-crust assimilation by the magma. An analogous correlation between the Nb and SiO₂ concentrations in the magmas of other associations was obviously caused by magma differentiation, because the evolutionary trajectories lie beneath CC.

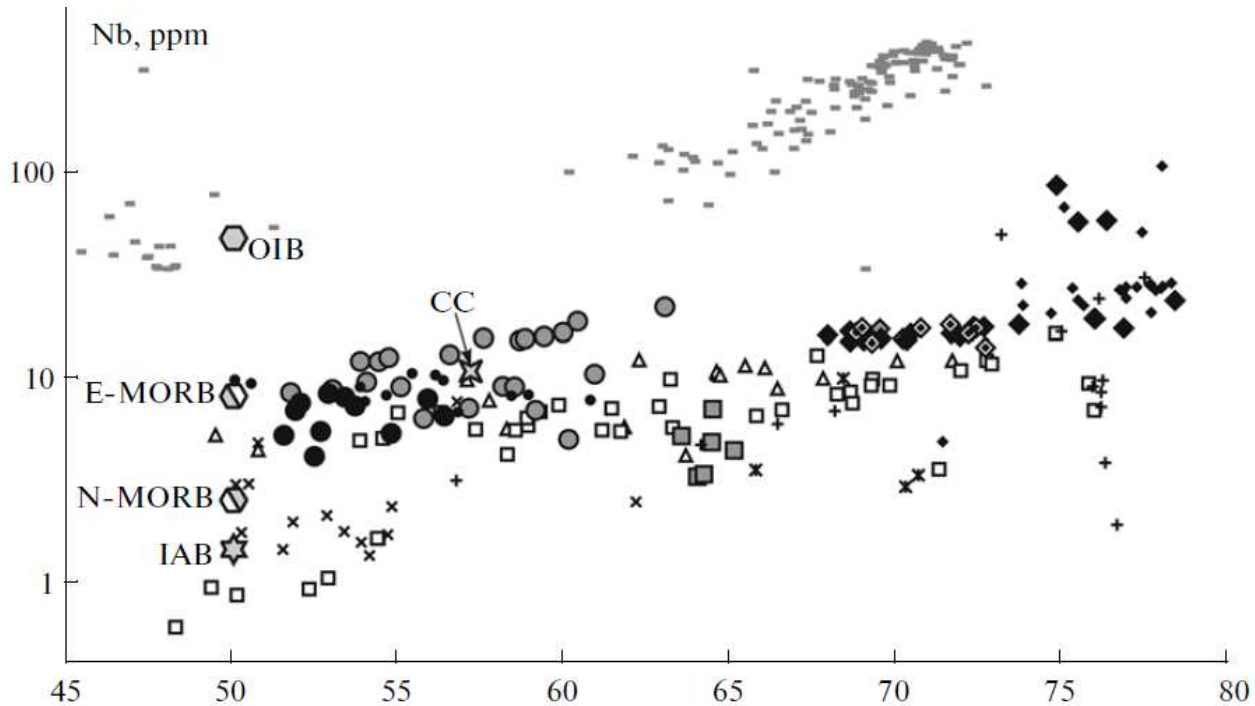


Fig. 13. Variations in the Nb versus SiO₂ concentrations in rocks of the han-Bogd area. See Fig. 4 for symbol explanations and Fig. 8 for model sources.

Finally, many comendite and trachyrhyolite compositions cluster around subduction component β at the same low Nb/U \sim 3–6 (Fig. 10b), which could be produced by the differentiation of basite magmas derived from a source of the IAB type. Since this differentiation trend for the comendites and trachyrhyolites continues with further Nb enrichment compared to composition β , it is unlikely that composition β is an occasional product of basite magma differentiation, and an individual source for composition β should have existed. Such a source could be either basites related to an IAB source [any of those listed above, including ophiolites, particularly those affected by spilitization (Kovalenko et al., 2009a) and anatexis] or the upper continental crust (Figs. 10b, 11b). If the latter was generated by evolving subduction magmas, as many researchers believe, it should have had canonical values typical of this environment (for instance, Nb/U = 3–6), which suggests either that the examined visible vertical section of the bimodal association is incomplete or that these acid volcanics were generated by the anatexis of spilitized ophiolitic basites, including compositions with such high Nb/U ratios.

Another distinctive feature of the Khan-Bogd depression is a La/Yb ratio elevated compared to the average IAB composition, perhaps, due to magma differentiation or a certain regional specifics of the sources. Figure 10c shows that the La/Yb ratio of the ACM volcanics increases with increasing degree of differentiation, which is, however, not the case with the rocks of the Devonian and bimodal associations. Moreover, the compositions of ACM, BLU, and BUU in Fig. 11c group within fields with similar La/Yb ratios, and these fields shift toward higher La/Yb ratios, with silicity increasing from ACM1 to BLU. We believe that these dependences can be accounted for by the addition of a progressively increasing fraction of sources like OIB or CC to sources of the IAB and MORB types (Fig. 11c). The further differentiation of all magmas, including BLU, perhaps, with the participation of upper-crust assimilation, resulted in an increase in the silicity of the residual magmas. Hence, we admit that the elevated values of the La/Yb ratio of the volcanic rocks can be related either to the addition of OIB to the magma source and the further differentiation of the magma or to the assimilation of the upper continental crust by these magmas and, again, the subsequent differentiation of the magmas.

The variations in the canonical ratios of incompatible trace elements in volcanic rocks of the Khan-Bogd depression suggest that the parental magmas were derived mostly from an IAB source, to which variable proportions of a MORB source were added. The greatest contribution of the latter was identified in the magmas of the bimodal association (BLU2–E-MORB for BLU1 and BUU-N-MORB). These data are consistent with the petrochemical characteristics of the rocks (see above), with the calcalkaline low-Ti Devonian and ACM series of normal alkalinity give way to the intermediate high- and moderate-Ti subalkaline BLU association and then to the moderate-Ti BUU association. The BLU and BUU associations are separated by IL, which is most likely of the calcalkaline series, a fact suggesting that bimodal volcanism continued simultaneously with normal andesite island arc volcanism (of the ACM1 type). Features of adakite compositions in the younger BLU and IL associations suggest that the magma source had an elevated temperature (hot lithosphere subduction).

Evolution of Geodynamic Environments in the Geological History of the Khan-Bogd Depression and the Origin of Comendites and Trachyrhyolites

Analysis of geological, geochronological, petrochemical, and geochemical data on volcanic rocks in the Khan-Bogd depression, first of all, in the southern surroundings of the Khan-Bogd alkali granite massif, indicates that, although geodynamic environments changed during the geological evolution of the depression, the predominant environment was that of a subduction one, and the source of volcanism was of the IAB type. The Devonian basement of the depression and the ophiolites of the southern Mongolian Hercynides as a whole were produced in an island-arc environment (Yarmolyuk et al., 2007; Khashgerel

et al., 2006), whereas the volcanics of the stratigraphically lowermost portion of the depression were produced in an ACM environment and are separated from the Devonian association by a conglomerate unit. Inasmuch as canonical ratios of incompatible trace elements used as indicators of geodynamic environments change only insignificantly in these associations, it is reasonable to admit that the early volcanic associations had similar sources. The subduction volcanic associations are differentiated and vary in composition from basites to dacites and rhyolites. We cannot rule out that the acid rocks of these associations were produced with the participation not only of the differentiation of the magma but also of the assimilation of acid continental crustal material by the magma. The ACM volcanic association is subdivided into the most primitive ACM1, which occurs in the northwestern peripheral part of the Khan-Bogd Massif, and ACM2, which has usual compositions and is predominant. With the transition from the ACM association to BLU, which is not accompanied by any significant stratigraphic or structural unconformity, the geodynamic situation changes: the BLU1 volcanics preserve all geochemical features of the ACM2 association, while the BLU2 rocks have elevated alkalinity, TiO₂ concentrations, are a transitional type from the calc-alkaline to tholeiite series, show evidence of the participation of mantle sources most likely of the E-MORB type, and are similar to adakites. It is commonly thought that such volcanic associations are generated when a subduction zone is approached by an mid-oceanic ridge (MOR), and hence, the convection cell in the asthenosphere between MOR and ACM becomes narrower, and volcanism of the E-MORB type is predominant in the MOR (Donnelly et al., 2004) and significantly adds to subduction volcanism. This unusual volcanism related to mixed sources alternates with normal subduction volcanism (IL dacites) and ends with tholeiitic moderate-Ti volcanism of normal alkalinity of BUU. In its basite part, this volcanism is weakly differentiated, with widespread comendites and trachyrhyolites, and is thus close to classic bimodal volcanism. The hypothetical similarity of this volcanism to a subduction source of the IAB type in terms of additional source (of the N-MORB type) testifies that the arc and MOR environments became even closer when the BUU was produced. The closeness of BLU and IL volcanics to adakites likely suggests that their magmatic source involved subducted oceanic crustal material (Hercynian ophiolites), and their origin is often thought to be related to the development of an asthenospheric window in a subduction zone, which is, in turn, caused by MOR subduction. The evolution of volcanism in the Khan-Bogd depression with the alternation of geodynamic environments and changes in the rock composition generally resembles the evolution of the western margin of North America in the Cenozoic (Zonenshain et al., 1973; Kovalenko et al., 1983; Yarmolyuk and Kovalenko, 1991) with an analogous evolutionary succession of volcanism: first, of normal subduction type and, then, bimodal, with vast volumes of comendites in the Basin and Range Province during the collision of the East Pacific Rise with the western margin of North America. If this analogy is realistic, it should prove the physical

probability of the origin of agpaitic acid rocks, which are unusual in subduction environments in an environment of subduction and MAR collision with a continental plate. In our earlier papers, we referred to such a complicated geodynamic environment as a Californian one, but this does not explain as to how comendites and trachyrhyolites can be formed in such environments.

The analysis of magma complexes (melt inclusions) from various geodynamic environments (Kovalenko et al., 2009b) indicates that acid agpaitic magmas can be generated in any geodynamic environments but occur in various proportions with acid nonagpaitic magmas. For example, although their fraction among acid magmas is higher in within-plate continental environments than in island-arc and ACM environments, these magmas occur in all of the environments. A precondition necessary for the derivation of acid agpaitic magmas in any environments, including arc ones, is the presence of basite magmas of elevated alkalinity, close to analogous magmas in continental environments, in which the proportion of agpaitic acid magmas is at a maximum. In normal arc magmas, the amount of such parental basite magma is low and, correspondingly, acid agpaitic rocks are rare and occur in subordinate amounts compared to nonagpaitic ones. Another prerequisite for the derivation of acid agpaitic magmas is the ability of the parental magmas to profoundly differentiate up to the derivation of acid melts, whose fraction increases with the evolution of the parental magmas. The former condition is met in natural magmatic systems, first of all, via Bowen's plagioclase effect (Bowen, 1945), if the agpaitic coefficient of a melt (Fig. 12a) in equilibrium with plagioclase is higher than that without plagioclase. This effect is manifested in practically all volcanic associations, as follows from the direct correlations between the agpaitic coefficient and the Eu/Eu^* ratio (Fig. 12b), with the parental basite magmas not necessarily being highly alkaline. The latter takes place in the volcanics of the BLU association, which includes all transitional rock compositions from basites through intermediate rocks to acid rocks. All of them have elevated alkalinity, comparable with that in model continental within-plate environments (as at Pantelleria Island in the Mediterranean Sea or the Gardar province in Greenland), and a small proportion of acid rocks compared to mafic and intermediate ones, as is typical of crystallization differentiation. The acid rocks of BLU have canonical ratios close to those in basite rocks, a fact testifying that the sources of the basite and acid magmas in this province were similar. Thus, we believe that acid agpaitic BLU rocks were produced by crystallization differentiation of magmas of elevated alkalinity. It is pertinent to mention that such crystallization differentiation should have proceeded at relatively shallow depths (under pressures of <9 kbar), because plagioclase effect needed for such differentiation can take place only within the plagioclase stability field.

This model is hardly applicable to BUU because, first, it includes associations of acid agpaitic magmas with tholeiitic basite magmas, whose crystallization differentiation does not lead to enrichment in silica to the level of acid magmas, and second, the alkalinity of these magmas is normal but not elevated, as is needed

to generate acid agpaitic magmas. Third, the volume of acid magmas in the BUU association is commensurable with the volume of basic magmas, which is at variance with the mechanism of crystallization differentiation. Fourth, the variations in the canonical ratios of concentrations of incompatible elements in the BUU acid magmas often differ from the analogous variations in the intermediate and basic magmas, a fact highlighting incomplete correspondence of the sources of the acid and basite magmas. To explain the genesis of the BUU association, we considered the model of the anatexis of basite rocks, particularly spilitized ones (Kovalenko et al., 2009a) or cumulates of their magmas, as was suggested for the bimodal association of Pantelleria Island (Mahood and Baker, 1986). The spilitization of basites results in an increase in their Na₂O concentrations, and this leads to an increase in the total alkalinity of the source to a level sufficient for trachyte. The differentiation of their magma can already bring about comendites and trachyrhyolites (Kovalenko et al., 2009a). The sources of BUU magmas in this model can be BLU basites, as well as spilitized BUU basites and even older subduction associations. It seems not to be coincidental that the comendite and trachyrhyolite compositions of the BUU include trachyte compositions close to primitive ones for acid agpaitic magmas. The differentiation of these or more silicic trachydacite magmas can result in the whole comendite–trachyrhyolite association in BUU.

The acid rocks of the BLU and BUU association were most probably generated by different mechanisms. The comendites and trachyrhyolites of the BLU association could admittedly be formed by the crystallization differentiation of a basite magma of elevated alkalinity, which, in turn, could be derived in an island-arc (subduction) environment that was modified by a MOR zone approaching the subduction zone (at IAB + E-MORB sources). The acid rocks of the BLU association were produced by the anatexis of tholeiitic basites of this association, particularly spilitized ones (as well as any other basites), and the subsequent crystallization differentiation of the anatectic magmas. The tholeiitic basalts of the BUU, which are only paragenetically related to the comendites and trachyrhyolites, were formed in a subduction environment that was even more significantly modified by the approaching subduction zone of the Hercynian MOR (at IAB + N-MORB source). It is pertinent to consider the possible participation of a plume source in the origin of the comendites (Yarmolyuk et al., 2000; Kovalenko et al., 2006). It was mentioned above that material with OIB characteristics (first of all, the La/Yb ratio) could be involved in the origin of these magmas, but available data indicate that the probability of the participation of an OIB source could not be high. We have already mentioned above that the vertical section of the bimodal volcanics is likely incomplete. From the geological standpoint, there is no difference between the model presented above and the model for the occurrence of a mantle plume in the subduction zone: in any event, the subduction environment gave way to rifting, or they could alternate. If subduction dominated over lithospheric extension, subduction should have suppress extension or the opening

of the asthenospheric window in both situations, and terminated rifting, of course, if the mantle plume did not further develop. We also cannot rule out that deep subduction induced the ascent of mantle plumes (Kovalenko et al., 2009c; *Modern...*, 2008). If the latter are of predominantly thermal nature, the source of magmatism induced by them should have characteristics of the latest compositional transformations but not simply a plume source of the OIB type.

CONCLUSIONS

(1) The comendite-bearing sequence of volcanic rocks examined in the Khan-Bogd depression in the southern Mongolian Hercynides is as follows: the basement of the depression (Devonian ophiolites older than 362 Ma); ACM volcanic associations (330 Ma); bimodal association (290 Ma), which is subdivided in a lower unit (BLU), dacite of the intermediate layer (IL), and the bimodal association of the upper unit (BUU).

(2) The Devonian and ACM volcanic associations are calc-alkaline, low-Ti; the transition from the Devonian association to ACM is not associated with any significant changes in the composition of the volcanic rocks. Starting in BLU, the very first discernible traces of bimodality appear, the contents of TiO₂ and alkalis in the magmas increase, the differentiation of the magmas is associated with the transition from the tholeiite to calc-alkaline series with the origin of comendites, trachyrhyolites, and rocks similar to adakites. Analogues of calc-alkaline magmas of the ACM type appear again in the form of IL dacites. The BUU volcanic association consists of moderate-Ti tholeiite basalts (of the MORB type), comendites, and trachyrhyolites, with a compositional gap between basic and acid rocks. Indications of adakite compositions in the BLU and IL associations suggest that an asthenospheric window occurred in the subduction zone due to the subduction of a Hercynian mid-oceanic ridge, and that hot lithospheric material was involved in the magma sources.

(3) Variations in canonical ratios of incompatible trace elements in the volcanic rocks of the Khan-Bogd depression and the petrochemical parameters of these rocks suggest that they were derived from a major source of the IAB type with variable proportions of a source of the MORB type. The most significant involvement of the latter was detected in the magmas of the bimodal association (BLU2-E-MORB for BLU1 and BUU-N-MORB). BLU and BUU are separated by IL, which most likely belongs to the calc-alkaline series, which suggests that normal andesitic bimodal and arc volcanism continued simultaneously.

(4) Analysis of geological, geochronological, petrochemical, and geochemical data on volcanics of the Khan-Bogd depression indicates that although the geological evolution of the depression was associated with changes in the geodynamic environments, the predominant one was a subduction environment with a source of volcanism of the IAB type. This environment practically did not change throughout the whole time span when the Devonian basement of the depression and ophiolites in the southern Mongolian Hercynides (island arcs) as a

whole were formed, as well as the stratigraphically lowermost part of the depression itself (ACM). The subduction volcanic associations generated thereby are differentiated, vary in composition from basites to dacites and rhyolites, and could be produced with the participation of CC assimilation. We admit that the bimodal volcanic association was generated when the subduction zone was approached by a mid-oceanic ridge (volcanism of the E-MORB type, whose material could be added in significant amounts to the subduction volcanism). The evolution of volcanism in the Khan-Bogd depression generally resembles the evolution of the western margin of North America in the Cenozoic in terms of the evolution of geodynamic environments and compositional specifics of volcanism.

(5) The acid rocks of the BLU and BUU associations were more likely formed in different manners.

The comendites and trachyrhyolites of the BLU association seem to be generated by the crystallization differentiation of basite magma of elevated alkalinity, which was, in turn, produced in an island-arc (subduction) geodynamic environment modified by a mid-ocean ridge approaching the subduction zone (IAB + E-MORB sources). The acid rocks of the BLU association resulted from the anatexis of the tholeiitic basites of this association (IAB + N-MORB sources), first of all, spilitized (as well as any other) basites and the subsequent crystallization differentiation of the anatectic magmas.

REFERENCES

1. Bowen, N.L., Phase Equilibria Bearing on the Origin and Differentiation of Alkaline Rocks, *Amer. J. Sci.*, 1945, vol. 248-A, pp. 75–89.
2. Donnelly, K.E., Goldstein, S.L., Langmuir, C.H., and Spiegelman, M., Origin of Enriched Ocean Ridge Basalts and Implications for Mantle Dynamics, *Earth Planet. Sci. Lett.*, 2004, vol. 226, pp. 347–366.
3. Dunbar, N.W. and Kyle, P.R., Volatile Contents of Obsidian Clast in Tephra from the Taupo Volcanic Zone, New Zealand: Implications to Eruptive Processes, *J. Volcanol. Geotherm. Res.*, 1992, vol. 49, pp. 127–145.
4. Durante, M.V., Zonenshain, L.P., Goreglyad, A.V., et al., Geological Position of the Khan-Bogd Alkaline Massif, Mongolia, *Byull. Mosk. O-va Ispyt. Prir., Otd. Geol.*, 1976, no. 4, pp. 85–104.
5. Ewart A., Taylor, S.R., and Capp, A.C., Geochemistry of the Pantellerites of Mayor Island, New Zealand, *Contrib. Mineral. Petrol.*, 1968, vol. 18, pp. 116–140.
6. Houghton, B.F., Weaver, S.D., Wilson, C.J.N., and Lanphere, M.A., Evolution of a Quaternary Peralkaline Volcano: Mayor Island, New Zealand, *J. Volcanol. Geotherm. Res.* 1992, vol. 51, pp. 217–236.
7. Khashgerel, B.E., Rye, R.O., Hedenquist, J.W., and Kavalieris, I., Geology and Reconnaissance Stable Isotope Study of the Oyu Tolgoi Porphyry Cu–Au System, South Gobi, Mongolia, *Econ. Geol.*, 2006, vol. 101, pp. 503–522.
8. Kovalenko, V.I., *Petrologiya i geokhimiya redkometal'nykh granitoidov* (Petrology and Geochemistry of Rare-Metal Granitoids), Novosibirsk: Nauka, 1977.
9. Kovalenko, V.I., Kozlovsky, A.M., and Yarmolyuk, V.V., Trace Element Ratios as Indicators of Source Mixing and Magma Differentiation of Alkali Granitoids

and Basites of the Haldzan-Buregtey Massif and the Haldzan-Buregtey Rare-Metal Deposit, Western Mongolia, *Petrologiya*, 2009a, vol. 17, no. 2, pp. 175–196 [*Petrology* (Engl. Transl.), vol. 17, no. 2, pp. 158–177].

10. Kovalenko, V.I., Kuz'min, M.I., Pavlenko, A.S., and Perfil'ev, A.S., South Gobi Belt of Rare-Metal Alkaline Rocks of Mongolia and its Structural Position, *Dokl. Akad. Nauk SSSR*, 1973, vol. 210, no. 4, pp. 911–914.

11. Kovalenko, V.I., Kuz'min, M.I., Zonenshain, L.P., et al., *Redkometal'nye granitoidy Mongolii (petrologiya, raspredelenie redkikh elementov i genesis)* (Rare-Metal Granitoids of Mongolia: Petrology, Trace-Element Distribution, and Genesis), Moscow: Nauka, 1971.

12. Kovalenko, V.I., Massakovskii, A.A., and Yarmolyuk, V.V., Petrochemical Zoning and the Reconstruction of Geodynamic Settings: Evidence from the Mongolian Segment of the Eurasian Late Paleozoic Volcanic Belt, *Geotektonika*, 1983, no. 6, pp. 13–29.

13. Kovalenko, V.I., Naumov, V.B., Girnis, A.V., et al., Peralkaline Silicic Melts of Island Arcs, Active Continental Margins, and Intraplate Continental Settings: Evidence from the Investigation of Melt Inclusions in Minerals and Quenched Glasses of Rocks, *Petrologiya*, 2009b, vol. 17, no. 4, pp. 437–456 [*Petrology* (Engl. Transl.), vol. 17, no. 4, pp. 410–427].

14. Kovalenko, V.I., Yarmolyuk, V.V., and Bogatikov, O.A., Regularities of Spatial Distribution of Mantle Hot Spots of the Modern Earth, *Dokl. Akad. Nauk*, 2009c, vol. 427, no. 5, pp. 654–658 [*Dokl. Earth Sci.* (Engl. Transl.), vol. 427, no. 6, pp. 924–928].

15. Kovalenko, V.I., Yarmolyuk, V.V., Kozlovsky, A.M., et al., Two Types of Magma Sources of Rare-Metal Alkali Granites, *Geologiya Rudn. Mestorozhd*, 2007, vol. 49, no. 6, pp. 506–534 [*Geol. Ore Dep.* (Engl. Transl.), vol. 49, no. 6, pp. 442–466].

16. Kovalenko, V.I., Yarmolyuk, V.V., Sal'nikova, E.B., et al., Geology, Geochronology, and Geodynamics of the Khan Bogd Alkali Granite Pluton in Southern Mongolia, *Geotektonika*, 2006, no. 6, pp. 52–72 [*Geotectonics* (Engl. Transl.), vol. 40, no. 6, pp. 450–466].

17. Liu, Y., Anderson, A.T., Wilson, C.J.N., et al., Mixing and Differentiation in the Oruanui Rhyolitic Magma, Taupo, New Zealand: Evidence from Volatiles and Trace Elements in Melt Inclusions, *Contrib. Mineral. Petrol.*, 2006, vol. 151, pp. 71–87.

18. Mahood, G.A. and Baker D.R., Experimental Constraints on Depths of Fractionation of Mildly Alkaline Basalts and Associated Felsic Rocks: Pantelleria, Strait of Sicily, *Contrib. Mineral. Petrol.*, 1986, vol. 93, pp. 251–264.

19. Martin, H., Adakitic Magmas: Modern Analogues of Archaean Granitoids, *Lithos*, 1999, vol. 46, pp. 411–429.

20. Naumov, V.B., Kovalenko, V.I., Babanskii, A.D., and Tolstykh, M.L., Genesis of Andesites: Evidence from Studies of Melt Inclusions in Minerals, *Petrologiya*, 1997, vol. 5, no. 6, pp. 654–665 [*Petrology* (Engl. Transl.), vol. 5, no. 6, pp. 586–596].

21. Nelson, S.A. and Hegre, J.A., Volcan Las Navajas, a Pliocene-Pleistocene Trachyte/Peralkaline Rhyolite Volcano in the Northwestern Mexican Volcanic Belt, *Bull. Volcanol.*, 1990, vol. 52, pp. 186–204.

22. *Noveishii vulkanizm Severnoi Evrazii: zakonomernosti razvitiya, vulkanicheskaya opasnost', svyaz' s glubinnymi protsessami i izmeneniyami prirodnoi sredy i klimata* (Youngest Volcanism of North Eurasia: Evolution Tendencies, Volcanic

Hazards, Relations with Deep Processes and Environmental and Climatic Changes), Kovalenko, V.I., Yarmolyuk, V.V., and Bogatikov, O.A., Eds., Vol. 2 of *Izmenenie okruzhayushchei sredy i klimata: prirodnye and svyazannye s nimi tekhnogennye katastrophy* (Environmental and Climatic Changes: Natural and Related Anthropogenic Catastrophes), Moscow: IGEM RAN, IFZ RAN, 2008.

23. *Tipy magm i ikh istochniki v istorii Zemli. Redkometal'nyi magmatizm: assotsiatsii porod, sostav i istochniki magm, geodinamicheskie obstanovki formirovaniya* (Magma Types and Their Sources in the Earth's History. Rare-Metal Magmatism: Rock Associations, Composition, and Sources of Magmas, and Geodynamic Settings of their Formation), Bogatikov, O.A. and Kovalenko, V.I., Eds., Moscow: IGEM RAN, 2006.

24. Vladykin, N.V., Kovalenko, V.I., and Dorfman, M.D., *Mineralogicheskie i geokhimicheskie osobennosti Khan-Bogdinskogo massiva shchelochnykh granitoidov (Mongol'skaya Narodnaya Respublika)* (Mineralogical and Geochemical Features of the Khan-Bogd Alkaline Granitoid Massif), Moscow: Nauka, 1981.

25. Workman, R.K. and Hart, S.R., Major and Trace Element Composition of the Depleted MORB Mantle (DMM), *Earth Planet. Sci. Lett.*, 2005, vol. 231, pp. 53–72.

26. Yarmolyuk, V.V., *Pozdnepaleozoiskii vulkanizm kontinental'nykh riftovykh struktur Tsentral'noi Azii* (Late Paleozoic Volcanism of Continental Rift Structures of Central Asia), Moscow: Nauka, 1983.

27. Yarmolyuk, V.V. and Kovalenko, V.I., *Riftogennyi magmatizm aktivnykh kontinental'nykh okrain i ego rudonosnost'* (Rift Magmatism of Active Continental Margins and its Ore Potential), Moscow: Nauka, 1991.

28. Yarmolyuk, V.V., Kovach, V.P., Kovalenko, V.I., et al., Isotopic Composition of the Hercynian Crust of Southern Mongolia: Substantiation of the Hercynian Juvenile Crust-Forming Event, *Dokl. Akad. Nauk*, 2007, vol. 416, no. 6, pp. 804–809 [*Dokl. Earth Sci.* (Engl. Transl.), vol. 416, no. 7, pp. 1178–1182].

29. Yarmolyuk, V.V., Kovalenko, V.I., and Kuz'min, M.I., North Asian Superplume Activity in the Phanerozoic: Magmatism and Geodynamics, *Geotektonika*, 2000, no. 5, pp. 3–29 [*Geotectonics* (Engl. Transl.), vol. 34, no. 5, pp. 343–366].

30. Yarmolyuk, V.V., Kovalenko, V.I., Kozlovsky, A.M., et al., Crust-Forming Processes in the Hercynides of the Central Asian Foldbelt, *Petrology*, 2008, vol. 16, no. 7, pp. 679–709.

31. Zonenshain, L.P., Kuz'min, M.I., Kovalenko, V.I., et al., Structural-Magmatic Zoning and Metallogeny of the Western Pacific Belt, *Geotektonika*, 1973, no. 5, pp. 3–21.

REDOX POTENTIAL OF DIAMOND FORMATION IN THE EARTH'S LOWER MANTLE

Ryabchikov I.D.

Institute of Geology of Ore Deposits, Petrography, Mineralogy, and Geochemistry, Russian Academy of Sciences, Staromonetnyi per. 35, Moscow, 119017 Russia;

Oxygen fugacity (f_{O_2}) is the main thermodynamic parameter controlling the processes of natural diamond formation. The formation of diamond in mantle rocks is possible within a limited range of f_{O_2} : increase of this value results in oxidation of diamonds with the formation of carbonates (magnesite in peridotite parageneses), whereas carbides may appear instead of diamond at very low values. In addition, at high values of thermodynamic hydrogen activity, diamond is resorbed with the formation of methane or other hydrocarbons.

It is established experimentally that, at ultrahigh pressures corresponding to the conditions of the lower mantle, magnesium metasilicate with a perovskite structure has such a high affinity to Fe^{3+} that Fe^{2+} should disproportionate with the formation of the metallic phase [1]. This process may be illustrated by the following reaction:



where *FP* is ferroperricite, *MPv* is magnesium metasilicate of the perovskite structure, and *FeNi* is a metallic iron–nickel alloy. The mineral association with participation of ferroperricite and metallic alloy controls at a level slightly lower than the iron–wüstite buffer according to the reaction



values calculated from the equilibrium constant depend on activities of FeO in ferroperricite and Fe in the metallic alloy. The behavior of nickel intensely incorporated in an iron rich alloy is a sensitive indicator of the presence of this alloy in equilibrium with iron–magnesium silicates. We calculated the distribution coefficient $K_d(Ni/Fe) = (Ni/Fe)^{FeNi}/(Ni/Fe)^{FP}$ characterizing nickel and iron exchange between metal and ferroperricite, from the equilibrium constant of the reaction



We applied thermodynamic data from the mutually consistent database in [2] for all materials participating in this reaction for calculations, except for stoichiometric iron oxide, for which thermodynamic characteristics were taken from [3].

The calculated value $K_d^{FeNi/FP}(Ni/Fe)$ is ~ 30 at 40GPa and 2000 K. A similar value is provided by calculations using thermodynamic constants from [4]. The behavior of nickel during the formation of the metallic alloy in equilibrium with

the mineral association of metaperidotite at the lower mantle parameters was modeled in the simplified Si–Fe–Mg–Ca–Ni–O system. The phase association of 79% *MPv* ($Mg\# = Mg/(Mg + Fe) \text{ (at)} = 0.96$), 16% *FP* ($Mg\# = 0.82$), and 5% of calcium metasilicate with the perovskite structure (*CPv*) was taken as a starting material before the segregation of this alloy according to the data of [5]. The concentration of nickel in the bulk composition of the system was accepted to be equal to the estimation for the primitive mantle [6]. To calculate the compositions of coexisting phases, we applied the equations of coefficients of Ni/Fe and Mg/Fe distribution between metallic alloy, *FP*, and *MPv*

$$K_d^{FP/MPv}(\text{Ni/Fe}) = (\text{Ni/Fe})_{FP} / (\text{Ni/Fe})_{MPv}, \quad (4)$$

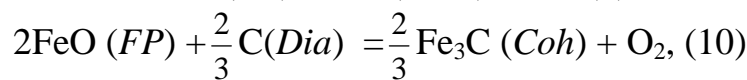
$$K_d^{FP/MPv}(\text{Mg/Fe}) = (\text{Mg/Fe})_{FP} / (\text{Mg/Fe})_{MPv}, \quad (5)$$

$$K_d^{FeNi/FP}(\text{Ni/Fe}) = (\text{Ni/Fe})_{FeNi} / (\text{Ni/Fe})_{FP}, \quad (6)$$

for which, according to our calculations (see above), $(\text{Ni/Fe}) = 30$ and, according to the experimental data [5], $(\text{Ni/Fe}) = 5$ and $(\text{Mg/Fe}) = 0.2$. In addition we applied equations of mass balance like $\sum C_i F_i = C_i^0$ where C_i is the concentration of this component in the i phase, F_i is the portion of the i phase in the system, and C_i^0 is the total concentration of the component in the system.

The solution of such system of equations allowed us to obtain the dependence between the concentration of nickel in the metallic alloy and its portion in the system (F_{met}) (Fig. 1). As is evident from this diagram, increase in the alloy portion results in decrease of the nickel concentration in it and synchronous decrease of this element concentration in the coexisting *FP* and *MPv*. This is explained by the transition of iron as a diluent for nickel dissolved in metal into the metallic alloy in an increasing concentration. This explains the remarkable increase of the Fe/Mg ratio in silicate and oxide solid solutions at high F_{met} values.

Based on the calculated compositions of the metallic alloy and ferropericlase for different proportions of the newly formed alloy, we estimated the values of oxygen fugacity for the equilibria with participation of *FP*, the metallic alloy, and carbon-bearing phases (magnesite, diamond, and cohenite). We applied the constants of equilibrium for the following reactions in these calculations:



where *MC* is magnesite, *Dia* is diamond, and *Coh* is cohenite. Thermodynamic constants for stoichiometric iron oxide and cohenite were taken from [3], and for the other components, from the database [2]. Parameters of the Margules equations describing deviations of the phases of variable compositions from the laws of ideal solutions were taken from [2, 7].

The results of these calculations are demonstrated as dependences of f_{O_2} (normalized to the values of oxygen iron–wüstite buffer, $\log(f_{\text{O}_2}/f_{\text{IW}})$) on the magnesium mole fraction of ferropericlase increasing with F_{met} growth. Decrease in f_{O_2} values occurs with an increase of F_{met} and the Mg/Fe ratio in ferropericlase

by synchronous decrease of FeO activity in the ferro-periclase and increase of the Fe activity in the metallic alloy.

The calculations given above were performed for one point on the adiabatic curve for the lower mantle [8] at 40 GPa and 1900 K. The relationships between the fields of magnesite, diamond, and cohenite stability will be the same as those demonstrated in Fig. 2 for other values of temperature and pressure typical for the upper part of the lower mantle.

Interpretation of experimental data on the concentrations in *MPv* equilibrated with metallic iron leads to the conclusion that metaperidotites of the lower mantle should contain ~1% of the metallic phase. In

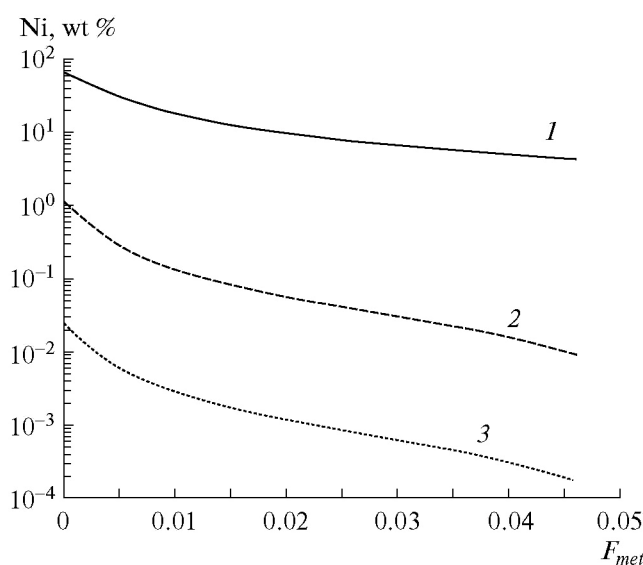


Fig. 1. Nickel concentration (wt %) in minerals of the phase association of the bulk metaperidotite composition at the lower mantle parameters depending on the weight portion of the newly formed metallic alloy (F_{met}). (1) *FeNi*; (2) *FP*; (3) *MPv*.

this case carbon should occur as iron carbide and the oxygen fugacity will correspond to the curve 3 (*FeNi* + *FP*) in Fig. 2. Curves 2 and 3 Fe_3C + *Dia* + *FP* and *FeNi* + *FP* approach a high nickel concentration in the metallic alloy (Fig. 2), and, within the uncertainty of applied thermodynamic constants, their crossing is not excluded. This demonstrates the possibility of existence of an iron–nickel alloy, iron carbide, and diamond. Actually the case of the presence of inclusions of iron carbides and the metallic alloy was registered in diamonds of the lower mantle origin [9]. However, in most cases inclusions in lower mantle diamonds comprise ferropericlase and high-pressure silicates (*MPv*, *CPv*, and *TAPP*), whereas metals and carbides are absent in them. This means that the oxygen fugacity in the zones of lower mantle diamond formation plots above curve 2 in Fig. 2.

The concentration of nickel in *FP* and *MPv* from inclusions in diamonds also provides evidence for more oxidized conditions relative to the equilibria including the iron–nickel alloy. As is evident from Fig. 1, at a portion of metallic alloy of

0.01 equilibrated with metaperidotite of the primitive mantle composition (estimation of the metal concentration in the lower mantle was performed on the basis of experimental data [1]), the concentration of Ni in *FP* and *MPv* decreases by an order of magnitude in comparison with the phase association without the iron–nickel alloy. However, the concentration of nickel in real fer-ropericlases from inclusions in diamonds is close to the estimations for the pyrolite bulk composition before the formation of the metallic alloy. Thus, ferro-periclases included in diamonds from the Kankan

790

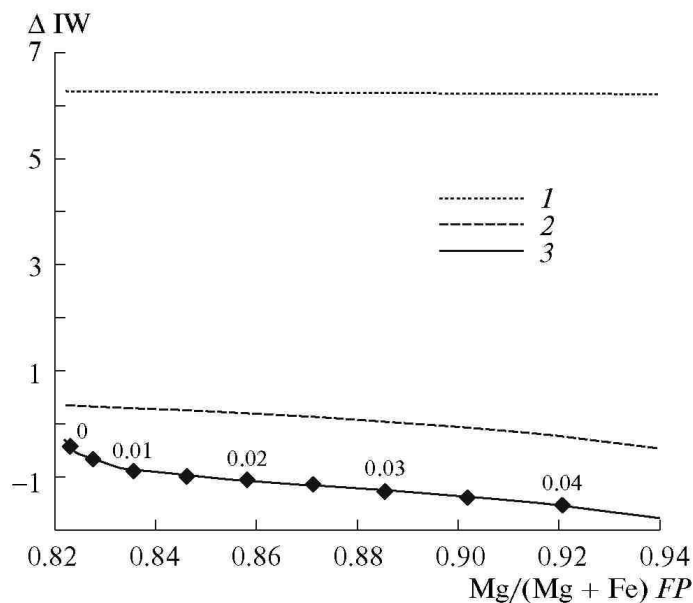


Fig. 2. Dependence of oxygen fugacity normalized by the iron–wüstite buffer ($\Delta IW = \log_{10}(f_{O_2}/f_{IW})$, where IW is the iron–wüstite oxygen buffer) for the phase equilibria described by the reactions (8)–(10) on the value of the atomic ratio $Mg/(Mg + Fe)$ in ferropericlase (*FP*). The compositions of metallic alloy and ferropericlase estimated for different portions of alloy formation in the mineral assemblage of lower mantle metaperidotite were applied for calculations (Fig. 1). (1) *MC + FP + Dia* (reaction (8)); (2) $Fe_3C + Dia + FP$ (reaction (10)); (3) *FeNi + FP* (reaction (9)). Rhombs denote points on curve 3 corresponding to the different values (numerals near symbols) of the weight portion of metallic phase F_{met} .

deposit (Guinea) are characterized by an average Ni concentration of 1 wt % [10], which is practically identical to the estimation at $F_{met} = 0$ (1.02 wt % Ni) illustrated by Fig. 1. The concentration of Ni in *MPv* crystals (Fig. 1, curve 3) is included in diamonds of the Kankan deposit (~0.02 wt %) and is close to the value on curve 3 (Fig. 1) at $F_{met} = 0$. This means that the pro-tolith in which diamonds of the Kankan deposit were formed did not contain a metallic alloy or its concentrations were very low.

As is evident from Fig. 2, the equilibrium of diamond with magnesium carbonate related to the upper boundary of the diamond stability (curve 1) lies

above the equilibrium of diamond with iron carbide (curve 3) by 6 logarithmic units of oxygen fugacity. Both iron carbides and carbonates are observed as inclusions in sublithospheric diamonds [9, 11, 12]. However, these finds are extremely rare, and in most cases crystalline inclusions in lower mantle diamonds are represented by *FP*, *MPv*, and *CPv*. Hence, it follows that typical values of oxygen fugacity in the zones of the lower mantle diamond formation lie between the values for the iron–wüstite buffer and the value of six logarithmic units above this level. Significant differences in f_{O_2} values for equilibria of lower mantle minerals with magnesite and the metallic alloy mean that carbonate activities should be extremely low ($\sim n \times 10^{-6}$) for typical lower mantle mineral parageneses including the iron–nickel alloy. Under these conditions, neither the appearance of crystalline carbonates nor the remarkable concentration of carbonate-ion in the melt is possible for the most part of the lower mantle.

Finds of diamonds of a lower mantle source in one case with inclusions of carbonate material and, in the other case, with carbides and the metallic phase provide evidence for processes resulting in variations of f_{O_2} values by several orders of magnitude in the lower mantle. As this takes place, the formation of lower mantle diamonds requires higher f_{O_2} values in comparison with those usual for the lower mantle.

Mechanisms responsible for redox differentiation in the lower mantle may comprise subduction of oxidized material of crustal origin, mechanical separation of the metallic phase and silicate–oxide mineral association enriched in ferric iron, as well as mantle transport of molten silicate material presumably enriched in Fe^{3+} .

The contribution of the material of the subducted oceanic crust in the formation of lower mantle meta-peridotite parageneses is neither supported by the major element composition of *FP* and metasilicates included in diamonds (consistent with the composition of lithospheric mantle peridotites) nor by the carbon isotope composition in diamonds containing inclusions of lower mantle minerals (usually the isotope composition of mantle carbon [13]).

The transportation of metallic components in the lower mantle may be gained by their partial dissolution in the mobile sulfide melt. We should account for the fact that the eutectic with the metallic phase in the Fe–S system is strongly shifted towards metallic iron (this is a practically diluted sulfide solution in metallic liquid), and its temperature is lower than estimations for the lower mantle adiabatic curve [14]. If this sul-fide–metal melt is accumulated in one area of the lower mantle and depleted in the other areas, decrease of pressure during the uprising transport of mantle material will result in the appearance of areas with low f_{O_2} values in the first case and high values, in the second case. The areas of the high redox potential formed in such a manner may be favorable for diamond formation.

Redox differentiation of the lower mantle material may result from the processes of partial melting of deep-seated material as well. In basaltic magmatism Fe^{3+} behaves as a moderately incompatible element enriching the melt relative to crystalline minerals. This is most likely true for processes of magma formation in

deep zones of the global silicate shell of the Earth as well. The zones enriched in melt as a result of its inter-granular filtration in mantle rocks, in this case, after ascent and decompression, will be characterized by relatively high f_{O_2} values, and consequently, they will be favorable for the formation of diamonds in the upper part of the lower mantle. Participation of near-solidus silicate melts in the formation of geochemical peculiarities of the zones of lower mantle diamond formation is supported by the observed increase of the concentration of more incompatible elements (LREEs in comparison with HREEs) in rocks from which sublithospheric diamonds were extracted [15].

The model geotherm for most of the lower mantle lies below the silicate solidus of metaperidotite in the absence of volatile components [8], which makes the magma formation problematic there. Partial melting becomes possible in the zone that is close to the mantle/core boundary with rapid growth of temperature with depth. Most likely, it is this place where redox differentiation takes place preparing conditions for the formation of diamonds during subsequent uprising transport of this material. It is not excluded that the formation of near-solidus melts may proceed during pressure decrease in the hot matter of uprising mantle plumes. In any case, the environment of the deepest mantle plumes going through the lower mantle from the zones close to the boundary with the metallic core is the most probable for the formation of lower mantle diamonds.

ACKNOWLEDGMENTS

This study was supported by the Russian Foundation for Basic Research (project no. 11-05-00247-a), the Earth Science Section, Russian Academy of Sciences (Program no. 2), and the Presidium of the Russian Academy of Sciences (Program no. 2).

REFERENCES

1. **D. J. Frost, C. Liebske, F. Langenhorst, et al.**, *Nature* 428, 409–412 (2004).
2. **T. J. B. Holland and R. Powell, J.** *Metamorphic. Geol.* 16, 309–343 (1998).
3. **R. A. Robie, B. S. Hemingway, and J. R. Fisher**, *Thermodynamic Properties of Minerals and Related Substances at 298.15 K and 1 bar (105 Pascals) Pressure and at Higher Temperatures* (United States Gov. Print. Office, Washington, 1978).
4. **A. J. Campbell, L. Danielson, and K. Righter**, *Earth Planet. Sci. Lett.* 286, 556–564 (2009).
5. **B. J. Wood**, *Earth Planet. Sci. Lett.* 174, 341–357 (2000).
6. **H. Palme and H. S. C. O'Neill**, *Treatise on Geochemistry. V. 2. The Mantle and Core* (Elsevier, Amsterdam, 2003), pp. 1–38.
7. **D. J. Frost**, *Am. Mineral.* 88, 387–397 (2003).
8. **S. Ono**, *Phys. Earth and Planet. Interiors* 170, 267–273 (2008).
9. **F. Kaminsky and R. Wirth**, *Acta Mineral.-Petrograph. (S z e g e d) . A b s t r. S e r.* 6, 180 (2010).
10. **T. Stachel, J. W. Harris, G. P. Brey, and W. Joswig**, *Contrib. Mineral. Petrol.* 140, 16–27 (2000).

11. **R. Wirth, F. Kaminsky, S. Matsyuk, and A. Schreiber**, *Earth Planet. Sci. Lett.* **286**, 292–303 (2009).
12. **F. Kaminsky, R. Wirth, S. Matsyuk**, et al., *Mineral. Mag.* **73**, 797–816 (2009).
13. **B. Harte**, *Mineral. Mag.* **74**, 189–215 (2010).
14. **L. Chudinovskikh and R. Boehler**, *Earth Planet. Sci. Lett.* **257**, 97–103 (2007).
15. **T. Stachel, G. P. Brey, and J. W. Harris**, *Elements* **1**, 73–78 (2005).

Petrology and composition of rare-metal alkaline complexes of the South Gobi, Mongolia

Vladykin N.V.

*Institute of Geochemistry, Siberian Branch of Russian Academy of Sciences, E-mail:
vlad@igc.irk.ru*

ABSTRACT

The belt of massifs containing alkaline granites [4] and the carbonatite province were earlier discovered in the southern Mongolia. The Lulingol massif of pseudo-leucite syenites with carbonatites was included into the alkaline granitic belt. The obtained new age determinations of the Lulingol massif indicates that it is 40 Ma younger than the Khan-Bogdo massif [26,12] and is separated from the alkaline granitic belt by a large fault. In addition to the Lulingol massif the same site of the south Gobi contains a series of dykes of alkaline K-shonkinites with a vein of rare-metal carbonatites located westwards of the Lulingol massif close to the Barun-Khasar-Ula city. To the north-east of the Lulingol massif there is a series of dykes of alkaline and nepheline syenites. These data allow distinguishing the intrusive complex of K-alkaline rocks - shonkinites and leucite syenites with the Upper Paleozoic TR-bearing carbonatites. Thus, 3 complexes of alkaline rocks of different age are found in the south Gobi. The article gives specified geologic maps of all three complexes. Massifs of all three complexes are deposits of rare elements (TR, Nb, Zr, Y and P). The chemical composition of silicate rocks of the complex, rare-metal apatitic pegmatites, carbonatitic and apatitic rare-metal ores is discussed in detail. Based on similar chemical, mineral and geochemical rare-metal composition of shonkinites of the Barun-Khasar-Ula and Mountain Pass (USA), their carbonatites and carbonatites of the Lulingol massif we came to the conclusions that all of them belong to a common formation complex of K-alkaline rocks and carbonatites. Using TR spectra and spider diagrams we demonstrate the generality and distinctions of rare-metal rocks from three complexes, as well as the difference in parageneses of their rare-metal minerals. We describe a rare process of transformation of rare-metal minerals into amorphous state. This process is associated with high-temperature of their crystallization in the chemical environment of anomalous silica content in pegmatites of the Khan-Bogdo massif. The source of the primary magmas of alkaline-carbonatite complexes is the contaminated EM-2 mantle, which underwent the recycling while for the Khan-Bogdo apatitic alkaline granites this source is the depleted mantle.

INTRODUCTION

The Soviet-Mongolian expedition of Academy of Sciences of former USSR and the Academy of Sciences of Mongolia that conducted prospecting works in Mongolia in the period from 1967 to 1988 discovered a number of alkaline complexes containing rare-metal mineralization. These discoveries are related to the name of the Russian scientist Academician **Vyacheslav Ivanovich Kovalenko** and the group of scientists from the laboratory of geochemistry of rare elements of IGC SB RAS headed by him. Li-F type of rare-metal granites was distinguished in Mongolia and the magmatic genesis of these formations which were earlier

[26]. However, alkaline leucite massifs do not occur separately thus the question concerning the formation type of the Luginol massif is still open. Later, in 30 km westwards of the Luginol massif close to Barun-Khasar-Ula city the Mongolian geologist Zeden discovered a dyke of rare-metal carbonatites containing bastnaesite, and V.I. Kovalenko found dykes of K-shonkinites. The author of the article discovered the dyke of nepheline syenites (40 % of nepheline) and 7 dykes

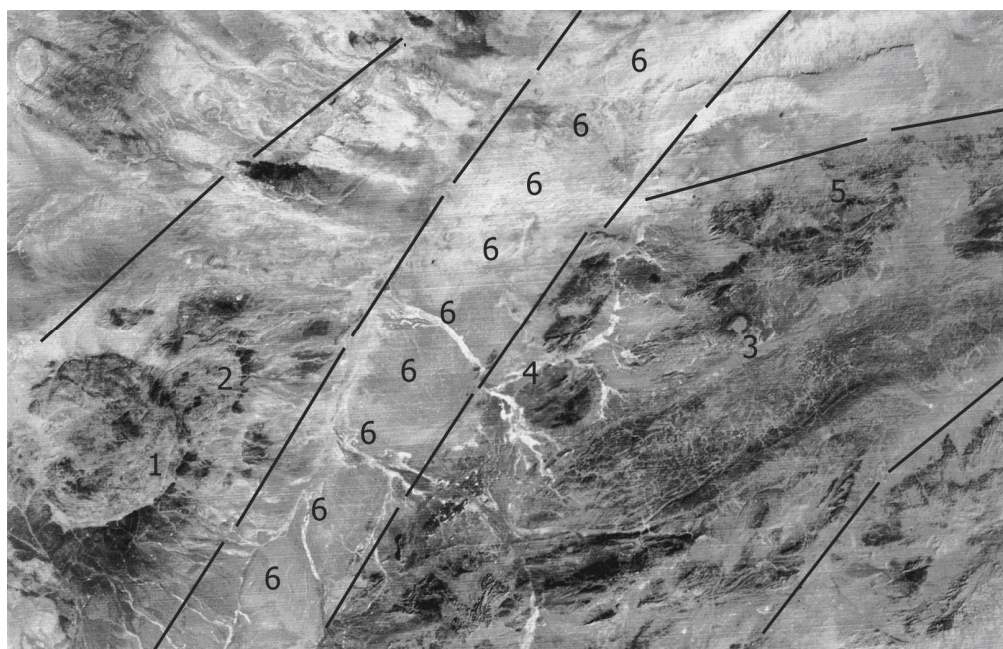


Fig. 2. Space picture of the South Gobi.

Khan-Bogdo massif: 1- Big ring, 2 – Small ring, 3 – Luginol massif, 4 – Barun-Khasar-Ula, 5 – area of alkaline dykes, 6 – Dzun-Bain regional fault.

of alkaline syenites in the area of Loon-Obo city in 40 km to the north-east of the Luginol massif. Thus, three occurrences of K-alkaline rocks are known by now in this area. So, it is enough to unite them into independent formation type of alkaline rocks in the South Gobi. In addition, the area of these massifs is separated from the Khan-Bogdo massif by a large Dun-Bain fault [27] which is well visible on space picture (Fig. 2). In the South Gobi Mongolia we suggest to distinguish ore-bearing complexes of three genetic formations:

1) the Mesozoic volcanogenic complex of K-Na alkaline rocks with carbonatites and hessonites with the Mushugai-Khuduk ore-bearing site (120-150 Ma);

2) the Upper Paleozoic intrusive complex of K-alkaline rocks (shonkinites and leucite syenites) with TR-ore-bearing carbonatites including the Luginol massif (250 Ma);

3) the Upper Paleozoic alkaline intrusive complex of agpaitic rocks with ore-bearing Khan-Bogdo massif (290-300 Ma) (Fig. 1).

All these complexes are associated with the Permian-Carbonaceous and Jurassic rifting of the South Gobi [27]. The ore-bearing carbonatites, apatite rocks (nelsonites) and agpaitic-pegmatite- ekerite granites are associated with large TR-F-P and Zr-Nb-TR deposits, which are unique in genesis [8, 9, 10]. Their studies are of great importance.

The South-Gobi carbonatite province [14] includes 7 sites which stretch from the east to the west over 300 km.

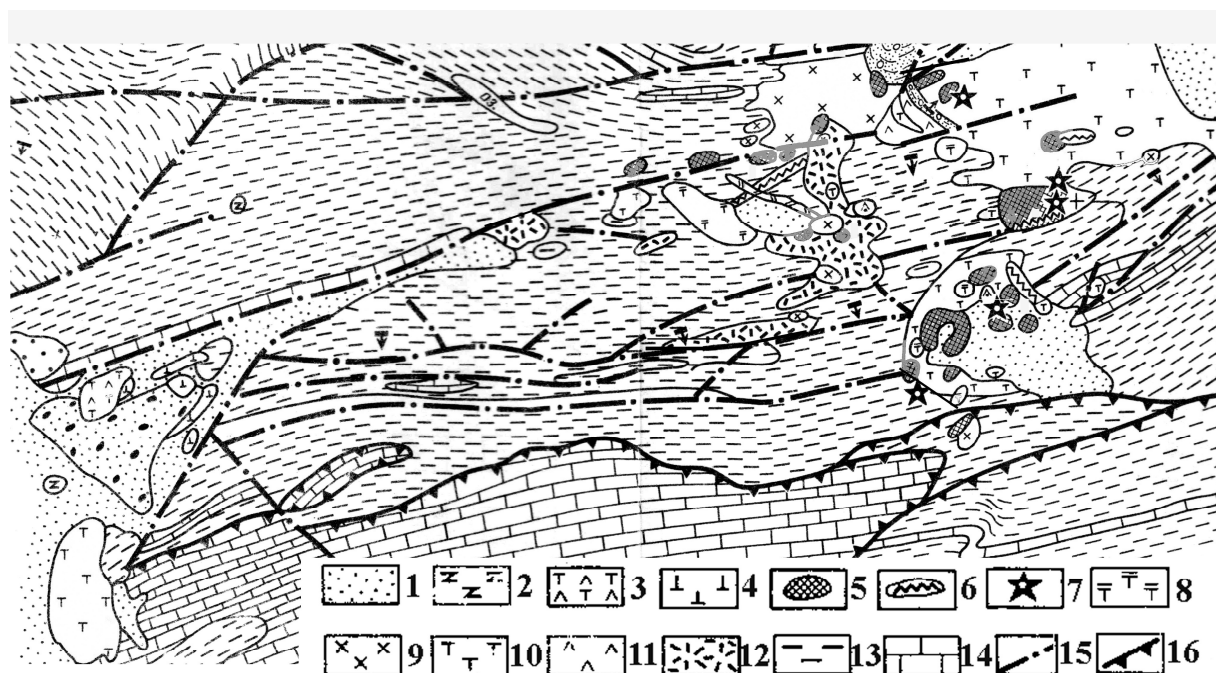


Fig. 3. Geologic structure of the Mushugai-Khuduk complex.[14].

1 – Quaternary sediments; 2 – olivine basalts; 3 – trachyte-latites ($MZ_2 tr_4$); trachyrhyodacite-trachytodacites ($MZ_2 tr_3$); 5 – ore potential sites; 6 - the largest ore-bearing sites; 7 – remnants of volcanoes; 8 - subvolcanic trachytes, trachyrhyodacites, syenite-porphyrines; 9 – syenites; 10 – subalkaline trachytes ($MZ_2 tr_2$); 11 – melenephelenites – melaleucites ($MZ_2 tr_1$); 12 – liparites (P_2); 13 – terrigenous-volcanogenic, 14 - carbonate; 15 – tectonic dislocations; 16 – thrust faults.

The Mushugai-Khuduk is the largest among the ore-bearing sites. The volcanic field Mushugai-Khuduk is located in 70 km to the northwest of the aimak Daland-zadgad. The geological map of the area is given on Fig. 3. The age of volcanic fields, intrusive stocks, small massifs of alkaline rocks is Jurassic (120 - 150 Ma). Several fields of volcanic flows and crater volcanic structures of different composition are distinguished [14]. The earliest among them is the volcano of K-Na alkaline-ultrabasic composition composed of intercalating tuff lavas, tuff breccias and lava flows of melaleucitite-melanephelenite composition. Lavas cut the dyke of micaceous shonkinites and numerous fine veins and dykes of calcite and calcite-fluorite carbonatites. The largest volcanic field of the trachytic composition occurs in the western part of the site. It contains lava and tuff-lava

flows and it is cut by numerous dykes (not less than 500) of volcanogenic fine and super-fine carbonatites of calcite and calcite- fluorite composition. This field also contains stocks of apatite – magnetite rocks (nelsonites) and apatite-fluorite-magnetite - celestine rocks [11]. Some small volcanic structures of teralites,

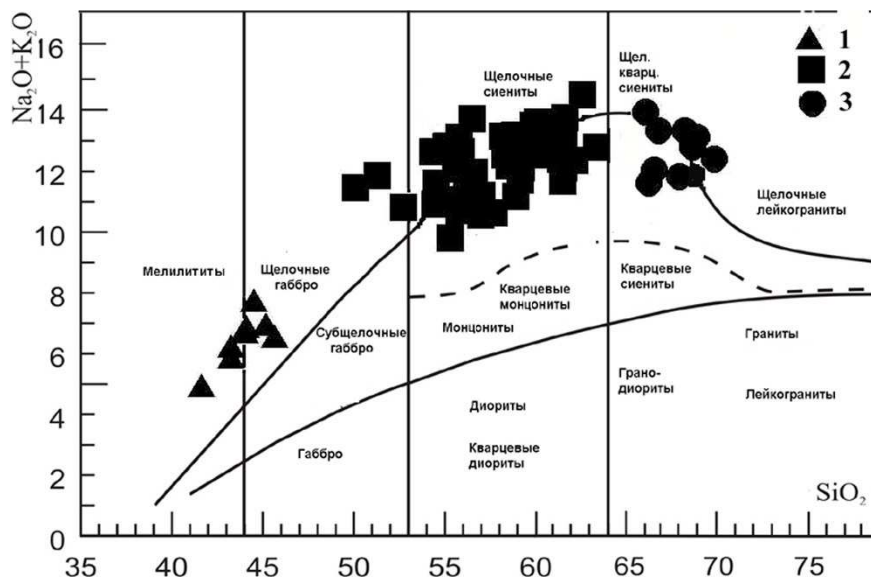


Fig. 4. Classification diagram of alkalis silica for the Mushugai-Khuduk rocks.

1 - melanephelenites-melaleucitite, 2 - trachytes, syenites, 3 - trachyrhyodacites-trachyliparites. (in wt.%)

craters of which are filled with potassium-feldspar breccias of stockwork type, which is cemented by calcite-fluorite-quartz carbonatites, containing up to 3 wt.% of TR. Fields of trachyte lavas cut three small stocks of nepheline and alkaline syenites, which possibly are strongly eroded volcanic structures and trachyte-phonolite lava in them is crystallized as nepheline and alkaline syenites, These crystallized rocks also cut the dykes of calcite and calcite-fluorite carbonatites. The latest magmatic rocks of the complex is the liparite dyke, cutting even the carbonatites. It is located in the central part of the Mushugai volcanic field. The eastern part of the field contains lava flows of phonolites, which overlap the older lavas of trachyrhyodacite composition. The eastern margin of the field is terminated by younger shield volcanoes of alkaline basaltic composition.

The representative analyses of silicate rocks of the Mushugui-Khuduk volcanic field are given in Table 1. On the classification alkali versus silica diagram the points of compositions of volcanics lie on the line of alkalis (Fig. 4), forming a common series from alkaline-ultrabasic rocks (melaleucitite-melanephelenites), with a greater field of rocks with average chemical composition (different trachytes, phonolites and their intrusive analogues - alkaline and nepheline syenites), up to rocks of acid composition (trachyrhyodacite-trachylaparites). Silicate volcanic rocks of the Mushugui-Khuduk field are thoroughly studied [14].

Table 1.

Chemical composition of silicate rocks (in wt.%) of the Mushugai-Khuduk field.

№	1	2	3	4	5	6	7	8	9	10	11	12	13
SiO ₂	45,1	44,4	44,0	54,1	55,0	56,3	57,0	58,9	61,0	61,7	61,6	67,6	69,8
TiO ₂	1,18	1,10	1,17	1,12	1,13	1,17	1,30	0,80	0,75	0,83	0,59	0,45	0,40
Al ₂ O ₃	14,2	13,9	13,9	16,7	16,1	14,8	15,5	17,6	17,0	17,1	17,2	14,9	14,7
Fe ₂ O ₃	4,08	4,77	4,13	3,80	3,03	3,27	4,61	3,31	3,45	2,26	2,56	0,20	2,87
FeO	4,13	3,05	4,49	2,15	3,51	2,51	1,62	0,72	0,90	2,33	1,25	2,35	0,28
MnO	0,16	0,16	0,15	0,09	0,13	0,10	0,09	0,10	0,06	0,10	0,09	0,10	0,08
MgO	5,04	5,27	6,21	2,91	2,25	2,91	3,66	0,71	0,54	0,59	0,96	0,45	0,33
CaO	8,67	8,34	9,72	4,20	5,21	6,0	4,47	3,96	1,79	1,61	2,04	1,29	0,12
BaO	0,70	0,81	0,60	0,46	0,62	0,50	0,44	0,40	0,36	0,30	0,31	0,06	0,06
SrO	0,89	0,93	0,70	0,54	1,36	0,57	0,40	0,56	0,46	0,44	0,32	0,11	0,07
K ₂ O	3,25	4,09	4,05	5,57	5,53	5,01	4,69	5,55	6,72	6,11	5,53	4,32	5,65
Na ₂ O	4,81	4,73	3,95	5,39	4,05	4,32	4,45	5,10	5,28	5,40	4,64	5,63	5,04
P ₂ O ₅	2,39	1,13	1,19	0,68	0,90	1,04	0,86	0,26	0,27	0,59	0,68	1,13	0,06
H ₂ O+CO ₂	4,46	6,06	4,87	1,41	1,12	1,03	0,28	1,80	0,23	1,0	1,79	0,93	0,22
F	0,75	0,85	0,80	0,95	0,23	0,35	0,75	0,40	1,05	0,23	0,12	0,13	0,20
Summa	100,3	100,2	100,2	100,6	100,3	99,99	100,6	100,4	100,5	100,7	99,7	99,7	100,1
	14	15	16	17	18	19	20	21	22	23	24	25	26
SiO ₂	71,1	56,4	55,5	56,2	56,4	67,3	69,0	55,8	58,3	60,8	60,3	60,4	70,1
TiO ₂	0,40	1,38	1,30	1,40	1,45	0,42	0,44	1,0	0,80	0,62	0,64	0,90	0,28
Al ₂ O ₃	14,0	16,0	15,1	15,9	16,8	11,9	12,1	16,9	18,0	18,0	17,9	16,4	14,4
Fe ₂ O ₃	1,65	4,22	6,43	5,57	5,82	1,67	0,62	2,99	3,44	2,87	2,93	3,40	0,67
FeO	0,28	1,37	0,92	1,26	0,70	1,15	1,29	3,05	2,08	1,29	1,15	1,44	0,43
MnO	0,02	0,07	0,09	0,08	0,08	0,37	0,08	0,13	0,10	0,11	0,08	0,07	0,03
MgO	0,27	2,89	2,66	2,31	1,95	0,55	0,52	2,04	1,49	0,97	0,82	1,38	0,36
CaO	1,11	4,76	6,07	4,72	2,72	2,62	2,48	3,76	2,87	2,53	2,09	2,80	1,40
BaO	0,01	0,45	0,43	0,47	0,73	0,10	0,11	0,49	0,30	0,10	0,15	0,10	0,05
SrO	0,08	0,44	0,37	0,45	0,45	0,22	0,18	0,57	0,56	0,20	0,26	0,20	0,02
K ₂ O	5,51	5,31	4,31	4,64	5,79	7,87	8,09	5,68	5,84	5,83	6,38	5,56	5,93
Na ₂ O	4,81	4,38	4,05	4,43	4,67	1,65	1,67	4,67	5,18	5,35	5,59	5,46	5,03
P ₂ O ₅	0,06	0,90	0,90	0,95	0,81	0,15	0,12	1,13	0,34	0,12	0,16	0,21	0,20
H ₂ O+CO ₂	0,51	0,47	1,47	0,41	1,01	0,46	0,92	2,15	0,69	0,24	0,86	1,17	0,48
F	0,25	0,65	0,50	0,85	0,75	2,0	1,50	0,12	0,35	0,40	0,30	0,30	0,40
Summa	100,2	100,1	100,4	100,2	100,5	99,6	99,98	100,6	100,6	99,8	99,7	99,9	99,95

Note: Rock names: 1-3 lavas of melanephelinites – melaleucites, 4 – veined shonkinites, cutting melanephelinite, 5 and 21 – subvolcanic teralite, 6-11 – lavas of trachytes, Eastern field, 12-14 – lavas of sanidine trachyrhyodacite of the Western field, 15-18 – lavas of phonolites of the western field, 19-20 – glassy trachyliparites of the Eastern field. Stocks of small intrusive massifs: 22 – nepheline syenites, 23-25 – alkaline syenites, 26 – quartz syenites. Data of chemical analysis, analyst is G. A. Pogudina, Institute of Geochemistry, SB RAS.

The phosphate-carbonate rocks i.e. carbonatites and apatite-magnetite nelsonites, though they possess a lot of an analytical information are less studied [11, 8, 9]. These rocks are similar in time of formation. Both carbonatites cut by veins of apatite-magnetites, and xenoliths of calcite-fluorite carbonatites in apotitolites are found. Among apatite rocks we can distinguish several varieties.

1. Two sufficiently large stock-like or volcano-like round bodies, with the size of 30 x70 m (Apatite-Camel body and magnetite ring).

The apatite body from the contact towards the center is composed of fine-grained trachytoid apatitolithes, containing 95 % of elongated apatite crystals, the interstices contain decayed glassy isotropic substance. The center of the body includes magnetolite with the size of 2 x 3 m, containing the magnetite and mica (5%) crystal aggregates. Apatitolithes contain from 7 up to 15 wt. % TR. From the contact with the host rocks towards the center the apatite rocks become more fine-grained (chilled), moreover TR concentration increases up to the highest values - 15 wt. %. In apatites the maximal TR concentration makes up 8 %, other rare earth elements are contained in an isotropic matrix.

The second body is located in 200 m southwestwards of the Apatite body. It is composed of apatitolithes with mica and magnetite. Magnetite forms a ring with a diameter of 10 m being 1-1.5m wide. This magnetolite contains aggregate of large dendritic magnetite crystals elongated along one of octahedron angles. The size of octahedrons is 5-10 sm. Such structural features of apatite and magnetite indicate their fast crystallization from the melt. High temperature of formation of apatite-magnetite rocks and their crystallization from the melt-fluid were confirmed by thorough thermobarogeochemical researches [1].

2. Some dykes of apatite-magnetite rocks of 0.2- 3 m thick and up to tens meters long. They contain apatite with magnetite endocontact margins. In the central part of large bodies of these rocks there are celestine and barite aggregates up to 0.3 m in size.

3. Veined body of fine-grained fluorite-magnetite-apatite rocks with celestine. The body is 5-20 m wide and up to 500 m long from south to north. The southern contact of the body is cut by a fault. The dyke of red trachyliparite was intruded here. Some outcrops of these rocks with varying concentrations of major minerals are found along the whole body. These rocks contain up to 2 - 4 wt. % TR, 5 - 10 wt. % of fluorine, 10 - 20 wt. % SrO and 10-20 wt. % P₂O₅. Probably these dykes are new type of ore-bearing rocks. The representative analyses of the chemical composition of the Mushugai-Khuduk ore complex are given in Table 2, while the contents of rare elements are presented in Tables 3 and 4.

By the mineral composition we can distinguish several varieties among the carbonatite occurrences of Mishugai-Khuduk field. All carbonatite veins (dykes) are leucocratic. The fine and micro-grained calcite carbonatites are abundant. They include the bodies which were intruded along fine cracks in the trachyte flow. They are from 10 sm up to 50 sm wide and 5-30 m long. They are composed of calcite. The accessory minerals include apatite, magnetite, fluorite and in cases quartz. The carbonatite, cutting the apatite dyke (site Terlitovyi) is enriched with

Table 2.

Chemical composition of carbonatites and apatite rocks of Mushugai-Khuduk area

№	1	2	3	4	5	6	7	8	9	10	11	12
SiO ₂	23,5	17,2	25,7	3,61	5,4	21,1	6,91	38,3	50,0	30,8	47,5	32,6
TiO ₂	0,05	0,05	0,15	0,10	0,05	0,09	0,05	0,05	0,05	0,10	0,05	0,13
Al ₂ O ₃	0,43	1,12	3,39	0,44	0,53	5,36	0,54	0,32	0,45	0,23	0,22	3,91
Fe ₂ O ₃	1,02	0,68	1,01	1,46	0,53	0,10	0,17	0,34	0,46	0,34	0,53	3,82
FeO	0,80	0,17	0,18	2,05	0,18	0,71	0,36	0,89	1,87	0,88	0,17	0,86
MnO	0,55	0,20	0,44	1,10	0,47	0,93	0,12	0,54	0,85	0,23	0,24	0,44
MgO	1,80	0,29	0,84	17,04	0,68	0,24	0,64	3,22	2,44	0,44	0,60	0,58
CaO	33,04	42,76	31,80	27,36	45,21	36,95	25,01	21,73	18,03	35,04	18,90	26,36
BaO	1,38	0,17	2,42	0,28	1,79	2,95	1,82	10,19	1,34	6,22	2,57	0,09
SrO	0,22	0,19	0,22	0,33	2,47	0,22	22,94	0,20	0,33	0,31	1,27	0,17
K ₂ O	0,00	н.о.	1,22	0,19	0,09	0,15	0,12	0	0	0,16	0	2,86
Na ₂ O	0,08	0,03	0,68	0,97	0,11	0,13	0,10	0	0,02	0,23	0	0,29
H ₂ O	0,12	0,90	1,25	1,39	0,49	1,59	0,21	1,13	1,28	1,13	0,61	1,29
CO ₂	32,28	33,70	27,81	41,01	18,17	24,18	12,89	15,96	16,64	8,09	9,58	24,41
P ₂ O ₅	0,27	1,35	1,22	0,27	0,22	0,63	0,95	0,00	0,23	2,01	1,28	0,00
SO ₄	0,82	0,15	1,45	1,20	11,41	1,30	20,46	0,69	2,15	1,61	6,08	0,20
TR	0,55	0,10	0,23	0,14	1,26	0,50	2,30	0,84	1,25	3,30	4,50	0,61
F	1,70	1,40	0,90	2,10	18,80	5,80	8,50	11,00	5,50	20,10	10,20	2,30
Summa	99,90	99,86	100,5	100,2	99,95	100,4	100,5	100,8	100,7	100,4	99,90	99,91
№	13	14	15	16	17	18	19	20	21	22	23	24
SiO ₂	26,6	23,6	21,3	5,22	11,8	19,2	32,8	19,5	4,53	7,42	10,5	41,7
TiO ₂	0,10	0,07	0,15	0,55	0,20	0,05	1,60	1,20	0,35	0,45	0,97	0,35
Al ₂ O ₃	3,28	5,02	5,40	2,97	2,85	2,51	2,31	2,45	2,21	5,20	5,93	1,09
Fe ₂ O ₃	4,11	4,45	2,15	29,70	35,18	19,37	22,39	19,35	7,50	9,42	15,61	5,73
FeO	0,36	0,89	0,90	3,77	0,53	1,07	1,10	1,41	0,70	2,10	2,07	1,08
MnO	0,39	0,05	0,53	0,42	0,28	0,13	0,36	0,78	0,10	0,10	0,11	0,02
MgO	0,68	0,60	0,84	1,49	1,31	0,24	1,02	1,12	0,07	0,11	0,10	0,72
CaO	32,13	20,27	32,35	22,58	18,88	22,16	14,08	25,23	35,12	25,27	21,56	4,74
BaO	0,82	6,08	6,18	2,24	2,46	3,45	0,66	0,96	3,76	2,65	2,07	3,04
SrO	0,13	10,50	0,22	3,41	0,26	3,11	0,14	0,11	2,84	9,96	9,26	0,20
K ₂ O	2,50	1,50	3,66	0,37	0,50	0,08	0,31	0,25	0,02	0,04	0,02	0,14
Na ₂ O	0,17	0,26	0,93	0,33	0,43	0,23	0,22	0,11	0,38	0,53	0,35	0,47
H ₂ O	1,23	0,21	0,34	1,73	1,12	3,43	1,86	2,39	1,83	3,55	1,30	3,12
CO ₂	24,06	7,83	21,23	0,88	1,47	1,90	0,49	9,00	0,37	0,58	0,30	12,01
P ₂ O ₅	0,00	8,04	0,38	20,41	14,69	18,88	14,01	7,91	26,99	18,51	17,38	1,27
SO ₄	1,07	9,27	1,15	1,09	1,30	2,51	0,33	0,50	1,50	6,50	6,40	4,83
TR	0,41	2,50	1,00	2,52	5,64	1,11	6,24	6,38	10,70	5,58	6,34	3,75
F	3,30	0,20	3,00	1,10	1,50	1,60	1,00	2,10	1,50	4,90	3,30	3,30
Summa	100,0	100,2	100,5	100,3	99,72	100,4	100,4	99,92	99,90	100,4	100,1	86,15

Note: in № 24 determined 14 wt.% PbO. №1,2,3 – calcite carbonatite with quartz, 4 – dolomitic carbonatite, 5-7 - fluorite-calcite carbonatite, 8-11 - calcite-fluorite carbonatites with quartz, 12-14 feldspar-calcite breccia sometime containing celestine, 15- calcite-feldspar-fluoritic carbonatite, veined, 16-20 - magnetite-apatite rocks (nelsonites), 21 - apatitilites, 22-23 – apatite-fluorite-magnetite rocks with celestine, 24 - jarosite-cerussite tuff. Data of the chemical analysis, analysts L.N. Matveeva, IGC SB RAS

Table 3.

Contents of rare elements (in ppm) in Mushugai-Khuduk apatite rocks and tuffs.

* №	1	2	3	4	5	6	7	8	9	10
Be	3,04	2,91	1,85	1,52	2,78	2,15	1,31	14,47	7,45	8,37
Sc	1,97	1,78	4,71	3,88	11,58	3,15	0,99	3,43	2,23	1,13
V	982,2	1025	57,50	59,99	82,75	57,42	9,79	44,05	41,68	30,60
Cr	17,62	53,67	14,06	54,23	32,29	38,65	4,46	22,21	10,87	15,45
Co	17,82	13,48	0,69	1,66	5,31	1,60	1,27	1,85	2,38	1,27
Ni	14,23	15,42	3,05	6,75	10,38	8,97	1,16	4,17	5,77	4,00
Cu	8,58	27,95	1,62	4,46	11,65	4,09	19,56	5,27	5,87	5,75
Zn	817,8	579,9	29,92	70,46	132,8	88,89	34,40	1013	86,71	113,7
Ga	29,50	36,07	2,96	3,69	4,05	3,54	3,72	13,53	18,12	8,56
Ge	0,35	0,38	0,06	0,10	0,20	0,10	0,12	0,68	0,62	0,34
Rb	12,18	19,47	3,56	8,53	41,89	5,42	4,11	102,7	126,5	64,43
Sr	1391	1149	9176	14337	5830	8747	1643	1489	2065	1844
Y	515,8	314,2	615,7	672,3	517,6	723,9	467,7	199,7	141,5	209,8
Zr	37,08	23,49	0,15	0,17	2,36	1,12	48,32	196,3	212,6	135,5
Nb	34,53	26,37	0,73	1,50	6,77	0,66	18,15	20,69	32,79	13,44
Mo	10,69	5,15	3,42	4,19	6,23	4,28	45,75	137,4	9,13	73,92
Sn	14,08	13,31	0,28	0,14	1,06	0,20	1,45	1,74	1,99	1,28
Sb	0,98	1,13	0,33	0,13	0,69	0,15	21,77	2,95	0,71	4,72
Cs	2,40	8,44	0,76	1,76	1,92	2,75	1,68	3,72	3,28	1,71
Ba	65,93	69,84	213,9	620,3	458,5	303,4	9468	13706	15452	17505
La	3764	2009	4632	4936	3823	5486	11438	4814	3202	6811
Ce	10628	5353	11748	12819	10659	12454	19710	7734	5252	8328
Pr	1052	498,9	1227	1363	1042	1470	1426	520,3	353,8	523,4
Nd	3668	1752	4239	4682	3655	5006	3673	1412	964,9	1275
Sm	466,2	213,9	547,1	569,0	471,6	632,4	331,4	129,8	89,90	102,3
Eu	47,32	24,85	75,38	84,19	68,20	88,40	51,43	28,25	19,88	21,15
Gd	243,7	120,1	331,6	345,9	253,6	332,1	194,7	76,14	53,30	65,53
Tb	23,04	11,84	32,34	33,69	24,55	32,20	16,03	6,36	4,22	4,80
Dy	108,1	58,02	140,6	147,8	113,8	153,6	71,03	31,34	20,38	23,20
Ho	19,15	10,30	22,92	23,72	19,68	25,96	12,23	5,79	3,87	4,44
Er	40,93	23,89	54,98	57,26	42,04	56,68	28,42	13,88	8,58	10,80
Tm	5,55	3,10	6,50	6,74	5,54	7,46	4,13	2,14	1,31	1,63
Yb	29,30	16,94	37,67	39,70	28,15	38,27	24,90	12,19	7,30	9,81
Lu	3,72	2,30	4,79	5,00	3,62	4,88	3,04	1,72	1,03	1,37
Hf	2,67	1,30	2,52	2,03	2,52	2,32	1,65	5,10	5,22	3,17
Ta	0,69	0,36	0,38	0,37	0,42	0,38	0,25	0,84	1,65	0,54
W	11,94	2,44	0,79	0,77	0,95	0,93	33,11	28,22	23,85	15,57
Tl	0,25	0,25	0,12	0,34	0,56	0,18	1,05	0,72	0,91	0,58
Pb	27,38	21,15	19,89	39,50	38,20	83,84	132701	2465	178,7	389,1
Th	637,0	287,3	318,3	362,8	276,5	412,6	278,2	85,44	77,13	45,34
U	50,10	34,58	23,48	28,15	19,58	34,83	499,8	164,7	24,31	53,08

Note. 1-6 – apatite rocks of the central field, 7 – jarosite-cerussite tuff, 8-10 – tuff-breccia with fragments of feldspar and fine fluorite phenocrysts. Data of ACP-MS analysis, analysts E.V. Smirnova and A.Yu. Mitrofanova, Institute of Geochemistry, SB RAS, 2010. * - Elements.

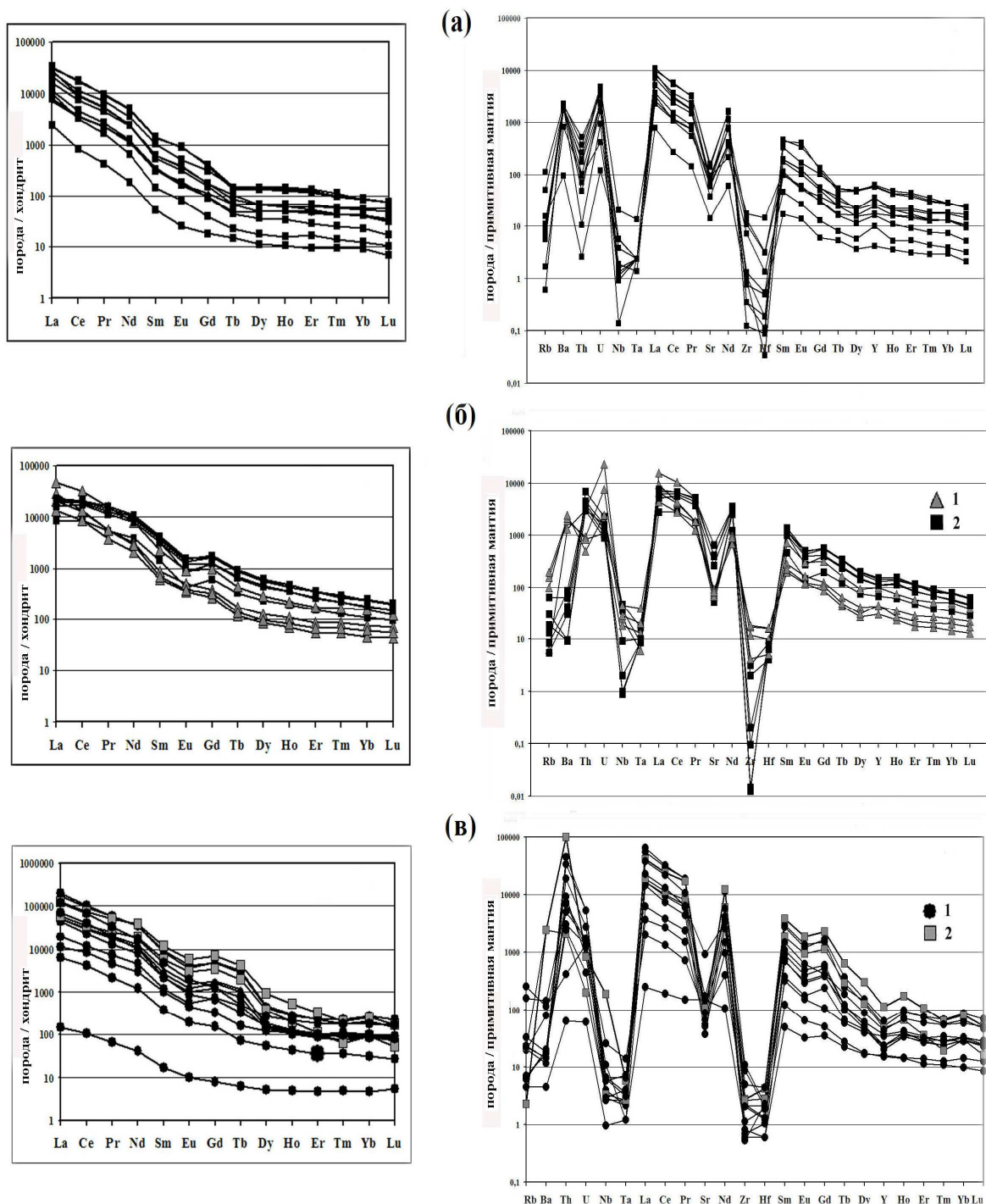


Fig.5. Diagrams of TR spectra TR (left plots) and spider-diagrams (right plots). (a) volcanogenic micro-grained rocks of fluorite-barite-cristobalite composition, (б) 1- jarosite cerussite tuffs and tuff breccias with fragments of feldspar and fine fluorite phenocrysts, 2 – carbonatites; (B) 1- Luginol carbonatites, 2 – Mauntin Pass carbonatites.

monazite. One carbonatite dyke containing up to 20 wt.% of potassium feldspar is observed.

The western part of the trachytic field contains a thick carbonatite dyke up to 1 km long and up to 1 m thick which is composed of fine-grained grains of calcite

with cavernous interstices. It is cut across by numerous tectonic fractures. The body possibly migrated vertically along these fractures. The most western part of this dyke includes the site being 2 meter long containing spherulite-like aggregates of the dolomitic composition which were cemented by calcite – quartz matrix (Table 2, the analysis 10). In 2 m from the dolomitic site this dyke is cut by the younger dyke of syenite-porphyry.

Another variety of carbonatites is of calcite-fluoritic composition. Fluorite forms idiomorphic crystals of cubic habit of crystal in the calcite matrix. Other minerals in these carbonatite include apatite and magnetite. Carbonatites are fine and micro-granular. They are found in the same site as calcitic carbonatites. Geological and petrographic data indicate the volcanic origin of carbonatites and their magmatic genesis is confirmed by thermobarogeochemical investigations [1]. In addition to K-Na carbonatites calcite-fluorite similar to carbonatites of the Mushugui-Khuduk massif [28] have been recently discovered on volcano Oldoinyo-Lengai in the Central Africa. The third variety of carbonatites is calcite-fluorite-quartz. The craters of small volcanoes of the teralite composition are filled with mineralized breccia of the potassium feldspar composition, which contains abundant veins and veinlets of quartz-calcite-fluoritic composition of the stockwerk type in numerous fractures. This type of carbonatites could possibly have formed from the explosive gas – hydrothermal mixture. The carbonatite melt - fluid transformed into this mixture when the temperature decreased. These rocks contain up to 3 wt. % TR.

In the Western part of the trachytic field we observed explosive formations of unusual composition. In 1 km to the north from the extended carbonate dyke there is one more site with carbonates. On the northern margin of this field we found several sublatitudinal dykes of 2-4 m thick and up to tens meters long. These are dykes of granosyenite-porphyries and sintered ignimbrites. Among them there are dykes of complex structure [16, 17]. The first dyke is up to 4 m thick. Its northern contact with trachytic flow contains glasses of trachyliparitic composition with phenocrysts of potassium feldspar, quartz and mica, being 0,5 - 1 m thick (Table 1, the analysis 19-20). The central part of the dyke comprises yellow original tuff-breccia material of explosive genesis, similar to carbonate tuff (Table 2, the analysis 11). There are 2 structural varieties of these formations. One of them includes tuff breccia with denser fragments of the same yellow substance, while another one comprises cavernous (vesicular) tuff, very light, with black spots of magnetite (?) dendrites or manganese oxides. By composition a yellow pelitic substance is similar to Pb-containing jarosite. In addition to jarosite it contains abundant (to 20-30 wt. %) of primary lead carbonate (cerussite). It forms transparent fine grains and their aggregates of pinkish color (up to 1 mm) being regularly disseminated in the rock. There are separate grains up to 3 - 5 mm. The concentration of PbO in this tuff reaches 15 - 18 wt. % and that of TR makes up to 5 wt. % (Table 3, the analysis 7). In addition to jarosite and cerussite the rocks

contains insignificant amount of magnetite opal-like disordered cristobalite, fluorite, barite, calcite. The southern part of the dyke is composed of ironshot

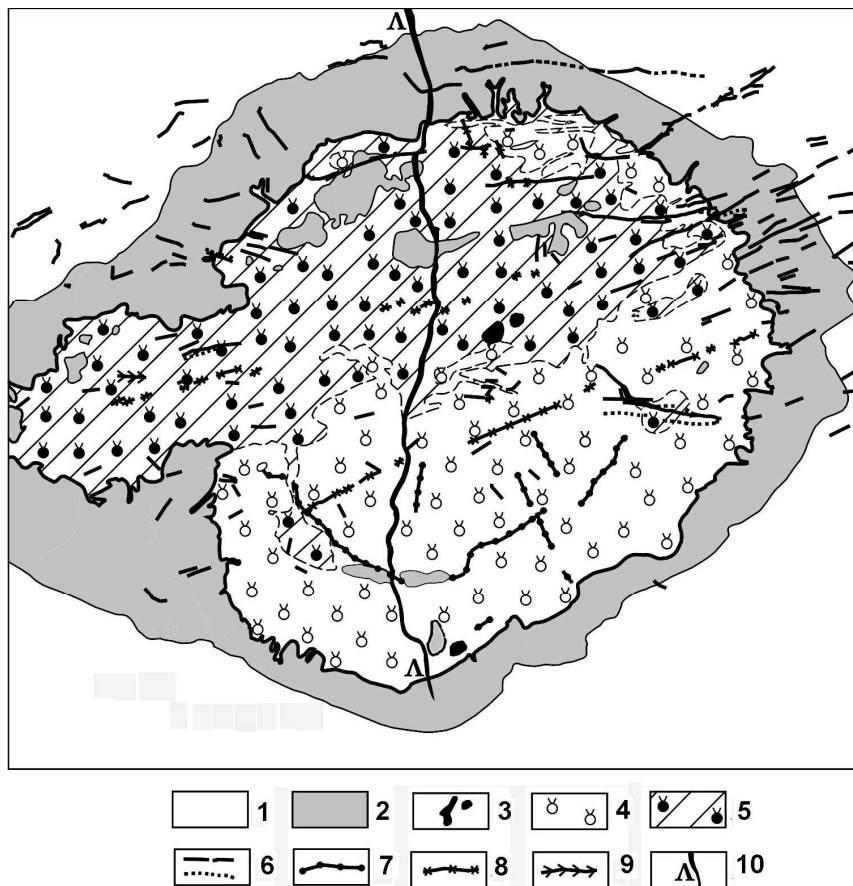


Fig.6. Geologic structure of the Luginol massif (from data [5] with adding G. Damdin и D. Batbold). 1 – host slates, 2 – near-contact hornfels, 3 – xenoliths of *Fsp-Pl* pyroxenites, 4 – nepheline syenites (pulaskites) of the main intrusive phase (MIPh) 5 – MIPh) carbonatized syenites, 6 – carbonatite veins and dykes, 7 – dykes of nepheline syenites and leucite syenites (leucitophyres), 8 – dykes of leucite tingvaites, 9 – dykes of micaceous syenites, 10 – trachylyparite dyke.

fluoritized pyroclast. It contains fragments of trachylyparite glasses, trachyte-feldspar lavas with abundant fine dark-blue fluorite crystals of cubic habitat. The fragments are often impregnated with brown manganese aggregate. These rocks are rich in TR, Pb, Ba (Table 3, analyses 7, 8, 9). Southwards the trachyte lavas comprise veinlets of microgranular black-violet fluorite-barite-cristobalite rocks. These veinlets are from 5 to 10 sm thick and 20-30 m long. Fluorite forms the faceted dark-blue cubic microcrystals. These veinlets contain up to 3 % TR. The concentrations of Sr, Ba, Pb, Y are high. Contents of rare elements in these unusual rocks are given in Table 4. These Pb-TR sulfate-carbonate tuffs and fluorite-barite-cristobalite rocks were formed at the final stage of eruptive-hydrothermal volcanic activity and as regard to the genesis they are similar to volcanogenic ores of the Tomtor massif [18, 25]. TR Spectra and spider diagrams of rare elements in rocks from the Mushugai-Khuduk massif are given on Fig. 5a, 5b.

The Upper Paleozoic intrusive complex of K-alkaline rocks - shonkinites and leucite syenites with TR ore-bearing carbonatites. The given complex includes three magmatic occurrences. They include the Luginol massif of pseudoleucite syenites with carbonatites, Zeden occurrence (Barun-Khasar Ula) of dykes of shonkinites with the carbonatite vein and dykes of nepheline and alkaline syenites in 40 km towards the north-east of the Luginol massif near Olon-Obo city.

The Luginol massif of the central type [5], has a round shape, its area is 10 km². The massif cuts the thickness of slates which are transformed into hornfels near the contact and are penetrated by various rocks of the veined series and carbonatite veins. Because of dark color of hornfels the massif is well visible in space pictures. The age of the massif determined from zircon and badeliite is 253-258 Ma. The main phase of the massif includes hastingsite nepheline-bearing and pseudoleucite syenites. In the central uplifted part of the massif there is an outcrop of coarse-grained leucites, gradually replaced by nepheline syenites. In potassium rocks of such composition leucite is first crystallized. It emerges in heavier magma and is accumulated in apical part of the massif, and then it is gradually dissolved in the same magma. The older rocks are found as well; they are outcropped in the central part of the massif as a large xenolith and smaller xenoliths near the southern endocontact. In the first case it is alkaline gabbroid (probably potassium feldspar pyroxenite), in the second they include biotite shonkinites. The geologic map of the massif is given on Fig. 6. A great number of radial and less abundant ring fractures which are filled with the rocks of the veined series is characteristic of the massif. The earliest among them include three dykes of leucite syenites (leucitophyres). Leucite in them is decayed into potassium feldspar and kalsilite or nepheline, therefore we call them pseudoleucitic. The dykes are 0.5 - 2 m thick and 0.1 - 1 km long. Two of them are chilled containing a glassy matrix. These dykes are cut by radial dykes of prismatic granular trachytoid nepheline syenites. The leucite porphyries are 0.5-1 m thick and 100-500 m long. The western part of the massif contains the dykes of melanocratic nepheline syenites enriched with biotite. It is up to 5 m thick and 200 m long. The younger dykes of dark green up to black pseudoleucite ingrates were intruded along the radial fractures and have vertical contacts. They include fine-grained (up to glassy) rocks, being up to 1 m thick and 0.1 - 2 km long. In the central part of the massif we found the youngest dykes of linarite to quartz porphyries which cuts all rocks of the massif. The dyke has a submeridional strike with a dip towards the west under the angle of 30°. In addition to dykes of the silicate rocks the Luginol massif contains the veined carbonatite bodies. They have a latitudinal strike with vertical contacts. They are from 0.2 up to 2 m thick and from 5 up to 200 m long. They are found in the northern part of the massif and outside its contacts. By composition they are calcite

Table 4.

Contents of rare elements (in ppm) in volcanogenic microgranular Mushugai-Khuduk fluorite-barite-crystalobalite rocks

№	1	2	3	4	5	6	7	8	9	10	11
Be	2,11	10,31	8,54	5,73	22,83	10,71	14,51	12,21	12,43	23,30	6,84
Sc	2,21	2,66	0,82	0,75	0,83	3,20	13,55	0,67	2,64	3,09	0,36
Ti	119,4	1734	308,4	271,2	111,7	376,6	204,9	95,78	85,07	90,80	199,1
V	48,32	28,76	15,86	49,16	25,35	66,31	41,77	39,62	75,28	59,77	26,50
Cr	49,37	45,75	42,87	40,98	41,66	44,15	46,27	46,43	23,66	28,11	65,43
Co	2,01	1,83	0,82	2,04	0,53	1,16	1,02	1,10	1,64	1,97	2,15
Ni	13,56	4,29	1,42	3,49	2,18	2,16	2,91	9,86	25,08	3,59	46,10
Cu	6,55	3,93	0,75	5,22	2,33	4,52	4,79	1,28	4,31	2,69	11,20
Zn	53,79	948,1	17,51	41,42	37,28	71,88	88,69	63,84	66,79	26,29	88,78
Ga	0,83	11,28	0,93	0,36	0,57	2,09	2,23	0,66	0,67	0,65	0,43
Ge	0,81	1,24	0,07	0,56	0,06	0,22	0,15	0,03	0,14	0,12	3,38
Rb	9,99	72,52	7,10	1,09	5,04	33,09	4,79	4,48	6,57	3,66	0,40
Sr	312,6	1312	1420	827,8	1790	2112	1782	1475	3521	3103	2048
Y	19,41	80,99	115,4	75,74	166,3	124,5	299,3	166,7	268,5	280,7	47,12
Zr	8,78	198,9	124,6	15,19	12,63	10,57	4,04	156,20	1,45	4,12	83,37
Nb	4,17	14,86	4,11	1,39	1,16	0,84	0,10	1,16	2,81	0,98	0,67
Mo	12,48	24,51	4,50	12,34	15,86	18,20	3,66	95,12	92,29	87,21	75,06
Sn	0,28	1,11	0,20	1,01	1,23	0,39	0,05	0,20	0,34	0,21	0,55
Sb	13,90	8,44	0,25	3,25	1,27	1,58	0,13	7,67	0,15	0,43	3,92
Cs	0,59	3,35	0,75	0,17	0,78	2,28	0,93	1,02	0,89	0,88	0,11
Ba	684,3	16411	15730	5859	12293	13704	14986	13866	14399	14125	14278
La	575,6	1670	2638	1892	5098	3780	6048	6640	7275	7993	2384
Ce	515,3	2142	2873	2249	5536	4525	6926	5857	10984	10293	2018
Pr	39,88	203,6	247,4	209,7	479,2	412,1	647,5	495,0	865,0	913,2	152,4
Nd	84,27	547,6	583,9	495,9	1105	1064	1629	1093	2201	2304	301,9
Sm	7,73	51,82	47,78	45,11	91,00	89,90	152,8	79,72	198,0	213,5	21,18
Eu	2,39	9,21	9,14	10,46	20,88	21,34	28,70	17,62	70,28	58,18	4,54
Gd	3,61	22,63	18,96	18,33	34,58	33,76	61,56	30,37	74,12	81,30	7,83
Tb	0,53	2,43	1,66	1,58	3,14	3,67	5,24	2,36	4,65	5,33	0,79
Dy	2,74	11,74	12,27	8,82	16,74	16,13	35,73	16,41	36,42	38,46	4,30
Ho	0,59	2,64	2,68	1,83	3,67	3,44	7,97	3,34	7,00	7,24	0,86
Er	1,52	7,21	7,71	4,52	10,85	8,41	21,70	9,86	18,42	20,20	2,65
Tm	0,23	1,02	1,05	0,62	1,47	1,08	2,80	1,39	2,38	2,50	0,35
Yb	1,47	6,59	6,47	3,63	9,10	6,51	14,07	8,68	13,57	14,25	1,96
Lu	0,17	0,84	0,82	0,41	1,35	0,75	1,91	1,17	1,84	1,88	0,25
Hf	0,16	4,65	0,98	0,17	0,06	0,01	0,06	1,01	0,03	0,04	0,43
Ta	0,03	0,57	0,03	0,06	0,10	0,10	0,10	0,10	0,10	0,10	0,10
W	1,09	31,69	4,26	0,47	12,40	11,77	4,64	15,22	18,95	11,90	5,67
Pb	41,11	5188	128,4	143,8	144,6	495,7	97,26	283,2	780,7	1193	181,2
Th	0,24	34,16	9,44	8,80	18,00	16,11	47,48	6,54	4,41	24,02	0,97
U	2,62	105,58	48,77	9,15	94,82	51,34	71,68	36,59	52,95	98,56	20,42

Note: data of ACP-MS analysis, analysts - E.V. Smirnova and A.Yu. Mitrofanova, IGC, SB RAS, 2009

Carbonatization is found in separate sites up to the depth of 750 m.

MINERAL COMPOSITION OF ROCKS OF THE LUGINGOL MASSIF.

Alkaline gabbroids. These are dark grey medium-grained rocks of the massive structure. The main minerals of rocks include plagioclase № 35 - 40 (60 %), light green augite (15 %), dark brown hastingsite (10 %), biotite (5 %), homogeneous potassium feldspar (5 %) and nepheline (5 %). Cancrinite and accessory minerals (sphene, apatite and zircon) are scarce. Non-plagioclase varieties, containing up to 50% of anorthoclase were observed as well. In the rock grains of plagioclase and dark-color minerals (2-6 mm) are cemented by the graphic aggregate of alkaline potassium feldspar and nepheline with separate xenomorphic cancrinite grains.

Shonkinites of the south endocontact contains 50 % of potassium feldspar, 30 % of pyroxene and 20 % of biotite.

Nepheline-bearing syenites of the main phase comprise large -and medium-grained rocks with massive, less often trachytoid structure. They consist of alkaline feldspar (70-80 %), nepheline (5-10 %), hastingsite (7-10 %) and zonal plagioclase № 10-20 (up to 10 %). The minor minerals include: augite, cancrinite, calcite and fluorite. Accessory minerals include apatite, sphene and zircon. Cancrinite is primary, regularly distributed in rocks and spatially is not connected with nepheline grains. In the zone of endocontact nepheline-bearing syenites become biotitic, and close to the southern contact there are sites, enriched up to 30 % by blue corundum – sapphire.

Pseudoleucite-containing syenites by composition are similar to nepheline-containing, but without plagioclase. They include coarse-grained pinkish-grey rocks with spherical or «leucite-like structure. Macroscopically they contain large (up to 10-20 sm in diameter) «phenocrysts» of pseudoleucite, cemented by the nepheline-bearing matrix. Other minerals include hastingsite, biotite, sphene and zircon.

Dyke pseudoleucite leucitophyres - dark grey rocks with large (2-8 sm in diameter) pink phenocrysts of pseudoleucite which are regularly distributed in the rock. The matrix is fine-grained up to microgranular, glassy. In addition to pseudoleucite it contains tabular grains of fine-pertite alkaline feldspar, isometric nepheline grains and prismatic hastingsite grains. Pseudoleucite phenocrysts demonstrate precise facet tetragontrioctahedron (Fig. 6) with sharp borders as regard to a matrix of the rock. They contain the graphic aggregate of alkaline feldspar, nepheline (in the ratio approximately 3:1), less often plagioclase № 15 - 20, cancrinite, fluorite and hastingsite.

The leucite tinguaites are dark green, to black, quite often porphyritic rocks with fine-grained, sometimes glassy texture of the matrix. Phenocrysts of tinguaites are up to 0,5-2,0 sm in size and include anorthoclase (1-10 %), light green augite (2-6 %), brown melanite (2-4 %), nepheline (2-10 %), less often analcite, pseudoleucite (crystals up to 1,5-2,5 sm in diameter). The matrix of

tinguaites is composed of tabular alkaline feldspar and prisms of hastingsite, isometric grains of nepheline and melanite which are cemented by phenocrysts of

Table 5.

Chemical composition of rocks (in wt. %) of the Luginol shonkinites, Barun-Khasar-Ula carbonatites and Mauntin Pass carbonatites.

N ₂	1	2	3	4	5	6	7	8	9	10	11	12
SiO ₂	52,1	45,4	55,4	57,3	55,4	52,4	54,4	51,3	51,6	70,9	3,46	7,69
TiO ₂	1,20	2,28	0,32	0,50	0,38	0,48	0,48	0,47	1,06	0,32	0,06	0,12
Al ₂ O ₃	16,0	13,30	20,25	19,29	22,20	21,84	21,84	20,60	20,38	13,83	0,50	1,80
Fe ₂ O ₃	2,13	8,93	1,72	1,00	1,00	1,76	1,02	2,78	1,60	0,83	0,50	1,40
FeO	4,17	3,49	3,59	2,87	1,36	1,99	3,59	2,08	2,33	0,28	0,05	0,04
MnO	0,17	0,53	0,18	0,15	0,10	0,26	0,15	0,19	0,18	0,07	0,36	1,58
MgO	3,15	1,30	0,92	0,42	0,50	1,00	0,79	1,01	0,75	0,53	0,20	0,20
CaO	5,98	14,50	2,45	2,45	1,58	1,75	2,60	4,08	4,57	1,02	59,34	45,13
BaO	0,23	0,30	0,13	0,11	0,20	0,20	0,25	0,23	0,20	0,06	0,10	0,10
SrO	0,30	0,60	0,17	0,14	0,20	0,22	0,27	0,43	0,60	0,03	0,40	0,47
Na ₂ O	5,40	3,58	2,86	3,79	2,83	8,10	5,26	6,67	6,56	3,51	0,46	0,44
K ₂ O	6,50	4,34	10,28	9,93	11,61	8,53	8,53	7,92	7,68	5,18	0,09	0,37
P ₂ O ₅	0,41	0,18	0,13	0,35	0,36	0,10	0,10	0,25	0,32	0,10	0,16	0,06
H ₂ O	1,60	1,38	1,30	1,40	1,85	0,90	1,05	2,00	1,80	3,45	1,13	1,68
F	0,40	0,05	0,52	0,43	0,24	0,54	0,17	0,40	0,35	0,10	18,00	2,70
CO ₂	0,46	0,34	0,68	0,72	0,72	0,66	0,20	0,39	0,38	0,22	22,68	32,62
TR	0,05	0,08	0,07	0,05	0,07	0,09	0,07	0,06	0,06	0,05	0,10	4,70
Σ	100,11	100,54	100,71	100,70	100,48	100,59	100,67	100,7	100,26	100,43	100,91	100,86
N ₂	13	14	15	16	17	18	19	20	21	22	23	24
SiO ₂	1,03	5,97	10,0	1,03	1,37	46,2	46,9	46,2	12,9	47,7	48,6	49,5
TiO ₂	0,01	0,05	0,12	0,02	0,06	1,13	1,10	1,17	0,09	1,35	1,26	1,17
Al ₂ O ₃	0,45	2,01	1,93	0,01	0,01	16,0	16,60	15,70	1,20	9,80	10,60	9,60
Fe ₂ O ₃	1,21	7,68	23,70	0,70	0,39	4,41	4,13	3,24	4,14	3,33	3,96	5,13
FeO	0,05	0,05	0,05	0,17	0,15	3,49	3,04	3,84	0,10	2,32	3,13	2,05
MnO	1,90	0,40	1,49	1,86	1,54	0,16	0,14	0,14	0,60	0,08	0,09	0,07
MgO	2,06	0,11	0,42	0,41	0,39	4,30	4,20	3,40	5,63	6,40	8,20	8,90
CaO	34,88	42,09	28,39	45,51	37,91	7,80	7,30	7,80	15,59	9,60	6,80	7,80
BaO	0,20	0,30	0,03	0,03	0,03	0,33	0,56	0,22	0,35	0,56	0,66	0,99
SrO	0,26	0,25	0,11	5,24	10,08	0,32	0,28	0,15	0,10	0,13	0,14	0,26
Na ₂ O	0,12	0,09	0,12	0,03	0,05	6,79	6,19	7,42	0,14	6,09	7,68	8,59
K ₂ O	0,12	0,43	1,08	0,12	0,19	2,64	3,30	2,39	0,62	1,21	1,56	1,56
P ₂ O ₅	0,14	0,14	0,23	0,07	0,03	0,84	0,82	0,84	0,19	1,52	1,31	1,31
H ₂ O	3,40	2,95	4,52	4,00	2,40	3,71	3,49	2,56	0,14	3,09	2,14	1,50
F	1,90	25,20	1,55	0,32	1,0	0,30	0,50	0,35	2,40	0,80	1,30	0,90
CO ₂	34,3	8,39	22,03	37,46	37,0	1,55	1,53	4,72	25,72	5,84	3,32	0,94
TR	17,5	14,40	4,24	2,89	6,83	0,42	0,68	0,38	30,11	0,21	0,12	0,16
Σ	98,73	99,90	99,36	99,74	99,01	100,29	100,55	100,39	99,02	99,69	100,29	100,13

Note. Luginol: 1- feldspar-plagioclase pyroxenite, 2 – garnet-pyroxene-nepheline melanosyenite, 3-4 – pulaskites of the main intrusive phase, 5 – MIPh pseudoleucite syenite; dykes of leucitophyres: 6 - chilled, 7 - crystallized; 8-9 – dykes of leucite tinguaites, 10 – trachyliparite dyke; carbonatites: 11-calcite-fluoritic, 12- calcitic, 13 - bastnasite-calcite, 14 – limonite-bastnasite-fluorite, 15- pyrite-calcite, 16- bastnasite-calcite, 17 – celestine-bastnasite-calcitic. Barun-Khasar-Ula: 18-20 – dykes of shonkinites, 21 – calcite-bastnasitic carbonatite. Mauntin Pass: 22-24 – shonkinites. Data of chemical analysis

cancrinite, calcite and fluorite. The latter are regularly distributed in rocks and do not show metasomatic features in the origin. Tinguaites, containing in addition to the above minerals arfvedsonite and albite are scarce.

The nepheline syenites of the main phase and veined rocks underwent the carbonatization. At the same time nepheline is replaced by the aggregate of shpriunstein and carbonate. Dark-color minerals are partially replaced by oxides of iron and carbonate.

Quartz porphyries, granosyenite-porphyries and liparites. These are pink porphyritic rocks with microgranular spherulitic matrix and sometimes with rare round "fused" phenocrysts of quartz and pertite potassium feldspar. The matrix contains microlites of potassium feldspar, as well as spherulitic aggregates, cemented by fine isometric quartz grains.

Carbonatites form veined bodies. By composition they are calcite and calcite-fluorite, containing frequently abundant TR fluorine-carbonates. Other minerals include limonitized and non-altered pyrite, potassium feldspar, barite, seldom mica. Carbonatites, containing up to 30 % of dark blue fluorite, 20 % of limonitized pyrite and 30 % of bastnasite are very similar to ore carbonatites of TR Bain-Obo deposit which is located in China in 100 km away from the Luggingol massif. They are different only in concentrations of calcite and limonitized pyrite instead of magnetite. Calcite-bastnasite carbonatites are similar to carbonatites of other large TR deposit – Mauntin Pass in the USA.

CHEMICAL COMPOSITION OF ROCKS FROM THE LUGINGOL MASSIF AND THEIR GEOCHEMICAL FEATURES.

All rocks of the massif belong to potassium series of alkaline rocks [16, 25]. Chemical compositions of the Luggingol rocks are given in Table 5. On the classification diagram 7 they lie in the field of alkaline rocks and form homodromic series. By the chemical composition xenoliths of shonkinites near the southern endocontact of the Luggingol massif are similar to xenoliths of shonkinites found by us in lavas of phonolite of the Mushugui field. Rare elements in the Luggingol carbonatites and in carbonatites of Mauntin Pass (USA) are given in Table 6, and plots of TR spectra and spider diagrams are given on Fig. 5c. Variations of concentrations of rare elements in carbonatites of the Luggingol massif are higher than the inclination of TR spectra and a configuration of spectra of rare elements on spider diagrams are similar. The spectra of the Luggingol carbonatites significantly enriched with rare elements are not different from spectra of carbonatites of Mauntin Pass complex.

In addition to the Luggingol massif on the east margin of the Dzun-Bain regional fault there are two more occurrences which can be regarded as the formation of K-alkaline rocks (Fig. 2).

First of them is Zeden located near Barun-Khasar-Ula city. It is located on low hill, which is composed of sandstones, approximately in 30 km to the west of the Luggingol massif. The host rocks including grey sandstones are cut by several dykes of K-alkaline shonkinites. The dykes are 1-3 m thick and up to tens meters long. Shonkinites are fine- and medium-grained, contain potassium feldspar, mica

and pyroxene. By the chemical composition shonkinites and minerals composing them are completely similar to Mauntin Pass shonkinites (Table 5, analyses 19-22 and 24-28) which are associated with the world's largest carbonatite deposit of rare elements. On the classification diagram 7 their compositions lie close to the compositions of the Luginol shonkinites. Concentrations of rare elements (Table 7) and TR spectra in shonkinites of these two sites are similar as well (Fig. 8a). In the same area the Mongolian geologist T. Zeden found the carbonatite vein of 1 m thick and 20 m long. The carbonatite comprises calcite and green bastnasite. TR concentrations in carbonatites reach as high as 30 %. Its chemical composition is given in Table 5, the analysis 19.

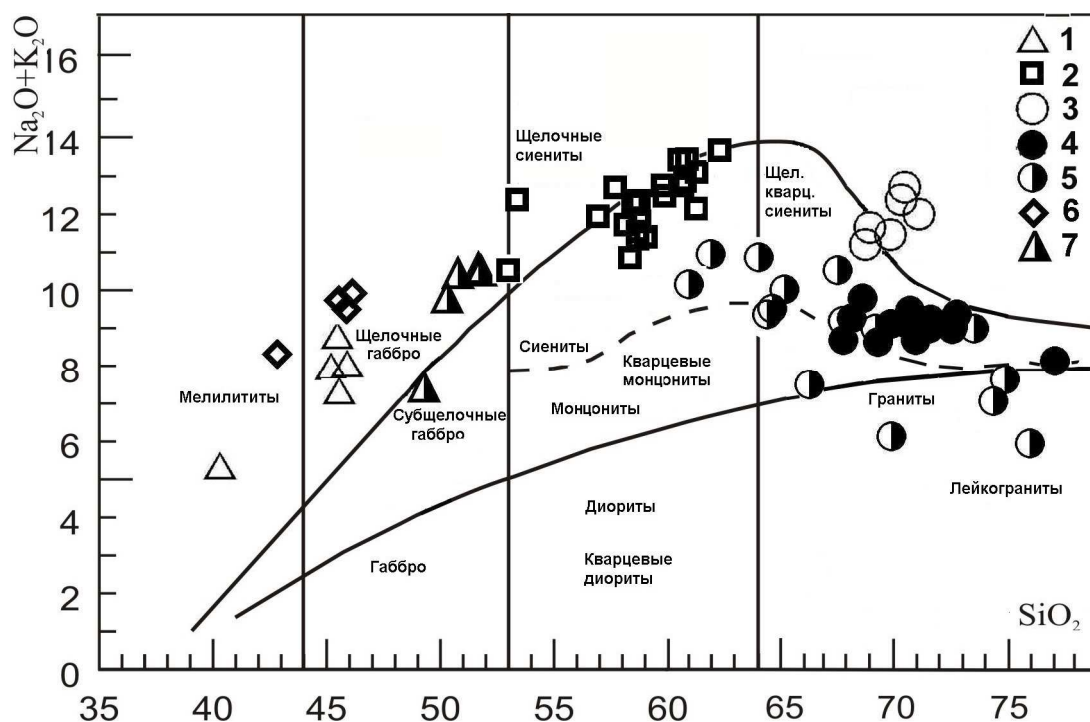


Fig. 7. Classification diagram alkalis – silica (in wt.%).

Luginol massif: 1- Fsp-Pl pyroxenites, 2- different syenites, 3 – trachyliparite dykes;
Khan-Bogdo massif: 4 - granites, 5 - pegmatites; 6 – shonkinites of Barun-Khasar-Ula massif, 7 – Mauntin Pass shonkinites.

The second occurrence is in 40 km north-westward of the Luginol massif near Olon-Obo hill. It was found by the author of the article in 1984. A small depression demonstrates some outcrops of submeridional dykes. One of dykes contains dark-green to black nepheline syenite. The dyke is up to 1 m thick and 30 m long. It is composed of nepheline (up to 40 %), green amphibole, mica (5 %) and potassium feldspar. Concentration of K_2O is 9,40 wt. %, that of Na_2O is 8,45 wt.

Table 6.

Contents of rare elements (in ppm) in Luginol carbonatites and Mauntin Pass.

№	1	2	3	4	5	6	7	8	9	10	11	12	13
Be	0,26	0,72	2,40	4,81	1,02	1,31	2,99	2,52	1,19	0,83	1,69	1,37	2,45
Ti	66,6	103,6	8,8	45,3	28,4	150	90,5					310	243
V	5,99	26,4	398	66,5	18,5	159	82,2	54,10	25,67	7,97	136,3	189	50,5
Cr	3,73	2,30	0,07	8,8	11,6	0,36	14,6	29,83	25,96	3,41	21,54	2,10	38,7
Co	2,45	3,49	5,56	10,3	3,35	3,16	20,0	9,04	1,74	1,71	7,61	3,91	13,2
Ni	17,4	13,1	9,15	17,8	16,0	11,8	18,9	2,51	2,02	3,19	1,20	48,1	60,0
Cu	6,04	3,10	9,40	8,90	4,36	8,57	10,7	6,56	3,95	3,43	4,26	32,3	18,8
Zn	20,1	21,2	166	425	221	183	602	433,3	32,28	852,9	274,4	61,8	258
Rb	2,89	15,09	4,51	13,2	4,30	104	12,6	165,0	21,10	14,37	3,97	1,46	14,1
Sr	3306	3755	2098	2300	2454	812	1103	1912	1213	20272	1457	1897	2340
Y	74,3	94,1	240	296	109	94,6	171	70,66	159,8	110,6	205,7	521	222
Zr	9,45	7,92	126	24,0	6,91	25,7	98,9	23,77	13,17	6,11	57,42	31,9	30,4
Nb	0,70	4,17	1,95	4,87	7,97	2,15	2,90	18,98	2,13	4,58	4,89	137	2,46
Cs	0,15	0,23	0,40	0,69	0,38	1,35	0,97	1,88	0,67	0,37	0,38	0,08	0,44
Ba	32,4	101	123	83,5	140	1030	567	819,3	129,6	102,9	143,7	17444	17593
La	182	12343	47261	40462	4609	10645	12339	1475	2655	16656	28031	30007	13875
Ce	360	18899	61243	58333	7226	13876	18103	2550	5088	24981	41696	45932	21662
Pr	41,9	1879	5324	5287	673	1225	1669	204,2	428,2	1798	2996	4817	2310
Nd	148	5843	15830	16179	2078	3686	5186	565,0	1372	4648	8062	17413	8449
Sm	22,6	504	1370	1271	173	323	415	55,66	147,6	332,4	686,3	1758	866
Eu	5,47	85,2	238	210	30,4	55,3	68,9	11,11	26,04	50,79	108,6	323	163
Gd	21,2	368	933	1016	146	247	328	30,89	64,79	235,2	252,3	1405	693
Tb	2,15	11,6	24,1	36,1	6,50	9,66	11,5	2,64	5,74	11,86	18,16	63,0	29,0
Dy	12,5	38,9	107	116	34,1	35,4	45,6	13,06	30,11	38,86	67,13	228	95,9
Ho	2,40	5,64	14,8	16,1	5,87	5,54	6,94	2,37	6,20	6,62	11,72	28,8	10,9
Er	6,84	13,3	37,7	36,9	15,7	13,8	16,7	5,54	15,99	14,10	29,28	52,1	17,7
Tm	0,99	1,88	5,40	4,45	2,28	1,90	2,18	0,86	2,72	2,35	4,35	5,14	1,52
Yb	6,98	14,6	43,3	32,8	16,2	14,3	15,9	4,88	16,03	13,73	28,96	40,6	14,6
Lu	1,00	1,87	5,43	3,71	2,21	1,82	1,98	0,68	2,25	1,97	4,06	4,07	1,27
Hf	0,19	0,33	0,73	0,68	0,19	0,42	0,64	0,39	0,59	0,72	1,40	1,34	0,89
Ta	0,05	0,30	0,11	0,15	0,05	0,09	0,09	0,58	0,17	0,13	0,27	0,24	0,11
Pb	125	792	1467	1393	621	455	2095	587,9	81,57	898,8	643,6	195	48,8
Th	5,76	845	4100	3117	279	640	460	38,16	225,6	682,0	1762	9139	192
U	1,33	18,4	117	116	29,5	26,8	37,4	29,85	9,75	31,79	60,29	18,3	4,35

Note. 1-11 – Luginol carbonatites, 12-13 – Mauntin Pass carbonatites. Data of ACP-MS analysis, Institute of Geochemistry SB RAS, Data of ACP-MS, E.V. Smirnova and A.Yu. Mitrofanova, Institute of Geochemistry, SB RAS, 2008-2010.

%. The rock is fine-grained, with fine phenocrysts of nepheline and potassium feldspar as well as needles and aggregates of greenish amphibole and brown mica. The accessory minerals include apatite and zircon. The same depression contains about ten others dykes of the syenite composition of the same strike and thickness.

They consist of phenocrysts and matrix of the potassium feldspar and insignificant amount (1 - 5 %) of green amphibole. Concentration of K_2O in rocks is 5,6 %, Na_2O is 6,9 %. Feldspars contain abundant fine inclusions of mica. Accessory minerals include apatite, sphene and zircon. It is most likely that this small depression is syenite massif overlapped by the quaternary sediments.

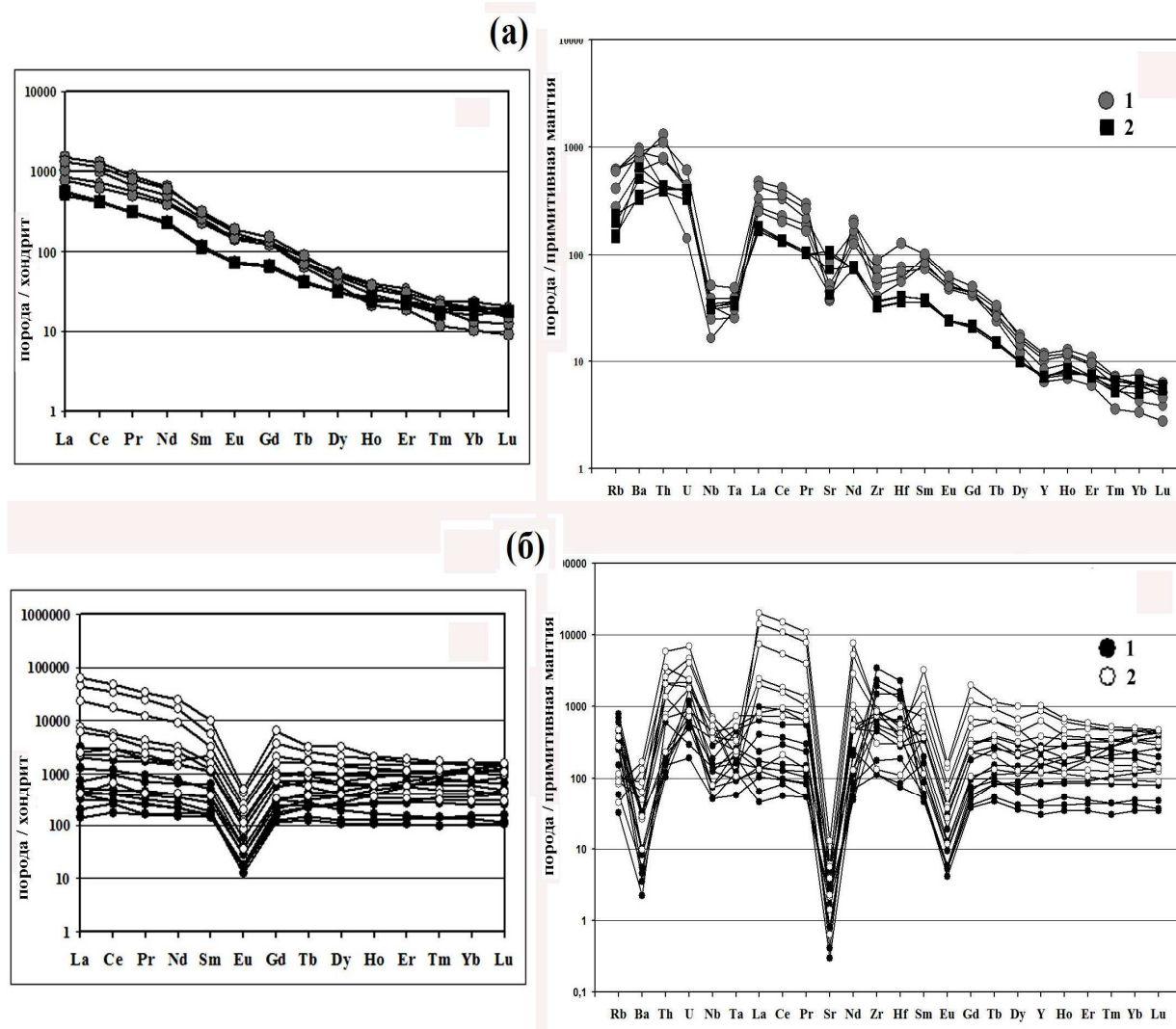


Fig. 8. TR spectra (left plots) and spider –diagrams (right plots). (a) shonkinites: 1 – Mauntin Pass, 2 – Barun –Khasar-Ula; (б) – Khan-Bogdo massif: 1 – MIPh) granites, 2 – pegmatites, pegmatitized hosting liparites.

Agpaitic alkaline- granite massifs of the third intrusive complex forms a belt stretching from the east to the west over hundreds kilometers [9]. It consists of eight massifs of alkaline granites of different size and various rare metal potential. The majority of massifs are non-rare-metal. The complex also contains a poor rare-metal Kharkhad massif and anomalously rare-metal Khan-Bogdo massif, which we will discuss in detail.

The largest in the world Khan-Bogdo massif of alkaline granitoids (more than 1500 km²) is located in the southern part of Gobi desert (Mongolia) [20] in 250 km from Dalan-Dzadgada aimak. On the northern margin of the massif there is

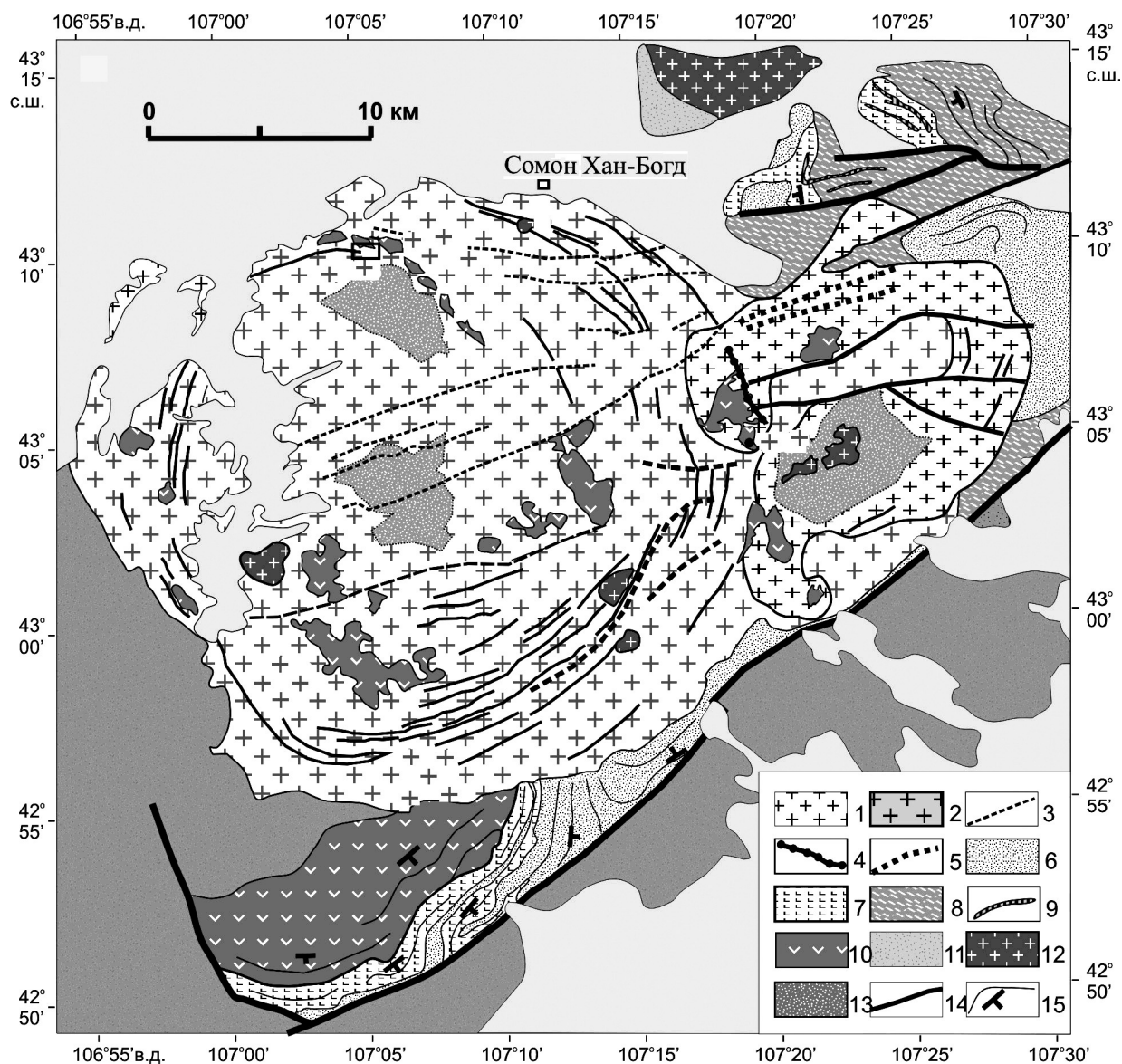


Fig. 9. Geological map of Khan-Bogdo massif [13]. 1–5 – rocks of the massif: 1 – alkaline granites of the main intrusive phase, 2 – fine-grained aegirine granites, 3 – dykes of micro-grained syenites and monzonites, 4 – late pantellerites, 5 – alkaline granite-porphyrries; 6–8 – volcanic rocks of the bimodal association: 6 – comendites, trachyrhyolites, their tuffs and ignimbrites, 7 – basalts, 8 – non-distinguished rocks of the association; 9 – rocks of island arc association (differentiated complex); 10 – Pre-Late Paleozoic complexes; 11–13 – massif roof: 11 – rocks of the differentiated complex transformed into hornfels, 12 – biotite and amphibole-biotite granites and granosyenites, 13 – sites of участки haematitization of alkaline granites of GIF (развития гематитизации щелочных гранитов ГИФ («red granites»); 14 – faults; 15 – borders of volcanic flows.

Khan-Bogdo settlement. The massif was formed within the Late Paleozoic active conti-nental margin of the Siberian paleocontinent. The location of the Khan-Bogdo massif is controlled by the area of crossing of Gobi-Tien-Shan

sublatitudinal rift zone and a large regional fault. It is the massif of the central type with ring and radial dykes (Fig. 8). It comprises two ring bodies (Western and Eastern), having sharp transversal magmatic contacts with the rocks of the hosting island arc sequence and tectonic broken borders with the bimodal sequence [12]. The internal ring structure is especially characteristic of the Western body and is emphasized here by ring dykes and deflection of the roof of the host sequence. The massif, by gravimetric data, is a flat body (laccolite) up to 10 km thick. The bottom is graded, dipping towards the north-west. A total succession of forming the magmatic rocks of the Khan-Bogdo massif is the following (from early to late): 1) light grey to pink alkaline medium-grained granites of the main intrusive phase (MIF) with accessory elpidite, composing the most part of the Western and a part of the Eastern bodies; 2) dykes of fine-grained ekerite, porphyry-like ekerites, layered granite-pegmatite bodies, pegmatoid alkaline granites, pegmatites, which are abundant in the Western body indicating its ring structure; 3) lilac fine- to medium-grained alkaline (usually aegirine or arfvedsonite-aegirine, frequently miarolitic) granites with accessory zircon, composing the most part of Eastern body; 4) dykes of micro-grained up to glassy dark-blue or dark green pantellerites. Rare-metal alkaline granitoids and alkaline-granite pegmatites occur in the ring dykes of the 2nd phase. These rocks also include ekerites being poor in rare elements as well as varieties transitional to rare-metal. The sites of the concentrated occurrence of rare-metal alkaline ekerites and pegmatites are frequently found under the deflections of roof composed of volcanic rocks of the basic to liparite composition. About 15 occurrences of rare-metal mineralization are observed. The mineralogy of which are thoroughly described in monographs [20, 15, 7]. A large deposit of Zr, deposits of Nb, TR and Y were discovered within rare-metal occurrences. The fine-grained rare-metal ekerites and medium-grained pegmatites of the layered complex contain up to 7% of Zr; the concentrators of Zr are zircon-silicates, elpidites and a new mineral (armstrongite). Nb concentration in some pegmatites reaches up to 0.5 wt/%, TR content makes up to 1 wt% and Y up to 0.5 wt%.

The main feature of this mineralization is its agpaitic character. It is proved, that in alkaline granites parageneses with zircon transit into parageneses with zircon-silicates (elpidites) with agpaitic coefficient (K_a) being more than 1,2 as opposed to alkaline and nepheline syenites in which eudialyte is crystallized instead of zircon if K_a is more than 1 [15]. Concentrators of Nb and TR are their alkaline silicates. Over 50 rare minerals have been discovered in the massif [20, 24]. A part of these minerals are new (armstrongite, mongolite and kovalenkoite). One more unique feature of mineral formation in this massif is transformation of some rare minerals into amorphous state. A dense effusive screen of the roof prevented volatile components together with rare elements to leave the massif and they were crystallized from the magmatic melt under high temperatures. If the alkalinity and silica content of the melt are high the minerals with high silica-

carbon radical are formed. When the temperature lowered they became unstable and decayed into re-

Table 7.

Contents of rare elements (in ppm) in Mauntin Pass and Barun-Khasar-Ula shonkinites

* №	1	2	3	4	5	6	7	8	9
V	123,6	88,7	99,1	67,8	97,4	114,3	119,6	106,4	103,5
Cr	247	274	300	280	299	17,7	33,7	25,8	27,5
Co	23,81	18,16	28,34	25,29	23,19	15,48	16,71	15,96	17,36
Ni	67,1	167,1	188,8	234,4	189,8	21,7	27,1	24,0	22,6
Cu	58,59	37,63	75,76	11,30	58,51	14,22	17,60	12,28	15,57
Zn	82,22	55,10	66,48	55,70	84,41	70,03	81,53	72,60	71,04
Ga	16,39	15,90	15,40	15,95	18,15	16,30	16,40	16,46	15,80
Ge	1,88	1,64	1,62	1,64	1,76	1,21	1,08	1,13	1,41
Rb	403	180	268	391	389	99,8	128	92,4	155
Sr	1128	810	976	1859	832	2364	1572	2198	912
Y	55	30	48	39	52	34	34	32	32
Zr	879	624	719	492	1067	398	431	439	379
Nb	27,9	24,0	18,2	12,0	37,3	22,2	25,0	23,9	23,0
Sn	10	10	8	14	17	8	36	8	19
Cs	8,81	1,99	1,72	5,35	8,34	2,49	13,72	20,44	3,69
Ba	5558	4397	6491	7108	6480	2585	3643	4658	2323
La	202,1	350,7	184,0	240,8	314,7	133,8	133,8	129,0	121,0
Ce	437,2	792,9	383,3	618,6	681,3	258,6	262,8	252,0	248,3
Pr	53,16	82,81	46,28	60,78	74,31	28,21	29,68	28,69	28,59
Nd	198,1	300,5	180,9	234,1	270,0	103,7	110,2	102,7	104,5
Sm	35,87	43,69	33,45	37,62	46,55	16,21	17,51	17,21	16,35
Eu	8,61	9,68	8,00	8,36	10,59	4,05	4,13	4,01	4,18
Gd	26,93	25,36	24,86	26,33	30,27	12,38	13,30	12,89	12,37
Tb	3,33	2,74	2,94	2,89	3,60	1,57	1,66	1,62	1,57
Dy	13,32	8,95	11,80	10,59	12,38	7,42	7,63	7,35	7,40
Ho	2,14	1,15	1,87	1,57	1,97	1,36	1,31	1,43	1,25
Er	5,39	2,95	4,54	3,57	4,71	3,59	3,69	3,44	3,70
Tm	0,57	0,29	0,48	0,45	0,56	0,52	0,53	0,41	0,42
Yb	3,73	1,95	3,02	2,47	3,24	3,27	2,90	3,14	2,96
Lu	0,50	0,22	0,41	0,31	0,37	0,48	0,44	0,42	0,44
Hf	24,27	18,93	21,95	17,34	40,84	11,45	12,78	12,96	11,21
Ta	1,62	1,06	1,06	1,25	2,01	1,38	1,52	1,43	1,51
Pb	86,18	26,80	33,66	39,93	258,45	74,39	153,69	83,67	96,20
Th	120,82	70,29	73,16	39,22	102,08	40,66	36,82	38,21	35,60
U	8,01	9,24	9,76	3,10	13,42	8,52	8,89	8,93	7,08

Note. 1-5 – Mauntin Pass shonkinites, 6-9 – Barun-Khasar-Ula shonkinites. Data of ACP-MS, E.V. Smirnova and A.Yu. Mitrofanova, Institute of Geochemistry, SB RAS, 2008-2010.

dundant quartz and amorphous oxides and, in rare cases, (with Nb) into quartz and

Table 8.

Chemical composition (in wt. %) of Khan-Bogdo granites and pegmatites

№	1	2	3	4	5	6	7	8	9	10	11
SiO ₂	74,1	74,2	73,3	75,2	71,1	73,8	72,4	73,2	76,7	75,4	73,5
TiO ₂	0,18	0,28	0,26	0,22	0,38	0,24	0,43	0,36	0,19	0,25	0,27
Al ₂ O ₃	10,44	11,35	11,64	10,25	11,57	10,79	11,61	10,95	10,72	10,20	11,57
Fe ₂ O ₃	5,56	4,04	4,11	4,44	5,47	4,99	5,06	4,89	3,34	4,57	5,32
MnO	0,18	0,16	0,13	0,12	0,22	0,19	0,16	0,19	0,09	0,12	0,15
MgO	0,09	0,08	0,10	0,15	0,26	0,20	0,47	0,18	0,10	0,10	0,10
CaO	0,26	0,32	0,33	0,21	1,00	0,49	0,61	0,34	0,20	0,17	0,18
Na ₂ O	4,19	4,31	4,15	4,21	4,74	4,29	4,25	4,55	3,70	4,46	7,62
K ₂ O	4,56	4,72	4,67	4,53	4,92	4,68	4,65	4,75	4,71	4,72	0,80
P ₂ O ₅	0,01	0,03	0,02	0,03	0,08	0,04	0,07	0,05	0,02	0,02	0,03
ZrO ₂	0,08	0,14	0,11	0,26	0,09	0,08	0,09	0,18	0,04	0,07	0,23
H ₂ O	0,38	0,47	1,36	0,45	0,25	0,27	0,25	0,28	0,19	0,13	0,35
Summa	100,05	100,09	100,20	100,06	100,05	100,07	100,01	99,96	99,99	100,19	100,13
№	12	13	14	15	16	17	18	19	20	21	22
SiO ₂	73,1	75,2	70,6	79,9	78,8	71,8	61,4	64,1	70,2	76,2	69,9
TiO ₂	0,34	0,37	0,39	0,11	0,14	0,51	2,52	0,91	0,52	0,13	0,26
Al ₂ O ₃	8,92	9,22	7,60	8,65	8,61	7,39	7,18	8,16	7,35	11,70	8,56
Fe ₂ O ₃	7,18	4,76	10,54	3,31	3,63	7,40	11,93	7,28	8,32	2,36	7,71
MnO	0,20	0,29	0,40	0,10	0,11	0,19	0,45	0,27	0,34	0,06	0,71
MgO	0,13	0,20	0,10	0,10	0,10	0,22	0,40	0,45	0,26	0,07	0,11
CaO	0,28	0,23	0,48	0,10	0,17	1,05	0,85	0,83	0,56	0,29	0,39
Na ₂ O	4,86	4,79	5,43	2,16	1,72	2,61	4,67	5,05	3,81	4,06	3,38
K ₂ O	4,03	4,01	3,64	5,61	3,58	5,74	5,08	5,95	5,17	4,69	7,13
P ₂ O ₅	0,02	0,01	0,04	0,01	0,03	0,09	0,04	0,03	0,04	0,03	0,03
ZrO ₂	0,68	0,57	0,42	0,03	0,05	1,51	4,21	5,12	2,52	0,05	0,38
H ₂ O	0,55	0,37	0,50	0,11	0,24	1,77	1,43	2,79	1,40	0,23	1,07
Summa	100,30	100,02	100,10	100,18	97,13	100,25	100,17	100,91	100,44	99,86	99,65
№	23	24	25	26	27	28	29	30	31	32	33
SiO ₂	77,6	66,9	68,6	71,6	67,5	91,6	72,4	88,1	77,1	66,7	66,3
TiO ₂	0,23	0,45	0,79	0,44	0,17	0,12	0,34	0,15	0,45	0,71	0,66
Al ₂ O ₃	5,10	4,76	2,98	6,56	12,12	1,75	3,84	3,00	3,22	10,30	10,83
Fe ₂ O ₃	8,01	14,90	13,58	10,36	5,23	1,99	5,12	1,98	10,12	6,53	6,93
MnO	0,30	0,27	0,86	0,23	0,95	0,80	0,79	0,53	0,49	0,46	0,52
MgO	0,07	0,23	0,28	0,15	0,20	0,07	0,40	0,13	0,10	0,72	0,89
CaO	0,17	0,45	0,94	0,48	0,86	0,31	1,00	0,47	0,43	2,44	0,70
Na ₂ O	3,29	6,60	5,23	4,99	7,00	0,70	3,88	1,83	4,16	5,72	3,53
K ₂ O	3,92	2,76	1,83	3,77	2,93	1,24	1,03	0,99	2,40	3,46	7,37
P ₂ O ₅	0,04	0,07	0,17	0,06	0,04	0,05	0,07	0,08	0,04	0,17	0,16
ZrO ₂	0,47	1,59	2,66	1,12	0,69	0,30	3,23	1,07	0,30	0,73	0,90
H ₂ O	0,80	1,53	2,30	0,62	2,14	1,02	3,86	1,69	1,04	2,17	1,31
Summa	100,00	100,53	100,24	100,42	99,78	99,90	95,95	100,01	99,83	100,09	100,09

Note. 1-10 – MIPh cataphorite granites with elpidite, 11 - MIPh granite with armstrongite, 12-16 – veined ekerites, 17 – veined granite, cutting ekerites, 18–20 – banded elpiditic ekerite-pegmatites, 21 – pegmatites with zircon, 22-26 – schlieren pegmatites with elpidite, 27-31 – different sites of schlieren pegmatite with TR, Zr, Nb, 32-33 – pegmatitized host liparite. Data of chemical analysis, Institute of Geochemistry, SB RAS, analyst – V.A. Pisarskaya.

another mineral with a smaller silica-oxygen radical. This process is characteristic of minerals (Nb, Ti, TR, Zr-TR). These minerals have the crystal facet filled after the decay with amorphous substance and quartz. As supply-removal did not occur during the mineral formation, the composition of “pseudomorphs” could be considered as a primary composition of minerals. There are three compositions of Ce-Zr minerals, five compositions of Ti-silicates, three compositions of TR-silicate [15]. High-silica Nb-silicate is decayed into quartz and kovalenkoite which is then replaced by mongolite. As the crystalline lattice is absent in these minerals it is impossible to prove that they are new minerals. Crystallization of elpidite instead of zircon is characteristic of granites of the main intrusive phase. The granites of this phase are monospathic. They contain microcline-perthite, quartz and alkaline amphibole - Ca-kataphorite. K-Na monospar was also crystallized at high temperature and non-stoichiometric ratio of Al and the sum of alkalis was available. Aluminum is more abundant than alkalis, though the ratio should be 1:1. Therefore at crystal lization of the main phase from magma (its volume is 90 % in relation to late rocks) the residual melt accumulated abundant alkalis, that led to such an intensive agpaitic rare-metal mineralization. Considering, that the area of the massif is more than 1500 km², it is possible to assume great volume of residual rare-metal magma that is responsible for the origin of huge deposits of rare elements. The representative analyses of rocks from the massif are given in Table 8, and those of rare elements are demonstrated in Table 9. On the classification diagram 7 the Khan-Bogdo granites and pegmatites lie lower than the alkaline line that is connected with abnormal concentrations of rare elements. Thus, the contents of alkalis are underestimated, with high agpaitic coefficient. Rare elements in granites and pegmatites of this massif show high Zr, Hf, Nb, TR, Y, U, Th and low Ba, Sr, Eu concentrations (Fig. 8b).

A huge volume of alkaline-granitic plutonic and volcanic rocks of the Khan-Bogdo massif and its ring structure resulted from the caldera mechanism of intrusion and evolution of its magmas.

Geochemical features of all of three rare-metal formations of South Gobi are visible on spider diagrams and TR-spectra plots (Fig. 5 and 8). Rare-metal ores of Mushugai-Khuduk and Lulingol carbonatite provinces have much in common as regard to distribution of rare elements on spider diagrams and TR spectra.

Insignificant europium fractionation is common to carbonatites and apatite ores of these provinces. In the volcanogenic fluorite-barite-cristobalite veins this fractionation is lack. On spider diagrams configuration of lines of distribution of rare elements also are similar for different concentrations of these elements. Barium distribution is a little bit unstable. Such uniform distribution of elements can be explained by their formation belonging to K-alkaline rocks, despite the fact that some of them belong to volcanogenic facie (Mushugai-Khuduk field), and others belong to intrusive facies (Lulingol massif) and have different age (259 and 120 Ma, correspondingly). Essentially different distribution pattern is typical of the

Table 9

Contents of rare elements (в ppm) in rare-metal Khan-Bogdo granitoids

№	1	2	3	4	5	6	7	8	9	
Li	22	41	9.0	326	16	321	231	246	230	
Be	10	14	16	13	20	9.5	8.9	15	15	
Sc	8.7	0.34	4.6	6.2	2.3	4.5	9.3	2.4	1.0	
Ti	2819	1263	2309	7696	1323	3075	6624	1942	1770	
V	2.8	1.6	75	20	6.0	14	32	2.4	0.02	
Cr	3.1	22	1.8	0.79	2.9	5.3	0.1	3.8	0.1	
Co	0.59	0.60	1.1	0.35	0.66	0.54	0.57	0.93	0.69	
Ni	0.59	20	4.9	1.0	0.05	2.4	2.8	0.60	6.7	
Cu	2.4	24	21	13	2.1	3.6	21	7.6	10	
Zn	145	327	552	275	324	444	687	349	476	
Ga	17	35	6	23	0.12	44	19	33	23	
Rb	170	21	231	511	244	38	304	456	294	
Sr	34	9.0	46	58	47	49	110	18	18	
Y	765	207	1111	1326	824	898	695	390	188	
Zr	39931	1293	7601	26845	3535	22698	17134	5980	2044	
Nb	91.3	104	209	138	284	37	91	57	55	
Cs	1.9	0.74	2.6	4.5	3.2	17	10	4.4	1.8	
Ba	64	16	229	197	189	40	234	60	33	
№	10	11	12	13	14	15	16	17	18	19
Li	146	46	13	314	116	328	67	861	6.8	383
Be	12	7.7	15	20	8.8	27	127	90	30	352
Sc	4.4	4.3	7.2	6.4	3.0	8.1	3.8	2.7	1.5	3.8
Ti	1330	4342	2297	2799	2436	3334	1936	843	189	124
V	2.4	3.6	141	125	38	145	23	17	15	12
Cr	1.9	0.82	0.1	7.8	0.56	7.2	0.79	2.9	0.1	0.7
Co	0.35	0.47	1.1	3.20	0.62	5.8	0.51	0.73	0.3	0.5
Ni	0.27	8.7	3.0	3.2	0.54	2.6	3.8	4.6	3.2	0.8
Cu	2.9	9.4	28	16	7.0	14	6.9	6.3	12	10.
Zn	341	414	613	466	207	836	1217	679	910	360
Ga	31	8.5	5.1	11	24	2.4	72	2.7	0.0	2.4
Rb	161	99	74	180	307	393	29	66	58	54
Sr	6.5	37	124	50	14	68	134	85	31	288
Y	142	401	1215	1813	553	1232	4103	2928	571	478
Zr	1292	6605	8522	9926	9735	5287	10625	8856	152	104
Nb	38	112	260	325	58	260	519	443	391	497
Cs	2.6	6.6	4.5	1.0	1.5	1.7	3.5	3.5	0.7	4.9
Ba	25	73	453	205	70	216	960	628	359	121

Table 9 Continued

№	1	2	3	4	5	6	7	8	9	
La	93	299	470	170	1762	33	126	101	105	
Ce	183	693	1048	559	3441	106	296	247	239	
Pr	24	84	155	65	381	15	42	35	29	
Nd	98	342	638	293	1449	75	187	159	120	
Sm	23	74	167	91	232	25	51	40	27	
Eu	0.9	2.2	6.5	3.2	7.1	1.0	1.6	1.6	0.9	
Gd	35	60	175	110	202	41	58	45	25	
Tb	8.1	9.6	36	25	32	11	15	8.9	5.2	
Dy	66	47	223	176	163	89	112	57	31	
Ho	21	9.0	48	46	33	26	31	14	6.8	
Er	89	24	140	159	90	93	115	42	21	
Tm	22	3.5	20	26	12	17	22	6.6	3.5	
Yb	187	21	113	196	75	115	170	40	24	
Lu	36	2.9	16	34	10	21	30	6.3	3.8	
Hf	725	27	213	521	95	416	490	110	60	
Ta	4.0	6.8	20	19	14	5.1	11	6.9	3.8	
Pb	76	53	152	27	232	33	161	24	40	
Th	11	55	192	21	191	9.5	15	14	20	
U	40	6.5	48	26	41	16	22	14	11	
№	10	11	12	13	14	15	16	17	18	19
La	75	47	536	596	96	717	10279	5415	1445	14626
Ce	182	155	1378	1795	402	1733	20751	10323	2991	28767
Pr	23	15	178	216	38	170	2204	1109	285	3081
Nd	99	68	787	649	184	697	7422	4038	1134	10842
Sm	24	21	330	168	53	156	802	471	174	1486
Eu	0.7	0.9	11	6.4	2.0	5.2	24	14	4.7	28
Gd	23	30	309	181	64	139	718	410	140	1218
Tb	4.5	8.0	61	38	13	27	91	62	20	115
Dy	27	61	370	243	90	155	504	328	97	771
Ho	5.7	15	78	58	22	32	103	66	19	113
Er	17	45	245	176	64	98	262	184	52	293
Tm	2.4	8.4	38	28	10	15	38	26	7.5	42
Yb	17	58	237	168	65	93	225	163	47	251
Lu	2.7	10	36	26	11	12	34	23	7.1	38
Hf	24	135	318	180	190	89	164	133	35	113
Ta	2.4	8.2	31	22	10	10	14	9.1	4.4	4.5
Pb	23	76	270	22	11	23	1438	1379	669	1049
Th	14	17	323	64	21	125	236	127	71	540
U	4.2	13	53	19	16	13	103	90	39	152

Note. 1 – MIPh granite with elpidite, 2 – MIPh granite with armstrongite, 3 – veined granite, cutting ekerites, 4 – elpidite ekerite-pegmatite, 5-9 – elpidite ekerites, 10-12 – elpidite pegmatites, 13-15 – pegmatitized host liparites, 16-19 – different sites of schlieren pegmatite with TR, Zr, Nb. Data of ACP-MS, E.V. Smirnova and A.Yu. Mitrofanova, Institute of Geochemistry, SB RAS, 2008

Khan-Bogdo agpaitic granites and ore-bearing pegmatites (Fig. 8b). The rocks of this formation show a sharp europium fractionation of TR spectra and anomalously low Ba and Sr concentrations. The difference is that rare elements are concentrated in alkaline-silicate pegmatites and granites, instead of carbonate-phosphate formations. Fluid modifiers in granites and pegmatites are H₂O and F, while in carbonatites they include CO₂, F and P₂O₅. These distinctions are connected with genetic difference in the origin and differentiation of these complexes.

Geochemistry of isotopes in these rare-metal massifs of the South Gobi is well studied [12, 13]. The Lulingol massif and the Mushugai-Khuduk volcanics originated in fold zones and the mantle source EM-2 is common to them [18, 23]. This source demonstrates high Sr⁸⁷/Sr⁸⁶ values (0,708 - 0,714). It is connected not with the contamination of sedimentary rocks by the alkaline magma but with the subduction of the crustal material into the mantle through Benioff zones. The mantle in these areas became contaminated and show high values of Sr isotopes. When alkaline magma is melted from such a mantle under a small degree of melting (less than 1 %) it demonstrates high Sr isotope ratio like the contaminated mantle. This process is related to unusual carbon and oxygen isotope values. High oxygen isotope values can result from the volcanogenic origin of massifs, when at the eruption of volcanoes we can observe «inleakage» of surface water into the volcano and their mixing with magma. High oxygen isotope values are characteristic of all volcanogenic carbonatites, and in particular of their tuff varieties when there is an exchange of isotopes and with air oxygen. Another distribution pattern of isotopes is observed in the Khan-Bogdo ore formations [13]. They demonstrate values of Nd epsilon being in the range from +5 up to +7 and strontium isotope values ranging as 0,703-0,705 that corresponds to the depleted mantle source, and isotopes of oxygen have mantle values as ranging from -6 to -8, that confirms no influence of surface water. Only the juvenile water proper containing mantle oxygen was accumulated under a dense “effusive” screen. As it was earlier shown [13], the Khan-Bogdo granites are related to the mantle source and generated from the differentiation of the basaltoid magma, which is verified by the bimodal alkaline-basalt-comendite series being of similar age as the Khan-Bogdo massif. This series occurs in the south-eastern exocontact of the massif [12].

There are there super-large TR deposits in the world: Mauntin-Pass, the USA, Bain-Obo, Mongolia and Tomtor in the Eastern Anabar Region, Russia. In our viewpoint these deposits belong to the formation of potassium alkaline rocks [25]. There are still disputes concerning the genesis of ores and type of formation. We believe that studies of carbonatites from the South Gobi will contribute to resolving these disputes .

CONCLUSIONS:

1. Three rare-metal complexes of different age are found in the South Gobi. They are associated with large deposits of rare elements. Various distribution patterns of rare elements and different mineral associations concentrating rare elements are characteristic.

2. The Mushugai - Khuduk and Lulingol carbonatite complexes like the large deposits Mauntin-Pass and Bain-Obo demonstrate common geochemical features in distribution of rare elements and they can be regarded as a common formation type of K-alkaline rocks.

3. Specific rocks enriched with Pb, TR, F, Ba are formed in the Mushugai-Khuduk complex during the volcanogenic - tuff process.

4. The source of Lulingol and Mushugai - Khuduk carbonatite complexes is the contaminated EM-2 mantle, while for the Khan - Bogdo agpaite granites and pegmatites this source is the depleted mantle.

REFERENCES

1. **Andreeva, I.A.** Silicate, silicate-salt and salt magmas of alkaline carbonatite-containing Mushugai-Khuduk complex, South Mongolia (data from studies of inclusions): Candidate Thesis. Moscow: Institute of Mineral Geology Petrography, Mineralogy and Geochemistry, Russian Academy of Sciences, 2000. 211 pp.
2. **Kovalenko, V.I., Kuzmin, M.I., Zeden, Ts., Vladykin, N.V.** Lithium-fluorine quartz keratophyre (ongonite)- a new variety of subvolcanic magmatic rocks // Year-book 1969. Irkutsk: Siberian Institute of Geochemistry. 1970. p. 85-88.
3. **Kovalenko, V.I., Kuzmin, M.I., Zonenshain, L.P., Nagibina, M.S., Pavlenko, A.S., Vladykin, N.V., Zeden, Ts., Gundsambuu, Ts, Goreglyad, A.V.** Rare-metal granitoids of Mongolia: petrology, distribution of rare elements and genesis. M.: Nauka, 1971, 148 pp.
4. **Kovalenko, V.I., Kuzmin, M.I., Pavlenko, A.S., Perfil'ev, A.S.** South Gobi belt of rare-metal alkaline rocks of Mongolia and its structural position // Doklady AN USSR. 1973. v. 210. № 4. p. 911-914.
5. **Kovalenko, V.I., Vladykin, N.V., Goreglyad, A.V., Smirnov, V.N.** Lulingol massif of pseudoleucite syenites in Mongolia // Izvestiya AN USSR. Geological Series 1974, №8. p.38-49.
6. **Kovalenko, V.I., Vladykin, N.V., Konusova, V.V., Smirnova, E.V., Goreglyad, A.V.** Occurrences of the concentrated rare-earth mineralization in the southern part of Gobi desert// Doklady AN USSR. 1976. v. 230.№1. v. 209-212.
7. **Kovalenko, V.I.** Petrology and geochemistry of rare-metal granitoids. Novosibirsk: Nauka, 1977. 190 pp .
8. **Kovalenko, V.I., Samoilov, V.S., Vladykin, N.V., Goreglyad, A.V., Makagon, L.D.** Geochemical characteristics of rocks of the surface carbonatite complex in Gobi desert // Geochemistry. 1977a. № 9. p. 1313-1326.
9. **Kovalenko, V.I., Vladykin, N.V., Goreglyad, A. V.** East Mongolia - a new province of rare metal mineralization // Geology and magmatism of Mongolia. 1977b. № 22. p. 189-205.

10. **Kovalenko, V.I., Vladykin, N.V., Samoilov, V.S., Smirnova, E.V., Goreglyad, A.V.** Rare-earth mineralization elements in rocks of surface carbonatite complexes of Mongolia // *Geochemistry*. 1977v. № 12. p. 1831-1842.
11. **Kovalenko, V.I., Samoilov, V.S., Vladykin, N.V., Goreglyad, A.V., Pisarskaya, A.V., Konusova, V.V.** Rare-metal carbonatites and apatite-magnetite rocks of Mongolia. // *Geology and magmatism of Mongolia*. 1979. № 30. p.158-167.
12. **Kovalenko, V.I., Yarmolyuk, V.V., Sal'nikova, E.B., Kozlovskiy, A.M., Kotov, A.B., Kovach, V.P., Vladykin, N.V., Savatenkov, V.M., Ponamarchuk, V.A.** Geology and age of the Khan-Bogdo massifs of alkaline granitoids in South Mongolia // *Deep-seated magmatism, its sources and plumes*. Irkutsk. 2006. p. 20-54.
13. **Kovalenko, V.I., Yarmolyuk, V.V., Kozlovskiy, A.M., Kovach, V.P., Sal'nikova, E.B., Vladykin, N.V., Kotov, A.B.** Two types of sources of magmas of rare-metal alkaline granitoids // *Alkaline magmatism, its sources and plumes*. Irkutsk. 2007. p. 5-37.
14. **Samoilov, V.S., Kovalenko, V.I.** Complexes of alkaline rocks and carbonatites in Mongolia. M.: Nauka, 1983.200 pp.
15. **Vladykin, N.V.** Mineralogical-geochemical features of rare-metal granitoid of Mongolia. Novosibirsk: Nauka, 1983.200 pp.
16. **Vladykin, N.V.** Petrology and ore potential of K-alkaline rocks of the Mongol-Okhotsk magmatic area. Candidate Thesis. Irkutsk: Institute of Geochemistry, Siberian Branch of Russian Academy of Sciences. 1997. p. 1 - 80.
17. **Vladykin, N.V.** Ore-bearing tuffs and volcanics of the carbonatite Mushugai-Khuduk complex, Gobi, Mongolia // *News of Universities of Siberia*. 1999. № 4-5. p. 84-86.
18. **Vladykin, N.V.** Geochemistry of Sr and Nd isotopes of alkaline and carbonatite complexes of Siberia and Mongolia and some geodynamic consequences // *Problems of sources deep magmatism and plumes*. Irkutsk. 2005. p. 13-29.
19. **Vladykin, N.V., Kovalenko, V.I., Kashaev, A.A., Sapozhnikov, A.N., Pisarskaya, V.A.** New silicate of calcium and zirconium - armstrongite // *Doklady AN USSR*. 1973. v. 209.№5. p. 1185-1188.
20. **Vladykin, N.V., Kovalenko, V.I., Dorfman, M.D.** Mineralogical and geochemical features of the Khan-Bogdo massif of alkaline granitoids (Mongolian National Republic). M.: Nauka, 1981.135 pp.
21. **Vladykin, N.V., Drita, V.A., Kovalenko, V.I., Malov, V.S., Gorshkov, A.I.** New silicate-mongolite // *ZVMO*, 1985. № 1. p.374-377.
22. **Vladykin, N.V.** Ore-bearing tuffs and volcanics of the Mushugai-Khuduk complex, Gobi, Mongolia // *News of Universities of Siberia*. 1999. № 4-5. p. 84-86.
23. **Vladykin, N.V., Tsypukova, S.S., Morikyo, T., Miuzaki, T.** Geochemistry of isotopes of carbon and oxygen in carbonatites of Siberia and geodynamics // *Deep seated magmatism, its sources and association with plume processes*. Irkutsk. 2004. p. 89-107.
24. **Vladykin, N.V., Agafonov, L.I., Maksimiyuk, I.E.** Minerals of Mongolia. M.: ECOST, 2006. 351 pp.
25. **Vladykin, N.V.** Petrology of K-alkaline lamproite-carbonatite complexes, their genesis and ore potential // *Geology and geophysics*, 2009. № 12. p. 1439-1451.
26. **Yarmolyuk, V.V., Kovalenko, V.I.** Rifting magmatism of active continental margins and its potential. M.: Nauka, 1991.
27. **Yarmolyuk, V.V.** Late Paleozoic volcanism of continental rift structures of the Central Asia. M.: Nauka, 1983.192 pp.
28. **Zaitsev, A.N., Petrov, S.V.** Carbonatites of volcano Oldoinyo-Lengai, Northern Tanzania // *Deep magmatism, its sources and plumes*. Irkutsk. 2008. p. 59-70.

A Pb isotope investigation of the Guli massif, Maymecha-Kotuy alkaline-ultramafic complex, Siberian flood basalt province, Polar Siberia.

Kogarko L.N.¹, Zartman R.E.²

¹ Vernadsky Institute of Geochemistry and Analytical Chemistry, Kosygin st 19, Moscow 495.

E-mail kogarko@geokhi.ru

² Max-Planck-Institute for Chemistry, Department of Cosmochemistry, P.O. Box 3060, 55020 Mainz, Germany

ABSTRACT

Covering a vast area of the northern Siberian platform are the Siberian flood basalts (SFB), which make up one of the world's largest magmatic provinces. Along the northeastern margin of the SFB province lies the Maymecha-Kotuy alkaline-ultramafic complex, consisting of a large volume of alkaline lavas, numerous dykes, and the Guli massif together with numerous other, smaller alkaline plutons. The genetic link between the SFB and the Maymecha-Kotuy complex continues to be a subject of active debate. Although the rocks in both units have essentially the same age close to the Permian-Triassic boundary, questions remain as to the relative order of emplacement and the contributing source materials of each lithology. This study builds upon earlier petrologic, geochemical, and isotopic work to further an understanding of the relationship between SFB and alkaline rocks.

A whole-rock U-Pb age of 250 ± 9 Ma was determined for the Guli massif, which lies within the range of ages previously reported for the SFB. The Pb isotopic composition of the Guli rocks plot mainly in the lower portion of the OIB field, and a dunite and carbonatite extend downward into the MORB field suggesting for them a more depleted source than produced the SFB. The combined Pb, Sr, and Nd isotopic systematics of the SFB and the Guli alkaline rocks enable the identification of several discrete source components. The first component dominates many of the Guli rocks and is characterized by low $^{87}\text{Sr}/^{86}\text{Sr}$ (0.7031 to 0.7038), high ϵ_{Nd} (+5.35 to +3.97), and relatively unradiogenic Pb ($^{206}\text{Pb}/^{204}\text{Pb} = 17.88$ -18.31; $^{207}\text{Pb}/^{204}\text{Pb} = 15.38$ -15.46; $^{208}\text{Pb}/^{204}\text{Pb} = 37.33$ -37.70), which we associate with the depleted (MORB source) mantle. The second component representing most of the SFB demonstrates a notable chemical and isotopic uniformity with $^{87}\text{Sr}/^{86}\text{Sr}$ values of 0.7046 to 0.7052, ϵ_{Nd} values of 0 to +2.5, and an average Pb isotopic composition of $^{206}\text{Pb}/^{204}\text{Pb} = 18.3$, $^{207}\text{Pb}/^{204}\text{Pb} = 15.5$, and $^{208}\text{Pb}/^{204}\text{Pb} = 38.0$. This component, making up the majority of SFB, is speculated to be a relatively primitive lower mantle plume with a near-chondritic signature. Contamination by upper and lower continental crustal material, designated as components 3 and 4, is postulated to explain the isotopic characteristics of some of the higher SiO_2 Guli rocks and SFB. Finally, metasomatic processes associated with the invasion of the Siberian super-plume add a fifth component responsible for the extreme enrichment in rare-earth and related elements found in some Guli rocks and SFB.

INTRODUCTION

Alkaline magmatism is sometimes observed in close proximity to continental flood basalt, for instance, in association with the Deccan (India), Etendeka (South

Africa), Parana (Brazil), and Siberian Flood Basalt (SFB) provinces. It has been speculated that both magmas are derivatives of ascending plumes [35, 3]. The SFB province with a volume of approximately $1.6 \times 10^6 \text{ km}^3$ [39] is exposed in the northern part of the Siberian Platform (Polar Siberia) between the Tunguska Basin on the west and the Archean and Proterozoic Anabar Shield on the east. The Putorana basalts, which are located in the central part of the SFB province, represent more than 90% of the SFB volcanism and are considered by Sharma et al. [27] to be an essentially pure derivative of the Siberian superplume. In the W part of the SFB province occurs the world-class Cu-Ni-Pt sulfide Norilsk-Talnakh deposits containing Cu-Ni-PGE resources each comparable to the Sudbury (Canada) and Bushveld (South Africa) complexes. The Maimecha-Kotuy Complex (MKC), one of the world's largest alkaline-ultramafic bodies, lies along the NE margin of the SFB province. The complex is comprised of a great volume of alkaline-ultramafic lavas, hundreds of dykes as well as several carbonatite bodies, and over 30 separate intrusive bodies, including the world's largest, ultramafic-alkaline intrusion, Guli [9]. Several kimberlitic diatremes are also found in the MKC, closely associated with ultramafic alkaline rocks, and farther east the Mesozoic diamond-bearing Yakutian kimberlite pipes occur. The compositional complexity of these Polar Siberian rocks, which comprise tholeiitic basalts, ultramafic alkaline rocks and their derivatives, carbonatites, kimberlites and various types of dykes suggests that this unique province may have resulted from the differentiation of a superplume-related continental magmatic system. However, the genetic connection between the flood basalts and the alkaline magmatism is still under debate [9, 39, 8, 1].

This alkaline volcanism is dated as being synchronous with [2], or slightly younger than [9, 1, 11], the continental flood basalts. Unfortunately, it is not possible on the basis of direct geological observation and mapping alone to establish the temporal relationship between the alkaline intrusions and the SFB. The radioactive age of the Siberian volcanics and related intrusive rocks, although broadly agreed upon, has given rise to some controversy. Kamo et al. [13] obtained a U-Pb age for zircon from the Norilsk intrusion of $251.2 \pm 0.3 \text{ Ma}$., and Dalrymple et al. [8] using the $^{40}\text{Ar}/^{39}\text{Ar}$ method found the age for a group of extrusive and intrusive rocks from the western margin of the Siberian craton to be $249 \pm 2 \text{ Ma}$. The latter authors also reported biotite ages for three intrusive Guli rocks of (1) $243.8 \pm 5.5 \text{ Ma}$ for a very Mg-rich alkaline volcanic maymechite, (2) $241.4 \pm 3.6 \text{ Ma}$ for an alkaline dyke, and (3) $437.0 \pm 3.1 \text{ Ma}$ for a carbonatite. [24] considers the apparently spuriously old biotite age of the carbonatite, which is here dismissed, most likely to have been caused by the presence of excess radiogenic argon. Kamo et al. [14, 15] and Basu et al. [2] have reported slightly older ages for melanephelinite flows of the Maimecha-Kotui area ($252.1 \pm 0.4 \text{ Ma}$ and $253.3 \pm 2.6 \text{ Ma}$). Although these results effectively constrain the age of all igneous activity to a value close to the Permian-Triassic boundary, they do not provide an unequivocal sequential ordering of the emplacement history.

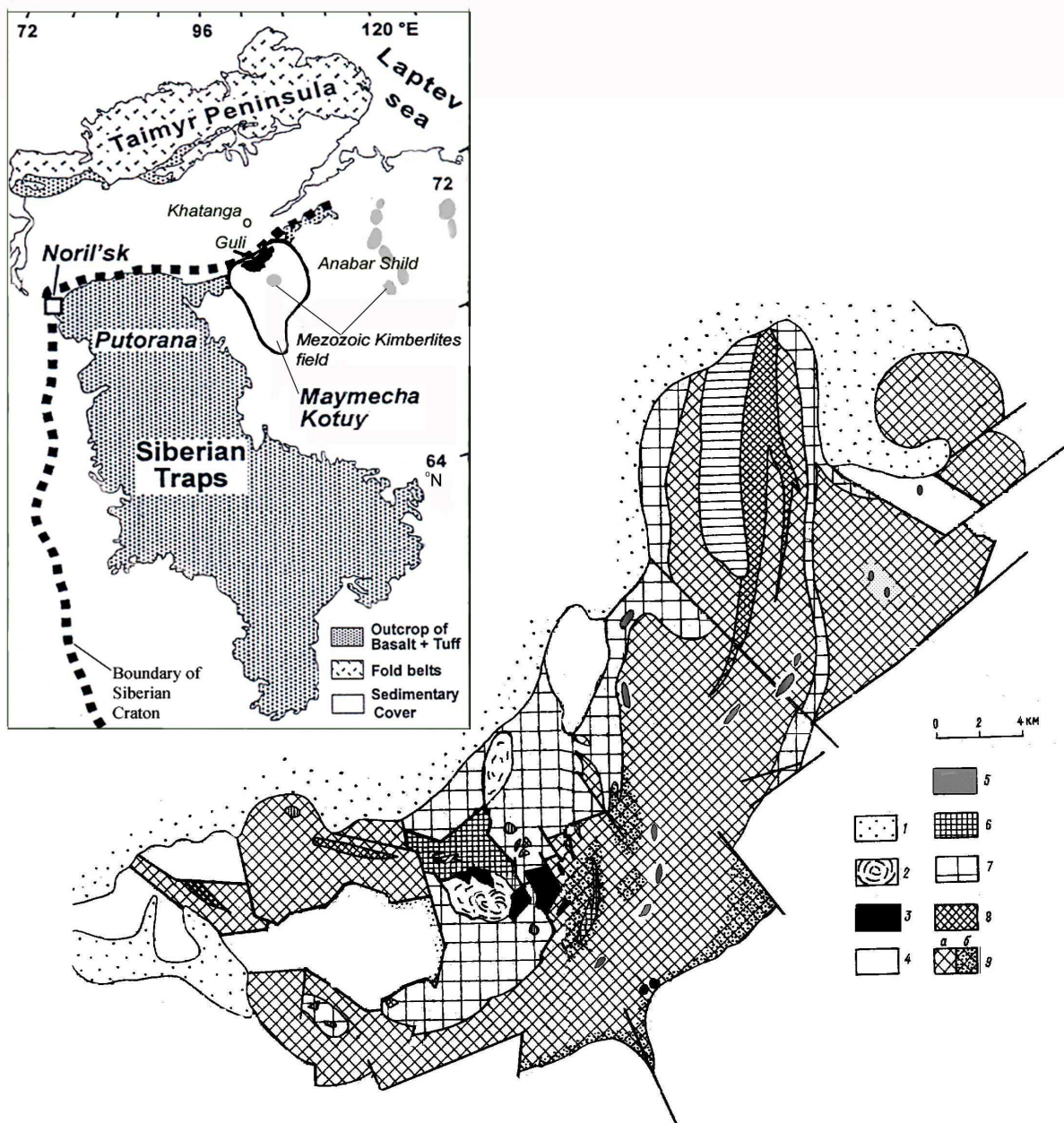


Fig. 1. Simplified geological map of Guli massif:

1- Mesozoic deposits, 2- Carbonatite complex, 3 - Melelite bearing rocks, 4 - Maymechite, 5- Syenite, quartz syenite, nepheline syenite, shonkinite, granite dykes, 6- Ijolite, melteigite, jucupirangite, 7- Melanephelinite, nepheline picrite, biotite-pyroxene picrite, 8 - Kosvite, 9 - Dunite (a), Altered dunite (b).

During the last decade several important geochemical and isotopic studies of the SFB were performed [1, 18, 33, 37], some of which included analyses of the apparently related alkaline rocks. This large volume of data on trace elements and

Rb-Sr, Sm-Nd, U-Pb, and Re-Os isotopic systems has generated several hypotheses for the origin of the SFB. The first systematic geochemical and isotopic investigation of the region was carried out by Sharma et al. [26, 27], who determined that most of the Putorana volcanics show a narrow range of initial ϵ_{Nd} (0 to +2.5) and $^{87}Sr/^{86}Sr$ (0.7046 to 0.7052), and an average initial Pb-isotopic composition of $^{206}Pb/^{204}Pb=18.3$, $^{207}Pb/^{204}Pb=15.5$ and $^{208}Pb/^{204}Pb=38.0$. These compositions lie close to chondritic values and were interpreted as identifying a lower mantle-derived plume as the main source for the SFB with crustal contamination playing no important role. An alternative model was proposed by Arndt et al. [1] and Wooden et al. [37], who advocated a very significant contribution of a crustal contaminant to the basalts by interaction with an asthenospheric melt in open-system magma chambers. They further conjectured that parental magmas to the alkaline series were generated much deeper, and bypassed the large crustal magma chambers during their ascension. Lightfoot et al. [18] suggest a third model whereby the geochemical and isotopic signatures of the SFB might be entirely derived from partial melting of lithospheric mantle containing a recycled sediment component. The osmium, lead, and neodymium isotope data obtained by Walker et al. [33] led them to propose that the primary SFB melts had a source similar to OIB, possibly a mantle plume ascending from the outer core-lower mantle boundary, which itself incorporated recycled oceanic crust.

In previous work by Kogarko et al. [17], Nd and Sr isotopic compositions showed only limited variation among all rocks of the Guli massif, except for several syenites and granites that appear to have been crustally contaminated. These results were interpreted as indicating a mantle source for the rocks, which were characterized by time-integrated light REE and Rb depletion. The significant present enrichment in alkalis and rare earth elements, especially the LREE, of the Guli rocks suggested that the depleted mantle source was subjected to intense metasomatism and an influx of rare earth elements and volatile components just before magma generation. In order for the primary isotopic signatures to remain unchanged, metasomatism must have preceded magmatism by no more than a few million years. As was shown by White and McKenzie [34] the majority of flood basalts can be modeled by single-stage melting of lower mantle-derived plumes with chondritic composition and the entrainment of depleted upper mantle material with a MORB isotopic and geochemical signature. Applying this approach to the Nd and Sr isotopic data, it was speculated that the Guli alkaline rocks required the involvement of about 70% of a depleted MORB-like component, which seemed reasonable for these alkaline rocks generated on the periphery of the Siberian plume. In this paper we present complementary Pb isotopic ratios for all six intrusive stages of the Guli alkaline rocks, and re-examine the genetic implications of the combined Sr-Nd-Pb data for the Guli rocks and previously published data for SFB rocks.

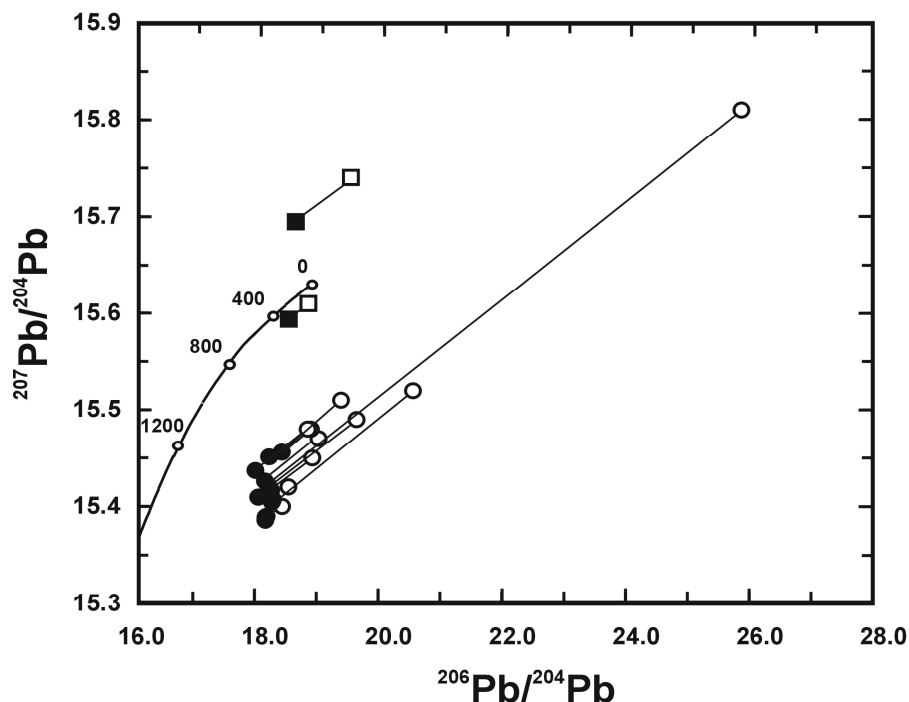


Fig. 2 $^{207}\text{Pb}/^{204}\text{Pb}$ vs. $^{206}\text{Pb}/^{204}\text{Pb}$ diagram showing measured (open symbols) and initial (solid symbols) isotopic composition. Initial ratios are calculated by correcting for 250 Ma of *in situ* radioactive decay. Circles: Silica unsaturated samples presumed to have minimal crustal contamination. Squares: Granite (#97) and quartz syenite (#91) presumed to have significant crustal contamination. Shown also is the Stacey and Kramers [29] model growth curve.

GEOLOGICAL SETTING

The MKC is one of the most extensive alkaline complexes in the world, extending over an area of 220 x 350 km (fig 1) and occupying the western slope of the Anabar shield from the margin of the middle Siberian platform in the north to the upper reaches of the Kotuy River in the S. Voluminous extrusive volcanic rocks dominate the MKC, and are cut by 30 intrusions and numerous dykes spread throughout the complex. The overall sequence of volcanic rocks comprises six distinct suites and have a cumulative thickness of up to 4000 m. Of the six suites the oldest two — the Aryzhangsky and Pravoboyarsky suites — are the most voluminous and are composed of ultramafic-alkaline and basic rocks. Above these two suites are rocks of the Kogotoksky suite, which is composed mostly of basalts and trachybasalts. At the top of the sequence are the Delcan suite represented by trachybasalts, trachyandesites and melanephelenites, and finally high Mg ultrabasic lavas and tuffs (maymechites) extending for more than 20 km along the Maymecha River. The Guli massif (fig 1) occupies a large area between the Maymecha and Kotui Rivers at the boundary of the Siberian platform with the Hatanga trough. It has a roughly oval shape of 35 x 45 km, and, including the two-thirds obscured by Quaternary deposits, has an area of 1500-1600 km² [9]. Geophysical evidence

indicates near vertical contacts and hence probably a stock-like form [16]. The surrounding country rocks are volcanics, and include an extensive area of maymechites.

The Guli massif, like many of the other alkaline-ultrabasic intrusions, is a composite, multi-stage pluton, as indicated in Table 1. The predominant rocks of the massif are dunites, which occupy about 60% of the total area, and a range of melanocratic alkaline rocks, which extend over about 30%. The other rock types, including melilitolite, ijolite, alkaline syenite and carbonatite, occupy less than 10% of the area. (1) The earliest rocks of the massif (first stage) are dunites, which

Table 1

Principal intrusive stages, sub-stages, and rock types in the Guli massif.

Intrusive Stage	Sub-stage	Rock types
Six (Youngest)	Fourth	Dolomite carbonatite
	Third	Fine-grained calcite carbonatite
	Second	Coarse-grained calcite carbonatite
	First	Phoscorite and ore forsteritite
Fifth	Second	Micro-shonkinite and solvsbergite
	First	Peralkaline syenite, nepheline syenite, quartz syenite
Fourth		Ijolite and ijolite pegmatite
Third	Third	Jacupirangite and melteigite
	Second	Melanephelinite, olivine melanephelinite, nepheline picrite, biotite-pyroxene picrite
	First	Melteigite, malignite, shonkinite
Second		Melilite rocks
First (Oldest)	Second	Ti-Fe-ore pyroxenite (kosvite), porphyritic olivine pyroxenite and peridotite
	First	Dunite

form an arcuate area with a width of 9-10 km that can be traced for 40 km. During the second sub-stage the dunite intrusives were cut by numerous bodies of Ti-Fe-ore pyroxenite (kosvite) that are composed mainly of pyroxene and titanomagnetite with accessory apatite and titanite, and form about 10% of the volume of the dunites. (2) The second stage of evolution is marked by the intrusion of melilitic rocks that occur as a 5 x 0.6 km partial ring body in the southern structural center of the massif and three smaller stocks 8 km to the southeast of the main ring. The composition of the rocks — melilitolite and kugdite — is characterized by the predominance of melilite over olivine, which in the melilitolite is up to 90 % of the volume. The accessory minerals are pyroxene, nepheline and titanomagnetite. (3) During the third intrusive phase a series of alkaline mafic and ultramafic rocks of rather closely related composition were emplaced in the following succession: sub-stage 1 — melteigite-malignite-shonkinite; sub-stage 2 — melanephelinite-alkaline picrite, and sub-stage 3 — jacupirangite-melteigite. The most widespread rocks of

this phase are the jacupirangites and melteigites, which are characterized by the presence of pyroxene — up to 90% in the jacupirangite, and nepheline—from 10 % up to 35-45% in the melteigite. The rocks of the melanephelinite-alkaline picrite series (second sub-stage) crop out in three large belts — up to 2 km across, and also occur as dyke-like bodies of alkaline picrite (containing nepheline and biotite-pyroxene, as well as olivine). The jacupirangite and melteigites of the third sub-stage are cut by (4) veins of ijolite and ijolite pegmatites, which represent the fourth intrusive stage. The pegmatites are composed mainly of nepheline (55-65%) and clinopyroxene (25-40%) with accessory titanomagnetite, phlogopite, perovskite, titanite and apatite. (5) In the center of the massif there are several bodies of fine- to medium-grained peralkaline syenite (the fifth stage), which are composed of up to 65% K-feldspar, aegirine and small amounts of nepheline. Syenites, quartz syenites, and granites form small dyke-like bodies in the central part of the massif. (6) Rocks of the sixth and final stage are essentially carbonatites and phoscorites. The rocks of the carbonatite group form two massifs – the Northern and Southern and are represented mostly by fine-grained calcite (third sub-stage) as well as dolomite carbonatite (fourth sub-stage). Apart from the dominant carbonate minerals, the carbonatites also contain apatite, magnetite, phlogopite, and, more rarely, forsterite, aegirinediopside, pyrrhotite, pyrochlore, dysanallyte, calzirtite and others.

ANALYTICAL METHOD

All samples used in this investigation are a subset of a larger suite of Guli alkaline rocks and carbonatites that have been previously analyzed for Sr and Nd isotopes [17]. The rocks had already been broken into small pieces, hand-picked free of weathered or altered material, cleaned in distilled water and 6N HCl, and pulverized to ~200 mesh. The resultant powders required no further preparation before being brought into the chemistry laboratory. X-ray spectrographic analyses that included Pb, U, and Th concentrations were available for about 2/3 of the samples, and this information was beneficial in determining appropriate sample size for dissolution and spiking. Generally, we tried to obtain ~1 ng Pb for mass spectrometric analysis, which usually required the digestion of 1-5 mg of the sample. One nepheline syenite (#863) with 108 ppm Pb would have far exceeded our target recovery amount; even so ~1 mg of the sample was dissolved but only a small aliquot taken for resin column separation.

The sample powders were weighed, transferred into 15 mL Teflon digestion vessels, and wetted with a few drops of milli-Q H₂O to avoid static dispersal. Next about 5 mL HF and 1 mL HNO₃ were added to the vessel, which was then capped and placed on a hotplate for 1-2 days. After evaporating the solution to dryness, 1 mL HNO₃ was added, the cap replaced, and the vessel put back on the hotplate for another day. The solution was cooled, and a fraction for concentration measurement was removed and spiked with either a ²⁰⁵Pb-²³⁵U or ²⁰⁵Pb-²³⁵U-²²⁹Th

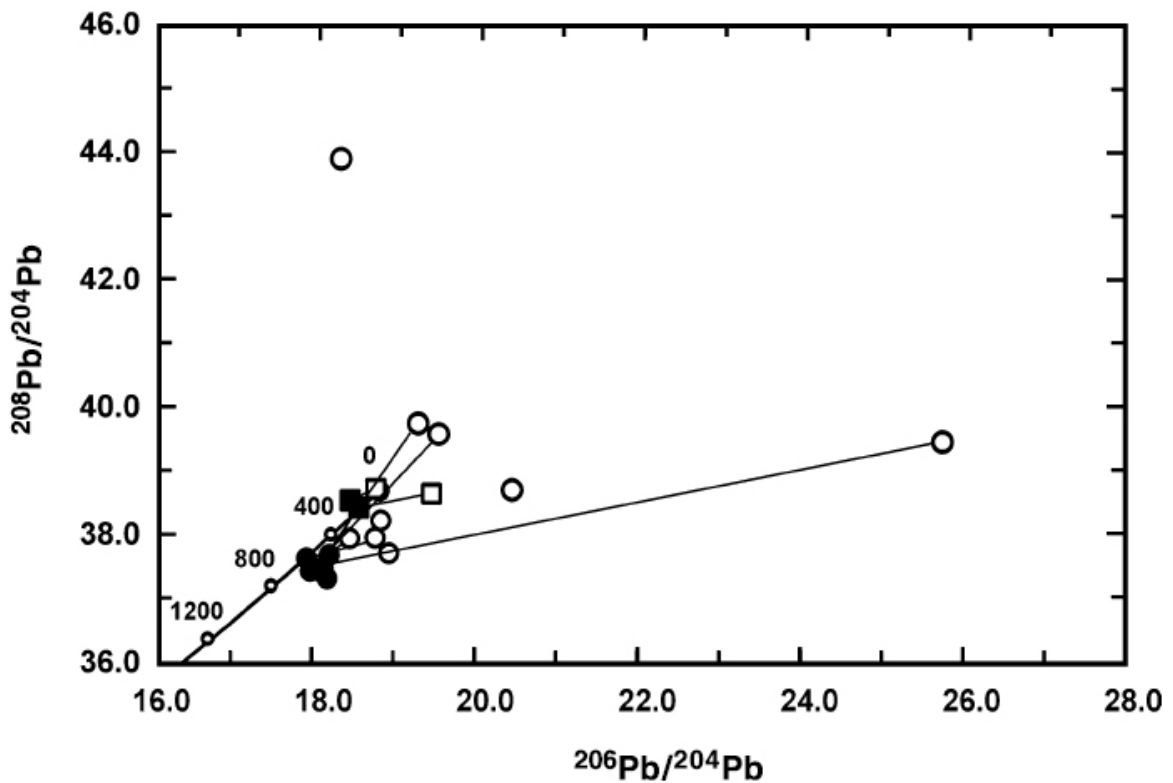


Fig. 3. $^{208}\text{Pb}/^{204}\text{Pb}$ vs. $^{207}\text{Pb}/^{204}\text{Pb}$ diagram showing measured (open symbols) and initial (solid symbols) isotopic composition. Initial ratios are calculated by correcting for 250 Ma of *in situ* radioactive decay. Circles: Silica unsaturated samples presumed to have minimal crustal contamination. Squares: Granite (#97) and quartz syenite (#91) presumed to have significant crustal contamination. Shown also is the Stacey and Kramers [29] model growth curve.

tracer solution. Both solutions were evaporated to dryness, and the residues re-dissolved in 0.5N HBr in preparation for anion resin exchange column separation of the Pb. The purified Pb was dried to a small droplet and loaded with a silica gel- H_3PO_4 activator on a single rhenium filament for mass spectrometry. The elutriate from the Pb concentration column, containing the spiked U (and Th), was dried, dissolved in 7N HNO_3 , re-dried, and re-dissolved in 7N HNO_3 in preparation for anion resin exchange column separation of the U and Th. Usually the same column as was used for Pb separation was converted to the nitrate form by multiple washings with 7N HNO_3 , and purification was effected by elutriation with several column volumes of 7N HNO_3 following which the U and Th were removed with H_2O and 0.1N HCl. The purified U and Th were dried and loaded as nitrates with aquadag on a single rhenium filament for mass spectrometry.

Isotopic analysis was performed at the Max Planck Institute on a 30 cm radius-of-curvature, 90° extended geometry mass spectrometer equipped with Faraday cup and electron multiplier detection systems. Depending on intensity of

the ion beam, Pb was measured on one or the other of the detectors, and U and Th were measured exclusively on the electron multiplier. The NBS 981 Pb standard was run repeatedly during the course of the investigation, and Pb ratios are reported normalized to that standard. Correction for the procedural blank of 10-15 pg for Pb and 0.5-1 pg for U and Th was small to negligible for all samples, but has been routinely applied in the data reduction. Uncertainties arising mainly from variable mass fractionation are estimated to be 0.1%, 0.15%, and 0.2% for $^{206}\text{Pb}/^{204}\text{Pb}$, $^{207}\text{Pb}/^{204}\text{Pb}$, and $^{208}\text{Pb}/^{204}\text{Pb}$, respectively. Concentrations of 1 ppm or higher are considered accurate to about 1% (95% confidence level), and proportionately less accurate for lower concentrations. Consequently, parent-daughters ratios have assigned an uncertainty of ~1.4% in the ISOPLOT [19] calculation of an isochron age. The concentration and isotopic data for the Guli alkaline rocks are summarized in Table 2.

RESULTS

Representative silicate rocks and carbonatites from all intrusive phases of the Guli massif have been analyzed (Table 2). The measured Pb isotope ratios exhibit substantial variations among samples ($^{206}\text{Pb}/^{204}\text{Pb} = 18.06\text{-}25.66$, $^{207}\text{Pb}/^{204}\text{Pb} = 15.38\text{-}15.74$, and $^{208}\text{Pb}/^{204}\text{Pb} = 37.45\text{-}43.91$), but upon correcting for 251 Ma of *in situ* U and Th radioactive decay the data plot as noticeably tighter clusters ($^{206}\text{Pb}/^{204}\text{Pb} = 17.88\text{-}18.52$, $^{207}\text{Pb}/^{204}\text{Pb} = 15.38\text{-}15.70$, and $^{208}\text{Pb}/^{204}\text{Pb} = 37.33\text{-}38.56$) on $^{207}\text{Pb}/^{204}\text{Pb}$ vs. $^{206}\text{Pb}/^{204}\text{Pb}$ (Fig.2) and $^{208}\text{Pb}/^{204}\text{Pb}$ vs. $^{206}\text{Pb}/^{204}\text{Pb}$ (Fig.3) diagrams. The five samples for which Th concentrations have not been determined could not be corrected for *in situ* growth of thorogenic Pb, and these samples are excluded from further discussion of initial $^{208}\text{Pb}/^{204}\text{Pb}$ ratios. An even more restricted range in isotopic composition ($^{206}\text{Pb}/^{204}\text{Pb} = 17.88\text{-}18.31$, $^{207}\text{Pb}/^{204}\text{Pb} = 15.38\text{-}15.46$, and $^{208}\text{Pb}/^{204}\text{Pb} = 37.33\text{-}37.70$) is observed by excluding the quartz syenite and granite and considering only the silica unsaturated rock samples. For most of the samples appreciable amounts of radiogenic Pb have grown since the rocks crystallized, requiring large corrections in calculating initial ratios and making it difficult to evaluate the remaining scatter in isotopic composition. However, when compared to the dunite (#8513), which requires almost no *in situ* decay correction, deviation in isotopic composition does not correlate with parent-daughter ratio as might be expected if the samples were chemically disturbed. In this regard the variation in $^{207}\text{Pb}/^{204}\text{Pb}$, although less than for the other ratios, is perhaps the most significant in that it is by far least affected by uncertainties in the parent-daughter ratio and can carry important petrogenetic information. As will be discussed below, most of the remaining $^{207}\text{Pb}/^{204}\text{Pb}$ scatter after *in situ* decay correction arises from two samples, a granite (#97) and a quartz syenite (#91), for which there is convincing geochemical and isotopic evidence of crustal contamination. These rocks are silica oversaturated and are also characterized by high $^{87}\text{Sr}/^{86}\text{Sr}$ and negative initial ϵ_{Nd} (-8.9 and -14.7) values [17].

Figure 4 is a $^{207}\text{Pb}/^{204}\text{Pb}$ vs. $^{206}\text{Pb}/^{204}\text{Pb}$ diagram on which are plotted the *in situ* decay corrected Guli alkaline massif samples together with the published Pb isotope compositions of SFB [1, 11, 18, 27, 33, 36, 37]. There is a general overlap in isotopic composition of the alkaline and basaltic rocks, although the silica unsaturated Guli samples appear to have a slight relative impoverishment in ^{207}Pb , which is most pronounced in the geochemically primitive dunite (#8513) and the carbonatite (#124). The other silica unsaturated alkaline rocks have isotopic compositions plotting in the lower portion of the Putorana basalt field. Interestingly, those basalt samples comprising the lower portion of the SFB isotopic field are from the oldest and most voluminous Gudchikhinsky and Ivakinsky Suites of the SFB [10].

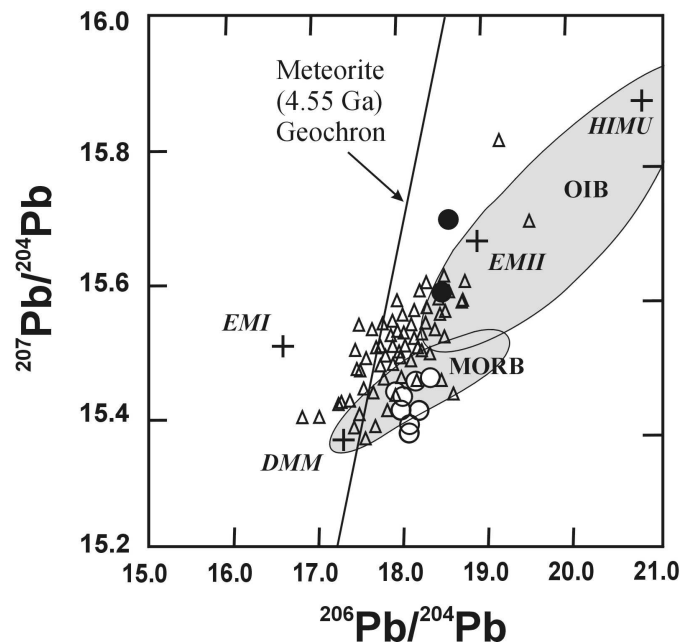


Fig. 4. $^{207}\text{Pb}/^{204}\text{Pb}$ vs. $^{206}\text{Pb}/^{204}\text{Pb}$ diagram showing the *in situ* decay corrected Guli alkaline complex samples (circles, open – silica unsaturated; solid – granite (#97) and quartz syenite (#91) together with the published Pb isotope compositions [27, 33, 36, 37] of SFB rocks (triangles). While there is a general similarity in isotopic composition of the alkaline and basaltic rocks, the silica unsaturated Guli rocks tend to plot beneath (i.e., with lower $^{207}\text{Pb}/^{204}\text{Pb}$) or in the lower portion of the SFB field. In contrast, the granite and quartz syenite, which are presumed to be crustally contaminated, plot near the top and above the SFB field.

In contrast, the granite and quartz-bearing syenite, which are quite probably contaminated by, or even the partial melts of, crustal material, are significantly enriched in ^{207}Pb . On the whole, the uncontaminated Guli rocks appear to have been derived from a slightly more depleted source than the SFB, and to have had a Pb isotopic composition close to that of the DMM reservoir. However, a few

analyses out of the 148 SFB analyzed for Pb are characterized by even more depleted compositions, but they are much more enriched in radiogenic Sr and have lower ϵ Nd values. It can be speculated that during upward migration some of the melt may have co-mingled with super-plume magma while undergoing differentiation, causing a mixing of Pb isotopic compositions. This same trend for Guli rocks is shown by the data for the Rb-Sr and Sm-Nd isotopic systems [17].

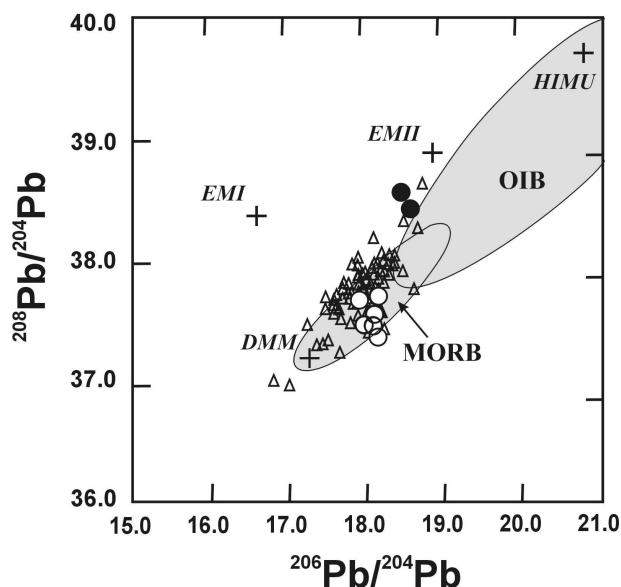


Fig. 5. $^{208}\text{Pb}/^{204}\text{Pb}$ vs. $^{206}\text{Pb}/^{204}\text{Pb}$ diagram showing the *in situ* decay corrected Guli massif rocks (circles, open – silica unsaturated; solid – granite (#97) and quartz syenite (#91) together with the published Pb isotope compositions [27, 33, 36, 37] of SFB rocks (triangles). Note that while there is a general similarity in isotopic composition of the alkaline and basaltic rocks, the silica unsaturated Guli rocks tend to plot beneath (i.e., with lower $^{208}\text{Pb}/^{204}\text{Pb}$) or in the lower portion of the SFB field. In contrast, the granite and quartz syenite, which are presumed to be crustally contaminated, plot near the top and above the SFB field.

Figure 5 is a $^{208}\text{Pb}/^{204}\text{Pb}$ vs. $^{206}\text{Pb}/^{204}\text{Pb}$ diagram on which are plotted a subset of eight *in situ* decay corrected Guli alkaline massif samples together with the published Pb isotope compositions of SFB. Because thorium concentrations have been determined on only six of the Guli silica unsaturated rock samples and the quartz-bearing syenite and granite, calculation of initial $^{208}\text{Pb}/^{204}\text{Pb}$ ratios can only be carried out for this subset of samples. As in the case of the $^{206}\text{Pb}/^{204}\text{Pb}$ ratios, there is no assurance that after correction for *in situ* radiogenic Pb growth the remaining small dispersion among the silica unsaturated samples represents a real heterogeneity in initial isotopic composition. Again, deviation in $^{208}\text{Pb}/^{204}\text{Pb}$ ratios from the dunite (#8513) value does not correlate with parent-daughter ratio, nor, indeed, with the corresponding $^{206}\text{Pb}/^{204}\text{Pb}$ ratios. In comparing the Guli results with the SFB isotopic field, a similar relationship as seen in Figure 4 emerges. That is, the silica unsaturated Guli samples lie either slightly below (i.e., are more

deficient in ^{208}Pb) or within the lower portion of the SFB field. Likewise, the granite and quartz-bearing syenite have $^{208}\text{Pb}/^{204}\text{Pb}$ ratios that plot distinctly apart in the upper-right of the SFB field. From the similarity in isotopic composition shown in Figures 4 and 5 of the quartz syenite and granite to the most radiogenic, enriched SFB, it might be deduced that a crustal component similar to that characterizing the Guli granite was also likely to have been the major contaminant for all the flood basalts. These plots also show that, except for the quartz syenite and granite, the alkaline rocks of the main intrusive phases of the Guli massif were not strongly affected by crustal contamination.

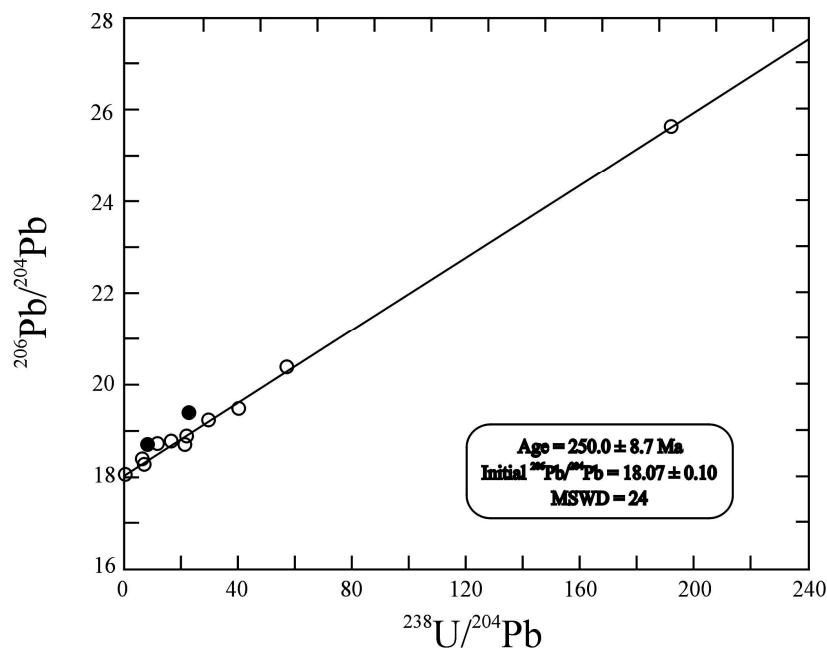


Fig. 6. $^{206}\text{Pb}/^{204}\text{Pb}$ vs. $^{238}\text{U}/^{204}\text{Pb}$ isochron diagram for the Guli massif rocks. The granite (#97) and quartz syenite (#91) shown in solid symbols, which have distinctly different initial isotopic compositions, are excluded from the age calculation.

Another way to examine our analyses is to plot the measured $^{238}\text{U}/^{204}\text{Pb}$ vs. $^{206}\text{Pb}/^{204}\text{Pb}$ on an isochron diagram (Fig. 6). If *in situ* radiogenic growth greatly exceeds the heterogeneity in initial isotopic composition and closed-system conditions have prevailed subsequently, the resulting isochron will yield an age for the Guli alkaline suite. Because it has already been determined that the quartz syenite and granite have an initial isotopic composition distinctly different from the silica unsaturated Guli rocks, these two samples were omitted from the isochron calculation. A York fit regression line through the remaining 11 silica unsaturated samples yields an isochron age of 250 ± 9 Ma [MSWD = 24], and lies within the range of ages of 232-253 Ma found for the SFB by previous workers [2, 8, 13, 14, 15]. However, because of the high MSWD and age uncertainty of the Guli isochron, which is largely controlled by one highly radiogenic jacupirangite (#131) and may also reflect significant scatter in initial isotopic composition, this

result is too imprecise to help in determining the relative order of emplacement. Instead, it is the very precise zircon and baddeleyite U-Pb ages on the SFB and Guli carbonatite recently reported by Kamo et al., [14, 15] that, in fact, leave little doubt but that the alkaline magmatism occurred essentially synchronously with the rapid eruption of the SFB at 251 Ma. Moreover, the obtained ages of Guli rocks and SFB, indicating that the bulk of both rock suites formed within a one million year time span, virtually coincide with the age of the Permian-Triassic boundary at 251.2 ± 1.7 Ma [7].

DISCUSSION

In order to investigate the lead isotope geochemistry of the Guli alkaline rocks and gain insight into their petrogenesis, we have made a compilation of all the published Pb, Sr, and Nd isotope data relating to the SFB province [1, 11, 18, 27, 33, 36, 37]. Our new Pb isotope results together with the relevant SFB data have then been plotted on $^{207}\text{Pb}/^{204}\text{Pb}$ vs. $^{206}\text{Pb}/^{204}\text{Pb}$ (Fig.4) and $^{208}\text{Pb}/^{204}\text{Pb}$ vs. $^{206}\text{Pb}/^{204}\text{Pb}$ (Fig. 5) diagrams. Also shown on the diagrams are the isotopic compositions of a number of widely recognized reference reservoirs and the fields of some major rock types. On the $^{207}\text{Pb}/^{204}\text{Pb}$ vs. $^{206}\text{Pb}/^{204}\text{Pb}$ diagram the SFB form an isotopic array that starts to the left of the meteoritic isochron where the earliest, undifferentiated picrites of the Norilsk area plot, follows along the MORB field, and continues slightly into the OIB field. The main volume of SFB and all of the Guli alkaline rocks plot to the right of the meteoritic isochron, requiring a multistage evolution of the U-Pb systems, produced possibly either by prior differentiation in the mantle source or by the recycling of crustal Pb back into the mantle. A few highly contaminated basalts and the Guli granite extend upward into the upper crustal field. The cluster of silica unsaturated Guli rocks extends below the MORB field and represent a more depleted mantle source, especially in respect to ^{207}Pb .

Mantle plumes are generally thought to be chemically, isotopically, and thermally very heterogeneous and zoned as a result of interaction with depleted MORB mantle, subducted slabs of oceanic crust, continental crust, and subcontinental lithosphere. Large isotopic variations exist in many continental flood basalts [20, 3], and, in the case of the Columbia River basalts, different members have very distinct isotopic compositions [5, 4]. Carlson [5] has used this heterogeneity to propose five isotopic sources for the Columbia River Flood Basalts. Likewise, Simonetti et al. [28] evaluated the variation in isotopic composition of the Deccan flood basalts and attributed the isotopic variations in those rocks to three distinct mantle sources.

On the basis of all existing Sr, Nd, and Pb isotopic data for the SFB and Guli alkaline rocks, we are able to recognize at least five different source components that have contributed to their formation. The first component, identified as the main contributor to the Guli alkaline rocks, is characterized by low $^{87}\text{Sr}/^{86}\text{Sr}$ (0.7031 to 0.7038), high ϵ_{Nd} (+5.35 to +3.97), and unradiogenic Pb ($^{206}\text{Pb}/^{204}\text{Pb} =$

17.88-18.31; $^{207}\text{Pb}/^{204}\text{Pb} = 15.38-15.46$; $^{208}\text{Pb}/^{204}\text{Pb} = 37.33-37.70$). This component bears a depleted mantle (MORB source) reservoir Pb isotopic signature, but with slightly more evolved Sm-Nd and Rb-Sr isotopic systems. Because of this divergence from pure MORB and the overlap in Pb isotopic composition with the second component described next, it cannot be ruled out that some contribution from the Siberian super-plume is also present in the Guli rocks. Based on Sr and Nd isotopes, Kogarko et al. [17] estimated the involvement of about 70% of upper mantle material (MORB source) and 30% of lower mantle material corresponding to primitive mantle as suggested by White and MacKenzie [34].

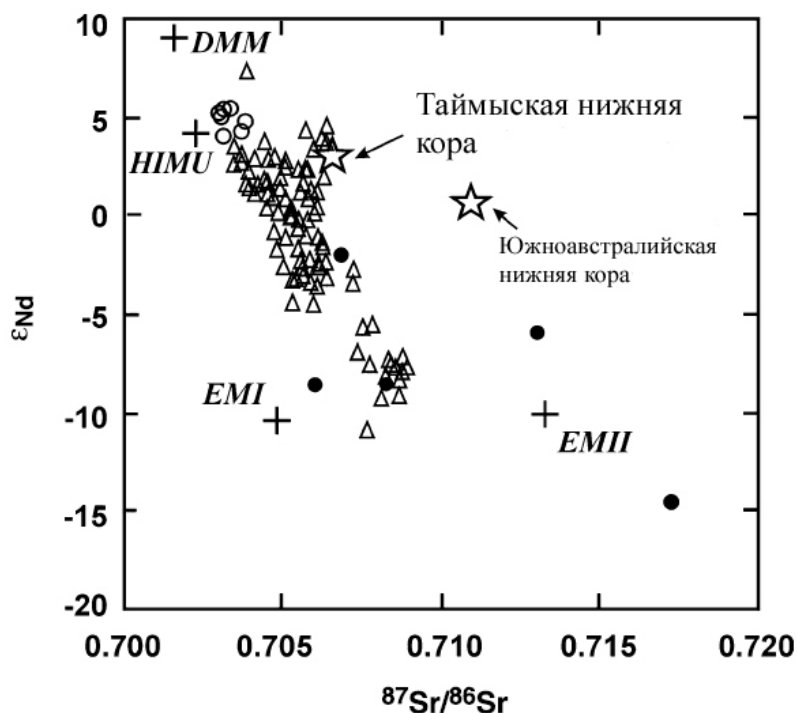


Fig. 7. ϵ_{Nd} vs. $^{87}\text{Sr}/^{86}\text{Sr}$ diagram showing a plot of the Guli massif rocks (circles, open – silica unsaturated; solid – granite (#97) and quartz syenite (#91) together with the published isotope compositions of SFB rocks [triangles; 1, 11, 18, 26, 27].

The second component, which can be attributed to the Siberian super-plume itself [27], is represented by the Putorana basalts making up 90-95% of the SFB province. These basalts demonstrate significant chemical and isotopic uniformity with ϵ_{Nd} ranging from -0 to +2.5, $^{87}\text{Sr}/^{86}\text{Sr}$ from 0.7046 to 0.7052, and an average Pb isotopic composition of $^{206}\text{Pb}/^{204}\text{Pb} = 18.3$, $^{207}\text{Pb}/^{204}\text{Pb} = 15.5$, and $^{208}\text{Pb}/^{204}\text{Pb} = 38.0$, suggesting that the majority of the SFB were derived from a relatively primitive lower mantle plume with a near-chondritic signature. Controversy still exists, of course, over the exact nature and origin of this near-chondritic mantle reservoir, which instead of being a remnant of the original, undifferentiated Earth could be material recycled into the mantle by subduction and/or lithospheric foundering processes. It may also be possible that this is the large moderately depleted reservoir (possible situated in the lower mantle), which supplies OIBs and other plume related magmas (PREMA- or FOZO-like material) [12].

Table 2

Strontium ,neodymium ,lead isotopic composition and Pb, U, and Th concentration of rocks from the Guli intrusion, Maymecha-Kotuy area, Siberia. Numerals in parentheses refer to the sequential stages/sub-stages of emplacement identified from field relationships.

Sample	Pb, ppm	U, ppm	Th, ppm	$\mu =$ ^{238}U / ^{204}Pb	$\kappa\mu =$ ^{232}Th / ^{204}Pb	Measured			Initial**			Initial ***	
						$^{206}\text{Pb}/$ ^{204}Pb	$^{207}\text{Pb}/$ ^{204}Pb	$^{208}\text{Pb}/$ ^{204}Pb	$^{206}\text{Pb}/$ ^{204}Pb	$^{207}\text{Pb}/$ ^{204}Pb	$^{208}\text{Pb}/$ ^{204}Pb	$^{87}\text{Sr}/$ ^{86}Sr ****	ϵ_{Nd} ****
8513 dunite (I/1)	1.65	0.01	0.03	0.38	1.17	18.06	15.38	37.45	18.05	15.38	37.44	0.703760	+4.08
37 maymechite (I/2)	1.25	0.43	--	21.9	--	18.89	15.47	37.73	18.03	15.43	--	-	-
118 melilitolite (II)	2.02	1.76	--	57.2	--	20.40	15.52	38.72	18.15	15.41	--	0.703174	+4.83
92 melteigite (III/1)	2,40	1.46	6.14	39,8	173	19.50	15.49	39,60	17,93	15.41	37.45	0.703170	+5.15
47 alkaline picrite (III/2)	7.88	1.45	--	11.8	--	18.77	15.48	38.71	18.31	15.46	--	0.703135	+5.33
861 alkaline picrite (III/2)	8,02	2.10	8.9*	16,6	72,8	18.79	15.45	38.24	18,13	15.42	37.33	0.703266	+4.81
131 jacupirangite (III/3)	2.18	5.90	4.7*	192	158	25.66	15.81	39.47	18.08	15.42	37.51	0.703116	+5.16
132 ijolite (IV)	1.46	0.49	0.57	21.2	25.5	18.72	15.48	37.97	17.88	15.44	37.65	0.703446	+5.35
863 nepheline syenite (V/1)	107	47.7	--	29.1	--	19.25	15.51	39.76	18.10	15.45	--	-	-
89 nepheline syenite (V/1)	1.40	0.14	0.45*	6.29	20.9	18.41	15.42	37.96	18.16	15.41	37.70	0.706771	-1.85
91 quartz syenite (V/1)	7.17	0.89	1.59	7.95	14.7	18.73	15.61	38.74	18.42	15.59	38.56	0.706261	-8.90
97 granite (VI)	11	3.81	2.83	22.4	17.2	19.41	15.74	38.66	18.52	15.70	38.45	0.717440	-14.69
124 carbonatite (VII/3)	2.26	0.23	--	6.92	--	18.31	15.40	43.91	18.04	15.39	--	0.703164	+4.88

Note: Th determined by x-ray spectrographic analysis. ** Corrected for 251 Ma of in situ radioactive decay. ****Kogarko et al [17]

Wooden et al. (1993), in a detailed investigation of the SFB in the Norilsk area, found a tendency for the more silica-rich samples to have higher Th/Ta ratios, relatively high $^{87}\text{Sr}/^{86}\text{Sr}$ ratios, and low $^{143}\text{Nd}/^{144}\text{Nd}$ and $^{206}\text{Pb}/^{204}\text{Pb}$ ratios. This shift was attributed to a significant interaction of the SFB with continental crust, and the ϵ_{Nd} vs. $^{87}\text{Sr}/^{86}\text{Sr}$ plot (Fig 7) shows this distinct trend toward the composition of continental crust. The SFB province is underlain by Paleozoic sedimentary rocks and a granite-gneiss Precambrian basement [9]. The Guli granite (#97) and, to a lesser extend, quartz syenite (#91), which were either contaminated by, or produced as an actual melt of upper crust, are here considered as the third component of SFB source.

Some samples of the Gudchikhinsky suite (basal member of the SFB) are characterized by low $^{206}\text{Pb}/^{204}\text{Pb}$ ratios and plot to the left of the meteoritic

isochron on the $^{207}\text{Pb}/^{204}\text{Pb}$ vs. $^{206}\text{Pb}/^{204}\text{Pb}$ diagram (Fig. 4). They also have high $^{87}\text{Sr}/^{86}\text{Sr}$ values relative to ϵ_{Nd} , and plot noticeably to the right of the main trend on the ϵ_{Nd} vs. $^{87}\text{Sr}/^{86}\text{Sr}$ diagram (Fig. 7). Lightfoot et al. [18] have also remarked that the rocks of the Gudchikhinsky suite show quite different geochemical features (e.g., high Ti, La/Sm, Ti/Y, Gd/Y) as compared to the other basaltic suites of the Norilsk area. Lightfoot et al. [18] noted that the Gudchikhinsky suite has chemical and isotopic characteristics resembling those of OIB, although they suggested that lithospheric mantle was the main component of all the SFB. However, Wooden et al. [37] proposed that these same characteristics were most readily explained by partial melting of crustal material. According to them the isotopic features of the Gudchikhinsky might then have been superimposed during post-crystallization alteration. In our opinion old lower crust is a more suitable candidate for being the exotic component in the source of the Gudchikhinsky suite. On the basis of a large Pb-isotope database for lower crustal xenoliths, Murphy et al. [23] determined that metamorphosed Archean lower crustal granulites contain very unradiogenic Pb, which often plot to the left of the meteorite isochron. Furthermore, Stolz and Davies [30], McCulloch et al. [22] and Stosch and Lugmair [31] found that the majority of garnet granulite xenoliths have relatively high $^{87}\text{Sr}/^{86}\text{Sr}$ in comparison with $^{143}\text{Nd}/^{144}\text{Nd}$ values and plot significantly to the right of the mantle array. For example, McCulloch et al. [22] calculate that the average South Australian lower crust has a $^{87}\text{Sr}/^{86}\text{Sr}$ of 0.7124 and a ϵ_{Nd} of +0.27 (recalculated to 250 Ma). The position of the South Australian lower crust on the ϵ_{Nd} vs. $^{87}\text{Sr}/^{86}\text{Sr}$ diagram (Fig.7) suggests that such a lower crustal component may be present in the SFB. Unfortunately there is no direct information about the isotopic composition of the Polar Siberian lower crust. However, a granite from the Taymir peninsula with the same approximate age, which is considered to be derived from lower crustal material remobilized by the Siberian super-plume, plots very close to the Gudchikhinsky basalts [32]. According to Vernikovskiy et al. [32] the isotopic signature of the Taymir granite probably resulted from the mixing of mantle and lower crustal components. Thus, we propose that old lower crustal material makes up a fourth component of the SFB.

The enormous concentration of rare-earth and related elements in alkaline rocks and carbonatites, such as those of the Guli massif, is thought to have occurred through the scavenging of metasomatically veined mantle material by melts or fluids associated with the upwelling plume. In order to preserve the primary isotopic signature of the depleted source of the Guli rocks, this metasomatizing event in Siberia must have occurred only shortly before 251 Ma. Subsequent to emplacement, however, considerable Pb isotopic growth has taken place in many of the rocks with high U/Pb and Th/Pb ratios. This metasomatically-derived component can be considered a fifth component found predominantly in some of the Guli alkaline rocks.

As it was mentioned before, a similar wide range in isotopic composition has been established for other flood basalt provinces [21, 5, 6, 4], suggesting the

contribution of isotopically distinct components in their genesis. Some of these components are very similar to those here identified as contributing to the SFB and the Guli alkaline massif. Collectively, all these data testify to the significant isotopic heterogeneity that is one of the main geochemical features of continental flood basalts.

CONCLUSIONS

1. The Pb isotope composition of the SFB and the Guli alkaline rocks on $^{207}\text{Pb}/^{204}\text{Pb}$ vs. $^{206}\text{Pb}/^{204}\text{Pb}$ and $^{208}\text{Pb}/^{204}\text{Pb}$ vs. $^{206}\text{Pb}/^{204}\text{Pb}$ diagrams lie almost entirely within the limits of the MORB and OIB fields, identifying the mantle as the dominant component in the source of these rocks. The new Pb isotopic compositions reported here for the Guli rocks overlap with those previously published for the SFB; however, they are mainly confined to a cluster plotting in the lower portion of the OIB field and extending slightly downward into the MORB field. We take this distinction to imply that the Guli rocks were derived from a more depleted source than produced the SFB. A similar implied source difference between the Guli rocks and the SFB based on the Rb-Sr and Sm-Nd isotopic systems had been shown by an earlier study.
2. A U-Pb age of 250 ± 9 Ma was determined for the Guli alkaline rocks, which lies within the range of ages previously reported for the SFB, and agree well with the recently published zircon and baddeleyite U-Pb ages of ~ 251 Ma found for both a Guli carbonatite and the bulk of the SFB. There thus remains little doubt that the Guli alkaline rocks were emplaced essentially synchronously with the Siberian trap basalts. The age of the Guli rocks and the SFB is also seen to coincide with that of the Permian-Triassic boundary.
3. The combined Pb, Sr, and Nd isotopic systematics of the SFB and the Guli alkaline rocks has enabled the identification of several discrete source components. The first component is characterized by low $^{87}\text{Sr}/^{86}\text{Sr}$, high $^{143}\text{Nd}/^{144}\text{Nd}$, and an unradiogenic Pb, which we associate with the depleted (MORB source) mantle with perhaps a slightly more evolved Rb-Sr and Sm-Nd isotopic system. The second component representing 90-95% of all SFB demonstrates notable chemical and isotopic uniformity with ϵ_{Nd} values of 0 to +2.5, $^{87}\text{Sr}/^{86}\text{Sr}$ values of 0.7046 to 0.7052, and an average Pb isotopic composition of $^{206}\text{Pb}/^{204}\text{Pb} = 18.3$, $^{207}\text{Pb}/^{204}\text{Pb} = 15.5$, and $^{208}\text{Pb}/^{204}\text{Pb} = 38.0$. This component is speculated to be a relatively primitive lower mantle plume with a near-chondritic isotopic signature. Contamination by upper and lower continental crustal material, designated as components 3 and 4, respectively, is postulated to explain the isotopic characteristics of some of the Guli rocks and SFB. Finally, metasomatic processes associated with invasion of the Siberian superplume produce a fifth component responsible for the extreme enrichment in rare-earth and related elements found in some Guli rocks and basalts.

ACKNOWLEDGMENTS

The authors are grateful to Professors G.W. Lugmair and E. Jaguts for the invitation to the Max Plank Institute (Mainz). We would like to thank K. Goodenough and T. Andersen for their constructive reviews. These investigations were supported by the Russian Foundation for Basic Research (grant N-05-05 64 144)

REFERENCES

1. **Arndt, N., Chauvel, C., Czamanske, G., and Fedorenko, V.** (1998) Two mantle sources, two plumbing systems: tholeiitic and alkaline magmatism of the Maymecha River basin, Siberian flood basalt province. *Contrib. Mineral. Petrol.* 133, 297-313.
2. **Basu, A. R., Poreda, R. J., Renne, P. R., Teichmann, F., Vasiliev, Y.R., Sobolev, N. V., and Turrin, B. D.** (1995) High-He-3 plume origin and temporal-spatial evolution. *Science* 269, 822-825.
3. **Bell, K.** (2001) Carbonatites: relationship to mantle-plume activity in Ernst, R.E. and Buchan, K.L., eds., *Mantle Plumes: their identification through time*, Geological Society of America Special Paper, 267-290.
4. **Brandon, A. D., Hooper, P. R., Goles, G. G., and Lambert, R. S.** (1993) Evaluating crustal contamination in continental basalts: the isotopic composition of the Picture Gorge Basalt of the Columbia River Basalt Group. *Contrib. Mineral. Petrol.* 114, 452-464.
5. **Carlson, R. W.** (1984) Isotopic constraints on Columbia River flood basalt genesis and the nature of the subcontinental mantle. *Geochim. Cosmochim. Acta* 48, 2357-2372.
6. **Carlson, R. W., and Hart, W. K.** (1988) Flood basalts volcanism in the Northwestern United States. in *Continental Flood Basalts*, Macdougall, J. D. (ed.), Kluwer Academic Publishers, 35-63.
7. **Claoue-Long, J. C., Zichao, Z., Guogan, M., and Shaohua, D.** (1991) The age of Permian-Triassic boundary. *Earth Planet. Sci. Lett.* 105, 182-190.
8. **Dalrymple, B. G., Czamanske, G. K., Fedorenko, V. A., Simonov, O. N., Lanphere, M. A., and Likhachev, A. P.** (1995) A reconnaissance $^{40}\text{Ar}/^{39}\text{Ar}$ geochronological study of ore-bearing and related rocks, Siberian Russia. *Geochim. Cosmochim. Acta* 59, 2071-2083.
9. **Egorov, L.S.** (1991) Ijolite carbonatite plutonism (case history of the Maimecha-Kotui complexes northern Siberia). Nedra, Leningrad, 260 pp.
10. **Fedorenko, V., Lightfoot, P.C., Naldrett, A.J., Czamanske, G.K., Hawkesworth, C.J., Wooden J.L., Ebel, D.S.** (1996) Petrogenesis of the Siberian Flood Basalt sequence at Noril'sk. *International Geology Review* 38, 99-135.
11. **Fedorenko, V., Czamanske, G., Zenko, T., Budahn, J., and Siems, D.** (2000) Field and geochemical studies of the melilite-bearing Arydzhangsky suite, and an overall perspective on the Siberian alkaline-ultramafic flood-volcanic rocks. *International Geology Review* 42, 769-804.
12. **Hofmann, A.W.**, 2003. Sampling mantle heterogeneity through oceanic basalts: isotopes and trace elements, *Treatise on Geochemistry*. Elsevier, pp. 61-10
13. **Kamo, S. L., Czamanske, G. K., and Krogh, T. E.** (1996) A minimum U-Pb age for Siberian flood-basalt volcanism. *Geochim. Cosmochim. Acta* 60, 3505-3511.
14. **Kamo, S. L., Czamanske, G. K., Amelin, Y., Fedorenko, V. A., and Trofimov, V. R.** (2000) U-Pb zircon and baddeleyite and U-Th-Pb perovskite ages for Siberian flood

- volcanism, Maymecha-Kotui area, Siberia (abs) Goldschmidt 2000, Oxford, UK. Journal of Conference Abstracts 5, no 2, 569.
15. **Kamo, S. L., Czamanske, G. K., Amelin, Y., Fedorenko, V. A., Davis, D. W., and Trofimov, V. R.** (2003) Rapid eruption of Siberian flood-volcanic rocks and evidence for coincidence with the Permian-Triassic boundary at 251 Ma. *Earth Planet. Sci. Lett.* 214, 75-91.
 16. **Kogarko, L. N., Kononova, V. A., Orlova, M. P., and Woolley, A. R.** (1995) The alkaline rocks and carbonatites of the world: former U.S.S.R., Chapman & Hall, UK, 224 pp.
 17. **Kogarko, L. N., Henderson, M., and Foland, K.** (1999) The Guli ultrabasic alkaline massif in polar Siberia: Evolution and isotope sources. *Doklady Earth Sciences* 364, 88-90.
 18. **Lightfoot, P. C., Hawkesworth, C. J., Hergt, J., Naldrett, A. J., Gorbachev, N. S., Fedorenko, V. A., and Doherty, W.** (1993) Remobilisation of the continental lithosphere by a mantle plume: major-, trace-element, and Sr-, Nd-, and Pb-isotope evidence from picritic and tholeiitic lavas of the Noril'sk district, Siberian trap, Russia. *Contrib. Mineral. Petrol.* 114, 171-188.
 19. **Ludwig, K. R.** (2000) Isoplot/Ex version 2.2, A geochronological toolkit for Microsoft Excel. Berkeley Geochron Center Spec. Publ. No. 1a.
 20. **Macdougall, J.D.** (1998) Continental flood basalts and MORB: a brief discussion of similarities and differences in their petrogenesis. *in* Continental Flood Basalts, Macdougall, J. D. (ed.), Kluwer Academic Publishers, 331-341.
 21. **Mahoney, J. J.** (1988) Deccan Traps, *in* Continental Flood Basalts, Macdougall, J. D. (ed.), Kluwer Academic Publishers, 151-195.
 22. **McCulloch, M. T., Arculus, R. J., Chappell, B.W., and Ferguson, J.** (1982) Isotopic and geochemical studies of nodules in kimberlite have implications for the lower continental crust. *Nature* 300, 166-168.
 23. **Murphy, D.T., Kamber, B.S., Collerson, K.D.** (2002) A refined solution to the first terrestrial Pb-isotope paradox. *J. Petrology* 44, 39-51
 24. **Renne, P. R.** (1995) Excess ⁴⁰Ar in biotite and hornblendite from the Noril'sk 1 intrusion, Siberia: implications for the age of the Siberian traps. *Earth Planet. Sci. Lett.* 131, 165-176.
 25. **Renne, P. R., and Basu, A. R.** (1991) Rapid eruption of the Siberian Traps flood basalts at Permo-Triassic boundary. *Science* 253, 176-179.
 26. **Sharma, M., Basu, A., and Nesterenko, G.V.** (1991) Nd-Sr isotopes, petrochemistry, and origin of the Siberian flood basalts, USSR. *Geochim. Cosmochim. Acta* 55, 1183-1192.
 27. **Sharma, M., Basu, A., and Nesterenko, G.V.** (1992) Temporal Sr-, Nd- and Pb-isotopic variations in the Siberian flood basalts: Implications for the plume-source characteristics. *Earth Planet. Sci. Lett.* 113, 365-381.
 28. **Simonetti, A., Goldstein, S.L., Schmidberger, S.S., Viladkar, S.L.** (1998) Geochemical and Nd,Pb, and Sr isotope data from Deccan alkaline complexes: Inferences for mantle sources and plume-lithosphere interaction. *J. Petrology* 39, 1847-1864
 29. **Stacey, J. S., and Kramers, J. D.** (1975) Approximation of terrestrial lead isotope evolution by a two-stage model. *Earth Planet. Sci. Lett.* 26, 207-221.
 30. **Stolz, A. J., and Davies, G.R.** (1989) Metasomatized lower crustal and upper mantle xenoliths from north Queensland: Chemical and isotopic evidence bearing on the composition and source of the fluid phase. *Geochim. Cosmochim. Acta* 53, 649-660.
 31. **Stosch, H. G., and Lugmair, G. W.** (1984) Evolution of the lower continental crust: granulite facies xenoliths from the Eifel, West Germany. *Nature* 311, 368-370.

32. **Vernikovsky, V. A., Victoria, L., Peaseb, V., Vernikovskaya, A. E., Romanov, A. P., Geed, D., and Travin, A.** (2003) First report of early Triassic A-type granite and syenite intrusions from Taimyr: product of the northern Eurasian superplume? *Lithos* 66, 23-36.
33. **Walker, R. J., Morgan, J.W., Horan, M. F., Czamanske, G. K., Krogstad, E. J., Bouse, R. M., Fedorenko, V. A., and Kunilov, V. E.** (1993) Re-Os isotopic evidence for an enriched-mantle source for the Norilsk-type, ore-bearing intrusions, Siberia. *Geochim. Cosmochim. Acta* 58, 4179-4197.
34. **White, R.S., Mc Kenzie, D.** (1995) Mantle plumes and flood basalts. *J. Geophys Research* 100, 17543-17585
35. **Wilson, M., and Patterson, R.** (2001) Intraplate magmatism related to short-wavelength convective instabilities in the upper mantle: Evidence from the Tertiary-Quaternary volcanic province of western and central Europe. *in* Mantle Plumes: Their identification through time. Geological Society of America Special Paper 352.
36. **Wooden, J. L., Czamanske, G. K., and Bouse, R. M.** (1992) Pb isotope data indicate a complex, mantle origin for the Norilsk-Talnakh ores, Siberia. *Econ. Geol.* 87, 1153-1165.
37. **Wooden, J. L., Czamanske, G. K., Fedorenko, V. A., Arndt, N. T., Chauvel, C., Bouse, R. M., King, Bi-Shia W., Knight, R. J., and Siems, D. F.** (1993) Isotopic and trace-element constraints on mantle and crustal contribution to Siberian continental flood basalts, Noril'sk area, Siberia. *Geochim. Cosmochim. Acta* 57, 3677-3704.
38. **Zindler, A., and Hart, S.** (1986) Chemical geodynamics. *Ann. Rev. Earth. Planet. Sci.* 14, 493-571.
39. **Zolotukhin, V.V., Almukhamedov, A.I.** (1988) Traps of the Siberian platform In *Continental Flood Basalts*, Macdougall, J. D. (ed.), Kluwer Academic Publishers, 273-310.

Paleozoic Alkaline Volcanism of the Northeastern Fennoscandia: Geochemical Features and Petrologic Consequences

Arzamastsev A.A., Petrovsky M.N.

Geological Institute, Kola Science Centre, Russian Academy of Sciences, 14 Fersmana St., Apatity, Murmansk Oblast, 184200 Russia, e-mail: arzamas@geoksc.apatity.ru

ABSTRACT

This paper presents the results of studying the Paleozoic volcanic series of the Kola Province, widespread in the areas of the Lovozero and Khibina massifs, the Kontozero caldera, and the Ivanovka volcano-plutonic complex. A distinctive feature of the volcanics is the presence of moderately alkaline basanites along with silica-undersaturated alkaline rock associations. All of the rocks are significantly enriched in incompatible elements: the contents of Rb, Ba, Sr, Nb, Zr and Y in the volcanics of the Lovozero and Kontozero formations. The Sm-Nd and Rb-Sr data suggest that the volcanics of the study area were derived from two different mantle sources: (1) superdepleted mantle material resulted from the multistage crustal growth over Archean and Proterozoic time in the Kola-White Sea rift-collision zone and (2) a source that had properties of moderately enriched EMI-type mantle. It is shown that the emplacement of the volcanics preceded the main pulse of alkaline magmatism in the region and can be referred to as the initial phase of the Paleozoic tectono-magmatic reactivation. According to geochronological data, the alkaline volcanic rocks were emplaced at least 20-30 m.y. before the intrusion of the alkaline plutonic rocks.

INTRODUCTION

A distinctive feature of the unorogenic continental series of alkaline ultramafic rocks and carbonatites is their spatial and temporal association with alkaline and subalkaline volcanics, the latter varying widely from silica-undersaturated alkaline ultramafics and nephelinite to normal basalt and trachyandesite. Examples of these associations are the Maimecha-Kotui Province and the alkaline province of East Africa, where in addition to ultrabasic lavas there are volcanics of the alkaline basalt, alkaline olivine basalt, and tholeiite basalt series [32, 36, 22]. Studies that were performed in these regions revealed the sources and evolution trends mainly for the series of alkaline ultramafics-carbonatites, for which comagmatic rocks of different depth facies were found. A more complicated problem is the role and place of subalkaline rocks, which are only represented by extrusive facies and have no plutonic equivalents in the magmatic complexes of the provinces. Geological observations and radiologic age determinations correlate the eruptions of alkaline olivine basalt and basanite with the initial phase of tectono-magmatic reactivation that preceded the plutonic phase of alkaline ultrabasic magmatism. It is obvious that the reconstruction of magmatic processes in the zones of ancient shield reactivation should be based on studies of

all of the components of mineralized magmatic systems, including rocks of volcanic origin.

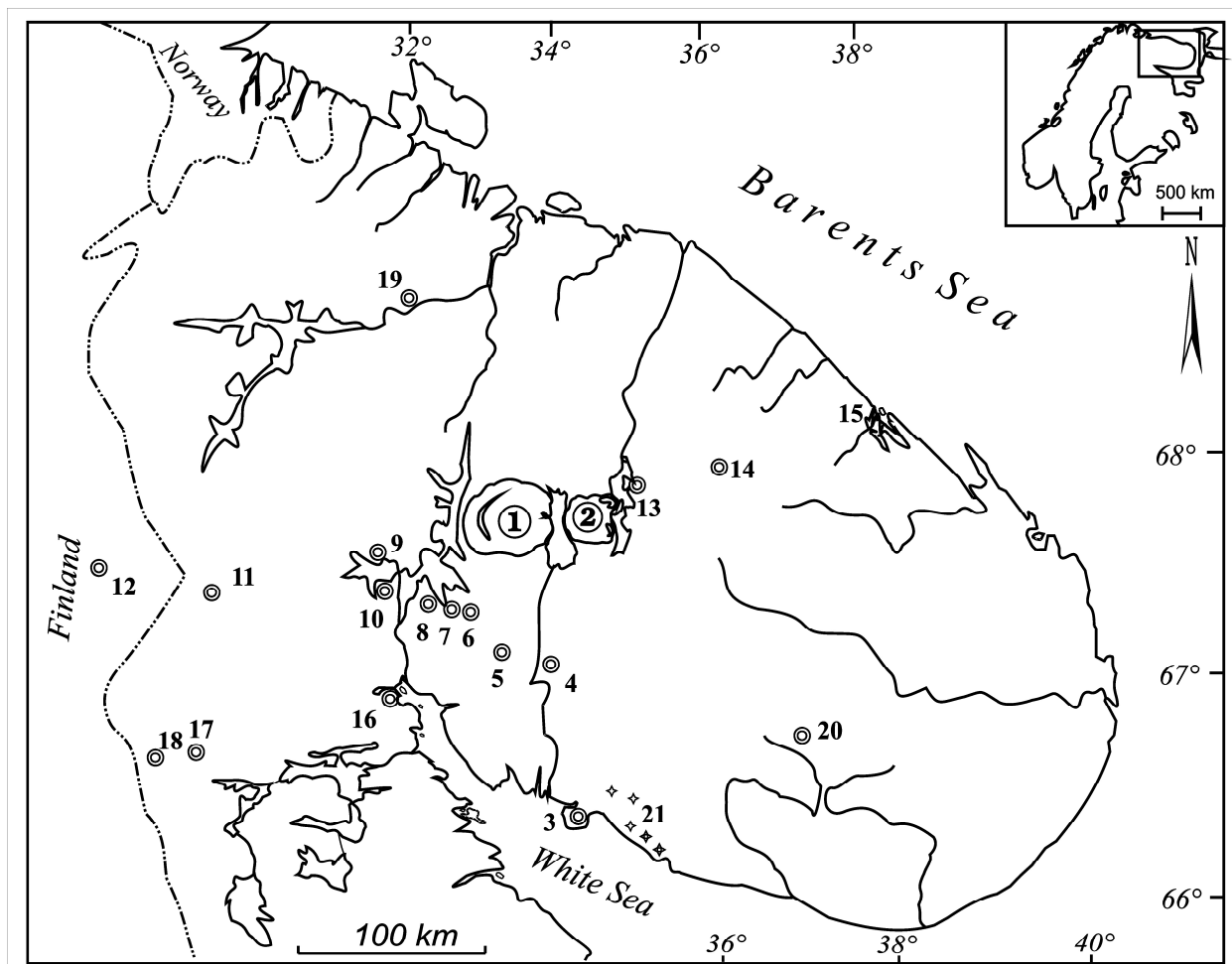


Fig. 1. Scheme of distribution of Paleozoic rocks in the northeastern Fennoscandian Shield. Plutonic series: 1 - Khibina, 2 - Lovozero, 3 - Turiy Mys, 4 - Ingozero, 5 - Salmagora, 6 - Lesnaya and 7 - Ozernaya Varaka, 8 - Afrikanda, 9 - Mavraguba, 10 - Niva, 11 - Kovdor, 12 - Sokli, 13 - Kurga, 14 - Kontozero, 15 - Ivanovka, 16 - Kandaguba, 17 - Vuoriyarvi, 18 - Sallanlatva, 19 - Seblyavr, 20 - Pesochny, 21 - dikes and pipes of the Tersky Coast.

The Paleozoic magmatic province of the Baltic Shield contains, in addition to the known alkaline intrusions, volcanic rocks that are spatially associated with large nepheline syenite plutons or are concentrated in zones of tectonic depressions. The prospecting and exploration operations conducted in recent years on the Kola Peninsula resulted in the discovery of new Paleozoic volcano-plutonic complexes [50] and also revealed a rather wide development of extrusive rocks in the Khibina and Lovozero massifs. The great lateral extent and substantial proportion of emplaced during the Paleozoic phase of the tectono-magmatic reactivation of the region were sufficient arguments for carrying out a study aimed at determining the evolution trends of the volcanic series of the province and

establishing relations between the volcanic and plutonic complexes, including the identification of intrusive equivalents of the extrusive rocks.

GEOLOGIC SETTING AND PETROGRAPHY

In the northeastern part of the Baltic Shield, Paleozoic volcanic rocks are restricted to a large NE-trending tectonic zone extending from the Sokli carbonatite massif in the north of Finland to the Ivanovka volcano-plutonic complex on the Barents Sea coast (Fig. 1). This zone also contains very large massifs of agpaite nepheline syenite. During this study, we investigated the structure of the Lovozero and Khibina massifs, the Kontozero Depression, and the Ivanovka volcano-plutonic complex, as well as the composition of the volcanic rocks composing them.

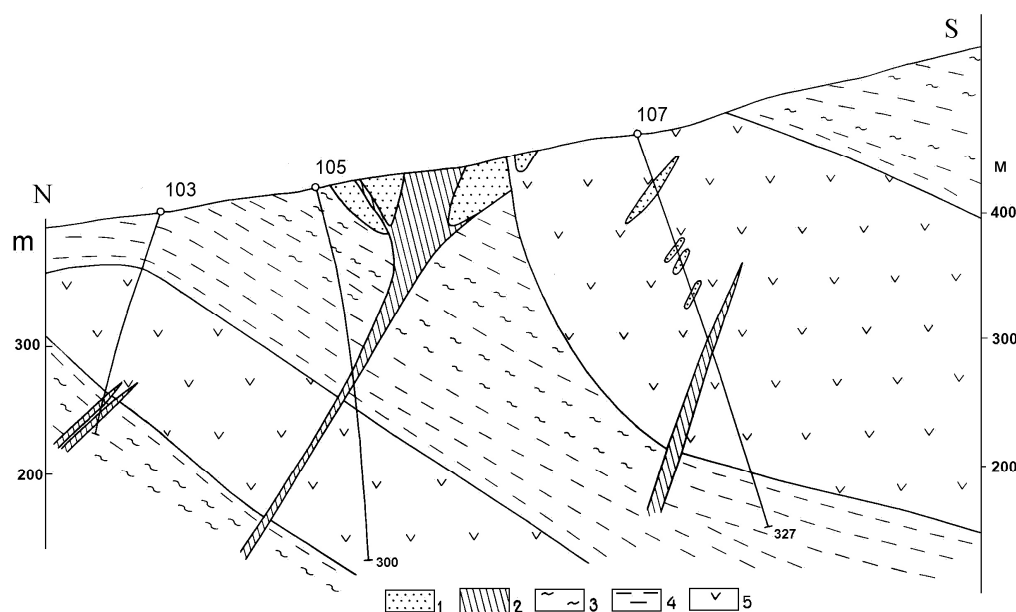


Fig. 2. Cross section of the northern slope of the Flora mountain in the Lovozero Massif. 1 - sandstone; 2 - albitization zone; 3 - foyaite; 4 - lujavrite; 5 - ultrabasic and basic volcanics.

Lovozero massif.

The volcanic rocks occurring in the outliers of the roof of this agpaite nepheline syenite pluton are most widely known among the volcanics of the region [16, 58, 13, 14]. According to the latest results of the Lovozero geological survey, the bulk of volcanic rocks as thick as 200 m are embedded in rocks of the differentiated lujavrite-foyaite-urtite complex and are spatially associated with the sediments of the Lovozero Formation. Elements of lateral zoning have been discovered in the distribution of compositionally varying rocks: ankaramite outliers dominate in the extreme northeastern part of the massif; alkaline basanite occurs further southward and superseded by phonolite porphyry in the Apuaiv and Kuamdespahk area. The structure of the sequence could be reconstructed only in its ultrabasic interval: the study of large volcanic outliers across the strike and at

depth (Fig. 2) revealed the predominance of ankaramite alternating with basanite. The thickness of each flow is no more than a few meters. The ankaramite contains phenocrysts or olivine and clinopyroxene and closed clusters of equant clinopyroxene crystals. There are also patches of picrite containing numerous

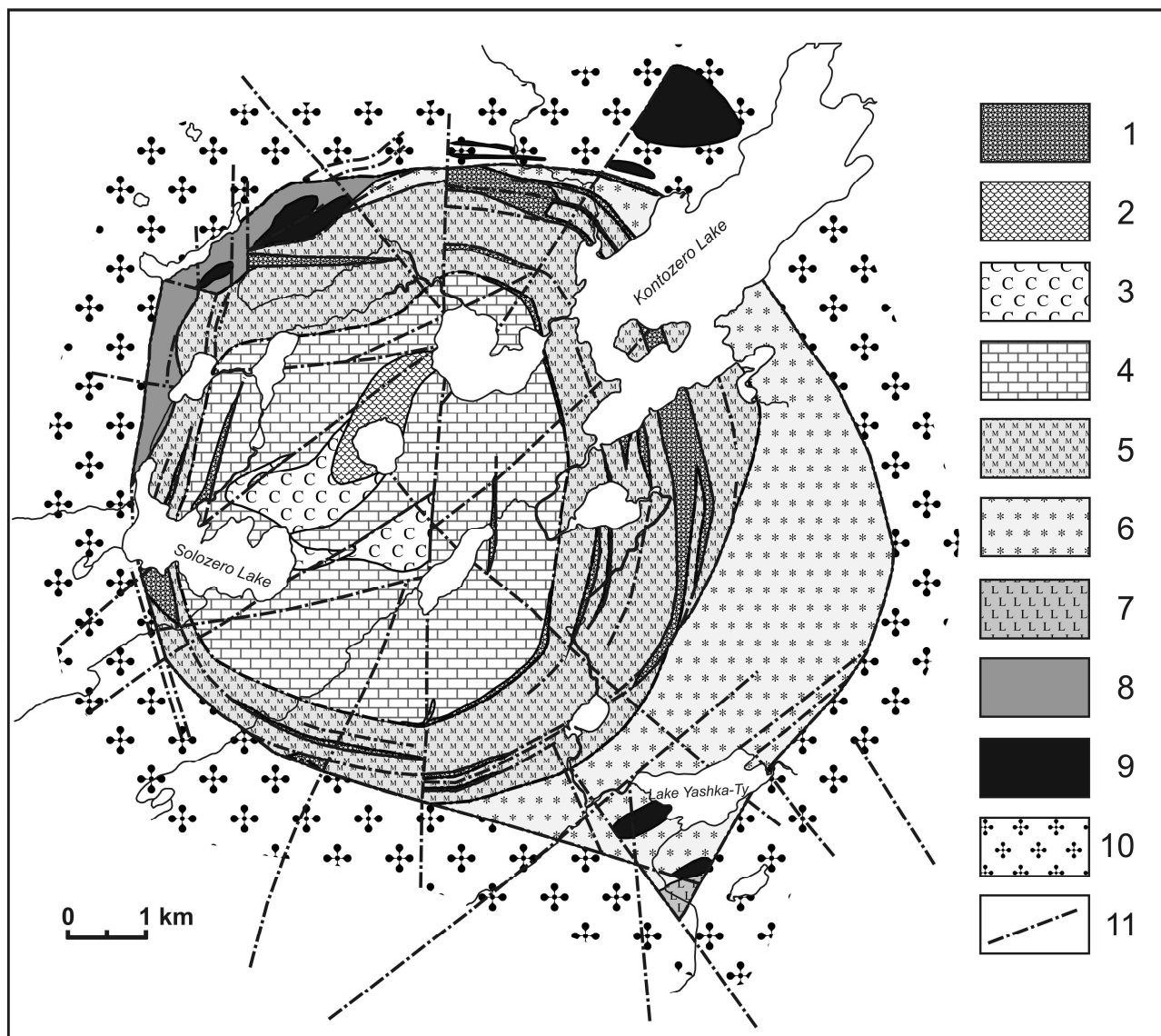


Fig. 3. Schematic map showing the geologic structure of the Kotozero caldera after Pyatenko and Saprykina [47] with author's supplements. (1) - ankerite-dolomite metasomatic rocks in the fault zones; (2) - explosion pipes filled with olivine-phlogopite picrite; Kotozero stratigraphic unit: (3) - carbonatite tuff and tuffitic breccia of the feeder channel; (4) - uppermost carbonatite series; (5) - intermediate melilititic series; (6) - lowermost augitite series; (7) - terrigenous and volcanogenic series composed by sandstone, alevrolite, argillite intercalated by basalt and trachybasalt; Plutonic unit: (8) - nepheline syenite, pulaskite, malignite; (9) - nepheline pyroxenite, melteigite, turyaite; Precambrian basement: (10) - AR gneiss and granite-gneiss. (11) - faults.

large olivine phenocrysts. The picrite is petrographically similar to the ankaramite and can be interpreted as its accumulative variety. All of the basaltoids contain small picrite and ankaramite xenoliths and were apparently emplaced during an independent phase of extensive activity. They are distinguished by the presence of large clinopyroxene phenocrysts enclosed in a subophitic groundmass of plagioclase, clinopyroxene, biotite, and ilmenite.

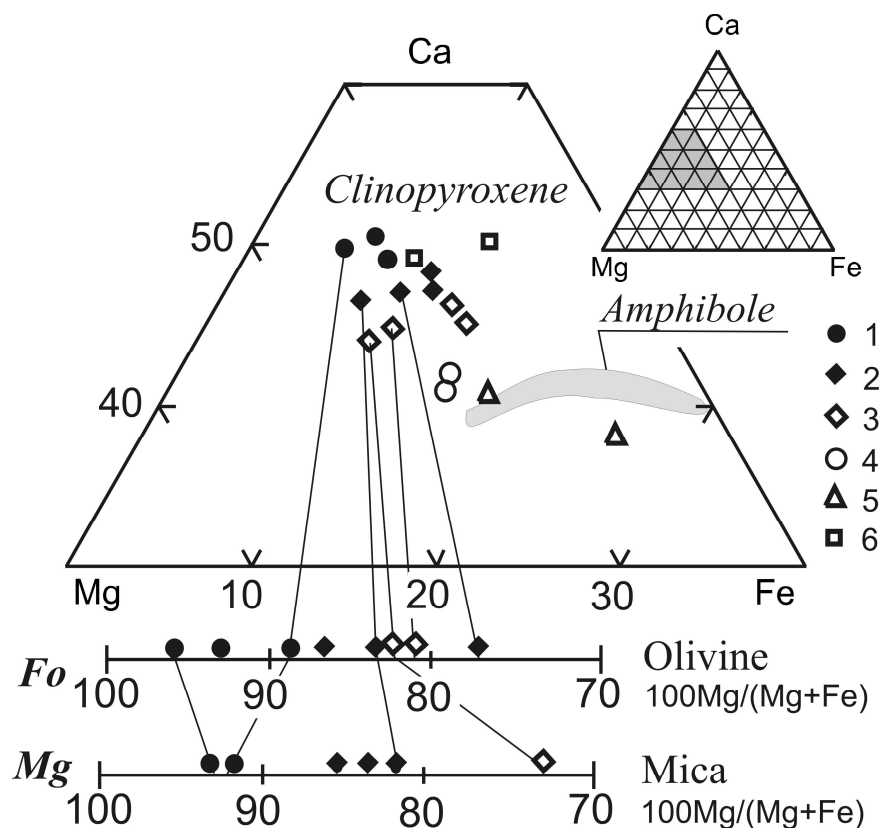


Fig. 4. Chemical composition of minerals from volcanic rocks. Kontozero: (1) - picrite; Lovozero (2) - picrite, (3) ankaramite, (4) basanite; Khibina: (5) phonolite porphyry; Ivanovka: (6) phonolite.

Ivanovka volcano-plutonic complex.

Alkaline rocks were discovered in Ivanovka Bay during prospecting work on the Barents Sea coast [50]. Remnants of volcanic rocks occur in localities as long as a few hundred meters along the bay shore and are traceable as far as 18 km from the mouth of the bay. The maximum thickness of the volcanogenic-sedimentary sequence is 30-40 m, the bedding is subhorizontal. The alkaline volcanics are represented by tuffs, tuffites, tufflavas, and lava breccias. The volcanic sequence is underlain by Archean granites, Riphean sedimentary rocks, and Riphean dolerites of a trap association. On a petrographic basis, the volcanics can be grouped into two main varieties: (1) nepheline basalts of an aphyric or a less common porphyritic texture consist of microcrystalline aggregates of feldspar laths and scarce grains of dark-colored minerals (clinopyroxene, mica, and amphibole) and

(2) alkaline trachytes closely associated spatially with the basalts and related to one another through a series of transitional varieties. The latter usually have a porphyritic texture: they contain phenocrysts of sodic plagioclase enclosed in a typically trachytic groundmass.

Khibina Massif.

Volcanic rocks occur as numerous xenoliths, generally concentrated in the less eroded areas of the massif. The largest exposure of the volcanic rocks, as long

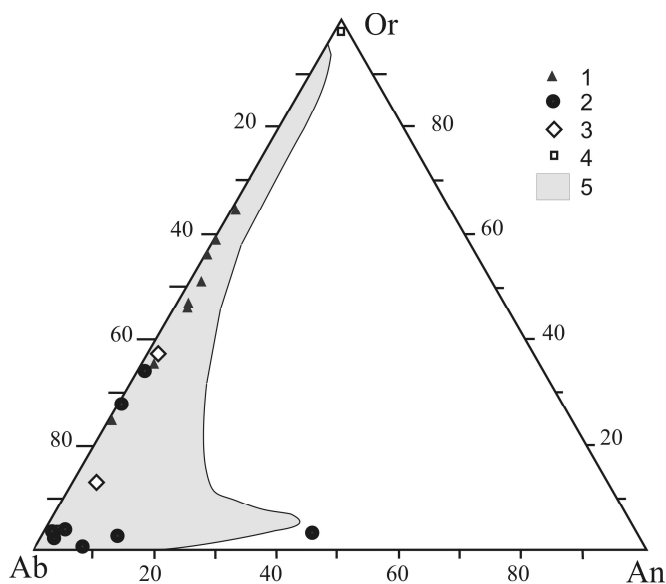


Fig. 5. Composition of feldspars from (1) - Khibina phonolite porphyry; (2) - Lovozero basanite; (3) - Ivanovka phonolite; (4) - Oslo basanite and (5) - Oslo rhomb porphyry. Data for the Oslo rocks are given after von Harnik [59].

as 10 km and having a maximum apparent thickness of 100 m, was discovered in the western part of the massif at a contact between the massive and trachytoid nepheline syenite (khibinite) of the peripheral zone of the intrusion. The lower interval of the sequence consists of metamorphosed volcanogenic-sedimentary rocks, the upper one is dominated by phonolite porphyry. Similar to the porphyritic rocks of the Lovozero Massif, the porphyries of the Khibina Massif cannot be interpreted as analogs of the rhomb-porphyry from the Oslo Graben: the latter is the volcanic facies of the larvikite-laurdalite series. Apart from the leucocratic varieties, Borutsky [15] found augite porphyry in the Chasnachorr-Yudichvumchorr block of the Khibina Massif.

Kontozero Depression.

The volcanic-sedimentary rocks of the Kontozero Formation fill a caldera 8 km across located in Archean granite-gneisses in the Lake Kontozero area 60 km

northeast of the Lovozero alkaline massif (Fig. 1). According to a gravity survey and 3-D density modelling based on its results, the caldera has a cone-shaped asymmetric structure and extends to a depth of 5 km (Fig. 3). The vent composed of rocks having a density of 2800 kg/m^3 is located in the eastern part of the caldera and has a diameter of 1-2 km. According to the data reported by Kirichenko [25], Borodin and Gladkikh [13], Pyatenko and Saprykina [47], and Pyatenko and Osokin [46], the Kontozero sedimentary-volcanic formation consists of three members: the lower (terrigenous-volcanic) argillite member, the middle (volcanic)

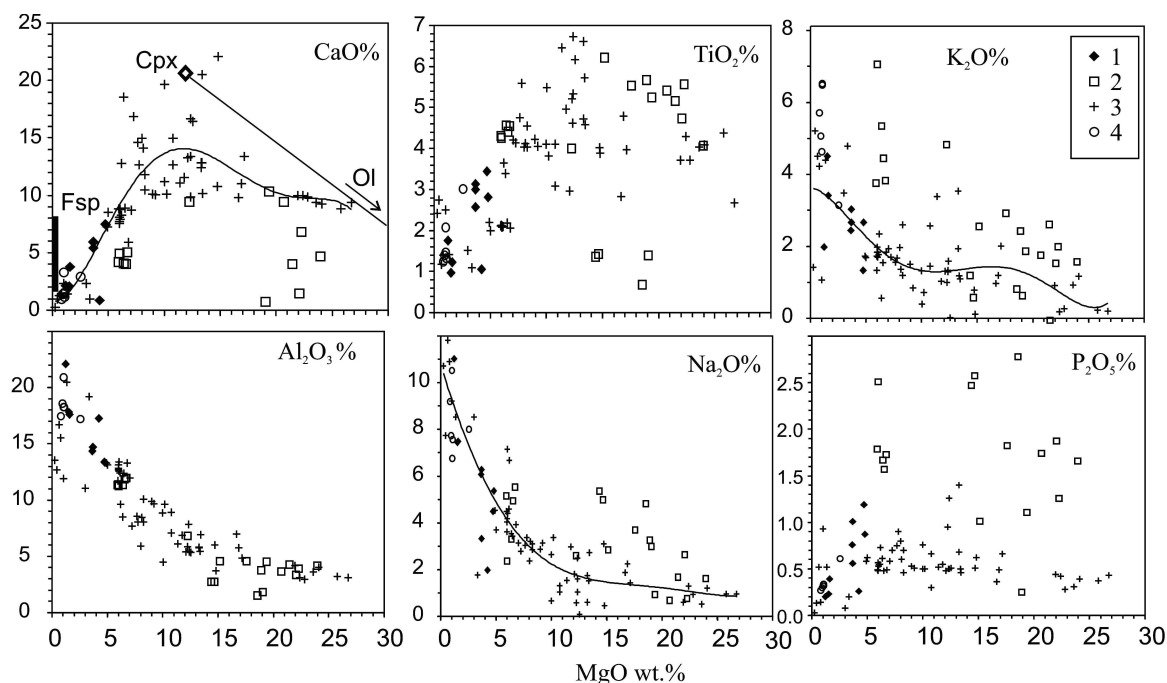


Fig. 6. Oxide-MgO (wt. %) variation diagrams for the Kola volcanic rocks. (1) - Ivanovka; (2) - Kontozero; (3) - Lovozero; (4) - Khibina. Analyses were recast on anhydrous and carbonate-free basis. Clinopyroxene (Cpx), olivine (Ol) and feldspar (Fsp) compositions are plotted in a MgO-CaO diagram. Polynomial trends of the 5 order are displayed.

melilitite-nephelinite member, and the upper (carbonate-terrigenous) carbonatite member. The lower member is composed mainly of augitite and melanephelinite tuffs and lavas alternating with siltstone and tuffstone layers and has a gradational contact with the overlying member of olivine nephelinite and melilitite. The upper member has an approximate thickness of 1000 m and consists of extrusive carbonatite (lavas and tuffs), picrite-carbonatite, and also calcareous tuffaceous siltstone, and tuffite. The thickness of the volcanic sheets ranges between 1 and 10 m. The study of the mineral composition of the volcanic rocks from the middle member revealed that the dominant rock was nephelinite rather than melilitite as had been inferred before. The X-ray diffraction and microprobe analyses of the groundmass from the bulk of the samples detected nepheline and feldspar instead of melilite. This result was confirmed by chemical analyses.

CHEMICAL COMPOSITION OF MINERALS

Olivine.

We studied olivine from the alkaline picrite and ankaramite of the Lovozero Formation and from the picrite-carbonatite of the Kontozero Formation (Table 1). Olivine phenocrysts of the Lovozero volcanics are distinctly zoned: the cores showed a composition of Fo93-92, the margins and small grains in the groundmass yielded Fo85-77. The evaluation of equilibrium between the olivine of the

Table 1

Chemical composition of olivine of the volcanic rocks.

Region	Kontozero					Lovozero									
Rock	PIC					ANK	PIC								
Sample	K-7/240		K-7/94			107/187	107/209		5053		5033a		50336		
Zone of phenocryst	C	C	C	C	C	C	C	R	C	R	C	R	C	R	
SiO ₂	41.23	39.10	40.65	40.92	41.00	39.11	40.47	39.22	40.84	40.73	40.51	39.18	39.98	38.94	
TiO ₂	-	-	-	-	-	-	0.05	0.05	0.04	0.04	-	0.06	-	0.04	
FeO	6.71	3.96	10.09	11.04	11.08	16.51	14.40	14.88	7.18	8.40	7.57	17.77	13.98	17.47	
MnO	0.48	0.50	0.14	0.11	0.12	0.18	0.36	0.36	0.12	0.10	0.11	0.40	0.24	0.41	
MgO	51.86	55.84	48.87	48.30	47.86	43.02	44.43	44.87	50.67	50.42	51.01	42.05	45.57	40.05	
CaO	0.07	0.19	0.12	0.15	0.08	-	0.51	1.11	0.20	0.18	0.43	0.60	0.54	1.85	
NiO	0.03	0.03	0.39	0.38	0.38	0.36	0.23	0.21	0.37	0.19	0.37	0.24	0.31	0.25	
CoO	0.03	0.01	0.02	0.02	0.02	0.03	0.02	-	-	-	-	-	-	-	
Cr ₂ O ₃	-	-	0.05	0.03	0.03	0.05	0.03	-	0.08	-	0.02	0.04	-	-	
Sum	100.41	99.63	100.33	100.95	100.57	99.26	100.50	100.70	99.50	100.06	100.02	100.34	100.62	99.01	
Fo %	93.24	96.18	89.63	88.64	88.51	82.30	84.63	84.31	92.64	91.46	92.32	80.85	85.33	80.35	

Note: Here and in other tables: C - core, I - intermediate, R - rim of the phenocryst, M - crystal in matrix. Rocks: PIC - picrite, ANK - ankaramite, NEPH - nephelinite, BAS - basanite, BAST - trachybasalt, PHN - phonolite, PHNP - phonolite porphyre.

Lovozero alkaline picrite and ankaramite and the magma corresponding with the country rock composition (with the Mg/Fe ratio in the coexisting magma KD = 0.3) showed that in the picrite-ankaramite-alkaline basanite succession, the olivine of Fo94-93, Fo92-90, and Fo87-80 respectively, must have been in equilibrium with the magma. The cores of the large crystals are consistent with this state. This points to an insignificant accumulation of the olivine crystals that settled out from the magma, from which the Lovozero volcanic ultramafic rocks were derived. The concentration of Ca in the olivine, which was empirically related to the formation depth of ultrabasic rocks [84], varies regularly from the low-Ca cores of large phenocrysts that originated during the plutonic phase of crystallization to the high-Ca margins of zoned crystals and the groundmass, consistent with near-surface crystallization. Olivine occurs in the Kontozero picrite and carbonatite as phenocrysts of Fo90-88 composition and also as xenocrysts with an unusually high

Table 2.

Chemical composition of clinopyroxene

Region	Lovozero								
Rock	PIC				ANK				BAS
Sample	105/290.3			107/209	107/187				133/315
Zone	C	R	M	M	C	R	M	M	M
SiO ₂	51.84	51.70	52.34	52.96	51.58	50.69	51.53	52.62	50.41
TiO ₂	1.65	1.82	1.40	1.68	1.96	2.28	1.86	1.40	1.48
Al ₂ O ₃	1.49	1.90	1.21	1.63	2.22	2.85	1.62	1.57	2.96
Cr ₂ O ₃	0.15	0.35	0.28	0.37	0.44	0.48	0.26	0.51	0.04
FeO	6.10	6.69	5.81	4.60	6.28	7.22	8.10	5.76	8.81
MnO	0.08	0.11	0.08	0.10	0.08	0.20	0.23	0.07	0.20
MgO	14.26	14.20	15.08	15.96	15.50	13.66	13.65	16.30	15.28
CaO	23.08	22.35	22.77	22.77	21.58	21.71	21.32	21.43	19.60
Na ₂ O	0.46	0.97	0.40	0.10	0.31	1.35	1.03	0.44	0.53
SrO	-	-	-	-	-	-	-	-	-
Sum	99.11	100.09	99.37	100.17	99.95	100.44	99.60	100.10	99.31
Cations per 6 oxygen ions									
Si	1.938	1.910	1.945	1.948	1.907	1.867	1.923	1.933	1.878
AlIV	0.062	0.083	0.053	0.052	0.093	0.124	0.071	0.067	0.122
AlVI	0.003	0.000	0.000	0.019	0.004	0.000	0.000	0.000	0.008
Ti	0.046	0.051	0.039	0.046	0.055	0.063	0.052	0.039	0.041
Fe ₃₊	0.000	0.055	0.000	0.000	0.000	0.097	0.046	0.006	0.068
Fe ₂₊	0.191	0.151	0.181	0.141	0.194	0.125	0.207	0.171	0.206
Cr	0.004	0.010	0.008	0.011	0.013	0.014	0.008	0.015	0.001
Mg	0.795	0.782	0.836	0.875	0.854	0.750	0.759	0.892	0.849
Mn	0.003	0.003	0.003	0.003	0.003	0.006	0.007	0.002	0.006
Ca	0.924	0.885	0.907	0.897	0.855	0.857	0.852	0.843	0.782
Na	0.033	0.069	0.029	0.007	0.022	0.096	0.075	0.031	0.038
Region	Kontozero			Ivanovka			Khibina		
Rock	PIC		NEPH	PHN	BAST	PHNP			
Sample	K-7/94		6/861	157B-86	12B-86	A-1045			
Zone	M	M	M	M	M	M			
SiO ₂	54.28	54.28	53.47	49.86	51.18	52.72			
TiO ₂	0.63	0.90	1.60	1.82	2.08	1.93			
Al ₂ O ₃	0.68	1.04	0.95	4.42	2.84	1.35			
Cr ₂ O ₃	0.02	-	-	0.06	-	-			
FeO	3.02	4.41	4.68	6.87	5.67	11.94			
MnO	0.08	0.10	0.16	0.26	0.11	0.66			
MgO	15.97	14.40	15.12	11.28	14.15	10.03			
CaO	24.20	24.28	23.90	21.32	23.01	14.74			
Na ₂ O	0.69	0.46	0.60	1.29	0.58	5.40			
SrO	-	-	0.10	-	-	0.24			
Sum	99.57	99.87	100.58	97.18	99.62	99.01			
Cations per 6 oxygen ions									
Si	1.986	2.004	1.959	1.907	1.899	1.960			
AlVI	0.015	0.045	0.000	0.106	0.023	0.019			
Ti	0.017	0.025	0.044	0.052	0.058	0.054			
Fe ₃₊	0.017	0.000	0.000	0.000	0.003	0.303			
Fe ₂₊	0.076	0.136	0.144	0.219	0.173	0.068			
Cr	0.001	0.000	0.000	0.002	0.000	0.000			
Mg	0.871	0.793	0.826	0.643	0.783	0.556			
Mn	0.002	0.003	0.005	0.008	0.003	0.021			
Ca	0.949	0.960	0.938	0.873	0.915	0.587			
Na	0.049	0.033	0.043	0.096	0.042	0.389			

Table 3.

Chemical composition of amphibole (1-6) and mica (7-12).

Region	Ivanovka					Khibina
Rock	BAS	BAST			PHN	PHNP
Sample	M-17-G	12B86			157B86	A-1045
Zone	M (1)	C (2)	I (3)	R (4)	M (5)	M (6)
SiO ₂	41.75	42.28	42.22	41.33	40.35	51.26
TiO ₂	5.66	5.90	4.98	5.68	4.01	3.45
Al ₂ O ₃	11.09	11.02	10.99	10.98	12.53	4.07
Cr ₂ O ₃	-	-	-	-	-	-
FeO	8.18	9.68	9.47	10.54	14.81	9.04
MnO	0.10	0.15	0.15	0.20	0.46	0.76
MgO	15.30	14.54	14.50	12.91	10.06	15.38
BaO	-	-	-	-	-	-
CaO	11.86	12.01	12.07	11.72	11.03	4.72
Na ₂ O	2.80	2.46	2.47	2.64	3.15	6.79
K ₂ O	1.13	1.25	1.32	1.04	1.14	1.32
Sum	97.87	99.29	98.17	97.04	97.54	97.02
Cations per 23 oxygen ions						
SiIV	6.027	6.121	6.177	6.148	6.095	7.437
AlIV	1.932	1.879	1.823	1.852	1.905	0.563
TiIV	0.630	0.642	0.000	0.000	0.000	0.000
AlVI	0.000	0.000	0.071	0.071	0.324	0.133
TiVI	0.000	0.000	0.548	0.635	0.456	0.377
Mg	3.374	3.138	3.163	2.863	2.265	3.327
Fe ₂₊	1.012	1.172	1.159	1.311	1.871	1.097
Mn	0.013	0.018	0.019	0.025	0.059	0.093
Ca	1.879	1.863	1.892	1.868	1.785	0.734
Na	0.803	0.691	0.701	0.761	0.923	1.910
K	0.213	0.231	0.246	0.197	0.220	0.244
Rock	Khibina	Kontozero				Lovozero
Sample	PHNP	PIC				ANK
Zone	A-1065	K7/240		K7/94		107/187
	M (7)	M (8)	M (9)	M (10)	M (11)	M (12)
SiO ₂	38.64	41.21	41.35	42.97	40.15	38.22
TiO ₂	7.32	0.82	0.46	0.76	2.84	4.84
Al ₂ O ₃	12.36	12.84	15.31	11.72	11.29	14.68
Cr ₂ O ₃	-	0.04	0.04	-	-	-
FeO	8.01	4.58	3.62	3.97	7.62	11.85
MnO	0.55	0.05	0.03	0.03	0.06	0.03
MgO	17.86	25.65	25.74	26.75	24.06	16.95
BaO	-	0.43	0.93	0.31	0.23	-
CaO	-	0.05	0.10	0.10	0.03	0.04
Na ₂ O	0.44	1.35	1.46	0.89	1.03	1.09
K ₂ O	9.48	9.15	8.73	8.48	8.47	8.85
Sum	94.66	96.17	97.77	95.98	95.78	96.55
Cations per 24 oxygen ions						
SiIV	5.652	5.820	5.710	6.000	5.760	5.550
AlIV	2.131	2.140	2.290	1.930	1.910	2.450
TiIV	0.217	0.050	0.000	0.070	0.310	0.000
AlVI	0.000	0.000	0.200	0.000	0.000	0.060
TiVI	0.588	0.040	0.050	0.010	0.000	0.530
Mg	3.895	5.400	5.300	5.570	5.150	3.670
Fe ₂₊	0.980	0.540	0.420	0.460	0.910	1.440
Mn	0.068	0.010	0.000	0.000	0.010	0.000
Ca	0.000	0.010	0.010	0.010	0.000	0.010
Na	0.125	0.370	0.390	0.240	0.290	0.310
K	1.769	1.650	1.540	1.510	1.550	1.640

content of the forsterite component (Table 1). We found olivine of this composition, having very low NiO concentrations, only in the phoscorite of the Kovdor Massif. We believe that the occurrence of olivine of this composition in the Kontozero caldera suggests that it contains a phoscorite-carbonatite complex.

Clinopyroxene.

According to the IMA classification [40] all of the pyroxenes from the Paleozoic volcanic rocks can be classed with the QUAD Ca-Mg-Fe group (Table 2). The Kontozero picrite contains the most magnesian diopside varieties. The clinopyroxene from the Khibina phonolite porphyry is aegirine-augite. The Lovozero rocks show a distinct dependence of their clinopyroxene chemistry on the composition of the host rocks: diopside is found in the picrite, diopside-augite in the ankaramite, and augite in the basanite (Fig. 4). The Al^{IV} value also varies in this rock sequence: the positive $Al^{IV} - TiO_2$ correlation suggests the growth of the $CaAl_2SiO_6$ component during magma differentiation; the highest Al^{IV} contents was found in the rocks of the Lovozero and Ivanovka massifs. The phenocrysts are poorly zoned. In the picrite and ankaramite, the variation of their compositions from margins to cores corresponds with the general evolution trend in the picrite-ankaramite-basanite succession.

Amphibole.

Amphibole. is scarce and occurs as phenocrysts in the Lovozero and Ivanovka basanites and in the Khibina phonolite porphyry. The chemical data (Table 3) suggest several amphibole varieties. The calculation of the formula shows that, according to Leake's classification, the amphiboles from the Ivanovka rocks can be referred to the Ca and Na-Ca groups: the basanite contains kaersutite, the phonolite bear ferropargasite. The amphibole from the Khibina phonolite porphyry is magnesiokataphorite.

Mica

Mica is represented by ferromagnesian varieties ranging from phlogopite ($Mg/Fe > 2$) to biotite (Table 3). Mica phenocrysts and groundmass grains of the Kontozero picrite and extrusive carbonatite is low-Ti phlogopite with an elevated Ba content, a feature typical of the micas from the carbonatite series of the region [48, 26]. The Khibina phonolite porphyry and the Lovozero ankaramite contain more ferrous phlogopite varieties with a higher Ti content. According to Spear (1984), this indicates that they crystallized under conditions of high temperature and elevated alkalinity (Fig. 4).

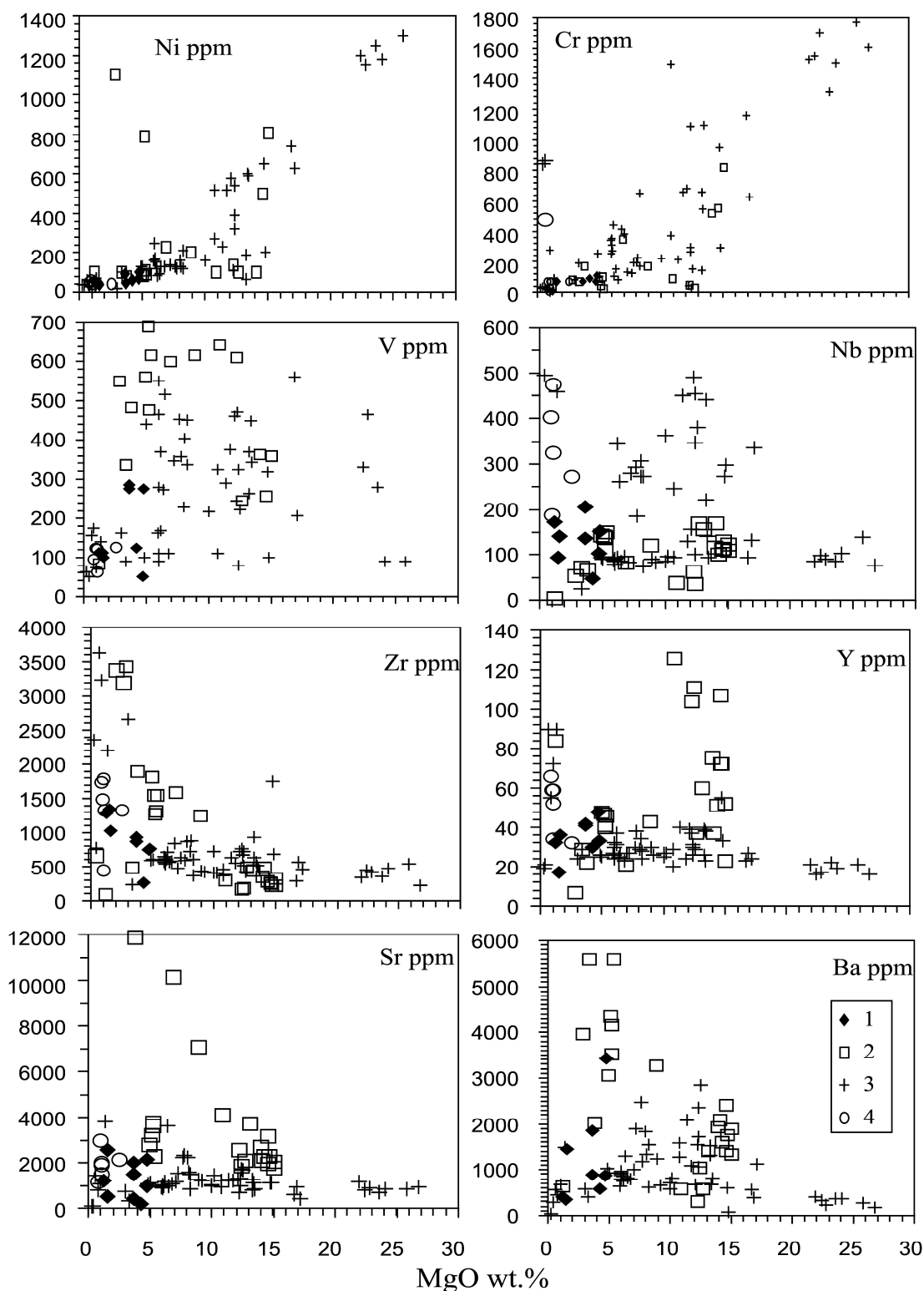


Fig. 7. Trace elements (ppm)-MgO (wt. %) variation diagrams for the volcanic rocks of the Kola Province. (1) - Ivanovka; (2) - Kontozero; (3) - Lovozero; (4) - Khibina.

Feldspar

Feldspar was found only in the Lovozero rocks of the ankaramite-basanite-

phonolite association and in the Khibina phonolite porphyry. In addition to the feldspar laths in the groundmass, this mineral occurs as rhomboid phenocrysts and resembles, in this respect, the feldspars from the rhomb-porphiry of the Oslo Graben [16]. In contrast to the Khibina and Lovozero plutonic nepheline syenites, where feldspar is represented by albite-orthoclase varieties, the Lovozero volcanics also contain plagioclase with a mole fraction of the An component as high as 46.3 % (Table 4, Fig. 5). Plagioclases of this composition were reported from the rocks fall regularly from the picrite to ankaramite and then to basanite, generally, in agreement with the evolution trend of these rocks.

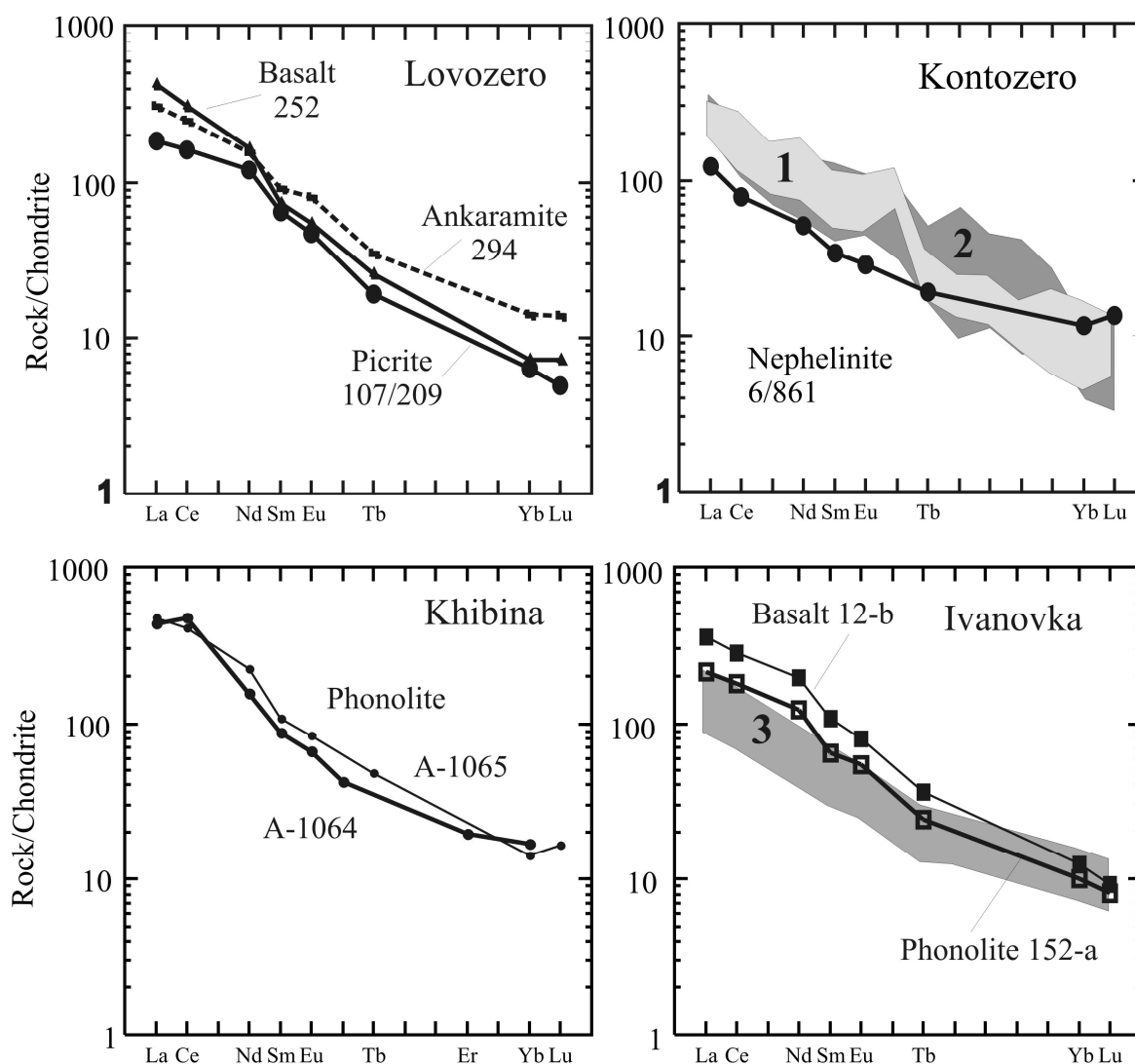


Fig. 8. REE distribution patterns for the volcanic rocks of the Kola Province. The fields of (1) the Kontozero melilitites and (2) carbonatites are plotted after Pyatenko and Osokin [46] and those of (3) the Oslo basalts after Neumann et al. [43]. The normalization factors of Taylor and McLennan [57] were used.

larvikite and laurdalite of the nearby Kurga intrusion, which are rocks comagmatic with the volcanics described [6].

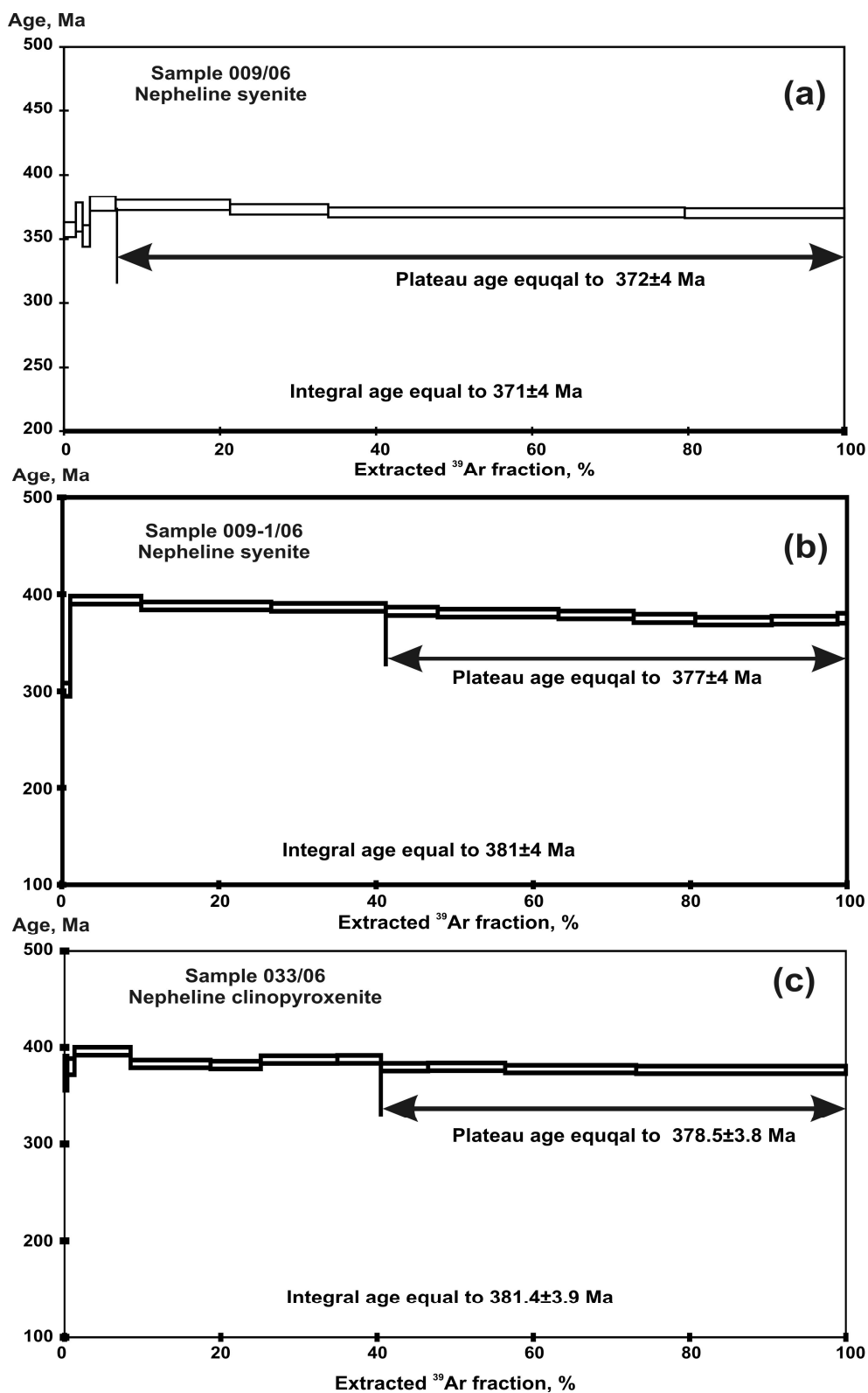


Fig. 9. Results of the $^{40}\text{Ar}/^{39}\text{Ar}$ step-heating study of a monomineral phlogopite fraction from nepheline syenite (a) and (b) and pyroxenite (c) of the Kontozero caldera.

Table 4.

Chemical composition of feldspars.

Region	Lovozero					Ivanovka	Khibina			
Rock	ANK	BAS	BAS	PHNP	PHNP	BAS	PHNP	PHNP	PHNP	PHNP
Sample	107/187	133/315	133/315	5505-G	5505-G	M-17-G	A-1045	A-1045	A-1065	A-1065
SiO ₂	66.00	57.03	64.34	66.97	65.93	63.97	66.20	66.45	66.50	64.04
TiO ₂	-	0.18	-	-	-	0.92	0.10	0.08	0.10	0.10
Al ₂ O ₃	20.24	27.27	21.94	19.24	21.15	22.13	18.80	18.66	19.95	20.36
FeO	0.11	0.17	0.18	-	0.12	1.42	0.71	0.75	0.19	0.18
CaO	1.52	8.95	2.59	0.07	0.49	0.37	-	0.02	0.33	0.54
Na ₂ O	11.39	5.59	9.75	7.21	9.27	5.90	3.82	4.46	7.14	5.82
K ₂ O	0.03	0.22	0.26	4.47	0.29	5.60	10.76	8.54	5.83	7.98
SrO	-	-	-	0.86	1.65	0.35	0.19	0.25	-	0.22
BaO	-	-	-	0.23	0.22	0.22	0.11	0.11	0.10	0.09
Sum	99.29	99.41	99.06	99.05	99.12	100.88	100.69	99.32	100.14	99.33
Si	11.696	10.262	11.437	12.008	11.737	11.396	11.961	12.039	11.847	11.653
Al	4.224	5.779	4.593	4.063	4.409	4.643	4.000	3.981	4.186	4.363
Ti	0.000	0.024	0.000	0.000	0.000	0.123	0.014	0.011	0.013	0.014
Fe ₊₂	0.016	0.026	0.027	0.000	0.018	0.212	0.107	0.114	0.028	0.027
Ba	0.000	0.000	0.000	0.016	0.008	0.015	0.008	0.008	0.007	0.006
Ca	0.289	1.725	0.493	0.013	0.093	0.071	0.000	0.004	0.063	0.105
Na	3.914	1.950	3.361	2.507	3.165	2.038	1.338	1.567	2.466	2.053
K	0.007	0.051	0.059	1.023	0.066	1.273	2.480	1.974	1.325	1.852
Ab	93.0	52.3	85.9	70.8	95.2	60.3	35.0	44.2	64.0	51.2
An	6.9	46.3	12.6	0.4	2.8	2.1	0.0	0.1	1.6	2.6
Or	0.2	1.4	1.5	28.9	2.0	37.6	65.0	55.7	34.4	46.2

Chrome spinel, magnetite, and ilmenite.

In addition to discrete magnetite and ilmenite crystals, the alkaline volcanic rocks contain chrome spinels. The chemical compositions of these minerals are given in Table 5. The calculation of equilibrium temperatures and oxygen fugacity for magnetite-ilmenite pairs from the Khibina phonolite porphyry (Sample A-1045) after Powell and Powell [45] and Anderson and Lindsley [2] yielded 450°C and $\log f_{O_2} = 29.5$, values corresponding to the latest cation equilibria of the Fe-Ti system.

Apatite

Apatite occurs as an accessory in all of the volcanic rocks of the province. The apatites from the Kontozero nephelinite and the Khibina phonolite porphyry showed the highest SrO contents (Table 6), At the same time, the Kontozero apatite is extremely low in rare earth elements, even though the contents of light lanthanides in the Khibina phonolite are abnormally high and exceed all of the known LREE values in apatite of the Kola alkaline province.

Table 5.

Chemical composition of magnetite, spinel and ilmenite.

Region	Kontozero					Lovozero						
	Mag	Spl	Mag	Spl	Mag	Spl		Mag		Spl	Mag	
Rock	PIC				NEPH	NEPH		PIC				PIC
Sample	K7/94		K7/240		6/861	105/290.3		5033	107/209		107/187	5053
SiO ₂	0.21	0.13	0.13	0.11	0.30	0.10	0.10	0.90	0.12	0.39	1.28	0.07
TiO ₂	8.24	8.99	2.05	2.25	9.74	4.66	4.68	2.79	1.16	0.31	3.71	2.84
Al ₂ O ₃	0.74	2.11	0.49	1.16	0.21	0.51	0.51	5.09	0.57	0.17	1.95	0.23
Cr ₂ O ₃	0.35	12.14	0.23	11.15	0.01	13.21	13.30	38.00	5.28	2.80	15.57	3.72
Fe ₂ O ₃	53.42	39.64	65.62	54.40	49.60	45.20	45.35	18.97	60.99	65.39	41.30	59.49
FeO	32.21	29.28	25.38	25.95	37.22	34.24	34.39	30.58	29.10	28.55	32.44	29.90
MnO	1.14	1.62	0.91	1.83	1.40	0.47	0.47	0.69	0.35	0.10	0.39	0.72
MgO	3.50	5.79	4.11	5.92	1.05	0.43	0.43	3.03	1.86	2.02	2.20	1.60
CaO	0.22	0.07	0.16	0.07	0.04	0.02	0.02	0.27	0.03	0.08	0.23	0.06
NiO	0.08	0.06	0.05	0.06	0.02	0.05	0.05	0.24	0.20	0.17	0.29	0.42
ZnO	0.10	0.17	0.13	0.42	0.13	-	-	-	0.16	0.07	0.28	-
V ₂ O ₅	0.28	0.14	0.29	0.16	-	-	-	-	0.32	0.33	0.34	-
CoO	0.06	0.04	-	-	-	0.07	0.07	-	0.00	0.00	0.04	-
Sum	100.54	100.18	99.55	103.48	99.71	98.96	99.37	100.56	100.13	100.38	100.01	99.05
Si	0.008	0.005	0.005	0.004	0.011	0.004	0.003	0.032	0.005	0.015	0.048	0.003
Ti	0.229	0.243	0.058	0.062	0.277	0.130	0.130	0.075	0.033	0.009	0.104	0.082
Al	0.032	0.089	0.022	0.050	0.009	0.020	0.020	0.213	0.025	0.008	0.085	0.010
Cr	0.010	0.345	0.007	0.322	0.000	0.400	0.400	1.067	0.158	0.084	0.457	0.112
Fe ₃₊	1.484	1.071	1.847	1.496	1.413	1.300	1.300	0.507	1.741	1.862	1.155	1.709
Fe ₂₊	0.994	0.879	0.793	0.671	1.179	1.100	1.100	0.908	0.920	0.903	1.008	0.955
Mn	0.036	0.049	0.029	0.057	0.045	0.020	0.020	0.021	0.011	0.003	0.012	0.023
Mg	0.193	0.310	0.229	0.323	0.059	0.020	0.020	0.160	0.105	0.114	0.122	0.091
Ca	0.009	0.003	0.006	0.003	0.002	-	-	0.010	0.001	0.003	0.009	0.002
Ni	0.002	0.002	0.002	0.002	0.001	-	-	0.007	-	-	-	0.013
Zn	0.003	0.005	0.004	0.011	0.004	-	-	-	-	-	-	-
Cr/Cr+Al	0.24	0.79	0.24	0.87	-	0.95	0.95	0.83	0.86	0.91	0.84	0.92

GEO THERMOBAROMETRY OF ROCKS

The crystallization temperatures of the rocks were determined using well-known geothermometers (Table 7). The highest values were obtained for the Kontozero picrite. It appears that the data used on the olivine-spinel assemblage characterize the earlier stages of this rock genesis, corresponding with the initial stage of the system crystallization. Phase equilibria temperatures for the Lovozero.

The pressures at which the mineral phases crystallized could be determined only for the Ivanovka basanite and phonolite. The approximate pressure estimation based on the Al_{IV} and Al_{total} values in the amphiboles [51] shows that amphibole phenocrysts of the Ivanovka rocks crystallized at pressures around 5 kbar, this value indicates that crystallization began at a depth as great as the intermediate magma reservoir.

Table 5. Continued

Region	Khibina		Lovozero		Khibina		Ivanovka
Mineral	Mag		Ilm				
Rock	PHNP		BAS		PHNP	PHNP	BAS
Sample	A1065	A1045	133/315		A1065	A1045	M17-G
SiO ₂	0.18	0.17	0.19	0.21	0.18	-	-
TiO ₂	7.95	5.05	51.30	51.71	53.88	52.54	47.74
Al ₂ O ₃	1.05	0.37	0.19	-	-	0.18	-
Cr ₂ O ₃	0.01	0.02	-	0.07	-	-	0.02
Fe ₂ O ₃	52.72	58.70	-	-	-	-	-
FeO	34.21	32.63	46.32	46.26	31.00	32.72	46.31
MnO	2.57	1.30	0.53	0.55	9.33	9.57	1.30
MgO	1.22	0.67	0.70	1.09	3.47	3.05	1.57
CaO	0.01	-	0.12	0.04	-	-	-
NiO	-	-	-	-	-	-	-
ZnO	0.22	0.69	-	-	-	-	-
V ₂ O ₅	-	-	-	-	-	-	-
CoO	-	-	-	-	-	-	-
Sum	100.14	99.60	99.18	99.93	98.68	98.06	96.94
Si	0.007	0.005	-	-	0.004	-	-
Ti	0.225	0.145	0.970	0.970	1.008	0.991	0.920
Al	0.046	0.017	0.010	-	-	0.005	-
Cr	-	-	-	-	-	-	-
Fe ₃₊	1.490	1.692	0.040	0.040	0.000	0.013	0.161
Fe ₂₊	1.075	1.046	0.940	0.920	0.687	0.674	0.831
Mn	0.082	0.042	0.010	0.010	0.197	0.203	0.028
Mg	0.068	0.038	0.030	0.040	0.129	0.114	0.060
Ca	-	-	-	-	-	-	-
Ni	-	-	-	-	-	-	-
Zn	0.006	0.020	-	-	-	-	-
Cr/Cr+Al	-	-	-	-	-	-	-

Note: Spinel formula calculated according to 3 cations, ilmenite - 2 cations. Fe₂₊/Fe₃₊ ratio calculated according to stoichiometry .

CHEMICAL COMPOSITION OF ROCKS

Major elements.

The least alkalic rocks of the alkaline volcanics emplaced during the Paleozoic episode of tectono-magmatic reactivation are the Lovozero rocks: the agpaitic coefficient (K + Na)/Al of the basanite averages 0.72; the associated ankaramite and picrite are also less alkalic than their Kontozero analogues. The norm (CIPW) calculation revealed nepheline-free varieties containing as much as 7% normative hypersthene among the Lovozero volcanics. The evolution of the Lovozero rock series was analyzed by means of a trend calculation based on computing the mass balance of major oxides using the conventional approach [41]. The results show that the evolution of the Lovozero series fits the model fairly well for the fractional crystallization of the initial ankaramite magma of the ANK-294

type (Table 8) with the formation of a series of basalt and phonolite derivatives during the successive crystallization of olivine, olivine + clinopyroxene, and salic minerals dominated by nepheline. In MgO-oxide (Fig. 6) and MgO-trace element (Fig. 7) diagrams, this succession is displayed by the following clearly expressed relationships: Ni-MgO (olivine crystallization), MgO-CaO and MgO-V (clinopyroxene), MgO-Na₂O, MgO-K₂O, etc. (crystallization of salic minerals).

Table 6.

Chemical composition of apatite.

Region	Kontozero		Lovozero		Ivanovka				Khibina	
Rock	PIC	NEPH	PHNP		PHN	BAST	BAS	BAS	PHNP	PHNP
Sample	7/152	6/861	5505-G	5505-G	157B-8	12B-86	M17-G	M17-G	A-1045	A-1065
SiO ₂	0.54	-	0.84	0.89	0.69	0.64	0.35	0.38	0.60	1.09
P ₂ O ₅	43.18	41.89	40.26	40.80	41.69	41.68	41.53	41.51	40.05	40.21
CaO	54.35	51.80	50.90	50.06	53.77	54.67	54.17	53.79	47.00	50.94
SrO	1.54	6.32	1.69	2.22	1.79	1.09	1.13	1.41	3.72	0.00
La ₂ O ₃	0.01	0.01	0.81	0.85	0.20	0.16	0.01	0.05	1.61	1.42
Ce ₂ O ₃	0.01	0.01	1.82	2.01	0.59	0.35	0.32	0.35	2.81	2.24
Pr ₂ O ₃	0.00	0.00	0.26	-	-	-	0.00	0.00	0.30	0.20
Nd ₂ O ₃	0.00	0.00	0.85	1.04	0.27	0.16	0.04	0.08	1.19	0.78
Cl	0.00	0.00	-	-	0.09	0.15	-	-	-	-
Sum	99.63	100.03	97.42	97.86	99.09	98.90	97.55	97.57	97.28	96.87

Table 7.

Estimation of temperature parameters of crystallization of volcanic rocks.

Region	Lovozero					Khibina	Kontozero		[Reference]
Sample	107/209	105/290	107/187	5033	133/315	A-1045	7/94	7/240	
Rock	PIC		ANK	BAS		PHNP	PIC		
Ol+Spl	1550°	-	1088°	777°	-	-	1717°	1815°	[18]
Ol+Spl	1488°	-	1157°	564°	-	-	-	-	[19]
Ol+Cpx	1087°	1346°	1277°	-	-	-	1116°	-	[39]
Cpx+Spl	993°	971°	1083°	-	-	-	-	-	[38]
Cpx + Ilm	-	-	-	-	505°	1120°	-	-	[11]

Trace elements.

A distinctive feature of the rocks under study is their significant enrichment with incompatible elements (Table 8). The concentrations of Rb, Ba, Sr, Zr, Nb, and Y in the Lovozero volcanics are more than twice as high as their contents in continental alkaline basalts from various provinces [21].

The rhomb-porphyrines and basalts of the Oslo Graben [43] and the basalts of (the Maimecha-Kotui Province) [22] have lower concentrations of incompatible elements. The Lovozero picrite and ankaramite and the Kontozero nephelinite are

2 to 8 times as high in Rb, Ba, Hf, Zr, and REE as the similar rocks of Arctic Siberia [22, 3].

The concentrations of incompatible elements increase regularly in the picrite-ankaramite-basanite-phonolite succession of the Lovozero, Khibina, and Ivanovka volcanic rocks. This regularity is especially pronounced for the Th concentrations, which increase from 7 ppm in the picrites to 40 ppm in the phonolites. Analysis of correlations between trace elements and Th revealed different evolution trends for the Kontozero and Lovozero series. Each of the series has a group of elements that have positive relations with Th and remained incompatible until the final derivatives evolved (paired correlation coefficients are given in parentheses): Rb (+0.67), Nb (+0.87), Ta (+0.64), U (+0.74), La (+0.75), and Ce (+0.87). In contrast to these, P_2O_5 (-0.67) and V (-0.59) remained compatible throughout the evolution of the series, because their concentrations in the residual magma were controlled by the crystallization of apatite and clinopyroxene, respectively. The trends of the Sr and Ba contents are different in the rocks of the Lovozero-Ivanovka-Khibina and Kontozero series: being compatible in the former series, they behave as incompatible elements in the Kontozero series and show distinct negative correlations with Th. Zr, Nb, and Ta. This can probably be explained by the crystallization of melilite $DSr = 1.0 - 1.12$ during the evolution of the Kontozero volcanogenic series.

All rocks of the province have low K and P and high Zr and Nb concentrations. Considering the low Rb contents, the depletion of the rocks in potassium could be caused by the separation of a potassium-bearing phase, apparently phlogopite, prior to the eruptive activity. The Zr and Nb distribution patterns show significant departures from the main fractionation trend ($Zr/Nb = 6.2-8.3$), which controlled the formation of the picrite, ankaramite, basanite, and phonolite. The low Nb concentrations can be explained by the separation of perovskite and ilmenite, which have very high Nb partition coefficients. Evidence in support of this idea comes from the occurrence of ilmenite-perovskite-olivine xenoliths in the Lovozero picrite and ankaramite, which seem to be the cumulates of the early crystallization phases.

The REE distribution in the rocks of the province is displayed in Fig. 8. All of the rocks show a high La/Yb ratio and no Eu anomaly. The degree of REE fractionation in the Kontozero rocks ($La/Yb = 15.5$) is lower than in the rocks of the other series (31.6 - 86.7). The positive correlation between REEs and SiO_2 ; suggests that the REE distribution in the rocks of the Lovozero, Khibina, and Ivanovka series was controlled mainly by silicate phases. The REE distribution patterns indicate that the enrichment of the more leucocratic derivatives in the light rare-earth elements was caused by the separation of olivine and, especially, clinopyroxene during the early fractionation stage and of nepheline and, to a lesser extent, Na-K-feldspar during the final fractionation phase. In addition to the

Table 8.

Chemical composition of volcanic rocks.

Region	Lovozero			Kontozero	Ivanovka		Khibina	
Rock	PIC	ANK	BAS	NEPH	BAST	PHN	PHNP	
Sample	107/209	294	252	6/861	12-B-86	152-a-86	A-1064	A-1065
SiO ₂	37.98	42.03	41.76	37.58	47.27	51.45	56.09	53.83
TiO ₂	4.29	4.02	4.54	3.83	2.81	1.75	1.39	2.08
Al ₂ O ₃	3.12	5.99	8.05	9.55	13.34	22.12	18.59	18.27
Fe ₂ O ₃	7.94	7.92	9.13	7.90	5.50	1.20	0.97	3.98
FeO	8.71	6.83	6.96	6.30	5.14	2.14	5.03	4.19
MnO	0.22	0.22	0.17	0.34	0.15	0.08	0.26	0.29
MgO	22.4	14.72	8.28	5.36	4.79	1.22	0.93	1.04
CaO	9.97	10.79	11.82	10.03	7.40	2.11	1.39	1.51
Na ₂ O	1.28	3.09	3.10	2.77	5.37	11.02	7.73	6.76
K ₂ O	0.18	0.79	2.59	4.49	2.66	1.98	5.07	6.52
P ₂ O ₅	0.42	0.51	0.70	1.40	0.87	0.20	0.30	0.34
CO ₂	0.18	0.33	0.05	5.18	0.22	0.45	0.08	0.13
S	0.15	0.05	0.06	0.67	0.15	0.05	0.02	0.18
Cl	0.01	0.01	0.19	0.01	-	-	-	-
F	0.15	0.14	0.3	0.36	-	-	0.29	0.18
H ₂ O+	2.01	1.44	1.55	2.31	3.5	3.48	0.8	0.57
H ₂ O-	0.28	0.19	0.22	0.63	0.19	0.14	0.14	0.02
Sum	99.29	99.07	99.47	98.71	99.36	99.39	99.08	99.75
Li	7	11	18	10	88	36	31	-
Rb	5	43	115	177	55	52	124	274
Cs	-	0.5	0.5	5	13	2.6	4.2	-
Sr	778	1111	1511	2283	2144	1200	2989	2009
Ba	332	594	1540	5600	3420	408	1030	1380
Sc	25	25	30	18	16	1.12	1.46	2
V	330	319	336	616	275	112	123	122
Cr	1550	948	170	24	107	8	8.1	26
Co	108	82	59	41	33	8.5	3.8	19
Ni	1154	650	120	90	100	53	60	27
Cu	191	-	-	-	-	-	-	53
Zn	123	-	-	-	-	-	-	193
Y	16	55	28	46	33	32	59	59
Nb	98	273	274	149	153	173	403	474
Ta	5.3	14	17	2.6	7.3	8	16	-
Zr	414	1748	602	1550	762	1290	1493	1784
Hf	9.2	29	11	27	17	22	25	-
Pb	7	-	-	-	-	-	-	34
U	1.9	3.9	2.2	2.1	3.7	6.8	7.6	6
Th	7.1	9.6	21	2.8	17	24	28	40
La	68	113	156	45	132	79	174	160
Ce	156	240	298	75	269	172	390	450
Nd	85	110	118	36	140	87	159	110
Sm	15	21	17	7.9	25	15	25	20
Eu	4.11	7.04	4.7	2.49	6.92	4.65	7.3	5.7
Gd	-	-	-	-	-	-	-	13
Tb	1.1	2	1.5	1.1	2.1	1.4	2.8	-
Er	-	-	-	-	-	-	-	4.9
Yb	1.6	3.5	1.8	2.9	3.1	2.5	3.5	4.2
Lu	0.19	0.53	0.28	0.52	0.35	0.31	0.63	-

Note: Oxides in mass. %, elements in ppm.

olivine-clinopyroxene control over REE distribution, an important factor in the Osokin [46] on the REE distribution in the Kontozero melilitites did show positive

Eu and Gd anomalies. At the same time, our data on the REE distribution in the nephelinites showed depletion of MREEs (Fig. 8). This fact indicates that the nephelinite and melilitite of the Kontozero series are complementary rocks.

ISOTOPIC SIGNATURES OF THE ROCKS

Analytical techniques.

Whole-rock samples, 100-200 mg in weight were decomposed using the technique we described earlier [10]. The subsequent Sm and Nd separation was performed by the conventional technique of two-step ion-exchange and extraction-chromatographic separation [1]. The isotopic composition and concentrations of Rb, Sr, Sm, and Nd were measured by isotopic dilution at the Institute of Precambrian Geology and Geochronology, Russian Academy of Sciences, using a "Finnigan MAT-261" solid-phase eight-collector mass spectrometer in static mode. The Nd isotope composition was corrected for fractionation in on-line operation using the ratio $^{148}\text{Nd}/^{144}\text{Nd} = 0.241570$. The occurrence of an Sm admixture in the Nd fraction was controlled using a $^{147}\text{Sm}/^{144}\text{Nd}$ ratio, whose value was not higher than $1 \cdot 10^{-5}$. The Nd isotope composition was measured as an average of 15-20 blocks (not less than 150 measurements). The isotope ratios were measured to better than $\pm 0.5\%$ (2σ) for $^{87}\text{Rb}/^{86}\text{Sr}$ and to $\pm 0.3\%$ (2σ) for $^{147}\text{Sm}/^{144}\text{Nd}$. The concentrations of elements were measured with an accuracy of $\pm 1\%$ (2σ). During the experiment, the values of the Nd isotope ratio were 0.511879 ± 14 ($n = 45$) for the La Jolla $^{143}\text{Nd}/^{144}\text{Nd}$ standard and 0.512673 ± 15 ($n = 10$) for BCR-1; the $^{87}\text{Sr}/^{86}\text{Sr}$ values were 0.705037 ± 50 ($n = 4$) for BCR-1 and 0.7102249 ± 18 for SRM-987. The total blanks were 0.03 ng for Rb, 0.1 ng for Sr, 0.03 ng for Sm, and 0.05 ng for Nd and did not have any significant effect on the composition and concentrations of the elements under study. The isochron parameters were calculated with a 95% confidence interval; the errors of data point location were 0.5% for the x-axis and 0.005% for the y-axis. The results of the measurements are summarized in Table 9.

Results.

The K-Ar age of 516 ± 50 Ma determined by Kukharenko et al. [30] confirms the old age of the Kontozero caldera. The regression based on three points (Table 9) yielded an age of 461 ± 39 Ma, but with the very small $^{87}\text{Rb}/^{86}\text{Sr}$ variation range. In order to get more reliable data we performed $^{40}\text{Ar}/^{39}\text{Ar}$ step-heating study of a monomineral phlogopite fractions from nepheline syenites and pyroxenites which are suggested to be comagmatic with the volcanic rocks. The obtained age (Fig. 9) falls within the time span of alkaline magmatism of the Kola Province and correspond to the age of the plutonic phoscorites recently obtained by Balaganskaya et al. [7].

The trend for the Rb-Sr ratios in the Lovozero rocks was not distinct enough to date them. It can be supposed, however, that their age approximates the age of the nearby Kurga intrusion: its Rb-Sr age was found to be 404 ± 12 Ma and is consistent with the K-Ar age reported earlier [30]. This supposition is supported by

Table 9.

Rb-Sr and Sm-Nd isotope characteristics of volcanic rocks.

Sam ple	Rock	[Sm], ppm	[Nd], ppm	[Rb], ppm	[Sr], ppm	$^{147}\text{Sm}/$ ^{144}Nd	$^{143}\text{Nd}/^{144}\text{Nd}$ $d \pm 2\sigma$	$^{87}\text{Rb}/$ ^{86}Sr	$^{87}\text{Sr}/^{86}\text{Sr}$ $\pm 2\sigma$
Rocks of the Lovozero complex									
107/ 187	ANK	14.24	80.75	46.93	594.4	0.10695	0.512599 ± 14	0.22835	0.704440 \pm 18
107/ 209	PIC	13.80	80.96	6.66	799.2	0.10337	0.512829 ± 15	0.02409	0.703079 \pm 12
105/ 287	PIC	16.69	94.71	33.24	1217	0.10684	0.512782 ± 12	0.07897	0.703943 \pm 14
133/ 315	BAS	21.31	65.27	29.25	824.6	0.11435	0.512618 ± 18	0.10258	0.703687 \pm 22
119/ 61.8	PIC	9.15	43.03	139.0	167.4	0.12893	0.512013 ± 13	2.40675	0.726735 \pm 17
Rocks of the Kontozero caldera									
7/81	CARB	6.36	23.50	0.49	17200	0.16415	0.512907 ± 13	0.00008	0.703124 \pm 24
7/88	PIC	13.8	82.92	44.00	1964	0.10091	0.512848 ± 17	0.06477	0.703542 \pm 17
6/ 863	NEPH	8.48	41.01	112.7 0	3914	0.12543	0.512816 ± 12	0.08325	0.703673 \pm 16
Plutonic rocks of the Kurga massif									
1/ 290	PRX	15.08	74.54	34.67	5428	0.12271	0.512692 ± 7	0.01023	0.703289 \pm 12
1/ 224	SYN	11.97	74.56	41.83	6966	0.09733	0.512576 ± 9	0.01736	0.703309 \pm 14

Note: CARB - calcite carbonatite, PRX - pyroxenite, SYN - nepheline syenite, the other rock abbreviations see Table 1.

the evidence that the Lovozero volcanic series and the Kurga intrusive series are comagmatic, as well as by the proximity of their geologic positions and geochemical characteristics [4].

DISCUSSION OF RESULTS

Mantle source characteristics.

The $\epsilon\text{Nd}(t) - ^{87}\text{Sr}/^{86}\text{Sr}(t)$ diagram plotted in Fig. 10 shows the compositions of spatially close igneous rocks of the Kola Peninsula: the kimberlite of the Tersky Coast, plutonic carbonatite intrusions, agpaitic complexes, and volcanic rocks of the province. The data points of these rocks form a trend, a fragment of which is a line plotted by Kramm and Kogarko [28] for the carbonatite association of the

region (KCL). Kramm [27] believes that the origin of this carbonatite association was related to the evolution of two isotopic components: a depleted mantle source, similar to the source reported for the Canadian carbonatites [9], and an EMI source enriched in LILE and incompatible elements. According to the data for the adjacent Arkhangelsk diamond-bearing province [37], the trend established for the aluminous kimberlite-melilitite series was specified by the contribution of a PREMA source and an old LREE-enriched EMI-type lithospheric mantle.

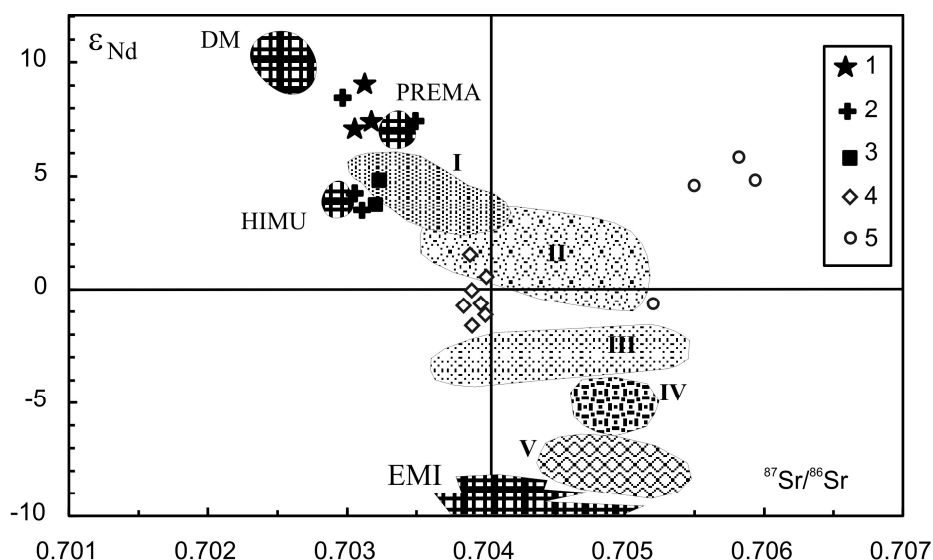


Fig.10. Diagram showing ϵNd vs. $^{87}\text{Sr}/^{86}\text{Sr}$ variations for (1) Kantozero volcanics, (2) Lovozero volcanics, (3) Kurga intrusive rocks, (4-5) kimberlites (4) and olivine melilitites (5) of the Tersky Coast. The fields are plotted for the plutonic rocks of the carbonatite and agpaitic complexes of the Kola Province (1) [29, 62] and for the kimberlites and picrites of the Fe-Ti series (II). Diamond-bearing mica kimberlites (III), olivine-phlogopite melilitites (IV), and olivine-nepheline melilitites (V) of the Arkhangelsk Province [44, 37].

All data were corrected for the age of 380 Ma.

Our data indicate that the mantle reservoir from which the primary magma of the volcanic rocks was derived was substantially more depleted in light lithophile elements when compared to the PREMA source and to all of the alkaline rocks of the province. The high $\epsilon\text{Nd}(t)$ values established for the volcanic rocks of the Kantozero caldera and the Lovozero Massif contradict the participation of a PREMA component in the mantle magma source and suggest a more depleted mantle material might be produced by multiphase crust-forming processes that operated during the Archean and Proterozoic history of the Kola-White Sea rift-collision zone. As a matter of fact, mantle source components having long depletion histories were reported from many continental plateau basalt regions of the world [35]. The direct evidence supporting the existence of this component in the Kola Province is the discovery of spinel harzburgite nodules, extremely depleted in the basalt component, in an explosion pipe cutting through the rocks of the Khibina Massif [6]. The Sm-Nd isotope characteristics of the nodules ($\epsilon\text{Nd}(t) =$

+17.8 for the age of 2054 Ma) classify them with remnants of the superdepleted mantle, which retained the features of an Archean protolith and bear signatures of later mantle transformations [5].

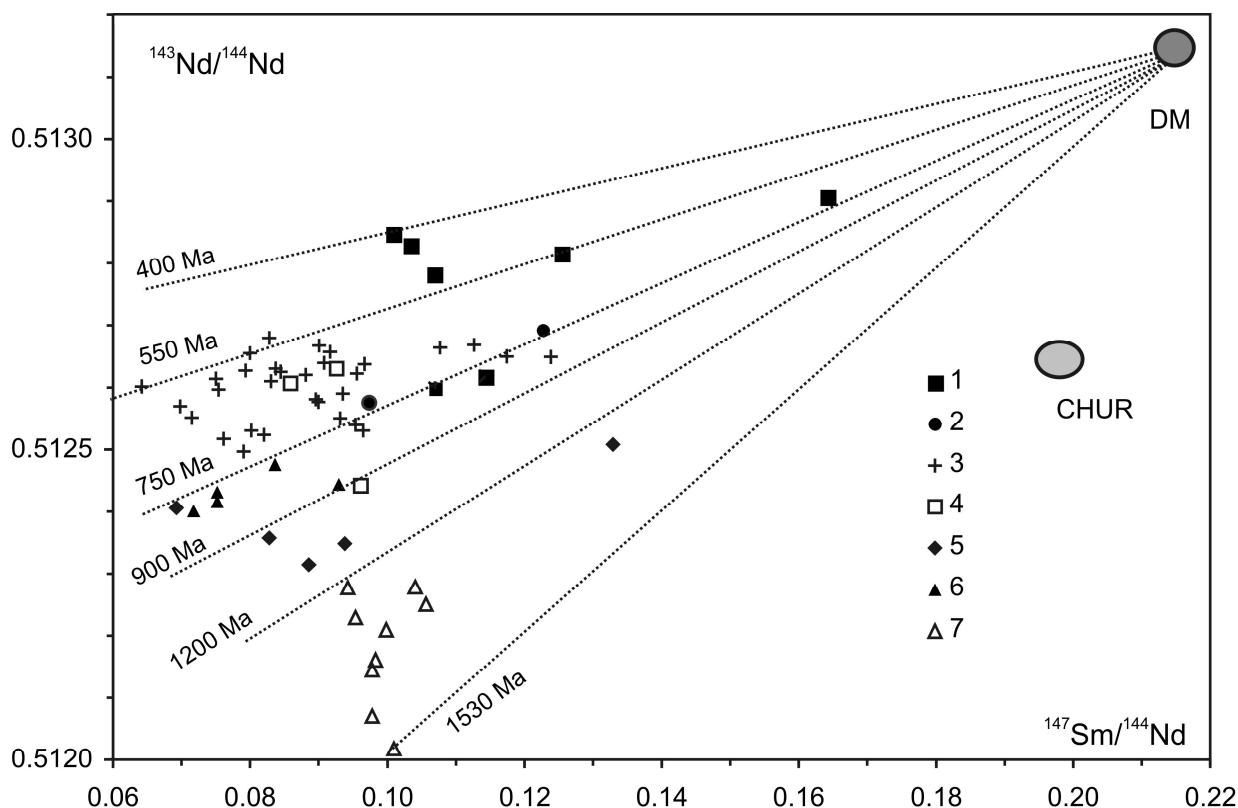


Fig. 11. $^{147}\text{Sm}/^{144}\text{Nd}$ - $^{143}\text{Nd}/^{144}\text{Nd}$ diagram for the Paleozoic rocks of the Kola alkaline province and adjacent regions. 1 - volcanic rocks of the Kola province; 2 - plutonic rocks of the Kurga massif; 3 - plutonic rocks of the agpaitic and carbonatite intrusions of the Kola province after [28, 62]; 4 - olivine melilitite and (5) kimberlite of the Tersky Coast; Arkhangelsk province: 6 - olivine-phlogopite and olivine-nepheline melilitite; 7 - diamond-bearing micaceous kimberlite after [44, 37].

The geochemical features of the volcanic rocks under study allowed us to identify another isotopic component which seems to be close to a moderately depleted mantle source of the EMI type. It was this component that was obviously responsible for the enrichment of the Paleozoic rocks of the province in LILE and incompatible elements. Its origin can be associated either with lower crust transformation under mantle conditions [24] or with mantle metasomatism [60, 34]. The indicator ratios of the rocks ($\text{Zr}/\text{Nb} = 5.4$, $\text{La}/\text{Nb} = 0.51$, $\text{Ba}/\text{Th} = 67$, $\text{Th}/\text{La} = 0.15$, $\text{Rb}/\text{Nb} = 0.42$) have values close to those of oceanic-island basalts (OIB) [52, 60]. Further evidence in support of the enrichment instead of the depletion of the mantle material are the negative values of the fractionation factor $f_{\text{Sm}/\text{Nd}} = [^{147}\text{Sm}/^{144}\text{Nd}(\text{sample})]/[^{147}\text{Sm}/^{144}\text{Nd}(\text{CHUR}) - 1]$ varying in the volcanic rocks from -0.17 to -0.49. The significant contribution of mantle metasomatic processes that operated under the entire region of the Paleozoic magmatic activity

is proved by the discovery of numerous hypoxenoliths showing traces of mantle metasomatism in various areas of the Baltic Shield [23, 20, 6 53].

The Sm-Nd and Rb-Sr isotopic characteristics of the Paleozoic magmatic rock associations in northeastern Fennoscandia are sufficient to outline the main evolution trends of the mantle magma sources, the reactivation of which resulted in the Paleozoic magmatic activity. The calculation of the model ages of the rocks with respect to TNd (DM) yielded a broad scatter of values for all of the magmatic rocks of the province. Considering that model ages are actually isochrons representing a relationship between the isotope ratios for a depleted mantle and the values measured for a particular sample, these ages can be plotted in a $^{143}\text{Nd}/^{144}\text{Nd}$ - $^{147}\text{Sm}/^{144}\text{Nd}$ diagram. The diagram presented in Fig. 11 shows the progressively younger ages in the following succession of rocks of different composition and different magma generation depths: (1) the diamond-bearing kimberlites of the Arkhangelsk District (1500-1200 Ma), (2) the poorly diamondiferous kimberlites at the Tersky Coast of the Kola Peninsula (1200-900 Ma), (3) the Kola olivine melilitites and the diamond-free kimberlites and picrites of the Arkhangelsk District (900-750 Ma), (4) the alkaline rocks of the Kola carbonatite and agpaite intrusions (750-550 Ma), and (5) the volcanic rocks of the Kola Province (750-400 Ma). Comparison with the model ages reported for continental flood basalts [61] shows that the mantle source was formed no later than one billion years before the first basalt eruptions. According to White and MacKenzie [61], a zone of magma generation at the head of a rising mantle plume originates at depth below 120 km in the region of garnet stability and descends as deep as the spinel-facies depth level (30-70 km). It can be supposed that, in the region of a long-cratonized lithosphere under north-eastern Fennoscandia, the vertical range of the magma generation zone was wider and extended as far as the diamond-facies depth. The successive separation of mantle magmas and the simultaneous rise of the magma generation level seem to represent the evolution of the mantle plume-lithosphere interaction and generally agrees with a dynamic model for a rising mantle plume.

Correlation with tectono-magmatic activity.

The results of isotopic dating proved that the alkaline intrusions of the Kola Peninsula were emplaced during a relatively short time interval, 380-360 Ma [29], a period that can be interpreted as the main phase of the Paleozoic tectono-magmatic activity in northeastern Fennoscandia. At the same time, geochronological data on minor lamprophyre intrusions from the Kandalaksha Graben [8] and dolerite dikes from the Rybachy and Sredny Peninsulas [49] suggest some local manifestations of the earlier magmatism in the region. In this context, the assignment of the alkaline volcanic rocks of the Kola Province and the intrusive rocks of the Kurga Pluton to the initial phase of the Paleozoic reactivation indicates that extensive subalkaline and alkaline magmatism was active not only in Late Devonian but also in Early Devonian. Relying on the available geochronological data, one can postulate that the initial phase of the endogenic

activity, responsible for the emplacement of volcanic rocks in northeastern Fennoscandia, occurred at least 20-30 Ma before the injection of alkaline intrusions.

CONCLUSION

1. The emplacement of volcanic rocks in the Kola alkaline province preceded the plutonic phase of alkaline magmatism in the region and can be referred to the initial phase of the Paleozoic tectono-magmatic reactivation. According to geochronological data, the volcanics were emplaced at least 20-30 Ma before the intrusion of plutons.

2. A distinctive feature of the volcanic rocks of the province is the occurrence of moderately alkaline basanites along with silica-undersaturated alkalic rock associations: the dominant rocks of the Lovozero and Ivanovka suites are nepheline-free miaskitic varieties (agpaitic coefficient 0.72). The volcanic rocks are significantly enriched in incompatible elements. The concentrations of Rb, Ba, Sr, Zr, Nb, and Y in them are considerably higher than those in continental alkaline basalts from various provinces.

3. The Sm-Nd and Rb-Sr isotopic data suggest the contribution of two different mantle sources to the genesis of the volcanic rocks: (1) superdepleted mantle material formed as a result of multiphase crust generation processes that occurred during the Archean and Proterozoic history of the Kola-White Sea rift-collision zone and (2) a moderately enriched EM I -type mantle source.

ACKNOWLEDGMENTS

Irina V. Bussen and Alexey S. Sakharov provided their collection of the Lovozero volcanics. Victor Yu. Kalachev's assistance during fieldwork was very fruitful. I.I. Kudryashova and A.S. Kurbangalieva (Luyavr Co.) and A.P. Lipov (Central Kola Geological Survey) added their samples to our collection. The assistance of A.B. Vrevsky (Institute of Precambrian Geology and Geochronology, Russian Academy of Sciences) in determining minor elements in volcanic rocks is appreciated. This work was supported by the Russian Foundation for Basic Research, project no. 09-05-00224.

REFERENCES

1. **Amelin, Ju.V., Neymark, L.A., Ritsk, E.Yu., Nemchin, A.A.** Enriched Nd-Sr-Pb isotopic signatures in the Dovyren layered intrusion (eastern Siberia, Russia): evidence for source contamination by ancient upper-crustal material. *Chem.Geology*, 1996, vol.129, p.39-69.
2. **Anderson, D.J., Lindsley, D.H.** New (and final!) models for the Ti-magnetite /ilmenite geothermometer and oxygen barometer // *EOS Transactions*. 1985. V.66. P.416.
3. **Arndt, N., Lehnert, K., Vasil'ev, Y.** Meimechites: Highly magnesian lithosphere-contaminated alkaline magmas from deep subcontinental mantle. *Lithos*, 1995, vol.34, no.1-3, p.41-59.

4. **Arzamastsev, A.A., and Arzamastseva, L.V.** Comagmatic Volcanic and Plutonic Alkali Basalt Series in the Kola Province, Dokl. Ross. Akad. Nauk, 1991, vol. 331, no. 6, pp. 699-702.
5. **Arzamastsev, A.A. and Belyatsky, B.V.** Evolution of the Mantle Source of the Khibina Massif: Evidence from a Rb-Sr and Sm-Nd Study of Mantle Xenoliths. Dokl. Ross. Akad. Nauk, 1999, vol. 331, no. 6, pp. 699-702.
6. **Arzamastsev, A.A. and Dahlgren, S.** Deep Mantle Mineral Associations in the Rocks of Dikes and Pipes of the Baltic Shield, Geochimya. 1993, no.8. pp.1132-1142.
7. **Balaganskaya, E.G., Timmerman, M., Liferovich, R.P., Kirnarsky, Yu.M.** $^{40}\text{Ar}/^{39}\text{Ar}$ dating of phlogopite from phoscorite of the Kontozero complex, Kola alkaline province. // Geokhimiya shchelochnykh porod. Shkola "Schelochnoi magmatism Zemli" (Geochemistry of alkaline rocks. School "Alkaline magmatism of the Earth"). Moscow, GEOKHI RAN publication, 2002. P. 16-17.
8. **Beard, A.D., Downes, H., Vetrin, V., Kempton, P.D., Maluski, H.** Petrogenesis of Devonian lamprophyre and carbonatite minor intrusions, Kandalaksha Gulf (Kola Peninsula, Russia). // Lithos, 1996, vol.39, P.93-119.
9. **Bell, K., Blenkinsop, J.** Nd and Sr isotope compositions of East African carbonatites: Implications for mantle heterogeneity. // Geology, 1987, vol.15, p.99-102.
10. **Belyatsky, B.V., Vinogradova, L.G., Krymsky, R.Sh., and Levsky, L.K.** Sm-Nd and Rb-Sr Isotopic Dating of the Tungsten-Rare-Metal Zabytoe Deposit, Primorie, Petrologiya. 1994, vol. 2, no. 3, pp. 243-250.
11. **Bishop, F.C.** The distribution of Fe^{+2} and Mg between coexisting ilmenite and pyroxene with applications to geothermometry. // Amer. J. Sci., 1980/ B, vol.280, p.46-77.
12. **Borodin, L.S. and Gladkikh, V.S.** New Data on the Petrography and geochemistry of the Alkaline Volcanic Rocks of the Kontozero Formation, in Novye dannye po geologii, mineralogii i geohimii shchelochnykh porod (New Data on the Geology, Mineralogy, and Geochemistry of Alkaline Rocks), Moscow, Nauka, 1973, pp. 48-55.
13. **Borodin, L.S., Gladkikh, V.S. and Egorova, N.F.** Petrology and Geochemistry of Exirusive Rocks of the Lovozero Alkaline Massif with Applications to its Genesis, in Novye dannye po geologii, mineralogii i geohimii shchelochnykh porod (New Data on the Geology, Mineralogy, and Geochemistry of Alkaline Rocks), Moscow, Nauka, 1973, pp.48-54.
14. **Borodin, L.S., Popov, V.S., Gladkikh, V.S., Pyatenko, I.K., Tugolesov, L.D., Soloviev V.A., Semina, V.A., Lyapunov, S.M., Nikolaenko, Yu. S.** Geokhimiya kontinental'nogo vulkanisma (Geochemistry of Continental Volcanism), Moscow: Nauka, 1987. 238 p.
15. **Borutsky, B.Ye.** Porodoobrazyushchie mineraly vysoko-shchelochnykh kompleksov (Rock-forming Minerals of Highly Alkaline Complexes), Moscow: Nauka, 1988. 215 p.
16. **Bussen, I.V. and Sakharov, A.S.** Lovozero Paleozoic Volcanic-Sedimentary Formation of the Luyavurt, Kola Peninsula, in Voprosy litologii fanerozaya Kol'skogo poluostrova (Lithologic Problems of Phanerozoic of the Kola Peninsula), Leningrad. 1972, pp. 5-37.
17. **Dallmeyer, R.D., Strachan, R.A., Henriksen, N.** $^{40}\text{Ar}/^{39}\text{Ar}$ Mineral Age Record in NE Greenland - Implications for Tectonic Evolution of the North Atlantic Caledonides. // Journ. Geol. Soc. London, 1994, vol.151, pt.4, p.615-628.
18. **Fabries, J.** Spinel-olivine geothermometry in peridotites from ultramafic complexes. // Contrib. Miner. and Petrol., 1979, vol.69, no.4, p.329-336.
19. **Fujii, T.** Fe-Mg partitioning between olivine and spinel. // Carnegie Inst. Geophys. Lab. Rep. 1976-1977, 1977, vol.76, p.563-569.

20. **Furnes, H., Pedersen, R.B., Maaloe, S.** Petrology and geochemistry of spinel peridotite nodules and host basalt, Vestspitsbergen. // Norsk. Geol. Tidsskr., 1986, v.66, n1, pp.53-68
21. **Gladkikh, V.S.** Geochemical Features of Alkali Olivine Basalts and Alkali Basaltoids of Various Tectonic Structures on Continents and Oceanic Islands, Geokhimiya, 1987, no. 7, pp. 928-945.
22. **Gladkikh, V.S.** Geochemistry of the Volcanic Rocks of the Maimecha-Kotui Province, Northern Siberian Craton, Petrologiya, 1994, no. 5, pp. 551-560.
23. **Griffin, W.L.** Lherzolite nodules from the Fen alkaline complex, Norway. // Contrib. Mineral. Petrol., 1973, vol.38, no.2, pp.135-146.
24. **Hergt, J.M., Peate, D.W., Hawkesworth, C.J.** The petrogenesis of Mesozoic Gondwana low Ti flood basalts. // Earth Planet. Sci. Lett., 1991, vol.105, p.134-148.
25. **Kirichenko, L.A.** Kontozerskaya seriya kamennougol'nykh porod na Kol'skom poluostrove (Carboniferous Kontozero Group on the Kola Peninsula). Leningrad: Nedra, 1970. 112 p.
26. **Kononova, V.A.** Yakupirangit-urtitovaya seriya shchelochnykh porod (Jacupirangite-Urtite Series of Alkaline Rocks), Moscow: Nauka, 1976. 215 p.
27. **Kramm, U.** Mantle components of carbonatites from the Kola Alkaline Province, Russia and Finland: A Nd - Sr study // Eur. J. Mineral. 1993. Vol.5. P.985-989.
28. **Kramm, U., Kogarko L.N.** Nd and Sr isotope signatures of the Khibina and Lovozero agpaitic centres, Kola Alkaline Province, Russia // Lithos. 1994. Vol.32. P.225-242.
29. **Kramm U., Kogarko, L.N., Kononova, V.A., Vartiainen, H.** The Kola Alkaline Province of the CIS and Finland: Precise Rb-Sr ages define 380-360 age range for all magmatism. // Lithos, 1993, vol.30, p.33-44.
30. **Kukhareno, A.A., Bulakh, A.C., Il'inskiy, G.A., et al.** Metallogenic Features of the Alkaline Associations of the Eastern Baltic Shield, Tr. Leningr. O-va Estestvoispyt., Leningrad: Nedra, 1971, vol. 72. no. 2. 280 p.
31. **Kukhareno, A.A., Orlova, M.P., Bulakh, A.G., et al.** Kaledonskiy kompleks ul'traosnovnykh-shchelochnykh porod i karbonatitov Kol'skogo poluost'rova i Severnoi Karelii (Caledonian Complex of Ultrabasic Alkaline Rocks and Carbonatites of the Kola Peninsula and Northern Karelia), Moscow: Nedra, 1965. 772 p.
32. **Le Bas, M.J.** Carbonatite-Nephelinite Volcanism. Wiley, New-York, 1977, 330p.
33. **Leake, B.E.** Nomenclature of amphiboles. // Mineral Mag., 1978, vol.42, no.324, pp.533-563.
34. **Lightfoot, P.C., Hawkesworth, C.J., Hergt, J.M., Naldrett, A.J., Gorbachev, N.S., Fedorenko, V.A., Doherty, W.** Remobilization of the continental lithosphere by a mantle plume: Major-, trace-element, and Sr-, Nd-, and Pb-isotope evidence from picritic and tholeiitic lavas of the Norilsk district, Siberian Trap, Russia. Contrib. Mineral. Petrol., 1993, vol.114, p.171-188.
35. **MacDougall, J.D.** Continental flood basalts and MORB: a brief discussion of similarities and differences in their petrogenesis. In: MacDougall J.D., ed., Continental flood basalts: Dordrecht, Netherlands, Kluwer, 1988, p.331-341.
36. **Kononova, V.A., Ed.** Moscow: Nauka, 1984. Magmaticheskie gornye porody. T. 2. Schelochnye porody (Igneous Rocks, vol.2. Alkaline Rocks), 415 p.
37. **Makhotkin, I.L., Zhuravlev, D.Z., Sablukov, S.M., et al.** Plume-lithospheric interaction as a Geodynamic Model for the Formation of the Arkhangelsk Diamond-bearing Province, Dokl. Russ. Acad. Nauk. 1997. vol. 353, no. 2, pp. 228-232.
38. **Mercier, J.-C.C.** Equilibrium state of diopside-bearing harzburgites from ophiolites: Geobarometric and geodynamic implications. // Contrib. Mineral. Petrol., 1984, vol.85, no.4, p.391-403.

39. **Mori, T., Green, D.H.** Laboratory duplication of phase equilibria observed in natural garnet lherzolites. // *J. Geol.*, 1978, vol.86, p.83-97.
40. **Morimoto, N.** Nomenclature of pyroxenes. // *Mineral.Mag.* 1988. Vol.52. №4. P.535-550.
41. **Morris, P.A.** MAGFRAC: a BASIC program for least-squares approximation of fractional crystallization. *Computers & Geosciences*. 1984, vol.10, no.4, pp. 437-444.
42. **Nagasawa, H., Schreiber H.D., Morris R.V.** Experimental mineral/liquid partition coefficients of REE, Sc and Sr for perovskite, spinel and melilite. *Earth Planet. Sci Lett.*, 1980, v.46, p.431-437.
43. **Neumann, E.-R., Sundvoll, B., Overli P.E.A.** Mildly Depleted Upper Mantle Beneath southeast Norway: Evidence from Basalts in the Oslo Rift. // *Tectonophysics*, 1990, vol.178, no.1, p.89-107.
44. **Parsadanyan, K.S., Kononova, V.A., and Bogatkov, O.A.,** Sources of the Heterogeneous Magmatism of the Arkhangelsk Diamond-bearing Province, *Petrologiya*. 1996, vol. 4, no. 5, pp. 496-517.
45. **Powell, R., Powell, M.** Geothermometry and oxygen barometry using coexisting iron-titanium oxides: a reappraisal. // *Mineral. Magazine*, 1977, Vol.41, p.257-263.
46. **Pyatenko, I.K. and Osokin, E.D.,** Geochemistry of the Kontozero Carbonatite Paleovolcano, Kola Peninsula, *Geokhimiya*, 1988, no. 5, pp. 723-737.
47. **Pyatenko, I.K. and Saprykina, L.G.,** Petrological Features of Alkali Basaltoids and Extrusive Carbonatites of the Russian Platform, in *Petrologiya i petrokhimiya rudonosnykh magmaticheskikh formacii (Petrology and Petrochemistry of Ore-bearing Igneous Associations)*, Moscow: Nauka, 1980, pp. 233-255.
48. **Rass, I.T.,** Parageneticheskiy analiz zonalnykh mineralov (Paragenetic Analysis of Zonal Minerals), Moscow: Nauka, 1986. 143 p.
49. **Roberts, D., Onstott, T.C.** Geochemistry and $^{40}\text{Ar}/^{39}\text{Ar}$ laser microprobe analyses of dolerite dykes from the Rybachi and Sredni Peninsulas, NW Kola, Russia. 1st Int. Barents Symp., Kirkenes, 21-24 Oct., 1993: Abstr.,-Trondheim, 1993, p.79.
50. **Rusanov, M.S., Arzamastsev, A.A., and Khmelinsky, V.I.** New Volcano-Plutonic Complex of the Kola Alkaline Province: Geology and Geochemistry, *Otechestvennaya Geologiya.*, 1993, no. 11, pp. 35-43.
51. **Rutter, M.J., Van der Laan S.R., Wyllie P.J.** Experimental data for a proposed empirical geobarometer: Aluminum in hornblende at 10 kbar pressure. // *Geology*, 1989, vol.17, no.10, p.897-900.
52. **Saunders, A.D., Norry, M.J., Tarney, J.** Origin of MORB and chemically depleted mantle reservoirs: trace element constraints. // *Journal of Petrology*, 1988, Special Lithosphere Issue, p.415-445.
53. **Shubina, N.A., Ukhanov, A.V., Genshaft, Yu.S., and Kolesov, G.M.** Trace and Major Elements in Peridotite Nodules from the Basalts of the Northwestern Spitsbergen with Implications for the Problem of Upper Mantle Heterogeneity, *Geokhimiya*, 1997, no. 1, pp. 21-36.
54. **Simkin, T., Smith, J.V.** Minor element distribution in olivine. // *J. Geology*, 1970, vol.78, no.3, p.304-325.
55. **Spear, A.J.** Micas in igneous rocks. // *Micas. Reviews in Mineralogy*, vol.13. 1984, pp.299-356.
56. **Stephens, M.B., Furnes, H., Robins, B., Sturt, B.A.** Igneous activity within the Scandinavian Caledonides. // *The Caledonide Orogen - Scandinavia and Related Areas.* (D.G.Gee & B.A.Sturt, ed.). Wiley & Sons, 1985, p.624-656.
57. **Taylor, S.R., McLennan, S.R.** The continental crust: its composition and evolution. 1985, Blackwell, Oxford. 312 p.

58. **Tikhonenkova, R.P.**, New Data on the Composition and Age of the Lovozero Formation, Kola Region, Dokl. Akad. Nauk SSSR. 1972, vol. 203, no. 4, pp. 903-907.
59. **von Harnik, A.B.** Strukturelle Zustände an den Anorthoklasen der Rhombenporphyre des Oslogebiets. // Schweizerische Mineralogische und Petrographische Mitteilungen. 1969, B.49, Heft 3, p.509-568.
60. **Weaver, B.L.** The origin of ocean island basalt end-member compositions: trace element and isotopic constraints. // Earth Planet. Sci. Lett., 1991, vol.104, p.381-397.
61. **White, R.S., McKenzie, D.** Mantle plumes and flood basalts. // Journ. Geophys. Res., 1995, vol.100, no.B9, p.17543-17586.
62. **Zaitsev, A.N., Bell, K.** Sr and Nd isotope data of apatite, calcite and dolomite as indicators of the source and the relationships of phoscorites and carbonatites from the Kovdor massif, Kola peninsula, Russia. // Contrib. Mineral. Petrol., 1995, vol.121, p.324-335.

A Possible Scenario of Material Differentiation at the Initial Stage of the Earth's Formation

Anfilogov V.N.¹ and Khachai Yu.V.²

¹ *Institute of Mineralogy, Ural Division, Russian Academy of Sciences, Miass, 456317 Russia;
e-mail: iminchf@ilmeny.ac.ru*

² *Institute of Geophysics, Ural Division, Russian Academy of Sciences, ul. Amundsena 100,
Yekaterinburg, 620016 Russia*

The formation of planets from protoplanet nebula is an extremely complex process. Substantial progress in the study of this process has been achieved in recent decade owing to the discovery of protoplanet nebulas and more than 100 planet systems of young stars. Decisive arguments have been adduced in favor of the formation of stars and planets in the course of a collapse of the dense cores of gas nebulas [1]. Modern models provide for several stages in the evolution of protoplanet nebula [1-3]: gravitational collapse; accretion of protostar nebula; settling of dust particles on the central region and the formation of a revolving disk; beginning of disk fragmentation with the formation of bodies and particles up to 1 cm in size; and the accretion stage at which the bodies, 0.1-10 km in size, grew into planetary dimensions.

The key problem that arises in the elaboration of models of the formation of the Earth and planets of the terrestrial group (TG) is related to the necessity of explaining the origin of a dense (mainly iron) core and silicate mantle. The various models that have been proposed for the solution of this problem may be classified into two groups: (1) models of homogeneous accretion (the formation of a quasi-homogeneous primordial Earth and its subsequent differentiation into the core and mantle after the completion of accretion) and (2) models of heterogeneous accretion (the formation of the Earth's iron core at the initial stage as a result of the coalescence of metallic particles).

The model of planet formation from dust and small particles leads to the homogeneous accretion. The fall of such materials is not accompanied by the formation of deep craters; the energy of collision that is released within a thin surface layer is largely dissipated by irradiation from the surface of a growing nucleus. Therefore, the temperature within the planet's interior remains below the solidus [2, 4, 5]. The fusion of its core could only have started in the Earth's upper layers, which were heated by large bodies falling on its surface [2-5]. Leaving aside the difficulties related to the physical substantiation of the mechanisms providing for the transport of core material to the Earth's center, let us only note that the time required for the submergence of such material into the core [3] turns out to be sharply overestimated in comparison with the age of the geomagnetic field and with the duration of core formation suggested by lead and some other

(e.g., W-Hf) isotopic systems [6]. The model of homogeneous accretion is also inconsistent with certain energy aspects of the problem [5].

Models of heterogeneous accretion meet another difficulty. Heterogeneous accretion should depend on the sequence of substance condensation in the protoplanet nebula and begin with initially condensating compounds. The sequence of condensation depends on *PT* conditions in the protoplanet nebula and represents an independent problem [1]. Modern estimates indicate that corundum, perovskite, melilite, and spinel are the first to condensate in the TG planets, whereas iron and silicates of Mg and Ca condensate later. Therefore, the problem of Fe transport to the Earth's center remains topical in this scenario too. In recent years, the model of megaimpact has been actively discussed towards explaining the distribution of matter in the Earth-Moon system. According to this model, the Earth collided with a body having the mass of Mercury or Mars at the final stage of its accretion. This promoted the heating of the Earth and the formation of its core. It is hard to believe that such a fortuitous event could be systematically repeated in the course of the formation of the cores of all TG planets. Some geochemical attributes that come into conflict with this model are noted in [7]. The model of the accretion of the Earth and other TG planets proposed in this communication is free of the aforementioned difficulties.

Meteorites bear the primary information on the composition and *PT* conditions of the protoplanet nebula. To develop an adequate model of planet formation, it is necessary not only to take into account the data on meteorite composition, but also to keep in mind their course of evolution—from their condensation from a gas nebula to the formation of parental bodies. In terms of the character of their evolution, primary and differentiated meteorites are recognized [8]. The first group is represented by carbonaceous chondrites composed of the substances that were released at the early (high-temperature) stage of nebular gas condensation. The iron meteorites, pallasites, and probably eucrites are related to the second group [8]. The mineral composition of the products of high-temperature condensation is best represented by coarse-grained CAI aggregates of carbonaceous chondrites composed of spinel MgAl_2O_4 (15-20 vol %), gehlenite $\text{Ca}_2\text{Al}[(\text{SiAl})_2\text{O}_7]$ (80-85 vol %), and perovskite CaTiO_3 (1-2 vol %) [8, 9]. Despite the rarity of such inclusions, their occurrence convincingly indicates that the sequence mentioned above was characteristic of condensation from gas nebula.

The state of protoplanet matter at the early stage and the character of its differentiation may be judged from the metamorphic grade of various meteorites. Occurrences of glass in chondrules of carbonaceous chondrites indicate that they experienced agglomeration and partial melting after their formation [8]. As follows from phase equilibria in the systems $\text{CaO-SiO}_2\text{-Al}_2\text{O}_3$, $\text{CaSiO}_3\text{-CaSiTiO}_5\text{-CaAlSi}_3\text{O}_8$, and $\text{Mg}_2\text{SiO}_4\text{-SiO}_2\text{-CaAl}_2\text{Si}_2\text{O}_8$ [9], they were heated up to 1800 ± 50 K. The eucritic material bears doubtless indications of crystallization from melt [8]. The melt in the diopside-anorthite-forsterite system, which mimics the mineral composition of eucrites, crystallizes at 1600-1550 K [10]. The material of iron

meteorites underwent total melting [8]. The melting temperature of the Fe-Ni alloy of these meteorites with an admixture of FeS is about 1720 K.

Iron meteorites and pallasites bear extremely important information on the differentiation of matter during the formation of parental bodies. First, the occurrence of such meteorites indicates that even relatively small parental bodies have been distinctly differentiated into their silicate and iron-nickel constituents. Second, the mineral composition of pallasites consisting of Fe-Ni alloy and olivine is consistent with the sequence of condensation in the gaseous protoplanet nebula. Third, the uniform distribution of olivine grains in the Fe-Ni alloy of pallasites indicates that the differentiation of matter during the formation of parental bodies was characterized by an absence of significant gravity field. This constrains the size of parental bodies by a few hundred kilometers. The Fe-Ni component of pallasites is undoubtedly of melt origin. However, the melting temperature of olivine is 1970-2070 K, and this mineral hardly experienced fusion. Most of the meteorites bear indications of the impacts that occurred during the collisions of parental bodies with one another. This process was accompanied by brecciation, shock metamorphism, and partial melting. However, only local heating was possible, because the parental bodies were small. The temperatures of metamorphism mentioned above are achieved in protoplanet nuclei already at their relatively small dimensions and not only at the final stage of planet accretion.

Table 1

Temperature in the center of a growing planet nucleus vs. radius and average Al₂O₃ content.

Radius, km	Temperature in the center, K			
	Al ₂ O ₃ content, wt %			
	1.0	3.0	4.6	9.0
50	1240	1701	1734	1825
100	1675	1752	1812	1978
150	1690	1793	1876	2104
200	1701	1828	1928	2206
250	1711	1856	1972	2290
300	1718	1878	2006	2359
400	1730	1912	2059	2461

Let us consider the possible sources of energy that functioned in the course of the formation of the parental bodies of meteorites and take them as a basis for the development of a thermal model. When developing such a model, we will consider only the early stage of planet accretion, when their size was not larger than a few hundred kilometers. The duration of this stage is estimated from various data at 10⁶-10⁷ Ma [1, 8]. The temperature of bodies at this stage was controlled by the following factors: (1) temperature of the environment at a given distance from the Sun, (2) energy of collision with other bodies and particles, and (3) heating related to the decay of short-lived radioactive isotopes. The contribution of energy that is released by impacts and that can be estimated from the most reliable Safronov

model [2] was small at this stage [2, 4, 5]. Therefore, the third factor is preferential as a source of energy. Isotope ^{26}Al with a half-life period $\tau = 7.38 \cdot 10^5$ yr and an energy of decay equal to $2.99 \cdot 10^6$ eV has attracted the most interest among the short-lived isotopes. A rather reliable estimate of ^{26}Al content in the parental material of meteorites is given in [11].

In order to describe the growth of a planet, let us use the Safronov model [2] that approximates the complex evolution of a planet nucleus in the course of multifold chaotic collisions with competing bodies and particles contained in the

$$\frac{dm}{dt} = 2(1 + 2\theta)r^2\omega\left(1 - \frac{m}{M}\right)\sigma_0,$$

protoplanet nebula at the accretion stage by the equation where $\omega = \frac{2\pi}{\tau}$ is the angular velocity of the orbital motion of the planet; τ is the period of circulation equal to $3.1 \cdot 10^7$ s; σ_0 is the surface density of material in the protoplanet feeding zone equal to 100 kg/m^2 [2]; m is the present-day mass of a planet; m is the mass of the growing planet; θ is the statistic parameter that takes into account the distribution of particles by their masses and velocities in the feeding zone; and r is the radius of the growing planet. To assess the energy contribution made by the decay of short-lived isotopes, we shall restrict our consideration to a spherical-symmetrical model. The convective heat transfer and the presence of alloy melting zones are taken into account parametrically, as in [5, 6], by introducing the effective heat capacity and thermal conductivity:

$$c_{\text{eff}}\rho\frac{\partial T}{\partial t} = \nabla(\lambda_{\text{eff}}\nabla T) + Q,$$

where ρ is the density of a body accepted to be 3000 kg/m^3 ; c_{eff} is the effective heat capacity; λ_{eff} is the effective thermal conductivity; and Q is the total power of internal heat sources provided by the decay of radioactive elements and the release of energy of falling bodies. The temperature on the outer surface of the growing body at minor masses is determined by the solar constant. A zero heat flow is set in the center of body.

Equation (2) was solved numerically for a sphere of increasing radius. The radius increment ΔR over one time step was assumed constant. The dimensional value ΔR was accepted as equal to $1/20\,000$ of the final radius. In the general case, a variable time step is chosen and found from (1) at the chosen distribution of model density at the accepted ΔR . The position of the partial melting zone is determined from the correlation of the calculated temperature distribution and the melting onset temperature at the protoplanet mass corresponding to a given temporal layer. An estimate of ^{26}Al concentration in the protoplanet nebula is important for further calculations. The isotope ratio $^{26}\text{Al}/^{27}\text{Al} = 5 \cdot 10^{-5}$ is accepted as the most highly substantiated value.

Our primary interest is the dependence of the maximum estimate of temperature in the center of the growing nucleus on its mass (or radius if density is

constant) at various Al_2O_3 concentrations in the initial matter. The calculation results are given in the table. As follows from the presented values, even a very low average Al content provides a temperature in the nucleus center above the melting temperature of Fe-Ni alloy (1720 K). The figure shows the calculated temperature distribution in the protoplanet interior for three radius values. As can be seen, even at a radius of 250 km and 4.6 wt % Al_2O_3 , the melting temperature of Fe-Ni alloy that accreted after the mineral assemblage in the central portion of the parental body is achieved at half-radius of the growing planet. Partial melting may also take place in a part of the next layer, which consists of diopside, forsterite, anorthite, and enstatite that condensed and accreted after iron. At the same time, the outer shell remains solid.

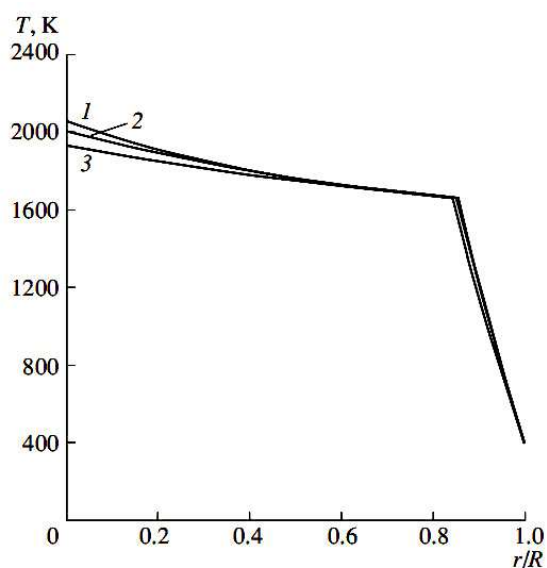


Fig 1. Temperature distribution in the nucleus of a growing planet. Radius of nucleus, km: (1) 400, (2) 300, (3) 250.

Let us consider further the process of accretion. In compliance with the Safronov model [1], a great number of chaotically moving parental bodies colliding with one another should be formed at the initial stage. The collision of two bodies that have similar dimensions, partially melted aluminosilicate core, completely fused middle shell composed of iron, and a solid outer shell leads to their destruction. Fragments of the solid outer shell can be partially lost, whereas the fragments of the fused iron merge and form the nucleus of a new body with a core composed of Fe-Ni alloy. As follows from the results shown in the figure, the thickness of the outer brittle shell is small. Therefore, the efficiency of coalescence is close to unity, as suggested by the model [2].

Thus, the proposed mechanism of planet formation is realized during two stages. Many parental bodies no larger than a few hundred kilometers across are formed at the first stage. In the process of their accretion, the primary bodies are heated as a result of the decay of short-lived radioactive isotopes, first of all, ^{26}Al . These bodies are partly destroyed in the course of collision with one another. The second stage is marked by the merger of melted shells mainly consisting of iron

derived from the destroyed parental bodies, and the new bodies serve as nuclei that accrete material of the destroyed parental bodies into planets. The quantitative description of this process requires an adaptation of scheme (1) and especially (2), in which such a process of separation is not taken into account in explicit form. The duration of the second stage might be 10^6 - 10^7 Ma. This scenario allows us to suggest that the formation of the Earth's core (at least, its central portion) and division of the planet into shells occurred in the beginning of the second stage. The proposed model does not rule out a continuation of the core formation during the further growth of the planet and after its completion. This principally new differentiation mechanism does not require the sort of catastrophic megaimpact that is often adduced in order to explain the formation of the Moon and initiation of the iron core formation in the Earth. Furthermore, our model opens the door to a rather simple solution of the geochemical problems discussed in [7]. In particular, the model suggests that the separation of lead and the division of the W-Hf system should have occurred in relatively small bodies that form over $\sim 10^7$ yr. Thus, our model eliminates the difficulties associated with such separation given the present-day dimensions of the core and mantle.

ACKNOWLEDGMENTS

This study was carried out as a part of integration projects of the Ural Division, Siberian Branch, and Far East Division of the Russian Academy of Sciences 2009-2011, (*no. 09-C-5-1014*).

REFERENCES

1. **V. A. Dorofeeva and A. B. Makalkin**, 2004. Evolution of the Early Solar System: Cosmochemical and Physical Aspects (Editorial, Moscow) [in Russian].
2. **V. S. Safronov**, 1982. *Izv. Akad. Nauk SSSR, Fiz. Zemli*, No. 6, 5.
3. **A. V. Vityazev, G. V. Pechernikova, and V. S. Safronov**, 1990. Planets of the Terrestrial Group: The Origin and Early Evolution (Nauka, Moscow) [in Russian].
4. **Yu. V. Khachai**, 1987. in Nuclear Geophysical and Geothermal Studies (Ural. Sci. Center, Sverdlovsk), pp. 38-44 [in Russian].
5. **W. M. Kaula, J. Geophys.** 1979. Res. 84, 999.
6. **S. Jacobsen and Q. Yin**, 2003. *Geophys. Res. Abstr.* 5, 13884.
7. **E. M. Galimov**, 2004. *Geokhimiya* 42 (7), 691. [*Geochem. Intern.* 42 (7), 595 (2004)].
8. **R. T. Dodd**, 1981. Meteorites. A Petrologic-Chemical Synthesis (Cambridge Univ. Press, Cambridge, ; Mir. Moscow, 1986).
9. **G. V. Voitkevich**, 1979. Principles of Theory of the Earth Origin (Nedra, Moscow [in Russian]).
10. **E. G. Ehlers**, The Interpretation of Geological Phase Diagrams (Freeman, San Francisco, 1972; Mir, Moscow, 1975).
11. **R. H. Nicols, Jr.**, *Space Sci. Rev.* 92, 113 (2000).

Chlorine from the mantle: magmatic halides in the Udachnaya-East kimberlite, Siberia

Kamenetsky V.S.^{1*}, Maas R.², Kamenetsky M.B.¹, Paton C.¹, Phillips D.², Golovin A.V.³

¹ARC Centre of Excellence on Ore Deposits and School of Earth Sciences, University of Tasmania, Hobart, Australia

²School of Earth Sciences, University of Melbourne, Vic 3010, Australia

³VS Sobolev Institute of Geology and Mineralogy, SB RAS, Novosibirsk, Russia

* Corresponding author. ARC Centre of Excellence on Ore Deposits and School of Earth Sciences, University of Tasmania, Hobart, 7001, TAS, Australia; Tel.: +61 3 62267649; fax: +61 3 62262547. E-mail address: Dima.Kamenetsky@utas.edu.au

ABSTRACT

The Devonian Udachnaya-East pipe (Siberia) presents a rare example of exceptionally fresh kimberlite rocks, containing a rich assemblage of alkali carbonate, chloride and sulphate minerals in its groundmass. Accordingly, bulk groundmass compositions have unusually high concentrations of sodium and chlorine (up to 6 wt.% each), while water contents are very low. High Na₂O and low H₂O are inconsistent with currently accepted model kimberlite magma compositions; and high Na and Cl contents in the Udachnaya-East pipe have been ignored by the geoscience community, because of possibility of contamination from sedimentary crustal rocks. New textural evidence suggests that the chloride and alkali carbonate minerals in this kimberlite are co-magmatic with perovskite.

Radiogenic isotope ratios for the perovskite (⁸⁷Sr/⁸⁶Sr ~0.7031, ε_{Nd}+5, ε_{Hf}+5.3, obtained by solution-mode and laser-ablation methods) are very primitive and provide no support for a crustal contaminant. The new perovskite data confirm previously published Sr-Nd-Pb isotopic evidence for the chlorides and alkali carbonates themselves, but are considered more reliable because of possible open system behaviour and analytical problems with unstable halide and carbonate minerals. Similar isotope ratios (⁸⁷Sr/⁸⁶Sr=0.70292, ε_{Nd}=+5, ε_{Hf}=+6.5) are recorded in a clinopyroxene macrocryst, which contains chlorides and alkali carbonates within melt inclusions, implying a similarly primitive isotopic signature for the host kimberlite. We infer that assimilation of evaporitic sediments is unlikely and that abundant chlorine and sodium in the kimberlite originated in the upper mantle. Our results and published experimental data on mantle chloride melts and presence of a chloride component in diamond-hosted fluid inclusions suggest a previously unrecognised role for mantle-derived halide melts in the genesis, composition and rheological properties of kimberlite primary melts.

INTRODUCTION

Kimberlites, the most important source of diamonds, are also a most enigmatic rock type. After a century of research, the nature, origin and evolution of their parent magmas are still controversial [27; 23; 2, 28]. “Archetypal” kimberlites (often referred to as group-I kimberlites) worldwide have ultramafic compositions (MgO >20 wt%), contain abundant volatiles (CO₂+H₂O >6 wt%) and incompatible trace elements (e.g., La >50 ppm), but have low levels of “basaltic” components

($\text{Na}_2\text{O} < 0.4 \text{ wt\%}$ and $\text{Al}_2\text{O}_3 < 5 \text{ wt\%}$) and elements of moderate incompatibility (e.g., $\text{Yb} < 1.5 \text{ ppm}$; the so-called “garnet” signature). Kimberlite parental melts are therefore believed to be high-Mg ultrabasic, hydrous, and highly enriched in incompatible trace elements [5, 39, 23, 9, 21, 28, 19].

A model magma of this nature, while capable of accounting for many of the compositional features of kimberlite rocks, presents a number of problems. For example, an ultrabasic magma composition is difficult to reconcile with models of kimberlite magma source compositions and melting conditions, with inferred magma temperatures and rheological properties, and with the style of kimberlite magma ascent and emplacement [27, 6, 46, 48, 28]. In our view, these inconsistencies indicate serious flaws in current models of kimberlite magma compositions.

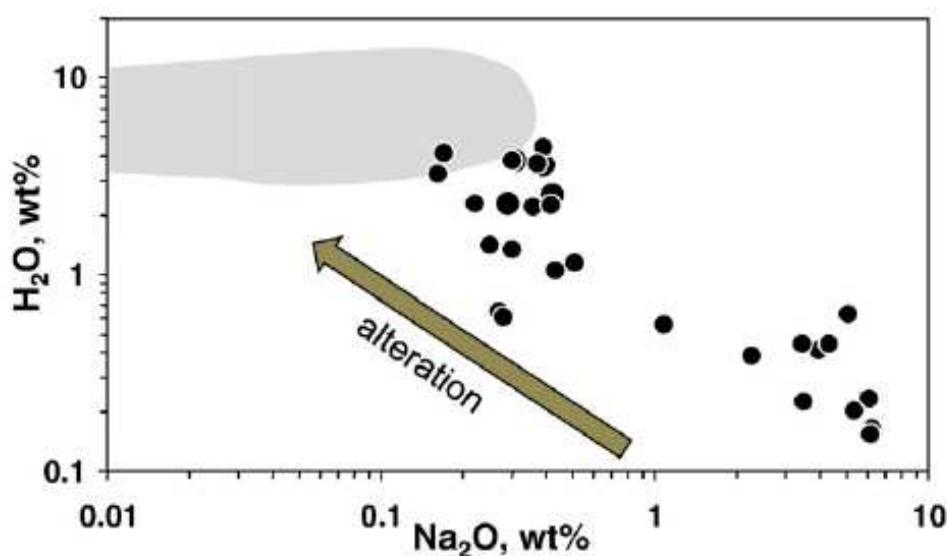


Fig. 1. Compositional co-variations of Na_2O and H_2O (in wt.%) in the Udachnaya-East pipe kimberlites and “archetypal” rocks from South Africa and Lac de Gras, Canada (shown as a field; e.g., [19]).

Much of the uncertainty over true kimberlite compositions may stem from the almost ubiquitous hydrous alteration of kimberlites. For example, two of the inferred key characteristics of kimberlitic magmas — low sodium and high water contents (Fig. 1; [19]) — may relate to postmagmatic alteration that affected most kimberlites worldwide.

A rare example of serpentine-free, but otherwise typical (group-I) kimberlite, is the diamondiferous Udachnaya-East pipe, Siberia [13, 14, 15, 16], in which unusual for kimberlites low H_2O abundances is coupled with extraordinary enrichment in Na_2O (up to 6 wt.%), and both components are negatively correlated (Fig. 1). In addition to common olivine and calcite the groundmass of this kimberlite contains abundant alkali carbonates (shortite $\text{Na}_2\text{Ca}_2(\text{CO}_3)_3$ and

zemkorite ($(\text{Na}, \text{K})_2\text{Ca}(\text{CO}_3)_2$). By contrast, hydrous minerals (phlogopite) are rare and serpentine is absent, consistent with very low intrinsic water content in the parent magma. Another key ingredient in this kimberlite is chlorine (total Cl up to 6 wt.%, 14, 15), which is mainly hosted in abundant groundmass halides (halite, sylvite). The halides are observed only in the deepest and freshest mine exposures in the pipe. They are relatively minor in kimberlite from shallower mine levels and the twin Udachnaya-West pipe [35], and have not previously been reported from other kimberlites, except olivine-hosted melt inclusions in the Canadian and Greenland kimberlites [17], presumably because they are so easily destroyed by alteration.

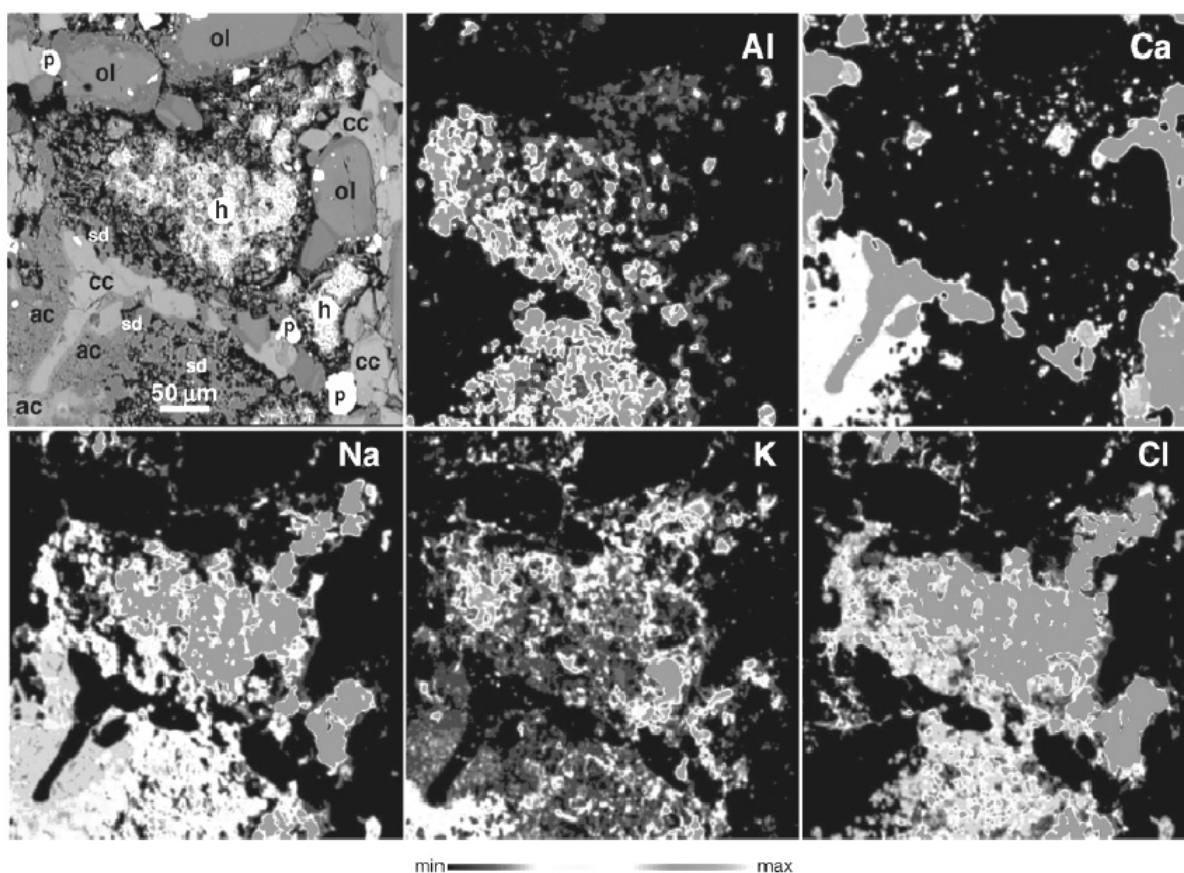


Fig. 2. Backscattered electron image and X-ray element maps showing intimate association of perovskite (p) with Na–K chlorides (h), alkali carbonates (ac), calcite (cc), sodalite (sd) and olivine (ol) in the groundmass of Udachnaya-East kimberlite.

We believe that observations from an unaltered kimberlite, such as Udachnaya-East, may hold the key to an improved understanding of kimberlite parent magma compositions. We have therefore argued that low water content, high sodium and high chlorine represent primary magmatic characteristics of the Udachnaya-East kimberlite, with important potential implications for kimberlite petrogenesis in general [13, 15, 16, 17].

Predictably, these claims have been received with some scepticism, simply because halides would not be expected to form primary minerals in igneous rocks.

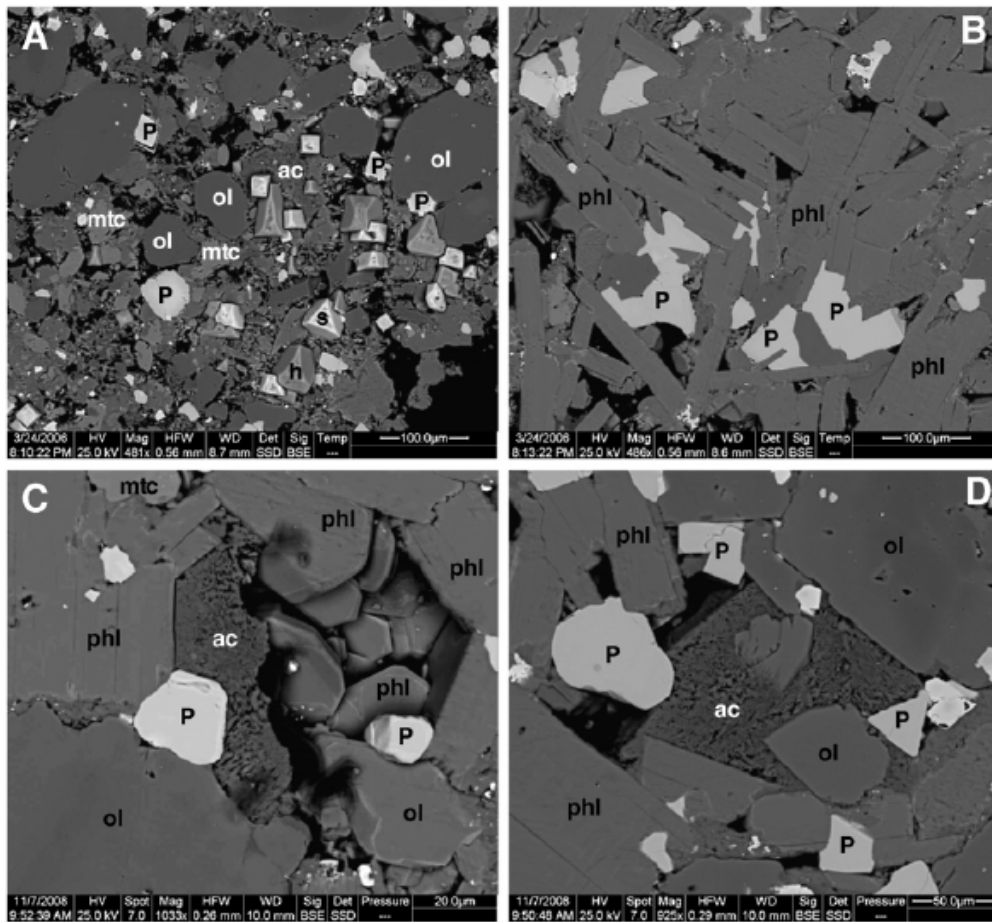


Fig. 3. Backscattered electron images of polished surfaces of the Udachnaya-East kimberlites (A — host kimberlite; B–D — perovskite- and phlogopite-rich clast), showing typical groundmass assemblage of co-crystallised chlorides, halite (h) and sylvite (s), alkali carbonates (ac), erovskite (P), phlogopite (phl), monticellite (mtc) and olivine (ol).

In fact, the halides at Udachnaya-East were attributed to reworking of crustal sediments of the Siberian Craton [35, 8, 38].

In efforts to support our hypothesis of primary, mantle-derived alkali- and Cl-bearing minerals (halides, sodalite and djerfisherite) in this kimberlite, we have presented evidence based on melt inclusions [13], and on stable and radiogenic isotopes [24, 14]. For example, Maas et al. [24] showed that easily soluble halides from the kimberlite have present-day $^{87}\text{Sr}/^{86}\text{Sr}$ ratios considerably lower than those of potential crustal (evaporitic) contaminants, and calculated initial Nd–Pb isotope ratios that are close to those of the silicate component in the same samples, consistent with a co-magmatic origin. Nevertheless, it has proved difficult to completely dispel alternative scenarios, most notably the possibility that crustal halides picked up at depth have been thoroughly assimilated and processed through the kimberlite magmatic system, to the extent that little of their crustal (isotopic)

heritage remains. In this regard, robust, high precision isotopic information for the halides and alkali chlorides becomes critical, yet is difficult to obtain, for two main reasons. Firstly, halides and alkali carbonates are highly unstable in air, even on the timescale of hours and days [e.g., 57]. This means that parent/daughter ratios could be changed by dissolution and reprecipitation processes in the laboratory; in fact, even present-day isotope ratios (Sr, Pb) might be affected, by incorporation of air- and surface-borne contaminants in reprecipitated material [e.g., 25, 24]. Secondly, halides are soluble in water and are therefore difficult to clean properly prior to isotopic work, complicating blank corrections to samples with low Sr, Nd or Pb contents. These factors compromise calculated initial isotope ratios for the halides and alkali carbonates from Udachnaya-East [24].

Table 1

Compositions of kimberlite clast, groundmass minerals and clinopyroxene macrocryst.

	1	2	3	4	5	6
SiO₂	32.36	0.03	0.02	37.89	37.73	54.98
TiO₂	5.24	54.30	55.56	2.83	3.52	0.20
Al₂O₃	5.36	0.28	0.13	14.95	15.40	2.01
FeO	7.85	1.39	1.17	5.03	6.19	4.13
MnO	0.13	n.d.	n.d.	0.03	0.07	0.12
MgO	31.07	0.07	0.07	22.84	22.93	16.17
CaO	5.96	37.13	37.95	0.15	0.04	20.68
Na₂O	1.47	0.59	0.54	0.17	0.10	1.74
K₂O	3.79	n.d.	n.d.	9.98	10.04	0.02
P₂O₅	0.14	n.d.	n.d.	n.d.	n.d.	n.d.
Cr₂O₃	0.26	n.d.	n.d.	0.64	0.21	0.31
BaO	0.46	n.d.	n.d.	0.77	0.76	n.d.
total	94.09 ^a	93.78 ^b	95.44 ^b	95.28	96.99	100.36

Note: (1) whole rock composition of clast UV31k-05; (2, 3) average compositions of perovskite in host kimberlite and kimberlite clast, respectively; (4, 5) average compositions of phlogopite in host kimberlite and kimberlite clast, respectively; (6) clinopyroxene macrocryst UV9774.

n.d. — not determined (but likely negligible).

^a Total exclude 3.22 wt.% CO₂ 1.21 wt.% H₂O and undetermined Cl.

^b Totals exclude 4–5 wt.% of REE, Sr, Th, Zr, Nb and Ta in perovskite (see Fig. 6).

An attempt to address the crustal contamination hypothesis with Cl isotopes proved inconclusive because of the similar ³⁷Cl/³⁵Cl ratios in mantle and crustal rocks [43]. Here we revisit the issue using a different isotope-based approach: we employ kimberlitic perovskite, closely associated with halide minerals to approximate the radiogenic isotopic signature of these halides. Perovskite (CaTiO₃) is a common groundmass mineral in kimberlites [e.g., 3] and is clearly derived from the melt. It has high Sr–Nd contents and Rb/Sr ≈ 0 [10] and should preserve the initial Sr–Nd isotope signature of the kimberlite melt during perovskite formation, even in altered kimberlite [33]. In our samples of

Udachnaya-East kimberlite, perovskite and associated halides/alkali carbonates can be shown to be co-magmatic based on textural relations. Radiogenic isotope signatures of the former should therefore provide valid high-precision constraints on the role of crustal material, if any, in the latter, while avoiding the analytical problems mentioned above.

SAMPLES FOR ISOTOPE STUDY

In the Udachnaya-East kimberlite, perovskite occurs as inclusions in the rims of olivine phenocrysts [16] and disseminated in the matrix in close association with groundmass phases (Figs. 2 and 3A), typical for all kimberlites (olivine, calcite, phlogopite, monticellite, apatite, Fe–Ti–Cr oxides and Fe–Ni sulphides) and alkali and Cl-bearing minerals, characteristic of the Udachnaya-East [13] and some other kimberlites (alkali carbonates and sulphates (aphthitalite $\text{NaK}_3(\text{SO}_4)_2$), chlorides, sodalite $\text{Na}_8\text{Al}_6\text{Si}_6\text{O}_{24}\text{Cl}$, and K-sulphides (djerfisherite $\text{K}_6(\text{Cu,Fe,Ni})_{25}\text{S}_{26}\text{Cl}$ and rasvumite KFe_2S_3 ; [44, 45]). Perovskite is particularly abundant (10%) in sample UV31k-05 (Fig. 3B–D, Table 1), a spherical ~3 cm phlogopite-olivine ‘clast’ recovered from fresh kimberlite. Mineral (olivine, phlogopite, perovskite) compositions in UV31k-05 and the host kimberlite are near-identical (Table 1), and groundmass assemblages are very similar, including interstitial carbonates, chlorides and perovskite (Figs. 2 and 3). We will therefore assume that UV31k-05 and the host kimberlite are genetically related. For example, UV31k-05 may represent a fragmented cumulate; accumulation of perovskite has been reported in a number of kimberlites [4, 27].

Textural relationships between perovskite and alkali carbonates and chlorides (Figs. 2 and 3) suggest their coprecipitation from the melt. A further link between a carbonate–chloride component and the kimberlite silicate–oxide assemblage is provided by melt inclusions. As documented earlier, the rims of zoned groundmass olivine in the Udachnaya-East kimberlite contain melt inclusions of carbonate–chloride composition, implying Cl-alkali-rich late-stage melt compositions [13, 7]. This evidence is also relevant to this study of perovskite, because its crystallisation partly overlaps that of the olivine (cf. perovskite inclusions in olivine rims, 16). Moreover, phlogopite-hosted melt inclusions in sample UV31k-05 (Fig. 4) are identical to olivine-hosted melt inclusions mentioned above, in having essentially carbonate–chloride compositions and low homogenisation temperatures (650–700 °C). This implies that all three minerals coexisted with a Cl-alkali-rich melt, in both host kimberlite and sample UV31k-05, and that UV31k-05 is indeed cogenetic (cognate clast) with the host kimberlite. We therefore used UV31k-05, with its abundance of phlogopite and perovskite, rather than the host kimberlite, to obtain high-quality separates of perovskite and phlogopite for Sr–Nd isotopic and Rb–Sr/Ar–Ar dating, respectively. Hafnium isotopic data were obtained for perovskite–phlogopite–olivine mixtures.

Sample UV9774 is large (~4 cm) clinopyroxene crystal (“macrocryst” thereafter instead of “megacryst” to avoid genetic implications; Table 1) from Udachnaya-East. It contains a number of cavities (Fig. 5), most likely melt inclusions, which have recrystallised into assemblages of halite, sylvite, tetraferriphlogopite, shortite, apatite, djerfisherite, barite, ilmenite, aphtitalite and olivine, all phases which also occur in the host kimberlite groundmass and would be expected to form from the type of melts trapped in the olivine- and phlogopite-hosted melt inclusion described above. Fragments of the clinopyroxene were used for Sr–Nd–Hf isotope work.

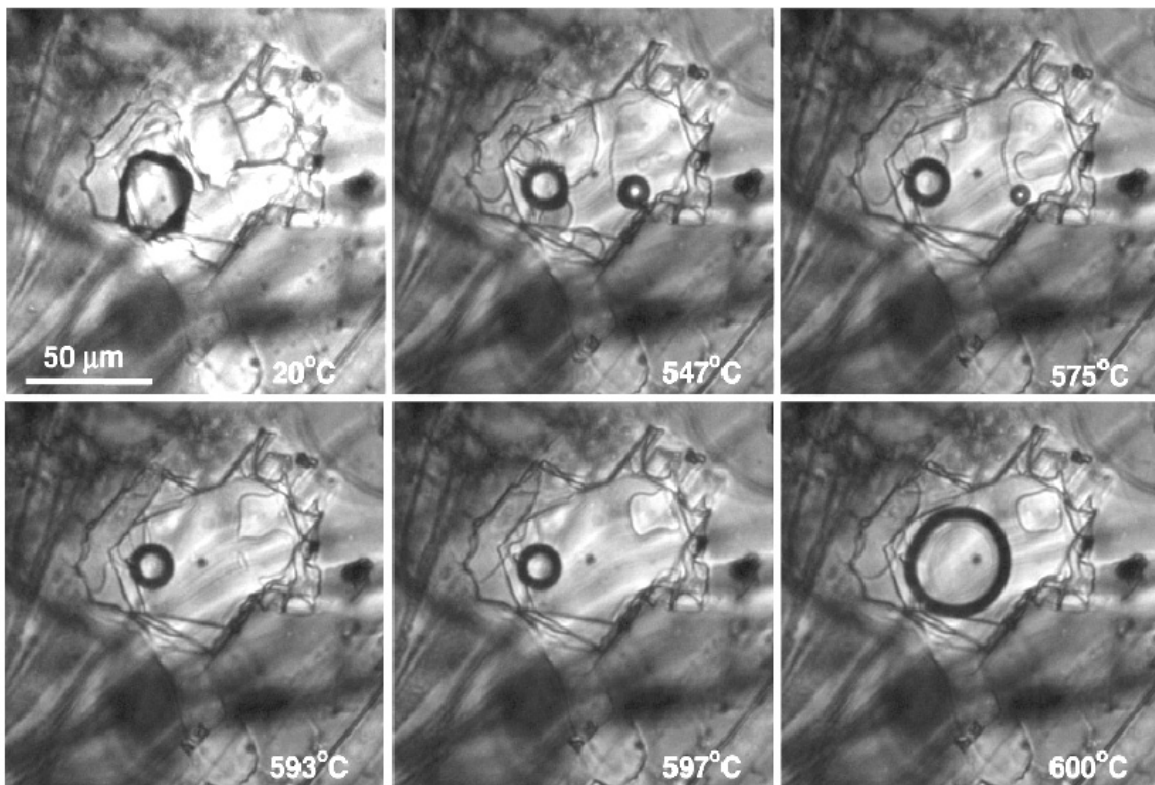


Fig. 4. Photomicrographs of a typical multiphase melt inclusion in phlogopite from clast sample UV31k-05 at room temperature and during experiment in a heating stage with visual control. At temperature N500 °C melting within melt inclusions is intense, vapour bubbles decrease in size, and possibly two liquids (carbonate-rich and chloride-rich) form. When the melt inclusion was close to homogenisation at ~600 °C, leakage of the liquid content and bubble increase occurred.

ANALYTICAL TECHNIQUES

^{40}Ar – ^{39}Ar , Rb–Sr, Sm–Nd and Lu–Hf isotope analyses were carried out at the University of Melbourne, following published analytical procedures [24, 34, 37]. Additional detail is given here and in Tables 2–4. Perovskite and phlogopite in UV31k-05 were handpicked from sized fractions after eliminating easily soluble salts and carbonates with cold 1.5 M HCl. Perovskite fractions (0.1 to 0.4 mg) were in the size range 30–200 µm, while phlogopite samples (0.3–1.5 mg) were

picked from the 50–200 μm (multiple single flakes) and 200–300 μm (small mica stacks) fractions. Larger mixed mineral fractions (olivine, phlogopite, perovskite, 100 mg) were used for Lu–Hf isotope work because pure perovskite fractions would have been too small to obtain good-quality Lu–Hf data. Assuming that olivine is very low in Lu and Hf, measured Hf isotope ratios for the mixed fractions should represent cogenetic perovskite and phlogopite. Acid-leached host kimberlite fractions for Lu–Hf were produced from bulk groundmass samples using cold 1M HCl. Mineral separates were cleaned in dilute nitric acid and dissolved (2:1 HF/HNO₃, 6 M HCl) on a hotplate; kimberlite groundmass samples were dissolved at high-pressure. Elemental separations were done using a combination of conventional cation exchange and EICHRON SR-resin (Rb–Sr),

RE-resin and LN-resin (Sm–Nd, Lu–Hf, 21, 24). Total blanks for all elements of interest were well below 100 pg and negligible in all cases. Sr–Nd–Hf isotopic analyses were carried out on a NU Plasma MC-ICPMS; for further details see Tables 2 and 4. Recent isotope dilution analyses for USGS basalts BCR-2 and BHVO-2 yield $^{176}\text{Lu}/^{177}\text{Hf}$ and $^{176}\text{Hf}/^{177}\text{Hf}$ of 0.01435, 0.282875 and 0.00878, 0.283113, respectively, very similar to results reported elsewhere [e.g., 56].
Parentdaughter

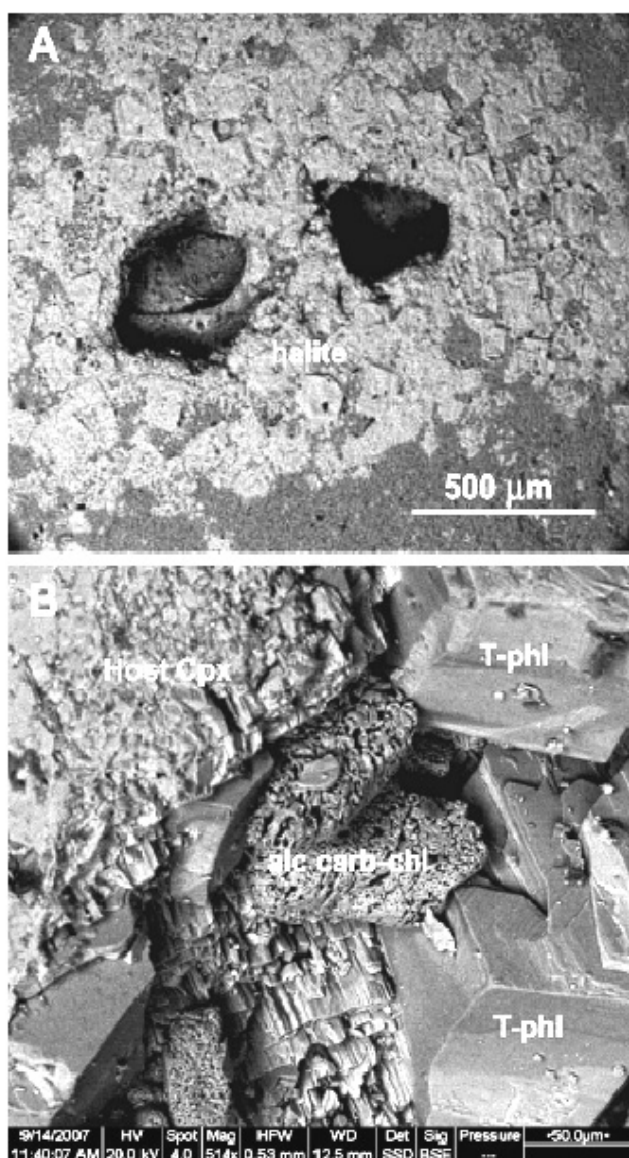


Fig. 5. Backscattered electron images of unpolished surface of clinopyroxene macrocryst (sample UV9774) showing: A — “negative crystal” shaped cavities, exposed by sawing and interpreted to have been large melt inclusions, with a microcrystalline aggregate of re-precipitated halite around them; B — remaining in cavities material represented by a porous mass (partly leached by water during sawing) of alkali carbonates and chlorides, intergrown with tetraferriphlogopite crystals.

Table 2

Rb-Sr, Sm-Nd and Lu-Hf isotope results for mineral and groundmass samples, Udachnaya-East kimberlite

	Host kimberlite, groundmass					Kimberlitic clast UV31k-05					UV9774			
	YBK-0 bulk		YBK-0 residue		YBK-3 bulk	YBK-3 residue		UP1 prv	UP2 prv	UP3 prv		UP4 prv/phl/ol	UP5 prv/phl/ol	Macrocryst cpx
Rb ppm	88.0	110.2	85.2	93.9									1.05	
Sr ppm	1122	64.6	933	55.4									154.8	
⁸⁷ Rb/ ⁸⁶ Sr	0.227	4.951	0.265	4.920				<0.001	<0.001	<0.001			0.0196	
⁸⁷ Sr/ ⁸⁶ Sr	0.70588	0.72956	0.70626	0.72907				0.70303	0.70308	0.70303			0.70302	
⁸⁷ Sr/ ⁸⁶ Sr ₃₆₃	0.70471	0.70397	0.70489	0.70364				0.70303	0.70308	0.70303			0.70292	
Sm ppm	10.57	12.77	11.58	10.52				591	4786	2123			2.13	
Nd ppm	79.85	98.56	80.62	82.11				4786	4786	149.11			9.08	
¹⁴⁷ Sm/ ¹⁴⁴ Nd	0.0800	0.0783	0.0869	0.0775				0.0782	0.0747	0.0861			0.1414	
¹⁴³ Nd/ ¹⁴⁴ Nd	0.512561	0.512591	0.512596	0.512568				0.512597	0.512595	0.512575			0.512761	
¹⁴³ Nd/ ¹⁴⁴ Nd ₃₆₃	0.512371	0.512405	0.512389	0.512384				0.512411	0.512417	0.512370			0.512425	
ε _{Nd363}	+3.9	+4.6	+4.3	+4.2				+4.7	+4.8	+3.9			+5.0	
Lu ppm	0.064	0.067	0.071	0.067				0.067	0.067	0.031			0.015	
Hf ppm	2.94	4.68	3.19	3.70				3.70	3.70	1.56			1.44	
¹⁷⁶ Lu/ ¹⁷⁷ Hf	0.00309	0.00204	0.00316	0.00256				0.00256	0.00256	0.00284			0.00148	
¹⁷⁶ Hf/ ¹⁷⁷ Hf	0.282701	0.282704	0.282706	0.282714				0.282714	0.282714	0.282713			0.282730	
¹⁷⁶ Hf/ ¹⁷⁷ Hf ₃₆₃	0.282680	0.282690	0.282685	0.282697				0.282697	0.282697	0.282694			0.282730	
ε _{Hf363}	+4.7	+5.1	+4.9	+5.3				+4.9	+5.3	+5.2			+6.5	

Note: Abbreviations: prv = perovskite; phl = phlogopite; ol = olivine; cpx = clinopyroxene; residue = residual after leaching with 1 M HCl. Concentrations in italics are by quadrupole ICP-MS; all other concentrations and parent/daughter ratios by isotope dilution. ⁸⁷Sr/⁸⁶Sr normalized to 88Sr/⁸⁶Sr = 8.37521 and reported relative to SRM987 = 0.71023. ¹⁴³Nd/¹⁴⁴Nd normalized to ¹⁴⁶Nd/¹⁴⁵Nd = 2.0719425 (equivalent to ¹⁴⁶Nd/¹⁴⁴Nd = 0.7219) and reported relative to LaJolla = 0.511860. ¹⁷⁶Lu/¹⁷⁷Hf normalized to ¹⁷⁹Hf/¹⁷⁷Hf = 0.7325 and reported relative to JMC475 = 0.282160. Internal precision (2se) is ± 0.00002 (Sr), ± 0.000012 (Nd) and ± 0.000010 (Hf); external precision (2sd) is ± 0.00004, ± 0.000020, ± 0.000015. External precision (2sd) is ± 0.5% (⁸⁷Rb/⁸⁶Sr), ± 0.2% (¹⁴⁷Sm/¹⁴⁴Nd), ± 1% (¹⁷⁶Lu/¹⁷⁷Hf); if quadrupole ICP-MS data are used (as for cpx macrocryst), Rb/Sr and Lu/Hf have errors of ± 3%. Present-day chondrite is: ¹⁴⁷Sm/¹⁴⁴Nd 0.1967, ¹⁴³Nd/¹⁴⁴Nd 0.512638; ¹⁷⁶Lu/¹⁷⁷Hf 0.0332, ¹⁷⁶Hf/¹⁷⁷Hf 0.282772 [1]. Rb-Sr and Sm-Nd data for host kimberlite groundmass samples from [Maas et al. \[24\]](#). Decay constants: ⁸⁷Rb 1.42 • 10⁻¹¹ yr⁻¹, ¹⁴⁷Sm 6.54 • 10⁻¹² yr⁻¹, ¹⁷⁶Lu 1.865 • 10⁻¹¹ yr⁻¹

ratios of some samples are based on quadrupole-ICPMS trace element data. Laser-ablation MC-ICP MS Sr isotope analyses of single perovskite grains were done following the published protocol [34]. Some of the 20 spot analyses (total Sr signals 0.9–2.8 V, 19–40 s ablations) produced spiky ^{85}Rb interference from impurities, but all calculated initial $^{87}\text{Sr}/^{86}\text{Sr}$ ratios were the same within errors (0.70312 ± 5 , MSWD 0.54). $^{84}\text{Sr}/^{86}\text{Sr}$ ratios, determined on small signals (4.5–14 mV) and corrected for REE++, ranged from 0.0563 to 0.0572, averaging 0.0569, slightly elevated compared to the natural ratio (~ 0.0565).

RESULTS AND DISCUSSION

As mentioned earlier, mineral compositions for groundmass olivine, phlogopite and perovskite in UV31k-05 and the host kimberlite are very similar. This similarity extends to trace elements (Table 1, Fig. 6). The data support accumulation of perovskite and phlogopite from the kimberlite parentmelt as the dominant mechanism to form clast UV31k-05 (Fig. 6). A further genetic link is provided by similar Nd–Hf isotope ratios in perovskite from the clast ($\epsilon_{\text{Nd}363}\sim +5$, $\epsilon_{\text{Hf}363}\sim +5.3$) and host kimberlite ($\sim +4.4$, $+5.0$, Table 2). ^{40}Ar – ^{39}Ar (362.7 ± 3.7 Ma, Table 3) and Rb–Sr (364.6 ± 4.1 Ma, Table 4) ages for phlogopite in UV31k-05 (Fig. 3B–D) are identical within error to the 367 ± 5 Ma SHRIMP U–Pb age of perovskite from the host kimberlite [18]. These phlogopite ages are the first independent high-precision confirmation of the perovskite U–Pb age of Kinny et al. [18]. We note that these ~ 363 Ma ages are older than a tentative age of 345 ± 5 Ma, estimated previously from U–Pb and Rb–Sr apparent isochron ages for the carbonate, chloride and silicate/oxide fractions of the kimberlite, and for a large halite crystal [24]. In light of our new phlogopite data and the analytical problems posed by halides (see above), we now attribute the ~ 20 Ma age offset largely to geological and laboratory-induced open system behaviour. This vindicates the approach taken in this study, i.e. the use of isotopic ratios in oxide and silicate minerals as proxies for halides and alkali carbonates.

The chemical and isotopic data for perovskite, phlogopite and olivine, together with textural (Figs. 2 and 3) and melt inclusion data (Fig. 4 and 13, 7) imply a close paragenetic relationship between alkali carbonates, chlorides and perovskite in both UV31k-05 and host kimberlite. In other words, chlorides and other Cl-bearing minerals (sodalite, djerfisherite) formed from the same parental melt as the perovskite. The initial Nd–Hf isotope ratios for halides and alkali carbonates should therefore be the same as, or be very similar to, those determined for the associated perovskite ($\epsilon_{\text{Nd}363}\sim +5$, $\epsilon_{\text{Hf}363}\sim +5.3$; Table 2). Likewise, initial $^{87}\text{Sr}/^{86}\text{Sr}$ ratios for perovskite, easily determined and highly reliable, should be a close proxy for the chloride and alkali carbonate minerals.

Three Sr isotope analyses of UV31k-05 perovskite by solution-mode average 0.70305 ± 7 (2σ , age-corrected; Table 2), similar to laser ablation MC-ICP MS results for 20 individual perovskite grains (average 0.70312 ± 5 , 2σ , age-corrected).

These $^{87}\text{Sr}/^{86}\text{Sr}$ ratios are lower than those for the host kimberlite (0.7043–0.7049, 36, 24, 22], although results for acid-leached kimberlite (0.7034–0.7037, 24) provide a closer match (Table 2). Such offsets between perovskite and host kimberlite were also noticed in other studies [e.g., 10, 33], and probably reflect minor disturbance of bulk rock Rb–Sr systems. In our samples, the elemental redistribution effects, associated with unstable chloride and alkali carbonate minerals, may be the main reason for these discrepancies. The perovskite-based $^{87}\text{Sr}/^{86}\text{Sr}$ is therefore considered as a more robust estimate for the kimberlite melt.

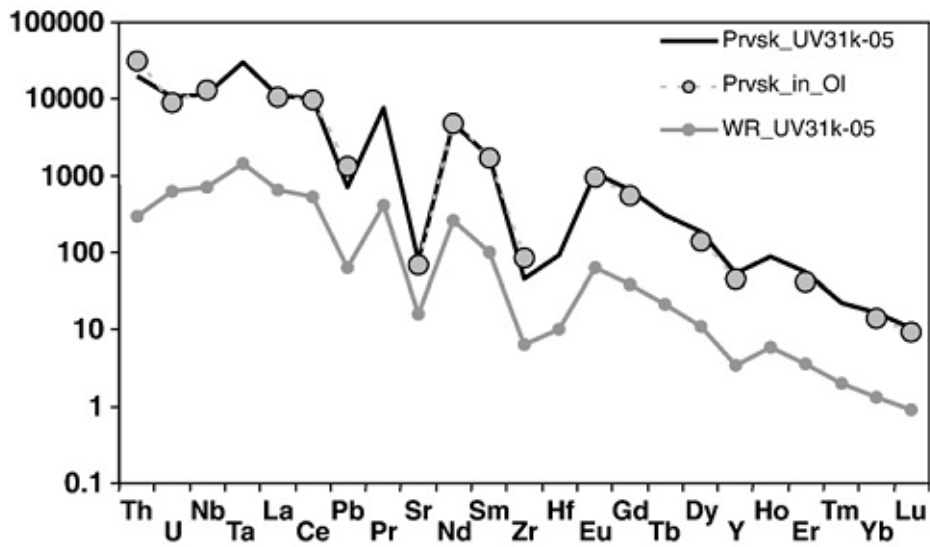


Fig. 6. Primitive mantle — normalised [53] trace element composition of clast sample UV31k-05 and average compositions (by in situ LA-ICPMS analysis of individual grains) of perovskite from clast and host kimberlite.

The measured ratio of ~ 0.7031 is similar to Sr isotope ratios reported from megacrysts in some (group-I) kimberlites [30] and lies at the unradiogenic end of the range for “archetypal” kimberlite bulk rock data [47, 30], including Siberian kimberlites [22]. The low $^{87}\text{Sr}/^{86}\text{Sr}$ and $\epsilon_{\text{Nd}}-\epsilon_{\text{Hf}}$ near +5 (Table 2) place the source of the parental magma at the edge of the global ‘MORB-OIB mantle array’ in both Sr–Nd and Nd–Hf space, within the field for modern HIMU ocean island basalts [11]. Material derived from old continental crust (high $^{87}\text{Sr}/^{86}\text{Sr}$, low $\epsilon_{\text{Nd}}-\epsilon_{\text{Hf}}$), if present, must be negligible, consistent with the lack of trace element evidence for such material (e.g., high Gd/Yb, no positive Pb anomaly, Fig. 6). By inference, the kimberlite melt shows no sign of crustal contamination, even at the time when perovskite and associated chlorides and alkali carbonates crystallised within clast UV31k-05. This in turn supports a mantle origin of such minerals in UV31k-05 and in the host kimberlite.

Similar results were obtained for clinopyroxene macrocryst UV9774. Initial Sr–Nd–Hf isotope ratios (0.7029, + 5.0, + 6.5, calculated at 363 Ma, Table 2)

Table 3

 $^{40}\text{Ar}/^{39}\text{Ar}$ furnace step-heating analytical results for phlogopite from Udachnaya-East clast UV31k-05.

Temp (°C)	Cum. % ^{39}Ar	^{40}Ar ($\times 10^{-13}$ mol)	^{39}Ar ($\times 10^{-14}$ mol)	^{38}Ar ($\times 10^{-16}$ mol)	^{37}Ar ($\times 10^{-16}$ mol)	^{36}Ar ($\times 10^{-16}$ mol)	Ca/K \pm	$\%^{40}\text{Ar}^{+}$	$^{40}\text{Ar}^{+}/^{39}\text{Ar} \pm$	Age (Ma)								
J-value =	0.013097	0.000036																
600	5.14	0.6760	0.0011	0.3148	0.0015	0.3768	0.0747	0.8320	0.1806	0.3317	0.0772	0.0463	0.0100	85.5	18.36	0.73	388.8	13.9
650	13.83	0.9279	0.0015	0.5319	0.0011	0.7194	0.0112	0.1228	0.0382	0.0939	0.0101	0.0040	0.0013	97.0	16.92	0.07	361.1	1.4
700	22.89	0.9755	0.0021	0.5555	0.0023	0.7726	0.0276	0.1573	0.1002	0.1490	0.0123	0.0050	0.0032	95.5	16.77	0.10	358.1	2.0
750	32.40	1.0807	0.0018	0.5820	0.0015	0.8993	0.0161	0.2573	0.1116	0.3223	0.0227	0.0077	0.0034	91.2	16.93	0.13	361.3	2.5
800	39.10	0.9503	0.0016	0.4106	0.0008	0.6980	0.0222	0.1652	0.0407	0.8074	0.0234	0.0070	0.0017	74.9	17.33	0.18	369.0	3.4
850	44.66	1.1127	0.0020	0.3407	0.0012	0.8067	0.0099	0.1018	0.0769	1.7412	0.0235	0.0052	0.0039	53.8	17.56	0.22	373.4	4.3
900	50.65	1.2744	0.0021	0.3664	0.0008	0.9679	0.0234	0.1423	0.0624	2.1907	0.0227	0.0068	0.0030	49.2	17.11	0.20	364.9	3.8
950	57.88	1.3722	0.0023	0.4431	0.0012	1.0362	0.0132	0.4366	0.1071	2.1637	0.0277	0.0172	0.0042	53.4	16.54	0.20	353.7	3.8
1000	65.82	1.2871	0.0022	0.4862	0.0006	0.9842	0.0173	0.6351	0.1140	1.5671	0.0537	0.0229	0.0041	64.0	16.95	0.33	361.6	6.4
1050	72.14	0.9748	0.0017	0.3870	0.0004	0.6555	0.0095	0.9762	0.0662	1.0492	0.0427	0.0441	0.0030	68.2	17.18	0.33	366.1	6.4
1100	79.68	1.0526	0.0019	0.4618	0.0011	0.8064	0.0159	4.1090	0.0455	0.9048	0.0190	0.1557	0.0018	74.6	17.01	0.13	362.9	2.6
1150	97.77	2.3103	0.0085	1.1085	0.0034	1.6790	0.0591	19.4273	0.3794	1.2808	0.0858	0.3067	0.0061	83.7	17.44	0.25	371.2	4.7
1250	99.99	0.7383	0.0013	0.1358	0.0006	0.5701	0.0134	3.9047	0.0623	1.7166	0.0203	0.5031	0.0084	31.3	17.04	0.46	363.4	8.9
1350	100.00	0.1757	0.0003	0.0005	0.0001	0.0004	0.0005	0.0193	0.0054	0.4863	0.0260	0.6297	0.2266	18.2	597.08	198.11	3927.5	530.7

Note: Irradiation of samples and flux monitor GAl550 biotite ([40]; age = 98.8 ± 0.5 Ma) was done in position 5c of the McMaster University reactor, Hamilton, Ontario, Canada. After cooling, a weighted aliquot of the phlogopite was loaded into a tin foil packet and step-heated in a tantalum resistance furnace. $^{40}\text{Ar}/^{39}\text{Ar}$ step-heating analyses were conducted on a VG3600 mass spectrometer, utilising a Daly detector. Mass discrimination values were monitored by analyses of purified air aliquots. Correction factors for interfering isotopes are: $(^{36}\text{Ar}/^{37}\text{Ar})\text{Ca} = 2.70 (\pm 0.04) \times 10^{-4}$; $(^{39}\text{Ar}/^{37}\text{Ar})\text{Ca} = 6.79 (\pm 0.05) \times 10^{-4}$; $(^{40}\text{Ar}/^{39}\text{Ar})\text{K} = 0.0005 \pm 0.0002$. Decay constants are those reported by [51]. Quoted errors are 2 σ and do not include uncertainty in J-value.

resemble those in UV31k-05 perovskite, suggesting either intrinsic isotopic similarities or equilibration of the macrocryst with the reactive kimberlitic melt. If the chlorides, alkali carbonates and other phases present within UV9774 do indeed represent melt inclusions (Fig. 5), as we infer, the unevolved mantle-like isotopic composition of the host clinopyroxene would support a mantle origin of this material.

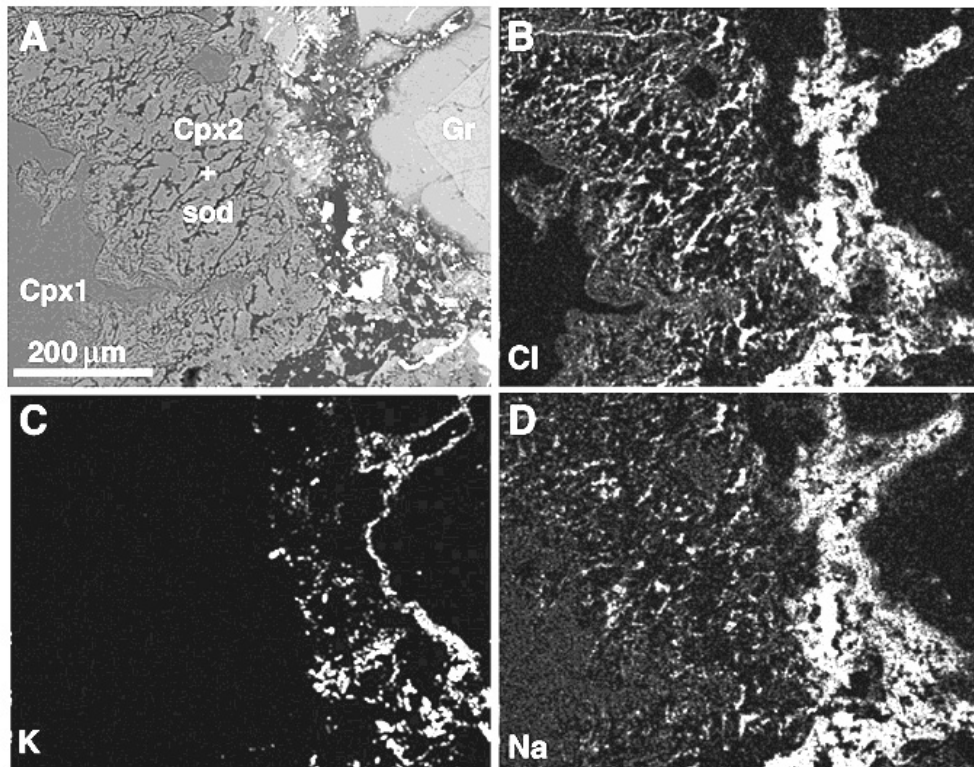


Fig. 7. Backscattered electron image (A) and X-ray element maps (B to D) showing "alteration" at the contact between omphacite (Cpx1) and garnet (Gr) in kimberlite-hosted eclogite xenolith

Further strong support for kimberlitic chlorine at mantle depths is provided by eclogite xenoliths from Udachnaya-East. While generally very fresh [50], these eclogite samples do show characteristic grain boundary alteration of primary omphacite and garnet, observed in many kimberlite-hosted eclogite suites. This includes "sieved" or "spongy" clinopyroxene depleted in Na and Al relative to original omphacite (Fig. 7), and multiphase "kelyphitic" rims around garnet.

Minerals present in this alteration (sodalite, calcite, phlogopite, halite, monticellite, apatite, spinel and different sulphates) also occur in the host kimberlite, with sodalite being the most important carrier of chlorine (Fig. 7). Grain boundary alteration is believed to be related to interaction of eclogite with Na–K–Ca–Cl–S-rich kimberlitic melt [26]. The presence and location of diamond within such "alteration" indicates that this interaction occurred at mantle depths, as noted by Spetsius and Taylor [50] on p. 129 "It is becoming increasingly evident that in eclogites, diamonds are NEVER in contact with primary garnet and/or omphacites.

Instead, they mostly occur along metasomatically induced alteration zones, sometimes in a linear fashion. Such zones would appear to be the avenues for permeation of the C–O–H–N–Smetasomatic fluids, as suggested by Haggerty (1986)”. We therefore suggest that a chloride component was present in protokimberlite melts, at least at the earliest recognisable stages of their derivation from and interaction with mantle rocks, and was possibly instrumental in the diamond formation [e.g., 54, 32].

Finally, carbonate–chloride-bearing melt inclusions within groundmass olivine [13] carry a neon isotope signature [52] similar to that found in deep mantle-derived magmas, thus providing another mantle link for the chloride component.

Table 4

Rb-Sr isotope results for phlogopite in clast UV31k-05.

	Rb (ppm)	Sr (ppm)	⁸⁷Rb/⁸⁶Sr	⁸⁷Sr/⁸⁶Sr	Age (Ma)
phl 2			15.33	0.78441	373.1
phl 3	570	95.61	17.40	0.79389	367.0
phl 4	337	63.16	15.55	0.78506	370.6
phl 5	590	104.6	16.44	0.78827	364.4
phl 6	888	128.8	20.13	0.80594	359.2
phl 7	656	98.6	19.43	0.80284	361.0
phl 8	506	75.0	19.73	0.80438	360.9
phl 9	437	66.2	19.29	0.80120	357.6

CONCLUDING REMARKS

Dry, chlorine-bearing alkali minerals in the Udachnaya-East kimberlite are products of crystallisation of the mantle-derived, uncontaminated melt. We suggest that essentially non-silicate compositions rich in alkalis, CO₂ and Cl may be a viable alternative to the currently favoured water-rich, high-Mg model primary melt. Entrainment of mantle silicates into such a melt en route to the surface, followed by gravitational accumulation of mantle olivine at the bottom of magma bodies after emplacement, would explain the observed properties of kimberlite magma/rock, notably enrichment in olivine in the hypabyssal kimberlite facies.

A “salty” carbonate composition of the kimberlite parental melt can account for trace element signatures consistent with low degrees of partial melting, low temperatures of crystallisation and the exceptional rheological properties that enable kimberlite magmas to rise with high ascent velocities, while carrying a large cargo of entrained xenoliths and crystals. Evidence for Cl and alkalis in the kimberlite melt is best preserved in unaltered rocks such as those from Udachnaya-East. Importantly, Cl- and Na-bearing minerals of the type reported here can be

found inside melt inclusions even in partly altered rocks, such as kimberlites from Canada and Greenland [17] and South Africa (our unpublished data).

The possible existence of chloride–carbonate liquids within the diamond stability field can be inferred from experiments in the model silicate system with addition of Na–Ca carbonate and K-chloride [41, 42]. These experiments also show that Cl-bearing carbonate–silicate and Si-bearing chloride–carbonate melts evolve towards Cl-rich carbonatitic liquids with decreasing temperature, providing a possible explanation for chlorine- and alkali-enriched microinclusions in some diamonds from Udachnaya-East [58] and other kimberlites in South Africa and Canada [12, 55, 20]. Brine inclusions in diamonds from various kimberlites, and the inferred role of chlorides in diamond nucleation and growth [54, 32] further illustrate the potential significance of mantle-derived “salty” fluids sampled by the kimberlite melt and fortuitously preserved at Udachnaya-East.

ACKNOWLEDGEMENTS

We are indebted to Victor Sharygin who collected and supplied sample UV31k-05 and mineral analyses for this study. We thank J. Woodhead, P. Robinson, S. Gilbert, K. McGoldrick, K. Gömann, and L. Danyushevsky for analysing the sample and providing help with microbeam analyses. The results and ideas were discussed with many participants of the 9th International Kimberlite Conference. In particular, we are grateful to A. Chakhmouradian, G. Yaxley, R. Mitchell, O. Navon, A. Sobolev, S. Kostrovitsky, S. Tappe, S. Matveev, M. Kopylova, D. Green, O. Safonov, L. Heaman, Ya. Fedortchouk and I. Veksler for advice, moral support and friendly criticism. Reviews by Michel Grègoire and an anonymous researcher, and editorial handling by Richard Carlson are greatly appreciated. The work was supported by an Australian Research Council Research and Professorial Fellowships and Discovery Grant to V. Kamenetsky and the Russian Foundation for Basic Research (project 07-05-00072) to A. Golovin.

REFERENCES

1. **Blichert-Toft, J., Albarede, F.**, 1997. The Lu–Hf isotope geochemistry of chondrites and the evolution of the mantle–crust system. *Earth Planet. Sci. Lett.* 148, 243–258.
2. **Canil, D., Bellis, A.J.**, 2008. Phase equilibria in a volatile-free kimberlite at 0.1 MPa and the search for primary kimberlite magma. *Lithos* 105, 111–117.
3. **Chakhmouradian, A.R., Mitchell, R.H.**, 2000. Occurrence, alteration patterns and compositional variation of perovskite in kimberlites. *Can. Mineral.* 38, 975–994.
4. **Dawson, J.B., Hawthorne, J.B.**, 1973. Magmatic sedimentation and carbonatitic differentiation in kimberlite sills at Benfontein, South Africa. *J. Geol. Soc. London* 129, 61–85.
5. **Edgar, A.D., Arima, M., Baldwin, D.K., Bell, D.R., Shee, S.R., Skinner, E.M.W., Walker, E.C.**, 1988. High-pressure–high-temperature melting experiments on a SiO₂-poor aphanitic kimberlite from the Wesselton Mine, Kimberley, South Africa. *Am. Mineral.* 73, 524–533.

6. **Eggler, D.H.**, 1989. Kimberlites: how do they form? In: Ross, J., et al. (Ed.), Kimberlites and Related Rocks: Their Composition, Occurrence, Origin and Emplacement. In Blackwell Sci. Publ., Sydney, pp. 489–504.
7. **Golovin, A.V., Sharygin, V.V., Pokhilenko, N.P.**, 2007. Melt inclusions in olivine phenocrysts in unaltered kimberlites from the Udachnaya-East pipe, Yakutia: some aspects of kimberlite magma evolution during late crystallization stages. *Petrology* 15, 168–183.
8. **Grishina, S.N., Polozov, A.G., Mazurov, M.P., Titov, A.T.** 2008. Origin of chloride Udachnaya-East kimberlite pipe, Siberia: evidence from fluid and saline melt inclusions. th Inter. Kimberlite Conf., Frankfurt, Germany, Extended Abstract 9IKC-A-00128.
9. **Harris, M., le Roex, A., Class, C.**, 2004. Geochemistry of the Uintjiesberg kimberlite, South Africa: petrogenesis of an off-craton, group I, kimberlite. *Lithos* 74, 149–165.
10. **Heaman, L.M.**, 1989. The nature of the subcontinental mantle from Sr–Nd–Pb isotopic studies on kimberlitic perovskite. *Earth Planet. Sci. Lett.* 92, 323–334.
11. **Hofmann, A.W.**, 2003. Sampling mantle heterogeneity through oceanic basalts: isotopes and trace elements. In: Holland, H., Turekian, K.K. (Eds.), *Treatise on Geochemistry*. In Elsevier-Pergamon, Oxford, pp. 61–101.
12. **Izraeli, E.S., Harris, J.W., Navon, O.**, 2001. Brine inclusions in diamonds: a new upper mantle fluid. *Earth Planet. Sci. Lett.* 187, 323–332.
13. **Kamenetsky, M.B., Sobolev, A.V., Kamenetsky, V.S., Maas, R., Danyushevsky, L.V., Thomas, R., Sobolev, N.V., Pokhilenko, N.P.**, 2004. Kimberlite melts rich in alkali chlorides and carbonates: a potent metasomatic agent in the mantle. *Geology* 32, 845–848.
14. **Kamenetsky, V.S., Kamenetsky, M.B., Sharygin, V.V., Faure, K., Golovin, A.V.**, 2007a. Chloride and carbonate immiscible liquids at the closure of the kimberlite magma evolution (Udachnaya-East kimberlite, Siberia). *Chem. Geol.* 237, 384–400.
15. **Kamenetsky, V.S., Kamenetsky, M.B., Sharygin, V.V., Golovin, A.V.**, 2007b. Carbonate–chloride enrichment in fresh kimberlites of the Udachnaya-East pipe, Siberia: a clue to physical properties of kimberlite magmas? *Geophys. Res. Lett.* 34, L09316. [doi:10.1029/2007GL029389](https://doi.org/10.1029/2007GL029389).
16. **Kamenetsky, V.S., Kamenetsky, M.B., Sobolev, A.V., Golovin, A.V., Demouchy, S., Faure, K., Sharygin, V.V., Kuzmin, D.V.**, 2008. Olivine in the Udachnaya-East kimberlite (Yakutia, Russia): types, compositions and origins. *J. Petrol.* 49, 823–839.
17. **Kamenetsky, V.S., Kamenetsky, M.B., Weiss, Y., Navon, O., Nielsen, T.F.D., Mernagh, T.P.**, 2009. How unique is the Udachnaya-East kimberlite? Comparison with kimberlites from the Slave Craton (Canada) and SW Greenland. *Lithos*. [doi:10.1016/j.lithos.2009.03.032](https://doi.org/10.1016/j.lithos.2009.03.032).
18. **Kinny, P.D., Griffin, W.L., Heaman, L.M., Brakhfogel, F.F., Spetsius, Z.V.**, 1997. SHRIMP U–Pb ages of perovskite from Yakutian kimberlites. *Russ. Geol. Geophys.* 38, 91–99.
19. **Kjarsgaard, B.A., Pearson, D.G., Tappe, S., Nowell, G.M., Dowall, D.P.**, 2009. Geochemistry of hypabyssal kimberlites from Lac de Gras, Canada: comparisons to a global database with applications to the primary magma problem. *Lithos*.
20. **Klein-BenDavid, O., Izraeli, E.S., Hauri, E., Navon, O.**, 2007. Fluid inclusions in diamonds from the Diavik mine, Canada and the evolution of diamond-forming fluids. *Geochim. Cosmochim. Acta* 71, 723–744.
21. **Kopylova, M.G., Matveev, S., Raudsepp, M.**, 2007. Searching for parental kimberlite melt. *Geochim. Cosmochim. Acta* 71, 3616–3629.
22. **Kostrovitsky, S.I., Morikiyo, T., Serov, I.V., Yakovlev, D.A., Amirzhanov, A.A.**, 2007. Isotope-geochemical systematics of kimberlites and related rocks from the Siberian Platform. *Russ. Geol. Geophys.* 48, 272–290.
23. **le Roex, A.P., Bell, D.R., Davis, P.**, 2003. Petrogenesis of group I kimberlites from Kimberley, South Africa: evidence from bulk-rock geochemistry. *J. Petrol.* 44, 2261–2286.

24. **Maas, R., Kamenetsky, M.B., Sobolev, A.V., Kamenetsky, V.S., Sobolev, N.V.,** 2005. Sr, Nd, and Pb isotope evidence for a mantle origin of alkali chlorides and carbonates in the Udachnaya kimberlite, Siberia. *Geology* 33, 549–552.
25. **Macdonald, R., Kjarsgaard, B.A., Skilling, I.P., Davies, G.R., Hamilton, D.I., Black, S.,** 1993. Liquid immiscibility between trachyte and carbonate in ash-flow tuffs from Kenya. *Contrib. Mineral. Petrol.* 114, 276–287.
26. **Misra, K.C., Anand, M., Taylor, L.A., Sobolev, N.V.,** 2004. Multi-stage metasomatism of diamondiferous eclogite xenoliths from the Udachnaya kimberlite pipe, Yakutia, Siberia. *Contrib. Mineral. Petrol.* 146, 696–714.
27. **Mitchell, R.H.,** 1986. *Kimberlites: Mineralogy, Geochemistry and Petrology.* Plenum Press, New York.
28. **Mitchell, R.H.,** 2008. Petrology of hypabyssal kimberlites: relevance to primary magma compositions. *J. Volcanol. Geotherm. Res.* 174, 1–8.
29. **Münker, C., Weyer, S., Scherer, E., Mezger, K.,** 2001. Separation of high field strength elements (Nb, Ta, Zr, Hf) and Lu from rock samples for MC-ICPMS measurements. *Geochem. Geophys. Geosyst.* 2. doi:10.1029/2001GC000183.
30. **Nowell, G.M., Pearson, D.G., Bell, D.R., Carlson, R.W., Smith, C.B., Kempton, P.D., Noble, S.R.,** 2004. Hf isotope systematics of kimberlites and their megacrysts: new constraints on their source regions. *J. Petrol.* 45, 1583–1612.
31. **Odin, G.S., et al.,** 1982. Interlaboratory standards for dating purposes. In: *Odin, G.S. (Ed.), Numerical Dating in Stratigraphy, Part I.* J. Wiley & Sons, New York, pp. 122–150.
32. **Palyanov, Y.N., Shatsky, V.S., Sobolev, N.V., Sokol, A.G.,** 2007. The role of mantle ultrapotassic fluids in diamond formation. *Proc. Natl. Acad. Sci. U.S.A.* 104, 9122–9127.
33. **Paton, C., Hergt, J.M., Phillips, D., Woodhead, J.D., Shee, S.R.,** 2007a. New insights into the genesis of Indian kimberlites from the Dharwar Craton via in situ Sr isotope analysis of groundmass perovskite. *Geology* 35, 1011–1014.
34. **Paton, C., Woodhead, J.D., Hergt, J.M., Phillips, D., Shee, S.,** 2007b. Strontium isotope analysis of kimberlitic groundmass perovskite via LA-MC-ICP-MS. *Geostand. Geoanal. Res.* 31, 321–330.
35. **Pavlov, D.I., Ilupin, I.P.,** 1973. Halite in Yakutian kimberlite, its relation to serpentine and the source of its parent solutions. *Dokl. Acad. Sci. USSR* 213, 178–180.
36. **Pearson, D.G., Shirey, S.B., Carlson, R.W., Boyd, F.R., Pokhilenko, N.P., Shimizu, N.,** 1995. Re–Os, Sm–Nd, and Rb–Sr Isotope evidence for thick Archaean lithospheric mantle beneath the Siberian craton modified by multistage metasomatism. *Geochim. Cosmochim. Acta* 59, 959–977.
37. **Phillips, G., Wilson, C.J.L., Phillips, D., Szczepanski, S.K.,** 2007. Thermochronological ($^{40}\text{Ar}/^{39}\text{Ar}$) evidence of Early Palaeozoic basin inversion within the southern Prince Charles Mountains, East Antarctica: implications for East Gondwana. *J. Geol. Soc. London* 164, 771–784.
38. **Polozov, A.G., Sukhov, S.S., Gornova, M.A., Grishina, S.N.** 2008. Salts from Udachnaya-East kimberlite pipe (Yakutia, Russia): occurrences and mineral composition. 9th Inter. Kimberlite Conf., Frankfurt, Germany, Extended Abstract 9IKC-A-00247.
39. **Price, S.E., Russell, J.K., Kopylova, M.G.,** 2000. Primitive magma from the Jericho Pipe, NWT, Canada: constraints on primary kimberlite melt chemistry. *J. Petrol.* 41, 789–808.
40. **Renne, P.R., Swisher, C.C., Deino, A.L., Karner, D.B., Owens, T.L., DePaolo, D.J.,** 1998. Intercalibration of standards, absolute ages and uncertainties in $^{40}\text{Ar}/^{39}\text{Ar}$ dating. *Chem. Geol.* 145, 117–152.
41. **Safonov, O.G., Perchuk, L.L., Litvin, Y.A.,** 2007. Melting relations in the chloride–carbonate–silicate systems at high-pressure and the model for formation of alkalic diamond-forming liquids in the upper mantle. *Earth Planet. Sci. Lett.* 253, 112–128.

42. **Safonov, O.G., Perchuk, L.L., Yapaskurt, V.O., Litvin, Y.A.,** 2009. Immiscibility of carbonate–silicate and chloride–carbonatemelts in the kimberlite–CaCO₃–Na₂CO₃–KCl system at 4.8 GPa. *Dokl. Earth Sci.* 424, 142–146.
43. **Sharp, Z.D., Barnes, J.D., Brearley, A.J., Fischer, T., Chaussidon, M., Kamenetsky, V.S.,** 2007. Chlorine isotope homogeneity of the mantle, crust and carbonaceous chondrites. *Nature* 446, 1062–1065.
44. **Sharygin, V.V., Golovin, A.V., Pokhilenko, N.P., Kamenetsky, V.S.,** 2007. Djerfisherite in the Udachnaya-East pipe kimberlites (Sakha-Yakutia, Russia): paragenesis, composition and origin. *Eur. J. Mineral.* 19, 51–63.
45. **Sharygin, V.V., Kamenetsky, V.S., Kamenetsky, M.B.,** 2008. Potassium sulfides in kimberlite-hosted chloride–“nyerereite” and chloride clasts of Udachnaya-East pipe, Yakutia, Russia. *Can. Mineral.* 46, 1079–1095.
46. **Skinner, E.M.W.,** 1989. Contrasting Group I and Group II kimberlite petrology: towards a genetic model for kimberlites. In: Ross, J., et al. (Ed.), *Kimberlites and Related Rocks: Their Composition, Occurrence, Origin and Emplacement*. Blackwell Sci. Publ., Sydney, pp. 528–544.
47. **Smith, C.B.,** 1983. Pb, Sr and Nd isotopic evidence for sources of southern African Cretaceous kimberlites. *Nature* 304, 51–54.
48. **Sparks, R.S.J., Baker, L., Brown, R.L., Field, M., Schumacher, J., Stripp, G., Walters, A.,** 2006. Dynamical constraints on kimberlite volcanism. *J. Volcanol. Geotherm. Res.* 155, 18–48.
49. **Spell, T.L., McDougall, I.,** 2003. Characterization and calibration of ⁴⁰Ar/³⁹Ar dating standards. *Chem. Geol.* 198, 189–211.
50. **Spetsius, Z.V., Taylor, L.A.,** 2008. *Diamonds of Yakutia: Petrographic Evidence for Their Origin*. Tranquility Base Press, Tennessee, U.S.A.
51. **Steiger, R.H., Jager, E.,** 1977. Subcommittee on geochronology: convention on use of decay constants in geochronology and cosmochronology. *Earth Planet. Sci. Lett.* 36, 359–362.
52. **Sumino, H., Kaneoka, I., Matsufuji, K., Sobolev, A.V.,** 2006. Deep mantle origin of kimberlite magmas revealed by neon isotopes. *Geophys. Res. Lett.* 33, L16318. doi:10.1029/2006GL027144.
53. **Sun, S.-S., McDonough, W.F.,** 1989. Chemical and isotopic systematics of oceanic basalts: implications for mantle composition and processes. In: Saunders, A.D., Norry, M.J. (Eds.), *Magmatism in the Ocean Basins: Geol. Soc. Spec. Publ.*, London, pp. 313–345.
54. **Tomlinson, E., Jones, A., Milledge, J.,** 2004. High-pressure experimental growth of diamond using C–K₂CO₃–KCl as an analogue for Cl-bearing carbonate fluid. *Lithos* 77, 287–294.
55. **Tomlinson, E.L., Jones, A.P., Harris, J.W.,** 2006. Co-existing fluid and silicate inclusions in mantle diamond. *Earth Planet. Sci. Lett.* 250, 581–595.
56. **Vervoort, J.D., Patchett, P.J., Soderlund, U., Baker, M.,** 2004. Isotopic composition of Yb and the determination of Lu concentrations and Lu/Hf ratios by isotope dilution using MC-ICPMS. *Geochem. Geophys. Geosyst.* 5. doi:10.1029/2004GC000721.
57. **Zaitsev, A.N., Keller, J.,** 2006. Mineralogical and chemical transformation of Oldoinyo Lengai natrocarbonatites, Tanzania. *Lithos* 91, 191–207.
58. **Zedgenizov, D.A., Ragozin, A.L.,** 2007. Chloride–carbonate fluid in diamonds from the eclogite xenolith. *Dokl. Earth Sci.* 415, 961–964.

Compositions of magmas and carbonate-silicate liquid immiscibility in the Vulture alkaline igneous complex, Italy

Solovova I.P.¹, Girnis A.V.¹, Kogarko L.N.², Kononkova N.N.²

¹*Institute of Geology of Ore Deposits, Petrography, Mineralogy, and Geochemistry, Russian Academy of Sciences, 35 Staromonetny, Moscow, 119017 Russia*

²*Vernadsky Institute of Geochemistry and Analytical Chemistry, Russian Academy of Sciences, 19 ul. Kosygina, Moscow, 117975 Russia*

ABSTRACT

Vulture Volcano is build up of a variety of mafic-ultramafic alkaline rocks and carbonatites. This paper presents a study of melt and fluid inclusions in minerals of Vulture basanite. The rock contains phenocrysts of olivine, clinopyroxene, apatite, and hauyne. We distinguished three generations of clinopyroxene differing in composition and morphology. All the phenocrysts bear primary and secondary melt and fluid inclusions, which recorded successive stages of melt evolution. The most primitive melts were found in the most magnesian olivine and the earliest clinopyroxene phenocrysts. The melts are close to primary mantle liquids and are rich in Ca, Mg and incompatible and volatile elements. Thermometric experiments with the melt inclusions suggested that melt crystallization began at temperatures higher than 1200°C and pressures of more than 5 kbar. Combined silicate-carbonate melt inclusions were found in apatite phenocrysts. They are indicative of carbonate-silicate liquid immiscibility, which occurred during melt differentiation. Large hydrous secondary melt inclusions were found in olivine and clinopyroxene. The inclusions in the phenocrysts recorded an open-system magma evolution in a magma chamber and a conduit including 2 crystallization, degassing, water input, oxidation, and liquid immiscibility processes.

INTRODUCTION

Carbonatites are usually considered as magmatic members of alkaline associations [6]. Several mechanisms of their genesis have been proposed including (i) partial melting of carbonated mantle; (ii) liquid immiscibility in carbonate-silicate magmatic systems; and (iii) extensive fractional crystallization and formation of volatile-rich residual liquids.

The possibility of carbonatite magma derivation during partial melting of carbonated peridotite has been supported by geochemical studies of mantle nodules and primary mantle carbonates [1, 23, 14], experimental data [29, 4, 10], and investigations of some carbonatitic complexes [3].

Experimental evidence suggests that liquid immiscibility may play a leading role in the genesis of carbonatites [11, 12, 13]. A wide field of two immiscible liquids exists in the system (SiO₂+Al₂O₃+TiO₂) - (MgO+FeO+CaO) - (Na₂O+K₂O) - CO₂. The immiscibility gap expands with increasing pressure and alkali content and decreasing magnesium concentration. Based on these data it was concluded that alkali-rich residual magmas may intersect the boundary of the silicate-

carbonate liquid immiscibility field under crustal conditions. Lee and Wyllie [17, 18] pointed out a number of limitations on this hypothesis and argued that there is no single process responsible for the formation of all carbonatites. According to Lee and Wyllie, fractional crystallization of carbonate-bearing alkaline magmas may be very important in the genesis of carbonatites, in agreement with the ideas proposed by Twyman and Gittins [28]. Kjarsgaard and Peterson [13] supposed that the alkali-poor carbonatites of Shombole Volcano (E. Africa) were the result of silicate-carbonate immiscibility.

Since the genesis of carbonatites still remains controversial, geological and mineralogical observations on the relationships between carbonate and silicate materials in magmatic rocks are very important. This paper presents data on the petrography, mineral composition, and carbonate-bearing microinclusions from Vulture Volcano, Italy.

GEOLOGICAL BACKGROUND

Vulture Volcano is situated at the eastern boundary of the Roman magmatic province. Its volcanic products are dominated by Na-K-rich undersaturated rocks, from basanite to trachyphonolite. Vulture is the only complex in this province where sodalite-group minerals occur as major phases of volcanic rocks [19].

The genesis of the primary mantle melts of Vulture Volcano was attributed to a subduction zone [9, 22] or continental rifting [16]. Cavarretta et. al. [7] proposed several magma sources for the Vulture volcanics. Some authors suggested a significant role of crustal assimilation [9]. However, recent Sr isotopic data [5] did not support this view and indicated a mantle origin for the volatile-rich Vulture magmas.

The volcanic activity of Vulture occurred between 0.8 and 0.42 Ma [15, 8, 9] and produced pyroclastic and lava flows and dikes of basanite, tephrite, foyadite, phonolite, and melilite-bearing rocks. In addition to silicate rocks, intrusive carbonatites (sövites) were found in the Monticcio Lake area [27, 26, 24]. The carbonatites were interpreted as products of crystallization of ultramafic carbonate liquid cognate with the silicate alkaline magmas of Mt. Vulture [24]. An alternative model implies carbonatite formation through interaction of alkaline magmas with sedimentary carbonates [22].

Direct evidence for the occurrence of liquid immiscibility can be obtained from a study of inclusions in minerals. The coexistence of silicate and carbonate liquids in melt inclusions was directly observed in a number of alkaline and carbonatite complexes [25, 20, 2, 21].

Samples of Vulture volcanics were collected during the Eurocarb-2002 workshop and field excursion. Melt and fluid inclusions were studied in minerals of olivine basanite from the Monticcio Lake area.

Table 1.

Chemical compositions of groundmass minerals and phenocrysts, wt.%

	Groundmass								Phenocrysts		
	Cpx	Cpx	Phi	Pl	Anor	Ab	Ne	Mt	Ol		
SiO ₂	43.39	49.97	38.97	59.99	62.74	63.23	45.00	0.75	39.90		
TiO ₂	1.63	0.95	4.00	0.11	0.10	0.09	0.01	8.05	0.00		
Al ₂ O ₃	13.41	4.85	13.11	23.59	20.64	23.71	33.74	4.08	0.00		
FeO	8.81	4.82	3.10	0.44	0.46	0.37	0.61	78.27	15.65		
MgO	10.18	14.86	19.95	0.00	0.01	0.00	0.01	2.22	43.89		
MnO	0.20	0.12	0.33	0.01	0.05	0.09	0.01	1.37	0.46		
CaO	22.87	24.55	0.16	4.72	2.08	0.32	2.28	0.21	0.42		
Na ₂ O	0.47	0.28	0.43	5.92	4.08	9.47	15.13	n.d.	0.00		
K ₂ O	0.01	0.02	9.50	2.96	3.94	0.61	4.63	n.d.	0.00		
BaO	0.66	0.00	0.00	0.00	0.00	0.00	0.00	n.d.	0.66		
SrO	0.00	100	0.00	0.00	100	0.00	0.00	n.d.	0.00		
P ₂ O ₅	n.d.	n.d.	n.d.	n.d.	n.d.	n.d.	n.d.	n.d.	n.d.		
Cl	6.00	6.00	6.00	6.00	0.00	6.00	6.00	n.d.	6.00		
F	n.d.	n.d.	n.d.	n.d.	n.d.	n.d.	n.d.	n.d.	n.d.		
SO ₃	0.00	0.00	0.00	0.00	0.00	0.00	0.00	n.d.	0.00		
Total	100.97	100.32	94.54	97.63	99.08	99.89	101.42	95.16*	100.31		
	Ol	Ol	Ol	Cpx 1	Cpx 1	Cox 1	Cpx 1	Cpx 2	Cpx 2	Cpx 2	
SiO ₂	39.16	41.80	42.67	51.12	49.00	46.87	51.40	45.42	45.36	47.24	
TiO ₂	0.00	0.00	0.00	0.89	1.36	1.62	0.64	1.96	1.95	1.23	
Al ₂ O ₃	0.00	0.00	0.00	5.89	7.35	7.78	3.61	9.41	9.41	7.38	
FeO	10.22	8.26	8.58	5.38	6.41	6.75	4.03	12.52	14.28	9.34	
MgO	49.00	49.70	49.67	15.04	14.41	13.70	15.97	8.73	8.00	12.51	
MnO	0.22	0.13	0.16	0.04	0.09	0.12	0.00	0.51	0.63	0.28	
CaO	0.34	0.40	0.26	21.87	21.68	22.91	23.28	19.42	20.20	21.62	
Na ₂ O	0.00	0.00	0.00	0.40	0.41	0.33	0.26	0.85	0.93	0.53	
K ₂ O	0.00	0.00	0.00	0.00	0.00	0.00	0.00	0.00	0.00	0.00	
BaO	0.00	0.00	0.00	0.04	0.01	0.00	0.09	0.08	0.09	0.05	
SrO	0.00	0.00	0.00	0.25	0.06	0.00	0.13	0.07	0.14	1.36	
P ₂ O ₅	n.d.	n.d.	n.d.	n.d.	n.d.	n.d.	n.d.	n.d.	n.d.	n.d.	
Cl	6.00	0.00	6.00	6.00	0.00	0.00	0.00	6.00	0.00	6.00	
F	n.d.	n.d.	n.d.	n.d.	n.d.	n.d.	n.d.	n.d.	n.d.	n.d.	
SO ₃	0.00	0.00	0.00	0.00	0.00	0.00	0.00	0.00	0.00	0.00	
Total	93.94	100.34	101.34	100.92	100.73	100.13	99.41	93.97	100.99	100.53	
	Cox 2	Cpx3	Cox 3	Cox 3	Ap	Ap	Ap	Ha	Ha	Ha	
SiO ₂	46.61	47.41	49.49	45.64	1.15	1.15	1.80	35.89	34.32	33.82	
TiO ₂	1.72	1.29	1.02	1.82	n.d.	n.d.	n.d.	0.00	0.04	0.04	
Al ₂ O ₃	7.89	6.58	5.16	7.43	n.d.	n.d.	n.d.	29.32	29.1;8	29.97	
FeO	6.96	6.33	4.57	7.33	1.36	0.75	0.30	2.80	0.38	1.08	
MgO	12.81	13.53	14.35	13.04	n.d.	n.d.	n.d.	0.07	0.01	0.01	
MnO	0.00	0.08	0.05	0.06	n.d.	n.d.	n.d.	100	0.01	0.02	
CaO	23.61	24.43	24.50	22.84	52.89	52.22	53.70	6.23	10.32	7.62	
Na ₂ O	0.33	0.35	0.26	0.31	n.d.	n.d.	n.d.	6.93	8.96	3.47	
K ₂ O	0.00	0.00	0.00	0.00	n.d.	n.d.	n.d.	3.08	1.04	3.71	
BaO	0.12	0.00	0.00	0.00	0.09	0.14	0.00	0.00	0.00	0.00	
SrO	0.06	0.00	0.00	117	0.27	0.44	0.47	0.16	0.00	0.00	
P ₂ O ₅	n.d.	n.d.	n.d.	n.d.	37.91	38.38	38.68	n.d.	n.d.	n.d.	
Cl	6.00	0.00	6.00	6.00	0.41	0.31	0.40	1.31	6.00	6.00	
F	n.d.	n.d.	n.d.	n.d.	4.11	3.93	2.50	n.d.	n.d.	n.d.	
SO ₃	0.00	0.00	0.00	0.00	n.d.	n.d.	n.d.	12.00	9.58	10.19	
Total	100.16	100.00	99.88	93.64	98.19	97.32	97.85	97.73	94.33	94.91	

Note. n. d. - not determined. Mineral symbols: Ab - albite, Ap - apatite, Anor - anorthoclase, Cpx - clinopyroxene (with phenocryst generation), Ha - hauyne, Mt - titanomagnetite, Ne - nepheline, Ol - olivine, Phl - phlogopite, Pl - plagioclase. *Including 0.21 wt % Cr₂O₃.

METHODS

Inclusions were studied in double-polished thin sections, 0.3 mm thick. Thermometric experiments were performed in small electric furnaces with Pt-Rh heaters (up to 1500°C) and graphite containers to prevent oxidation, and a Linkam microscopic heating stage. Temperature was calibrated against the melting point of gold (1063°C). Heating rate varied from 5 to 80°C/min, and samples were held for 10 to 60 min (usually, 15 min) at desired temperatures. Fluid inclusions were explored on a Linkam microscopic stage cooled with liquid nitrogen. This stage was calibrated using synthetic inclusions of CO₂ and aqueous NaCl solutions of known concentrations. Cooling and heating rates varied from 0.5 to 50°C/min.

The compositions of minerals and glasses were determined on a Cameca MS-46 electron microprobe with four spectrometers at the Vernadsky Institute of Geochemistry and Analytical Chemistry, Russian Academy of Sciences. The measurement conditions were as follows: an accelerating voltage of 15 kV, a beam current of 20 nA, and a counting time from 10 to 40 sec. Minerals were analyzed with a focused beam and glasses were scanned over an area of 12 * 12 μm. Sodium was analyzed first in order to minimize its migration. The concentrations of oxides were calculated using the ZAF procedure.

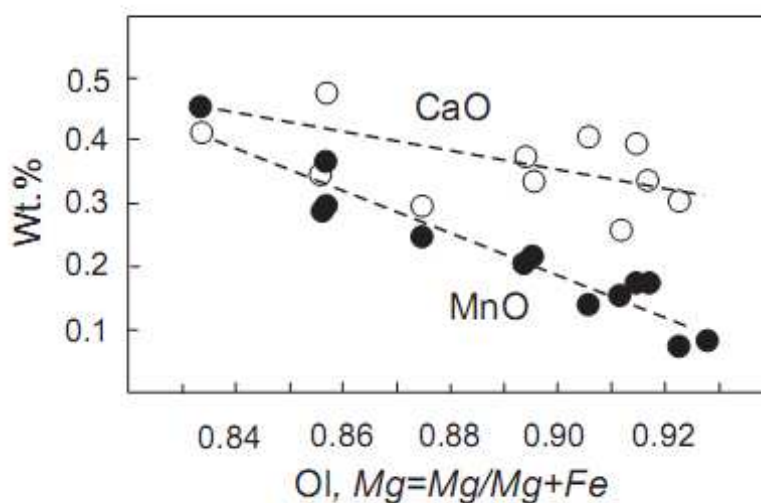


Fig. 1. Correlations of CaO and MnO concentrations with Mg/(Mg+Fe) for olivine phenocrysts.

MINERALOGY AND PETROGRAPHY

The olivine basanite sample studied is a dark gray rock without any visible secondary alteration. Its phenocryst assemblage is dominated by olivine and clinopyroxene. The holocrystalline groundmass is composed of clinopyroxene, plagioclase (An₅₈ to An₁₀, some crystals with up to 2 wt % BaO and SrO), phlogopite, nepheline, alkali feldspars, and Ti-magnetite (Table 1). The mineralogy of Vulture rocks was reported in detail by Melluso et al. [19] and Beccaluva et al. [5]. We only briefly describe here the phenocrysts that host melt and fluid

inclusions and provide selected analyses of groundmass minerals important for further discussion.

Olivine

Olivine phenocrysts are strongly fractured and some crystals show smooth rounded outlines. Most olivine crystals are up to 0.6 mm in size. The composition of olivine varies from $Fe_{0.83}$ to $Fe_{0.91}$ with up to 0.48 wt % CaO (Table 1). The concentrations of CaO and MnO correlate negatively with $mg = Mg/(Mg+Fe)$ (Fig. 1). In addition, there are very large crystals (up to 5-6 mm) of $Fe_{0.92-0.93}$ with 0.20-0.35 wt % CaO. These crystals are devoid of primary inclusions and are often angular. Most likely, they are xenocrysts.

Clinopyroxene

Clinopyroxene is the most common phenocryst mineral occurring in three generations differing in morphology and composition. Clinopyroxene 1 forms large (2-6 mm) strongly fractured homogeneous crystals, colorless or light yellow without pleochroism. Its narrow (no wider than 100 μm) colorless or light green rim zones are stuffed by small crystalline inclusions of fresh hauyne and apatite no larger than 10 μm in size.

Clinopyroxene 2 forms phenocrysts up to 1 mm in size pleochroic from dark green to amber yellow. Some grains are strongly resorbed. Crystals of clinopyroxene 2 are mantled by finely banded zones of colorless clinopyroxene 3.

The compositions of all clinopyroxene phenocrysts (Table 1) form a single trend in variation diagrams (Fig. 2). However the distinguished clinopyroxene types fall within different segments of this trend. Clinopyroxenes 1 and 3 form a compact cluster at high MgO and low Al_2O_3 , Na_2O and MnO (Fig. 2). The compositions of clinopyroxene 2 are lower in MgO and much richer in FeO, Al_2O_3 , Na_2O , and MnO. The central zones of dark green clinopyroxene 2 are characterized by the maximum concentrations of FeO, Na_2O and Al_2O_3 , whereas colorless clinopyroxene 3 contains up to 14.3 wt % MgO, which is similar to clinopyroxene 1 (Fig. 3).

The mg values of groundmass clinopyroxene vary from 0.85 to 0.67, and its TiO_2 content is no higher than 1.8 wt %.

Hauyne

Large (up to 0.5 mm) hauyne grains are surrounded by opaque rims (Fig. 4a). They are often strongly altered and depleted in CaO and Na_2O (Table 1).

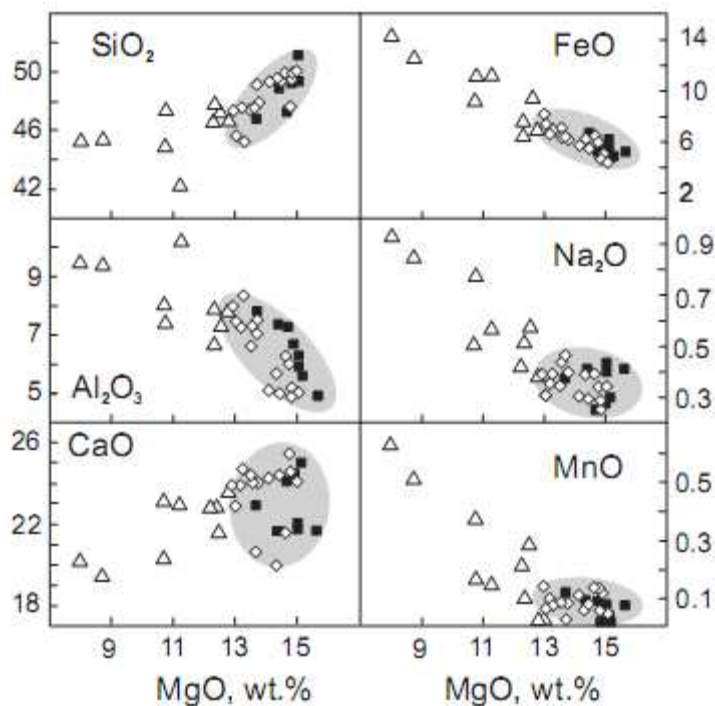


Fig. 2. Variations of major element contents as functions of MgO in clinopyroxene phenocrysts. Filled squares – clinopyroxene 1; unfilled diamonds – clinopyroxene 2; and triangles – clinopyroxene 3. The shaded field show outlines the compositions of clinopyroxene 1 and 3.

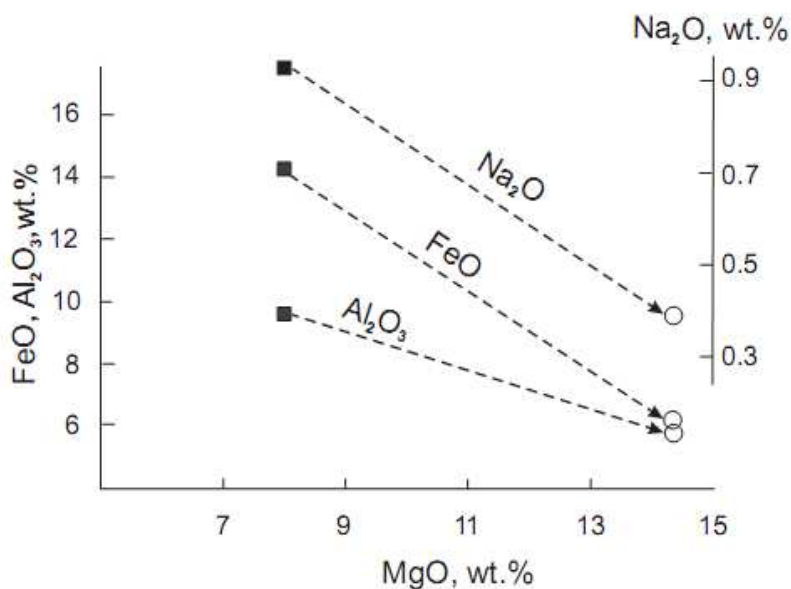


Fig. 3. Variations in FeO, Al₂O₃, and Na₂O concentrations as functions of MgO for clinopyroxene 2 (squares) and clinopyroxene 3 (circles) in three phenocrysts.

4.4. Apatite

Anhedral F-apatite phenocrysts are up to 700 μm in size (Table 1). They contain numerous tiny (less than 1 μm) tubular secondary inclusions with a rough optic relief (low-density fluid). There are also elongated inclusions of salt phases, occasionally with aqueous solution, up to 20 μm in size. These inclusions are

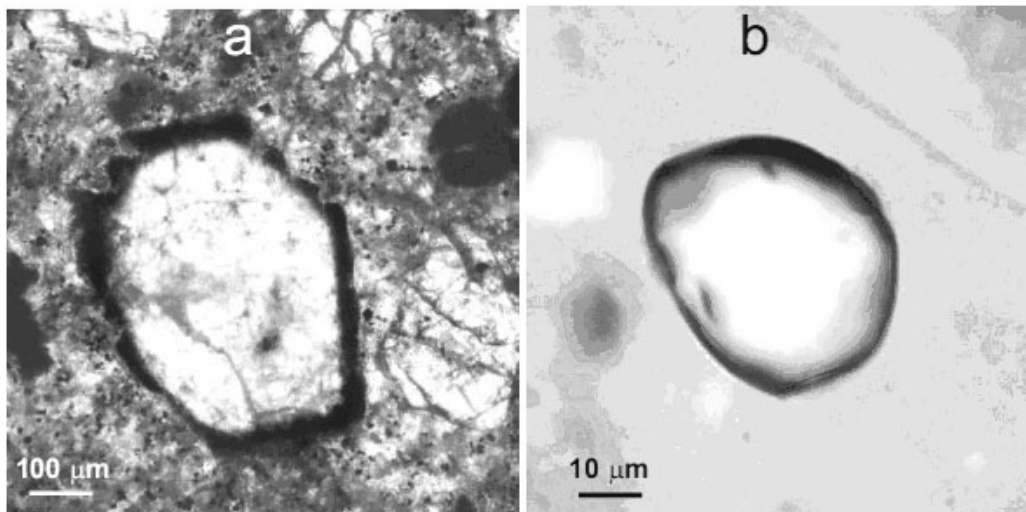


Fig. 4. **Photomicrographs of (a) hauyne phenocryst with a dark reaction rim in rock groundmass, (b) a hauyne crystalline inclusion in clinopyroxene 2 and. Plane-polarized transmitted light.**

aligned parallel to cleavage planes and were interpreted as secondary. Because of the strong alteration of apatite crystals, thermometric experiments failed, the inclusions were opened both during cooling to -50°C and heating to 600°C .

INCLUSIONS IN MINERALS

Crystalline inclusions

Early olivine (Fo_{90-91}) contains crystalline inclusions of Cr spinel with up to 46 wt % Cr_2O_3 (Table 2). Similar spinels were found in early clinopyroxene phenocrysts (clinopyroxene 1). Later olivine crystals and colorless rims of clinopyroxene 3 around green crystals of clinopyroxene 2 contain only low-Cr Ti-rich spinel (less than 1 wt % Cr_2O_3 and up to 17 wt % TiO_2). Clinopyroxene 2 hosts crystalline inclusions of Ti-magnetite identical to the opaque phase from the rock groundmass (Table 1 and 2).

Crystalline inclusions of clinopyroxene in olivine show high mg = 0.89 and contain up to 0.91 wt % Na_2O (Table 2). The concentration of Cr_2O_3 in one of such inclusions was about 0.38 wt %, in contrast to <0.05 wt % in the clinopyroxene phenocrysts.

Table 2.

Chemical compositions of crystalline inclusions in phenocrysts, wt.%

	Inclusions in clinopyroxene 1		Inclusions in clinopyroxene 2		Mt	Mt	Ap	Ha	Ha	Ha	Cpx
	Sp	Ap									
SiO ₂	1.21	1.37			0.72	1.04	1.6 ₀	30.43	31.74	31.24	43.06
TiO ₂	0.86	0.0			4.59	4.67	0.0	0.0	0.0	0.0	1.86
Al ₂ O ₃	14.73	0.00			5.91	5.45	0.00	30.43	31.74	31.24	8.93
FeO	31.28	0.39			80.64	80.20	0.37	1.01	0.85	0.79	12.28
MgO	10.34	0.00			3.31	6.11	0.00	0.40	0.16	0.16	8.32
MnO	0.41	0.00			0.64	0.59	0.00	0.00	0.00	0.00	0.48
CaO	1.09	40.35			0.71	0.97	51.94	10.27	10.09	8.39	23.37
Na ₂ O	0.00	0.00			0.00	0.00	0.00	10.46	9.73	13.72	0.68
K ₂ O	0.00	0.00			0.00	0.00	0.00	2.47	1.73	2.29	0.00
BaO	0.00	0.06			0.00	0.00	0.04	0.00	0.00	0.00	0.00
SrO	0.00	0.43			0.00	0.00	0.33	0.30	0.24	0.39	0.00
Cl	0.00	0.38			0.00	0.00	0.41	0.88	1.08	1.25	0.00
SO ₃	0.00	0.00			0.00	0.00	0.00	12.30	11.72	11.86	0.00
Cr ₂ O ₃	39.73	n.d.			0.07	0.11	n.d.	n.d.	n.d.	n.d.	0.02
Total	99.65	42.98			96.59	99.14	54.69	98.95	99.08	101.33	98.99

	Phi	Amf	Inclusions in clinopyroxene 3				Inclusions in olivine		Sp	Sp
			Sp	Ha	Ha	Ha				
SiO ₂	37.65	41.32	0.99	34.83	32.90	33.41		0.49	0.80	
TiO ₂	1.27	2.50	4.93	0.00	0.00	0.00		0.75	0.77	
Al ₂ O ₃	15.3	15.21	11.43	28.29	28.36	27.26		10.83	14.52	
FeO	10.55	10.99	71.86	0.53	0.48	0.62		37.72	26.72	
MgO	19.33	14.70	8.12	0.36	0.44	0.39		6.03	12.56	
MnO	0.24	0.16	0.39	0.00	0.00	0.00		1.21	0.25	
CaO	0.34	12.52	0.77	11.92	12.63	12.20		0.15	0.00	
Na ₂ O	0.4	2.06	0.00	8.61	10.37	9.98		0.00	0.00	
K ₂ O	9.76	1.37	0.00	5.43	6.09	5.80		0.00	0.00	
BaO	0.92	0.16	0.00	0.08	0.08	0.00		0.00	0.00	
SrO	0.02	0.31	0.00	0.26	0.26	0.46		0.00	0.00	
Cl	0.00	0.00	0.00	0.50	0.39	0.76		0.00	0.00	
SO ₃	0.00	0.00	0.00	9.23	9.30	8.35		0.00	0.00	
Cr ₂ O ₃	n.d.	n.d.	1.38	n.d.	n.d.	n.d.		41.94	44.30	
Total	98.43*	101.30	99.87	100.04	101.30	99.23		99.12	99.92	

	Sp	Sp	Sp	Sp	Sp	Cpx	Cpx	Grt
SiO ₂	0.80	0.68	0.83	0.53	0.58	53.00	52.25	38.32
TiO ₂	0.77	0.61	0.64	16.91	15.07	0.13	0.40	3.13
Al ₂ O ₃	14.52	15.19	14.63	5.51	6.88	4.58	3.94	16.15
FeO	26.72	24.53	25.67	66.30	65.30	4.31	3.64	7.34
MgO	12.56	13.16	12.21	7.84	7.20	16.49	16.45	10.77
MnO	0.25	0.26	0.30	0.34	0.49	0.03	0.07	0.09
CaO	0.00	0.00	0.00	0.00	0.00	21.35	22.84	22.14
Na ₂ O	0.00	0.00	0.00	0.00	0.00	0.91	0.42	0.48
K ₂ O	0.00	0.00	0.00	0.00	0.00	0.08	0.00	0.18
BaO	0.00	0.00	0.00	0.00	0.00	0.00	0.00	0.04
SrO	0.00	0.00	0.00	0.00	0.00	0.13	0.00	0.02
Cl	0.00	0.00	0.00	0.00	0.00	0.00	0.00	0.00
SO ₃	0.00	0.00	0.00	0.00	0.00	0.00	0.00	0.00
Cr ₂ O ₃	44.30	45.87	45.28	2.05	1.15	n.d.	0.38	n.d.
Total	99.92	100.30	99.56	99.48	96.67	101.01	100.39	98.66

Note: Amf - amphibole, Grt - garnet, Sp-spinel; other mineral symbols are the same as in Tab.1.
 *Including 0.48 wt % Ce₂O₃ and 2.17 wt % F.

Table 3.

Compositions of daughter phases in primary and secondary melt inclusions, wt. %

Phase	Primary melt inclusions <i>In Olivine</i>				<i>In clinopyroxene 1</i>				<i>In clinopyroxene 2</i>			
	1	2	3	4	5	6	7	8	9			
	Cpx	Cpx	Anor	Glass	Amf	Phi	Anor	Glass	Cpx			
SiO ₂	42.14	53.00	56.99	57.79	40.03	36.41	63.34	50.93	42.00			
TiO ₂	2.80	0.13	0.01	0.00	2.17	3.18	0.04	0.12	2.07			
Al ₂ O ₃	12.18	4.58	24.67	22.47	14.07	18.55	18.09	23.33	9.62			
FeO	6.46	4.31	0.56	0.85	8.90	7.44	0.28	1.57	13.59			
MgO	12.31	16.49	1.03	0.35	15.94	18.17	0.26	1.64	9.59			
MnO	0.06	0.03	0.04	0.00	0.25	0.29	0.00	0.00	0.54			
CaO	22.51	21.35	2.81	1.85	13.21	0.67	2.41	5.20	20.49			
Na ₂ O	0.29	0.91	5.42	7.76	2.48	0.58	1.93	3.04	0.82			
K ₂ O	0.16	0.00	8.69	8.34	1.99	11.45	15.41	2.23	0.03			
BaO	0.00	0.13	0.07	0.00	0.11	2.04	0.00	0.00	0.00			
SrO	0.00	0.00	0.21	0.54	0.21	0.11	0.55	0.00	0.23			
Cl	0.00	0.00	0.00	0.25	0.00	0.00	0.13	2.46	0.00			
SO ₃	0.00	0.00	0.00	0.85	0.00	0.00	0.00	3.25	0.00			
Total	98.91	100.93	100.50	101.05	99.36	98.89	102.44	93.77	98.98			

Phase	<i>In clinopyroxene 3</i>					<i>In apatite, silicate inclusions</i>		
	10	11	12	13	14	15	16	17
	Cpx	Cpx	Anor	Or	Glass	Cpx	Cpx	Cpx
SiO ₂	43.47	40.54	60.54	62.68	56.19	47.22	46.80	49.23
TiO ₂	1.72	1.54	0.00	0.06	0.47	1.15	1.21	1.09
Al ₂ O ₃	8.43	9.28	20.61	19.91	16.12	7.82	7.00	7.74
FeO	12.50	13.50	0.64	0.00	3.00	8.61	8.91	4.79
MgO	11.04	9.56	1.51	0.20	4.00	14.06	13.58	13.74
MnO	0.41	0.27	0.00	0.00	0.09	0.10	0.00	0.32
CaO	20.93	23.28	4.96	0.46	9.56	21.63	23.37	22.43
Na ₂ O	0.94	0.62	6.19	0.47	2.18	0.59	0.67	0.66
K ₂ O	0.00	0.00	3.90	15.52	6.20	0.05	0.09	0.00
BaO	0.00	0.00	0.78	0.12	0.00	0.10	0.08	0.00
SrO	0.00	0.00	1.10	0.65	0.00	0.00	0.00	0.00
Cl	0.00	0.00	0.00	0.00	0.00	0.00	0.00	0.00
SO ₃	0.00	0.00	0.00	0.00	0.00	0.00	0.00	0.00
Total	99.44	98.57	100.23	100.07	97.81	101.33	101.71	100.00

Phase	<i>In apatite, silicate - carbonate inclusion</i>		<i>In clinopyroxene 3</i>							
	18	19	20	21	22	23	26	27	28	29
	Grt	Glass	Cpx	Cpx	Cpx	Glass	Phi	Carb	Carb	Carb
SiO ₂	34.71	60.57	40.25	44.37	44.91	56.18	35.44	0.22	0.12	0.07
TiO ₂	1.63	0.07	1.62	1.11	0.85	0.27	2.96	0.00	0.00	0.00
Al ₂ O ₃	13.39	24.71	13.00	11.29	12.73	24.84	19.06	0.00	0.00	0.00
FeO	16.36	0.38	10.08	7.85	7.89	1.90	9.26	0.23	2.09	0.81
MgO	5.90	0.27	9.32	10.20	10.63	1.68	16.90	43.69	25.29	1.64
MnO	0.55	0.00	0.19	0.16	0.21	0.03	0.17	0.00	0.11	0.18
CaO	22.73	1.81	23.48	23.36	23.86	5.24	1.35	2.55	28.81	55.30
Na ₂ O	0.88	3.07	0.51	0.74	0.25	8.93	0.24	0.01	0.30	0.09
K ₂ O	0.07	4.42	0.06	0.05	0.12	1.32	14.39	0.01	0.01	0.01
BaO	0.05	0.00	0.23	0.17	0.09	0.00	1.56	0.00	0.02	0.03
SrO	0.24	0.22	0.00	0.00	0.00	0.00	0.00	0.00	0.18	0.00
Cl	0.00	0.50	0.00	0.00	0.00	0.03	0.00	0.02	0.04	0.10
SO ₃	0.00	0.00	0.00	0.00	0.00	0.03	0.00	0.05	0.13	0.20
Total	96.52	96.02	98.73	99.31	101.54	100.44	101.33	46.78	57.10	58.42

Table 3. Continued

	30	Secondary melt inclusions <i>In oivine</i>		31	<i>In clinopyroxene 1</i>		32	33	34	35	36	37
Phase	Carb			Carb			Cpx	Cpx	Cpx	Amf	Phi	Phi
SiO ₂	0.19			0.80			43.42	44.61	46.48	38.52	33.70	37.00
TiO ₂	0.00			0.00			11.61	2.21	1.39	1.73	4.05	1.98
Al ₂ O ₃	0.00			0.00			9.13	8.85	7.98	16.40	16.67	14.28
FeO	7.08			8.95			9.41	8.38	8.79	9.04	13.66	7.24
MgO	1.52			41.07			12.35	12.29	13.62	14.39	15.77	19.94
MnO	0.32			0.12			0.23	0.08	0.15	0.34	0.39	0.16
CaO	43.54			0.14			24.23	21.04	21.22	13.71	0.27	0.66
Na ₂ O	0.28			0.34			0.95	0.37	0.36	3.06	0.41	0.82
K ₂ O	0.09			0.00			0.00	0.00	0.00	2.77	13.70	11.52
BaO	0.00			0.00			0.06	0.00	0.00	0.00	2.57	3.33
SrO	0.11			0.00			0.00	0.00	0.15	0.20	0.12	0.07
Cl	0.00			0.00			0.00	0.00	0.00	0.00	0.00	0.00
SO ₃	0.88			0.28			0.00	0.00	0.00	0.00	0.00	0.00
Total	54.01			51.70			101.39	97.95	100.33	100.27	101.31	101.00
	38	39	40	41	42	43	44	45	46			
Phase	Anor	Or	Ne	Ap	Mt	Ze	Ze	Ze	Ze			
SiO ₂	64.34	65.24	46.82	1.80	0.94	41.09	47.04	48.38	42.41			
TiO ₂	0.00	0.00	0.00	0.00	9.02	0.00	0.00	0.00	0.00			
Al ₂ O ₃	21.47	18.99	33.06	0.00	1.97	24.44	0.00	21.93	24.38			
FeO	0.26	0.39	0.70	0.34	78.27	0.25	19.86	0.32	0.35			
MgO	0.13	0.33	0.15	0.00	1.13	0.44	2.76	0.40	0.18			
MnO	0.00	0.00	0.00	0.00	1.59	0.00	3.47	0.00	0.00			
CaO	0.97	1.08	2.95	53.90	0.59	8.56	0.00	9.27	8.11			
Na ₂ O	7.13	0.48	15.79	0.00	0.00	0.09	12.18	0.05	0.15			
K ₂ O	5.36	12.03	1.11	0.00	0.00	4.00	0.65	1.48	2.08			
BaO	0.00	0.90	0.00	0.06	0.00	0.17	3.35	2.80	3.49			
SrO	0.26	0.95	0.00	0.67	0.00	6.27	0.71	4.82	5.22			
Cl	0.00	0.00	0.00	0.17	0.00	0.00	0.85	0.00	0.00			
SO ₃	0.00	0.00	0.00	0.00	0.00	0.00	0.00	0.00	0.00			
Total	99.92	100.39	100.58	97.59*	93.62**	89.31	96.37	89.45	87.47***			
	47	48	49	50	<i>In clinopyroxene 2</i>							
Phase	Carb	Carb	Carb	Carb	51	52	53					
					Cpx	Cpx	Or					
SiO ₂	0.62	0.80	1.03	0.82	42.00	42.25	60.28					
TiO ₂	0.00	0.00	0.00	0.00	2.07	1.61	0.00					
Al ₂ O ₃	2.83	0.00	0.00	0.00	9.62	9.70	18.73					
FeO	22.17	16.46	8.44	0.15	13.59	14.40	0.31					
MgO	0.23	2.41	2.49	0.55	9.59	9.68	0.12					
MnO	40.52	1.43	0.48	0.00	0.54	0.00	0.00					
CaO	0.27	40.45	43.48	52.87	20.49	20.51	2.19					
Na ₂ O	0.26	0.21	0.11	0.07	0.82	0.52	2.49					
K ₂ O	0.00	0.09	0.12	0.05	0.00	0.03	14.34					
BaO	0.00	0.13	0.11	0.03	0.03	0.00	0.72					
SrO	0.00	0.00	0.14	0.13	0.23	0.27	0.42					
Cl	0.00	0.00	0.00	0.00	0.00	0.00	0.00					
SO ₃	0.40	0.28	1.02	0.00	0.00	0.00	0.00					
Total	67.30	62.26	57.42	54.67	98.98	98.97	99.60					

Note: Carb - carbonate, Or - orthoclase, Ze - zeolite; other abbreviations are the same as in Tables 1 and 2.
 *Including 36.53 wt % P₂O₅, 3.41 wt % F, 0.52 wt % Ce₂O₃, and 0.19 wt % La₂O₃. **Including 0.11 wt % Cr₂O₃.
 ***Including 1.1 wt % Ce₂O₃

A crystalline inclusion of pyrope garnet (Py₄₀And₃₂Gros₂₈) was found in olivine. This garnet is different from the Ti-rich garnets (melanite and shorlomite) described by Melluso et al. [19] and Beccaluva et al. [5] in the volcanic rocks of the Vulture complex.

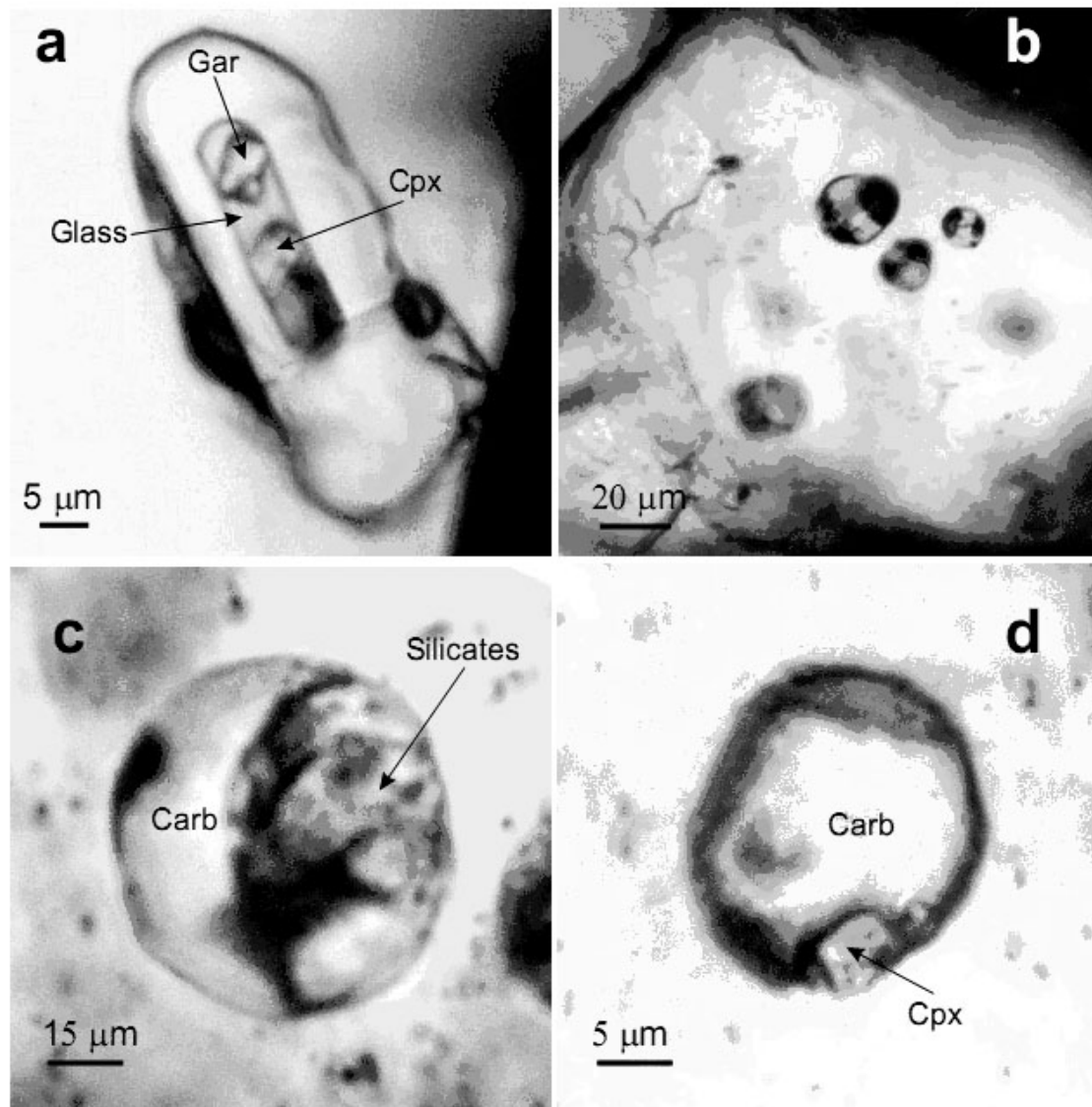


Fig. 5. Photomicrographs of inclusions in apatite crystals. (a) Primary inclusion of silicate melt in a prismatic apatite grain enclosed by clinopyroxene 2. (b)-(d) Primary silicate-carbonate melt inclusions in apatite phenocrysts ranging from (b) predominantly silicate through (c) 50% silicate – 50% carbonate to (d) predominantly carbonate composition.

Green clinopyroxene 2 bears numerous crystalline inclusions of hauyne, apatite, and rare grains of Ba-rich phlogopite (Table 2) and amphibole. The amphibole is strongly resorbed and contains numerous gas bubbles.

Fresh rounded inclusions of hauyne in clinopyroxene 2 are up to 50 μm across (Fig. 4b). Compared to the hauyne inclusions in the marginal zones of

clinopyroxene 1 (smaller than 10 mm in size), they are enriched in SO_3 , Cl, Na_2O , and Al_2O_3 (Table 2).

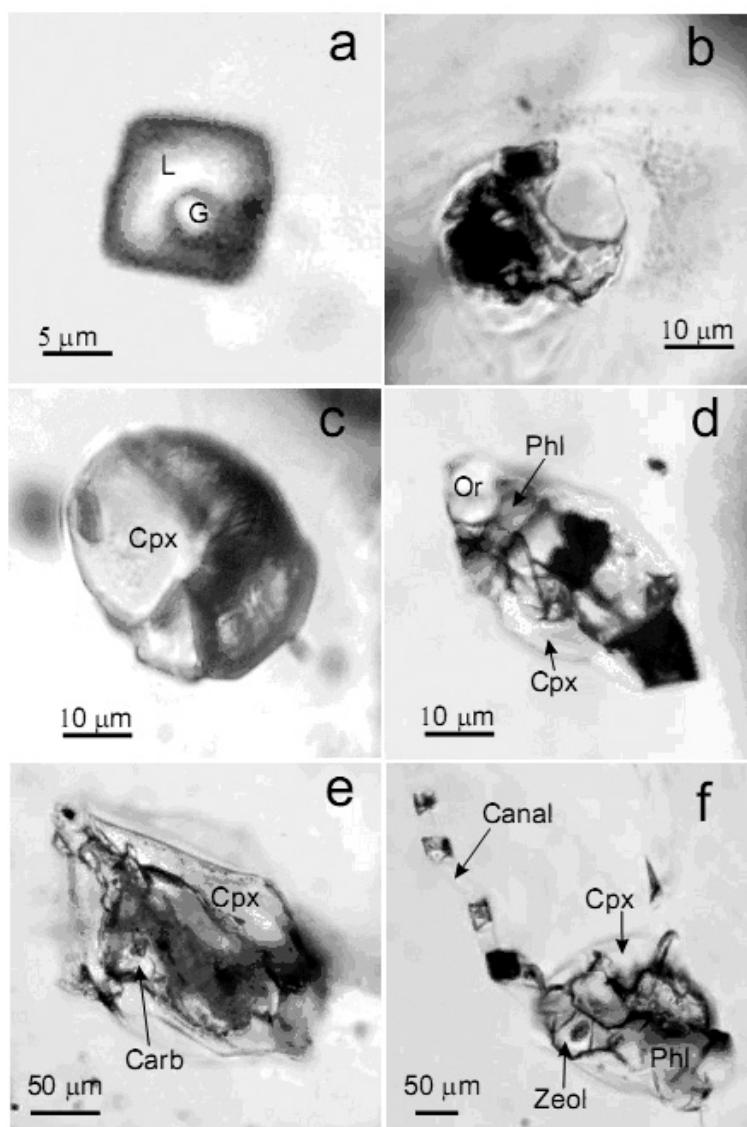


Fig. 6. Photomicrographs of inclusions in olivine and clinopyroxene. (a) Primary high-density CO_2 inclusion in olivine. (b) Partially leaked melt inclusion in olivine surrounded by the halo of small tiny inclusions impregnated into the host mineral. (c) Primary melt inclusion in olivine. (d) Primary melt inclusion in clinopyroxene 2. (e), (f) Secondary melt inclusions in clinopyroxene 1.

Clinopyroxene 2 contains numerous prismatic randomly distributed inclusions of apatite (Table 2), up to $70 \mu\text{m}$ in size. They are partially resorbed and show smoothed faces (Fig. 5a).

Fluid inclusions

Rare primary fluid inclusions were found in olivine and clinopyroxene 1. They are often decrepitated and contain gas phase only. However one small inclusion,

less than 20 μm across, contained liquid and gaseous CO_2 (Fig. 6a). Its homogenization temperature (29°C) suggests a density of 0.63 g/cm^3 . Assuming that it was captured by the clinopyroxene crystal at a temperature of about 1200°C (see thermometric experiments), pressure during olivine and pyroxene 1 crystallization is estimated as about 3.5 kbar.

One partially leaked secondary CO_2 inclusion containing liquid and gas was also found in clinopyroxene 2. Its density is 0.33 g/cm^3 , which corresponds to 1.2 kbar at a temperature of $1100 - 1150^\circ\text{C}$.

5.3. Primary melt inclusions in clinopyroxene and olivine

5.3.1. Phase composition

Primary melt inclusions in olivine and clinopyroxene are fully crystallized. The daughter phases of melt inclusions are colorless clinopyroxene and alkali feldspars in olivine (Fig. 6c); clinopyroxene, amphibole, phlogopite, and orthoclase in clinopyroxene 1; and clinopyroxene, alkali feldspars and orthoclase in clinopyroxene 2 (Fig. 6d, Table 3). All the inclusions contain minor amounts of residual glass and a gas phase accounting for no more than 7 vol %.

The daughter clinopyroxene crystals in melt inclusions from clinopyroxene are always more intensely colored than the host pyroxene. They occupy up to 40% of inclusion volume and are enriched in FeO, MnO, Al_2O_3 , Na_2O , and SrO at the expense of SiO_2 . The daughter clinopyroxene of olivine-hosted melt inclusions shows a high BaO content, whereas daughter clinopyroxene in inclusions from clinopyroxene 2 is SrO-rich (up to 0.23 wt %).

5.3.2. Thermometric experiments

The complete homogenization of melt inclusions was never reached in thermometric experiments. The temperatures listed in the table 4 correspond to the point of complete melting of daughter phases. Iron sulfide was present in some melt inclusions in olivine at a temperature of 1200°C . Primary melt inclusions are sometimes decrepitated (Fig. 6b). In some cases hermetic inclusions in olivine contained up to five gas bubbles at 1180°C , which is indicative of melts enriched in volatile components. The temperatures of partial homogenization (melt + gas) are $1180-1240^\circ\text{C}$ for olivine and clinopyroxene 1, and $1160-1190^\circ\text{C}$ for clinopyroxene 2.

5.3.3. Composition of initial melt in olivine and clinopyroxene 1

The composition of primary melt was estimated using the analyses of glasses from heated melt inclusions in olivine and clinopyroxene 1. The glasses of melt inclusions in olivine were recalculated to equilibrium with the host mineral by adding the appropriate amount of olivine to attain $K_D = (\text{Fe}/\text{Mg})^{\text{Ol}} (\text{Mg}/\text{Fe})^{\text{Liq}} \sim 0.3$ (Table 4). The compositions show moderate MgO (about 10 wt %), low SiO_2 (40 –

44 wt %) and TiO₂ (no more than 1.5 wt %), and high Al₂O₃ (up to 22 wt %) and CaO contents (up to 17 wt %). The total of alkalis is up to 11 wt % with about equal sodium and potassium contents. The initial magma was enriched in F (up to 0.6%), S (up to 0.43%), Cl (up to 0.55%), BaO (up to 0.5%), SrO (up to 0.52%), and Ce₂O₃ (up to 0.15%). The high concentrations of S in the melts resulted in sulfide appearance during early stages of crystallization and sulfates during late stages (hauyne).

The residual glasses of primary melt inclusions in olivine contain up to 57 wt % SiO₂ (Table 4).

5.3.4. Compositions of melt inclusions in clinopyroxene 2

Table 5 shows the compositions of glasses from heated melt inclusions in clinopyroxene. They are richer in SiO₂ (45-50 wt %) compared to the inclusions in olivine and poorer in CaO and K₂O at the same MgO content. However, the concentrations of BaO, SrO, F, S, and Cl are similarly high. The melts also show high P₂O₅ concentrations, up to 1.3 wt %. The residual glasses of melt inclusions in clinopyroxene coexisting with daughter phases contain up to 57 wt % SiO₂.

5.4. Primary silicate melt inclusions in apatite

Primary tubular melt inclusions often occur in the central parts of apatite grains enclosed in clinopyroxene 2. One of such inclusions, 5 x 20 μm in size, contained glass and euhedral daughter crystals accounting for 40-50 vol % (Fig. 5a). Among the daughter phases, garnet Alm₆And₅₃Gros₁₅Py₂₅ and clinopyroxene were identified. The residual glass is Na-K-rich (Table 3). The bulk composition of this inclusion is roughly estimated as 45 wt % SiO₂, 15 wt % Al₂O₃, 10 wt % FeO, 6-7 wt % MgO, and 16 wt % CaO. Na₂O + K₂O is no higher than 4 wt % and Na₂O > K₂O. It is similar to the composition of tephrite reported by Meluso et. al. [19].

5.5. Primary silicate--carbonate melt inclusions in apatite

Large tabular apatite crystals identical to individual phenocrysts are sometimes completely enclosed by clinopyroxene 1 and are much better preserved in such a case. Primary silicate-carbonate melt inclusions (up to 70 μm in size) were found in such crystals (Fig. 5b-d). The silicate and carbonate materials show variable proportions and are always clearly separated. Some inclusions display a meniscus-shaped boundary between the silicate and salt parts (Fig. 5c). Daughter clinopyroxene, phlogopite and residual glass were analyzed in the silicate part of these inclusions (Table 3). Electron microscope examination revealed a SrO, S and Cl enriched zone in the host apatite in contact with the carbonate portion of one inclusion.

Calcite from the inclusions is enriched in FeO (up to 7 wt %) and SrO (up to

Table 4.

Compositions of glasses from heated primary melt inclusions in olivine, wt.%

	1	2	3	4	5	6	7
SiO₂	43.62	41.24	41.45	40.73	42.09	41.66	42.97
TiO₂	1.23	1.29	1.25	1.31	1.28	1.36	1.37
Al₂O₃	20.75	17.37	18.22	18.85	17.05	16.25	16.83
FeO	5.79	5.60	5.87	6.28	6.48	5.93	5.82
MgO	6.45	8.24	7.03	7.18	8.04	7.09	7.84
MnO	0.03	0.01	0.04	0.11	0.11	0.09	0.05
CaO	10.51	15.97	13.39	14.09	16.48	16.56	16.91
Na₂O	5.24	3.38	5.71	4.18	4.28	3.83	3.60
K₂O	3.61	2.42	3.18	2.93	3.95	3.88	3.73
BaO	0.46	0.32	0.22	0.20	0.28	0.26	0.22
SrO	0.18	0.09	0.31	0.44	0.16	0.31	0.06
La₂O₃	0.04	0.07	0.03	0.00	0.07	0.07	0.00
Ce₂O₃	0.13	0.04	0.12	0.00	0.15	0.06	0.08
Cl	0.46	0.23	0.53	0.55	0.50	0.40	0.38
F	0.60	0.24	0.28	n.d.	0.12	0.00	0.16
S	0.18	0.34	0.17	0.18	0.20	0.22	0.26
Total	99.27	96.84	97.77	97.05	101.22	97.96	100.28
T°C exp.	1200	1200	1200	1200	1240	1240	1240
mg# of host 01	0.86	0.92	0.85	0.85	0.90	0.90	0.90
	8	9	10	11	12	13	
SiO₂	42.35	43.11	41.41	42.96	39.91	39.14	
TiO₂	1.38	1.46	1.42	1.12	1.45	4.25	
ai₂o₃	16.75	16.89	18.18	17.48	15.64	15.45	
FeO	4.93	5.18	5.94	8.27	7.23	10.12	
MgO	8.35	7.77	7.29	7.25	9.21	7.64	
MnO	0.11	0.05	0.11	0.13	0.11	0.11	
CaO	17.06	15.50	13.99	12.27	13.35	13.44	
Na₂O	3.68	2.84	5.07	4.62	5.15	4.89	
K₂O	3.58	4.06	5.69	3.66	4.60	4.51	
BaO	0.32	0.34	0.39	0.33	0.33	0.14	
SrO	0.35	0.24	0.29	0.38	0.40	0.24	
La₂O₃	0.01	0.00	0.00	0.00	0.00	0.00	
Ce₂O₃	0.04	0.00	0.00	0.01	0.00	0.08	
Cl	0.44	0.26	0.59	0.48	0.55	0.12	
F	0.16	0.00	n.d.	0.38	0.29	0.11	
S	0.18	0.33	0.00	0.41	0.33	0.16	
Total	99.69	98.01	100.37	99.75	98.55	100.40	
T°C exp.	1200	1210	1180	1200	1200	1180	
mg# of host 01	0.90	0.90	0.88	0.85	0.89	0.85	

0.2 wt %). Magnesite was identified among the daughter phases in primary silicate-carbonate inclusions in apatite and in a magnesite-zeolite lens in the groundmass. It always contains variable amounts of FeO and CaO. In addition,

dolomite and ankerite were found in primary melt inclusions. Such a diversity of carbonates is certainly nonequilibrium and probably reflects a prolonged evolution of the carbonate system during changes in P-T conditions.

Secondary melt inclusions in clinopyroxene 1, olivine and clinopyroxene 2

Phenocrysts of olivine and clinopyroxene contain large melt inclusions up to 200 μm in size (Fig. 6e, f). The phase composition and morphology of these inclusions are very different from those of the “normal” melt inclusions that are described above. In addition to much larger sizes comparable with that of the host crystal, they show irregular outlines and are not confined to certain mineral zones. Some of these “inclusions” are connected with the groundmass through thin channels filled with daughter minerals and are strictly speaking not inclusions (Fig. 6f). However, many of them are certainly completely isolated within crystals. We believe that such inclusions record a stage of partial dissolution of phenocrysts; they are thus fundamentally different from small syn-crystallization inclusions and referred to as secondary.

The secondary melt inclusions contain large daughter crystals and glass (Table 3). No less than 40 vol % of yellowish green clinopyroxene occur on the walls. This clinopyroxene is much lower in MgO and higher in FeO, Al_2O_3 , TiO_2 , and Na_2O than host clinopyroxene 1. Their daughter phase association is also different from those of primary melt inclusions and includes F-apatite, amphibole, F-phlogopite, Na-K feldspar, orthoclase, nepheline, Ba-Sr zeolites, Ti-magnetite, and carbonates. Characteristic features of the daughter minerals in such aggregates are high contents of SrO (in apatite, clinopyroxene, feldspars, and amphibole), BaO (in phlogopite, feldspar, and amphibole) and Ce_2O_3 (in apatite) (Table 3). The zeolite is rich in BaO (3.5 wt %), SrO (5.2 wt %), and Ce_2O_3 (1.1 wt %). There is always a distinct gas bubble accounting for no more than 7-9 vol %.

DISCUSSION AND CONCLUSIONS

The diversity of mineral compositions suggests a complex history of crystallization of the basanite sample studied. The investigation of melt and fluid inclusions in the minerals provided some constraints on this process. It is evident that the earliest magmatic minerals of this rock are olivine and clinopyroxene 1, which form large and rather homogeneous phenocrysts. The high maximum mg values of olivine phenocrysts (up to 0.91) suggest that the magma that arrived into a magma chamber was almost undifferentiated and similar to the primary mantle melt. The high Ca contents of the most magnesian olivine phenocrysts (Fig. 7) indicate that high Ca is a pristine characteristic of the mantle melt rather than the result of assimilation of crustal carbonates. The composition of primary mantle

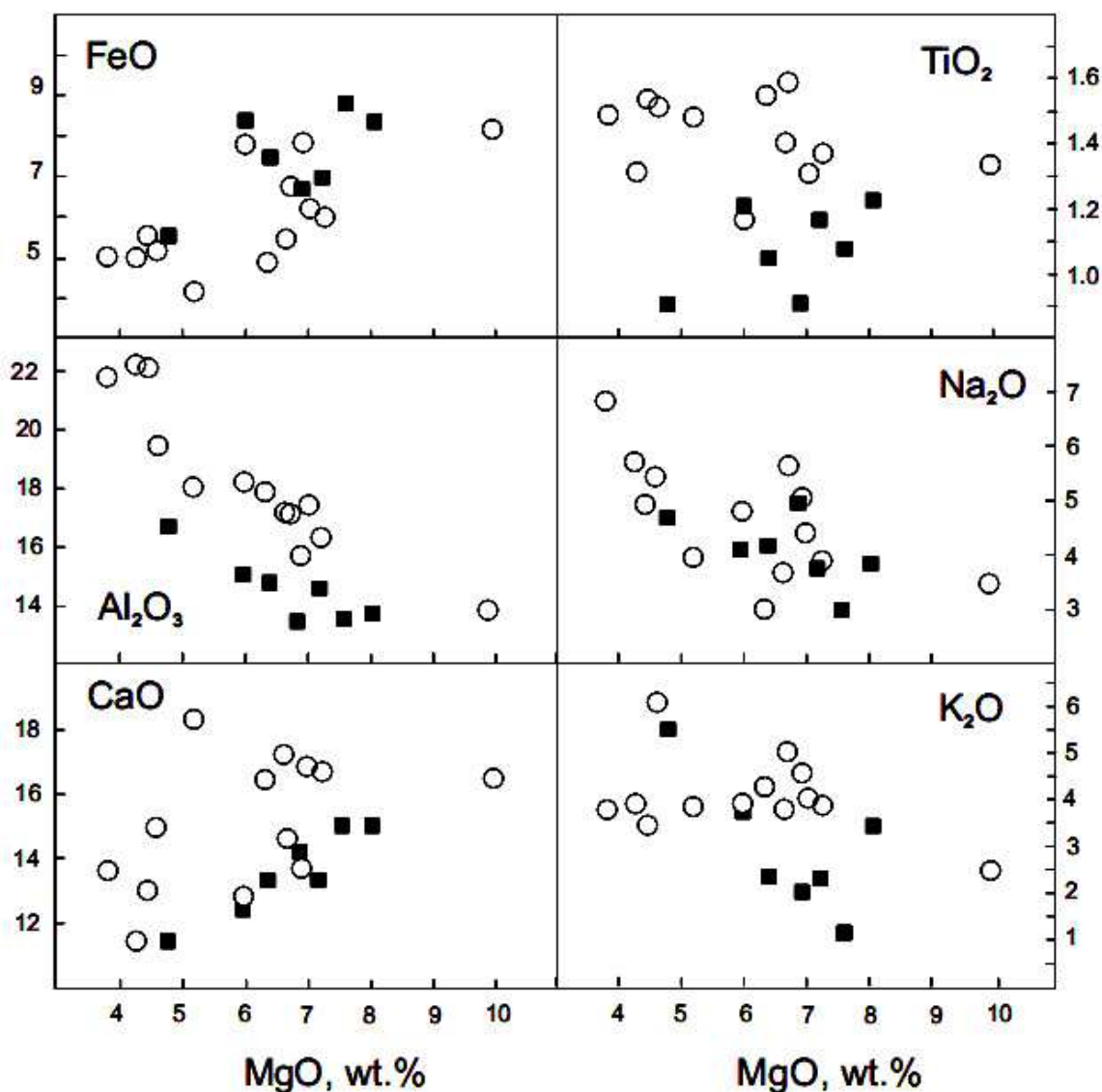


Fig. 7. Variations in the concentrations of major elements as functions of MgO for homogenized melt inclusions in olivine and clinopyroxene phenocrysts.

melt was characterized by high K_2O , Na_2O , F, Cl and S contents, which were inherited by all later derivatives and are recorded in melt inclusion compositions. The conditions of the beginning of magma crystallization in a transitional magma chamber are estimated from the results of thermometric experiments with melt and fluid inclusions. The highest crystallization temperature recorded by melt inclusions in olivine is $1240^{\circ}C$. Because of the partial leakage of all primary fluid inclusions, the pressure of crystallization is constrained only from below as >5 kbar.

The compositions of clinopyroxene grains suggest that clinopyroxene 2

Table 5

Compositions of glasses from heated primary melt inclusions in clinopyroxene, wt.%

	1	2	3	4	5	6	7
SiO₂	46.53	45.86	46.92	45.71	50.04	44.75	47.85
TiO₂	1.17	0.91	1.08	1.05	0.91	1.23	1.21
Al₂O₃	14.64	13.45	13.57	14.81	16.73	13.73	15.08
FeO	6.98	6.68	8.81	7.48	5.54	8.35	8.37
MgO	7.22	6.91	7.61	6.41	4.79	8.08	6
MnO	0.14	0.11	0.21	0.11	0.32	0.33	0.3
CaO	13.37	14.21	15.03	13.31	11.42	14.99	12.44
Na₂O	3.76	4.92	2.98	4.15	4.71	3.84	4.11
K₂O	2.32	2.03	1.15	2.34	5.51	3.44	3.78
BaO	0.19	0.08	0.11	0.25	0.26	0.23	0.26
SrO	0.21	0.31	0.21	0.08	0.26	0.43	0.3
Cl	0.12	0.67	0.03	0.38	0.54	0.39	0.51
F	0.23	0.22	0.04	0.14	0.42	0.22	0.39
S	0.32	0.19	0	0.34	0.03	0.48	0.37
P₂O₅	1.28	1.01	1.33	1.08	0	0	0
La₂O₃	0.01	0.04	0.04	0.05	0	0	0
Ce₂O₃	0.06	0.11	0.07	0.08	0.15	0.13	0.27
Total	98.54	97.71	99.2	97.77	101.63	100.62	101.24
T^oC exp	1165	1180	1180	1180	1195	1190	1160

crystallized after olivine and clinopyroxene 1. The limited data on the compositions of melt inclusions in clinopyroxene 2 indicate that it crystallized from a melt similar to that parental of clinopyroxene 1 but more evolved (clinopyroxene 2 are lower mg, higher Ti, etc.). In addition to melt differentiation, the sharp difference of compositions and appearances of the two pyroxene generations could be related to a change in physicochemical crystallization conditions (pressure, redox potential, or water activity). This is suggested by the partial resorption of olivine and clinopyroxene 1 before or during clinopyroxene 2 crystallization. This process was most extensive when large secondary melt inclusions in olivine and clinopyroxene were formed. A remarkable feature of these inclusions is elevated water and CO₂ contents, which resulted in carbonate crystallization and formation of zeolites during their postmagmatic closed-system evolution. It is important that such high water contents could not be derived by fractional crystallization of melts trapped as primary melt inclusions in olivine and clinopyroxene 1. These inclusions also evolved under closed-system conditions to low temperature, but they never contain zeolites and only minor amphibole and F-phlogopite as hydrous phases.

The conditions and compositions of crystallization of these hydrous melts are difficult to constrain, because the secondary melt inclusions could not be homogenized. Rough estimates of their bulk compositions from the proportions and compositions of daughter minerals suggest that they were similar to other melts. This is further supported by the specific chemical characteristics of the minerals, such as high Ba, Sr, F, and S contents.

The last stage of crystallization is recorded by clinopyroxene 3, which overgrows both clinopyroxene 1 and 2, and groundmass minerals. The compositions of these minerals indicate again a sharp change in crystallization conditions. The high mg of clinopyroxene 3 suggests that the parental magma was strongly depleted in Fe owing to extensive crystallization of titanomagnetite, which is abundant in groundmass. The mineralogy of the groundmass is indicative of almost water-free conditions. This conclusion is corroborated by the absence of low-temperature hydrous minerals in the groundmass, except for the deep inlets in pyroxenes cogenetic with secondary melt inclusions. This implies that most of water gained after clinopyroxene 1 and 2 crystallization was lost by the moment of eruption.

Thus, the complex mineralogy of the rock mirrors primary mantle magma crystallization under open-system conditions, with strong variations in water (probably, also oxygen) potential. Silicate-carbonate liquid immiscibility occurred during some phase of this process. This is recorded in the melt inclusions in apatite containing silicate and carbonate materials in varying proportions. Primary silicate-carbonate inclusions in calcites were also reported from the Mt. Vulture sövites by Rosatelli et al. [24]. Their carbonate component is dominated by dolomite. The compositions of carbonate and silicate liquids from the apatite were not determined, but the main mineral of the carbonate part is calcite. The carbonate melt coexisting with alkaline silicate melt must contain substantial amounts of alkalis. According to the available experimental data, the partition coefficients of Na and K between carbonate and silicate liquids are close to one, if Na₂O and K₂O contents lower than 10 wt %. The carbonatite liquids trapped together with silicates in apatite must therefore contain 5-10 wt % of Na₂O and K₂O. These components could be consumed by the crystallization of nepheline and potassium feldspar or (and) be dissolved in aqueous fluid separating during inclusion crystallization.

REFERENCES

1. **Amundsen, H.**, 1987. Evidence for liquid immiscibility in the upper mantle. *Nature* 327, 692 – 695.
2. **Andreeva, I.A., Naumov, V.B., Kovalenko, V.I., Kononkova, N.N.**, 1998. Fluoride-sulfate and chloride-sulfate salt melts of the carbonatite-bearing complex Mushugai-Khuduk, Southern Mongolia. *Petrology* 6, 284-292.
3. **Bailey, D.K.**, 1993. Carbonate magmas. *Journal of Geological Society London* 150, 637 – 651.
4. **Baker, M., Wyllie, P. J.**, 1990. Liquid immiscibility in a nephelenite-carbonate system at 25 kbar and implications for carbonatite origin. *Nature* 346, 168–170.
5. **Becculava, L., Coltorti M., Di Girolamo, P., Melluso, L., Milani, L., Morra, V., Siena, F.**, 2002. Petrogenesis and evolution of Mt. Vulture alkaline volcanism (Southern Italy). *Mineralogy and Petrology* 74, 277 – 297.
6. **Bell, K.** (ed), 1989. *Carbonatites: Genesis and evolution*. London: Unwin Hyman.

7. **Cavarretta, G., Lombardi, G.,** 1990. Origin of sulphur in the Quaternary perpotassic melts from Italy: evidence from hauyne sulphur isotope data. *Chemical Geology* 82, 15 – 20.
8. **Cortini, M.,** 1975. Eta K - Ar del Monte Vulture. *Rivista Italiana di Geofisica* 2, 45 – 46.
9. **De Fino, M., La Volpe, L., Peccerilo, A., and Poli G.,** 1986. Petrogenesis of Monte Vulture volcano (Italy) inferences from mineral chemistry, major and trace element data. *Contributions to Mineralogy and Petrology* 92, 135 – 145.
10. **Eggler, D.H.,** 1989. Carbonatites, primary melts, and mantle dynamics. In Bell, K. (ed), *Carbonatites: Genesis and evolution*. London: Unwin Hyman, 561–579.
11. **Freestone, I.C., Hamilton, D.L.,** 1980. The role of liquid immiscibility in the genesis of carbonatites – an experimental study. *Contributions to Mineralogy and Petrology* 73, 105 – 117.
12. **Hamilton, D.L., Kjarsgaard, B.A.,** 1993. The immiscibility of silicate and carbonate liquids. *South African Journal of Geology* 96, 139 – 142.
13. **Kjarsgaard, B.A., Peterson, T.,** 1991. Nephelinitic – carbonatite liquid immiscibility at Shombole volcano, East Africa: petrographic and experimental evidence. *Mineralogy and Petrology* 43, 293 – 314.
14. **Kogarko, L.N., Henderson, C.M., Pacheco, H.,** 1995. Primary Ca-rich carbonatite magma and carbonate –silicate – sulfide liquid immiscibility in the upper mantle. *Contributions to Mineralogy and Petrology* 121, 267 – 274.
15. **La Volpe, L., Patella, D., Rapisardi, L., Tramacere, A.,** 1984. The evolution of Monte Vulture volcano Southern Italy: inferences from volcanological, geological and deep dipole electrical sounding data. *Journal of Volcanology and Geothermal Research* 22, 147 – 162.
16. **Lavecchia, G., Stoppa, F.,** 1990. The Tyrrhenian zone: a case of lithosphere extension control of intra-continental magmatism. *Earth and Planetary Science Letters* 99, 336–350.
17. **Lee, W.–J., Wyllie, P.J.,** 1994. Experimental data bearing on liquid immiscibility, crystal fractionation, and the origin of calciocarbonatites and natrocarbonatites. *International Geological Review* 36, 797–819.
18. **Lee, W.–J., Wyllie, P.J.,** 1996. Liquid immiscibility in the join NaAlSi₃O₈ – CaCO₃ to 2.5 GPa and the origin of calciocarbonatite magmas. *Journal of Petrology* 37, 1125 – 1152.
19. **Melluso, L., Morra, V., Di Girolamo, P.,** 1996. The Mt. Vulture volcanic complex (Italy): evidence for distinct parental magmas and for residual melts with melilite. *Mineralogy and Petrology* 56, 225 – 250. 15
20. **Nielsen, T.F.D., Solovova, I.P., Veksler, I.V.** 1997. Parental melts of melilitolite and origin of alkaline carbonatite: evidence from crystallized melt inclusions, Gardiner complex. *Contributions to Mineralogy and Petrology* 126, 331–344.
21. **Panina, L. I., Usol'tseva, L. M.** 1999. Alkaline high – Ca sulfate – carbonate melt inclusions in melilite – monticellite – olivine rocks from the Malomurunskii alkaline massif, Aldan. *Petrology* 7, 610 – 625.
22. **Peccerillo, A.,** 1998. Relationships between ultrapotassic and carbonate – rich volcanic rocks in central Italy: petrogenetic and geodynamic implications. *Lithos* 43, 267 – 279.
23. **Pyle, J. M., Haggerty, S.E.,** 1994. Silicate – carbonate liquid immiscibility in upper – mantle eclogites: implications for natrosilicic and carbonatitic melts. *Geochimica et Cosmochimica Acta* 58, 2997 – 3011.
24. **Rosatelli, G., Stoppa, F., Jones, A.P.,** 2000. Intrusive calcite – carbonatite occurrence from Mt. Vulture volcano, southern Italy. *Mineralogical Magazine* 64, 615 – 624.

25. **Solovova, I.P., Girnis, A.V., Ryabchikov, I.D.**, 1996. Inclusions of carbonate and silicate melts in minerals of alkali basaltoids from the east Pamirs. *Petrology* 4, 319 – 341.
26. **Stoppa, F., Principe, C.**, 1998. Eruption style and petrology of a new carbonatite suite from the Mt. Vulture, Southern Italy: the Monticcio Lake formation. *Journal of Volcanology and Geothermal Research* 80, 137 – 153.
27. **Stoppa, F., Wooley, A.**, 1997. The Italian carbonatites: field occurrence, petrology and regional significance. *Mineralogy and Petrology* 59, 43 – 67.
28. **Twyman, J.D., Gittins, J.**, 1987. Alkalic carbonatite magmas: parental or derivative? In: Fitton, J. G. & Upton, B.G.J. (eds) *Alkaline igneous rocks*. Geological Society, London, Special Publication 30, 85 – 94.
29. **Wyllie, P.J.**, 1989. Origin of carbonatites: evidence from phase equilibrium studies: In Bell, K. (ed), *Carbonatites: Genesis and evolution*. London: Unwin Hyman, 500 – 545.

Average Compositions of Igneous Melts from Main Geodynamic Settings According to the Investigation of Melt Inclusions in Minerals and Quenched Glasses of Rocks

Naumov V.B.¹, Kovalenko V.I.², Dorofeeva V.A.¹, Girnis A.V.²,
and Yarmolyuk V.V.²

¹ Vernadsky Institute of Geochemistry and Analytical Chemistry, Russian Academy of Sciences, ul. Kosygina 19, Moscow, 119991 Russia; email: naumov@geokhi.ru

² Institute of Geology of Ore Deposits, Petrography, Mineralogy, and Geochemistry (IGEM), Russian Academy of Sciences, Staromonetnyi per. 35, Moscow, 119017 Russia; e-mail: vik@igem.ru

ABSTRACT

We compiled a database containing more than 480 000 determinations for 73 elements in melt inclusions in minerals and quenched glasses of volcanic rocks. These data were used to estimate the mean contents of major, volatile, and trace elements in igneous melts from main geodynamic settings. The following settings were distinguished: (I) oceanic spreading zones (mid-ocean ridges); (II) zones of mantle plume activity on oceanic plates (oceanic islands and plateaus); (III) and (IV) settings related to subduction processes, including (III) zones of island-arc magmatism generated on the oceanic crust and (IV) magmatic zones of active continental margins involving the continental crust into magma generation processes; (V) intracontinental rifts and continental hot spots; and (VI) back-arc spreading centers. The histogram of SiO₂ contents in the natural igneous melts of all geodynamic settings exhibits a bimodal distribution with two maxima at SiO₂ contents of 50–52 wt % and 72–74 wt %. The range 62–64 wt % SiO₂ comprises the minimum number of determinations. Primitive mantle normalized spidergrams were constructed for average contents of elements in the igneous melts of basic, intermediate, and acidic compositions from settings I–V. The diagrams reflect the characteristic features of melt compositions for each geodynamic setting. On the basis of the analysis of data on the composition of melt inclusions and glasses of rocks, average ratios of incompatible trace and volatile components (H₂O/Ce, K₂O/Cl, Nb/U, Ba/Rb, Ce/Pb, etc.) were estimated for the igneous melts of all of the settings. Variations of these ratios were determined, and it was shown that, in most cases, the ratios of incompatible elements are significantly different between settings. The difference is especially pronounced for the ratios of elements with different degrees of incompatibility (e.g., Nb/Yb) and for some ratios with volatile components (e.g., K₂O/H₂O).

In 2004, Naumov et al. [1] published the first generalization for the mean contents of major, volatile, and trace elements in igneous melts from main geodynamic settings on the basis of a database including the analyses of glasses from homogenized melt inclusions and quenched glasses of volcanic rocks assembled in the Paradox for Windows system. The total number of analyses, i.e., the number of the natural objects (melt inclusions and quenched glasses), was then almost 14000. Overall, the database contained 190 500 determinations representing 60 elements. During the past five years, the investigations of melt inclusions in minerals have rapidly increased, which is illustrated by Table 1. The total number

of publications exceeds 1000, and the number of objects analyzed reaches 33 000. Note that more than 50% of these papers have been published and 70% of the determinations have been obtained during the last decade. This attention to the investigation of inclusions in minerals is explained by the fact that they provide, perhaps, the most reliable method for the estimation of the composition and physicochemical parameters of igneous melts. These investigations became especially efficient after the advent of the methods of local quantitative analysis (electron, ion, and proton microprobes, Raman spectroscopy, LA ICP-MS, local infrared spectroscopy, etc.). Some recent studies (e.g., [2–7]) reported even isotopic characteristics for some elements in individual melt inclusions.

Table 1.

Numbers of publications and analyses of melt inclusions in minerals and quenched glasses of rocks for various time periods

Period	Number of publications	%	Number of analyses	%
1970–1979	26	2.5	295	0.9
1980–1989	112	10.6	1465	4.4
1990–1999	361	34.2	8310	25.2
2000–2009	555	52.7	22935	69.5
1970–2009	1048	100.0	33005	100.0

As of the beginning of May 2009, the database contained more than 480 000 determinations representing 73 elements, including 295 000 for major elements, 47000 for volatile components (H₂O, Cl, F, S, and CO₂), 88 000 for trace and ore elements (44 elements), and 52 000 for rare earth elements. In addition, the database comprises 7700 determinations of temperatures and more than 2000 determinations of pressures for natural igneous melts. Given the variable abundances of natural minerals, the number of determinations for particular minerals is, of course, also variable, which is illustrated by Table 2. The maximum amounts of data were obtained for inclusions in olivine, feldspars, quartz, and pyroxenes. Overall, the database comprises melt inclusion analyses from 40 minerals. The analyses of quenched glasses of volcanic rocks account for 43% of all determinations (Table 2). The following main geodynamic settings differing in conditions of formation and evolution of igneous melts are considered in this paper: (I) oceanic spreading zones (mid-ocean ridges); (II) zones of mantle plume activity on oceanic plates (oceanic islands and plateaus); (III) and (IV) settings related to subduction processes, including (III) zones of island-arc magmatism and (IV) magmatic zones of active continental margins; (V) intracontinental rifts and continental hot spots; and (VI) back-arc spreading centers related to subduction.

Figure 1 shows the histogram of SiO₂ contents in homogenous melt inclusions in minerals and quenched glasses of volcanic rocks for all geodynamic settings.

Figure 1a is based on 13 500 determinations available by 2004 and discussed in [1]. A bimodal distribution was observed for the available data on natural igneous

Table 2.

Numbers of analyses of major, volatile, and trace elements in the quenched lasses of rocks and melt inclusions in various minerals

Object	Number of analyses	Object	Number of analyses
Quenched glasses	14227	Magnetite and	
Olivine	7570	ilmenite	59
Feldspars	3912	Melilite	53
Quartz	3383	Monticellite	42
Pyroxenes	2369	Topaz	41
Spinel	305	Titanite	40
Amphibole	244	Perovskite	32
Apatite	221	Garnets	24
Zircon	169	Cordierite	16
Feldspathoids	105	Corundum	16
		Other 19 minerals	177

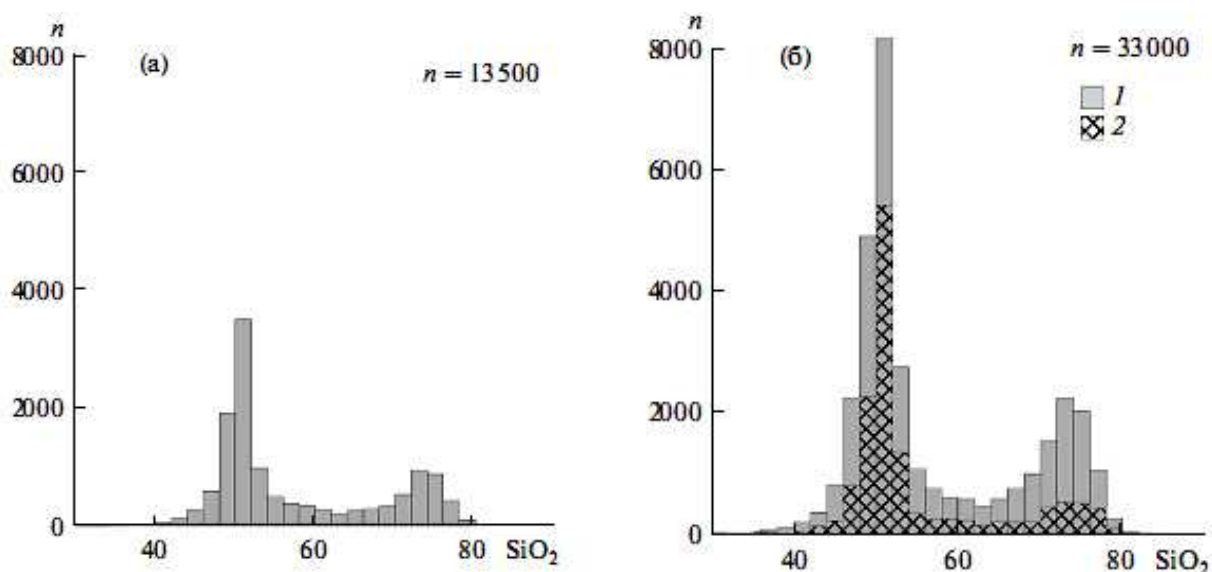


Fig. 1. Histogram of SiO₂ contents in natural igneous melts from all geodynamic settings according to the investigation of homogeneous melt inclusions in minerals and quenched glasses of rocks *n* is the number of determinations. (a) Data of [1] and (b) data of this study. (1) Melt inclusions in minerals and (2) quenched glasses of rocks.

melts. Figure 1b presents the results of 33 000 SiO₂ determinations available now. It is clearly seen that (1) the two diagrams are completely equivalent, although a number of new natural objects from various geodynamic settings were involved into analysis, and (2) the distribution of SiO₂ contents in natural igneous melts is bimodal. There are two maxima at SiO₂ contents of 50–52 wt % and 72–74 wt %.

The lowest number of determinations corresponds to SiO₂ contents of 62–64 wt %. The bimodal character of natural melts was detected by us [8] on the basis of 3465 analyses and was confirmed using an extended data set of 11 500 analyses [9]. It can probably be concluded that such a type of distribution of SiO₂ contents will not be changed by future investigations. (3) A bimodal distribution is characteristic of both melt inclusions in minerals (Fig. 1b, 1) and quenched glasses of rocks (Fig. 1b, 2).

The histograms of Fig. 2 show the distribution of SiO₂ contents in natural igneous melts from particular geodynamic settings (I–VI). Setting I (mid-ocean ridges) is practically devoid of intermediate and acidic melts (there are only 61 such analyses in our database, i.e., 1.2%). Setting II (ocean islands) is also dominated by basic and ultrabasic melts. Similar types of distribution were observed in settings III, IV, and V (island arcs, active continental margins, and intraplate continental regions). They contain igneous melts with widely variable SiO₂ contents from 40 to 80 wt %. Data for back-arc basins (setting VI) are still limited (908 determinations), but the dominance of basic melts is evident. Keeping in mind such a distribution of SiO₂ contents (Figs. 1, 2), we calculated the mean contents of major, volatile, trace, and rare earth elements for three types of igneous melts of basic (40–54 wt % SiO₂), intermediate (54–66 wt % SiO₂), and acidic (>66 wt % SiO₂) compositions.

For each melt type, mean contents were calculated for the particular geodynamic settings that were distinguished above. Naumov et al. [1] showed that geometric mean contents are more adequate than arithmetic mean values, because the contents of many elements have an approximately lognormal distribution. Such a distribution is exemplified by Fig. 3, which shows 1348 determinations of Cl content in basic igneous melts from geodynamic setting I. The lognormal distribution of element contents, irrespective of the geodynamic setting, was also observed for Nb, Ce, Yb (setting I), Sr, Cr, and Dy (setting II) in Fig. 4 and for Ba, Nd, Sm (setting III), Rb, B, and Th (setting V) in Fig. 5. Therefore, the abundances of elements were calculated as geometric means, under the conditions that any particular measurement will not deviate from the mean by more than 2σ with a probability of 95%. The determinations that did not meet this requirement were rejected and the mean was recalculated. The obtained mean contents of major, volatile, and trace elements are given in Tables 3–5. Each of the obtained mean contents in the tables is accompanied by two values characterizing the confidence interval (the first and second values are to be added to and subtracted from the mean, respectively). Mean contents were calculated if at least 10 determinations were available. Otherwise, the tables give only the number of available analyses by the time of calculations.

How significantly did the mean contents of elements change owing to the investigation of new natural objects and the significant increase of the number of

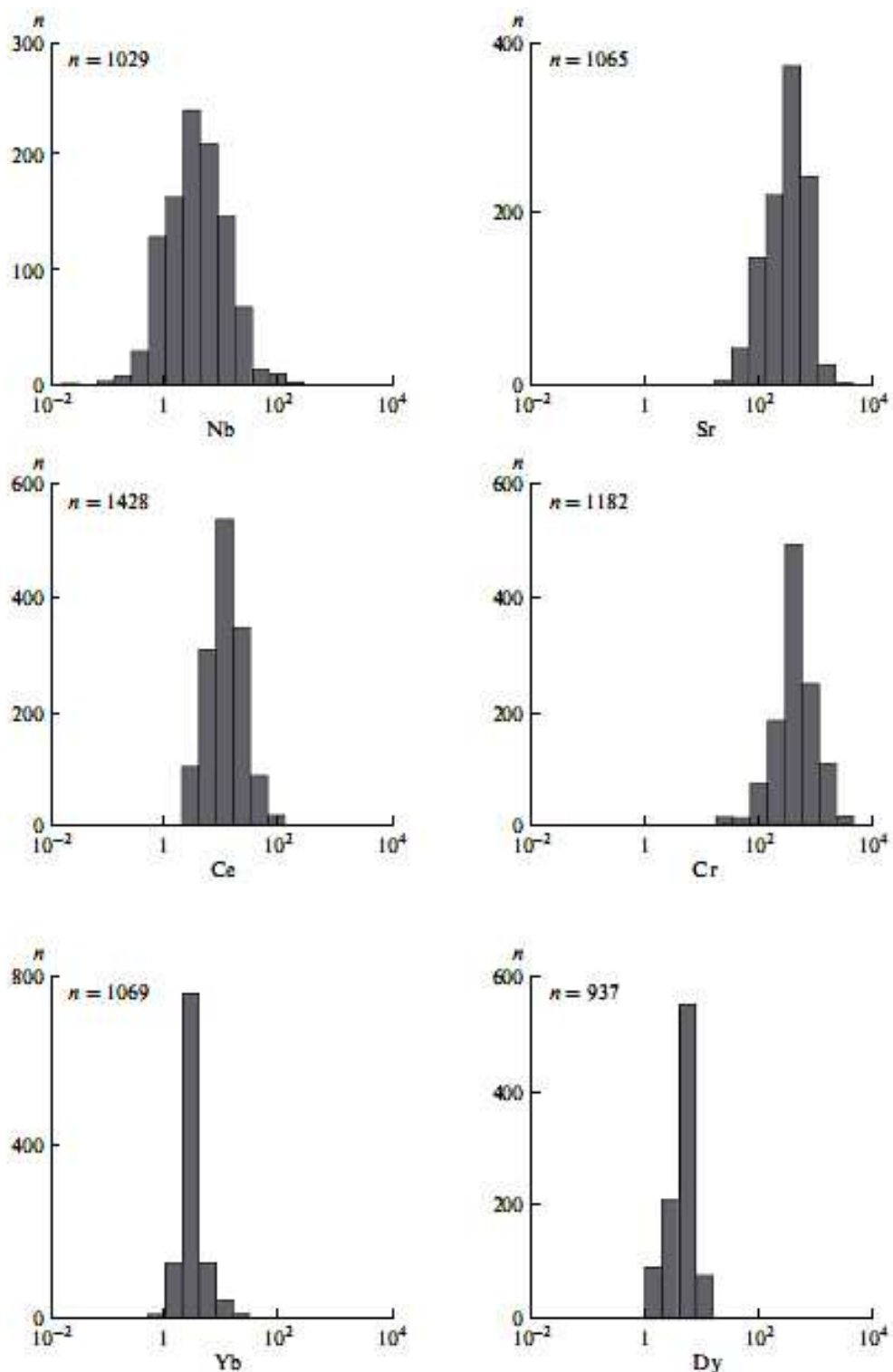


Fig. 2. Histograms of SiO₂ contents in natural igneous melts from the main geodynamic settings (I–VI) according to the investigation of homogeneous melt inclusions in minerals and quenched glasses of rocks; *n* is the number of determinations. Geodynamic settings: (I) mid-ocean ridges, (II) ocean islands, (III) island arcs, (IV) active continental margins, (V) intracontinental rift and hot-spot regions, and (VI) back-arc basins.

determinations compared with those available previously? In order to estimate this effect, let us compare the mean compositions of basic melts from geodynamic setting I reported in [1] with those for the same setting presented in Table 3. Discrepancies higher than 10% rel. were obtained for volatile components, K₂O, B, Nb, and Ba. The remaining 43 elements showed differences of no higher than 10% rel. On the other hand, the difference appeared to be much higher than 10% rel. for the contents of many elements in basic melts from geodynamic settings II and V, because the number of determinations discussed in [1] was much lower. In addition, this fact indicates a higher diversity for the compositions of natural melts from geodynamic settings II and V compared with geodynamic setting I.

In addition to the elements presented in Tables 3–5, the first analyses of other trace elements (Re, Os, Ir, Pt, Pd, Ru, Cd, Br, and Tl) were recently reported for basic igneous melts (40–54 wt % SiO₂). These data are summarized in Table 6, which shows the geodynamic setting, the number of determinations, mean contents (ppb), and confidence limits (first number has to be added to the mean, and the second number has to be subtracted from the mean). Despite the limited number of determinations, the data of Table 6 provide insight into the level of concentrations of these elements in the igneous melts of the main geodynamic settings.

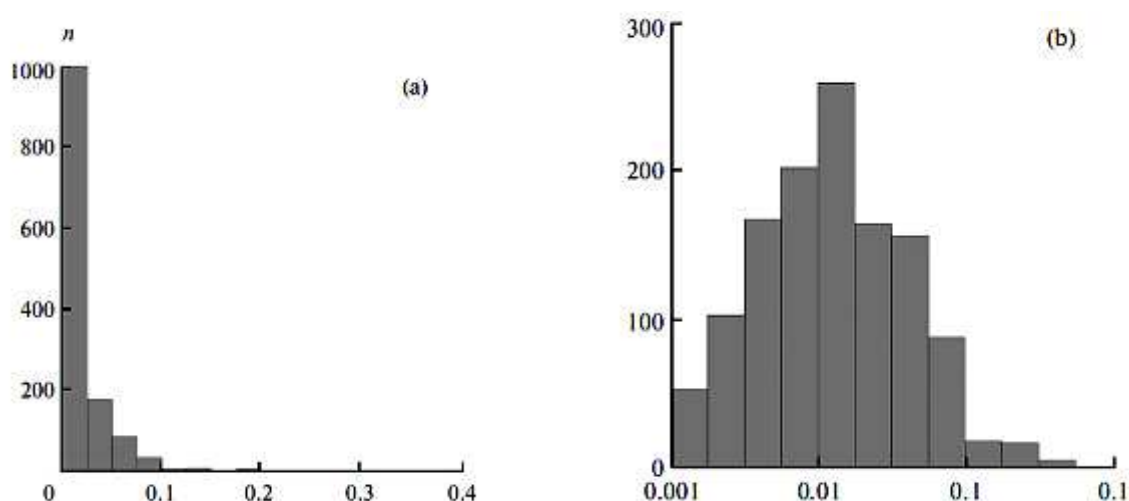


Fig. 3. Histogram of the distribution of 1348 determination of Cl content in basic igneous melts from geodynamic setting I on (a) linear and (b) logarithmic scales.

Figures 6–8 present spidergrams constructed using the data of Tables 3–5 for the mean contents of elements in the igneous melts of the main geodynamic settings (I–V). The results for back-arc settings (VI) are not shown in these diagrams, because, as was noted above, the number of available analyses is still low. The comprehensive analysis of the distribution of trace elements in melts of various compositions from various geodynamic settings is beyond the scope of this contribution. Many relevant problems have been discussed in the papers that focused on data for particular settings [11–17]. We only emphasize here some

general relations, which were revealed during the analysis of the whole data set on the compositions of inclusions and glasses of rocks.

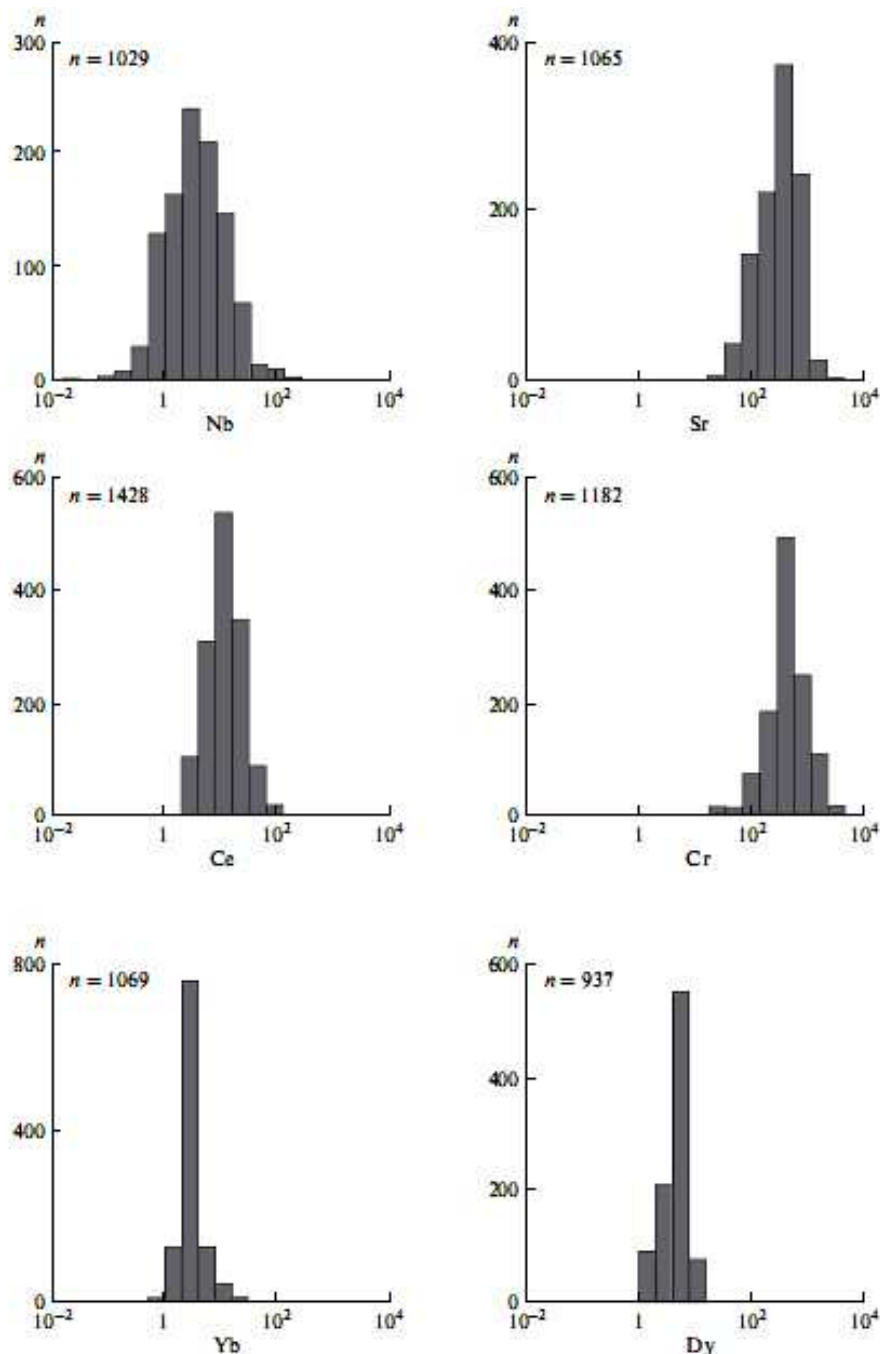


Fig. 4. Histograms of the contents of Nb, Ce, Yb (setting I), Sr, Cr, and Dy (setting II).

(1) The mean compositions of inclusions and glasses of rocks confirm the existence of geochemical signatures for the melts of each of the settings. This is primarily demonstrated by the radiating arrangement of the set of the spectra of mean contents in the melts of basic and intermediate compositions. The maximum differences are observed between the melts of settings I and V.

(2) In general, the distributions of trace elements in intermediate and basic melts are similar to each other and different from the distribution observed in acidic rocks. This may indicate that the sources of the intermediate and basic magmas were similar. It can be supposed that the main mechanism of the formation of intermediate melts was the differentiation of basic (mantle) magmas, whereas the sources and processes of the formation of acidic magmas were different (crustal rocks).

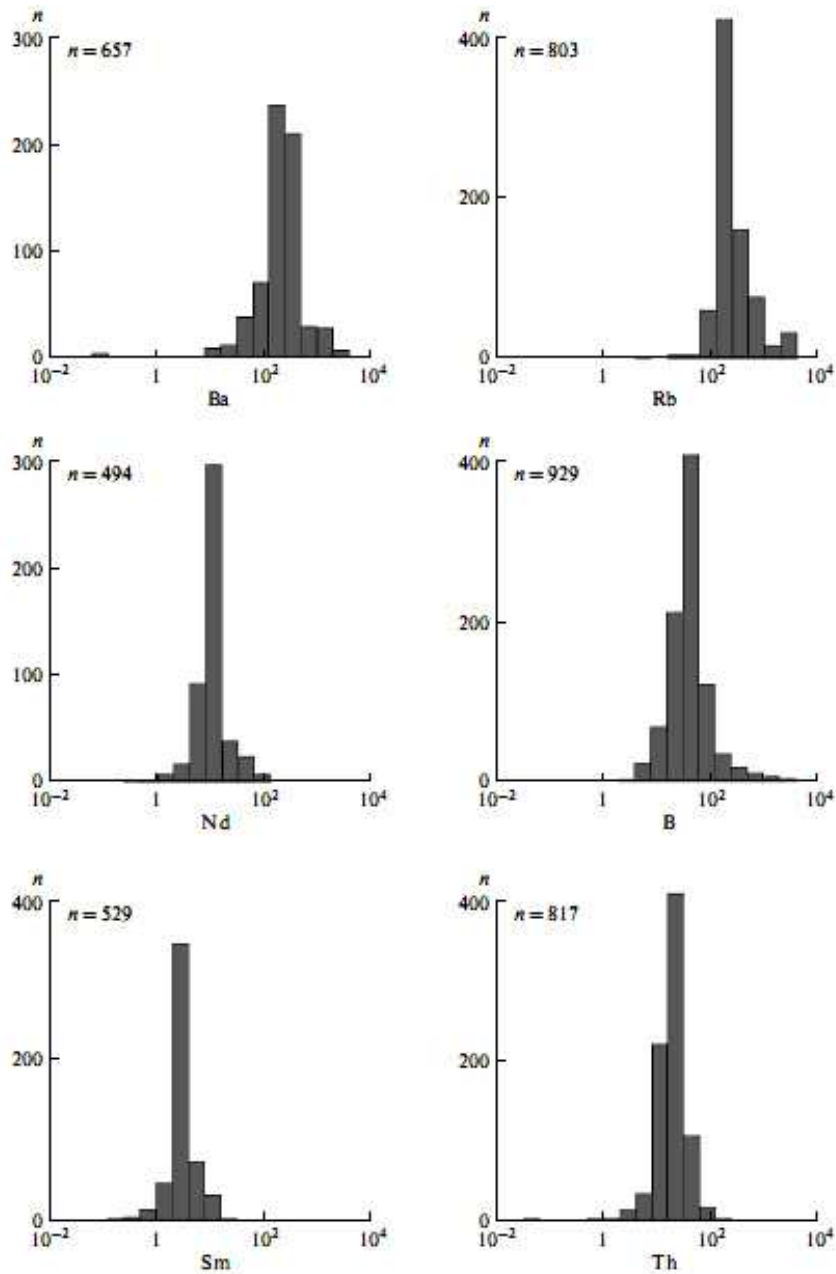


Fig. 5. Histograms of the contents of Ba, Nd, Sm (setting III), Rb, B, and Th (setting V).

(3) A remarkable feature of the diagrams, especially those for basic melts, is the very limited variations in the contents of the least incompatible elements in

the right part of the distribution patterns (from Tb to Lu). Such uniformity indicates that the sources of magmas were, on average, similar. It should be kept in mind

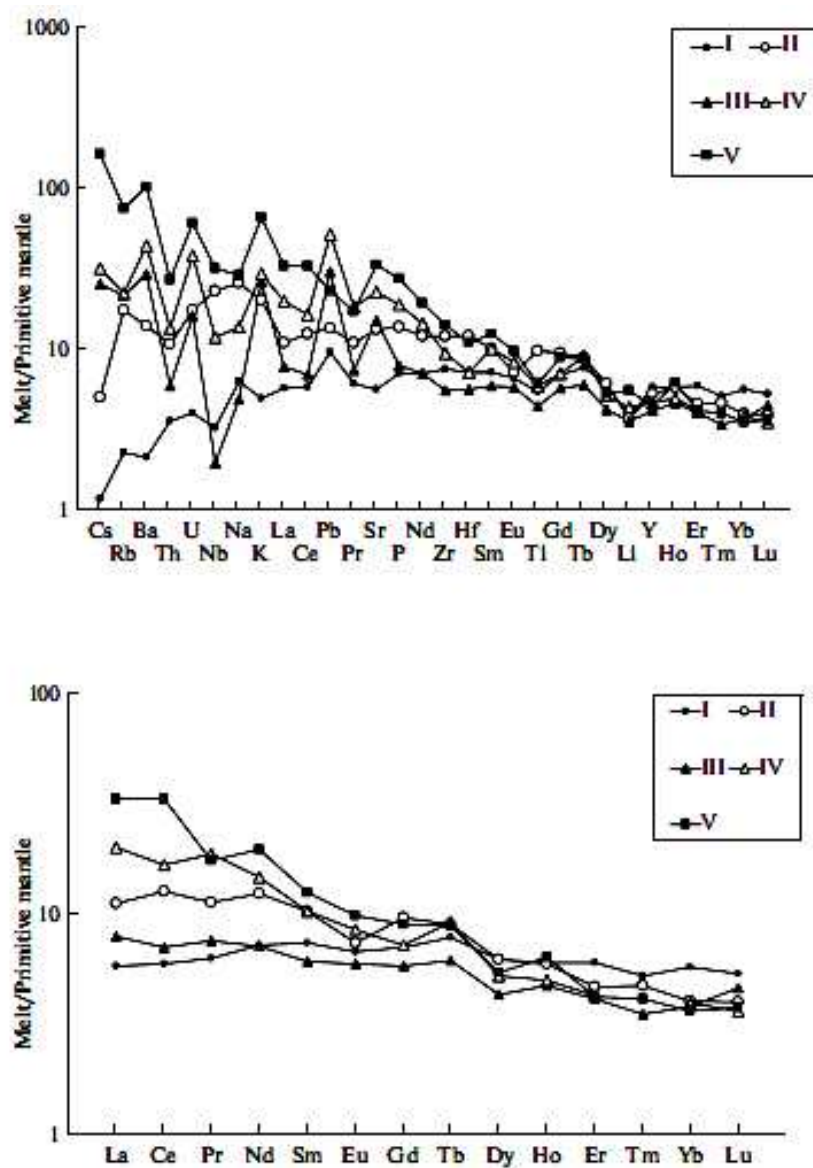


Fig. 6. Primitive mantle normalized [10] distribution patterns of trace and rare earth elements in the basic melts of (I) midoceanridges, (II) ocean islands, (III) island arcs, (IV) active continental margins, and (V) intracontinental rifts and continental hotspots.

that the relative contents of these elements are least affected by the processes of crustal contamination, modification of source composition under the influence of fluid and melt mass transfer, etc. Although minor, the differences in these parts of patterns are also interesting. The melts of mid-ocean ridges appear to be most enriched in these elements.

Table 3.

Mean contents of major, volatile, and trace elements in basic (40–54 wt % SiO₂) igneous melts from the main geodynamic settings (I–VI) according to the investigation of melt

Component	<i>n</i>	I	<i>n</i>	II	<i>n</i>	III
SiO ₂	4815	50.33 + 1.05/-1.03	5197	49.82 +2.49/-2.37	2468	50.59 +2.83/-2.68
TiO ₂	3593	1.22 +0.52/-0.36	4977	2.15 +0.97/-0.67	2385	0.98 +0.51/-0.34
Al ₂ O ₃	3522	15.53 + 1.28/-1.18	4988	13.92 + 1.60/-1.44	2385	16.08 +2.84/-2.41
FeO	3591	9.19 + 1.66/-1.40	5024	10.87 +2.34/-1.92	2390	8.63 +2.48/-1.93
MnO	2233	0.16 +0.06/-0.04	3878	0.17 +0.06/-0.05	1922	0.16 +0.10/-0.06
MgO	3869	7.80 + 1.54/-1.29	5111	7.27 +2.84/-2.04	2417	6.56 +4.19/-2.56
CaO	3522	11.53 + 1.271.43/-	4988	11.12 + 1.79/-1.54	2385	10.79 +2.92/-2.30
Na ₂ O	3575	2.68 +0.66/-0.53	4975	2.38 +0.64/-0.50	2385	2.64 + 1.03/-0.74
K ₂ O	4460	0.14 +0.30/-0.10	5029	0.57 +0.57/-0.28	2401	0.74 +0.86/-0.40
P ₂ O ₅	3074	0.15 +0.15/-0.08	4521	0.29 +0.26/-0.14	1959	0.17 +0.20/-0.09
H ₂ O	1216	0.29 +0.34/-0.16	1238	0.52 +0.68/- 0.29	1044	1.80 + 1.49/-0.82
Cl	1348	110 + 390/-90	1856	300 +620/-200	1459	960 +700/-400
F	395	150 +210/-90	1002	650 + 1110/-410	601	330 +480/-200
S	762	1000 +450/-310	2797	620 +1280/-420	1276	1350 + 1160/-620
CO ₂	479	160 +150/ - 80	848	100 +220/-70	194	250 +1180/- 200
Total		99.17		99.24		99.43
T, °C	541	1226 +43/-42	1051	1200 +60/-57	1014	1172 +84/-78
Li	453	6.13 + 1.82/-1.40	145	6.11 + 3.35/-2.16	478	5.88 +4.1 1/-2.42
Be	407	0.58 +0.38/- 0.23	78	0.69 +0.42 /-0.26	373	0.55 +0.21/-0.15
B	212	1.39 + 1.07/-0.61	224	1.70 + 1.80 /-0.87	582	12.85 +7.59/-4.77
Sc	730	38.30 + 5.17/-4.56	232	34.79 +12.36/-9.12	87	31.66 +19.72/ 12.15

Table 3. Continued

Component	<i>n</i>	IV	<i>n</i>	V	<i>n</i>	VI
SiO ₂	1304	49.64 +2.77/-2.62	2143	48.57 +3.82/-3.54	704	50.15 +2.19/-2.10
TiO ₂	1303	1.31 +0.48/-0.35	2077	1.36 + 1.20/-0.64	661	0.99 +0.61/-0.38
Al ₂ O ₃	1304	17.01 +2.99/-2.84	2107	15.42 +5.83/-4.23	661	15.07 +2.75/-2.32
FeO	1303	8.87 +3.19/-2.34	2091	8.41 +4.66/-3.00	661	8.13 +2.17/-1.71
MnO	1189	0.14 +0.09/-0.05	1551	0.16 +0.15/-0.08	520	0.15 +0.06/-0.04
MgO	1303	6.21 +2.86/-1.96	2080	5.07 +4.62/-2.42	683	7.83 +2.58/-1.94
CaO	1304	10.07 +2.15/-1.77	2108	9.61 +4.85/-3.22	661	11.92 +2.28/-1.92
Na ₂ O	1304	3.06 + 1.33/-0.93	2117	2.81 +2.77/-1.40	661	2.58 +0.63/-0.50
K ₂ O	1304	0.82 +0.69/-0.38	2143	1.84 +3.18/-1.16	683	0.74 + 1.90/-0.53
P ₂ O ₅	1227	0.40 +0.49/-0.22	1562	0.58 +0.93/-0.36	653	0.20 +0.20/-0.10
H ₂ O	430	1.96 +2.36/-1.07	550	1.64 +2.42/-0.98	196	0.92 +0.91/-0.46
Cl	1068	680 +920/-390	1187	2000 +7150/-1560	142	970 +960/-480
F	97	1160 +5880/-970	430	2090 +5650/-1530	35	80 +90/-40
S	1032	1170 + 1150/-580	964	1020 +2350/-710	103	790 + 550/-320
CO ₂	152	930 + 1550/-580	241	1330 + 1900/-780	39	420 +960 /-290
Total		99.89		96.11		98.91
T, °C	757	1207 +24/-23	982	1194 +69/-66	32	1181 +59/-57
Li	133	7.08 + 5.52/-3.10	175	9.11 + 18.60/-6.1 1	17	5.70 + 2.10/-1.53
Be	35	0.47 + 3.7/-0.21	139	4.04 +9.57/-2.84	11	0.54 +0.34/-0.21
B	102	10.21 + 10.30/-5.13	216	10.71 +37.6/-8.33	-	- -
Sc	137	27.77 +9.44/-7.04	105	33.45 +20.12/-12.6	54	40.59 +6.12/-5.32

Table 3. Continued

Component	<i>n</i>	I	<i>n</i>	II	<i>n</i>	III
V	619	268 + 8 8/-66	453	297 + 120/-86	203	314 +90/-70
Cr	1106	313 + 251/-139	1182	398 +533/-228	437	236 +609/-171
Co	324	44.1 +4.8/-4.4	87	50.5 + 10.0/-8.4	31	37.5 +25.3/-15.1
Ni	534	102 + 52/-35	464	148 +220/-88	61	59 +160/-43
Cl	371	73.0 + 14.6/-12.2	192	100.2 +60.8/-37.8	27	145.1 + 133.6/-69.6
Zn	351	80.2 +28.9/-21.3	206	108.0 +34.9/-26.4	18	71.8 +22.2/-16.9
Ga	341	17.8 + 1.9/-1.8	61	21.7 +2.6/-2.3	-	- -
Rb	719	1.52 + 3.11/-1.02	661	11.44 + 28.37/-8.15	184	14.2 + 32.3/-9.9
Sr	1078	127 +61/-41	1065	296 +403/-170	531	340 +266/-149
Y	1041	27.8 + 12.8/-8.8	940	25.2 + 13.3/-8.7	653	20.0 +6.4/-4.8
Zr	1153	89.6 +75.6/-41.0	1053	142 +180/-79	647	65.7 +43.7/-26.2
Nb	1029	2.47 +4.37/-1.58	897	17.1 +33.4/-11.3	621	1.49 + 1.50/-0.75
Mo	22	0.90 + 1.22/-0.52	-	- -	-	- -
Cs	336	0.04 +0.13/-0.03	110	0.17 +0.34/-0.11	118	0.85 +3.00/-0.66
Ba	973	15.9 +45.5/-11.8	932	102 +247 /-72	656	214 +256 /-116
La	1318	4.26 +5.28/-2.36	1096	8.11 +22.74/-5.98	647	5.76 +5.55/-2.82
Ce	1428	11.3 + 12.3/-5.9	939	24.0 + 74.0/-18.1	513	13.4 + 12.7/-6.5
Pr	285	1.76 + 1.20/-0.71	466	3.14 +2.14/-1.27	130	2.12 +2.49/-1.14

Table 3. Continued

Component	<i>n</i>	IV	<i>n</i>	V	<i>n</i>	VI
V	91	274 +67/-54	1 14	276 + 176/-108	104	265 +50/-42
Cr	56	125 +690/-106	491	482 +1722/-377	327	470 +675/-277
Co	-	- -	46	56.2 + 131.8/-39.4	60	44.6 +22.6/-15.0
Ni	-	- -	250	316 +717/-219	106	106 +7S/-44
Cl	24	209 + 1088/-175	31	646 + 1200/-420	92	102 +43/-30
Zn	21	117.3 +51.5/-35.8	27	88.4 +80.6/-42.2	39	68.8 +25.3/-18.5
Ga	-	- -	26	16.4 +2.7/-2.3	21	15.5 +2.3/-2.0
Rb	190	14.7 +40.3/-10.8	251	49.0 + 192.5/-39.1	166	3.27 + 3.54/-1.70
Sr	288	502 +427/-231	445	740 +1110/-444	172	182 +83/-57
Y	287	22.4 +S.6/-6.2	311	21.2 + 11.9/-7.6	167	21.3 + 16.4/-9.3
Zr	288	111 +134/-61	386	167 +271/-103	142	57.7 + 79.4/-33.4
Nb	235	8.89 + 10.48/-4.81	310	23.6 + 55.9/-16.6	142	0.82 + 1.15/-0.48
Mo	-	- -	-	- -	30	0.59 +0.33/-0.21
Cs	38	1.06 +2.93/-0.78	1 12	5.39 +15.12/-3.97	22	0.03 +0.11/-0.02
Ba	295	322 +493 /-195	470	740 +4230/-630	180	45.5 +42.0/-21.8
La	245	14.62 +23.61/-9.03	289	24.2 +64.4/-17.6	146	4.92 +4.09/-2.23
Ce	287	31.6 +54.1/-20.0	350	62.6 +109.1/-39.8	99	11.35 +9.29/-5.11
Pr	156	5.21 +7.71/-3.11	81	4.85 +3.03/-1.86	34	1.11 +0.66/-0.41

Table 3. Continued

Component	<i>n</i>	I	<i>n</i>	II	<i>n</i>	III
Nd	1 133	10.14 +6.43/-3.94	939	17.4 + 33.8/-11.5	505	10.09 +6.94/-4.11
Sm	1212	3.39 + 1.81/-1.18	955	4.72 + 5.35/-2.51	529	2.80 + 1.41/-0.94
Eu	1045	1.16 +0.52/-0.36	917	1.27 +1.12/-0.59	499	1.02 +0.49/-0.33
Gd	775	4.31 + 1.61/-1.17	669	5.86 + 3.08/-2.02	272	3.55 +1.64/-1.12
Tb	350	0.77 +0.27/-0.20	378	0.88 +0.23/-0.18	71	0.60 +0.20/-0.15
Dy	1032	4.72 +2.13/-1.47	937	4.73 + 2.79/-1.76	494	3.30 + 1.01/-0.77
Ho	274	1.00 +0.36/-0.26	464	0.99 +0.28/-0.22	69	0.79 +0.30/-0.22
Er	889	2.99 + 1.18/-0.85	840	2.31 +1.12/-0.76	494	2.04 +0.60/-0.47
Tm	228	0.42 +0.14/-0.10	378	0.38 +0.12/-0.09	93	0.28 +0.12/-0.08
Yb	1069	2.88 + 1.29/-0.89	1049	2.02 +0.88/-0.61	532	1.91 +0.66/-0.49
Lu	565	0.43 +0.15/-0.11	420	0.32 +0.12/-0.09	100	0.37 +0.21/-0.13
Hf	608	2.33 + 1.24/-0.81	485	3.92 + 2.63/-1.57	359	1.84 +0.92/-0.61
Ta	518	0.27 +0.48/-0.17	343	1.09 +1.12/-0.55	100	0.21 +0.27/-0.12
W	52	0.02 +0.02/-0.01	13	0.29 +0.46/-0.18	-	- -
Pb	459	0.69 +0.38/-0.24	380	0.96 +0.96/-0.48	324	2.13 +2.11/-1.06
Th	736	0.34 +0.71/-0.23	471	1.00 + 2.52/-0.72	542	0.56 +0.52/-0.27
U	588	0.09 +0.17/-0.06	450	0.39 +0.64/-0.24	400	0.36 +0.36/-0.18

Table 3. Continued

Component	<i>n</i>	IV	<i>n</i>	V	<i>n</i>	VI
Nd	228	20.6 + 29.0/-12.0	286	27.4 + 31.9/-14.8	172	9.61 +4.41/-3.02
Sm	210	4.72 +4.83/-2.39	325	5.78 +6.57/-3.07	186	2.68 + 1.10/-0.78
Eu	177	1.45 +0.83/-0.53	247	1.70 + 1.33/-0.75	131	0.94 +0.33/-0.24
Gd	177	4.39 + 2.95/-1.76	200	5.47 +4.82/-2.56	120	3.07 + 1.70/-1.09
Tb	15	0.90 +0.21/-0.17	79	0.87 +0.41/-0.28	21	0.73 +0.30/-0.21
Dy	196	3.98 + 1.86/-1.27	236	4.13 + 2.71/-1.64	99	4.08 + 1.97/-1.33
Ho	10	0.84 +0.20/-0.16	47	1.06 +0.22/-0.18	51	0.67 +0.31/-0.21
Er	203	2.11 +0.79/-0.58	202	2.10 +1.00/-0.68	100	2.50 + 1.32/-0.86
Tm	-	- -	30	0.33 +0.02/-0.02	60	0.21 +0.07/-0.05
Yb	211	1.97 +0.88/-0.61	281	1.82 +1.02/-0.66	146	1.97 + 1.26/-0.77
Lu	34	0.29 +0.29/-0.14	117	0.30 +0.11/-0.08	39	0.36 +0.28/-0.16
Hf	124	2.36 +1.51/-0.92	165	3.58 +4.17/-1.92	83	0.86 +0.36/-0.25
Ta	143	0.59 +0.38/-0.23	173	1.22 +2.99/-0.87	94	0.04 +0.06/-0.02
W	-	- -	-	- -	12	0.05 +0.02/-0.02
Pb	202	3.63 + 8.03/-2.50	113	1.62 + 3.44/-1.10	110	1.08 +0.66/-0.41
Th	193	1.27 + 2.43/-0.84	299	2.51 +8.07/-1.91	68	0.29 +0.32/-0.15
U	168	0.84 +1.49/-0.54	242	1.35 +4.02/-1.01	76	0.18 +0.15/-0.08

Note: In Tables 3–5, the contents of major oxides and water are in wt %, and other elements are in ppm; *n* is the number of determinations; geometric means are calculated under the condition that a particular determination does not deviate from the mean by more than 2σ with a probability of 95%; and the numbers beneath the mean values are standard deviations (the first number has to be added to, and the second number, subtracted from the mean).

(4) In general, an increase in the normalized element contents with increasing incompatibility mimics the character of element variations in the mean composition of the continental crust. However, a simple model based on the direct contamination of mantle melts (similar to the depleted melts of setting I) by crustal

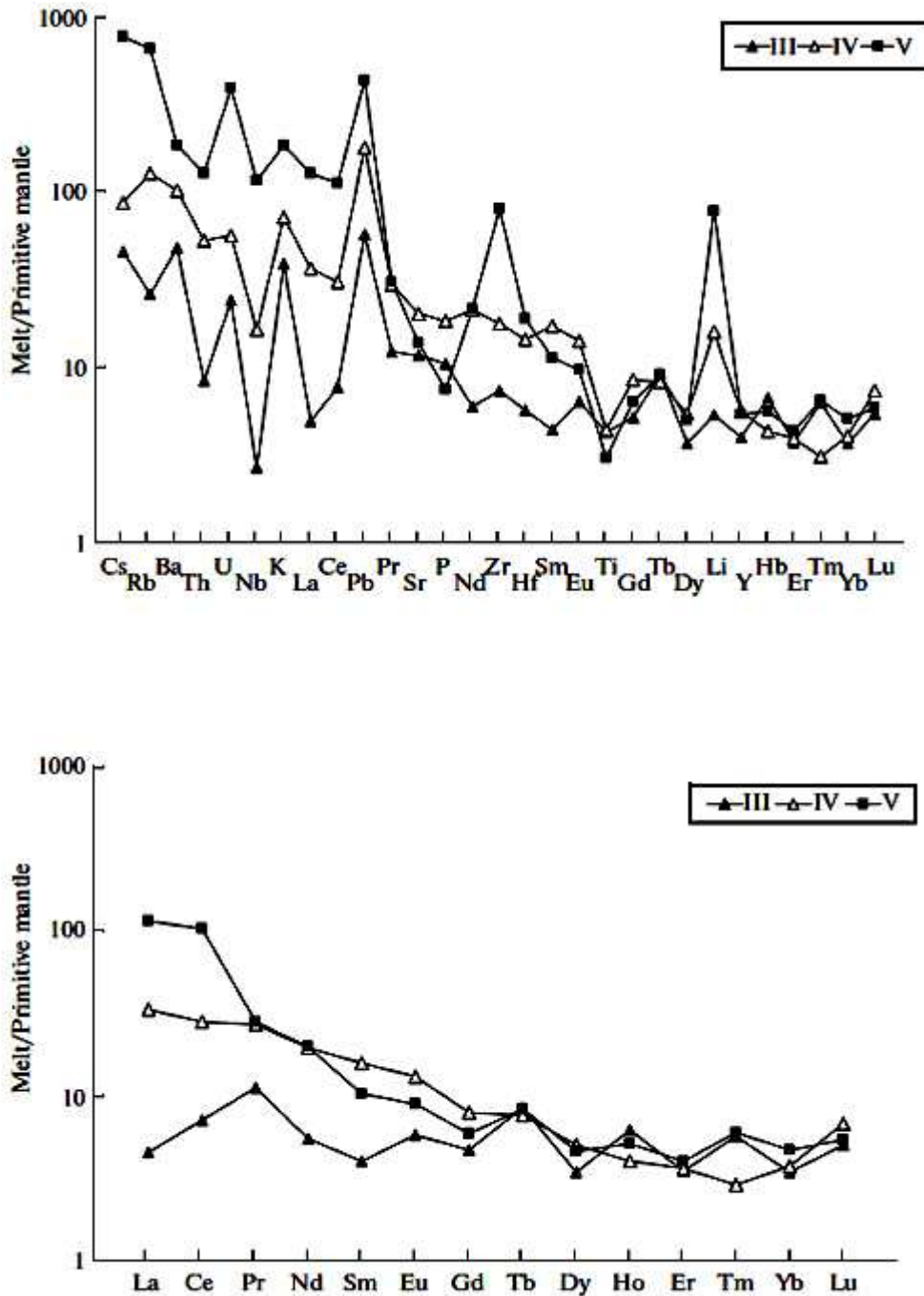


Fig. 7. Primitive mantle-normalized [10] distribution patterns of trace and rare earth elements in the intermediate melts of (III) island arcs, (IV) active continental margins, and (V) intracontinental rifts and continental hot spots.

Table 4.

Mean contents of major, volatile, and trace elements in intermediate (54–66 wt % SiO₂) igneous melts from the main geodynamic settings (I–VI) according to the investigation of melt inclusions in minerals and quenched glasses of volcanic rock

Component	n	I	n	II	n	III
SiO₂	59	56.52 +2.50/-2.40	349	58.57 +4.51/4.18	1520	57.84 +4.17/-3.89
TiO₂	55	1.57 + 1.26/-0.70	344	1.01 + 1.51/-0.61	1505	0.89 +0.81/-0.42
Al₂O₃	54	14.51 +5.48/-3.98	347	16.86 +4.56/-3.59	1511	15.23 +2.53/-2.17
FeO	55	7.96 +3.38/-2.37	349	3.98 +4.15/-2.03	1519	7.44 +4.36/-2.75
MnO	42	0.14 +0.06/-0.04	285	0.10 +0.22/-0.07	1054	0.16 +0.14/-0.08
MgO	59	4.33 +5.02/-2.32	348	1.72 +2.50/-1.02	1510	2.15 +2.40/-1.14
CaO	55	6.18 +5.51/-2.91	347	3.28 +4.89/-1.96	1511	6.38 + 3.19/-2.13
Na₂O	55	3.22 + 1.45/-1.00	344	4.41 +2.95/-1.77	1510	3.17 + 1.44/-0.99
K₂O	58	0.68 + 1.54/-0.47	349	2.09 +3.1/-1.25	1511	1.05 + 1.74/-0.65
P₂O₅	35	0.28 +0.39/-0.16	285	0.26 +0.52/-0.17	1056	0.21 +0.40/-0.14
H₂O	4	- -	47	1.58 + 3.43/-1.08	433	1.87 + 1.61/-0.87
Cl	20	2710	187	1430 +1980/-830	901	1450 + 1820/-810
F	0	- -	94	800 +1280/-490	322	380 + 960/-270
S	17	730 +700/-360	148	340 +620/-220	589	430 + 1070/-310
CO₂	0	- -	3	- -	41	70 +160/-50
Total		95.73		96.20		96.63
T, ° C	11	1250 0/0	60	1203 +55/-53	331	1134 +77/-72
Li	5	- -	15	4.76 + 1.91/-1.36	163	8.26 +6.29/-3.57
Be	4	- -	0	- -	142	0.54 +0.21/-0.15

Table 4. Continued

Component	n	IV	n	V	n	VI
SiO₂	698	60.92 + 5.50/-5.04	918	58.80 +3.58/-3.38	131	56.77 +2.98/-2.83
TiO₂	689	0.92 +0.90/-0.46	1097	0.64 + 1.07/-0.40	123	0.76 +0.41/-0.27
Al₂O₃	694	16.38 +2.36/-2.07	1 118	17.85 +5.75/-4.35	123	16.71 +3.04/-2.57
FeO	690	4.62 + 3.41/-1.96	1 114	2.56 +3.01/-1.38	123	6.23 +4.38/-2.57
MnO	562	0.10 +0.12/-0.05	845	0.12 +0.26/-0.08	106	0.13 +0.09/-0.05
MgO	683	2.05 +2.74/-1.17	1086	1.06 +4.47/-0.86	131	1.92 +2.22/-1.03
CaO	689	4.42 +3.68/-2.01	1 104	2.11 +2.89/-1.22	123	6.34 +2.53/-1.81
Na₂O	694	4.26 +1.75/-1.24	1 118	4.30 +3.35/-1.88	123	2.82 + 1.31/-0.89
K₂O	694	1.94 + 1.53/-0.86	1 118	4.94 +4.72/-2.41	112	0.81 +0.58/-0.34
P₂O₅	534	0.37 +0.40/-0.19	740	0.15 +0.74/-0.13	117	0.20 +0.20/-0.10
H₂O	312	1.65 +2.95/-1.06	264	1.61 +2.68/-1.00	77	1.55 +0.37/-0.30
Cl	286	1140 +1820/-700	799	2850 +6330/-1970	76	2410 +950/-680
F	114	3360 + 16690/-2800	414	3630 +7010/-2390	53	140 +2020/-130
S	177	460 +1850/-370	415	370 +690/-240	25	430 +1560/-340
CO₂	34	1790 + 9720/-1510	4	- -	3	- -
Total		98.31		94.83		94.53
T, ° C	123	1144 +96/-8S	414	1124 +167/-145	1	- -
Li	40	24.50 +36.64/-14.68	60	120 +905/-106	0	- -
Be	18	1.88 +6.03/-1.43	48	15.7 +98.5/-13.6	3	- -

Table 4. Continued

Component	n	I	n	II	n	III
B	3	-	15	2.15 +0.60/-0.47	164	18.2 +22.1/-10.0
Sc	15	36.7 + 5.53/-4.81	4	-	30	21.5 +32.6/-12.9
V	6	-	11	27.8 +328/-25.6	87	271 + 530/-179
Cr	6	-	41	284 +1002/-222	198	170 + 735/-138
Co	1	-	2	-	16	24.8 + 15.9/-9.7
Ni	1	-	45	222 +353/-136	38	43.0 +295/-37.5
Cu	1	-	8	-	13	93.6 +285/-70.5
Zn	11	-	14	150 +99/-60	13	77.7 + 12.1/-10.4
Rb	15	7.31 +28.22/-5.81	21	33 +276/-29	102	16.3 +58.2/-12.7
Sr	18	187 +208/-98	36	341 +258/-147	174	250 +490/-166
Y	18	16.8 + 12.0/-7.0	21	34.6 +48.5/-20.2	159	18.0 +22.2/-10.0
Zr	18	130 +232/-83	36	252 +798/-191	157	82.7 + 147.1/-52.9
Nb	16	8.73 +37.05/-7.07	36	23.3 + 106.3/-19.1	151	1.90 +3.34/-1.21
Mo	-	-	-	-	-	-
Sn	-	-	-	-	-	-
Cs	4	-	5	-	35	1.46 +6.37/-1.19
Ba	17	63.7 +370/-54.3	47	245 +1125/-201	196	338 +1936/-288
La	19	6.65 + 16.40/-4.73	32	21.4 +107.7/-17.8	160	3.46 +9.06/-2.50
Ce	19	14.8 +27.0/-9.6	22	142 +393/-104	164	14.2 + 54.4/-11.3

Table 4. Continued

Component	<i>n</i>	IV	<i>n</i>	V	<i>n</i>	VI
B	42	36.9 +78.2/-25.1	59	84 +539/-72	0	- -
Sc	20	15.23 +6.03/-4.32	23	2.90 +3.84/-1.65	14	22.4 + 13.4/-8.4
V	36	167 + 194/-90	27	42.3 + 171.3/-34.0	12	290 +159/-103
Cr	46	151 +1958/-141	88	149 +-1532/-135	25	43.7 +223.9/-36.6
Co	12	14.5 + 16.7/-7.8	24	1.66 +2.02/-0.91	10	29.0 +7.11/-5.71
Ni	8	- -	45	101 +4720/-99	18	13.0 + 18.8/-7.7
Cu	72	197 +358/-127	6	- -	27	56.3 + 116/-37.9
Zn	54	69.3 +40.2/-25.4	14	107.0 +68.8/-41.9	13	81.0 +77.0/-39.4
Rb	119	80.1 + 159/-53.3	89	414 +3030/-364	18	9.42 +7.82/-4.28
Sr	117	429 + 304/-178	187	292 +2180/-258	20	168 +231/-97
Y	111	25.2 +25.3/-12.6	81	24.5 +65.8/-17.8	19	30.2 + 17.4/-11.0
Zr	115	199 +146/-84	182	900 +3486/-716	20	106.4 +95.8/-50.4
Nb	114	11.7 + 16.9/-6.9	90	83.2 + 166.9/-55.5	34	1.30 +1.26/-0.64
Mo	12	1.78 +2.48/-1.04	16	3.15 +5.18/-1.96	5	- -
Sn	-	- -	19	22.7 +208.2/-20.4	-	- -
Cs	87	2.76 +4.85/-1.76	64	24.8 +684/-23.9	8	- -
Ba	137	719 +415/-263	206	1293 -	34	140 + 172/-77
La	104	25.9 + 18.9/-10.9	108	90.1 +406/-73.7	16	5.78 +9.00/-3.52
Ce	111	56.4 +40.6/-23.6	133	208 +754/-163	15	21.1 +35.0/-13.2

Table 4. Continued

Component	<i>n</i>	I	<i>n</i>	II	<i>n</i>	III
Pr	6	- -	10	4.22 +7.40/-2.69	41	3.32 +6.48/-2.20
Nd	17	8.31 +7.54/-3.95	22	56.5 + 148/-40.8	151	8.14 + 17.70/-5.57
Sm	17	1.95 + 1.47/-0.84	22	10.2 + 18.5/-6.6	147	1.94 +2.48/-1.09
Eu	17	0.93 +0.58/-0.36	22	2.26 +2.40/-1.16	131	1.05 + 1.08/-0.53
Gd	17	2.36 + 2.28/ 1.16	20	8.56 + 13.84/-5.29	83	3.02 + 1.97/-1.19
Tb	5	- -	7	- -	31	0.87 +0.30/-0.22
Dy	17	2.62 +2.51/-1.28	22	7.05 +8.95/-3.94	145	2.72 +2.47/-1.29
Ho	7	- -	10	0.99 +0.76/-0.43	28	1.08 +0.29/-0.23
Er	18	1.55 + 1.04/-0.62	21	3.07 +3.05/-1.53	133	1.80 + 1.24/-0.74
Tm	5	- -	5	- -	18	0.48 +0.16/-0.12
Yb	18	1.88 + 1.49/-0.83	32	2.25 + 1.55/-0.92	152	1.78 + 1.35/-0.77
Lu	9	- -	8	- -	52	0.42 +0.38/-0.20
Hf	9	- -	6	- -	80	1.75 + 1.52/-0.81
Ta	6	- -	6	- -	48	0.31 +0.92/-0.23
Pb	11	1.10 + 1.89/-0.69	15	5.25 +27.46/-4.41	70	3.90 +4.63/-2.12
Th	14	1.20 + 3.49/-0.89	6	- -	101	0.74 + 1.16/-0.45
U	10	0.82 + 1.63/-0.55	6	- -	64	0.51 +0.51/-0.25

Table 4. Continued

Component	<i>n</i>	IV	<i>n</i>	V	<i>n</i>	VI
Pr	20	8.06 +6.86/-3.71	50	8.30 +28.67/-6.44	14	2.44 +2.34/-1.19
Nd	90	29.0 +21.6/-12.4	76	29.5 +86.8/-22.0	17	13.4 + 16.6/-7.4
Sm	52	7.69 +6.68/-3.58	82	5.00 + 15.88/-3.80	17	3.18 +2.02/-1.24
Eu	49	2.37 + 1.35/-0.86	70	1.61 +2.26/-1.08	15	1.10 +0.29/-0.23
Gd	31	5.04 +2.60/-1.72	46	3.76 +8.46/-2.60	14	2.99 + 2.19/-1.26
Tb	20	0.78 +0.30/-0.22	48	0.86 +2.53/-0.64	13	0.64 +0.34/-0.22
Dy	30	4.00 + 1.84/-1.26	75	3.68 +7.31/-2.45	10	3.36 +3.80/-1.78
Ho	12	0.70 +0.38/-0.25	47	0.90 +2.66/-0.67	13	0.99 +0.60/-0.38
Er	28	1.88 +0.66/-0.49	67	2.08 +3.87/-1.35	15	2.54 + 1.68/-1.01
Tm	14	0.24 +0.07/-0.05	25	0.50 + 1.33/-0.36	6	- -
Yb	66	1.96 + 1.80/-0.94	76	2.44 +4.56/-1.59	15	2.63 +2.06/-1.15
Lu	26	0.57 +0.67/-0.31	51	0.45 +0.94/-0.30	14	0.64 +0.59/-0.31
Hf	25	4.47 +5.44/-2.48	45	5.82 +7.97/-3.36	14	2.30 +2.51/-1.20
Ta	49	0.97 + 1.74/-0.62	35	8.33 +27.72/-6.29	22	0.06 +0.03/-0.02
Pb	73	12.21 +7.27/-4.86	21	29.5 +94.0/-22.5	28	2.45 +2.58/-1.26
Th	76	4.72 +6.90/-2.80	69	11.38 +21.64/-7.46	28	0.70 +0.40/-0.26
U	66	1.21 + 1.41/-0.65	56	8.34 +20.99/-5.67	28	0.45 +0.47/-0.23

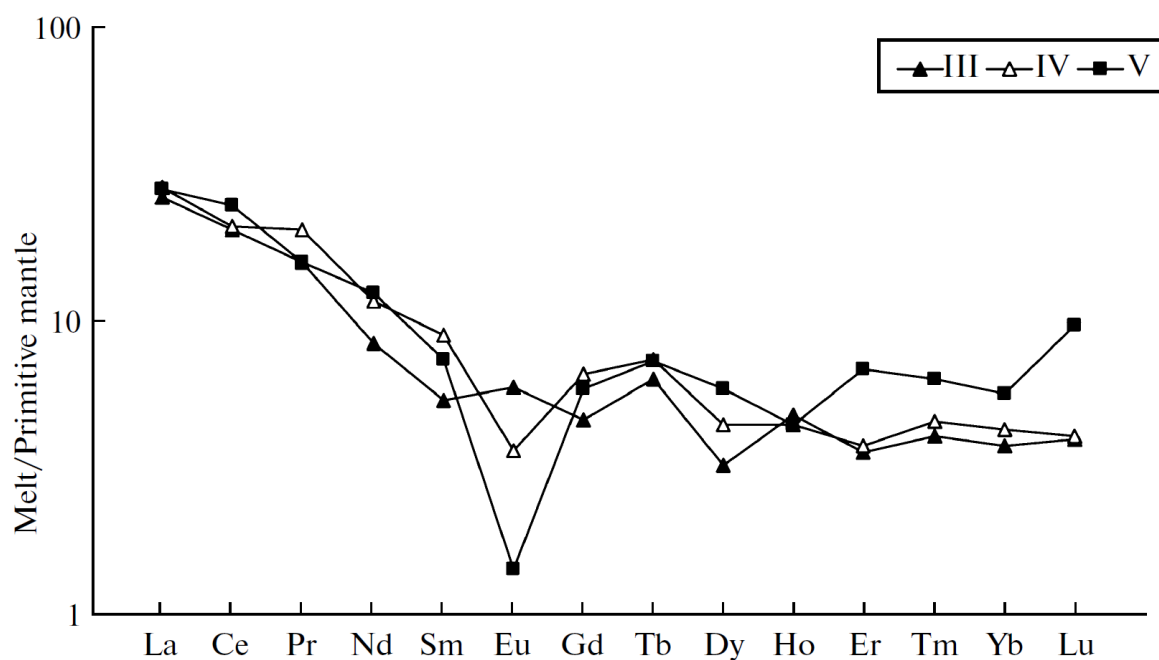
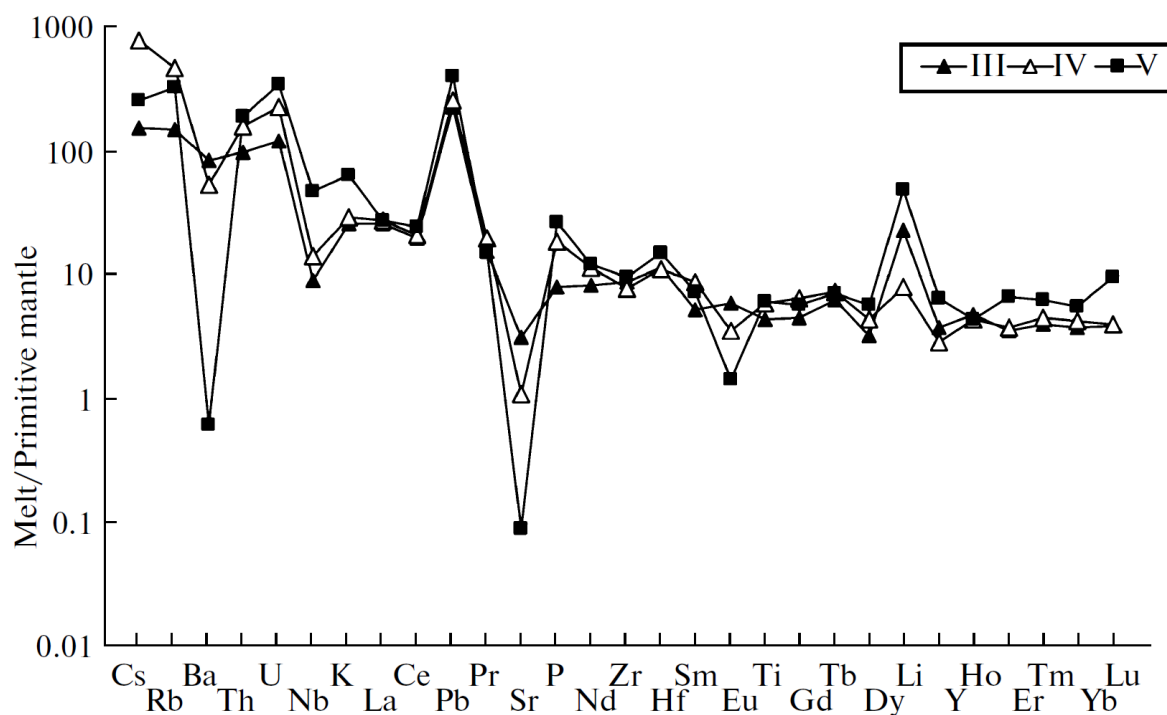


Fig. 8. Primitive mantle-normalized [10] distribution patterns of trace and rare earth elements in the acidic melts of (III) island arcs, (IV) active continental margins, and (V) intracontinental rifts and continental hot spots.

Table 5.

Mean contents of major, volatile, and trace elements in acidic ($\text{SiO}_2 > 66$ wt %) igneous melts from the main geodynamic settings (II–VI) according to the investigation of melt inclusions in minerals and quenched glasses of volcanic rocks

Component	<i>n</i>	II	<i>n</i>	III	<i>n</i>
SiO ₂	205	70.48 +2.35/-2.28	3364	73.40 +3.33/-3.18	2856
TiO ₂	201	0.29 +0.21/—0.12	3155	0.28 +0.58/-0.19	2429
Al ₂ O ₃	205	12.97 +2.98/-2.43	3277	12.57 + 1.52/-1.36	2694
FeO	205	3.29 + 1.29/-0.93	3283	1.35 + 1.04/-0.59	2419
MnO	172	0.12 +0.08/-0.05	2088	0.06 +0.10/-0.04	1688
MgO	205	0.12 +0.90/-0.11	3138	0.23 +0.54/-0.16	2397
CaO	205	1.20 + 1.93/-0.74	3303	1.16 +0.75/-0.46	2665
Na ₂ O	203	5.11 + 1.44/-1.12	3275	3.72 + 1.1 1/-0.85	2678
K ₂ O	205	3.21 + 1.46/-1.00	3292	3.05 + 1.30/-0.91	2727
P ₂ O ₅	102	0.05 +0.27/-0.04	1135	0.06 +0.17/-0.04	1521
H ₂ O	31	1.72 +3.66/-1.17	1131	2.39 +2.84/-1.30	1576
Cl	102	2330 +2860/-1280	2050	1110 + 1820/-690	912
F	82	1150 +3330/-860	667	320 +400/-180	555
S	73	130 + 200/-80	535	120 +250/-80	367
CO ₂	1	- -	168	90 +120/-50	323
Total		98.92		98.43	
T, °C	1	- -	483	989 +206/-170	599
Li	13	61.4 +73.4/-33.4	694	38.2 +62.0/-23.7	435
Be	13	12.49 + 1.92/-1.66	410	1.22 +0.99/-0.55	156

Table 5. Continued

Component	IV	<i>n</i>	V	<i>n</i>	VI
SiO₂	72.71 + 3.28/-3.14	2123	73.82 +2.88/-2.77	61	68.89 +3.39/-3.24
TiO₂	0.19 +0.57/-0.14	1751	0.10 +0.17/-0.06	60	0.59 +0.26/-0.18
Al₂O₃	13.40 +2.28/-1.95	2017	12.16 + 1.92/-1.66	60	13.70 + 1.76/-1.56
FeO	1.11 + 1.34/-0.61	2009	0.98 + 1.32/-0.56	60	3.84 + 1.74/-1.20
MnO	0.05 +0.10/-0.03	1301	0.04 +0.12/-0.03	55	0.10 +0.14/-0.06
MgO	0.19 +0.68/-0.15	1934	0.04 +0.07/-0.02	61	0.87 + 1.14/-0.49
CaO	0.97 + 1.35/-0.56	1855	0.40 +0.42/-0.20	60	2.73 + 1.35/-0.90
Na₂O	3.66 + 1.74/-1.18	2014	3.91 + 1.38/-1.02	60	3.36 + 1.34/-0.96
K₂O	4.06 + 1.87/-1.28	2017	4.54 + 1.05/-0.85	61	1.61 +0.56/-0.42
P₂O₅	0.07 +0.26/-0.06	812	0.03 +0.05/-0.02	47	0.11 +0.12/-0.06
H₂O	2.06 + 2.20/-1.06	1385	2.58 + 2.78/-1.34	36	1.41 +0.48/-0.36
Cl	1280 +1160/610	1230	1680 +2580/-1020	41	5110 +2160/-1520
F	870 +2480/-640	1376	2080 +7730/-1640	11	520 +1090/-350
S	90 +270/-70	197	70 +160/-50	11	40 +240/-40
CO₂	20 +50/-10	155	140 +310/-100	1	- -
Total	98.70		99.00		97.77
T, °C	898 +129/-113	807	840 +210/-168	-	- -
Li	13.3 +45.2/-10.3	922	80.6 + 174.2/-55.1	-	- -
Be	2.40 +2.16/-1.14	540	7.38 + 10.97/-4.41	-	- -

Table 5. Continued

Component	<i>n</i>	II	<i>n</i>	III	<i>n</i>
B	13	17.75 +3.91/-3.20	673	31.0 +36.2/-16.7	441
Sc	3	- -	191	4.39 + 2.40/-1.55	38
V	3	- -	224	5.71 + 8.02/-3.34	19
Cr	12	421 +1059/-301	130	2.15 +4.19/-1.42	64
Co	-	- -	44	1.78 + 1.64/-0.86	8
Ni	3	- -	52	1.60 + 1.83/-0.85	5
Cu	-	- -	63	27.5 +40.3/-16.3	399
Zn	2	- -	57	54.0 + 38.5/-22.5	364
Ga	-	- -	43	16.73 + 3.63/-2.98	29
As	-	- -	18	8.32 +4.27/-2.82	258
Rb	18	170 +84/-56	745	100 +87/-46	677
Sr	20	4.99 + 122.2/-4.8	792	71.3 + 84.1/-38.6	644
Y	19	76.6 + 382.6/-63.8	711	18.1 + 12.3/-7.3	365
Zr	20	1600 +2311/-945	704	105.0 +79.7/-45.3	427
Nb	19	190 +409/-129	783	6.78 +4.70/-2.78	334
Mo	-	- -	131	1.52 +0.63/-0.45	275
Sn	13	42.73 +7.88/-6.65	10	2.08 + 1.35/-0.82	276
Sb	-	- -	16	0.84 +0.57/-0.34	233
Cs	16	3.42 +4.03/-1.85	236	5.26 + 3.06/-1.94	349
Ba	6	- -	825	619 +528/-285	508
La	7	- -	768	19.4 + 13.2/-7.8	341

Table 5. Continued

Component	IV	<i>n</i>	V	<i>n</i>	VI
B	77.0 +466/-66.1	929	40.1 +45.1/21.2	-	- -
Sc	7.23 + 1 1.28/-4.40	237	2.74 + 1.74/-1.06	13	10.42 +4.56/-3.17
V	21.4 + 150.8/-18.8	287	4.08 +2.08/-1.38	-	- -
Cr	3.75 + 12.07/-2.86	100	3.04 + 5.02/-1.89	12	5.01 +2.35/-1.60
Co	- -	22	0.65 + 1.30/-0.43	-	- -
Ni	- -	14	4.08 37.50/-3.68	-	- -
Cu	25.9 + 50.7/-17.1	64	92.8 + 1002/-84.9	34	19.3 + 17.0/-9.0
Zn	45.0 + 38.6/-20.8	38	1 1.4 +212/-10.8	13	18.7 +40.7/-12.8
Ga	22.54 + 14.31/-8.75	16	61.6 +55.2/-29.1	-	- -
As	1200 -	12	88.9 +258.S/-66.2	13	1.35 + 1.23/-0.64
Rb	317 +1451/-260	803	217 +230/-112	14	9.9 +32.9/-7.6
Sr	24.3 +337/-22.7	873	2.01 +4.22/-1.36	14	305 +72/-58
Y	13.7 + 17.8/-7.7	830	31.3 +66.0/-21.2	13	31.4 + 12.1/-8.7
Zr	92.9 + 148.0/-57.1	770	113 +179/-69	13	106 +38/-28
Nb	10.7 + 10.6/-5.3	871	36.3 +76.9/-24.6	34	1.61 +0.47/-0.36
Mo	21.8 +81.3/-17.2	173	4.88 +5.17/-2.51	12	0.86 +0.41/-0.28
Sn	207 +808/-165	178	23.0 +42.8/-14.9	-	- -
Sb	316 +1710/-267	21	1.08 +8.18/-0.95	-	- -
Cs	26.8 + 1137/-26.2	401	8.66 +21.78/-6.19	-	- -
Ba	398 +1065/-290	739	4.49 +20.59/-3.68	35	376 + 150/-107
La	20.9 + 13.9/-8.3	475	20.7 +28.9/-12.0	14	11.0 + 13.6/-6.1

Table 5. Continued

Component	<i>n</i>	II	<i>n</i>	III	<i>n</i>
Ce	20	172 +178/-88	800	39.1 +27.3/-16.1	385
Pr	2	- -	243	4.46 +4.67/-2.28	75
Nd	7	- -	396	12.0 + 10.5/-5.6	225
Sm	7	- -	398	2.50 + 2.12/-1.15	106
Eu	6	- -	341	1.03 + 3.18/-0.78	100
Gd	6	- -	144	2.83 +3.50/-1.56	77
Tb	2	- -	87	0.63 +0.54/-0.29	43
Dy	7	- -	268	2.49 +2.66/-1.29	90
Ho	2	- -	84	0.81 +0.79/-0.40	34
Er	3	- -	249	1.79 + 1.56/-0.83	89
Tm	2	- -	83	0.33 +0.64/-0.22	25
Yb	19	4.41 + 21.04/-3.65	274	1.90 + 1.87/-0.94	127
Lu	-	- -	86	0.32 +0.67/-0.22	61
Hf	-	- -	101	3.77 + 2.55/-1.52	73
Ta	12	19.68 +3.12/-2.70	162	0.83 +0.79/-0.40	229
W	-	- -	4	- -	230
Pb	-	- -	324	16.2 +11.0/-6.6	180
Bi	-	- -	2	- -	225
Th	13	14.83 +6.98/-4.75	390	9.26 + 16.98/-5.99	268
U	13	4.38 + 1.27/-0.98	339	2.70 +2.38/-1.27	299

Table 5. Continued

Component	IV	n	V	n	VI
Ce	40.4 +27.4/-16.3	786	47.3 +44.4/-22.9	14	25.7 +27.2/-13.2
Pr	5.76 + 3.18/-2.05	275	4.51 +3.31/-1.91	13	1.95 + 1.62/-0.88
Nd	16.7 + 13.5/-7.5	448	17.7 +22.1/-9.8	14	17.6 + 15.4/-8.2
Sm	4.17 + 3.14/-1.79	397	3.43 +5.40/-2.10	14	3.54 +2.82/-1.57
Eu	0.63 +0.82/-0.36	377	0.25 + 1.20/-0.20	14	1.24 +0.27/-0.22
Gd	4.04 +2.62/-1.59	257	3.60 +6.13/-2.27	14	4.67 + 1.89/-1.35
Tb	0.73 +0.51/-0.30	170	0.72 +0.70/-0.38	13	0.82 +0.24/-0.18
Dy	3.39 +2.86/-1.55	298	4.50 +9.71/-3.08	1	- -
Ho	0.75 +0.34/-0.24	154	0.75 +0.64/-0.35	13	1.18 +0.40/-0.30
Er	1.89 + 1.60/-0.87	281	3.43 +7.46/-2.35	14	2.62 + 1.13/-0.79
Tm	0.37 +0.29/-0.16	147	0.51 +0.49/-0.25	-	- -
Yb	2.17 + 2.29/ 1.12	316	2.87 +6.12/-1.95	14	2.89 + 1.86/-1.13
Lu	0.33 +0.20/-0.13	206	0.78 + 1.65/-0.53	13	0.46 +0.58/-0.26
Hf	3.66 + 3.84/-1.88	267	4.90 +8.06/-3.05	13	3.06 +1.10/-0.81
Ta	12.0 +274/-11.5	111	7.10 + 19.06/-5.17	21	0.11 +0.03/-0.02
W	60.8 +99.1/-37.7	55	11.1 +27.6/-7.9	-	- -
Pb	18.6 + 11.8/-7.2	300	29.1 +30.7/-14.9	35	5.38 +3.28/-2.04
Bi	8.24 +27.53/-6.34	15	2.89 + 14.87/-2.42	-	- -
Th	15.02 +20.94/-8.75	817	18.11 + 14.62/-8.09	34	1.22 +0.40/-0.30
U	5.17 +7.84/-3.11	533	7.91 + .97/-3.4	34	0.84 +0.30/-0.22

materials is implausible, because the mean contents of the most incompatible elements in the basic melts are higher than those in the continental crust (for instance, the mean Ba content is 645 ppm in the continental crust [18] and 740 ppm in the melts of setting V). The formation of small portions of strongly enriched mobile melts or fluids modifying the compositions of mantle sources and (or) mantle magmas is probably a more viable model [19].

(5) The melts related to continental margin environments (III and IV) are distinguished by strong variations in the left parts of the trace element distribution patterns, which are usually described in terms of geochemical anomalies. A spectacular example of such anomalies is the well-known negative Ta–Nb anomaly. Its origin is still disputable. Perhaps, Nb and Ta were retained in the solid residue during melting. These elements are selectively concentrated, for instance, in rutile, but basic melts in equilibrium with rutile must be significantly enriched in Ti, which is not observed.

Table 6.

Mean contents of trace elements (ppb) in basic (40–54 wt % SiO₂) igneous melts from the main geodynamic settings (I–VI) according to the investigation of inclusions in minerals and quenched glasses of volcanic rocks

Element	Geodynamic setting	<i>n</i>	Average content	2σ
Re	I	34	0.97	+0.37/-0.27
Re	II	16	0.80	+0.55/-0.32
Re	III	30	1.32	+0.68/-0.45
Re	VI	55	1.03	+0.81/-0.45
Pt	I	23	0.23	+0.39/-0.14
Pt	II	15	5.04	+3.52/-2.08
Ir	I	22	0.03	+0.05/-0.02
Ir	V	20	4.35	+5.53/-2.43
Pd	I	24	0.66	+ 1.55/-0.48
Os	I	34	0.004	+0.005/-0.002
Cd	II	15	122	+27/-22
Ru	I	27	0.03	+0.07/-0.02
Br	I	56	280	+450/-170
Tl	I	26	15.8	+21.9/-9.2

(6) Another intriguing feature of melts from settings III and IV is the positive Pb anomaly (high Pb/Ce ratio). The nature of this anomaly is also controversial. During crystallization of silicate minerals from a melt, both Pb and Ce are strongly incompatible. The fractionation of these elements is possible in the presence of a sulfide phase, because Pb is a typical chalcophile element [20]. However, sulfide phases are common in the basic magmas of all settings, whereas a Pb anomaly is distinctly observed only in two of them. Another possible

Table 7.

Ratios of components in basic (40–54 wt % SiO₂) igneous rocks from the main geodynamic settings (I–VI) according to the investigation of melt inclusions in minerals and quenched glasses of volcanic rocks

Ratio	<i>n</i>	I	<i>n</i>	II	<i>n</i>	III	<i>n</i>	IV	<i>n</i>	V	<i>n</i>	VI
H ₂ O/ Ce	649	190 +80/- 50	204	130 +130/- 60	300	1310 +3040/- 910	124	950 +4100/- 770	152	70 +520/- 60	63	880 +1000/- 470
Ce/Pb	421	23.1 +8.4/- 6.2	378	25.6 +16.8/- 10.1	251	6.2 +3.8/- 2.3	172	7.4 +6.1/-3.3	116	32.3 +15.5/- 7.1	69	14.9 +9.9/- 6.0
K ₂ O/ H ₂ O	1177	0.6 +0.4/- 0.2	1194	1.0 +1.5/- 0.6	872	0.4 +0.7/- 0.2	429	0.7 +1.9/-0.5	553	1.9 +4.2/- 1.3	196	0.3 +0.2/- 0.10
K ₂ O/ CL	1288	11.7 + 18.4/- 7.1	1855	22.6 +26.7/- 12.2	1459	7.9 +8.3/- 4.1	1068	14.5 +13.4/-7.0	1219	14.7 +24.0/- 9.1	142	3.2 +2.3/- 1.3
La/Yb	1028	1.2 +1.1/- 0.6	1044	2.7 +5.1/- 1.8	526	2.4 +2.4/- 1.2	211	6.1 +10.0/-3.8	236	13.9 +36.0/- 10.0	123	1.6 +1.5/- 0.8
Nb/U	477	42.7 + 10.7/- 8.5	446	50.7 +14.0/- 11.0	391	5.4 +3.1/- 2.0	164	12.8 +18.0/-7.5	222	25.4 +49.6/- 16.8	76	2.3 +1.4/- 0.9
Nb/Yb	733	1.1 +2.2/- 0.7	835	6.0 +8.8/- 3.6	494	0.9 +0.6/- 0.4	208	3.7 +5.2/-2.2	257	11.6 +36.5/- 8.8	78	0.4 +0.2/- 0.2
Zr/Nb	892	24.2 +38.3/- 14.8	897	8.8 +6.6/- 3.8	616	38.1 +20.2/- 13.2	235	17.9 +20.3/-9.5	313	6.4 +8.9/- 3.7	132	47.1 +58.4/- 26.1
Th/Ta	503	1.0 +0.3/- 0.2	343	1.0 +0.4/- 0.3	100	6.6 +12.6/- 4.3	129	2.8 +5.9/-1.9	170	1.4 +1.0/- 0.6	64	3.9 +16.4/- 3.1
Th/Yb	632	0.1 +0.2/- 0.1	464	0.6 +0.9/- 0.4	421	0.3 +0.4/- 0.2	167	0.7 +1.2/-0.4	255	1.5 +4.0/- 1.1	41	0.1 +0.6/- 0.1
Th/U	578	2.7 +0.8/- 0.6	463	3.5 +1.4/- 1.0	343	1.7 +1.0/- 0.6	171	2.5 +1.2/-0.8	248	3.4 +1.4/- 1.0	48	2.6 +0.8/- 0.6
Ba/Rb	636	11.1 +2.9/- 2.3	629	11.4 +5.2/- 3.6	184	13.5 +8.8/- 5.3	190	28.0 +28.6/- 24.2	194	11.1 +8.7/- 4.9	165	10.5 +6.2/- 3.9
P ₂ O ₅ /F	309	7.6 +5.0/- 3.0	1000	5.3 +3.8/- 2.2	527	4.0 +4.2/- 2.0	95	4.2 +5.0/-2.3	412	2.6 +8.4/- 2.0	-	-
TiO ₂ / Dy	1030	2800 +840/- 650	929	4100 +1900/- 1300	494	2900 +750/- 600	196	3400 +1000/- 790	239	3300 +2700/- 1500	99	2700 +490/- 420

Note: The ratios were calculated as geometric means under the condition that a particular value does not deviate from the mean by more than 2σ with a probability of 95%; the numbers beneath the mean values are standard deviations (the first number has to be added to, and the second number, subtracted from the mean).

mechanism of magma (or source) enrichment in Pb relative to Ce is mass transfer with an aqueous fluid [21]. Note that a Pb anomaly is also characteristic of intermediate and acidic melts, and in the latter it is even more pronounced than the Nb anomaly Table 7 shows some mean ratios of components in the magmas of various settings. This information provides a quantitative illustration to the conclusions drawn on the basis of the examination of the spidergrams. First, there are rather significant variations in the ratios of basic melts. In many cases, the variation ranges overlap to a large extent, and there is a group of ratios showing very minor variations between settings. Among them are K_2O/Cl , Th/U , P_2O_5/F , and TiO_2/Dy . These ratios are insensitive to geodynamic settings, and their significant variations are probably related to local processes. Other ratios are more setting specific, but it should be noted that there is no ratio that could have been used for the unequivocal assignment of a particular composition to one of the five settings. Moreover, with respect to many parameters, the settings are combined into larger groups, the differences within which are insignificant. For instance, settings related to plate boundaries (III and IV) are significantly different from settings related to mantle plumes with respect to the Ce/Pb , Nb/U , Zr/Nb , and Th/Ta ratios. Setting I is similar to plume settings in some parameters (e.g., Th/Ta) and to settings III and IV in other parameters (e.g., Zr/Nb). Setting I is significantly different from all other settings in showing very low La/Yb and Th/Yb values (these ratios can be used as indicators of the depleted mantle). It is remarkable that this depletion is not accompanied by significant changes in the ratios of strongly incompatible elements: for instance, the H_2O/Ce and Ce/Pb ratios are similar in settings I and II but significantly different from those of settings III and IV. The quantitative interpretation of these differences is a difficult problem, because they could be related to the redistribution of components under the influence of melts and fluids formed under various thermodynamic conditions. Some differences could probably be inherited from the early stages of the evolution of geospheres. In this context, it would be interesting to track time variations in element ratios in melts of similar compositions, but such data are still very rare for ancient complexes.

CONCLUSIONS

(1) We compiled a database containing more than 480 000 determinations for 73 elements in melt inclusions in minerals and quenched glasses of volcanic rocks. Using this database, we estimated the mean contents of major, volatile, and trace elements in igneous melts from main geodynamic settings.

(1) Six main geodynamic settings were distinguished: (I) oceanic spreading zones (mid-ocean ridges); (II) regions of mantle plume activity within oceanic plates (oceanic islands and plateaus); (III) and (IV) environments related to subduction processes, including (III) zones of island-arc magmatism formed on the oceanic crust and (IV) magmatic zones of active continental margins, where the

continental crust is involved in magma formation; (V) intracontinental rifts and continental hot spots; and (VI) backarc spreading centers.

(2) A bimodal distribution of SiO₂ content in natural igneous melts was established for all geodynamic environments: there are two maxima at 52–52 wt % and 72–74 wt % SiO₂. The minimum of the distribution of SiO₂ determinations was observed at 6264 wt %.

(3) Spidergrams were constructed for the mean contents of elements in the igneous melts of basic, intermediate, and acidic compositions for settings IV normalized to primitive mantle values. These diagrams reflect the characteristic features of melts from each of the geodynamic setting.

(4) Based on the analysis of data on the compositions of melt inclusions and glasses of rocks, mean ratios of some incompatible and volatile components were estimated (H₂O/Ce, K₂O/Cl, Nb/U, Ba/Rb, Ce/Pb, etc.) in the igneous melts of the distinguished settings. Variations in these ratios were examined, and it was shown that most incompatible element ratios are significantly different in different settings. The discrepancies are especially significant for the ratios of elements with different degrees of incompatibility (e.g., Nb/Yb) and some ratios including volatile components (e.g., K₂O/H₂O).

ACKNOWLEDGMENTS

We are grateful to A.V. Sobolev for helpful comments and discussion of the materials of our investigation. This study was financially supported by the Russian Foundation for Basic Research, project nos. 07-05-00497 and 08-05-00472; the Department of Earth Sciences of the Russian Academy of Sciences; and the Program for the Support of Leading Scientific Schools.

REFERENCES

1. **V. B. Naumov, V. I. Kovalenko, V. A. Dorofeeva, and V. V. Yarmolyuk**, “Average Concentrations of Major, Volatile, and Trace Elements in Magmas of Various Geodynamic Settings,” *Geokhimiya*, No. 10, 1113–1124 (2004) [*Geochem. Int.* 42, 977–987 (2004)].
2. **J. M. Eiler, P. Schiano, J. W. Valley, et al.**, “Oxygen-Isotope and Trace Element Constraints on the Origins of Silica-Rich Melts in the Subarc Mantle,” *Geochem. Geophys. Geosyst.* 8 (9), 1–21 (2007).
3. **A.-S. Bouvier, N. Metrich, and E. Deloule**, “Slab-Derived Fluids in the Magma Sources of St. Vincent (Lesser Antilles Arc): Volatile and Light Element Imprints,” *J. Petrol.* 49 (8), 1427–1448 (2008).
4. **M. Le Voyer, E. F. Rose-Koga, M. Laubier, and P. Schiano**, “Petrogenesis of Arc Lavas from the Rucu Pichincha and Pan de Azucar Volcanoes (Ecuadorian Arc): Major, Trace Element, and Boron Isotope Evidences from Olivine-Hosted Melt Inclusions,” *Geochem. Geophys. Geosyst.* 9 (12), 1–27 (2008).
5. **R. Harlou, D. G. Pearson, G. M. Nowell, et al.**, “Combined Sr Isotope and Trace Element Analysis of Melt Inclusions at Sub-ng Levels Using Micro-Milling, TIMS and ICPMS,” *Chem. Geol.* 260 (3–4), 254–268 (2009).
6. **G. D. Layne, A. J. R. Kent, and W. Bach**, “ $\delta^{37}\text{Cl}$ Systematics of a Backarc Spreading System: The Lau Basin,” *Geology* 37 (5), 427–430 (2009).

7. **J. Wittenbrink, B. Lehmann, M. Wiedenbeck, et al.**, “Boron Isotope Composition of Melt Inclusions from Porphyry Systems of the Central Andes: A Reconnaissance Study,” *Terra Nova* 21 (2), 111–118 (2009)
8. **V. B. Naumov, V. I. Kovalenko, A. D. Babansky, and M. L. Tolstykh**, “Genesis of Andesites: Evidence from Studies of Melt Inclusions in Minerals,” *Petrologiya* 5 (6), 654–665 (1997) [*Petrology* 5, 586–596 (1997)].
9. **M. L. Tolstykh, V. B. Naumov, A. D. Babansky, et al.**, “Chemical Composition, Volatile Components, and Trace Elements in Andesitic Magmas of the Kurile-Kamchatka Region,” *Petrologiya* 11 (5), 451–470 (2003) [*Petrology* 11, 407–425 (2003)].
10. **S. S. Sun and W. F. McDonough**, “Chemical and Isotopic Systematics of Oceanic Basalts: Implications for Mantle Composition and Processes,” in *Magmatism in the Ocean Basins*, Ed. by A. D. Saunders and M. J. Norry, *Geol. Soc. Spec. Publ.* 42, 313–345 (1989).
11. **V. I. Kovalenko, V. B. Naumov, A. V. Girnits, et al.**, “Estimation of the Average Contents of H₂O, Cl, F, and S in the Depleted Mantle on the Basis of the Compositions of Melt Inclusions and Quenched Glasses of Mid-Ocean Ridge Basalts,” *Geokhimiya*, No. 3, 243–266 (2006) [*Geochem. Int.* 44, 209–231 (2006)].
12. **V. I. Kovalenko, V. B. Naumov, A. V. Girnits, et al.**, “Average Contents of Incompatible and Volatile Components in Depleted, Oceanic Plume, and Within-Plate Continental Mantle Types,” *Dokl. Akad. Nauk* 415 (3), 389–393 (2007) [*Dokl. Earth Sci.* 415, 880–884 (2007)].
13. **V. I. Kovalenko, V. B. Naumov, A. V. Girnits, et al.**, “Average Compositions of Magmas and Mantle Sources of Mid-Ocean Ridges and Intraplate Oceanic and Continental Settings Estimated from the Data on Melt Inclusions and Quenched Glasses of Basalts,” *Petrologiya* 15 (4), 361–396 (2007) [*Petrology* 15, 335–368 (2007)].
14. **V. I. Kovalenko, V. B. Naumov, A. V. Girnits, et al.**, “Volatiles in Basaltic Magmas of Ocean Islands and Their Mantle Sources: I. Melt Compositions Deduced from Melt Inclusions and Glasses in the Rocks,” *Geokhimiya*, No. 2, 131–149 (2007) [*Geochem. Int.* 45, 105–122 (2007)].
15. **V. I. Kovalenko, V. B. Naumov, A. V. Girnits, et al.**, “Volatiles in Basaltic Magmas of Ocean Islands and Their Mantle Sources: II. Estimation of Contents in Mantle Reservoirs,” *Geokhimiya*, No. 4, 355–369 (2007) [*Geochem. Int.* 45, 313–326 (2007)].
16. **V. I. Kovalenko, V. B. Naumov, A. V. Girnits, et al.**, “Peralkaline Silicic Melts of Island Arcs, Active Continental Margins, and Intraplate Continental Settings: Evidence from the Investigation of Melt Inclusions in Minerals and Quenched Glasses of Rocks,” *Petrologiya* 17 (4), 437–456 (2009) [*Petrology* 17, 410–427 (2009)].
17. **V. I. Kovalenko, V. B. Naumov, A. V. Girnits, et al.**, “Canonical Ratios of Trace Elements in Basic Magmas of Various Geodynamic Settings: Estimation from Compositions of Melt Inclusions and Rock Glasses,” *Dokl. Akad. Nauk* 426 (2), 222–225 (2009) [*Dokl. Earth Sci.* 426, 611–614 (2009)].
18. **R. L. Rudnick and S. Gao**, “Composition of the Continental Crust,” in *Treatise on Geochemistry* (Elsevier, Amsterdam, 2003), Vol. 3, pp. 1–64.
19. **R. J. Arculus**, “Island Arc Magmatism in Relation to the Evolution of the Crust and Mantle,” *Tectonophysics* 75, 113–133 (1981).
20. **S. R. Hart and G. A. Gaetani**, “Mantle Pb Paradoxes: The Sulfide Solution,” *Contrib. Mineral. Petrol.* 152, 295–308 (2006).
21. **J. Ayers**, “Trace Element Modeling of Aqueous Fluid-Peridotite Interaction in the Mantle Wedge of Subduction Zones,” *Contrib. Mineral. Petrol.* 132, 390–404 (1998).

Sources for the Il'meno-Vishnevogorsky Alkaline Complex: Evidence from Lu–Hf Isotopic Data for Zircons.

Nedosekova I.L.¹, Belousova E.A.², Sharygin V.V.³

¹ *Zavaritskii Institute of Geology and Geochemistry, Ural Division, Russian Academy of Sciences, Yekaterinburg, Russia*

² *GEMOS ARC National Key Centre, Macquarie University, Sydney, Australia*

³ *Sobolev Institute of Geology and Mineralogy, Siberian Branch, Russian Academy of Sciences, Novosibirsk, Russia e-mail: vladi49@yandex.ru*

The composition of hafnium isotopes in zircons is currently an important instrument for reconstruction of the source of magmatic rocks. Zircon is stable in many hypogene and hypergene processes. Metamictization and later processes of alteration practically do not affect the composition of Hf isotopes in zircon [12]. The relative stability of Hf isotopes in zircons makes them a powerful instrument for the study of the source age, as well as the origin and isotopic evolution of various rocks [6, 11]. The combination of dating of an individual zircon grain by the U–Pb method with the study of Hf isotopes of the same grains (with application of local isotopic methods, such as SHRIMP, SIMS, and laser ablation) is the most effective. Such a combination provides important information on the rock source even in the case when other isotopic systems are significantly disturbed.

We obtained the first Lu–Hf isotopic data (in combination with the U–Pb isotopic data) by the method of laser ablation for zircons from carbonatite and alkaline rocks of the Il'meno-Vishnevogorsky Complex in order to study the age of rocks and the source of their material. Since the Sm–Nd and Rb–Sr isotopic systems were disturbed to various degrees during the Hercynian collision [5, 9], we considered application of the Lu–Hf isotopic system as the most stable and informative to be especially important.

The Il'meno-Vishnevogorsky Complex occurs at the boundary between the Middle and Southern Urals and is located within the Sysert–Ilmeny Precambrian block, which has a two level structure and a long history of the formation. The core of the block is composed of granulitic gneiss and migmatite of the Selyankino Series (the U–Pb age of its zircons is 1820 ± 70 Ma), as well as plagiogneiss and amphibolite of the Vishnevye Gory Series (PR1). The frame (the upper structural level) is represented by the Ilmeny Series in the south and Shumikhin and Chernov Series in the north composed of amphibolite, plagiogneiss, and quartzite, which are presumably Pre-Uralian paleovolcanic complexes with a U–Pb zircon age of 643 ± 46 (Ilmeny Series) and 576 ± 65 (Shumikhin Series) Ma [1]. The age of the miaskite and carbonatite formation for the Il'meno-Vishnevogorsky Complex obtained by Rb–Sr and U–Pb geochronology is 440–410 Ma. In addition, later

metamorphic processes related to Hercynian orogeny (360–320 Ma) and subsequent postcollision spreading (260–240 Ma) are dated by the U–Pb and Rb–Sr methods [2, 9, 10].

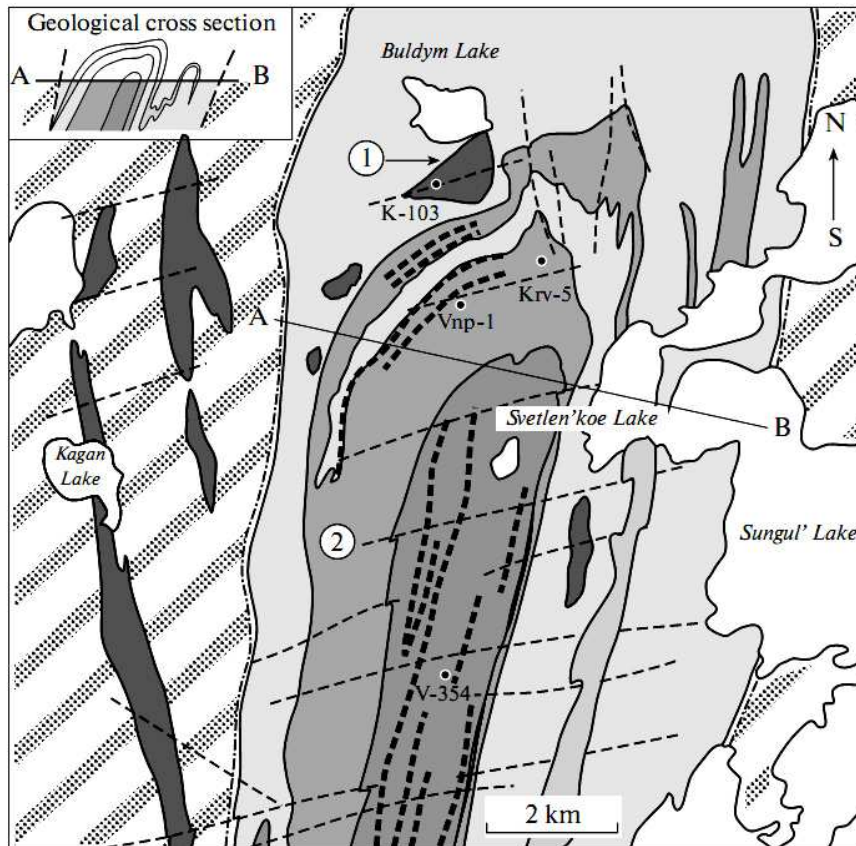


Fig. 1. Scheme of the geological structure of northern part of the Il'meno-Vishnevogorsky complex, after [3]. (1) Plagioclase schist and quartzite of the Igish, Sait, Arazin, and Kyshtym series (R_{1-2}); (2) plagiogneiss and amphibolite of the Vishneve Gory series (PR_1); (3) meta-ultrabasic rocks ($PR_1?$); (4) alkaline metasomatic rocks of the central alkaline band (fenite, carbonate-silicate rocks, miaskite, and carbonatite); (5) miaskite of the Vishneve Gory massif; (6) zones of carbonatite and carbonate-silicate rocks; (7) massifs: (1) Buldym ultrabasic, (2) Vishneve Gory miaskitic; (8) lines of tectonic dislocations; (9) places of sampling and sample numbers.

According to the model of crustal anatexis [3], the Il'meno-Vishnevogorsky alkaline complex was formed under the influence of a powerful flow of juvenile alkaline hydrous–carbon dioxide fluids on the gneiss–amphibolite substrate of the Sysert–Ilmeny block and subsequent evolution of the crustal anatectic processes controlling the formation of carbonatite–miaskite intrusions.

The model of mantle anatexis is based on mantle O, C, S, Sr, and Nd markers and suggests that the formation of the Il'meno-Vishnevogorsky miaskite–carbonatite complex results from the introduction of deep alkaline

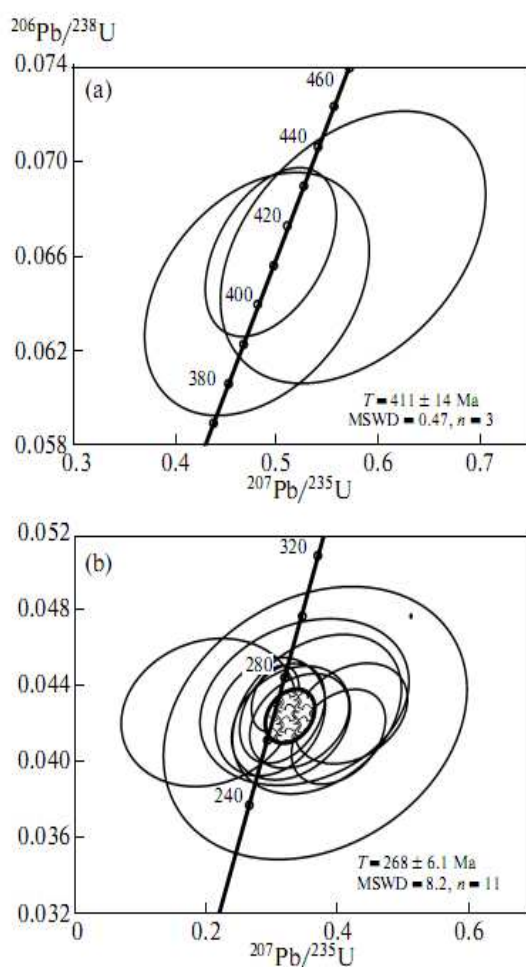


Fig. 2. U—Pb diagram for zircons from the Il'meno-Vishnevogorsky complex: (a) Sample V-354, from calcitic carbonatite of the Vishnevye Gory miaskitic massif; (b) Sample K-103, from dolomitic carbonatite of the Buldym ultrabasic massif.

K-103) (Fig. 1).

Zircon in miaskite, miaskitic pegmatite, and carbonatite of the Vishnevye Gory massif is represented by crystals of several morphological types: xenomorphic, prismatic, and dipyrmidal which are also different in color, the presence of inclusions, and transparency. The early zircon I, most likely formed during the crystallization of the miaskitic massif, is represented by xenomorphic, poor-transparent grains with nonuniform color, usually darker cathodoluminescence (CL), spotty on back-scattered electron (BSE) images, with relics of oscillatory zonation. Late newly formed zircon II is characterized by short-tabular grains of round shape, transparent, with primary zonation, homogeneous on BSE images, and clear cathodoluminescence. Most zircon grains are represented by intermediate varieties illustrating various degrees

magma; palingenesis processes are dependent [9].

The study of the Lu–Hf and U–Pb isotopic compositions of zircons from the Il'meno-Vishnevogorsky complex was performed by the laser ablation method at the National Key Centre of Geochemical Evolution and Metallogeny of the Continents (GEMOC) of Macquarie University (Sydney, Australia). An ultraviolet laser UP213 New Wave/Merchantek together with a multicollector MC_ICPMS Nu_Plasma were applied for the Hf isotopic analysis and U–Pb dating. Analyses were performed with a beam diameter of $\sim 50 \mu\text{m}$. The ablation time was 100–120 s; the depth of the crater was 40–60 μm . The methodology of U–Pb dating and Hf isotope measurements were previously described in detail [8].

We studied zircons from miaskite (Samples Vnp-1 and Vnp-2), miaskitic pegmatite (Sample Krv-5), and carbonatite of the Vishnevye Gory miaskitic massif (Sample V-354), as well as zircons from dolomitic carbonatite of the Buldym ultrabasic massif (Sample

of transformation of early zircon generations and their replacement by later ones. Zircon crystals contain inclusions of thorianite, pyrochlore, xenotime, and monazite.

Zircons from miaskite and carbonatite of the Vishnevye Gory massif were previously dated by the classic U–Pb method studying bulk samples with acid decomposition of grains [10] and were studied on a SHRIMP-II as well [2]. Zircons from carbonatite of the Buldym massif were not studied previously.

The U–Pb age of early zircon I from carbonatite of the Vishnevye Gory massif was determined by the laser ablation method as 411 ± 14 Ma (Fig. 2a). An age of 408 ± 8 Ma was obtained by the U–Pb–SHRIMP dating of early zircon generations from miaskite [2]. Late zircon II provided an age of 282 Ma. The U–Pb age of zircons from dolomite carbonatite of the Buldym massif was determined as 268 ± 6 Ma (Fig. 2b).

The results of the Hf isotopic composition analysis of the studied zircons are given in the table and Fig. 3.

The initial ratios of Hf isotopes in early zircons (the same grains that were used for the U–Pb dating) demonstrate insignificant variations of $(^{176}\text{Hf}/^{177}\text{Hf})_{410} = 0.282617\text{--}0.282678$, $\epsilon_{\text{Hf}} = 3.5\text{--}5.7$ and provide evidence for the formation of zircon from a moderately depleted source. Zircons from miaskite, miaskitic pegmatite, and carbonatite have

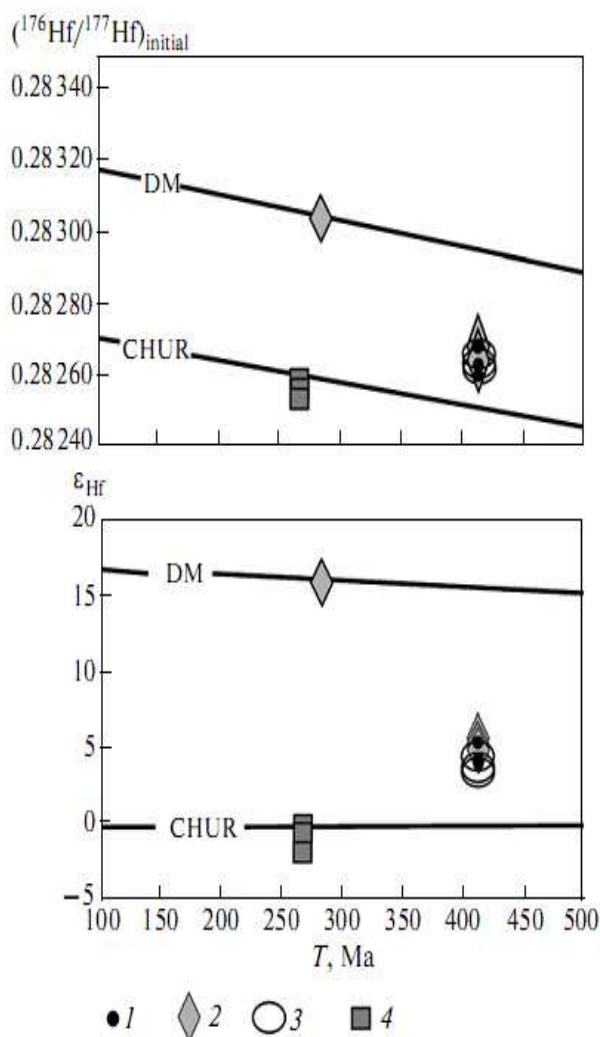


Fig. 3. Initial $^{176}\text{Hf}/^{177}\text{Hf}$ isotopic ratios and ϵ_{Hf} in zircons from the Il'meno-Vishnevogorsky complex. (1)—(3) Zircons of the Vishnevye Gory massif: (1) from miaskite, (2) from carbonatite, (3) from miaskitic carbonatite; (4) zircons of the Buldym massif (from dolomitic carbonatite). Lines of the DM and CHUR mantle reservoir isotopic evolution are shown for comparison. A decay constant of ^{176}Lu $\lambda = 1.865 \times 10^{-11}$ [14] is applied for the calculation of DM and CHUR isotopic evolution.

close values of the Hf isotopic parameters, which points to the same source of their material.

Hf isotopes were also analyzed in the zircon II crystal (a U–Pb age of 282 Ma) from carbonatite of the Vishnevye Gory massif. Zircon II differs significantly from early zircon I, it has high values of $(^{176}\text{Hf}/^{177}\text{Hf})_{282} = 0.283055$, $\varepsilon_{\text{Hf}} = 16$ corresponding to those of a depleted mantle that may provide evidence for the different, juvenile source participating in miaskite and carbonatite transformations. However, this question requires statistical substantiation and further study.

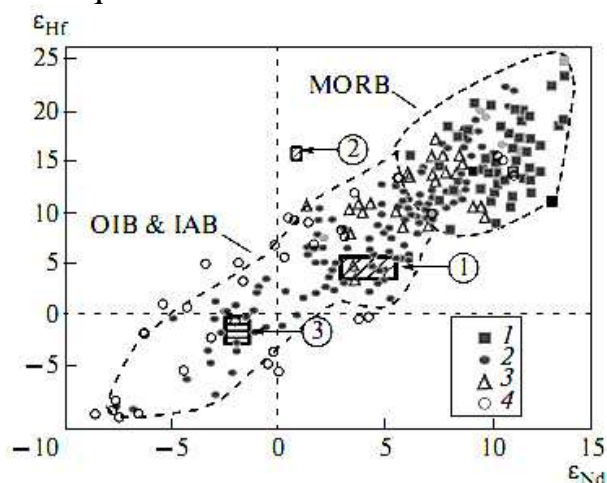


Fig. 4 ε_{Hf} — ε_{Nd} diagram for zircon from rocks of the Il'meno-Vishnevogorsky complex. Isotopic compositions of MORB (1), OIB (2), and IAB (3) [12, 13, and others] and lower crustal rocks (4) [15] are shown for comparison. Fields of zircon compositions: (1) and (2) from miaskite, miaskitic pegmatite, and carbonatite of the Vishnevye Gory massif and (3) from dolomitic carbonatite of the Buldym massif; U–Pb zircon age: (1) 410 Ma, (2) 282 Ma, (3) 268 Ma.

The composition of Hf isotopes in zircons from dolomitic carbonatite of the Buldym massif $(^{176}\text{Hf}/^{177}\text{Hf})_{268} = 0.282525\text{--}0.282555$, $-0.2\text{--}1.8$ is close to that of chondrite and differs significantly from zircons of the Vishnevye Gory massif by the lower initial ratios of Hf isotopes and ε_{Hf} , which provides evidence for participation of various sources in their formation.

The isotopic composition of Nd in rocks of the Il'meno-Vishnevogorsky complex is also different for carbonatites of the Vishnevye Gory and Buldym massifs. Carbonatite and miaskite of the Vishnevye Gory massif have higher values of $(^{143}\text{Nd}/^{144}\text{Nd})_T = 0.512232\text{--}0.512364$, $\varepsilon_{\text{Nd}} = 2.4\text{--}4.9$ ($n = 10$) typical for a moderately depleted mantle. Dolomitic carbonatite of the Buldym massif has quite low values of $(^{143}\text{Nd}/^{144}\text{Nd})_T = 0.512197\text{--}0.512149$ ($n = 2$) and negative ε_{Nd} from -1.9 to -2.8 corresponding to the parameters of an enriched source of the EM1 type [5]. We cannot exclude that the differences in isotopic parameters of zircons from the Vishnevye Gory and Buldym massifs result of contamination during the evolution of carbonatitic melts/fluids of the Il'meno-Vishnevogorsky complex.

Table 1

Lu—Hf isotopic data for zircons of the Il'meno-Vishnevogorsky complex

No.	Sample	Lu, ppm	Yb, ppm	Hf, ppm	$^{176}\text{Lu}/^{177}\text{Hf}$	$^{176}\text{Hf}/^{177}\text{Hf}$	$^{206}\text{Pb}/^{238}\text{U}$ -age, Ma	$^{176}\text{Hf}/^{177}\text{Hf}$ (T)	$\epsilon_{\text{Hf}}(T)$	T_{DM} , Ga	T_{DMC} , Ga
1	Vnp-2	2	17	10430	0.000030	0.282623	411	0.282623	3.8	0.87	1.17
2	Vnp-1A	4	29	12126	0.000044	0.282633	411	0.282633	4.1	0.86	1.15
3	Vnp-1B	2	15	7980	0.000034	0.282668	411	0.282668	5.4	0.81	1.07
4	Krv-5-1*	2	16	6623	0.000045	0.282617	411	0.282617	3.5	0.88	1.17
5	Krv-5-2*	2	16	7683	0.000039	0.282632	411	0.282632	4.1	0.86	1.15
6	Krv-5-3*	2	19	7929	0.000043	0.282654	411	0.282654	4.8	0.83	1.10
7	V-354-3	9	91	6445	0.000204	0.282680	411	0.282678	5.7	0.79	1.04
8	V-354-6	12	125	6530	0.000265	0.282660	411	0.282658	5.0	0.82	1.09
9	V-354-8*	76	673	5190	0.002028	0.282679	411	0.282663	5.2	0.84	1.08
10	V-354-10*	3	26	6869	0.000060	0.282673	411	0.282673	5.5	0.80	1.06
11	V-354-12*	13	124	5978	0.000306	0.282664	411	0.282662	5.1	0.82	1.08
12	V-354-2	3	23	6614	0.000057	0.283055	282	0.283055	16.2	0.27	0.27
13	K-103-02	31	274	8734	0.000488	0.282593	268	0.282591	-0.5	0.92	1.33
14	K-103-03	16	132	8649	0.000251	0.282587	268	0.282586	-0.7	0.92	1.34
15	K-103-10	16	139	8013	0.000282	0.282589	268	0.282588	-0.6	0.92	1.34
16	K-103-12	26	215	8225	0.000438	0.282601	268	0.282599	-0.2	0.91	1.31
17	K-103-13	23	199	8480	0.000371	0.282589	268	0.282587	-0.7	0.92	1.34
18	K-103-15	22	184	8819	0.000353	0.282557	268	0.282555	-1.8	0.97	1.41

Note: Errors of values for the $^{176}\text{Hf}/^{177}\text{Hf}$ ratio are ± 0.00002 (2σ), which is equal to $\pm 0.7 \epsilon_{\text{Hf}}$ based on zircon standard no. 91500. Isotopic characteristics for chondrites after [14] were accepted for calculations of primary Hf isotopic ratios and ϵ_{Hf} . Asterisks denote points at which the $^{206}\text{Pb}/^{238}\text{U}$ age was not determined but was extrapolated for the calculation of the initial $^{176}\text{Hf}/^{177}\text{Hf}$ ratios and $\epsilon_{\text{Hf}}(T)$. (1)—(12) Zircons from Vishnevye Gory miaskitic massif; (1)—(3) from miaskite, (4)—(6) from miaskitic pegmatite, (7)—(12) from cal-citic carbonatite; (13)—(18) zircons from dolomitic carbonatite of the Buldym massif

The composition of Hf and Nd isotopes for rocks of the Il'meno-Vishnevogorsky complex is shown on the $\epsilon_{\text{Nd}}-\epsilon_{\text{Hf}}$ diagram (Fig. 4). The mantle trend of isotopic compositions of depleted mantle (MORB), enriched mantle and island arc basalts (IAB) is shown for comparison [12, 13, and others]. In addition, the data for lower crustal rocks, particularly isotopic compositions of granulites, which are close to mantle isotopic compositions [15], are plotted on the diagram.

Points of the compositions of early zircon generations from the Il'meno-Vishnevogorsky complex plot on the mantle trend of the evolution of moderately depleted mantle compositions and lower crustal rocks on the $\epsilon_{\text{Nd}}-\epsilon_{\text{Hf}}$ diagram. Only one point (V-354-2, late zircon II with an age of 282 Ma from carbonatite of the Vishnevye Gory massif) is outside the "terrestrial array" [15] (Fig. 4). The initial ratios of the Hf and Nd isotopes for the Il'meno-Vishnevogorsky complex form discrete compositional fields on the diagram. Miaskite, miaskitic pegmatite, and carbonatite of the Vishnevye Gory massif have isotopic compositions of a moderately depleted mantle. Dolomitic carbonatite of the Buldym massif has isotopic parameters of an enriched source. Significant differences in the isotopic parameters of carbonatites from the Vishnevye Gory and Buldym massifs provide evidence for their formation from various sources and multistage carbonatite formation in the Il'meno-Vishnevogorsky complex.

Lu-Hf model ages T_{DM} and T_{DMC} were calculated for the estimation of the time of melt generation, i.e., the separation of parent magmas for the Il'meno-Vishnevogorsky complex from the depleted mantle. To calculate the model age T_{DM} based on melting of rocks from the depleted mantle, we accepted the model with $(^{176}\text{Hf}/^{177}\text{Hf})_{\text{initial}} = 0.279718$ in 4.56 Ga and $^{176}\text{Lu}/^{177}\text{Hf} = 0.0384$, which provides modern values of $^{176}\text{Hf}/^{177}\text{Hf} = 0.28325$ close to the average MORB values [8]. Since the calculation of T_{DM} may provide only a minimal age for the magma source from which zircon crystallized, we also calculated the two-stage model age T_{DMC} suggesting melting of parental magma from the middle continental crust previously formed from the depleted mantle ($^{176}\text{Lu}/^{177}\text{Hf} = 0.015$; Geochemical Earth Reference Model database, <http://www.earthref.org/>).

The calculation of Lu-Hf model ages provides an age estimation of melt source producing the earliest zircons of the Il'meno-Vishnevogorsky complex ($T_{\text{DM}} = 790-880$ Ma). If the two-stage model of the evolution of Hf isotopic composition is applied, the protolith age of the Il'meno_Vishnevogorsky complex is $T_{\text{DMC}} = 1040-1170$ Ma. Note that the model T_{DM} age of the late zircon II generation in carbonatite from the Vishnevye Gory massif is 270 Ma and well consistent with the U-Pb age of these zircons. Such similarity may provide evidence for the formation of the late zircon generation during the collision processes.

Thus, Lu-Hf isotopic data obtained by the early zircon generations (in addition to the previously obtained Sr-Nd isotopic data [4, 5]) confirm the mantle character of matter source for magma of the Il'meno-Vishnevogorsky complex and provide evidence for participation of material of depleted mantle (DM) and enriched source (most likely a lower crustal component) in magma generation. Mixing of materials from these sources may provide the whole spectrum of isotopic compositions of rocks from the Il'meno-

Vishnevogorsky complex. The model age of the protolith of the Il'meno-Vishnevogorsky complex corresponds to the initial stages of the Riphean riftogenesis resulting in destruction of the Rodinia supercontinent, at that time the Riphean–Vendian crust (upper structural level of the Syssert–Ilmeny block). Thus, we may suggest that the protolith of the Il'meno-Vishnevogorsky complex was most likely represented by Riphean oceanic or rifting-related series with close Sr–Nd characteristics and a model Sm–Nd age of the source [7]. Their melting provided magma generation in the Il'meno-Vishnevogorsky complex at the initial stages of Paleozoic riftogenesis in the Urals.

Thus, we may suggest that the protolith of the Il'meno-Vishnevogorsky complex was most likely represented by Riphean oceanic or rifting-related series with close Sr–Nd characteristics and a model Sm–Nd age of the source [7]. Their melting provided magma generation in the Il'meno-Vishnevogorsky complex at the initial stages of Paleozoic riftogenesis in the Urals.

ACKNOWLEDGMENTS

The authors are grateful to B.V. Belyatskii for consultation and discussion of the materials. This study was supported by an interdisciplinary project of the Ural Division, Siberian Branch, and Far East Division, Russian Academy of Sciences, in 2009–2011 (no. 09-C-5-1014).

REFERENCES

1. **A. Krasnobaev and V. A. Davydov.** (2000) Dokl. Akad. Nauk 372 (1), 89–94 [Dokl. Earth Sci. 372, 672 (2000)].
2. **A. Krasnobaev, A. I. Rusin, S. V. Busharina, et al..** (2007) Yearbook (Inst. Geol. Geokhim., Yekaterinburg, 2008), pp. 264–268 [in Russian].
3. **V. Ya. Levin, B. M. Ronenson, V. S. Samkov, et al..** (1997) Alkaline–Carbonatitic Complexes of the Urals (Uralgeolkom, Yekaterinburg,) [in Russian].
4. **L. Nedosekova, N. V. Vladykin, S. V. Pribavkin, et al..** (2009) Geol. Rudn. Mestorozhd. 51 (2), 157–181 [Geol. Ore Deposits 51, 139].
5. **S. V. Pribavkin and I. L. Nedosekova.** (2006) Dokl. Akad. Nauk 408 (3), 381–385 (2006) [Dokl. Earth Sci. 408, 627].
6. **Y. Amelin, D. C. Lee, A. N. Halliday, and R. T. Pidgeon.** (1999) Nature 399 (6733), 252–255.
7. **H. P. Echtler, K. S. Ivanov, Y. L. Ronkin, et al..** (1997) Tectonophysics 276, 229–251.
8. **W. L. Griffin, N. J. Pearson, E. A. Belousova, et al..** (2000) Geochim. Cosmochim. Acta 64, 133–147.
9. **U. Kramm, A. B. Blaxland, V. A. Kononova, et al..** (1983) J. Geol. 91, 427–435.
10. **U. Kramm, I. V. Chernyshev, S. Grauert, et al..** (1993) Petrology 1 (5), 474–485.
11. **O. Nebel, Y. Nebel-Jacobsen, K. Mezger, et al..** (2007) Chem. Geol. 241, 23–37.
12. **P. J. Patchett and M. Tastumoto.** (1980) Geophys. Rev. Lett. 7 (12), 1077–1080.
13. **V. J. M. Salters and W. M. White.** (1998) Chem. Geol. 145, 447–460.
14. **E. Scherer, C. Munger, and K. Mezger.** (2001) Science 293 (5530), 683–687.
15. **J. D. Vervoort, J. P. Patchett, F. Albarede, et al..** (2000) Earth Planet. Sci. Lett. 181, 115–129 .

Reconstruction of mantle sequences beneath the Wyoming craton using xenocrysts from Sloan and Kelsey Lake - 1 kimberlite pipes, northern Colorado.

Ashchepkov I.V.¹, Downes H.², Vladykin N.V.³, Mitchell R.⁴,
Nigmatulina E.¹, Palessky S.V.¹

¹*Institute of Geology and Mineralogy, SD RAS Novosibirsk 630090, Russia*

²*Dept. of Earth and Planetary Sciences, Birkbeck University of London Malet Street London, UK*

³*Institute of Geochemistry SD RAS, Favorsky str. 1a, Irkutsk*

⁴*Lakehead University, Canada*

ABSTRACT

Xenocrysts from two Paleozoic kimberlite pipes Sloan and Kelsey Lake - 1 in northern Colorado were analyzed by EPMA and LAM ICP-MS. Their pyrope compositions relate to lherzolitic field (up to 14 Wt % Cr₂O₃). Clinopyroxenes from these pipes differ in major and trace element compositions as well as chromites and ilmenites. All minerals were used to reconstruct the mantle section in this part of the Wyoming craton with monomineral thermobarometry. The minerals from Sloan show three branches in the lower part of the mantle lithosphere, one of which is close to sheared peridotites, the second represents a refertilization trend under the influence of protokimberlite melt, and last one represents metasomatized peridotites. Heating was found near 40 kbar and starting from 30 kbars within the garnet-spinel facies. Trace element patterns in minerals from the lower part of the mantle section suggest a high degree of interaction with protokimberlite melts. The mantle lithosphere beneath Sloan originally contained a large amount of subducted material which was later metasomatized and homogenized under the influence of fluids and protokimberlite melts which left several refertilization trends in the lower part of the mantle section.

Comparison of the PT diagrams for mantle sections derived from other kimberlite occurrences, e.g. the Chicken Park (Vendian), Iron Mountain (Ordovician), Williams and Homestead (Eocene) show the onset of intrusion of ultramafic plumes then development of feeder system for mantle-derived melts. This was followed by formation of mantle diapirs which intruded the level upper above the graphite-diamond boundary.

INTRODUCTION

Information about the sub-cratonic lithospheric mantle (SCLM) is available now for many cratons but mostly for those cratons which were intensively explored for diamonds, such as the Kaapvaal and other Africa [34] and Slave [3] craton. Similar information is now available for the Dharwar [19, 38, 41], Australian and Siberian [2, 39, 40, 48-53] cratons and even for South America [10]. In North America, the Wyoming craton has rather long story of investigation of kimberlites, mantle mineralogy and petrology [5-24, 28-29, 42-49]. But the more productive kimberlites in the Slave and Superior cratons have received more attention from petrologists.

Numerous studies of the xenocrysts and xenoliths by petrologists [12-19, 42-48] and prospecting geologists [11, 20, 27] show not only details of the general

variations of the minerals and position of the geotherm but also the evolution and reduction of the mantle lithosphere beneath the Wyoming Craton. Here we present

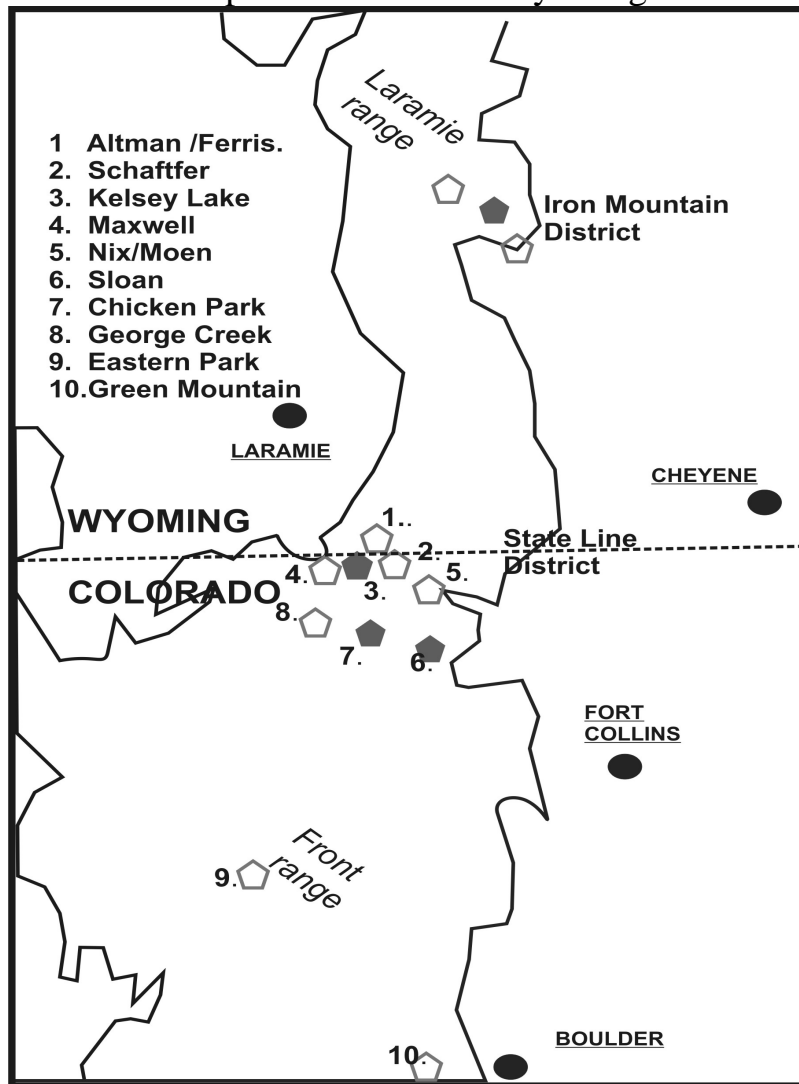


Fig.1. Scheme of the location of kimberlite pipes in Wyoming craton in State Line district and surrounding area.

more detailed information for the Sloan and Kelsey Lake- 1 pipes [1] than was done previously [11 and references therein]. The Wyoming craton gives a unique example for studying of the evolution of the upper mantle because of the possibility to find kimberlites from Late Proterozoic through Late Paleozoic to Eocene and Miocene time [11, 22, 27]. Reported petrologic reconstructions suggest continuous destruction of the craton by subduction tension, tectonic and plume forces with reduction of the cratonic keel [7-9, 11]. Here using mainly monomineral thermobarometry and geochemical features of mineral we will show the reconstructions of the sub-cratonic lithospheric mantle (SCLM) of the Wyoming craton and further evidence for its evolution.

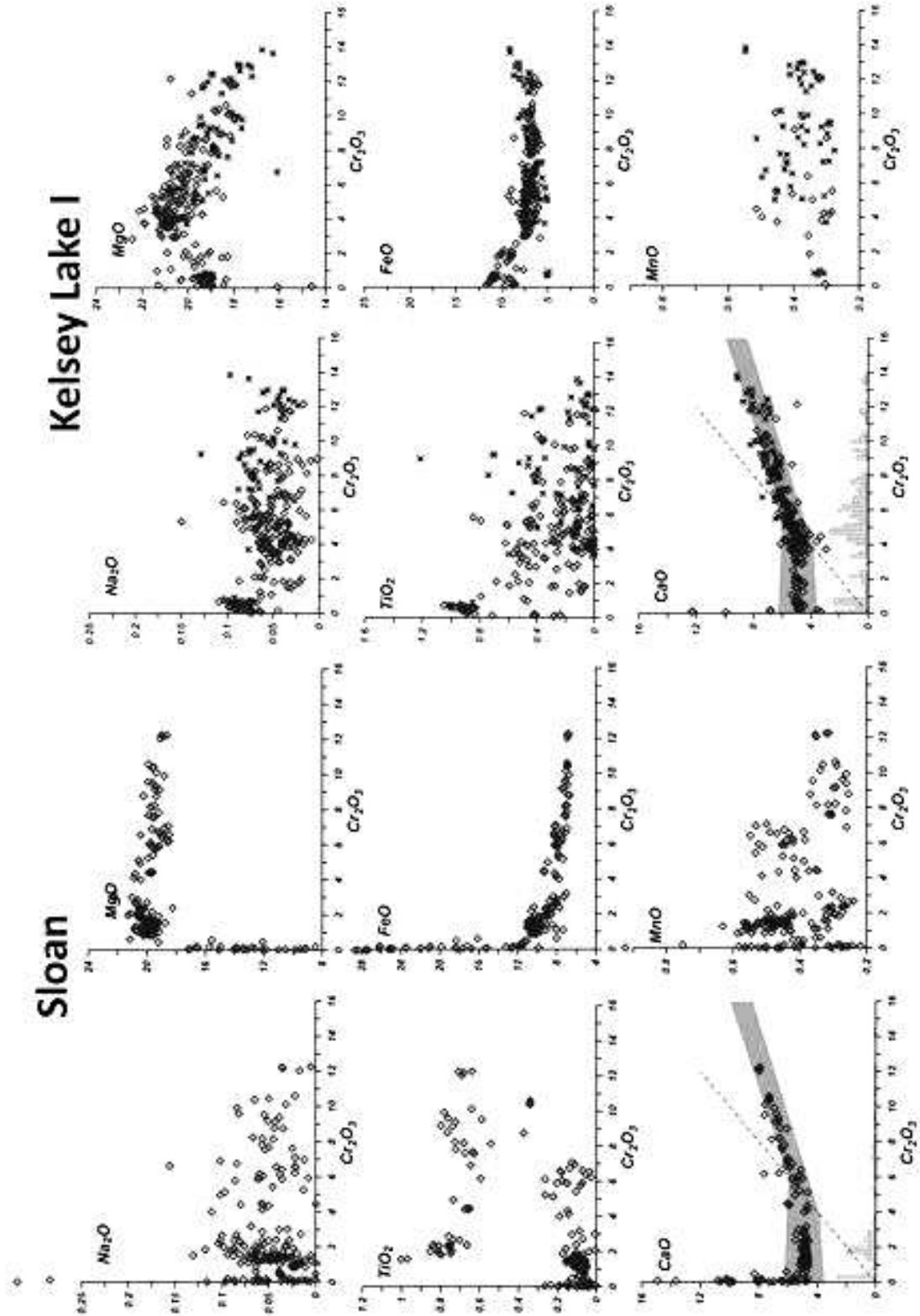


Fig.2. Variations of major element compositions from garnets from Sloan (a) and Kelsey Lake 1 (b)

LOCATION AND GEOLOGY

The Wyoming craton has experienced mantle-derived volcanism over a long period of time, including kimberlites [11, 48] (Vendian to Eocene), lamproites [32], minettes [14-15, 42] and alkaline basalts [35], and most of these contain various sets of deep seated xenoliths. The Sloan and Kelsey Lake kimberlite groups are located in the southern part of the Wyoming craton in the State Line kimberlite district. They both consist of several kimberlites bodies (Sloan-5 and Kelsey Lake-8), some of them relatively large (up to 400 meters) which contain diamonds [11]. Most of them carried abundant xenocrysts and their intergrowths which are more frequent and fresh in the Sloan pipes. Large peridotite xenoliths are not frequent and in KL - 1 pipe they are mostly altered.

DATA SET AND ANALYSES

We made EPMA analyses (>2000) of mineral grains from coarse grained concentrate (+2) and discrete xenocrysts and intergrowth. All analyses for Sloan (990 grains) and from Chicken Park (~80 grains) were made on Jeol Superprobe with the standard procedure. Silicate minerals were analyzed for 10 components using silicate scheme. For the ilmenites and spinels the set of elements include Ti, Al, Cr, Fe, Mn, Mg and in addition Ni, V, Ta, Zn. The analytic uncertainty for minor components was not high because they show good correlations with the main components with relatively low dispersion. For the megacrysts from KL-1 kimberlite (>1100) most analyses were made on Camebax Micro machine. A new series of Cr-rich garnets, ilmenites and chromites was obtained in comparison on Jeol Superprobe. Some published analyses [16-17, 18, 44-49] were included for the thermobarometric reconstructions. To increase the precision mostly natural ilmenite standard GF -55 [26] was taken, analyzed by chemical methods and in many EPMA laboratories. The accelerating voltage 15 kV and a focused beam current 20 nA, 1 μm beam diameter and counting times of 20 s were used. Reduction procedure using PAP correction was applied to the analyses. The relative standard deviation did not exceed 2 %, the precision was close to 0.02-0.015% for minor (Al, Ni, Mn, V) elements. Analyses of the grains (garnet, clinopyroxenes, ilmenites etc) were obtained in the Analytic Centre of UIGGM on a Finnigan Element ICPMS with a UV LaserProbe (wave length 233) and UP 213 (wl 213) laser ablation systems using international reference standards NIST 612 SRM and NIST 614 SRM. The background was obtained from measurements of argon. Corrections were introduced from analyses of samples analyzed by EPMA.

The ^{40}Ca was used for corrections for garnets and clinopyroxenes and Ni and V for ilmenites.

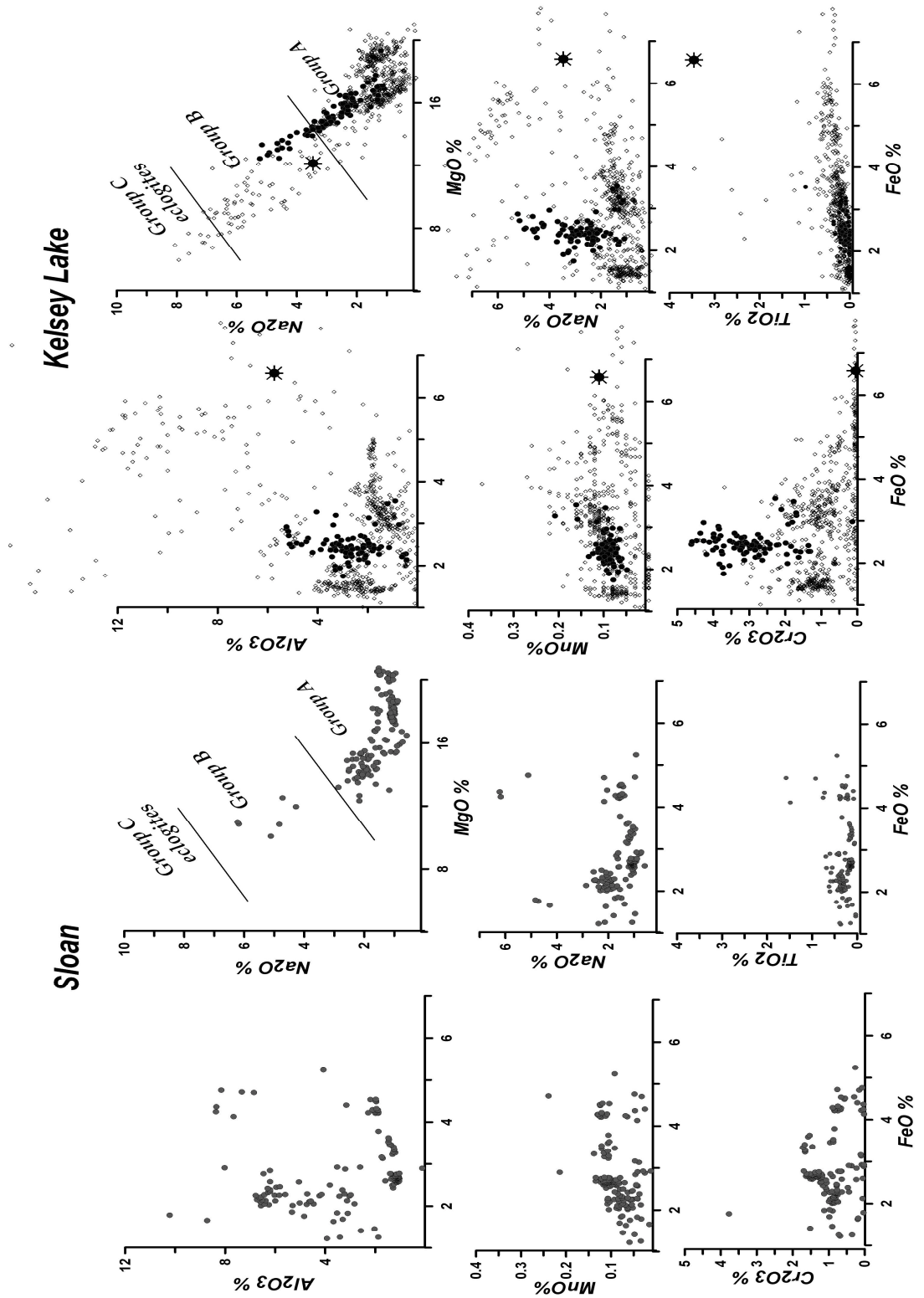


Fig.3. Variations of major element compositions of clinopyroxenes from Sloan (a) and Kelsey Lake 1 (b) signs 1- previous data [1], 2 -with new data for Cr-rich xenocrysts and in (3) comparison with published associations from Udachnaya pipe.

MINERALOGY OF XENOCRYSTS

Garnets from Sloan (fig. 2a) mainly fall into the lherzolite field according to [52] with up to 12.5 Wt % Cr_2O_3 . Compared to the KL- garnets which reach 13 Wt Cr_2O_3 and show deviations to the harzburgite fields, this is less favorable for the diamond grade. But this is possibly the result of the large grain size of the concentrates because reported diagrams for garnets from Front Range kimberlites including these pipe show more sub-calcic garnets in the concentrate and a similar range of Cr_2O_3 . Amount of the eclogitic garnets [46, 51] showing large nearly continuous range of the FeO (8-27 Wt %) is much higher Sloan pipes. garnets showing TiO_2 to 1.2 Wt % and some enrichment in Na_2O to 0.125 Wt % which is more typical for megacrysts [16, 45]. Garnets from KL pipe (fig. 2b) show essential enrichment in FeO and more continuous and dispersed enrichment in TiO_2 , gradually decreasing to the high-Cr part of the diagram.

Cr-diopsides from these two pipes (fig. 3) are much less depleted than those in Siberia, for example from the Daldyn area, see plot for Udachnaya pipe (fig. 3b). Cpx from Sloan are divided into two groups corresponding to different parts of the mantle sections. Those with lower Al are from the lower part of the mantle section and show a trend similar to those for sheared peridotites. The other more Mg-rich group differs from the common trend for the Kelsey Lake clinopyroxene, demonstrating much less enrichment in Cr, but they are richer in Al. The KL diopside show a rather interesting trend of restricted FeO values and sharp growth of Al-Cr, Na together with Fe, which looks like a mixing trend between eclogitic and peridotitic material.

Cr-Spinels from Sloan (fig. 4) demonstrate the common peridotitic trend but with very interesting behavior of TiO_2 and V_2O_3 which increase together with Cr_2O_3 . The opposite behaviour is shown by NiO which rises together with Al_2O_3 . ZnO negatively correlates with temperatures and is higher in the middle part of the mantle section. Nb_2O_3 shows high dispersion but in general it shows a rise together with Al_2O_3 . Chromites from the KL pipe practically coincide in their plot (fig.4) with those from the Cr-rich part of the Sloan spinel trend. They both have very high dispersion of TiO_2 and related elements showing a trend to the ulvospinel. But in general chromites from KL -1 are higher in FeO and MnO, some of them with up to 7 Wt % MnO.

Ilmenites from Sloan pipe (fig. 5a) are restricted in TiO_2 from 56 to 44 Wt % and show two definite branches, one of which is Cr-rich and the other Cr-poor. Ilmenites from the first one show a decrease of Al_2O_3 as well as FeO, a flat trend in NiO together with an increase in Cr. These types of ilmenites are probably from the common metasomatic association and represent the trend of interaction with the peridotites [2]. But this trend in general divides into 3-4 parts with nearly equal FeO and Cr_2O_3 contents. NiO demonstrates two branches decreasing with Fe increase, V_2O_3 is slightly rising but in each part there are arrays of rapid decrease. Mn negatively correlates with Fe in this trend.

The KL-1 ilmenite trend (fig. 5b) is more extended (36-60% TiO₂) than those found for Sloan ilmenites. These ilmenites are much more dispersed because many

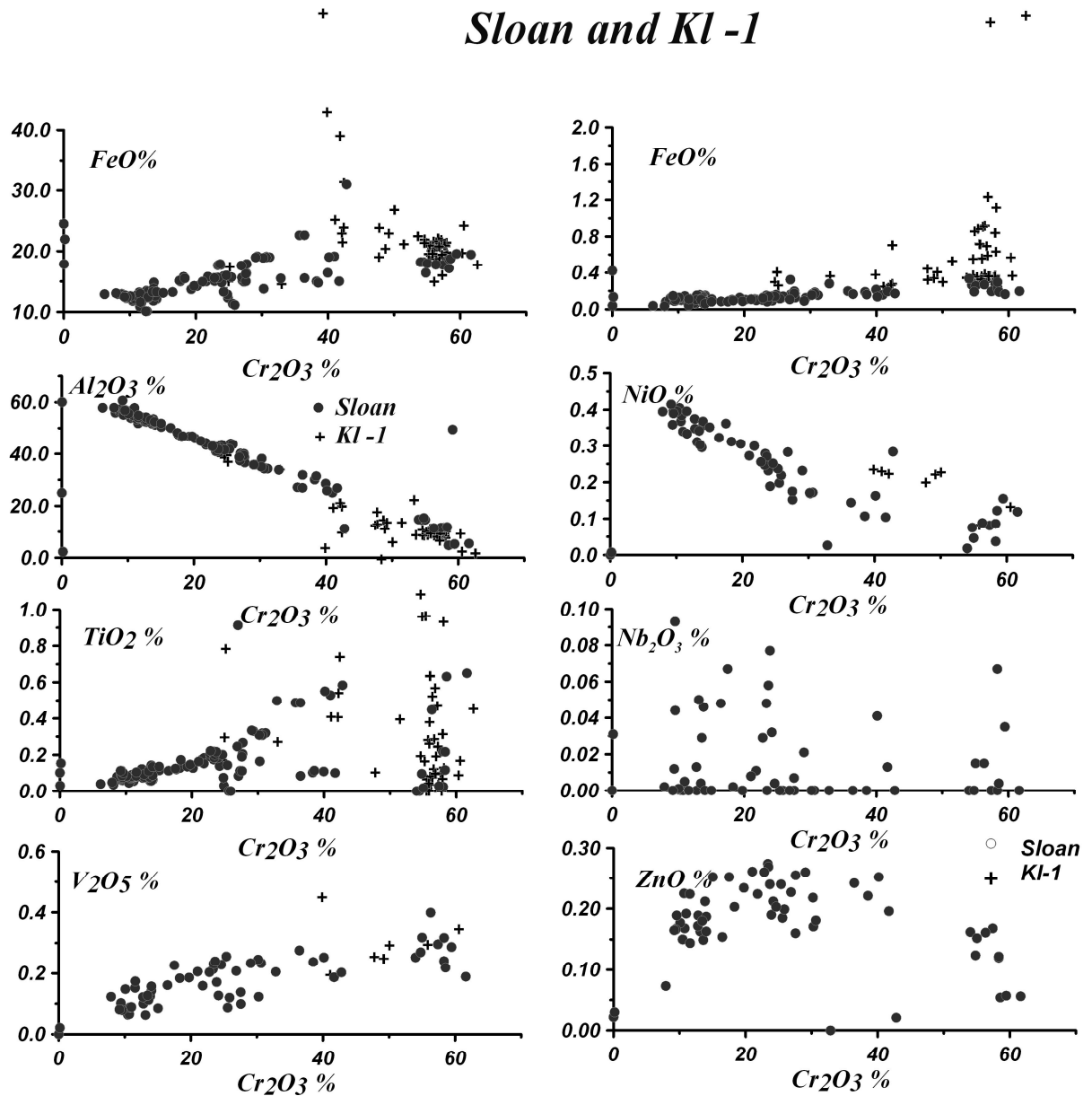


Fig.4 Variations of major element compositions for Cr- spinels from 1 Sloan and 2 KL-1 pipes

are in intergrowths with exsolved rutile [1, 45] and are not constant in composition. Nevertheless the general tendencies are similar as for Sloan ilmenites. They are very are enriched in Cr in Ti-rich part but many of them demonstrate essential enrichment in MnO sometimes up to 8 Wt %. Ilmenites from Chicken Park are mildly Mg (8-10 Wt %) and TiO₂-rich. They are slightly enriched in Al₂O₃ and show relatively low Ni content and highly varying V₂O₃.

THERMOBAROMETRY

Using our new analyses the SCLM sequences beneath the Sloan and Kelsey Lake (fig. 6) and Chicken Park kimberlites were reconstructed by set of thermobarometers [2]. Further diagrams were constructed using published analyses for Iron Mountain (Wyoming), and Williams and Homestead (Montana) [16-17, 23-24] (fig. 8) kimberlites. The SCLM beneath Sloan reveals a sharp division into two large parts which are divided by the PT estimates for Opx and some eclogitic pyroxenes (omphacites having up to 6 Wt % Na₂O) and to Al-augites from Ga-Cpx cumulates) at the 40-10 kbar interval. They do not differ much those found in ultramafic diatremes [49] in young basalts and alkali minettes [55]. But lawsonite eclogites which are Na-rich [55] show much colder subduction gradients. They also differ from diamond eclogites [44, 46] and diamond inclusions from Sloan [47] which are rich in TiO₂ and show the heated condition of the convective branch. Similar high temperature PT conditions were found for Mg, Cr-rich ilmenites and some diopsides which are close to those from sheared peridotites [36, 50]. Estimates for Cr-rich garnets forming Iherzolitic trend (G11) enriched in TiO₂ show the position near heating base of SCLM. The common peridotites and metasomatites and Cr-rich ilmenites reflect the conditions $\sim 37\text{mw/m}^2$. In the lower part of the section, two branches for the Cr-diopsides close to sheared and Ti-enriched garnets mark the heating of the mantle base at 75 kbars. The deeper Cr-spinels show variations from 60 Wt% Cr₂O₃ to Ti-enriched ulvospinel with linear enrichment of Ti with estimated pressures. Enrichment in NiO for the peridotitic Cr-picotites from shallow horizon increases with decreasing pressures.

The PT conditions for low-Cr diopsides and ilmenites at the base of the SCLM which form a dispersed sub-adiabatic branch probably reflect the conditions of protokimberlite fractionation in the vein conduits [2]. In the lower part they coincide with the PT conditions for low-Cr pyroxenes and in the upper part with Fe-rich Opx and some hot eclogites. Ilmenites showing PT conditions close to the metasomatitic peridotitic minerals were probably derived from the major magmatic system. Trends of Fe# enrichment with decreasing depth for ilmenites and Cr-poor clinopyroxenes may indicate coeval crystallization of these minerals which is proved by their intergrowths [16].

Three major branches for Cr-diopsides and ilmenites are evident in the P-Fe#Ol diagram at the base of SCLM. The branch with 17% Fe# reflects evolution of protokimberlite melts which formed Cr-diopsides with the chemical features close to those from the sheared peridotites. The branch of the metasomatites shows a relatively constant Fe#= 12%, while typical mantle peridotites and some ilmenites reflect the Fe# branch near 8-10%.

The upper level of the mantle column > 30 kbar reveals three branches of PT paths. First is the most heated marked by the Opx and Cpx, then the lower in Ti for garnets and Cpx, and the last is the lowest temperature Sp, Cpx and Gar. Fe# variations from 9 to 11% possibly reflect disequilibrium of the heated minerals in

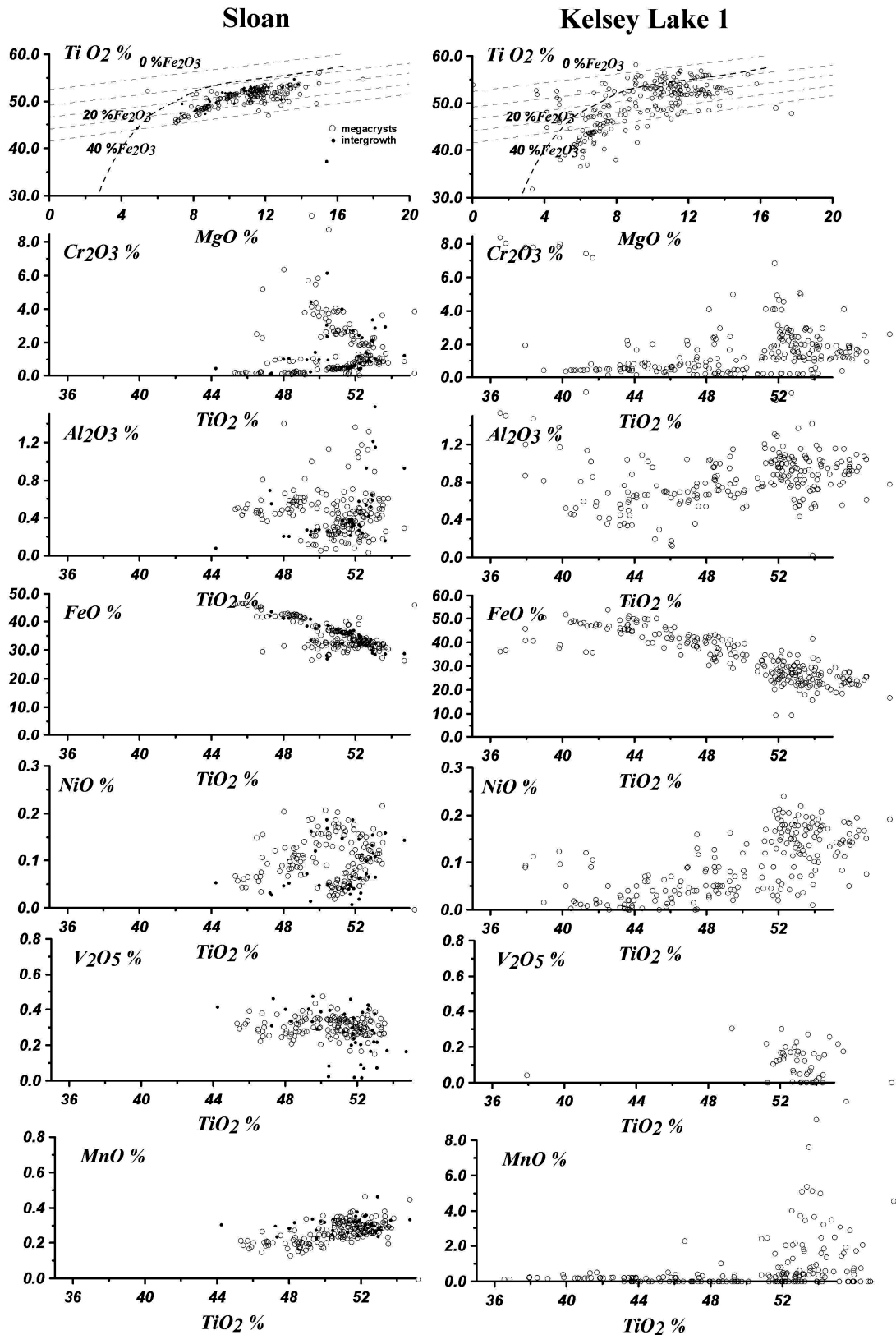


Fig.5. Variations of major element compositions of ilmenites from Sloan (a) (1 – xenocrysts 2 - intergrowths) and Kelsey Lake (b)

associations. In general the heated PT conditions for the shallow mantle from 1000 to 600°C are common for spinel peridotites beneath cratons and modern platforms worldwide and for the Colorado plateau as well [13]. Note that the Colorado Plateau is located far away from the Wyoming craton!!

This mantle sequence beneath the KL-1 (fig. 6b) pipe shows lower temperature conditions with some deviations to $< 35 \text{ mw/m}^{-2}$ geotherm. Relatively HT branches for Cr-rich garnets in the base of SCLM reflect high-Ca pyroxenitic tendencies. Several joined ilmenites and Cr diopsides trends (Fe#~15-17%; 11-14%; 9-10%) resulting from refertilization at 65 to 30 kbar interval are reconstructed. PT conditions have also tendency for the division to relatively low heated and those overheated at the shallow level. Chromite PT estimates show split trends (Fe#~10%; 12%) at 55-40kbar. The HT conditions with sub-adiabatic path are detected for some ilmenites in the middle and upper parts of the lithospheric mantle section. Most ilmenites from KL-1 which usually form aggregates and intergrowths probably reflect the freezing conditions in the vicinity of the magmatic chambers or veins. Several trends of Fe# enrichment with decreasing depth for ilmenites and clinopyroxenes probably show several coeval crystallization PT paths of these minerals. Garnets in these both pipes demonstrate enrichment in Ca with increasing estimated depth.

Interesting examples for two more pipes from State Line districts (fig. 7) give some imagination about development of the mantle sections. Chicken Park is probably one of the earliest pipes in the Wyoming craton [21]. The SCLM obtained with the restricted analyses shows the subdivision into two parts at 40 kbar where the garnet PT trend reveals an inflection. The base of the lithosphere judging by PT conditions for two Opx is heated to 1500°C. The Fe# enrichment is restricted to 5 kbar and is not seen in the upper level. The next heated horizon is at 40 kbar.

The SCLM beneath Iron Mountain (Wyoming) is similar with a sharp division at 40 kbar. Garnets in the upper section demonstrate an increase in FeO and equal amounts of CaO while in lower part there is dispersion in CaO and increase in Fe within 50-70 kbar pressure interval. The high temperature convective branch is pronounced there for PT estimates from both garnets and The pipes from the Northern part of the craton referred to the Paleocene (48 Ma) (Williams) and Homestead in Montana show thinner SCLM. The mantle sequence beneath the Williams pipe reveals high heating but it still keeps its lithospheric root at about 60 kbar as calculated for garnets and ilmenites and is proved also by CPx estimates [24], but most xenoliths were brought from the heated upper part of the mantle section. The northern Homestead kimberlite [23] shows a very similar configuration of the PT plot but relates mainly to the mantle section above the graphite-diamond transition and 45 mw/m^{-2} geotherm from 40 to 20 kbars. The xenoliths demonstrate disequilibrium between garnets and pyroxenes, the Cpx are

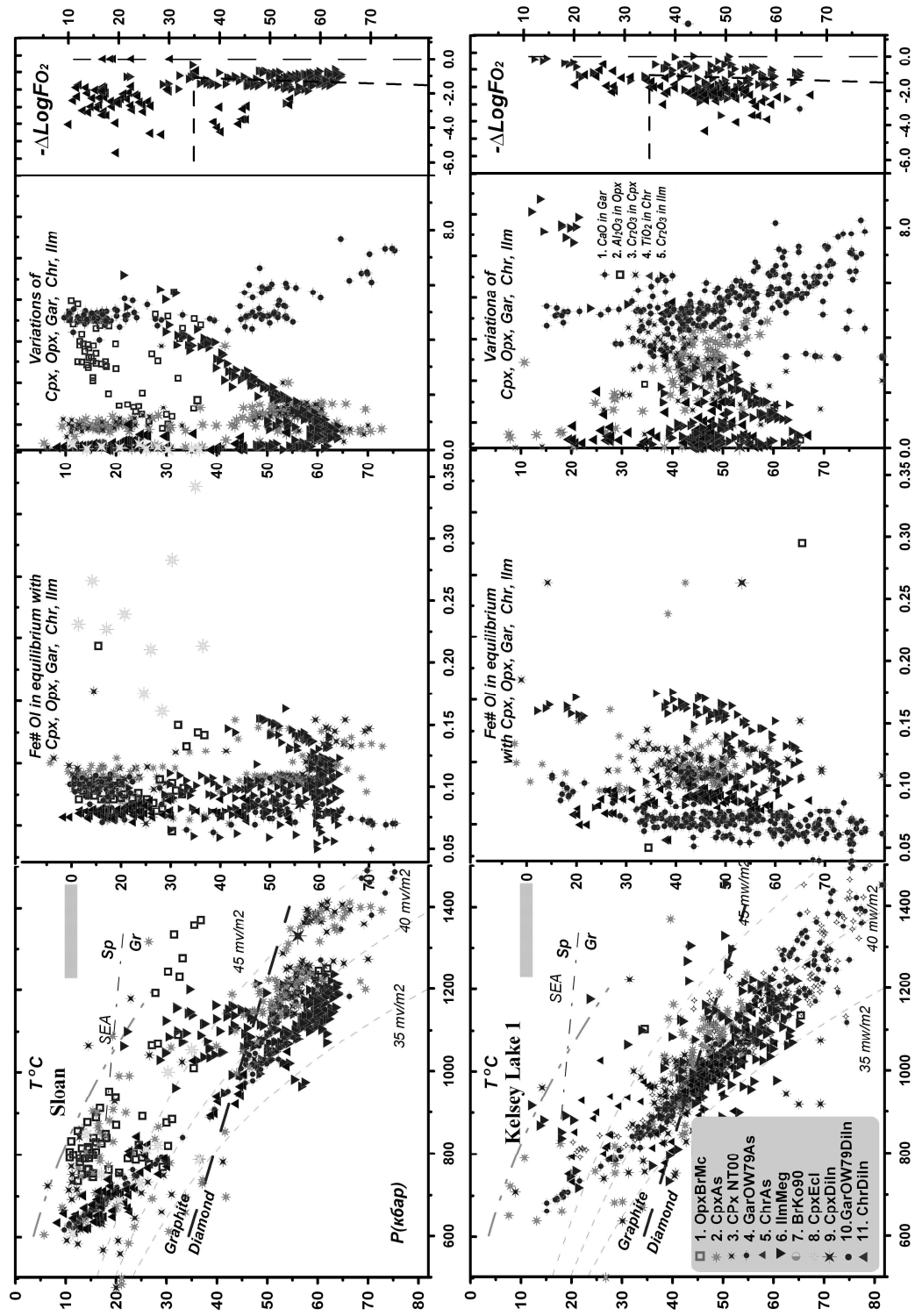


Fig.6. PTXFO2 conditions for the new data and for all previous data set of deep seated inclusions from kimberlite pipes Sloan (a) and Kelsey Lake 1 pipes (b) Symbols: 1. Opx T°C[2]- P(kbar) [31], 2. Cpx: T°C [33]- P(kbar) [2]; 3. T°C P [33], 12. Garnet [36]- P(kbar) [2]; 5. Chromite T°C [37]- P(kbar) [2]; 6. Ilmenite [54]- P(kbar) [2]; 7. T°C P(kbar) [31] ; 8. T°C [33]- P(kbar) [2] Cpx [2] for eclogites; 9. the same for diamond inclusions; 10. Gar [36]- P(kbar) [2] for diamond inclusions; 11. Chr T°C [37]- P(kbar) [2] for diamond inclusions.

higher than Opx and garnets in Fe# and definitely were formed as a result of fertilization.

TRACE ELEMENTS

The trace elements determined for the minerals from the Sloan pipe reveal rather uniform configuration of the spiderdiagrams for peridotitic garnets and clinopyroxenes. Garnets show mainly common rounded distributions corresponding to those equilibrated with Cpx which was formed from 1-2 % partial melting. Small humps (enrichment) from Nd to Gd for several grains may be a sign of their origin from pyroxenites. Such grains reveal small enrichment in U, Ba and less in Nb and Ta and very small fluctuations in Zr, Hf and have no Pb anomalies. The concentration of such components is lower for one even more depleted sample.

Most Cpx show the inclination $50 < \text{Gd/Yb} < 80$ which corresponds to the garnet mode of about 10-15% due to fluctuations in HREE. The spideragrams show small depletion in left part but without peaks. The small troughs of Zr are typical for all of them. The enrichment in Ba is due the presence of fluid inclusions – evaporation of fluids with Ba was visible during the laser ablation of the grain. The trace elements for ilmenites are also very uniform with the strong peaks in Ta-Nb, less in Hf-Zr and evident for Pb. But some ilmenites have higher Rb and Ba, probably due to metasomatism. One ulvospinel show inclined REE patterns and moderate enrichment in HFSE.

Eclogitic minerals demonstrate different behavior in trace elements. One of the eclogites shows common rounded patterns for garnets and clinopyroxene without Eu anomalies. The next one with high amount of modal Cpx demonstrates a spoon-like distribution common for garnet-poor or-free associations. Two Cpx show a distribution typical for plagioclase and probably result from the inversion of this mineral without high influence of garnet partitioning. The spiderdiagrams for most of them show peaks in Ba, U, Sr, Pb, which is typical for subduction-related fluids but they have no essential negative anomalies in HFSE.

Sloan minerals differ in geochemical features. Garnets with high-Cr content demonstrate increase in LREE and progressive S-shaping, with pressure increase. The peak in U is higher for garnets having common rounded REE.

Clinopyroxenes REE patterns show the rotation in Gd (La/Yb variations) suggesting a different percentage of garnet in melting/precipitation assemblages. Zr-Hf depletion was found for two grains while Ta-Nb minima are common. Depletion in HFSE coincides with the growth of the U peaks. Cpx with one order of magnitude REE enrichment displays LREE and Th enrichment probably derived from carbonatite melt. The pattern for Cpx from Sp lherzolites with flattened HREE show LREE enrichment or depletion and U, Ba peaks marking subduction processes. Spinels have very low concentrations of REE, with higher LREE and HFSE peaks. Ilmenites from this pipe are very enriched in trace elements espe-

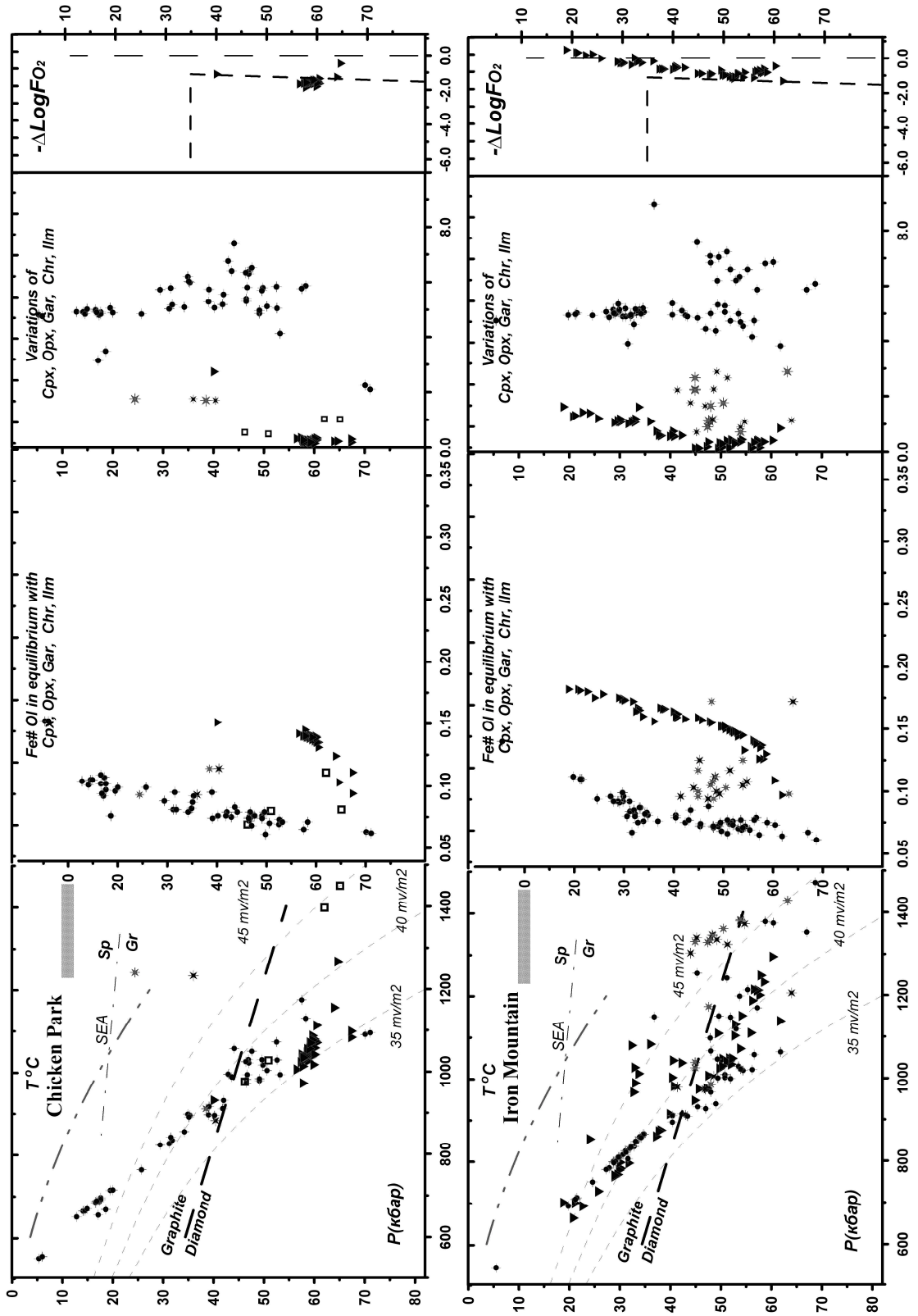


Fig.7. PTXFO2 diagrams for the Vendian Chicken Park and Ordovician Iron Mountain pipes.

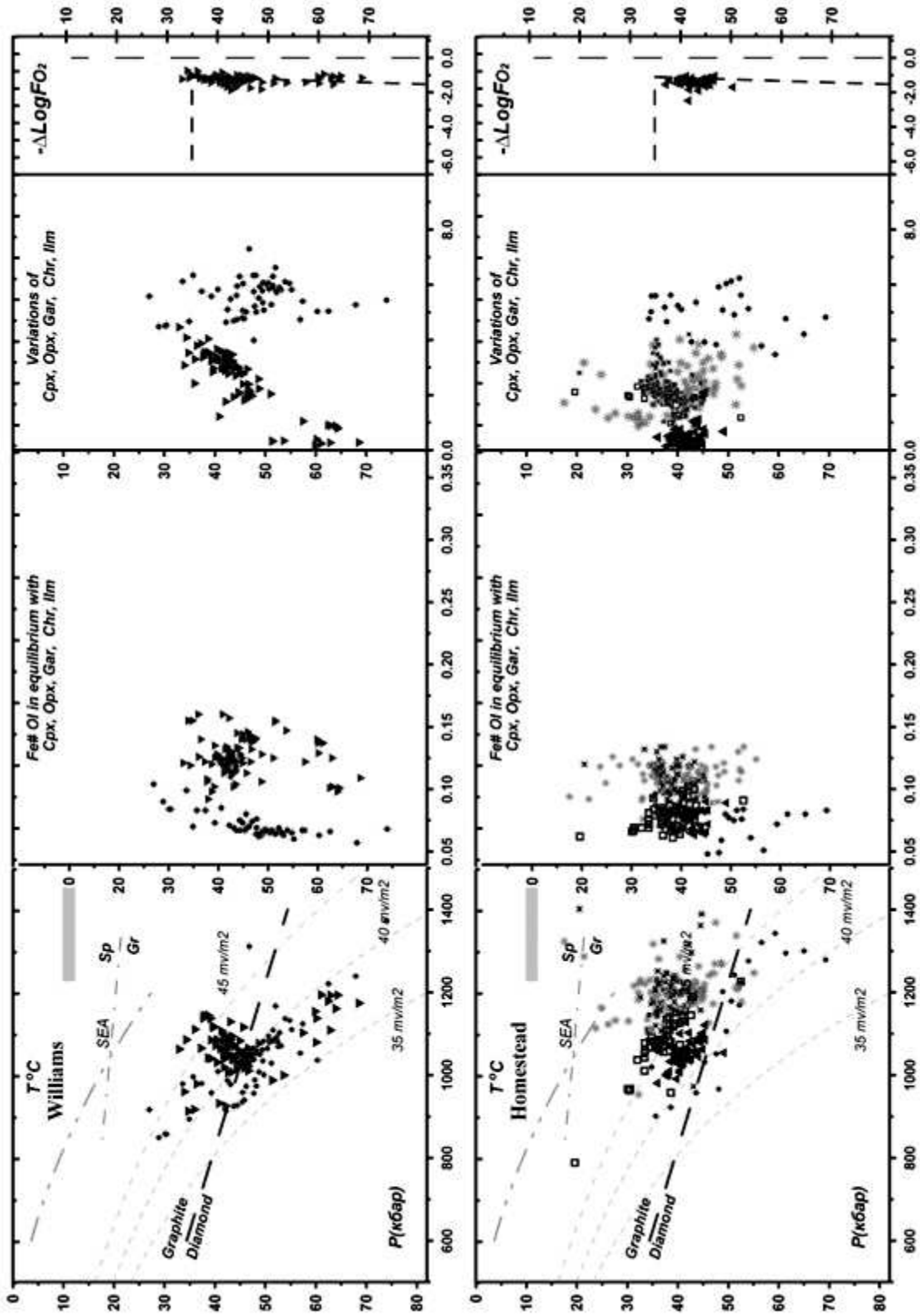


Fig.8. PTXFO2 diagrams for the minerals from concentrates Eocene Williams and Homestead kimberlite pipes (Montana) Symbols see Fig 6.

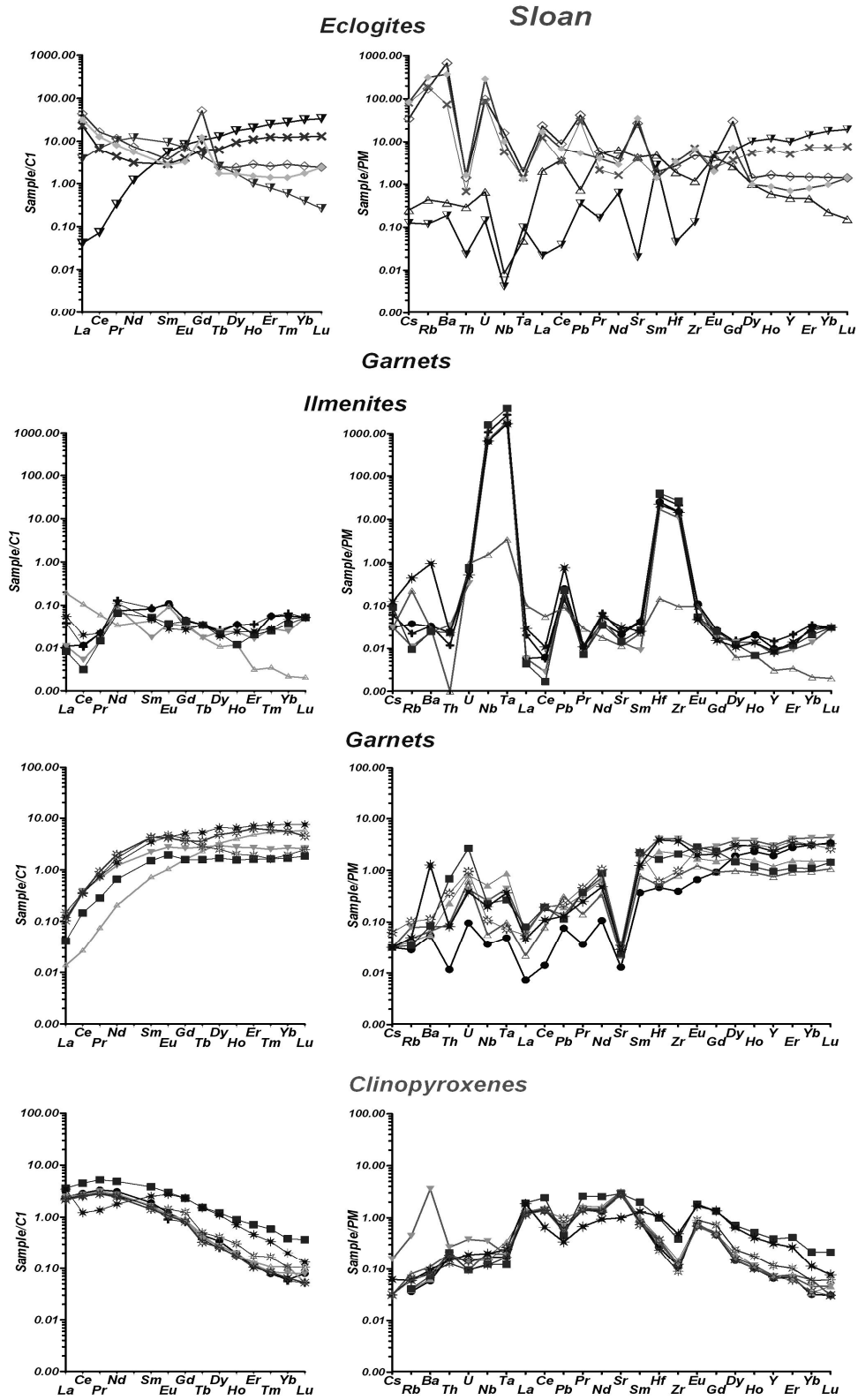


Fig. 9. Trace element pat-terns for minerals from deep seated inclusion from Sloan pipe

cially in LREE. The inclination of their REE patterns (La/Yb)_n is greater for the less enriched grains. Divergence in HREE may mean the garnet dissolution because other components especially Ta-Nb-Zr-Hf show very high concentrations.

DISCUSSION

Two pipes from different parts of the State Line region of the Wyoming craton have different mineralogical and geochemical features of the xenocrysts captured from the upper mantle. The SCLM under Sloan has a definite division to three units with contrasting structure of SCLM. Grouping of the minerals corresponds to these divisions. One can suppose a general scheme of the mantle

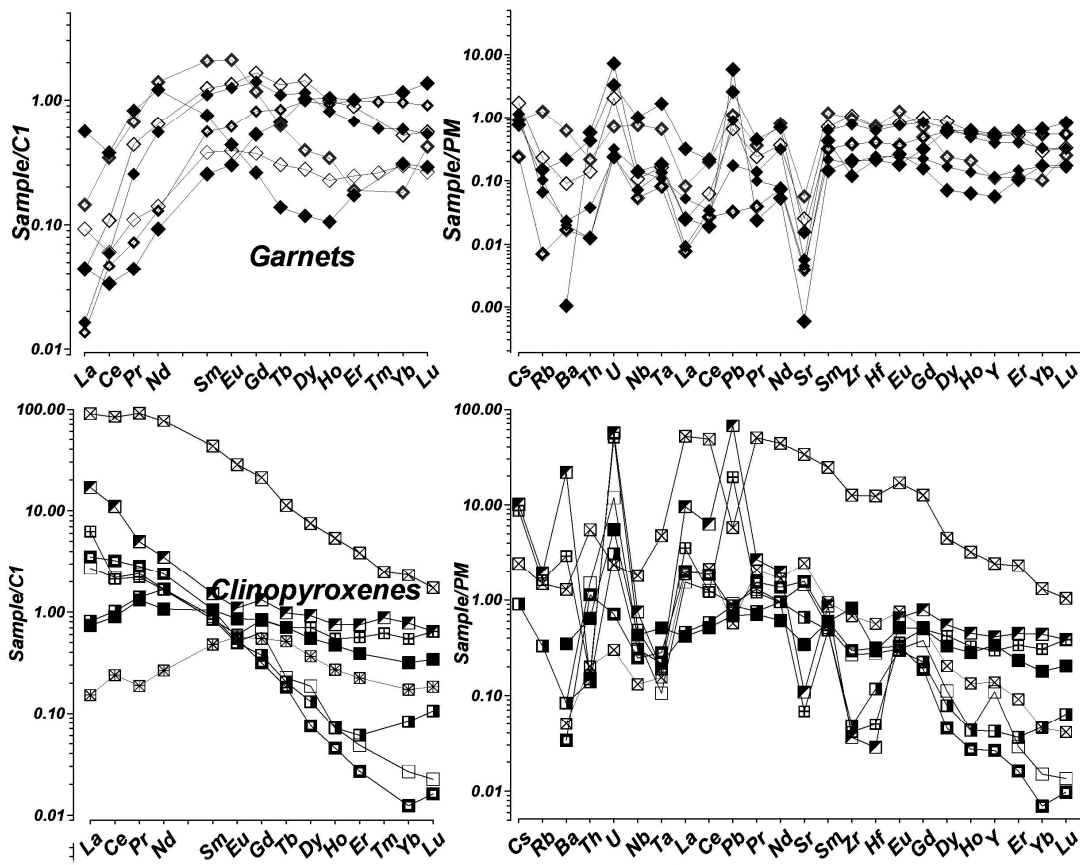


Fig. 10a. Trace element patterns for minerals from deep seated inclusion from Kelsey Lake-1 pipe.

structure development. Division at 40 kbar into the lower and upper section of typical for all mantle sections [2]. The SCLM beneath Chicken Park shows the first step with the high heating of the base of the mantle section and beginning of formation of deformed peridotites and the influence of plume melts marked by ilmenites. The next step of development of mantle section probably is shown by the Iron Mountain SCLM where probably a long protokimberlite vertical channel was traced by ilmenites and accompanied by local fertilization. The next step was

shown by the Williams SCLM in Montana where abundant melts likely created a mantle diapir which intruded the upper part of the mantle section, the more complete and homogenized type of such process are reflected by the Homestead SCLM, also in Montana. The story of the craton growth and destruction [9, 11] can be reconstructed in detail for its different parts.

The Sloan and KL-1 pipes reveal different processes of the extensive reaction of the mantle protolith with different matter. For Sloan the lower part is subjected to reactions with the rather uniform melt which was probably close to the protokimberlites. Cpx samples analysed for trace elements were from the lower part of the section and probably reflect this process. The KL – 1 SCLM was

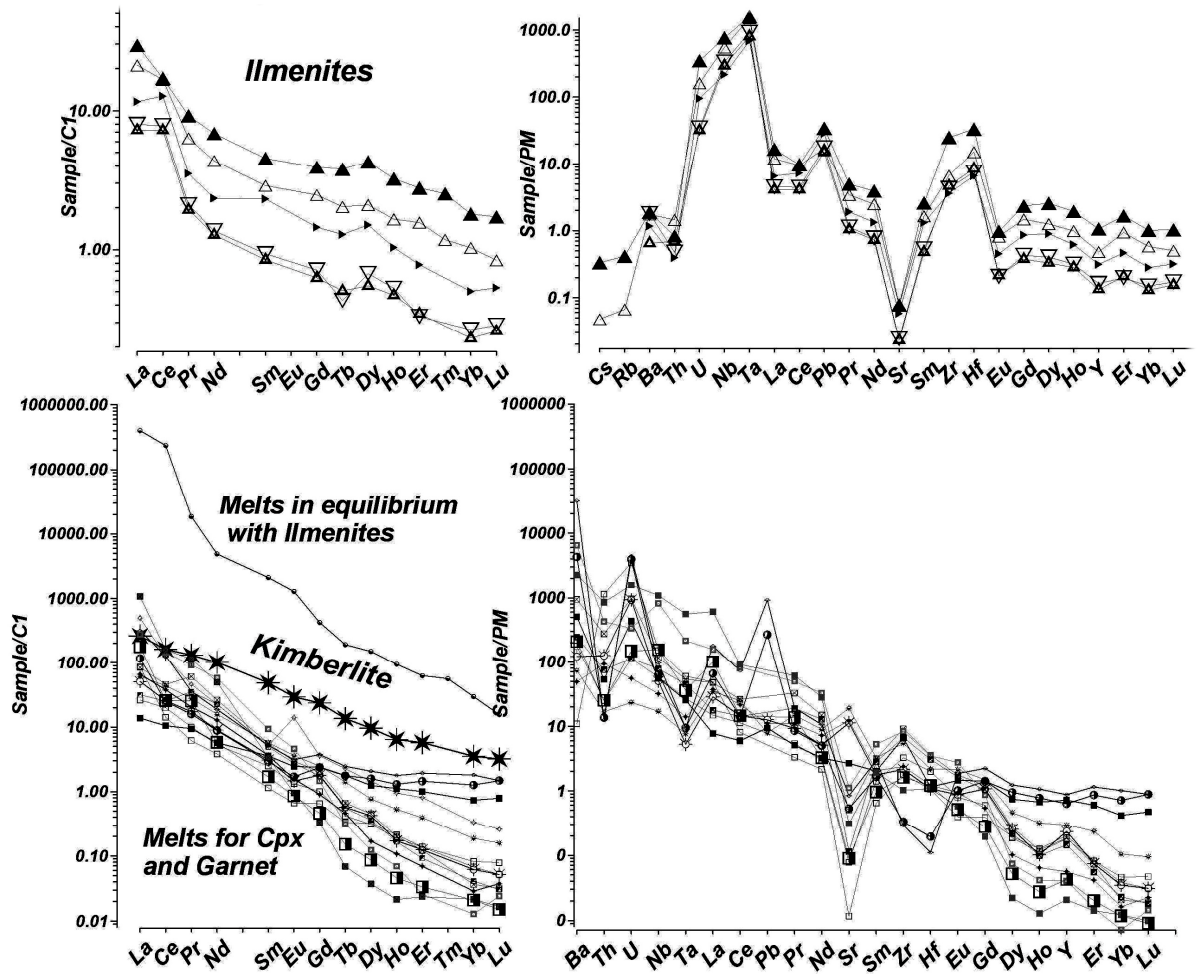


Fig. 10b. Trace element patterns for minerals from deep seated inclusion from Kelsey Lake-1 pipe.

probably much more diverse in composition and the section was later metasomatized and homogenized by protokimberlite melts. Originally it contained a lot of subduction material. This is visible by the high Mn Ba and Sr contents, and especially high Pb and U. This probably corresponds to the subduction not only eclogites but sediments. Trace element peaks correspondent to the subducted fluids how primary high degree metasomatism of the mantle. The metasomatism dated by

zircons reveals mainly the ages of the kimberlite formation [7, 8, 43]. Mantle xenoliths from the spinel facies which are depleted in some cases [13] and seems to be more enriched in the Sloan SCLM may give the most ancient ages for the craton growth.

The high heterogeneity of the mantle beneath the Wyoming craton was probably an original feature of the Wyoming craton keel which was composed from several high angle slabs joined together in craton margins. Position and compositions of the eclogites in the mantle section of different pipes is unstable and this also probably most interesting thing now to determine the ages of the eclogites, The Os ages for the peridotitic minerals indicate Archean to Proterozoic events [7-9].

ACKNOWLEDGEMENTS

We thank H Coopersmith for samples and concentrates, and the analytic laboratories of IGM SD RAS. This work was supported by grant 11-05-00060.

REFERENCES

1. **Ashchepkov, I.V., Vladykin, N.V., Mitchell, R.H., Howard, C., Garanin, V.G., Saprykin, A.I., Khmelnikova, O.S., Anoshin, G.N.** Mineralogy of the mantle xenocrysts from KL-1 (Kelsey lake) kimberlite pipe, Colorado // *Revista Brasileira de Geociencias*, 2001, v.31, pp. 645-652.
2. **Ashchepkov, I.V., Pokhilenko, N.P., Vladykin, N.V., Logvinova, A.M., Kostrovitsky, S.I., Afanasiev, V.P., Pokhilenko, L.N., Kuligin, S.S., Malygina, L.V., Alymova, N.V., Khmelnikova, O.S., Palessky, S.V., Nikolaeva, I.V., Karpenko, M.A., Stagnitsky, Y.B.** Structure and evolution of the lithospheric mantle beneath Siberian craton, thermobarometric study. // *Tectonophysics*. 2010. v. 485, pp.17-41
3. **Aulbach, S., Griffin, W.L., Pearson, N.J., O'Reilly, S.Y., Kivi, K., Doyle, B.J.** Mantle formation and evolution, Slave Craton: constraints from HSE abundances and Re-Os isotope systematics of sulfide inclusions in mantle xenocrysts.// *Chem. Geol.* 2004, v 208, pp. 61-88.
4. **Brey, G.P., Kohler, T.** Geothermobarometry in four-phase lherzolites. II. New thermobarometers, and practical assessment of existing thermobarometers. // *Journal of Petrology*, 1990. v.31, pp.1353-1378.
5. **Carlson, R.W., Irving, A.J.** 1994. Depletion and enrichment history of subcontinental lithospheric mantle: an Os, Sr, Nd, and Pb isotopic study of ultramafic xenoliths from the northwestern Wyoming craton. // *Earth Planet Sci Lett* v.126 pp.457-472
6. **Carlson, R.W., Irving, A.J., Hearn, B.C., Jr.** Chemical and isotopic systematics of peridotite xenoliths from the Williams kimberlite, Montana: clues to processes of lithospheric formation, modification and destruction. /In *Proc.7th Int.Kimberlite Conf.*(eds. J.J.Gurney, J.L.Gurney, M.D.Pascoe, and S.H.Richardson). Red Roof Design, Cape Town, 1999 .v.1, pp. 90-98.
7. **Carlson, R.W., Irving, A.J.** Depletion and enrichment history of sub-continental lithospheric mantle: Os, Sr, Nd and Pb evidence for xenoliths from the Wyoming Craton.// *Earth Planet. Sci.Lett.* 1994. v.126, pp. 457-472.
8. **Carlson, R. W., Irving, A.J., Schulze, D.J., Carter, B., Hearn, J.** Timing of Precambrian melt depletion and Phanerozoic refertilization events in the lithospheric mantle of the Wyoming Craton and adjacent Central Plains Orogen. // *Lithos* 2004. v.77. pp.453- 472

9. **Carlson, R. W., James, D. E.** 2011. Craton Destruction: An Ongoing Example in Western North America. /International Conference On Craton Formation And Destruction Abstracts, pp.14-15.
10. **Carvalho, J.B., Leonardos, O.H.** Garnet peridotites from the Três Ranchos IV kimberlitic pipe, Alto Paranaíba igneous province, Brazil: geothermobarometric constraints. //Russian Geol. Geophys., 1997. v.38/1, pp. 159-172.
11. **Coopersmith, H. G., Mitchell, R.H., Hausel W. D.** Kimberlites And Lamproites Of Colorado And Wyoming, Usa./ Guidebook for the VIIIth International Kimberlite Conference, Colorado and Wyoming Field Trip. 2003. 32 p.
12. **Davies, R.M., Griffin, W.L, O'Reilly, S.Y., Doyle, B.J.** Mineral inclusions and geochemical characteristics of microdiamonds from the DO27, A154, A21, A418, DO18, DD17 and Ranch Lake kimberlites at Lac de Gras, Slave Craton, Canada. //Lithos 2004. v.77, pp.39– 55.
13. **Downes, H., Macdonald, R., Upton, B. G. J., Cox, K.G., Bodinier, J-L., Mason, P. R. D., James, D., Hill, P.G., Hear, B. C. Jr.** Ultramafic Xenoliths from the Bearpaw Mountains, Montana, USA: Evidence for Multiple Metasomatic Events in the Lithospheric Mantle beneath the Wyoming Craton //J. Petrology, 2004, v.45, pp. 1631 - 1662.
14. **Ehrenberg, S.N.** Rare earth element geochemistry of garnet lherzolite and megacryst all in nodules from minette of the Colorado Plateau province.// Earth Planet. Sci.Lett. 1982., v.57 , pp.191–210.
15. **Ehrenberg, S.N.** Petrogenesis of garnet lherzolite and megacrystalline nodules from the Thumb, Navajo Volcanic Field. // J.Petrol., 1982, v.23, pp.507-547
16. **Eggler, D.H., McCallum, M.E., Smith, C.B.** Megacryst assemblages in kimberlite from northern Colorado and southern Wyoming: petrology, geothermometry –barometry and areal distribution. /In Kimberlites, Diatremes, and Diamonds: Their Geology, Petrology, and Geochemistry (eds. F.R.Boyd and H.O.A.Meyer). American Geophysical Union, Washington, DC, 1979. V. 1, pp. 213–226.
17. **Eggler, D.H., McCallum, M.E., Kirkley, M.B.** Kimberlite-transported nodules from Colorado-Wyoming: A record of enrichment of shallow portions of an infertile lithosphere. In: Morris, E.M. and Pasteris J.D., eds., Mantle metasomatism and alkaline magmatism// Geol. Soc. Am. Spec. Paper 1987, v.215, pp.77-90.
18. **Griffin, W.L., Suzanne O'Reilly, Y., Doyle, B.J., Pearson, N.J., Coopersmith, H., Kivi, K., Malkovets, V., Pokhilenko, N.** Lithosphere mapping beneath the North American plate //Lithos,2004, v.77, pp.873-922
19. **Griffin, W.L., Kobussen, A.F., Babu, E.V.S.S.K., O'Reilly, S.Y., Norris, R., Sengupta, P.** A translithospheric suture in the vanished 1-Ga lithospheric root of South India: Evidence from contrasting lithosphere sections in the Dharwar Craton // Lithos, 2009. 112, 2, 2009, 1109-1119
20. **Hausel, W.D.** Diamonds and mantle source rocks in the Wyoming Craton, with a discussion of other US occurrences/ Wyoming State Geological Survey Report of Investigations 53, 1998. 93 p.
21. **Heaman, L.M., Kjarsgaard, B.A., Creaser, R. A.** The temporal evolution of North American kimberlites.// Lithos. 2004. v.76. p. 377– 397.*
22. **Heaman, L.M., Kjarsgaard, B.A., Creaser, R.A.** The timing of kimberlite magmatism in North America: implications for global kimberlite genesis and diamond exploration. //Lithos. 2003. Vol. 71. Iss. 2-4. P. 153-184.
23. **Hearn, B. C.** The Homestead kimberlite, central Montana, USA: mineralogy, xenocrysts, and upper-mantle xenoliths. //Lithos, V.77, 2004, 473-491

24. **Hearn, B. C. Jr., McGee, E. S.** 1984 Garnet peridotites from Williams kimberlites, north-central Montana, USA /in Kornprobst, J., ed., *Kimberlites II: The Mantle and Crust-Mantle Relationships*: Amsterdam, Elsevier, 1984, p. 57-70.
25. **Kopylova, M.G., Caro, G.** Mantle xenoliths from the Southeastern Slave craton: Evidence for chemical zonation in a thick, cold lithosphere. // *J. Petrol.* 2004. Vol. 45. Iss. 5. pp. 1045-1067.
26. **Lavrent'ev, Yu. G., Usova, L.V.** New version of KARAT program for quantitative X-ray spectral microanalysis. // *Zhurnal Analiticheskoi Khimii*, 1994., v.5, pp.462–468.
27. **Lester, A., Larson, E.** New geochronological evidence for the Late Proterozoic emplacement of Colorado Wyoming kimberlites belt. // *EOS Trans. Am. Geoph. Union*, 1996, v.77(41), pp. 821
28. **McCallum, M.E., Eggler, D.H.** Diamonds in an upper mantle peridotite nodule from kimberlite in southern Wyoming. // *Science*. 1976. V. 192. P. 253-256.
29. **McCallum, M. E., Eggler, D. H., Burns, L. K.** Kimberlitic diatremes in northern Colorado and southern Wyoming. // *Physics and Chemistry of The Earth*, V. 9, 1975, P. 149-161
30. **McDonough, W.F., Sun, S.S.** The Composition of the Earth. // *Chemical Geology*. 1995. V.120, pp. 223-53.
31. **MacGregor, I.D.** 1974. The system MgO-Al₂O₃-SiO₂: solubility of Al₂O₃ in enstatite for spinel and garnet peridotite compositions.// *Am Mineral*. 1974. v.59. pp. 110±119
32. **Mitchell, R. H., Bergman, S. C.** / *Petrology of Lamproites*; Plenum Press, New York, 1991, 447 p.
33. **Nimis, P. Taylor, W.** Single clinopyroxene thermobarometry for garnet peridotites. Part I. Calibration and testing of a Cr-in-Cpx barometer and an enstatite-in-Cpx thermometer. // *Contrib. Mineral. Petrol.* , 2000. v.139 (5), pp.541-554.
34. **Nixon, P.H., Boyd, F.R.** Petrogenesis of the granular and sheared ultrabasic nodule suite in kimberlites./ In: Nixon PH (ed) *Lesotho kimberlites*. Lesotho Nat Dev Corp Maseru, Lesotho, 1973, pp 48-56.
35. **O'Brien, H. E., Irving, A. J., McCallum, I. S., Thirwall, M. F.** Sr, Nd and Pb isotopic evidence for the interaction of post-subduction asthenospheric potassic mafic magmas of the Highwood Montana, Montana, USA, with ancient Wyoming craton lithospheric mantle. // *Geochimica et Cosmochimica Acta*. 1995. V.59, 4539-4556.
36. **O'Neill, H. St. C. & Wall, V. J.** 1987. The olivine orthopyroxene-spinel oxygen geobarometer, the nickel precipitation curve, and the oxygen fugacity of the Earth's upper mantle. // *Journal of Petrology*, 1987. v. 28, pp.1169-1191
37. **O'Neill, H.St.C, Wood, B.J.** An experimental study of Fe-Mg- partitioning between garnet and olivine and its calibration as a geothermometer. // *Contrib. Mineral. Petrol.* 1979. v.70, pp.5970
38. **Patel, S.C., Ravi S., Anilkumar, Y., Pati, J.K.** Major element composition of concentrate garnets in Proterozoic kimberlites from the Eastern Dharwar Craton, India: Implications on sub-continental lithospheric mantle. // *Journal of Asian Earth Sciences*. 2010. v.39, pp. 578-588
39. **Pokhilenko, N. P., Sobolev, N.V., Kuligin, S. S., Shimizu, N.** Peculiarities of distribution of pyroxenite paragenesis garnets in Yakutian kimberlites and some aspects of the evolution of the Siberian craton lithospheric mantle.// *Proceedings of the VII International Kim-berlite Conference*. The P.H. Nixon volume. 1999. pp. 690-707.
40. **Pokhilenko, N. P., Pearson, D. G., Boyd, F. R. & Sobolev, N. V.** Megacrystalline dunites: sources of Siberian diamonds. /*Carnegie Inst. Washington Yearbook*, 1991. pp.11-18.

41. **Rao K.R.P., Rao K.N., Dhakate M.V., Nayak S.S.** Petrology and mineralogy of mantle xenoliths of Wajrakarur and Narayanpet kimberlite fields, Andhra Pradesh, India. //Geol Surv India Special Publication 2001. v.58, pp. 577–591
42. **Roden, M. R., Shimizu, N.** Trace element abundances in mantle-derived minerals which bear on compositional complexities in the lithosphere of the Colorado Plateau. /Chemical Geology 2000. v.165, pp. 283–305
43. **Rudnick, R.L., Ireland, T.R., Gehrels, G., Irving, A.J., Chesley, J.T., Hanchar, J.M.** Dating mantle metasomatism: U–Pb geochronology of zircons in cratonic mantle xenoliths from Montana and Tanzania. /In Proc.7th Int. Kimberlite Conf.(eds. J.J.Gurney,J.L.Gurney, M.D.Pascoe, and S.H.Richardson). Red Roof Design, Cape Town, 1999. vol. 2, pp. 728–735.*
44. **Schulze, D. J.** Diamond Eclogite from Sloan Ranch, Colorado and its Bearing on the Diamond Grade of the Sloan Kimberlite.// Economic Geology, 1992. v. 87, p. 2175-2179.
45. **Schulze, D. J., Anderson, P. F. N., Hearn, B. C., Jr., and Hetman, C. M.** Origin and Significance of Ilmenite Megacrysts and Macrocrysts from Kimberlite.// International Geology Review, 1995v. 37, p. 780-812.
46. **Schulze, D. J.** The Significance of Eclogite and Cr-poor Megacryst Garnets in Diamond Exploration. //Explor. Mining Geol., 1997.v. 6, pp. 349-366,
47. **Schulze, D. J., Coopersmith, H. G., Harte B., Pizzolato, L.-A.** Mineral inclusions in diamonds from the Kelsey Lake Mine, Colorado, USA: Depleted Archean mantle beneath the Proterozoic Yavapai province. // Geochimica et Cosmochimica Acta, 2008, v. 72, pp.1685–1695.
48. **Smith, C.B., McCallum, M.E., Coopersmith, H.G., Eggler, D.H.** Petrochemistry and structure of kimberlites in the Front Range and Laramie Range, Colorado-Wyoming, /in Boyd, F.R. and Meyer, H.O.A., eds, Kimberlites, diatremes, and diamonds; Their geology, petrology, and geochemistry, American Geophysical Union, Washington. D.C.: American Geophysical Union, 1979. pp. 178-189.
49. **Smith D., Griffin W.L.** Garnetite Xenoliths and Mantle–Water Interactions Below the Colorado Plateau, Southwestern United States. //J. Petrology. 2005, v.46 , pp. 1901–1924
50. **Sobolev, N.V.** Deep-Seated Inclusions in Kimberlites and the Problem of the Composition of the Mantle./ 1977, Amer. Geophys.Union, Washington, DC. 279 p.
51. **Sobolev, V.N., Taylor, L.A., Snyder, G.A., Sobolev, N.V.** Diamondiferous eclogites from the Udachnaya pipe, Yakutia // International Geology Review, 1994, v. 36, N 1, pp. 42-64
52. **Sobolev, N.V., Lavrent'ev, Yu.G., Pokhilenko, N.P., Usova, L.V.** 1973. Chrome-rich garnets from the kimberlites of Yakuti and their parageneses. // Contrib Mineral Petrol., 1973, v.40; pp. 39–52.
53. **Sobolev, N.V., Sobolev, V.N., Snyder, G.A., Yefimova, E.S., Taylor, L.A.** Significance of eclogitic and related parageneses of natural diamonds. //Intern Geol Rev 1973, v.41, pp. 129–140
54. **Taylor, W.L., Kamperman, M., Hamilton, R.** New thermometer and oxygen fugacity sensor calibration for ilmenite and Cr-spinel- bearing peridotite assemblage. /In: Gurney, J.J., Gurney, J.L., Pascoe, M.D., Richardson, S.H. (Eds.)/7th International Kimberlite Conference. In: Red Roof Design, Capetown, 1998. pp.986–988
55. **Usui, T., Kobayashi, K., Nakamura, E., Helmstaedt, H.** Trace element fractionation in deep subduction zones inferred from a lawsonite-eclogite xenolith from the Colorado Plateau Chemical Geology, 2007, 239, pp. 336–351

The RHA coding of mineral compositions of alkaline rocks exemplified by the nepheline syenite family

Krasnova N., Petrov T., Korolev N.

Dept of Mineralogy, Saint-Petersburg State University, University Embankment 7/9, Saint Petersburg 199034, Russia

ABSTRACT

Alkaline igneous rocks have a notoriously complex nomenclature. A new method of coding the mineralogical compositions of alkaline rocks is offered. Normative compositions of 418 alkaline rocks calculated using program NORM-4 provided the input data. They were processed on RHA method (program PETROS-2). This provides the following information: R (the rank formula) which is a sequence of components ordered in decreasing content in the normative analysis (e.g. (Ab>Ne>Ort>...)); H which is a measure of the complexity or “entropy” of the composition; A which is a measure of purity of the composition (i.e. how closely it approaches being a monomineralic rock). The set of R values provided by the program can be considered analogous to words, e.g. AbNeOrt (Ab>Ne>Ort>...). They are ordered “alphabetically” to give the R-classification of mineralogical composition of rocks (see: <http://geology.spbu.ru/department/scientific/rha-language-method/>). This method can serve as a universal language for worldwide communication of geologists, and applies particularly well to the complex nomenclature of alkaline igneous rocks.

INTRODUCTION

It is known that the names given to the same rock by different authors differ considerably, not only by macroscopic description but also even after microscopic study. D’Alessandro et al. [4] proved this by sending identical specimens of 23 different rocks for independent examination by petrographers in 18 different geological institutes in various parts of the world. The resulting petrographic names of these specimens and their descriptions varied widely, viz. 22 of the 23 rocks received at least four different petrographic names. This clearly showed that differences in nomenclature and description mainly arise due to the “manner of observing”, i.e. by subjective factors. This can cause significant difficulties in the worldwide exchange of geological or geochemical data based on rock names. The situation has not essentially changed for the past 30 years. The existing rules of rock classification are not universal, and consequently are at best suitable for ordering only within the limits of individual rock groups, not covering all their variety.

Natural borders between chemical compositions of “different” rocks do not exist. There is an important distinction between chemical and mineral compositions. According to the known Russian geochemist Vernadsky [21], the wide dispersion of elements should be considered as characteristic property of

Table 1

The names of some rocks of nepheline syenite group and their mineral composition according to [11, 2].

localynames	locality	Rock name and mineral composition
borolanite	Loch Borolan, Scotland	Ne syenite [Ort, Bt, Andr, Ps-Lct
ditroite	Ditro, Romania	Ne syenite [Cen, Bt, Cal
foyaite	Mt Foya, Portugal	Ne syenite trachytoid [Ort, Aeg, Arf, Ab
juvite	Juvet complex, Norway	Ne syenite [Ort.>Ab
kakortokite	Kakortok, Grenland	Ne syenite [Eud, Arf
khibinite	Khibina, Russia	Ne syenite [Aeg, Eud, Amf
litshfieldite	Lithfield, St. Maine, USA	Ne syenite [K, Fsp, Ab,Cen, Sld, Lpdm
lujavrite	Mt. Lujavr, Lovosero, Russia	Ne syenite melanocrate [Eud, Aeg, Arf
malignite	R. Malign	Ne syenite fg [Ort, Aeg, Aug, Cen, Amf
mariupolite	Mariupol, Ukraine	Ne syenite leucocrate [Ab, Aeg (no K-Fsp!)
miaskite	Miass, Russia	Ne monzosyenite (12 QAPF) [Bt,Ort, Olig
naujaite	Naujakasik, Greenland	Ne-Sdl syenite [Ort, Arf, Aeg, Eud
pulaskite	Raglan, Ontario, Canada	Ne diorite [Olig, Bt
rischorrite	Mt.Rischorr, Khibina, Russia	Ne syenite poikilitic [Bt, Aeg-Aug, Ap
saibarite	Sabar, Siberia, Russia	Ne syenite trachytoid [Aeg, K, Fsp, Ab, Amf
shonkinite	Shonkin, Montana, USA	Ne syenite (II QAPF) [Ort, Aug, Ol, Bt, Hbl

Note: Ab – albite, Aeg – aegirine, Amf – amphibole, Arf – arfvedsonite, Aug – augite, Bt – biotite, Cen – cancrinite, Crn – corundum, Di – diopside, Eud – eudialite, Fa – fayalite, Hbl – hornblende, K-Fsp – potassium feldspar, Ne – nepheline, Ol – olivine, Olig – oligoclase, Ort – orthoclase.

substance of our planet. In the first quarter of previous century he pointed out that in any geological object, there are all elements of the periodic table. At the same time, rocks contain mixtures of compounds of elements (minerals) in which the variety of minerals is sharply limited. Eight to ten elements are required for the description of a rock using its chemical composition, and often additional data, but only 3-5 minerals are often sufficient for the same task using mineral compositions. The natural limits both of rock-forming oxides and mineral contents in any given rock family usually overlap, and the definition of the different types within the family causes difficulties. Besides this, unequivocal identification of rock types is confused also by the fact that classifications published in reference books [e.g., 11; 2] are based on different principles (mineral and/or chemical composition, texture and structure, agpaite coefficient, etc.). The data about rock compositions are not systematized, which makes the uniform ordering and searching of information about the rock's composition impossible (Table 1). In addition, the rigid criteria used to unequivocally define a rock variety are not fixed to traditional names of nepheline syenites rocks [2]. The alkaline rocks, and in particular the representatives of the nepheline (feldspathoid) syenite group, often sharply reveal contradictions connected with definition of the rock name [8].

Uncertainty of rock names in relation to their mineral composition will be shown using the example of the nepheline syenites rock family. The main task of this article is to present a way of describing a rock's mineralogical composition, which will help to produce a more improved nomenclature.

INITIAL DATA AND METHOD OF PROCESSING

The practical absence of parallel chemical and mineral analyses of alkaline rocks has compelled us to use normative rock compositional data, calculated by means of program Norm-4 applied by many geologists. We will not discuss the problem of conformity of the mineral composition derived from the CIPW method to real rock compositions, since normative calculations are standard petrographic practice. It is sufficient that use of similar chemical rock analyses leads to similar normative mineral compositions, irrespective of the method by which they have been calculated.

Normative compositions have been calculated for 418 chemical analyses of many alkaline rock varieties taken from six literature sources and two databases of our own. They are given in volumetric % (Vol. %), which most closely corresponds to the visual definition of the rock.

The systematisation of chemical and mineral compositions has been made using the rank-entropy RHA method [14]. It is based on a principle of ordering of components ranged according to decreasing content in the analysis – R. The symbol “=” between two components shows that $p_i/p_{i+1} \leq 1,15$, which corresponds to the difference between the neighbouring components not more than 15% relative. The entropy and purity characteristics (H and En, respectively) describe a kind of ranged distributions (rank distribution). The closer H is to zero, the closer the rock is to being monomineralic; the closer En is to unity, the closer is its composition to a uniform distribution of volumes of different minerals (uniform distribution of volume %). The method is described in more detail by Petrov [15] and Petrov and Farafonova [16]. The results are abbreviated as RHACHem and RHAMin respectively.

From the ranking we receive the rank formulas (Rmin) which are sequences of minerals, e.g. of type AbNeOrt... that corresponds to decreasing volume fractions (percents) of minerals in a rock $Ab > Ne > Ort$. (Table 2). Such an arrangement of mineral symbols in the description puts the dominant components into first place, in other words, the building material defines the major properties of the object. Such components of some of the analyses shown in Table 2 are specially marked to facilitate the understanding the rank formulas formation. The ordered set of symbols of the components corresponds to the visual definition of the rock's composition. The rank formula set can be seen as being analogous to a word, which can be ordered under a specially chosen or created alphabet.

In the case of alkaline rocks, the rank formula sets are ordered under a certain “alphabet, using the sequence of minerals in their chemical R-classification of all minerals [17; also see a file R-Min-Catalogue-2010.rar at the same web-site].

Horizontal lines (classifiers), which begin from each new component in their vertical succession, divide distinct groups of Rmin's.

RESULTS

Table 2 represents the calculated normative compositions and corresponding rank formulas (Rmin) of foyaites and some other nepheline syenites. Three normative minerals (namely Ne, Ab and Ort) dominate the first three ranks. Only in the rank formulas of two foyaites is the third rank occupied by Di (diopside) and in one Crn (corundum). The variety of compositions sharply increases when the 4th component is considered and further changes a little: the only new component Mag (magnetite) occupies the 5th rank. The file RHA-Min comp_alkaline rocks.rar on the web-site <http://geology.pu.ru/> shows the full version of our results.

Table 3a-e with reduced up to 3 positions rank formulas show the predominance in their composition of nepheline (Ne), orthoclase or microcline (Ort) and alkaline plagioclase (Ab) assemblages. Comparison of R-data for all syenite family rocks shows similarity of many rank formulas. Thus, formulas AbNeOrt and AbOrtNe are present in the following groups: foyaites (Table 3a), khibinites (Table 3b), mariupolites (Table 3c), miaskites (Table 3d) and lujavrites (Table 3e). In contrast, the formula OrtNeAb is common in foyaites, khibinites, rischorrites and juvites (data on the latter two are available only in the full table on the web-site). The formula OrtAbNe is seen in foyaites, khibinites, miaskites and lujavrites. Thus, it is clear that, using such short rank formulas, it is impossible to define a rock variety in the nepheline syenites rock family. The similarity of rank formulas within the limits of the three first components in Table 3a-e illustrates a generality of representatives from this rock group. On the other hand, the variety of names of such rocks in Table 1 is mostly caused by distinctions of minor minerals, many of which contain volatile components. Concentrations of these minerals are impossible to calculate using the program NORM-4. The solution to this problem requires either significant improvement to this program, or direct definition of the real mineral contents of rocks. The latter is more desirable, as it corresponds more closely to nature. First, it will allow us to consider the present minerals, instead of virtual components such as K_2SiO_3 , Na_2CO_3 , corundum, etc., derived sometimes from the norm calculations. Secondly, it will provide an account of the minerals including volatile components, among which in the rocks under consideration usually occur micas, amphiboles, cancrinite, etc. Presence of these minerals does not come to light by using of program Norm-4. Semenov [20] already pointed out the great significance of the melanocratic minerals for the classification of alkaline rocks.

Using the visual definition of mineral content in a sample (Figure a) or in thin section (Figure b), it is possible to represent the real composition of rock. Such a

Table 2

Rank formulas of normative mineral volume % for foyaites and other, nepheline syenites. Values of En – information entropy and An – anentropy are calculated for first 4 components.

Rank formula_Min			En	An	Description	Cal	Nts	Oi	Crn	Ne	Ab	Aeg	Di	Ort	Ap	Ilm	Mag	An%
Ne	Ab	Ort Nts Aeg	0.899	0.030	10-19-41_ foyaites Sdl	4	9	6	0	30	26	7	1	17	0	1	0	0
Ne	Ort	Ab= Cal Oi	0.558	0.181	14-1061-t30_ foyaites Aeg-Hd	3	0	2	0	54	3	0	0	38	0	0	1	7
Ne	Ort	Ab Oi Cal	0.731	0.116	6-1061-t19_ syenite Ne	2	0	3	0	41	24	0	0	28	0	0	1	26
Ne	Ort	Ab Oi Aeg	0.702	0.101	4-1061-t32_ foyaites peg.	0	2	4	0	53	14	3	1	22	0	0	0	0
Ne	Ort	Di= Ab Cal	0.804	0.066	8-1061-t30_ foyaites Aeg-Hd	4	0	2	0	38	6	0	16	31	0	1	3	24
Ab	Ne=	Ort Di= Oi	0.732	0.125	3-1061-t32_ foyaites Aeg-Arf	0	0	2	0	29	34	1	2	29	1	0	1	0
Ab	Ort=	Ne Oi Di	0.685	0.169	6-1061-t31_ foyaites Ab	0	0	1	0	29	38	0	1	30	0	0	1	4
Ab	Ort	Ne Oi Mag	0.707	0.135	6-1061-t18_ foyaites av.4	1	0	3	0	21	40	0	1	33	0	0	1	12
Ab	Ort=	Ne Oi Mag	0.672	0.158	9-2008-t8_ miaskite	0	0	2	1	23	48	0	0	24	0	0	1	5
Ab	Ort	Ne Di= Cal	0.748	0.080	11-1061-t30_ foyaites Aeg-Hd	4	0	4	0	9	43	0	4	32	0	1	3	22
Ab	Ort	Ne Di Oi	0.686	0.145	3-19-t35_ foyaites-fenite	0	0	1	0	17	43	0	3	34	0	0	1	17
Ort	Ne=	Ab Cal Di	0.783	0.089	6-1061-t30_ foyaites Aeg-Hd	6	0	1	0	25	24	0	3	38	0	1	1	6
Ort	Ne	Ab Oi Aeg	0.725	0.085	10-2009-t41_ foyaites Aeg-Amf	0	2	5	0	19	14	4	3	53	0	0	0	0
Ort	Ne=	Ab Aeg= Oi	0.616	0.143	7-1061-t28_ foyaites	0	3	3	0	23	21	3	1	44	0	1	0	0
Ort=	Ne	Ab Aeg= Di	0.821	0.063	38-19-t41_ foyaites	0	0	3	0	31	20	6	5	34	1	0	0	0
Ort	Ne	Ab Aeg Di	0.767	0.079	2-19-t36_ foyaites	1	3	2	0	25	15	4	4	43	2	1	0	0
Ort=	Ne	Ab Di Oi	0.712	0.140	4-19-t5_ foyaites	0	0	1	0	32	26	0	2	36	0	1	1	8
Ort	Ne=	Ab Di Aeg	0.772	0.093	46-2025-t1_ khibinite	0	0	2	0	28	25	3	4	36	0	1	1	0
Ort	Ne=	Ab Di= Aeg	0.706	0.140	5-19-t37_ foyaites Bt	0	0	1	0	29	26	2	2	39	0	1	0	0
Ort=	Ne	Ab Ap Crn	0.739	0.111	154-2025-t1_ foyaites Amf-Aeg	0	0	2	2	32	23	0	0	37	3	1	1	1
Ort	Ne	Di= Ab Cal	0.856	0.052	9-1061-t30_ foyaites Aeg-Hd	4	0	0	0	28	11	0	18	33	0	2	3	6
Ort	Ab	Crn Ne Cal	0.742	0.095	12-2009-t41_ foyaites peg.	3	0	2	12	7	32	0	0	44	0	0	1	6
Ort	Ab	Ne Oi Cal	0.740	0.100	4-19-t36_ foyaites	2	0	5	0	18	24	0	1	45	1	1	2	28
Ort	Ab=	Ne Oi= Aeg	0.774	0.091	160-2025-t1_ foyaites Amf-Bt	0	0	3	0	27	29	3	2	34	0	1	0	0
Ort	Ab=	Ne Oi Mag	0.689	0.166	18-2025-t1_ khibinite	0	0	2	0	29	31	0	0	36	0	1	1	16
Ort	Ab	Ne Oi Mag	0.636	0.186	9-2009-t41_ foyaites	0	0	3	0	17	23	0	0	55	0	0	1	34
Ort	Ab	Ne Aeg Oi	0.838	0.055	2-1061-t28_ phase II_ foyaites	0	3	4	0	21	26	6	4	34	0	1	0	0
Ort=	Ab	Ne Aeg Oi	0.728	0.121	168-2025-t1_ foyaites Ab	0	1	2	0	24	33	2	1	35	1	1	0	0
Ort	Ab	Ne Aeg Di	0.714	0.132	4-19-t37_ foyaites Bt-Pyx	0	1	1	0	25	31	2	2	38	0	0	0	0
Ort	Ab=	Ne Di Oi	0.756	0.078	8-2009-t41_ foyaites Bt	0	0	4	0	17	17	0	8	51	1	1	2	18
Ort=	Ab	Ne Di Oi	0.745	0.112	13-1061-t18_ foyaites	1	0	2	0	25	32	0	3	34	0	0	1	7

Note see table 1 and also: Ap – apatite, Cal – calcite, Ilm – ilmenite, Mag – magnetite, Nts – natrosilite, Wo – wollastonite. Description: No of analysis; No of reference: 19 – [3], 1061 – [7], 2009 – [5], 2025 – [6]; author's rock name. An% – anorthite % in plagioclase.

definition more or less corresponds to the calculation of volumetric % of minerals in the rock and can be represented in the form of rank formulas. In the present

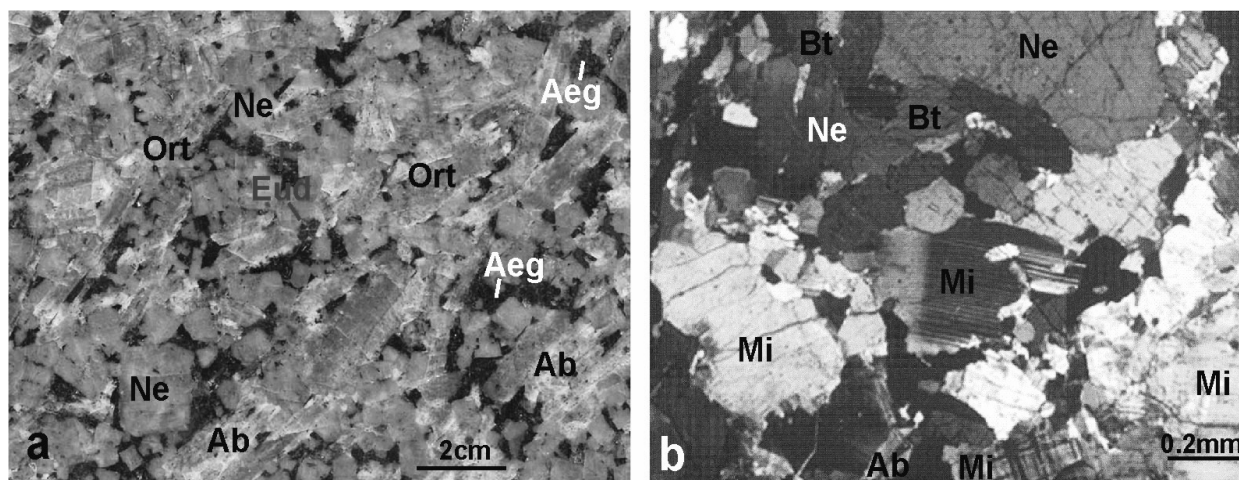


Fig. a. The sample: the composition (in Vol.%): Ne-36,Ort-33,Ab-14,Aeg-13,Eud-5 Rank formula: Ne=OrtAb=AegEud. The rocks identification: Nepheline syenite aegirine-eudialyte (Ne-syenite Aeg-Eud).

Fig. b. The thin section: the composition (in Vol.%): Mi-54, Ne-25, Bt-16, Ab-5 Rank formula: MiNeBtAb. The rock: Nepheline syenite biotite (Ne-syenite Bt).

case, the first three predominant minerals mostly define only the rock group (nepheline syenite): NeOrtAb, AbOrtNe, OrtNeAb etc. In order to determine the classification of alkaline rock varieties, we need to use the longer rank formulas of mineral composition, not less than of four ranks. It is possible to create a simple rock name by adding to the term «nepheline syenite» the name of mineral (or some minerals) occupying the fourth or fifth rank positions. For example, a rock with the rank formula «OrtAbNeBt» can receive the name “nepheline syenite Bt”. Such names can be formed basing on quantitative calculations of their real mineral composition. Obvious, a high precision of these calculations is not required, but only creation of rank formula on the basis of visual estimation of the relative amounts of rock-forming minerals.

It will be possible to work out a rational nomenclature for various rock groups within this family after critical revision of such representative RHAmin collections from different regions. The values of complexity (En) and purity (An) of composition, showing the degree of approach to monominerality, can be used for specification of the description in the form of rank formulas.

The RHA-method allows us to create a uniform, unequivocal classification of mineral compositions not only of nepheline syenite groups, but also all set of rocks. Such a classification is open for addition of new types, which were previously unknown. The opportunity to create an unequivocal rock classification based on mineral composition using the mineral composition rank formulas has been shown earlier on the example of phoscorites and carbonatites [9, 18], rocks which had no standard nomenclature. In addition, success of the application of this

method can be shown on an example of well-studied rocks such as granites (77 analyses), diorites (59) and gabbros (33 analyses). These results are accessible on separate pages of file RHA-Min comp_alkaline rocks.rar.

Table 3a-e

The reduced rank formulas of mineral composition (R-min) for different representatives of nepheline-syenite family (N – quantity of analyses corresponding of given analysis)

a. foyaite			b. khibinite			c. mariupolite			d. miaskite			e. lujavrite		
Rmin		N	Rmin		N	Rmin		N	Rmin		N	Rmin		N
Ne	Ab Ort	1	Ne	Ort Ab	3	Ne	Ort Ab	1	Ab	Ne Ort	1	Ab	Ne Ort	1
Ne	Ort Ab	3	Ne	Ort Di	1	Ne	Ort Di	1	Ab	Ort Crn	1	Ab	Ort Aeg	1
Ne	Ort Di	2				An	Ort Ne	1	Ab	Ort Ne	14	Ort	Ab Ol	1
						Ab	Ol Ne	1						
Ab	Ne Ort	1	Ab	Ne Ort	1	Ab	Ne Ort	7	Ort	Ab Ne	5	Ort	Ab Ne	1
Ab	Ort Ne	9	Ab	Ort Ne	1	Ab	Ort Ne	5						
Ort	Ne Ab	12	Ort	Ne Ab	18									
Ort	Ne Di	1												
Ort	Ab Crn	1	Ort	Ab Ne	4									
Ort	Ab Ne	15												
Ort	Ab Di	2												
total		47	total		28	total		16	total		21	total		6

A fragment of such an RHA classification of mineral composition for some typical rock groups is shown in table 4. Increasing details of the description (rank formula length) will allow the peculiarities of a rock's mineral composition to be taken into consideration, significant for some cases. The unambiguity of our alphabetic ordering of RHA-descriptions of compositions allows us to store numerous data sets and to reveal groupings of similar rocks by their composition, to estimate the completeness of data for various groups, and to reveal different types of error. The existence of sufficiently representative arrays of rock types stipulates the opportunity of their identification by real modal composition.

CONCLUSIONS

The authors do not suggest replacing the standard generally accepted names of rocks. However they suggest that the RHA language is only a way of coding of analytical information, based on which its unequivocal, hierarchical, periodic ordering can be made. Such standardisation of representation of chemical and mineral compositions of a rock based on the RHA method will promote the ordering and systematisation of most geological data. Simplicity and clearness of rules for using the RHA method allows the construction of a uniform systematisation of various rock compositions in different geological institutes independently. It will be necessary to coordinate only two questions – general

Table 4.

The RHA classification of normative mineral composition (Vol. %) for some rock types.

Rank formula Min					En	An	Description	An%
Ne	Ort	Ab	Di	Ilm	0.722	0.113	16-2025-t1_khibinite	0
Ne=	Ort	Ab	Di	Ilm	0.708	0.146	32-2025-t1_syenite Ne	7
Ne	Ort	Ab	Di	Mag	0.642	0.149	30-19-t41_syenite Ne	0
Ne=	Ort	Ab	Di	Mag	0.728	0.130	148-2025-t1_syenite	0
Ne=	Ort	Di	Ab	Wo	0.845	0.058	4-676-p310_Ne syenite	2
Ne=	Ort	Di	Ab	Wo	0.832	0.062	10-1061-t30_foyaite	0
An	Ol=	Ilm	Ap	Mag	0.816	0.048	23-2052-t16_peridotite	100
An	Ol	Ilm	Mag	Ne	0.785	0.079	22-2052-t16_gabbro Ol	100
An	Ol	Ilm=	Mag	Kls	0.696	0.097	19-2052-t11_gabbro	100
An=	Ol	Ilm=	Mag	Kls	0.849	0.061	10-2052-t11_peridotite	100
An	Ol	Mag	Ilm	Ne	0.757	0.090	9-2052-t11_peridotite	100
Qtz	Ab	Ort	Crn	Hyp	0.725	0.116	1002-1024_Bt granite	17
Qtz	Ab	Ort	Crn	Hyp	0.698	0.146	1008-1024_granite	5
Qtz=	Ab	Ort	Crn	Hyp	0.690	0.172	1074-1024_Bt granite	11
Qtz	Ab	Ort	Hyp	Crn	0.706	0.153	1070-1024_granite	13
Qtz=	Ab=	Ort	Hyp	Crn	0.694	0.169	1054-1024_Bt granite	8
Qtz	Ab	Ort	Hyp	Crn	0.690	0.140	1057-1024_aplite	21
Qtz=	Ab	Ort	Hyp	Crn	0.688	0.171	1024-1024_granite	9
Ab	Ne	Ort	Aeg	Ol	0.821	0.061	9-19-t41_lujavrite	0
Ab	Ne	Ort	Aeg	Ol	0.785	0.080	5-1061-t32_mariupolite	0
Ab	Ne	Ort	Aeg	Ol	0.920	0.023	3-19-t41_kakortokite	0
Ab	Ne=	Ort	Aeg	Ol	0.702	0.139	15-2009-t41_mariupolite	0
Ab=	Qtz	Ort	Hyp	Crn	0.687	0.171	1078-1024_granite	9
Ab=	Qtz	Ort	Hyp	Crn	0.665	0.205	1035-1024_Bt granite	15
Ab	Qtz	Ort	Hyp	Crn	0.660	0.200	1069-1024_granite	11
Ab	Qtz	Ort	Hyp	Di	0.697	0.163	1029-1024_aplite	2
Ab=	Qtz	Ort	Hyp	Di	0.680	0.177	1037-1024_granite	11
Ab	Qtz=	Ort	Hyp	Di	0.660	0.204	1044-1024_granite	3
Ab	Qtz	Ort	Hyp	Mag	0.671	0.187	1075-1024_granite	7
Ab=	Qtz	Ort	Hyp	Mag	0.664	0.217	1046-1024_granite	11
Ab	Qtz=	Ort	Hyp	Mag	0.659	0.224	1010-1024_granite	7
Ab	Qtz=	Ort	Hyp	Mag	0.670	0.199	1040-1024_granite	2
Ab	Qtz=	Ort	Hyp	Mag	0.660	0.226	1052-1024_Bt granite	8
Ab	Qtz	Ort	Hyp	Mag	0.652	0.208	1014-1024_granite	5
Ab=	Qtz	Ort	Hyp	Mag	0.675	0.209	1051-1024_granophyre	10
Ab	Qtz	Ort	Hyp	Mag	0.672	0.201	1063-1024_granite	7
Ab	Qtz=	Ort	Hyp	Mag	0.649	0.244	1023-1024_granite	5
Ab	Ort	Ne	Ol	Crn	0.615	0.173	5-2008-t8_miaskite	7
Ab	Ort	Ne	Ol	Crn	0.582	0.157	7-2008-t8_miaskite	9
Ab	Ort	Ne	Ol	Crn	0.657	0.143	20-2009-t41_mariupolite	3
Ab	Ort=	Ne	Ol	Crn	0.537	0.153	22-2009-t41_mariupolite	7
Ab	Ort	Ne	Ol	Di	0.693	0.115	3-1061-t31_foyaite-peg	16
Ab	Ort	Ne	Ol	Di	0.571	0.186	5-2009-t41_syenite Ne	4
Ab	Ort	Ne	Ol	Hem	0.671	0.169	1-2008-t8_miaskite	20
Ab	Ort	Ne	Ol	Hem	0.582	0.170	5-2008-t28_syenite	18
Ab	Ort	Ne	Ol	Mag	0.715	0.126	29-19-t41_syenite	10
Ab	Ort	Ne	Ol	Mag	0.707	0.135	6-1061-t18_foyaite	12

Table 4. Continued

Rank formula Min					En	An	Description	An%
Ab	Ort	Ne	Di	Ol	0.719	0.122	1-19-t13_syenite Ne	29
Ab	Ort	Ne	Di	Ol	0.704	0.132	3-2008-t28_miaskite Bt	30
Ab	Ort	Ne	Di	Ol	0.704	0.125	1-19-t35_tinguaite	8
Ab	Ort	Ne	Di	Ol	0.621	0.144	3-19-t28_nephelinite Lct	8
Ab=	Ort	Ne	Di	Aeg	0.833	0.056	40-19-t41_hedrumite	0
Ab	Ort	Ne	Di	Aeg	0.716	0.121	6-19-t29_phonolite	0
Ab	Ort	Di	Ne	Ol	0.800	0.068	1-2009-t41_syenite Bt	24
Ab	Ort	Di	Ne	Ol	0.691	0.108	8-19-t12_ordanchite	15
Ab	Ort	Di	Ne	Ol	0.645	0.124	21-19-t41_syenite Ne	13
Ands	Hyp	Qtz=	Di	Ort	0.637	0.106	4-2052-t5_diorite Qtz	45
Ands	Hyp	Di	Ort	Qtz	0.769	0.069	3-1144-t2_gabbronorite	46
Ands	Hyp	Di	Ort	Qtz	0.740	0.078	1-1144-t2_gabbronorite	41
Ands	Hyp	Ort=	Qtz	Di	0.814	0.061	2-1144-t2_monzogabbro	51
Ort	Ne=	Ab	Aeg	Ol	0.770	0.094	42-2025-t1_khibinite	0
Ort	Ne=	Ab	Aeg	Ol	0.756	0.089	7-1061-t28_foyaite	0
Ort	Ne	Ab	Aeg	Di	0.767	0.079	2-19-t36_foyaite	0
Ort=	Ne	Ab	Aeg	Di	0.728	0.108	39-2025-t1_khibinite	0
Ort=	Ne	Ab	Aeg	Di	0.821	0.063	38-19-t41_foyaite	0
Ort	Ne=	Ab	Aeg	Di	0.770	0.098	166-2025-t1_foyaite	0
Ort=	Ne	Ab	Aeg	Di	0.731	0.118	17-2025-t1_khibinite	0
Ort=	Ne	Ab	Di	Aeg	0.757	0.101	3-19-t5_syenite Ne	0
Ort=	Ne	Ab	Di	Aeg	0.736	0.107	5-19-t5_Khibina av.	0
Ort	Ab	Ne	Ol	Crn	0.659	0.105	4-19-t40_syenite Ne	14
Ort	Ab	Ne	Ol	Crn	0.577	0.174	2-19-t40_syenite Ne	0
Ort	Ab=	Ne	Ol	Crn	0.657	0.206	1-2009-t26_Mi-Ne peg.	5
Ort=	Ab	Ne	Ol	Crn	0.625	0.176	1-19-t9_miaskite	16
Ort	Ab=	Ne	Ol	Di	0.689	0.164	11-2009-t26_Mi-Ne peg.	10
Ort	Ab	Ne	Aeg	Ol	0.838	0.055	2-1061-t28_foyaite	0
Ort=	Ab	Ne	Aeg	Ol	0.741	0.118	168-2025-t1_foyaite	0
Ort	Ab=	Ne	Aeg	Di	0.734	0.118	45-2025-t1_khibinite	0
Ort	Ab=	Ne	Aeg	Di	0.734	0.118	46-2025-t1_khibinite	0
Ort	Ab=	Ne	Aeg	Di	0.774	0.095	167-2025-t1_foyaite	0
Ort	Ab=	Ne	Aeg	Di	0.739	0.123	158-2025-t1_foyaite	0
Ort=	Ab	Ne	Di	Ol	0.770	0.096	2-19-t8_syenite Ne	6
Ort	Ab=	Ne	Di	Ol	0.756	0.078	8-2009-t41_foyaite Bt	18
Lbr	Hyp	Qtz=	Di	Ort	0.741	0.073	4621-1024_diorite	50
Lbr	Hyp	Qtz	Di	Ort	0.631	0.104	4649-1024_diorite Qtz	63
Lbr	Hyp	Qtz	Ort	Di	0.752	0.074	4602-1024_diorite	58
Lbr	Hyp	Qtz	Ort	Di	0.537	0.140	4622-1024_diorite Qtz	47
Lbr	Hyp	Ort	Qtz	Di	0.784	0.067	4623-1024_diorite Qtz	56
Lbr	Hyp	Ort=	Qtz	Di	0.663	0.101	4612-1024_diorite	45
Lbr	Hyp	Ort	Qtz	Di	0.631	0.113	4618-1024_diorite	46
Lbr	Ort	Hyp	Qtz	Di	0.764	0.074	4605-1024_granodiorite	50
Lbr	Ort=	Hyp	Qtz	Di	0.651	0.102	4639-1024_diorite	49
Lbr	Ort	Hyp=	Di	Qtz	0.805	0.061	4617-1024_diorite Hbl	48
Lbr	Ort=	Hyp	Di	Qtz	0.715	0.083	4651-1024_diorite	50
Lbr	Ort=	Hyp	Di	Mag	0.655	0.127	4624-1024_diorite Qtz	33

Note: Both En – measure of composition complexity and An – measure of purity were calculated for 4 first components. Description: No of analysis, No of reference see table 2, in addition: 676 – [10], 1002 – [13], 1024 – [22], 1144 – [19], 2008 – [12], 2052 – [1]; (No of table/page); rock name.

abbreviations of mineral names and specification of boundaries between mineral species in isomorphic series.

Using this RHA language, the definition of rocks finally has a chance to become unequivocal. It is possible to determine the strict specification of limits between mineral varieties of rocks on the presence of changes in their rank formulas (e.g. on rearrangements of mineral symbols). Thus, as pointed by D'Alessandro et al. [4], we can envisage the creation of a reliable universal language for communication among all geologists.

REFERENCES

1. **Bogachev, A.I., Zack S.I., Safonova, G.I. & Inina, K.A.** 1963. Geology and petrology of gabbroid rocks of Elet'ozerskyi massif, Karelia. Moscow-Leningrad. AN SSSR. (In Russian).
2. **Bogatikov, O.A., Petrov, O.V. & Sharpenok, L.N. (Eds.)** 2008. Petrographic code of Russia. Magmatic, metamorphic, metasomatic, impact rock-assemblages. Second edition. VSEGEI Press. Saint-Petersburg. (In Russian).
3. **Borodin, L.S.** 1974. (Ed.) The main provinces and formations of alkaline rocks. Nauka Press, Moscow. (In Russian).
4. **D'Alessandro, M., Potenza, R., Hubaux, A. & Hugli, T.** 1977. Cogeodata Inquiry on Rock Names and Descriptions. N. Jb. Miner. Abh. 129. 43-65.
5. **Donskoy, A.N.** 1982. Nepheline complex of Oktyabrsky massif. Kiev. Naukova Dumka Press. (In Russian).
6. **Galakhov, A.V.** 1975. Petrology of Khibina alkaline massif. Leningrad. Nauka Press. (In Russian).
7. **Kononova, V.A. (Ed.)**. 1984. Magmatic rocks. Alkaline rocks. Nauka Press. Moscow. (In Russian).
8. **Krasnova, N.I., Korolev, N.M. & Petrov, T.G.** 2009. Ambiguity of nepheline syenite family rock names and how to cope with this problem. In: Geochemistry of magmatic rocks. XXVI Int. Conf. School "Geochemistry of alkaline rocks". Abstr. Vol. 11-15 May. 78-80.
9. **Krasnova, N.I., Petrov, T.G., Balaganskaya, E.G., Garcia, D., Moutte, J., Zaitsev, A.N. & Wall, F.** 2004. Introduction to phoscorites: occurrence, composition, nomenclature and petrogenesis. In: Phoscorites and carbonatites from the mantle to mine: the key example of Kola alkaline province. Wall, F. & Zaitsev A.A. (Eds.). Publ. Min. Soc. of GB et Irl., London. 45-74.
10. **Le Bas, M.J.** 1977. Carbonatite-nephelinite volcanism. London, John Wiley.
11. **Le Maitre, R.W., Bateman, P., Dudek, A., Keller, J., Lameyre, U., Le Bas, M.J., Sabine, P.A., Schmid, R., Sørensen, H., Streckeisen, A., Woolley, A.R. & Zanettin, B. (Eds.)** 1989. A classification of igneous rocks and glossary of terms. Recommendations of the International Union of Geological Sciences Subcommittee on the Systematics of Igneous rocks. Int. Geol. Sci. Oxford, London.
12. **Levin, V.Ya., Ronenson, B.M. & Samsonov, V.S. et al.,** 1997. Alkaline-carbonatite complexes of Ural. Ekaterinburg. (In Russian).
13. **Moutte, J., Garcia, D. & Gallice, F.** Unpublished data of different rocks from Kola alkaline-ultrabasic with carbonatite complexes (Ecole de Mines de Saint Etienne, XRF and ICP-AES methods). Original data are available on Web site: <http://www.emse.fr/~moutte>

14. **Petrov, T.G.** 1971. The justification of variant of general classification for geochemical systems. Vestnik of Leningrad State University. 18. 30-38. (In Russian).
15. **Petrov, T.G.** 2008. RHA-method as a problem solution of systemizing analytical data on material composition of geological targets. Otechestvennaya Geologiya. 4. 98-105. (In Russian).
16. **Petrov, T.G. & Farafonova, O.I.** 2005. Information-component analysis. RHA method. Textbook. Saint-Petersburg. (In Russian).
17. **Petrov, T.G. & Krasnova, N.I.** 2010. R-dictionary-catalogue of chemical mineral composition. Saint-Petersburg. (In Russian).
18. **Petrov, T.G. & Krasnova, N.I.** 2006. Principle of creation of mineral rock classification using the RHA-method (on an example of phoscorites and carbonatites). In: Geochemistry, petrology, mineralogy and genesis of alkaline rocks. Abstr. of Allrussian Conf. 18-23 Sept. Miass. 191-196. (In Russian).
19. **Ryborack, M.V.** 2002. Composition of rockforming minerals of differentiated gabbro-norite – quartzmonzonite series of Olkhovkiy ring pluton (Central Russia, Voronezh crystalline massif). In: Geology and environment: investigations of young scientists. Apatity. 72-83. (In Russian).
20. **Semenov, Ye.I.** 1967. Mineralogical-geochemical types of nepheline-syenite derivatives. In: Mineralogy of pegmatites and hydrothermolites of alkaline massifs. Moscow. Nauka Press. 52-71. (In Russian).
21. **Vernadsky, V.I.** 1954. The selected works. V. I. Academy Nauk SSSR Press. Moscow. (In Russian).
22. **Vistelius, A.V.** 1995. (Ed.) The scientific date that led to the opening of the mineral wealth of Siberia and Mongolia. Theophrastus Publ. S.A. Athens.